Les terres rares et les isotopes radiogéniques comme traceurs d'échange et de transfert dans les cycles géochimiques externes

Marc Steinmann

Habilitation à diriger des recherches

Les terres rares et les isotopes radiogéniques comme traceurs d'échange et de transfert dans les cycles géochimiques externes

présentée par

Marc STEINMANN

Mémoire présenté le 3 décembre 2008 devant un jury composé de :

M. Pierre-Marie BADOT (président du jury)
Professeur, UMR 6249 Chrono-environnement, Besançon

M. François CHABAUX (rapporteur)
Professeur, UMR 7517 Centre de Géochimie de la Surface-EOST, Strasbourg

M. Gérard GRUAU (rapporteur)
Directeur de Recherche au CNRS, UMR 6118 Géosciences, Rennes

M. Didier MARQUER
Professeur, UMR 6249 Chrono-environnement, Besançon

M. Thomas NÄGLER (rapporteur)
Professeur, Institut für Geologie der Universität Bern, Suisse

M. Peter STILLE
Directeur de Recherche au CNRS, UMR 7517 Centre de Géochimie de la Surface-EOST, Strasbourg

Sommaire

Avant-Propos

Ce mémoire de HDR est organisé en 3 parties :

- **"A Cadre général"** regroupe le curriculum vitae ainsi qu'un résumé de l'ensemble de mes activités et responsabilités, menées parallèlement à la recherche (enseignement, tâches administratives, etc.) et qui sont aussi le quotidien d'un enseignant-chercheur.
- **"B Synthèse scientifique"** constitue la partie principale de ce mémoire. Elle présente un résumé et une synthèse de mes activités de recherche depuis la thèse.
- **"C Sélection de publications"** fournit les originaux des principales publications, à la base de la partie B.

La rédaction du présent mémoire me donne l'opportunité de faire un bilan de mon cursus professionnel et de penser à tous ceux, qui l'ont influencé ou marqué. Tout a commencé à la rentrée 1984 avec le début de mes études en géologie à l'ETH de Zürich, j'y suis resté jusqu'à ma soutenance de thèse en avril 1994. Ma période "zurichoise" a été positivement influencée par mes 4 co-directeurs de thèse : Wilfried Winkler (ETH Zürich), Daniel Bernoulli (ETH Zürich), Stefan Schmid (université de Bâle) et Peter Stille (CGS-CNRS Strasbourg). Ma thèse a balayé une thématique très vaste, allant de la cartographie régionale jusqu'à la reconstitution paléogéographie de la Téthys alpine, en intégrant une analyse tectonique, sédimentaire et géochimique des terrains. Wilfried Winkler m'a guidé dans ce vaste assemblage avec beaucoup de calme et une perception imperturbable de l'essentiel. Daniel Bernoulli m'a appris la rigueur scientifique, à coup de séances d' "advocatus diaboli" et de slogan "always keep observation and interpretation apart". Stefan Schmid m'a montré, que tout problème scientifique doit être affronté avec une intensité et une rigueur impitoyable. Peter Stille m'a fait découvrir, avec beaucoup de fascination, l'univers de la géochimie et de la géochimie isotopique. Il a ainsi induit une réorientation complète de mon cursus. Cette découverte m'a incité à quitter la géologie sédimentaire pour devenir géochimiste. Merci Peter, je n'ai jamais regretté ce changement cap.

Mes années post-doctorales au Centre de Géochimie de la Surface (CGS) de Strasbourg, de mai 1994 à juillet 1998, ont été marquées par une étroite collaboration avec Peter Stille. Celle-ci continue encore aujourd'hui et se reflète dans ma liste de publication. Avec Peter Stille, j'ai appris à toujours garder une curiosité scientifique, au delà de ma propre spécialité de recherche et à oser aborder sans complexes de nouvelles thématiques. L'intégration de la biosphère à mes projets de recherche en est le fruit. Mes années au CGS de Strasbourg, m'ont aussi formé sur le volet analytique de la géochimie. Merci aux « rois du laboratoire », Urs Schaltegger (maintenant université de Genève) et les ingénieurs Daniel

Tisserand et Bernard Kiefel pour leur patience et pertinence en salle blanche et au spectromètre de masse.

Au delà de l'aspect scientifique, mes années strasbourgeoises ont été pour moi des années de découverte et d'ouverture à un pays, une culture et une langue. Le cercle des doctorants et post-doctorants du CGS était particulièrement chaleureux et sympathique, j'en garde d'excellents souvenirs. Je ne dresserai pas de liste de noms, elle serait trop longue. Juste un petit mot pour la femme que j'y ai rencontré et qui ma suivi pour le meilleur et pour le pire (comme devoir rendre se mémoire plus digeste).

Mon arrivée à Besançon en 1998 s'est faite dans une équipe en pleine restructuration, avec de nombreux collègues récemment nommés. J'ai beaucoup apprécié l'esprit "pionnier" de cette jeune équipe et la volonté de construire quelque chose de nouveau sur les remblais du passé. Grand merci à Catherine Bertrand, pour son aide à l'intégration du petit immigré. En 10 ans j'ai vu grandir l'EA2642 Géosciences et les différents axes de recherche se dessiner dans un climat d'échange et de collaboration, constructif et amical. Je suis content d'avoir pu participer à cette construction, qui a abouti cette année à la fusion en UMR Chrono-environnement. Je trouve cette évolution positive et je suis optimiste pour l'avenir.

La rédaction d'une habilitation à diriger des recherches est très peu compatible avec l'emploi de temps d'un maître de conférences. Avancer signifiait donc jongler ! Merci mes filles d'avoir essayé de comprendre que papa avait les pieds, les mains et la tête dans son HDR.. Merci aussi à mes parents d'avoir toujours soutenu dans mes projets professionnels.

Je remercie Gérard Gruau, Thomas Nägler, François Chabaux, Peter Stille, Didier Marquer et Pierre-Marie Badot d'avoir accepté de juger ce travail. J'attends que les discussions scientifiques, lors de la soutenance, soient riches et source d'inspiration pour de futurs projets.

Morteau, fin octobre 2008

Résumé

Ce mémoire présente une vue d'ensemble de mes travaux de recherche, réalisés depuis 1995 en tant que post-doctorant au Centre de Géochimie de la Surface de Strasbourg et depuis 1998 en tant que Maître de Conférences à l'université de Franche-Comté de Besançon. Dans toutes ces études, je me suis intéressé aux échanges et transferts chimiques dans les cycles géochimiques externes, avec comme principaux outils de traçage les terres rares (TR) et les isotopes radiogéniques du Sr et du Nd.

J'ai suivi une formation classique de géologue-sédimentologue, que j'ai complété au cours de ma thèse, par les outils de traçage de la géochimie élémentaire et isotopique. Le début de mes années post-doctorales marque une rupture avec mes thématiques de recherche antérieures : j'ai abandonné les problématiques de reconstitutions paléogéographiques et paléotectoniques, pour me consacrer entièrement aux processus de transferts et d'échanges chimiques dans les couches géologiques superficielles, en contexte naturel ou anthropisé.

Cette réorientation a commencé par l'étude d'un sol contaminé de la région de Bâle (Suisse), suivi par un projet sur les transferts chimiques dans des gisements de sel, dans le cadre d'études de faisabilité sur le stockage de déchets radioactifs dans des dômes de sel en Allemagne. Elle s'est poursuivie par des études de circulations d'eau de mer dans le récif corallien de Tahiti et en contexte hydrothermal de basse température, sur la plaque des Cocos. Après cette incursion dans le milieu marin, je suis revenu, ces dernières années, en milieu continental avec des projets portant sur le transport des TR dans des ruisseaux du Massif Central et sur le transfert des TR à l'interface géosphère-biosphère sur des sites du Jura, des Vosges et du Kaiserstuhl (volcan inactif près de Freiburg, Allemagne). L'ensemble de ces travaux de recherche a été le fruit de nombreuses collaborations.

Malgré la diversité des objets, nous avons souvent rencontré des mécanismes de transferts et d'échanges chimiques très similaires. L'identification de ces mécanismes était basée sur une utilisation combinée des TR, des isotopes et d'autres outils, tels que les éléments majeurs ou les données minéralogiques. Nous avons ainsi constaté que la mobilité des TR et d'autres métaux traces est le plus souvent liée à la présence et à la stabilité de phases accessoires, telles que l'apatite et des oxyhydroxides Fe-Mn. En ce qui concerne le transport en phase liquide, nos résultats suggèrent une influence importante de la fraction colloïdale et de la végétation. Celles-ci se combinent à d'autres paramètres de contrôle plus "classiques" (pH, Eh, complexes solubles, sorption etc.). C'est la raison pour laquelle, nous souhaitons à l'avenir intégrer d'avantage l'étude du rôle de la phase colloïdale et de la végétation à nos projets de recherche.

Les TR représentent aujourd'hui un outil de traçage particulièrement pertinent dont l'analyse s'est simplifiée. Leur dosage peut, dans la plupart des cas, être intégré à une analyse de routine par ICP-MS, sans générer ni sur-coûts ni complément de travail. Il serait aujourd'hui dommage de ne pas intégrer ces dosages de TR aux analyses chimiques par ICP-MS. Toutefois, les spectres des TR doivent parfois être combinés avec des données isotopiques du Sr et du Nd afin d'écarter toute ambiguïté dans leur interprétation.

Abstract

This habilitation thesis is entitled **"tracing of exchange and transfer processes in surface geochemistry by rare earth elements (REE) and radiogenic isotopes"**. It presents a summary of my research realized since 1995 as post-doctoral fellow at the "Centre de Géochimie de la Surface" in Strasbourg and since 1998 as lecturer ("Maître de conférences") at the university of Franche-Comté in Besançon. The common topic of all these studies are chemical exchange and transfer processes in surface environments, using as principal tracers the rare earth elements (REE) and the radiogenic isotopes of Sr and Nd.

I have followed a classical formation in geology and sedimentology, that I completed during my PhD thesis with the tools of elementary and isotope geochemistry. The beginning of my post-doctoral years marks a break with my previous research: I abandoned the problems of palegographic and paleotectonic reconstructions and switched completely to surface geochemistry.

This reorientation started with a study of a heavy-metal contaminated soil near Basel (Switzerland), followed by a project on the migration of REE in salt deposits in Germany, within the framework of feasibility studies on the storage of radioactive waste in salt diapirs. I continued my research with projects on interstitial fluid circulation in the barrier reef of Tahiti and on low temperature hydrothermal processes on the Cocos plate. After this incursion to the marine environment, I returned to the continents with projects on REE transport in streams of the Massif Central and REE exchange processes between soils and vegetation. This latter study is actually running on field sites in the Jura and Vosges mountains, and on the inactive volcano of Kaiserstuhl (in the Rhine plain near Freiburg, Germany). All these projects were realized in numerous collaborations.

In spite of the variety of study objects and environments, we regularly found that the chemical exchange and transfer processes were controlled by similar mechanisms. The identification of these mechanisms was based on a combined approach using REE, radiogenic isotopes and complementary tools, such as major elements or mineralogy. In many cases, the mobility of the REE and other trace metals was directly related to the presence and the stability of accessory minerals, such as apatite or Fe-Mn oxyhydroxides. For water samples, we found an important role of colloidal particles and vegetation, in addition to more "classic" parameters such as pH, Eh, solution complexation, or sorption. Therefore, our future research will be focused more precisely on the importance of colloids and vegetation for REE transport and fractionation in surface environments.

The REE are today a powerful geochemical tracer, that can be determined in most samples by ICP-MS without specific preparation procedures and additional costs. Therefore, we think that the REE should systematically be included in routine chemical analyses by ICP-MS. However, in some cases, the REE data should be combined with isotope data in order to eliminate ambiguities in the interpretation of the REE patterns.

A Cadre général

1 Curriculum vitae

Marc STEINMANN
Maître de conférences
rattaché à la 36e section du CNU
UMR 6249 Chrono-environnement
Université de Franche-Comté
16, route de Gray
25030 Besançon Cedex*

Nationalité française et suisse
44 ans, marié, 3 enfants

Géologue-Géochimiste, Docteur ès Sciences

Expérience et formation

depuis 1998	**Maître de conférences** à l'université de Franche-Comté, Besançon.
1994-1998	**Post-doctorant** dans la section de géochimie isotopique du Centre de Géochimie de la Surface (CGS-CNRS), Strasbourg, en collaboration avec P. Stille (DR CNRS).
1989-1994	**Doctorant et moniteur** à l'école polytechnique fédérale de Zürich (ETH Zürich, Suisse), thèse soutenue en avril 1994, mention "très bien" (No. 10668)
	Titre: "Les schistes lustrés nord-penniques des Alpes centrales des Grisons (Suisse): Tectonique, stratigraphie et évolution du bassin". Direction de thèse : W. Winkler (ETH), D. Bernoulli (ETH), S. Schmid (université de Bâle), P. Stille (CNRS Strasbourg).
1989	**Diplôme de géologie** (dipl. Natw. ETH), mention "très bien"
	Titre : "Les faciès lombard de Ballino (Italie du Nord): sédimentation et resédimentation au pied d'une faille synsédimentaire". Direction de diplôme : D. Bernoulli (ETH), H. Thierstein (ETH).
1984-1989	Étudiant **en géologie** à l'ETH de Zürich.
1983-1984	Service militaire en Suisse, depuis 1992 Premier Lieutenant (600 jours de service).
1971-1983	École primaire et lycée en Suisse, baccalauréat en 1983.

Centres d'intérêt en recherche

Cycles biogéochimiques naturels et anthropisés des terres rares (TR) et d'autres éléments traces en milieu continental et marin. Traçage des processus d'échanges et de transferts chimiques par les TR et les isotopes radiogéniques (Sr, Nd, Pb). Plus précisément la spéciation des éléments traces et des terres rares dans la phase solide et liquide et les mécanismes, menant à la mise en solution et la fixation des éléments traces et au fractionnement des TR.

* Tél. 03 81 66 65 46 - FAX 03 81 66 65 58 - E-mail: marc.steinmann@univ-fcomte.fr

Compétences

- ✗ **Géochimie:** Comportement des éléments traces, en particulier des terres rares, dans les roches sédimentaires, les sols et les eaux (de surface et souterraines); adsorption par les oxydes et les argiles.
- ✗ **Géochimie isotopique:** Rb-Sr, Sm-Nd, Pb-Pb
  Création, organisation, fonctionnement et suivi scientifique de la salle blanche.
- ✗ **Géologie générale:** Cartographie (15 mois de terrain durant la thèse), sédimentologie, tectonique, géodynamique.
- ✗ **Méthodes:** Spectrométrie de masse, ICP-E, ICP-MS, coulométrie (mesure des teneurs en carbonates et carbone organique total) - chromatographie ionique et extraction liquide-liquide pour la séparation et l'enrichissement d'éléments traces.

Langues

Allemand : langue maternelle
Français et **Anglais** : courant (lu, écrit, parlé)
Italien (bonnes notions), **Espagnol** (notions de base)

2 Publications et communications

Articles catégorie A :

[A1/1] **Steinmann, M.** & Stille, P. 1997: Rare earth element behavior and Pb, Sr, Nd isotope systematics in a heavy metal contaminated soil. Applied Geochem. 12, 607-624.

[A1/2] **Steinmann, M.** & Stille, P., 1998. Strongly fractionated REE patterns in salts and their implications for REE migration in chloride-rich brines at elevated temperatures and pressures. C.R. Acad. Sci. Paris, série II a, 327: 173-180.

[A1/3] **Steinmann, M.**, Stille, P., Bernotat, W. & Knipping, B., 1999. The corrosion of basaltic dykes in evaporites: Ar-Sr-Nd isotope and REE evidence. Chem. Geol., 153, 259-279.

[A1/4] **Steinmann, M.** & Stille, P, 1999. Geochemical evidence for the nature of the crust beneath the eastern North Penninic basin of the Mesozoic Tethys ocean. Geol. Rundsch. 87, 633-643.

[A1/5] **Steinmann, M.**, Stille, P., Mengel, K. & Kiefel, B, 2001. Trace element and isotopic evidence for REE migration and fractionation in salts next to a basalt dyke. Applied Geochem. 16, 351-361.

[A1/6] **Steinmann, M.** & Déjardin, P, 2004. Temporal evolution of fluid flow through the Tahiti barrier reef traced by Sr isotopes and pore water chemistry. Chem. Geol. 203, 51-73.

[A1/7] **Steinmann, M.**& Stille, P., 2004. Basaltic dykes in evaporites: a natural analogue. In: Gieré, R. and Stille P. (eds): Energy, waste, and the environment: a Geochemical Perspective. Geol. Soc. London Spec. Publ. 236, 135-141.

[A1/8] **Steinmann, M.** & Stille, P., 2008. Controls on transport and fractionation of the Rare Earth Elements in stream water of a mixed basaltic-granitic catchment basin (Massif Central, France). Chem. Geol. 254, 1-18.

[A2/1] Stille, P., **Steinmann, M.** & Riggs, S.R. 1996: Nd isotope evidence for the evolution of the paleocurrents in the Atlantic and Tethys Oceans during the past 180 Ma. Earth Planet. Sci. Lett. 144, 9-20.

[A2/2] Stille, P., **Steinmann, M**., Pierret, M.C., Gauthier-Lafaye, F., Chabaux, F., Viville, D., Pourcelot, L., Matera, V., Aouad, G. and Aubert, D., 2006. The impact of vegetation on REE fractionation in stream waters of a small forested catchment (the Strengbach case). Geochim. Cosmochim. Acta, 70(13): 3217-3230.

[A2/3] Bodeï, S., **Steinmann, M**., Buatier, M. Nd-Sr isotope and REY geochemistry of metalliferous sediments in a low-temperature off-axis hydrothermal environment (Costa Rica margin). en préparation.

[A3/1] Tricca, A., Stille, P. & **Steinmann, M.**, Kiefel, B., Samuel, J. & Eikenberg, J. 1999: Rare earth elements and Sr and Nd isotopic compositions of dissolved and suspended loads from small river systems in the Vosges mountains (France), the river Rhine, and groundwater. Chem. Geol. 160, 139-158.

[A3/2] Bodeï, S., Buatier, M., **Steinmann, M.**, Adatte, T. & Wheat, C., 2008. Characterization of metalliferous sediment from a low-temperature hydrothermal environment on the Eastern Flank of the East Pacific Rise. Marine Geology 250, 128-141.

[A6/1] Denimal, S., Bertrand, C., Mudry, J., Paquette, Y., Hochart, M. & **Steinmann, M**., 2005. Evolution of the aqueous geochemistry of mine pit lakes - Blanzy-Montceau-les-Mines coal basin (Massif Central, France): origin of sulfate contents; effects of stratification on water quality. Applied Geochem., 20(5): 825-839.

Articles catégorie B :

[B1/1] **Steinmann, M.** 1994: Ein Beckenmodell für das Nordpenninikum der Ostschweiz (Modèle de bassin sédimentaire du faciès nord-pennique de la Suisse orientale). Jb. Geol. B.-A. 137/4, 675-721.

[B1/2] **Steinmann, M.** & Stille P., 2006. Rare earth element transport and fractionation in small streams of a mixed basaltic-

granitic catchment basin (Massif Central, France). J. Geochem. Exploration, 88(1-3), 336-340 (extended abstract)

[B2/1] Jacobs. E., **Steinmann M.**, Stille P. & Pika-Biolzi, M. 1996: Sr isotope stratigraphy and variations in the Nd isotopic composition of foraminifera from the Lemme-Carrosio section (northern Italy). Giornale di Geologia, 58, 111-117.

[B2/2] Buatier M., **Steinmann M.**, Bertrand, C., 2001. Fluid-sediment interaction and clay authigenesis along the flank of the Juan de Fuca Ridge. In: Cidu, R. (Eds.), Tenth international symposium on water-rock interaction, Villasimius, Italy, pp. 615-618.

[B2/3] Rahn, M., **Steinmann, M.** & Frey, M. 2002. Chloritoid composition and formation in the eastern Central Alps: a comparison between Penninic and Helvetic occurrences. Schweiz. Mineral. Petrogr. Mitt. 82, 409-426.

[B2/4] Stille, P., **Steinmann, M.**, Pierret, M.C., Gauthier-Lafaye, F., Aubert, D., Probst, A., Viville, D. & Chabaux, F., 2006. The impact of vegetation on fractionation of rare earth elements (REE) during water-rock interaction. J. Geochem. Exploration, 88(1-3), 341-344 (extended abstract).

[B3/1] Rahn, M., Potel, S. & **Steinmann, M.** 2003. Chloritoid in the Penninic Tomül nappe: HP or LP formation? A reply to a comment by R. Oberhänsli, R. Bousquet and B. Goffé. Schweiz. mineral. petrogr. Mitt., 83(3), 345-348.

Résumés de congrès :

Steinmann, M., Stille, P. & Winkler, W. 1991: Neodymium isotopes applied to the stratigraphy of a metamorphic series. Terra abstracts, EUG VI meeting, Strasbourg, France, March 1991.

Steinmann, M., Stille, P. & Winkler, W. 1992: Neodymium isotopes as a stratigraphic working tool in "Bündnerschiefer" series. Terra abstracts, ALCAPA meeting, Graz, Austria, July 1992.

Steinmann, M. 1993: Formation and disappearance of a basin: the case of the "Bündnerschiefer" series in the Alps of eastern Switzerland. Terra abstracts, EUG VII meeting, Strasbourg, France, April 1993.

Steinmann, M. & Stille, P. 1994: Isotopengeochemische Untersuchungen an Schwermetall-belasteten Böden. In: Umweltgeowissenschaften - eine Kursbestimmung. Kurzfassungen der Posterbeiträge zur Tagung vom 7. und 8. Oktober 1994 (Ed. by G. Müller & J. Matschullat). Heidelberger Geowiss. Abh. 78, Heidelberg, 15.

Steinmann, M. & Stille, P. 1995: Isotopic evidence for origin, mobility and exchange behaviour of heavy metals in contaminated soils. Terra abstracts, EUG 8 meeting, Strasbourg, France, April 1995.

Steinmann, M. & Stille, P. 1995: Trace metal behaviour in a contaminated soil studied with isotopic methods and REE distribution patterns. Third international conference on the biogeochemistry of trace elements, Paris, 15-19 May 1995.

Steinmann, M. & Stille, P. 1996: Speciation of Rare Earth Elements in a heavy metal contaminated soil using geochemical and isotopic methods. 6th V.M. Goldschmidt Conference, Heidelberg 31 March-4 April 1996.

Steinmann, M., Bernotat, W., Stille, P. & Knipping, B. 1997: Exchange and corrosion behaviour of basaltic dykes in evaporites: a natural analogue for the long-term stability of HLW glass products in a salt repository. Terra abstracts, EUG 9 meeting, Strasbourg, France, 23-27 March 1997.

Steinmann, M., Stille, P., Mengel, K., Siemann, M. & Bernotat, W. 1997: Nd-Sr Isotope and REE Evidence for the Long-Term Stability of HLW Glass Products and Trace Metal Migration in a Salt Repository: Corroding Basaltic Dykes in Evaporites as Natural Analogues. 21st International Symposium on the Scientific Basis for Nuclear Waste Management, Davos, Switzerland, September 28th - October 3rd 1997.

Steinmann, M., Stille, P. & Mengel, K. 1998: Trace element and Nd-Sr isotope evidence for REE migration and fractionation in chloride-rich brines at elevated T and P. 8th V.M. Goldschmidt Conference, Toulouse (France), 30 August-3 September 1998, Min. Magazine, Vol. 62A, 1453.

Steinmann, M., Stille, P. & Mengel, K. 1999: REE Mobility During the Corrosion of Basaltic Dykes in Salt Formations: A Natural Analogue for Radionuclide Behaviour in a Salt Repository. Terra abstracts, EUG 10 meeting, Strasbourg, France, 28 March - 1 April 1999.

Steinmann, M. & Déjardin P. 2000: Fluid flow through the Tahiti barrier reef traced by Sr isotopes and pore water chemistry. 10th V.M. Goldschmidt Conference, September 3rd–8th, 2000 Oxford, UK. Journal of Conference Abstracts Vol. 5(2), 956.

Steinmann, M. & Stille, P. 2004: REE patterns in small streams from a mixed basaltic-granitic catchment area (Massif Central, France), V.M. Goldschmidt Conference, June 5-11, 2004 Copenhagen, Geochim. Cosmochim. Acta 69/10, Suppl. 1, 429.

Steinmann, M. & Stille, P. 2004: Transport and fractionation of the rare earth elements in small streams of the massif central, France. Réunion des Sciences de la Terre, Strasbourg – France, September 20-25, RSTGV-A-00187.

Steinmann, M. & Stille, P. 2005: Rare earth element transport and fractionation in small streams of a mixed basaltic-granitic catchment basin (Massif Central, France). 7th International Symposium on the geochemistry of the Earth's surface (GES-7). Aix-en-Provence, France, August 23-27, 2005.

Steinmann, M., Stille, P. & Pierret, M-C. 2007: Biogeochemical Cycling of Rare Earth Elements in Surface Soils . V.M. Goldschmidt Conference, August 20-24, 2007 Cologne, A972.

Bodeï, S., **Steinmann, M**., Buatier, M. & Wheat, C.G. 2004: Fluid-sediment interaction in a low temperature off-axis hydrothermal environment (Cocos plate, Costa Rica margin); V.M. Goldschmidt Conference, June 5-11, 2004 Copenhagen, Geochim. Cosmochim. Acta 69/10, Suppl. 1, 351.

Bodeï, S., Buatier, M., **Steinmann, M.**, Walter, A.-V. & Manceau, A.. 2004: Origine et mode de formation des dépôts métallifères marins au large de la Péninsule de Nicoya (Costa Rica). Réunion des Sciences de la Terre, Strasbourg – France, September 20-25, RSTGV-A-00169.

Bodeï, S., **Steinmann, M**. & Buatier, M. 2006: Nd-Sr isotopic and REY geochemistry of metalliferous sediments in a low-temperature off-axis hydrothermal environment. 16th annual Goldschmidt Conference, Melbourne, Australia.

Brioschi, L. **Steinmann, M.**, Lucot, E., Badot, P.M. & Stille, P. 2008: Absorption and fractionation of REE by spruce and beech: a comparative study on specimens grown on brown acidic soils and calcareous soils. Réunion des Sciences de la Terre, Nancy – France, April 21-24.

Buatier, M., Bodeï, S., Manceau, A., **Steinmann, M**., Karpoff, A.M., Guillaume, D., Wheat, GC. 2005: Fluid sediment interaction and formation of Mn oxi-hydroxide related to a ridge flank hydrothermal system. AGU FALL Meeting. San Francisco, USA

Déjardin, P., **Steinmann, M.**, Destrigneville, C., Fritz, B. & Rougerie, F. 1997: Internal circulation pattern in the Tahiti insular reef geosystem traced by interstitial fluid geochemistry. Terra abstracts, EUG 9 meeting, Strasbourg, France, 23-27 March 1997.

Ferreux J.-M., **Steinmann, M**., Bertrand, C., Dubois, C. 2000: Mobilisation of arsenic in mine tailings subjected to spontaneous

combustion. 10th V.M. Goldschmidt Conference, September 3rd–8th, 2000 Oxford, UK. Journal of Conference Abstracts Vol. 5(2), 398.

Jacobs, E., **Steinmann, M.**, Gauthier-Lafaye, F. & Stille, P. 1997: Paleoclimate and paleoceanic evolution of the Mediterranean sea during the Neogene: Sr-Nd and stable isotope evidence. Terra abstracts, EUG 9 meeting, Strasbourg, France, 23-27 March 1997.

Rodot, S., Denimal, S. & **Steinmann, M.** 2006: Dispersion et dynamique des métaux traces d'origine anthropique dans le lac de Saint Point (Doubs). Réunion des Sciences de la Terre, Dijon – France.

Stille, P. & **Steinmann, M**. 1995: Nd-Sr isotope stratigraphy in phosphorites and evidence for changes of paleo-currents in the Atlantic and the Tethys during the past 100 Ma. The First SEPM congress on Sedimentary Geology, August 13-16, St. Petersburg Beach, Florida.

Stille, P. & **Steinmann, M.** 1997: Nd-Sr isotopic compositions of phosphates as tracers for oceanic paleocurrents. Terra abstracts, EUG 9 meeting, Strasbourg, France, 23-27 March 1997.

Stille, P., Gauthier-Lafaye F., Schaltegger U., **Steinmann, M.** & Bros, R. 1996: Processes leading to Sr, Nd and Pb isotopic homogenization in sediments. AAPG annual convention 1996, San Diego, June 1996.

Stille, P., M. **Steinmann, M.**, Pierret, M.-C., Gauthier-Lafaye, F., Aubert, D. & Probst, A. 2005: The impact of vegetation on fractionation of REE during water-rock interaction. 7th International Symposium on the geochemistry of the Earth's surface (GES-7). Aix-en-Provence, France, August 23-27, 2005.

Tricca, A., **Steinmann, M.,** Stille, P. & Eikenberg, J. 1997: Origin and exchange of REE between suspended and dissolved load in freshwater: Sr-Nd isotope evidence. Terra abstracts, EUG 9 meeting, Strasbourg, France, 23-27 March 1997.

Tricca, A., Stille, P. & **Steinmann, M.** 1998: Rare earth elements and Sr and Nd isotopic compositions of dissolved and suspended loads from small river systems in the Vosges mountains (France), the river Rhine and the groundwater. 8th V.M. Goldschmidt Conference, Toulouse (France), 30 August-3 September 1998.

3 Reviews pour des revues de catégorie A

- ✗ Septembre 1999 : Manuscrit AG 99-704 pour **Applied Geochemistry**
- ✗ Février 2000 : Manuscrit AG 00-775 pour **Applied Geochemistry**
- ✗ Avril 2000 : Manuscrit GCA W0233 pour **Geochimica et Cosmochimica Acta**
- ✗ Juin 2000 : 1 Manuscrit pour **Eclogae geologicae Helvetiae**
- ✗ Février 2003 : Manuscrit AG 03-1241 pour **Applied Geochemistry**
- ✗ Octobre 2003 : Manuscript MS-03-09 pour **Clay Minerals**
- ✗ Février 2004 : Manuscrit GCA W2506 pour **Geochimica et Cosmochimica Acta**
- ✗ Janvier 2006 : Manuscrit AG 05-1893 pour **Applied Geochemistry**
- ✗ Mai 2007 : Manuscrit NAWI_07_0035 pour **Naturwissenschaften**

4 Encadrements d'étudiants et de doctorants

4.1 Post-Doc au Centre de Géochimie de la Surface de Strasbourg

- ✗ **1995-1996** : Participation à l'encadrement de la **thèse** de P. Déjardin, 1996 (ULP Strasbourg) sur la caractérisation des fluides interstitiels d'un récif corallien par les isotopes du Sr.
  Directeurs de thèse : B. Fritz (CGS-CNRS, Strasbourg), F. Rougerie (ORSTOM Tahiti).
- ✗ **1995-1997** : Participation à l'encadrement de la **thèse** de A. Tricca (ULP Strasbourg) sur le comportement chimique des terres rares dans les eaux.
  Directeurs de thèse : P. Stille (CGS-CNRS, Strasbourg), J. Eikenberg (Institut Paul Scherrer, Suisse).
- ✗ **1995 et 1997** : Encadrement de stages de 2ème année d'ingénieurs chimistes de l'École des Hautes Etudes des Industries Chimiques de Strasbourg (EHICS, aujourd'hui « Ecole Européenne de Chimie, Polymères et Matériaux » ECPM).

4.2 Maître de Conférences à l'université de Franche-Comté

- **1999** : Co-encadrant du **DEA** de M. Hochart (DEA PAE3S de Nancy) : « Hydrogéologie d'un site minier en cours de réaménagement : caractérisation des différents réservoirs et leurs échanges »
  Encadrement : C. Bertrand, Y. Guglielmi, **M. Steinmann**, J. Mudry, Y. Paquette.
- **2000** : Co-encadrant **DEA** de J.-M. Ferreux (DEA Physique – Chimie UFC) : « Relargage de l'arsenic par lixiviation de terrains houiller après combustion »
  Encadrement : C. Bertrand, **M. Steinmann**, C. Dubois, Y. Paquette.
- **2003/2004** : Co-encadrant du **DEA** de S. Bodeï (DEA Environnement, santé, société UFC) : « Transfert de matière et interactions eau-sédiments en environnement océanique ».
  Encadrement : M. Buatier, **M. Steinmann**, A.-V. Walter
- **2004-2007** : Co-encadrant de la **thèse** de S. Bodeï (ED Homme - Environnement - Santé UFC) :
  « Genèse et évolution des sédiments métallifères en contexte hydrothermal hors axe (exemple des dépôts de la marge du Costa Rica, Pacifique Equatorial) ».
  Encadrement : M. Buatier, **M. Steinmann**
- **2006** : Co-encadrant du **Master 2** de S. Rodot (Master Environnement, santé, société UFC) : « Dispersion et dynamique des métaux traces d'origine anthropique dans le Lac St. Point ».
  Encadrement : S. Denimal, **M. Steinmann**
- **2006** : Co-encadrant du **Master 2** de S. Bontemps (Master Environnement, santé, société UFC) : « Mobilisation et transfert des éléments majeurs, en traces et terres rares au cours de l'altération dans le bassin versant de Malaval (Massif Central) ».
  Encadrement : **M. Steinmann,** A.-V. Walter, P. Stille
- **2007** : Co-encadrant du **Master 2** de L. Brioschi (Master Environnement, santé, société UFC) : « Absorption et fractionnement des terres rares par la végétation, en fonction des conditions de sol ».
  Encadrement : **M. Steinmann**, E. Lucot, P.M. Badot
- **depuis 2007** : Co-encadrant de la **thèse** de L. Brioschi (ED Homme - Environnement - Santé UFC) :
  « Les transferts des terres rares à l'interface géosphère – biosphère ».
  Encadrement : **M. Steinmann**, E. Lucot, P.M. Badot

---

5 Activités et responsabilités d'enseignement

5.1 Période 1998 – 2003 (« Ante LMD »)

Filière	Thématique	CM	TD	TP	horaires
DEUG ST-SV1	Outils Informatiques			15	
DEUG STU1	Cycles externes	12			
MST géol. appl. 1	Stage cartographie Alpes (Barles)		33		
MST géol. appl. 1	Sols contaminés	10			
MST géol. appl. 2	Stage cartographie Pyrénées (Rouffiac)			68	
MST géol. appl. 2	Géodynamique	20	5	50	
DESS géol. appl.	Métaux traces environnement		10		
IUP génie env.	Métaux traces environnement		3	3	
	total annuel (heures étudiant)	**42**	**51**	**136**	**229**
	total ETD annuel	**63**	**51**	**91**	**205**

Responsabilités particulières :

- Responsable de l'unité "outils informatiques" (DEUG ST-SV1), environ 240 étudiants
- Responsable du stage de cartographie dans le Alpes (MST géol. appl. 1), environ 20 étudiants, 9 jours
- Responsable du stage de cartographie dans les Pyrénées (MST géol. appl. 2), environ 20 étudiants, 9 jours

5.2 Période 2004 – 2007 (LMD1)

Filière	Thématique	CM	TD	TP	horaires
Lic. Géosciences 1	Cycles externes	12	6	8	
Lic. Géosciences 2	Sédimentologie marine	3	7	31.5	
Lic. Géosciences 2	Stage cartographie Pyrénées (Rouffiac)			55	
Lic. Géosciences 3	Stage cartographie Jura (Besançon)			44	
Lic. Géosciences 3	Géodynamique	5		18	
Master géol. appl. 1	Métaux traces environnement	4	8		
Master SVT 1	Géochimie		9		
Master SVT 1	Géodynamique	10	8	18	
Agreg ST SVU	Sédimentologie marine		4		
	total annuel (heures étudiant)	**34**	**42**	**175**	**251**
	total ETD annuel	**51**	**42**	**116**	**209**

Responsabilités particulières :

- ✗ Responsable du semestre 4 de la Lic. Geosciences, environ 35 étudiants
- ✗ Responsable du stage de cartographie dans les Pyrénées (Lic. Geosciences 2), environ 35 étudiants, 8 jours

5.3 Depuis 2008 (LMD2)

Filière	Thématique	CM	TD	TP	horaires
Lic. Terre et env. 1	Cycles externes	12	6	8	
Lic. Terre et env. 2	Sédimentologie marine	3	7.3	8	
Lic. Terre et env. 2	Stage cartographie Pyrénées (Rouffiac)			55	
Lic. Terre et env. 3	Stage cartographie Jura (Besançon)			40	
Lic. Terre et env. 3	Géodynamique	5		18	
Master Sci.Environ./Géol.Appl. 1	Métaux traces environnement	4	8		
Master Sci.Env./VTESS-SVT	Géochimie		9		
Master Sci.Env./VTESS-SVT	Géodynamique	10	8	18	
Master VTESS 2	Systèmes écologiques	4	18		
Prépa CAPES	Sédimentologie marine	1.5	1.5		
	total annuel (heures étudiant)	**40**	**58**	**147**	**244**
	total ETD annuel	**59**	**58**	**98**	**215**

Responsabilités particulières :

- ✗ Responsable du semestre 4 de la Lic. Terre et environnement, environ 45 étudiants
- ✗ Responsable du stage de cartographie dans les Pyrénées (Lic. Terre et environnement 2), environ 45 étudiants, 8 jours

6 Responsabilités administratives et techniques

L'infrastructure analytique et informatique du laboratoire de Géosciences de l'université de Franche-Comté était très rudimentaire à mon arrivée en 1998. Les compétences acquises pendant mes années de thèse et de post-doctorat me pressentaient pour participer à l'installation d'une salle blanche et à la mise en place d'une infrastructure informatique. Je me suis lancé avec beaucoup d'énergie dans la réalisation de ces 2 projets, dont j'ai rapidement hérité de la responsabilité, mais aussi la quasi-totalité de la charge de travail.

Rétrospectivement, j'avais en 1998 très largement sous-estimé l'investissement en temps, qui ne se comptait pas en jours ou semaines, mais en mois et années. Cet investissement a sûrement contribué à moderniser l'infrastructure commune du laboratoire, mais il a considérablement ralenti mes activités de recherche.

6.1 Installation et gestion d'une salle blanche

La disponibilité d'une salle blanche est indispensable à mes projets de recherche en géochimie. Le projet avait été initié par mon collègue P. Henry dès 1997, mais la réalisation a été retardé jusqu'en 2001 - 2002, essentiellement pour des problèmes de locaux.

Je me suis occupé de la réalisation de la salle blanche à partir de 2001. Avec les travaux de transformation du local, l'achat et l'installation du matériel de laboratoire, ainsi que la mise au point de protocoles analytiques. L'amélioration de l'équipement et la mise au point de nouveaux protocoles représentent encore aujourd'hui une charge de travail considérable.

La disponibilité de cet équipement a permis à l'ensemble du laboratoire d'intégrer à ses problématiques de recherche des approches analytiques nécessitant des préparations d'échantillons en salle blanche. Notamment pour les analyses d'éléments traces par ICP-MS et pour les analyses isotopiques (Sr, Nd, Ca).

6.2 Mise en place et gestion de l'infrastructure informatique

L'infrastructure informatique du laboratoire de Géosciences consistait à mon arrivée en 1998 en un parc hétérogène de postes isolés et de quelques imprimantes locales. Seul un nombre limité de postes était raccordé à internet. Dès mon arrivée, j'ai commencé avec la mise en place d'une l'infrastructure cohérente qui consiste aujourd'hui en :

- environ 50 postes de travail dans les bureaux et labos (Windows, Mac, Linux), tous raccordés au

réseau local et à internet.

- 1 salle informatique commune avec 2 PC équipés de scanners (A4, A3, diapos) et d'imprimantes à jet d'encre couleur (A4, A3, A0), entièrement intégrés dans le réseau local.
- 1 salle destinée aux étudiants de Master2 et aux visiteurs avec plusieurs postes.
- 4 imprimantes laser réseau A4 noir et blanc, une imprimante laser réseau couleur A3.
- 1 copieur numérique avec interface informatique accessible par le réseau local.
- 1 serveur de fichier (Linux/Samba), qui gère également les droits d'accès au niveau du réseau local (contrôleur de domaine) et le routage DHCP.

En tant que responsable informatique, je gère le planning et la réalisation des investissements en matériel informatique et de l'achat et de la gestion des licences de logiciels. Il faut ajouter à cela le suivi et la maintenance au quotidien du serveur et du matériel commun, ainsi que le dépannage des postes individuels. Depuis 2003, je partage une partie de ces tâches avec mon collègue Ph. Goncalves. Avec la fusion en UMR Chrono-environnement en 2008, l'infrastructure informatique de l'ancien laboratoire de Géoscienses est passée sous la responsabilité de J.D. Tissot (ingénieur informatique CNRS). Toutefois, nous ne disposons que d'un informaticien pour les 170 personnels statuaires et temporaires de l'UMR. Nous continuons donc, pour le moment, à assurer une bonne partie de nos anciennes tâches.

B Synthèse scientifique

1 Introduction

Ce chapitre a pour objectif de présenter le cadre et la chronologie des projets de recherche réalisés depuis ma thèse, de mettre en évidence les liens existants entre les projets et de mentionner les travaux de DEA/Master et de thèse associés. Avant de résumer chaque projet dans les chapitres B3 à B8, je décris dans le chapitre B2 les principaux outils de traçage, que sont les TR et les isotopes radiogéniques. Une synthèse de l'intégralité des travaux est présentée dans le chapitre B9 et un aperçu des projets de recherche à venir dans le chapitre B10.

1.1 Les années d'études et de thèse à l'ETH de Zürich (1984-1994)

J'ai réalisé l'intégralité de mon cursus universitaire et ma thèse à l'institut de géologie à l'ETH de Zürich (Suisse), dans l'équipe de géologie sédimentaire de Daniel Bernoulli et de Wilfried Winkler. Mes travaux de DEA et de thèse traitaient des problématiques de reconstitutions paléogéographiques et paléotectoniques dans le cadre de la Téthys alpine. J'avais choisi cette thématique, parce que j'étais fasciné par la géodynamique. L'analyse de ces processus par le biais de l'étude de séries sédimentaires me semblait être une approche particulièrement intéressante.

Mon sujet de thèse portait sur l'origine paléogéographique des schistes lustrés du domaine nord-penniques (Bündnerschiefer) de l'Est de la Suisse. Ces "Bünderschiefer" sont des sédiments terrigènes argilo-carbonatés faiblement métamorphisés d'une épaisseur de plusieurs milliers de mètres, sans repères stratigraphiques évidents. Il s'agissait d'établir une organisation stratigraphique et de déterminer l'origine des niveaux basaltiques, intercalés entre les sédiments. Pour répondre à ces questions, nous avions choisi d'utiliser des traceurs chimiques et isotopiques. Dans le cadre de ces analyses, j'ai été accueilli par Peter Stille (un de mes co-directeurs de thèse), pour plusieurs mois au Centre de Géochimie de la surface de Strabourg (CGS), afin de me familiariser avec les outils de la géochimie et de la géochimique isotopique. La finesse et l'efficacité de ces outils, tout comme l'aspect objectif et quantitatif qu'ils représentent, m'ont rapidement convaincu.

Les reconstitutions paléogéographiques et paléotectoniques représentent une problématique pour

laquelle il y a plus d'inconnues que d'équations. Il en découle qu'au delà d'un certain niveau d'argumentation, les cheminements et interprétations peuvent vite devenir plus sensitifs qu'objectifs. J'étais conscient de ces limites et j'avais aussi besoin de travailler sur des thématiques plus appliquées, plus au service des problèmes des sociétés modernes. J'imaginais, au delà de la fascination pour les traceurs géochimiques, leur potentiel de traçage des phénomènes de surface et des problèmes environnementaux. J'ai donc opté pour un changement complet dans mes orientations de recherche.

1.2 Les projets de post-doctorat réalisés au Centre de Géochimie de la Surface (1994-1998)

Des études, réalisées à la fin des années 1970, ont montré que certains outils de traçage de la géochimie élémentaire et isotopique pouvaient être pertinents dans les problématiques environnementales. Ce potentiel novateur, associé à l'importance croissante des problèmes environnementaux, nous ont motivé à monter un projet d'étude de suivi d'une contamination. Mon premier projet post-doctoral concernait le comportement des TR et des traceurs isotopiques dans un sol contaminé. Ce projet s'est déroulé de 1994 à 1995 au CGS de Strasbourg en collaboration avec P. Stille, il a été financé par une bourse du fond national suisse. Ce travail est décrit dans le chapitre B3.

A la suite de ce premier projet, nous étions en contact avec B. Knipping de l'université de Clausthal-Zellerfeld et W. Bernotat du Centre de recherche de Karlsruhe (Allemagne), ils étaient à la recherche de partenaires pour une étude de la mobilité des TR dans les gisements de sel. Ce projet s'inscrivait dans une approche d'analogie naturelle pour le stockage de déchets radioactifs dans des dômes de sel en Allemagne (voir chap. B4.1.1). Il s'agissait plus particulièrement d'étudier la migration des TR au niveau de contacts entre le sel et des intrusions basaltiques. Ce cadre nous semblait bien adapté pour compléter notre approche du comportement des TR et des isotopes radiogéniques, dans des problématiques environnementales. Le projet est décrit dans le chapitre B4. Il a été réalisé au CGS de Strasbourg de 1995 à 1998 (date de ma nomination à Besançon), avec des financements du Centre de recherche de Karlsruhe et du fond national suisse.

Pendant mon séjour post-doctoral à Strasbourg, j'ai également continué à exploiter les données de ma thèse (Steinmann et Stille, 1999; Rahn *et al.*, 2002) et collaborer à des projets sur l'évolution de la composition isotopique du Nd dans l'eau de mer (Stille *et al.*, 1996; Jacobs *et al.*, 1996). En tant que post-doctorant j'ai aussi participé à l'encadrement scientifique d'étudiants et de doctorants, avec notamment les travaux de thèse de A. Tricca sur les TR dans les ruisseaux vosgiens (Tricca, 1997; Tricca *et al.*, 1999) et de P. Déjardin sur la circulation des fluides dans le récif barrière de Tahiti (Déjardin, 1996). P. Déjardin ayant quitté la recherche après sa thèse sans avoir publié ses résultats, j'ai repris et publié ultérieurement une partie de ces données (chap. B5; Steinmann et Déjardin, 2004).

1.3 Les projets de recherche réalisés à l'université de Franche-Comté (depuis 1998)

J'ai été nommé Maître de Conférences, à l'université de Franche-Comté, en 1998. En absence de moyens analytiques (notamment d'une salle blanche ; voir chap. A6.1), j'ai été obligé d'interrompre mes projets antérieurs et j'ai choisi, dans un premier temps, de m'associer à des projets en cours. Pendant cette période, j'ai travaillé sur l'impact de l'altération dans le contexte de versants instables (glissements de la Clapière, 06) et sur la mobilisation des éléments traces métalliques (ETM) dans des remblais charbonneux de sites miniers en cours de ré-aménagement (site de Blanzy - Montceau-les-Mines, 71). Dans le cadre de ces collaborations j'ai co-encadré 2 stages de DEA (M. Hochart, 1999 ; J.-M. Ferreux, 2000 ; chap. A4). Toutefois, les retombés scientifiques ont été moins riches que prévues et une seule publication de rang A est sortie de sur ces thématiques (Denimal *et al.*, 2005).

La salle blanche a commencé à être opérationnelle fin 2002. A partir de ce moment, j'ai pu relancer des projets autour des TR et des traceurs isotopiques. Dans un premier axe de recherche nous avons étudié en collaboration avec M. Buatier (Besançon) un site d'activité hydrothermale de basse température au niveau de la plaque Cocos, dans l'océan Pacifique au large du Costa Rica. Dans ce projet j'ai co-encadré avec M. Buatier le stage de DEA (Bodeï, 2004), puis la thèse de S. Bodeï (Bodeï, 2007; Bodeï *et al.*, 2008; Bodeï *et al.*, in prep). Les résultats de ces travaux sont présentés dans le chapitre B6.

Le 2ème axe de recherche lancé fin 2002 est un projet sur le comportement des TR dans des ruisseaux du Massif Central. Ce projet fait, en quelque sorte, suite à la thématique de thèse de A. Tricca, suivie pendant mes années post-doctorales. Dans le cadre de ce projet Massif Central, j'ai co-encadré avec A.V. Walter (Besançon) le stage de recherche de Master 2 de S. Bontemps (Bontemps, 2006). Ce travail de Master avait pour objectif de compléter l'étude des TR dans l'eau des ruisseaux, par une d'étude des TR dans les profils d'altération, afin d'établir un lien entre les spectres de TR dans la roche et dans l'eau. Les premiers résultats sur les TR dans l'eau des ruisseaux ont été publiés récemment (Steinmann et Stille, 2008) et sont présentés dans le chapitre B7.

Depuis 2005, les laboratoires de Geosciences, de Biologie environnementale et de Chrono-écologie de Besançon, ont commencé à se rapprocher pour former, depuis janvier 2008, l'actuelle UMR de Chrono-environnement. Ce rapprochement m'a donné l'opportunité d'intégrer le monde vivant à mes thématiques de recherche. J'ai ainsi eu la possibilité de m'investir dans des collaborations avec mes collègues biologistes. Un premier projet a porté sur la mobilité des ETM dans le lac St. Point et un second projet sur le transfert des TR à l'interface géosphère-biosphère. Dans le cadre de la thématique sur le Lac St. Point, j'ai co-encadré avec S. Denimal (Besançon) le stage de recherche de Master 2 de S. Rodot (Rodot, 2006). Un autre stage de recherche de Master 2, sur ce même lieu et avec la même équipe d'encadrement, va démarrer en janvier 2009 (E. Dhivert).

Dans le cadre de la thématique sur les transferts des TR à l'interface géosphère-biosphère, j'ai co-encadré, avec E. Lucot et P.M. Badot, le stage de recherche de Master 2 de L. Brioschi (Brioschi, 2007).

Ce travail de Master 2 a abouti en septembre 2007 à l'attribution d'une bourse de thèse par le Ministère de la recherche pour L. Brioschi. Cette thèse est actuellement en cours et un aperçu des premiers résultats est donné dans le chapitre B8.

2 Les terres rares et les isotopes radiogéniques dans les cycles géochimiques externes

2.1 Les terres rares (TR)

2.1.1 Historique

Les terres rares (TR) sont des éléments traces métalliques (ETM) regroupant les lanthanides, éléments 57 à 71 de la classification périodique, avec l'yttrium et le scandium. Toutefois, les termes "TR" et "lanthanides" sont souvent utilisés comme synonymes dans la littérature scientifique. En géochimie, les TR ont d'abord été utilisées dans l'étude des roches magmatiques. Les premières applications, aux cycles géochimiques externes, portaient essentiellement sur le processus de l'altération (ex. Nesbitt, 1979; Braun *et al.*, 1990). A partir des années 1990 et avec l'arrivée de l'ICP-MS, de plus en plus d'études se sont intéressés à la géochimie des TR dans les fleuves, dans les estuaires et dans l'eau de mer (ex. Sholkovitz, 1995; Bau, 1999; Alibo et Nozaki, 1999). Aujourd'hui, les TR sont devenues un outil très polyvalent dans le traçage des processus chimiques et minéralogiques des enveloppes internes et externes de la Terre.

2.1.2 Fondements chimiques

La spécificité et la cohérence du comportement géochimique des TR est liée à la structure de leur couche électronique. Les TR et plus précisément les lanthanides sont, avec les actinides, les seuls éléments du système périodique pour lesquels les électrons ajoutés à la structure ne se placent pas dans les couches s, p ou d, mais dans la couche f, située en-dessous de la couche des électrons de valence. Dans le milieu naturel, les TR apparaissent essentiellement sous forme trivalente, à l'exception du cérium et de l'europium qui existent aussi sous la forme respectivement tétra et bivalente. Malgré la cohérence du comportement chimique du groupe des TR, le remplissage de la couche électronique 4f provoque une diminution continue du rayon ionique du lanthane au lutétium ; cette "lanthanide contraction" induit des variations systématiques du comportement chimique à l'intérieur du groupe. La couche des électrons de valence garde, pour toutes les TR trivalentes, la configuration du gaz noble xénon ($5s^2\ 5p^6$).

Dans les systèmes magmatiques anhydres, le comportement chimique des TR est essentiellement contrôlé par leur charge et par la diminution de leur rayon ionique. Dans les systèmes contentant une phase aqueuse, la complexation des TR est un facteur additionnel très important. La stabilité des complexes de TR ne dépend plus uniquement de leur charge et de leur rayon ionique, mais aussi du degré

de remplissage de la couche 4f (Bau, 1996). De ce fait on observe des constantes de complexation avec des ligands inorganiques et organiques, qui varient de façon régulière au sein du groupe des TR (Cantrell et Byrne, 1987; Lee et Byrne, 1992; Millero, 1992; Byrne et Kim, 1993; Bau, 1999; Davranche *et al.*, 2005; Sonke et Salters, 2006; Stern *et al.*, 2007; Davranche *et al.*, 2008).

Outre leur faible réactivité chimique, l'avantage des TR, par rapport à d'autres traceurs non-isotopiques, est que leur distribution, dans les différents compartiments de la Terre, présente peu de variations. Une réaction chimique ou un processus d'échange abouti donc à une modification partielle de la distribution des TR et non à leur transformation complète. Cela permet de caractériser respectivement le type de réaction chimique ou la nature des réservoirs impliqués dans le processus d'échange ou de mélange. Ces faibles variations dans leurs distributions permettent également de limiter l'influence des modifications secondaires sur le traçage.

2.1.3 Les TR dans le cycle exogène continental

Les spectres des TR dans les sols, les sédiments et l'eau de rivière sont couramment utilisés pour étudier les transferts chimiques et particulaires issus de l'érosion continentale vers les océans (ex. Goldstein et Jacobsen, 1988; Allègre *et al.*, 1996; Dupré *et al.*, 1996; Gaillardet *et al.*, 1997; Sholkovitz *et al.*, 1999; Pokrovsky *et al.*, 2006). Ils sont aussi un outil efficace dans l'étude des mécanismes d'altération et d'interaction eaux-roche (ex. Braun *et al.*, 1998; Dupré *et al.*, 1999; Land *et al.*, 1999; Viers *et al.*, 2000). Les travaux menés dans ce domaine ont démontré que les spectres de TR de la fraction particulaire des rivières reflètent la présence de certains minéraux de la roche initiale (e.g. Tricca *et al.*, 1999; Aubert *et al.*, 2001), alors que les spectres de la fraction dissoute sont contrôlés par des processus qui interviennent lors de l'interaction eau-roche et du transport dans l'eau. Les processus, capables de fractionner les spectres des TR, les plus fréquemment cités sont (1) la dissolution préférentielle de certaines phases minérales lors de l'altération, (2) les variations de stabilité des complexes lors du transport dans l'eau et (3) l'adsorption et l'intégration différentielle des TR dans les minéraux néoformés ou dans les phases colloïdales (Dia *et al.*, 2000; Ingri *et al.*, 2000; Nozaki *et al.*, 2000a; Andersson *et al.*, 2001; Aubert *et al.*, 2001; Harlavan et Erel, 2002; Gruau *et al.*, 2004; Andersson *et al.*, 2006; Dahlqvist *et al.*, 2007; Steinmann et Stille, 2008).

Les spectres des TR dissoutes montrent, dans la plupart des rivières et des fleuves, un appauvrissement en TR légères (La – Sm) par rapport à la moyenne des roches du bassin versant (Dupré *et al.*, 1996; Gaillardet *et al.*, 1997; Tricca *et al.*, 1999). Des études menées dans le bassin versant du Strengbach, dans les Vosges, indiquent que ce fractionnement est, au moins en partie, lié à la dissolution préférentielle de l'apatite au cours de l'altération de la roche (Aubert *et al.*, 2001), puis à l'adsorption préférentielle des TR légères sur les particules du sol et en suspension (Stille *et al.*, 2006). Toutefois, l'ensemble de ces processus ne permet pas d'expliquer entièrement l'appauvrissement en TR légères observé dans l'écoulement de surface. C'est la raison pour laquelle Stille *et al.*, (2006) ont suggéré, que l'absorption préférentielle des TR légères par la végétation puisse contribuer à l'appauvrissement en TR

légères de l'eau de surface. Cette étude a également montré que la quantité de TR absorbée, par la végétation à l'échelle du bassin versant et chaque année, est du même ordre de grandeur que celle exportée par l'écoulement superficiel. D'autres études ont mis en évidence qu'une grande partie des TR transportées dans l'écoulement de surface et souterrain en période de crue est liée à la fraction particulaire et colloïdale issue de la dégradation de la végétation dans les sols (Ingri *et al.*, 2000; Andersson *et al.*, 2001; Andersson *et al.*, 2006).

2.1.4 Les TR dans les végétaux

Les végétaux absorbent essentiellement des TR apportées par l'eau du sol ou par des retombées atmosphériques (Aubert *et al.*, 2002b; Aouad *et al.*, 2006). Les teneurs absolues en TR dans les végétaux varient fortement, allant pour le La de 10 ng/g dans des aiguilles d'épicéas (Wyttenbach *et al.*, 1996; Wyttenbach *et al.*, 1998) à 1 mg/g dans certaines fougères (Koyama *et al.*, 1987; Guo *et al.*, 1996; Zhang *et al.*, 2002).

A l'heure actuelle, il existe très peu d'informations dans la littérature sur un éventuel rôle métabolique, de la translocation et d'éventuels effets des TR sur les végétaux. Les résultats disponibles sont en partie contradictoires (ex. Zhang et Shan, 2001; Liang *et al.*, 2005). Ces divergences sont sans doute liées au fait, que des gammes de concentrations en TR très variées ont été utilisées pour ces différentes études. Sur la base des données disponibles dans la littérature, on peut émettre l'hypothèse, que de fortes concentrations en TR seraient inhibitrices, tandis que des faibles teneurs pourraient être favorables à la croissance végétale. Toutefois, les seuils sont très mal définis et à priori variables d'une espèce à l'autre. Certains travaux ont ainsi suggéré que la présence de TR dans l'eau du sol diminue l'impact d'un manque de Ca et de Mn (Maheswaran *et al.*, 2001), que les TR stimulent la croissance de chloroplastes, qu'elles augmentent la croissance racinaire et foliaire (Guo *et al.*, 1996), qu'elles facilitent le transfert du Ca à travers les membranes cellulaires (Zeng *et al.*, 2003) et qu'elles améliorent l'efficience de l'utilisation de l'eau et la résistance stomatique en condition de sécheresse (Maheswaran *et al.*, 2001). Toutefois, d'autres études suggèrent au contraire que la présence de TR bloque les canaux calciques (Ding et Pickard, 1993) à cause de leur rayon ionique voisin de celui du Ca, ce qui ferait des TR plutôt un inhibiteur de croissance.

2.1.5 L'utilisation des TR par l'homme et le transfert de ces TR anthropiques vers l'environnement

La spécificité chimique des TR (chap. B2.1.2) leur confère un intérêt grandissant pour l'industrie de pointe (électronique, optique etc.), comme pour la médecine et l'agriculture. L'utilisation des TR par l'homme est en forte augmentation depuis 1980. La Chine est aujourd'hui le premier et quasi l'unique producteur de TR ; ce pays assure environ 97 % des besoins mondiaux et la production de l'industrie minière est passée de 30 kt de TR extraites en 1980 à 124 kt en 2007 (Fig. 1 ; Haxel *et al.*, 2002; Hedrick, 2008). Les applications industrielles sont multiples (Tableau 1), elles vont de produits "grand public"

(ex. briquets, abrasifs, écrans CRT et LCD, ampoules à basse consommation et LED, revêtements phosphorescents, pots catalytiques…), à d'autres plus sophistiqués (lasers, fibres optiques, aimants, piles La-Ni-H, réfrigération magnétique) ou même futuristes (supra conducteurs, piles à hydrogène ; Haxel *et al.*, 2002). Dans la plupart des cas, une TR unique ou un mélange de plusieurs TR est ajouté en faible quantité à un matériau afin en optimiser ses performances. Les quantités de TR utilisées sont en augmentation exponentielle, par exemple un produit de technologies innovantes tel que la voiture hybride Toyota Prius contient environ 20 kg de TR (Degraaf, 2006).

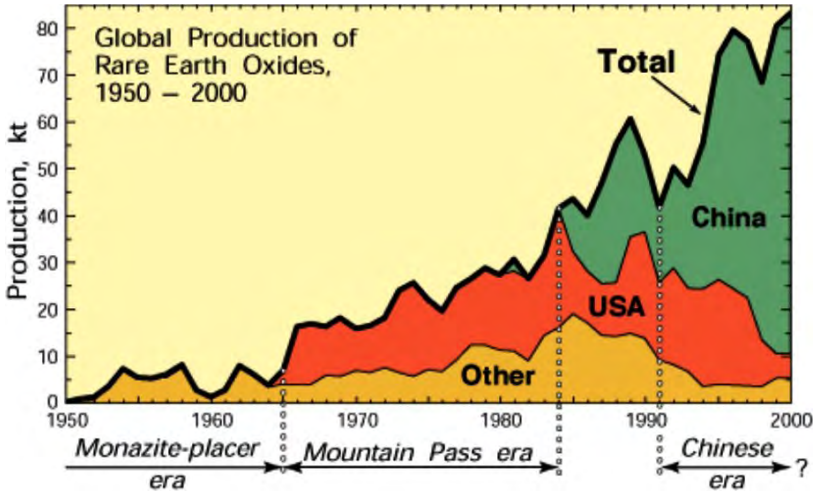

Fig. 1 : Production globale de terres rares par l'industrie minière de 1950 à 2000 en kilotonnes (Haxel et al., 2002). La Chine est depuis 1990 le principal producteur. La production global a atteint 124 kt en 2007 (Hedrick, 2008).

En médecine, des complexes organiques au gadolinium sont employés pour les IRM comme agent de contraste (Bau et Dulski, 1996; Kümmerer et Helmers, 2000) et des comprimés de carbonate de lanthane sont commercialisés pour traiter des insuffisances rénales (Fosrenol ; www.fosrenol.com ; D'Haese *et al.*, 2003; Hutchison *et al.*, 2004; Bernard *et al.*, 2005).

Les travaux scientifiques postulant pour un effet bénéfique des TR sur la croissance des végétaux ont incité l'agriculture chinoise à utiliser des engrais dopés en TR. Ainsi 1030 tonnes de ces engrais ont été épandues sur 1 million d'hectares de terres agricoles en 1993 (Barry et Meehan, 2000) et cette superficie est passée à 4 millions d'hectares en 2004 (Liang *et al.*, 2005). Toutefois, les bases physiologiques sont très mal comprises et les études sur l'efficacité des TR sont contradictoires. La seule étude de terrain visant à évaluer l'efficacité des engrais dopés en TR, par rapport aux engrais traditionnels, n'a montré aucune amélioration (Maheswaran *et al.*, 2001). Toujours en Chine, des additifs de chlorures de TR sont ajoutés à la nourriture d'animaux d'élevage (bovins, porcs, volaille) afin d'optimiser leur croissance (Liu *et al.*, 2007). En Europe, des essais avec de la nourriture d'animaux dopée en TR ont été menés en Allemagne et en Suisse (He *et al.*, 2001; He *et al.*, 2003; Redling, 2006; Feldhaus, 2006 ; www.lanthanoide.de). Un premier produit de ce type est commercialisé en Suisse depuis 2003 et sa certification par l'UE est actuellement en cours (Lancer 500 ; http://www.zehentmayer.ch/fileadmin/ documents/Tier/Vitalstoff-Forum/VF_Lancer.pdf).

Application	2004	2005	2005 % of total	2010	2005-2010 CAGR* %
Neo Magnets	13,650	17,150	18.0%	31,100	12.64%
NiMH batteries	6,200	7,200	7.6%	27,300	30.55%
Catalysts	20,440	21,230	22.3%	25,960	3.78%
Phosphors	3,652	4,007	4.2%	7,512	13.00%
Glass	13,440	13,590	14.3%	13,990	0.57%
Polishing compounds	14,100	15,150	15.9%	23,500	9.2%
Other	15,365	16,935	17.8%	24,950	8.00%
Total	86,847	95,262	100%	154,312	10.10%

Source: BCC Research
**Compound Application Growth Rate*

Tableau 1 : Principales utilisations de TR par l'industrie en 2005 et perspectives pour 2010. Les valeurs absolues sont en kilotonnes. La catégorie "phosphors" correspond principalement aux revêtements phosphorescents des ampoules basse consommation, aux écrans LCD et pour des diodes lumineuses. On attend à court terme les plus fortes croissances pour les batteries NiMH (voitures hybrides), suivi par les revêtements phosphorescents et les aimants dopés aux TR, utilisés pour les moteurs électriques et les générateurs des voitures hybrides (Lunn, 2006).

On connaît à l'heure actuelle plusieurs cas concrets de contaminations de TR d'origine anthropiques dans l'environnement. Des teneurs élevées en gadolinium, probablement d'origine médicale, ont été détectées dans des rivières et lacs et en milieu côtier en Europe (Bau et Dulski, 1996; Elbaz-Poulichet *et al.*, 2002; Möller *et al.*, 2000; 2002; 2003; Hennebrüder *et al.*, 2004; Knappe *et al.*, 2005; Rabiet *et al.*, 2005; Kulaksiz et Bau, 2007), aux États Unis (Verplanck *et al.*, 2003; Bau *et al.*, 2006) et au Japon (Nozaki *et al.*, 2000b). Dans certaines régions de Chine, en raison de la forte utilisation d'engrais dopés en TR, des teneurs anormales ont été détectées chez certains animaux et végétaux (Zhang et Shan, 2001) et des auteurs rapportent que les enfants vivants dans ces régions montrent des performances intellectuelles anormalement basses (Zhu *et al.*, 1997). Des expériences sur l'effet du lanthane chez les souris et les rats montre une inhibition du développement cérébrale (Briner *et al.*, 2000; Feng *et al.*, 2006). La toxicité des TR n'a pas été étudiée de manière extensive, cependant des travaux montrent, que certaines TR exercent des effets toxiques chez de nombreux organismes vivants (Spencer *et al.*, 1997; Wilde *et al.*, 2002). Chez les végétaux, des effets inhibiteurs sur la croissance de différentes espèces ont été rapportés par différents auteurs, mais leurs mécanismes ne sont pas connus (Wheeler et Power, 1995; Diatloff *et al.*, 2008).

Il est fort probable que le nombre de cas de contaminations des milieux naturels par les TR va suivre, dans un proche avenir, la croissance exponentielle de leur production, et on ignore pour l'instant complètement l'impact sanitaire de telles contaminations.

2.2 Les isotopes du Sr et du Nd

Les systèmes isotopiques $^{87}Sr/^{86}Sr$ et $^{143}Nd/^{144}Nd$ sont des systèmes isotopiques dits "radiogéniques", parce que les isotopes ^{87}Sr et ^{143}Nd sont les produits stables issus de la désintégration radioactive respectivement du ^{87}Rb et du ^{147}Sm. Les systèmes isotopiques du Sr et du Nd ont à l'origine servi pour la datation de roches magmatiques, mais ils sont depuis une vingtaine d'années également

beaucoup utilisés comme outils de traçage dans les cycles géologiques externes. Des compilations récentes sur ces applications ont été publiées par Blum et Erel (2003) et Banner (2004).

L'intérêt de l'utilisation des isotopes radiogéniques du Sr et du Nd, comme outil de traçage dans les enveloppes géochimiques externes, tient à leur caractéristique chimique, qui reflètent uniquement des processus d'échange et de transfert. Les rapports $^{87}Sr/^{86}Sr$ et $^{143}Nd/^{144}Nd$ sont complètement indépendants des réactions chimiques ou processus biologiques. Ils sont ainsi des outils très performants pour retracer l'origine des éléments chimiques dans les cycles biogéochimiques. Les rapports isotopiques du Nd ont notamment montré leur performance dans le traçage précis de l'origine des TR dans des profils d'altération et des profils pédologiques (Macfarlane *et al.*, 1994; Steinmann et Stille, 1997) ou en contexte hydrothermal (Mills *et al.*, 2001). Les compositions isotopiques du Sr fournissent des informations complémentaires quant à l'origine des fluides et à l'importance des échanges avec les différents substrats traversés (Albarède et Michard, 1987; Goldstein et Jacobsen, 1987; Blum *et al.*, 1994; Allègre *et al.*, 1996). Le rapport $^{87}Sr/^{86}Sr$ est aussi un outil très performant pour le contrôle et la caractérisation des phases lessivées au cours de l'extraction séquentielle des échantillons (chap. B3.2 ; Steinmann et Stille, 1997).

3 Le comportement des terres rares et des isotopes du Sr, du Nd et du Pb dans un sol contaminé

Publication associée :

- **Steinmann, M.** & Stille, P. 1997: Rare earth element behavior and Pb, Sr, Nd isotope systematics in a heavy metal contaminated soil. Applied Geochem. 12, 607-624.

3.1 Problématique

Ce travail de Steinmann et Stille (1997) avait pour objectif d'évaluer le potentiel de traçage des TR et des isotopes du Sr, du Nd et du Pb dans un sol contaminé en éléments traces métalliques (ETM) à proximité d'une fonderie. Le site se trouve en Suisse au sud de Bâle, dans une plaine alluvial au pied des montagnes du Jura (Swissmetall Dornach). Il s'agit d'un fluvisol calcique d'une épaisseur d'environ 50 cm (Fig. 2). Le site avait été échantillonné dans le cadre d'une thèse au laboratoire d'écologie terrestre à l'ETH de Zürich (Federer et Sticher, 1991; Federer, 1993) et les échantillons ont été mis à notre disposition. Le site de Dornach est devenu, entre temps, un des sites de référence pour l'étude et le suivi de sols contaminés dans le cadre du programme européen CEEM soil (Comparative evaluation of European methods for sampling and sample preparation of soils; Wagner *et al.*, 2001; Desaules *et al.*, 2001).

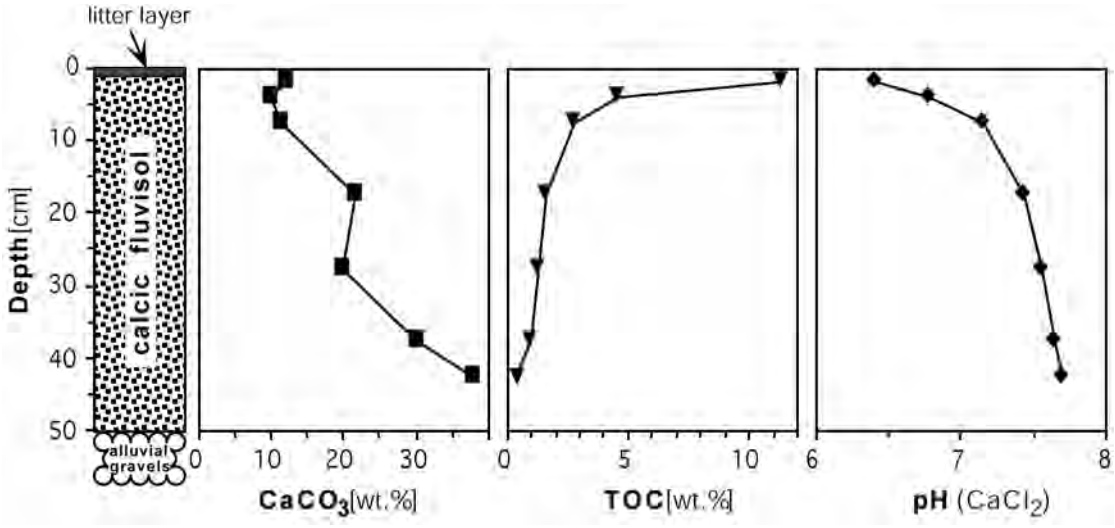

Fig. 2 : Profil de sol du site Swissmetall à Dornach (Figure 1 de Steinmann et Stille, 1997).

3.2 Principaux résultats

Le travail analytique concernait à la fois des échantillons de roche totale et des fractions séparées par extraction séquentielle ; de manière à distinguer les différentes phases porteuses de la contamination. Ce type d'approche est couramment utilisé dans l'étude de sols contaminés (Tessier *et al.*, 1979; Ure *et al.*, 1993; Quevauviller *et al.*, 1994). Toutefois, pour notre étude, ces méthodes ont été adaptées afin de réduire le blanc analytique et de mobiliser à chaque étape suffisamment de matière pour les analyses isotopiques. Une autre difficulté était de travailler avec des extractants, qui ne modifient pas les spectres des TR. Après plusieurs essais nous avons retenu un protocole à 3 étapes d'extractions : une première à l'acide acétique 1 M (HAc 1M), suivi d'une seconde à l'acide chlorhydrique 1M (HCl 1M), et une dernière à l'acide nitrique 1M (HNO_3 1M). La comparaison de nos résultats avec ceux obtenus par les méthodes "classiques" (à 5 étapes d'après Tessier *et al.*, 1979 utilisée par Federer pour les mêmes échantillons), ne montre pas de différences fondamentales et permet de valider notre méthode.

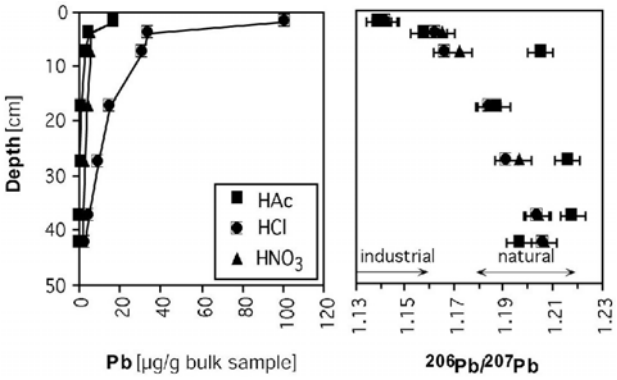

Fig. 3 : Composition isotopique du Pb dans un profil de sol contaminé. Le Pb anthropique reste fixé dans les premiers 10 cm du sol riche en matière organique. Les groupes "HAc", "HCl" et "HNO3" correspondent aux différentes fractions extraites lors de l'extraction séquentielle par acide acétique, acide chlorhydrique et acide nitrique (Figure 5 de Steinmann et Stille, 1997).

Les isotopes du Pb ont permis de distinguer facilement le Pb anthropique du Pb naturel. Les données montrent notamment, que l'essentiel du Pb anthropique reste immobilisé dans la matière organique des 10 premiers centimètres du sol (Fig. 3). Une analyse de corrélations dans les différentes fractions de l'extraction séquentielle met en évidence un comportement similaire pour le Cu et le Zn (Fig. 4).

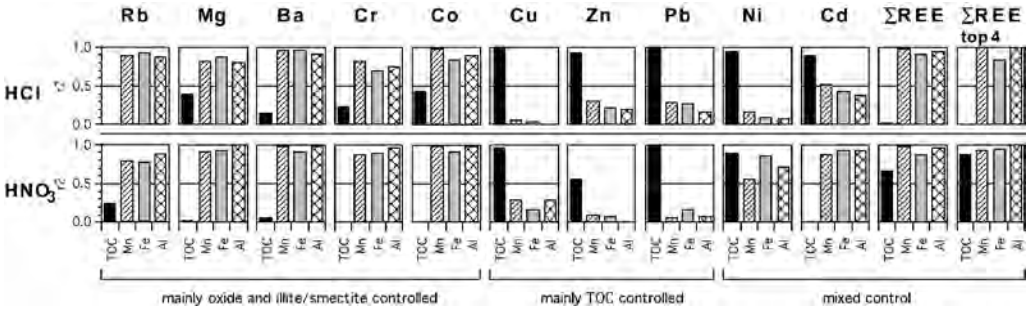

Fig. 4 : Facteurs de corrélation r2 entre les teneurs de divers ETM et les teneurs en matière organique (TOC), Fe, Mn et Al. Le Fe, le Mn et l'Al proviennent essentiellement d'hydroxides de Fe (goethite). Un bon facteur de corrélation avec la matière organique indique que l'ETM en question est essentiellement fixé dans la phase organique, tandis qu'une bonne corrélation avec Fe, Mn et Al suggère une spéciation dans la goethite (Figure 4 de Steinmann et Stille, 1997).

La composition isotopique du Sr, contrairement à celle du Pb, caractérise principalement les phases minérales extraites lors de la procédure d'extraction. Les résultats montrent que la fraction extraite par HAc est essentiellement composée de Sr issu de la fraction carbonatée du sol (Fig. 5). Les fractions extraites par HCl et HNO_3 ont des valeurs $^{87}Sr/^{86}Sr$ plus élevées que les fractions HAc, indiquant que ces étapes ont également attaqué des phases silicatées naturelles du sol (micas, argiles).

Fig. 5 : Composition isotopique du Sr du même profil de sol que dans la Fig. 3. Les valeurs 87Sr/86Sr d'environ 0.7077-0.7078 sont typiques pour la phase carbonatée naturelle du sol. Des rapports légèrement plus élevés indiquent surtout un lessivage de minéraux silicatés (Figure 6 de Steinmann et Stille, 1997).

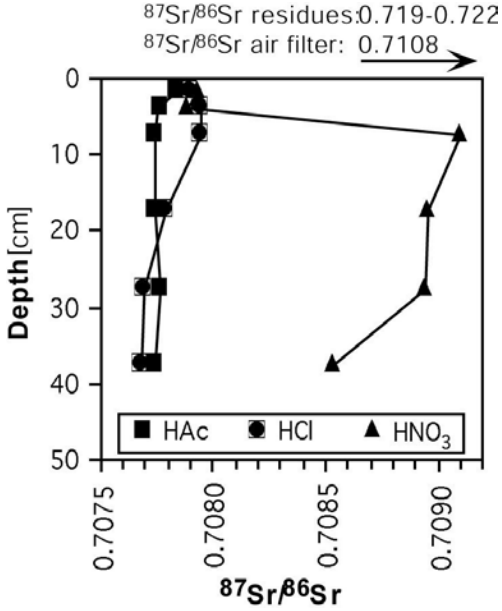

Fig. 6 : Corrélation entre les TR et le pH du sol pour les fractions HAc - entre les TR et le Mn pour les fractions HCl et HNO3 (Figure 8 de Steinmann et Stille, 1997).

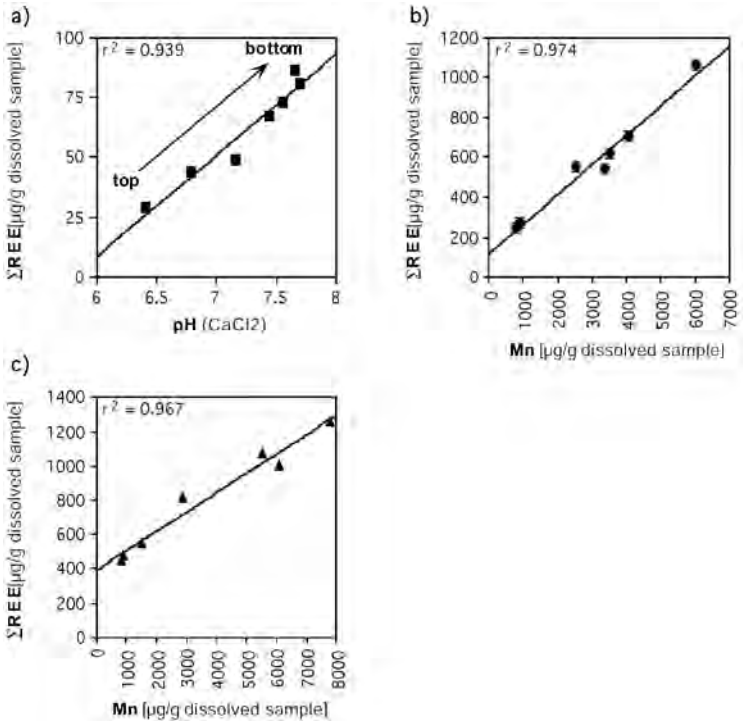

L'étude des TR et des isotopes du Nd représente la partie la plus importante de l'étude. L'analyse des corrélations indique que les TR des fractions extraites à l'acide chlorhydrique et à l'acide nitrique

sont associées principalement à des oxyhydroxydes Fe-Mn (Fig. 4). Une partie des TR de la fraction HNO_3 semble également être fixée dans la matière organique. La seule corrélation que l'on observe pour les TR de la fraction HAc est avec le pH du sol (Fig. 6). Ces deux paramètres augmentent avec la profondeur. Le rapport $^{143}Nd/^{144}Nd$ de la fraction HAc évolue d'un pôle naturel en surface vers un pôle anthropique en profondeur (Fig. 7). Dans le diagramme de mélange $^{143}Nd/^{144}Nd$ vs. 1/Nd, les TR de ces mêmes échantillons définissent une droite de mélange entre un pôle naturel en surface et un pôle anthropique en profondeur (Fig. 8). La fraction HAc est également caractérisée par une anomalie négative en Ce, qui s'accentue avec la profondeur (Fig. 9). Pour les fractions HCl et HNO_3 on n'observe pas d'évolution régulière du rapport isotopique du Nd avec la profondeur. On constate que les niveaux avec les teneurs maximales en Nd (5-10 cm pour la fraction HCl et 25-30 cm pour la fraction HNO_3) correspondent à des niveaux, où les 3 fractions ont des compositions isotopiques identiques avec une signature de Nd naturel (phase B; Fig. 7).

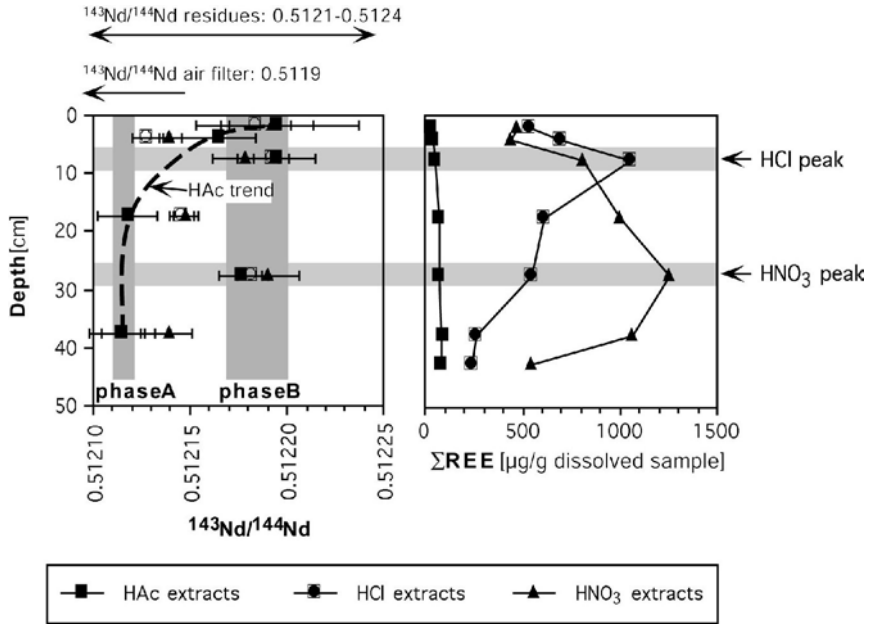

Fig. 7 : Évolution du rapport 143Nd/144Nd et des teneurs en TR avec la profondeur pour les fractions HAc, HCl et HNO3. La phase A désigne un pôle anthropique, la phase B un pôle naturel (Figure 10 de Steinmann et Stille, 1997).

Toutes ces informations suggèrent, que des TR d'origine anthropique se sont déposées en surface, d'où elles ont migré en profondeur et précipité avec l'augmentation du pH du sol. Les TR anthropiques ne sont donc pas restées fixées dans la matière organique du sol superficiel, mais elles étaient mobiles, contrairement au Pb, Zn et Cu. Pendant cette migration, le Ce a précipité plus rapidement que les autres TR à cause de sa charge de 4+, contre celle de 3+ pour les autres TR. Cette mobilité des TR est probablement liée d'une part à une saturation de la capacité d'absorption des horizons superficiels du sol, du fait des fortes teneurs en Pb, Zn et Cu et d'autre part à la formation de complexes carbonatés solubles. Les teneurs en TR des fractions HCl et HNO_3 sont beaucoup plus élevées que dans les fractions HAc.

Mais les compositions isotopiques du Nd montrent, que seules les TR de la fraction HAc sont d'origine anthropique.

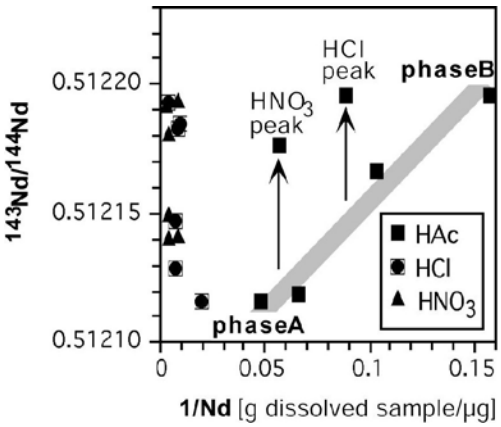

Fig. 8 : Diagramme de mélange 143Nd/144Nd vs. 1/Nd. Les échantillons de la fraction HAc sont issus d'un mélange entre un pôle de Nd anthropique (phase A) et un pôle naturel (phase B). Les points "HCl peak" et "HNO3 peak" correspondent à des niveau de sol où les 3 fractions d'extraction sont dominées par une phase minérale contenant des fortes teneurs en Nd naturel (voir Fig. 7) (Figure 11 de Steinmann et Stille, 1997).

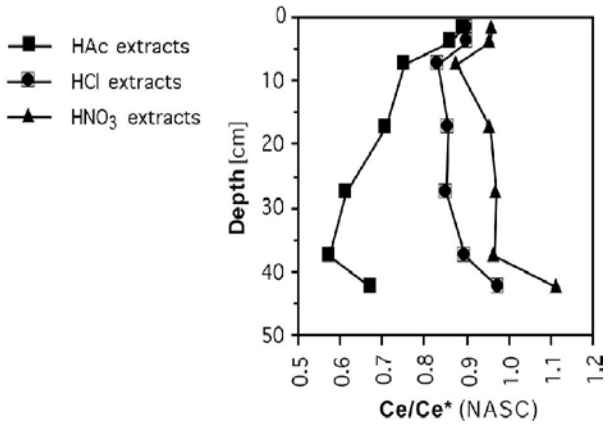

Fig. 9 : Évolution de l'anomalie en Ce des fractions HAc, HCl et HNO3 avec la profondeur (Figure 13 de Steinmann et Stille, 1997).

3.3 Perspectives de la thématique

L'étude de Steinmann et Stille (1997) a contribué à démontrer que les isotopes radiogéniques ont un important potentiel pour les études environnementales. La publication a notamment illustré que ces traceurs ne permettent pas uniquement de distinguer entre origine naturelle ou anthropique des ETM, mais également de caractériser leur spéciation et d'identifier les processus qui interviennent dans la migration de la contamination.

L'étude a aussi montré que les TR d'origine anthropique peuvent, sous certaines conditions, être mobiles dans les sols. Ce constat est particulièrement d'actualité avec l'utilisation de plus en plus importante des TR dans l'industrie, en médecine et en agriculture (chap. B2.1.5). Nos recherches en cours sur le transfert des TR à l'interface géosphère - biosphère et sur leur impact sur le fonctionnement physiologique des végétaux (chap. B8) sont en partie basées sur l'approche développée dans de l'étude de Steinmann et Stille (1997).

4 La mobilisation des terres rares lors de l'altération de filons de basalte en milieu salifère et leur migration dans le sel adjacent

Publications associées :

- **Steinmann, M.** & Stille, P., 1998. Strongly fractionated REE patterns in salts and their implications for REE migration in chloride-rich brines at elevated temperatures and pressures. C.R. Acad. Sci. Paris, série II a, 327: 173-180.
- **Steinmann, M.**, Stille, P., Bernotat, W. & Knipping, B., 1999. The corrosion of basaltic dykes in evaporites: Ar-Sr-Nd isotope and REE evidence. Chem. Geol., 153, 259-279.
- **Steinmann, M.**, Stille, P., Mengel, K. & Kiefel, B, 2001. Trace element and isotopic evidence for REE migration and fractionation in salts next to a basalt dyke. Applied Geochem. 16, 351-361.
- **Steinmann, M.** & Stille, P., 2004. Basaltic dykes in evaporites: a natural analogue. In: Gieré, R. and Stille P. (eds): Energy, waste, and the environment: a Geochemical Perspective. Geol. Soc. London Spec. Publ. 236, 135-141.

4.1 Problématique

4.1.1 Le principe de l'analogie naturelle

Le stockage des déchets radioactifs est l'un des grands enjeux auxquels nos sociétés sont actuellement confrontée. La plupart des nations, qui exploitent l'énergie nucléaire, envisagent, faute d'alternatives opérationnelles concrètes (ex. transmutation), de stocker leurs déchets radioactifs de haute activité et à vie longue (HAVL) et de moyenne activité et à vie longue (MAVL) dans des dépôts géologiques profonds. Ces déchets devront être complètement isolés de l'environnement pendant une période d'environ 200'000 à 1'000'000 ans.

L'eau est le vecteur principal de transfert des radionuclides vers l'environnement. Pour assurer la sûreté d'un site de stockage, il faut donc pouvoir garantir que les déchets radioactifs ne soient jamais en contact avec de l'eau, pendant toute la durée du stockage. Pour atteindre cet objectif, toute une série de barrières techniques et géologiques sont prévues. Faire des pronostics sur la fiabilité de ces barrières sur une durée de 200'000 ans est un défi auquel personne n'a été confronté auparavant. L'une des grandes difficultés est de faire des extrapolations sur la stabilité mécanique et chimique des différentes barrières et de modéliser la migration de radionuclides dans le cas d'une infiltration accidentelle d'eau au sein du site de stockage.

Ce contexte a conduit Ewing (1979) à établir le concept de l'analogue naturel. Cette approche consiste à étudier des processus naturels sur des objets géologiques ou archéologiques montrant une forte analogie avec les processus et les matériaux présents dans un site de stockage de déchets radioactifs. L'avantage de l'approche est qu'elle intègre parfaitement l'échelle du temps géologique, ses défauts sont qu'aucun analogue naturel ne reflète parfaitement les caractéristiques d'un site de stockage et que de

nombreux paramètres physico-chimiques restent mal définis. Malgré ces limitations, les études d'analogues naturels (menées depuis maintenant bientôt 30 ans) ont considérablement contribué à améliorer notre connaissance de la problématique du stockage de déchets radioactifs dans des dépôts géologiques profonds.

Certaines TR, notamment le Sm^{3+}, le Nd^{3+} et l'Eu^{3+} ont des rayons ioniques et une configuration électronique très proches de ceux de l'Am^{3+} et du Cm^{3+}. C'est la raison pour laquelle ces TR sont souvent considérées comme analogues chimiques des actinides (Ewing, 1979; Choppin, 1983; 1989 Krauskopf, 1986; Seaborg, 1993). L'étude de leur comportement au sein d'un site d'analogue naturel donnera par conséquent des indications sur le comportement des actinides dans le contexte d'un site de stockage de déchets radioactifs à l'échelle du temps géologique. De nombreux travaux ont été réalisés sur l'altération de verres basaltiques et sur la mobilité des TR au cours de cette altération, en considérant ces processus comme analogues naturels de l'altération de colis de déchets radioactifs vitrifiés (ex. Crovisier *et al.*, 1992; 2003; Abdelouas *et al.*, 1994; Daux *et al.*, 1997; Advocat *et al.*, 2001; Munier *et al.*, 2004; Curti *et al.*, 2006). D'autres études se sont focalisées sur la migration des TR et de l'U au contact de roches enrichies en ces éléments, telles que le réacteur nucléaire fossile d'Oklo au Gabon (Gauthier-Lafaye *et al.*, 1996; Hidaka et Gauthier-Lafaye, 2000; Stille *et al.*, 2003; Bros *et al.*, 2003; Kikuchi *et al.*, 2007) ou des gisements d'Uranium tels que le site de Poços de Caldas au Brézil (Waber, 1992; Bonotto *et al.*, 2007) ou le site de Cigar Lake au Canada (Smellie et Karlsson, 1999; Gauthier-Lafaye *et al.*, 2004).

4.1.2 Le stockage des déchets nucléaires dans les diapirs de sel en Allemagne

La majorité des pays envisage l'installation d'un site de stockage de déchets radioactifs dans des formations argileuses. Les avantages incontestés des argilites sont : 1) l'étanchéité et l'auto-scellage de fractures par gonflement des argiles en cas d'infiltration d'eau, 2) le comportement plastique sous contrainte tectonique, et 3) l'important pouvoir d'adsorption en cas de fuites de radionuclides.

Certains pays, qui ne disposent pas de formations argileuses appropriées, envisagent l'installation d'un site de stockage dans des granites (pays scandinaves, option "granite" en Suisse). L'avantage principal du granite est la disponibilité de gisements granitiques étendus (notamment en Scandinavie) et sa réputation de solidité et longévité auprès du grand public. Les défauts de l'option granite sont liés au comportement cassant sous contrainte tectonique et à la faible capacité d'adsorption du granite, rendant un site de stockage en milieu granitique très vulnérable aux infiltrations d'eau.

L'Allemagne ne dispose ni de formations argileuses ni de granites appropriés à l'installation d'un site de stockage. C'est la raison pour laquelle les autorités allemandes se sont mis à la recherche d'alternatives. Ces recherches se sont orientées, depuis 1973, vers un stockage dans les diapirs de sel, présents en nombre important en Allemagne du nord. L'option sel est avant tout basée sur le constat que les mines de sel exploitées à grande échelle par l'industrie chimique depuis le 19ème siècle sont parfaitement sèches. La bonne conductivité thermique du sel est un autre argument souvent avancé en

faveur d'un tel site. Toutefois, les arguments contre le stockage dans le sel sont nombreux : 1) Des sondages dans les dômes de sel ont mis en évidence la présence de nombreuses poches d'eau à l'intérieur du dôme (Herrmann et Knipping, 1993), provenant probablement de l'infiltration d'eau météorique lors des dernières glaciations. 2) Les sels sont très solubles dans l'eau et un site de stockage dans le sel serait donc très vulnérable à toute infiltration d'eau. 3) Les évaporites marines sont caractérisées par une stratigraphie cyclique, dans laquelle chaque cycle correspond à une séquence d'évaporation d'eau de mer. L'halite (NaCl) est considérée comme idéal pour le stockage de déchets radioactifs, par contre, les sels de potasse tels que la sylvite (KCl) ou la carnallite ($KMgCl_3 * 6H_2O$) ont des caractéristiques défavorables à cause de leur forte solubilité à l'eau, surtout à des températures > 100 °C (Braitsch, 1971; Herrmann et Knipping, 1993). L'extension latérale et verticale d'un gisement d'halite peut facilement être évaluée dans une série évaporitique autochtone. Par contre, lors de la mise en place des dômes de sel, cette stratigraphie initiale est complètement perturbé (halocinèse). De ce fait, il est très difficile de connaître l'extension exacte en 3 dimensions des différents sels à l'intérieur du dôme et donc de certifier l'absence de sels potassiques à proximité d'une masse d'halite sélectionnée pour accueillir un site de stockage.

Ces arguments décrédibilisent l'option des diapirs de sel pour le stockage de déchets nucléaire, qui reste pourtant maintenue faute d'alternatives sur le territoire allemand. Dans ce contexte, et étant donné la focalisation des pouvoirs publiques sur un seul site potentiel (le dôme de Gorleben), les opinions publiques et une partie de la classe politique allemande maintiennent une forte opposition. Le sujet du stockage des déchets nucléaire reste très controversé et les investigations pour un site de stockage potentiel dans les diapirs de sel sont en standby depuis 2000 ("Gorleben-Moratorium").

4.1.3 Objectif de l'étude et contexte géologique

L'étude de la mobilisation des TR lors de l'altération de filons de basalte en milieu salifère présentée ici, s'inscrit dans l'approche des analogues naturels pour le stockage de déchets nucléaires dans les gisements de sel. Elle a pour objectif d'obtenir des renseignements sur le comportement des radionuclides à l'échelle du temps géologique, si un colis de déchets radioactifs vitrifiés se trouve accidentellement en contact direct avec des saumures provenant du sel. Dans ce contexte nous avons utilisé les TR naturelles du basalte comme analogue chimique pour des actinides radioactifs. L'étude avait été initiée au milieu des années 1990 par B. Knipping de l'université technique de Clausthal-Zellerfeld (Allemange) et W. Bernotat du Centre de recherche de Karlsruhe (Allemagne). Dans le cadre de ce projet, j'ai eu l'opportunité d'étudier la mobilité des TR au sein des filons de basalte lors de l'altération ainsi que leur migration dans le sel voisin. L'approche a été complétée par un traçage par les isotopes du Sr et du Nd. Tous les échantillons de sel et de basalte avaient déjà fait l'objet d'études minéralogiques antérieures à l'université technique de Clausthal-Zellerfeld.

Les objets d'études sont des contacts entre les filons de basalte (dykes) et le sel encastrant. Ces filons de basalte sont d'âge Miocène et recoupent les séries salifères du Zechstein dans le secteur de

Werra-Fulda en Allemagne (Fig. 10). Ils peuvent être suivis latéralement sur plusieurs kilomètres et ils ont à la fois été cartographiés à la surface et dans les mines de sel à des profondeurs d'environ 800 m (Knipping, 1989). Les bords des filons de basalte sont vitrifiés par le refroidissement rapide du basalte lors de l'intrusion et ressemblent ainsi à des colis de déchets radioactifs vitrifiés. Les séries salifères du Zechstein ont une épaisseur totale d'environ 400 m.

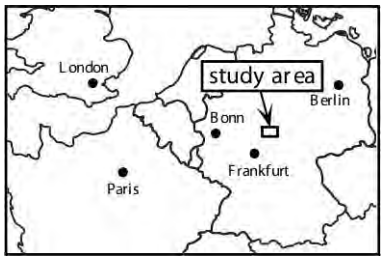

Fig. 10 : Localisation du secteur d'étude dans la zone minière de Werra-Fulda en Allemagne (a) (Fig. 1 de Steinmann et al., 1999).

La lithologie principale est l'halite (NaCl), avec des niveaux plus fins de sel de potasse et d'anhydrite ($CaSO_4$). Dans le secteur de Werra-Fulda deux niveaux de sel de potasse, essentiellement composés de carnallite ($KMgCl_3 * 6H_2O$) et d'une épaisseur de 2 à 10 m, sont exploités dans des galeries sous-terraines à des profondeurs d'environ 800 m. Les contacts basalte-sel étudiés ont été échantillonnés dans ces 2 niveaux dans la mine de Hattorf (http://www.kali-gmbh.com/profil/hattorf_en.cfm).

Sur le terrain on observe une zone d'interaction entre basalte et sel uniquement dans les niveaux de sel de potasse et pas dans les niveaux de halite et d'anhydrite. Cette différence s'explique par le fait que les fluides, qui accompagnaient l'intrusion du basalte, avaient traversé, avant d'arriver au niveau des galeries de mine, un niveau de halite épais d'une centaine de mètres, mais pas de sels de potasse. Par conséquent, les fluides étaient saturés par rapport à l'halite et pas par rapport aux sels de potasse, ils ont donc uniquement interagi avec ces derniers (Knipping et Herrmann, 1985; Gutsche, 1988; Knipping, 1989).

Nous avons étudié dans ce contexte à la fois la mobilité des TR au sein du basalte vitrifié (Steinmann *et al.*, 1999) et dans le sel voisin (Steinmann *et al.*, 2001). Cette mobilité des TR semble dans les 2 cas être associée à la circulation des fluides saturés en NaCl, qui lors de l'intrusion du basalte, se sont mélangés avec des fluides provenant des sels de potasse. Des indications précises sur le durée de la circulation et sur la température de ces fluides manquent. Toutefois, on sait que la température du basalte au moment de l'intrusion était d'environ 1150 °C et des modélisations basées sur refroidissement par conductivité thermique suggèrent, que les températures du sel à 1 m du contact au basalte ne dépassaient jamais 200 °C (Knipping, 1989). Ces températures correspondent à peu près à la température maximale attendu pour un site de stockage de déchets nucléaires dans des gisements de sel.

4.2 Principaux résultats

4.2.1 La mobilité des TR lors de l'altération du basalte

La mobilité des TR dans le filon de basalte a été étudiée dans une coupe détaillée à travers un filon de basalte, qui est conservé en forme d'un boudin tectonique dans la mine de Hattorf (Fig. 11) et dont la pétrographie avait été étudiée par Knipping et Herrmann (1985). Au niveau du contact basalte-sel, on observe la présence de fines paillettes d'argiles néoformées et dans la bordure du filon basaltique apparaissent des petites bulles remplies de sel (Knipping et Herrmann, 1985). Afin d'enlever ces traces de sel, toutes les poudres de basalte ont été lavées à l'eau ultra-pure avant l'attaque pour l'analyse chimique. Un aliquot de chaque échantillon a en plus subi une traitement de leaching à l'HCl 1.5 M. L'objectif du leaching était de caractériser séparément la composition chimique et isotopique des phases minérales secondaires, qui sont préférentiellement mobilisées par le leaching (Clauer *et al.*, 1993; Stille et Clauer, 1994; Innocent *et al.*, 1999). Les analyses chimiques et isotopiques ont à la fois été réalisées sur la roche totale lavée à l'eau ultrapure, ainsi que sur la solution et sur la phase résiduelle issues des expériences de leaching.

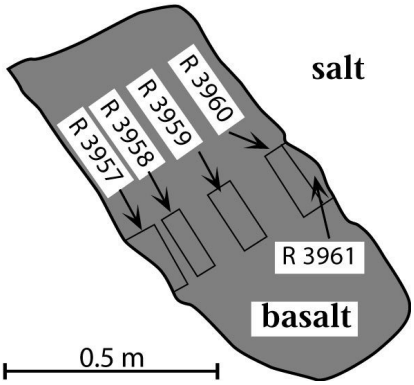

Fig. 11 : Coupe détaillée à travers un filon de basalte en contact des sels de potasse (essentiellement carnallite, KMgCl3 * 6H2O) et localisation des échantillons R3957 à R3961 étudiés. Le filon conservé en forme d'un boudin tectonique a été échantillonné dans la mine de Hattorf (Fig. 2 de Steinmann et al., 1999).

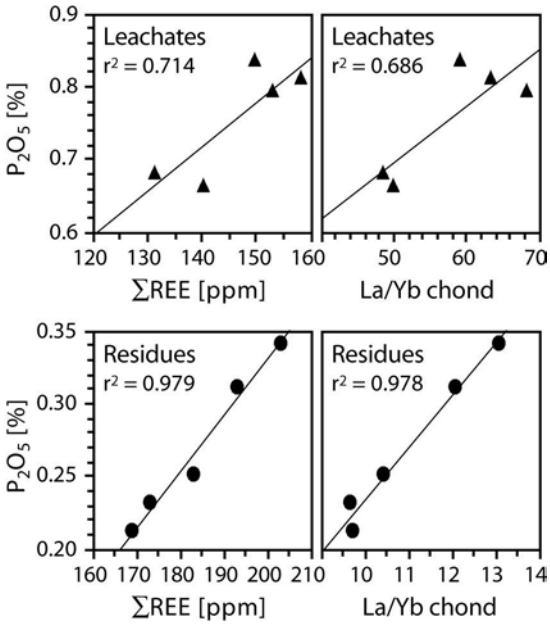

Fig. 12 : Corrélation entre ΣREE et P2O5 respectivement La/Yb et P2O5 dans les leachates et résidus du profil de basalte. Dans les 2 cas le TR semblent associées à une phase phosphatées enrichies en TR légères (La/Yb élevé) (Fig. 8 de Steinmann et al., 1999).

Une des difficultés principales de l'étude était de faire la distinction entre variations chimiques et minéralogiques dues à la cristallisation fractionnée au sein du filon et variations dues à l'altération lors de

l'échange avec les saumures. Une analyse détaillée des données a finalement montré que les variations chimiques observées dans la phase résiduelle des basaltes après leaching étaient essentiellement dues à la cristallisation fractionnée, tandis que les variations observées dans les leachates reflétaient les variations liées à l'altération du basalte (Steinmann *et al.*, 1999).

Fig. 13 : Comparaison entre les spectres moyennes des TR, des leachates et des résidus du profil de basalte (Fig. 9 de Steinmann et al., 1999).

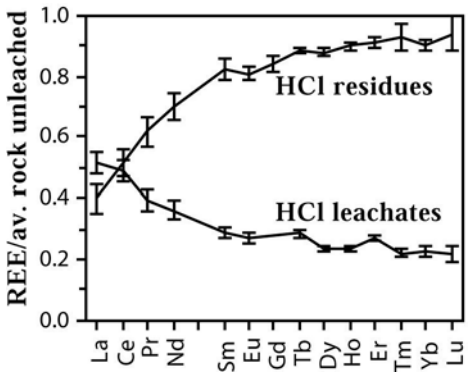

La phase porteuse des TR semble, dans les résidus et dans les leachates, être une phase phosphatée, qui est dans les 2 cas enrichie en TR légères (Fig. 12). Une comparaison entre les spectres de TR de ces 2 phases montre, que cet enrichissement en TR légères est plus accentué pour les leachates et que les spectres des leachates et des résidus sont complémentaires (Fig. 13). La Fig. 13 montre également, qu'environ 50 % des TR légères se trouvent dans le leachates et que cette valeur baisse à environ 20 % pour les TR lourdes. La phase phosphatée porteuse des TR correspond probablement, dans la phase résiduelle, à des apatites aciculaires d'origine magmatique et visibles sous lame-mince. Des analyses MEB ont permis d'identifier des apatites secondaires, qui se trouvent systématiquement dans des franges d'altération autour de bulles de sel (Fig. 14). Des analyses dispersives en énergie (EDX) montrent que ces apatites secondaires sont très riches en TR (Fig. 15) et qu'il s'agit de chlorapatites de TR ($Ca_2La_{0.5}Ce\ Nd_{0.5}(PO_4)_3Cl$).

Toutes ces données indiquent, que ce sont les TR légères des apatites magmatiques primaires du basalte, qui ont principalement été mobilisées lors de l'altération du basalte et qu'elles ont ensuite, aussitôt, été immobilisées par la précipitation de chlorapatites secondaires. La stabilité d'apatites primaires, ainsi que la précipitation d'apatites secondaires, sont donc les processus clés qui contrôlent la mobilité et le fractionnement des TR dans le basalte.

En se basant sur les données du basalte, il n'était pas possible de savoir, si l'immobilisation in situ des TR a été intégrale ou si une partie des TR avait migré vers le sel. C'est la raison pour laquelle nous nous sommes intéressé, dans un second temps de l'étude, à la migration des TR dans le sel voisin.

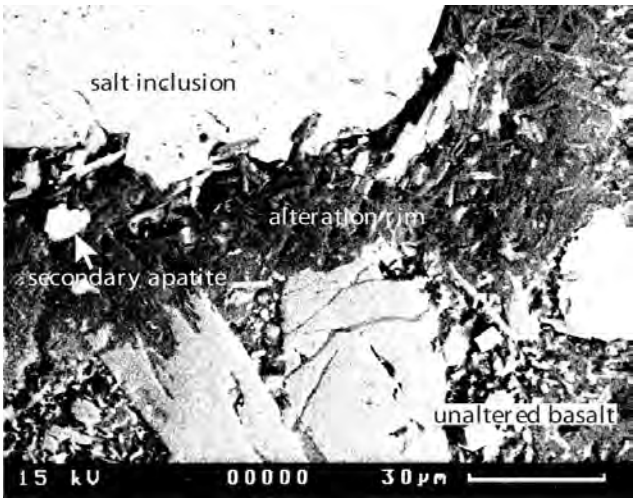

Fig. 14 : Photo MEB montrant la présence d'apatites secondaires dans des franges d'altération autour de bulles de sel (Fig. 17 de Steinmann et al., 1999).

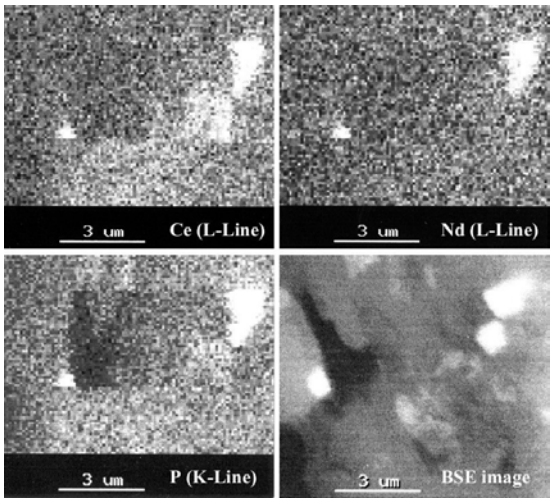

Fig. 15 : Carte élémentaire d'apatites secondaires de la Fig. 14 avec les teneurs en P, Ce et Nd indiquant que ces apatites secondaires sont très riches en TR. Ces fortes teneurs font ressortir les apatites secondaires dans l'image à électrons rétrodiffusés (image BSE) (Fig. 18 de Steinmann et al., 1999).

4.2.2 La migration des TR dans le sel

Afin d'identifier la part des TR d'origine basaltique dans les sels, nous avons étudié un profil de sel en contact d'un filon basaltique (Fig. 16). Étant donné les très faibles teneurs en TR et les rapports Rb/Sr très élevés dans les sels, il a d'abord été nécessaire de développer des méthodes analytiques adaptées pour les analyses des TR et des rapports isotopiques du Nd et du Sr (Steinmann et Stille, 1998).

Fig. 16 : Profil de sel étudié à proximité d'un filon de basalte, localement élargi en apophyse. Le profil de sel (échantillons R4250-R4254) se situe dans un niveau de sel de potasse (Fig. 2 de Steinmann et al., 2001).

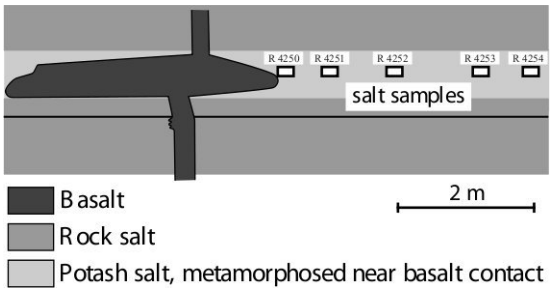

Une étude minéralogique détaillée du profil de sel avait été réalisée auparavant (Gutsche, 1988). La composition minéralogique et les concentrations en éléments majeurs ont mis en évidence que le niveau de sel étudié avait à l'origine entièrement été composé de carnallite ($KMgCl_3 * 6H_2O$). Lors de l'intrusion du basalte, la carnallite a été transformée en halite (NaCl) et sylvite (KCl) par des fluides riches en NaCl, qui accompagnaient la remontée du magma basaltique. Le NaCl de ces fluides provenaient de la dissolution partielle d'un niveau de halite épais d'environ 150 m et situé en-dessous de l'horizon de carnallite étudié (Knipping et Herrmann, 1985; Knipping, 1989). Cette transformation de la

carnallite primaire par les fluides est très bien illustrée par la composition minéralogique des échantillons (Fig. 17), mais aussi par la composition isotopique du Sr (Fig. 18). Ces données montrent, que la transformation de la carnallite primaire est presque intégrale au niveau du contact avec le basalte et qu'elle diminue avec la distance.

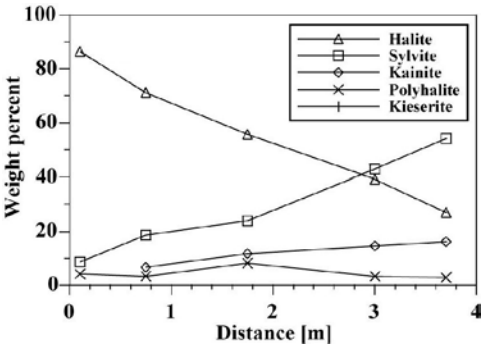

Fig. 17 : Composition minéralogiques du sel en fonction de la distance au filon de basalte. On observe que la carnallite d'origine (KMgCl3 * 6H2O) a été entièrement remplacée par de la halite (NaCl) et de la sylvite (KCl). La répartition de la halite retrace l'avancée de fluides enrichis en NaCl (données de Gutsche, 1988, Fig. 3 de Steinmann et al., 2001).

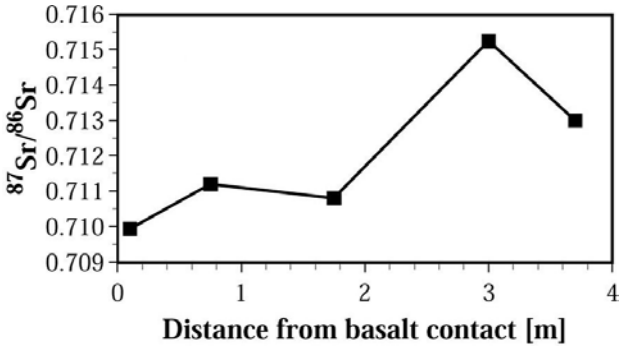

Fig. 18 : Composition isotopique du Sr du sel en fonction de la distance au filon de basalte. La répartition des valeurs indique également l'avancée d'un fluide de composition isotopique moins radiogénique provenant du contact au basalte. Toutefois, même les rapports isotopiques les plus faibles sont plus élevées que dans le basalte (87Sr/86Sr ≈ 0.7035, Steinmann et al., 1999), indiquant que le Sr contenu dans les fluides n'est pas d'origine mantellique, mais issu de l'interaction avec des roches de la croûte supérieure (Fig. 4 de Steinmann et al., 2001).

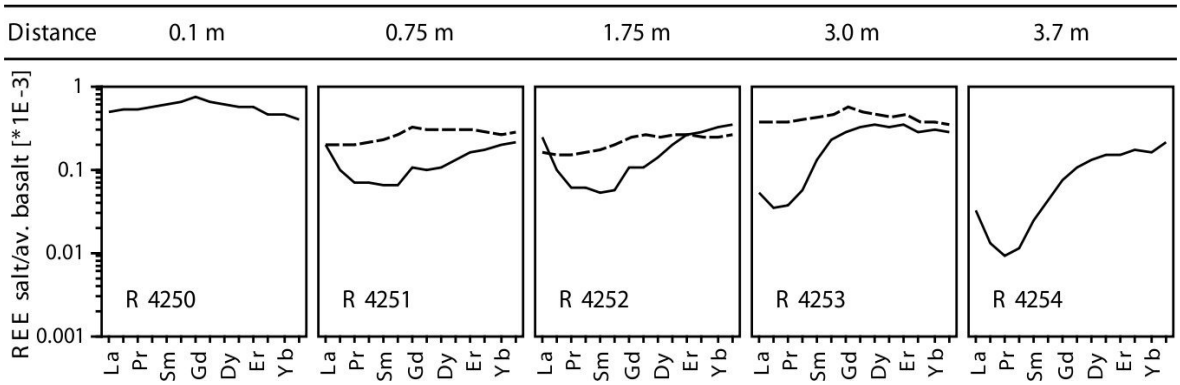

Fig. 19 : Spectres de TR des sels normalisés par rapport au basalte moyen. Le spectre du sel près du contact du basalte est plat, quasiment identique à celui du basalte. Avec la distance, on constate un fort appauvrissement en TR légères, notamment en Ce, Pr, Nd, Sm et Eu. Les pointillées (échantillons R4251-4253) correspondent à des spectres de mélange calculés, leur signification est discutée dans le texte (Fig. 6 de Steinmann et al., 2001).

L'évolution des spectres des TR et des compositions isotopiques du Nd de ces mêmes échantillons sont présentés respectivement dans les figures 19 et 20. On observe un fort appauvrissement en TR légères avec la distance, notamment en Ce, Pr, Nd, Sm et Eu, tandis que les données isotopiques indiquent clairement que ces TR proviennent essentiellement du basalte. Afin de vérifier, si les spectres observés ne sont pas des spectres de mélange entre un pôle basaltique et un pôle de sel, des spectres de

mélange ont été calculés pour les échantillons intermédiaires (R4251 à R4254) en utilisant les échantillons R4250 et R 4254 des 2 extrémités du profil comme pôles de mélange. La figure 19 montre que les spectres calculés sont quasiment plats et complètement différents des spectres observés, démontrant ainsi que les spectres des échantillons intermédiaires (R4251 à R4254) ne sont pas issus d'un mélange, mais le résultat d'un fractionnement de TR d'origine basaltique lors du transport dans les sels.

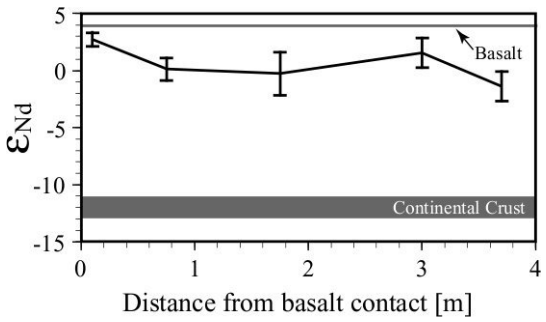

Fig. 20 : Composition isotopique du Nd dans les sels. Les valeurs restent toujours proche des valeurs typique du basalte (εNd ≈ 5, Steinmann et al., 1999) et loin de la croûte continentale, montrant que les TR analysées dans le sel proviennent essentiellement du basalte (Fig. 7 de Steinmann et al., 2001).

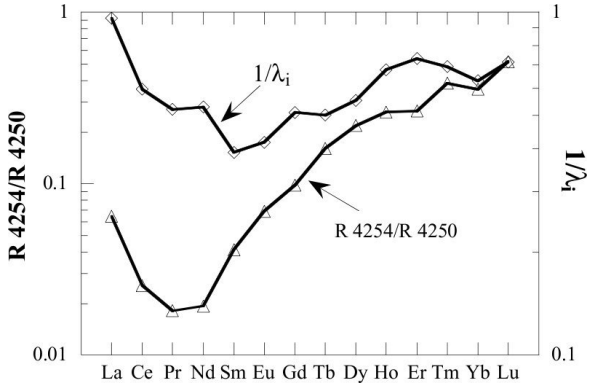

Fig. 21 : Comparaison du fractionnement des spectres de TR dans les sels et de facteurs de fractionnement déterminés expérimentalement pour des TR coprécipitées avec des apatites (Byrne et al., 1996). Le facteur de fractionnement expérimentale λi est présenté en forme inverse afin de montrer le fractionnement dans la solution résiduelle (Fig. 11 de Steinmann et al., 2001).

Nous avons montré dans le chap. B 4.2.1 que les TR sont mobilisés au sein du basalte par la dissolution d'apatites magmatiques suivi d'une immobilisation par la précipitation d'apatites néoformées. Il était donc raisonnable de suggérer que la migration des TR dans le sel a également été contrôlée par les apatites. La figure 20 compare le fractionnement des TR observé avec des facteurs de fractionnement déterminés expérimentalement pour des TR co-précipitées avec des apatites (Byrne *et al.*, 1996). Les 2 courbes sont très similaires, ce qui semble confirmer, que le fractionnement des TR observé dans les sels a été causé par la précipitation préférentielle des TR légères avec des phosphates secondaires. Il a été impossible d'identifier directement ces apatites présumées dans le sel, pour confirmer cette hypothèse.

4.2.3 Signification des résultats pour le stockage de déchets radioactifs dans les sels

L'étude de la mobilité des TR dans les filons de basalte et dans les sels adjacents montre que la mobilité et le fractionnement des TR est avant tout contrôlée par la dissolution d'apatites primaires et la précipitation d'apatites secondaires. Premier renseignement pour un site de stockage : la mobilité des actinides pourrait également dépendre de la stabilité de quelques phases accessoires. Il est donc nécessaire de s'assurer que les radionuclides ne soient pas associés à des phases minérales instables. D'autre part, l'étude de la migration des TR montre que la précipitation de minéraux phosphatés est un processus très efficace dans l'immobilisation des TR et donc, par analogie, des radionuclides. Par

conséquent, il serait envisageable d'intégrer de l'apatite dans la bentonite du remplissage de galeries, autour des colis de déchets radioactifs vitrifiés. Dans le cas d'une infiltration d'eau, ces apatites seraient en partie dissoutes et immobiliseraient ensuite d'éventuels radionuclides par co-précipitation. Une étude récente basée sur des arguments minéralogiques et thermodynamiques est arrivée à une conclusion très similaire (Oelkers et Montel, 2008).

4.3 Perspectives de la thématique

Le stockage des déchets nucléaires reste un problème non-résolu et il fait partie des problématiques complexes atour de la question de l'utilisation de l'énergie nucléaire comme source de production énergétique. Dans certains pays, ce sujet atteint un tel niveau de polémique, qu'il en devient tabou et qu'il est tout simplement exclus du discours politique. Mais les déchets radioactifs sont là et même dans les pays, qui ont choisi d'abandonner cette source d'énergie à moyen terme (Autriche en 1978, la Suède en 1980, l'Italie en 1987, la Belgique en 1999 et l'Allemagne en 2000) et il est nécessaire de trouver des solutions fiables pour leur stockage.

Les décideurs en ont conscience et les programmes de recherche des différents organismes nationaux chargés de la gestion des déchets radioactifs continuent d'exister (Andra, Enresa, DBE, Nagra ...). Pourtant, ils semblent en veille ou tout au moins ne plus mobiliser la même énergie que par le passé. L'argument officiel est l'absence d'urgence, parce que la chaleur produite par la fission résiduelle dans les combustibles usés est pour l'instant trop importante pour un stockage définitif et nécessite un stockage intermédiaire dans des bassins d'eau pendant plusieurs dizaines d'années. Toutefois, il ne semble pas abusif de penser, que les décideurs jouent aussi la carte du temps, espérant que des solutions techniques (ex. transmutation) ou politiques (ex. centre de stockage européen) soient prochainement trouvées, qui permettraient de simplifier l'épineux problème du stockage définitif.

A ce jour, le seul site de stockage géologique de déchets HAVL en exploitation est un site américain pour des déchets militaires. En Europe, certains pays sont en train de définir l'emplacement d'un site de stockage pour des déchets HAVL, mais aucune décision définitive n'est prise à l'exception de la Finlande (construction en cours sur le site d'Olkiluoto).

La thématique de recherche sur les analogues naturels est directement dépendante des décisions politiques prises sur le stockage des déchets HAVL. L'absence actuelle de prises de position claires sur ce sujet fait que les programmes existants continuent, mais peu de financements sont alloués à de nouveaux projets. En ce qui concerne le stockage dans les dômes de sel, de plus en plus de données scientifiques remettent en question l'aptitude de ces gisements pour le stockage de déchets HAVL. Dans ce contexte, il me semble inopportun de continuer la recherche sur la migration des TR en milieu salifère en tant qu'analogue naturel. Sur la base des connaissances actuelles il vaut mieux concentrer les efforts de recherche sur les analogues naturels dans les formations argileuses.

5 La migration des fluides interstitiels dans un récif corallien

Publication associée :

- **Steinmann, M.** & Déjardin, P, 2004. Temporal evolution of fluid flow through the Tahiti barrier reef traced by Sr isotopes and pore water chemistry. Chem. Geol. 203, 51-73.

5.1 Problématique

Cette étude trace la circulation des fluides interstitiels dans le récif barrière de Tahiti (Fig. 22). La circulation des fluides dans les récifs coralliens est importante d'une part pour la diagenèse et la conservation de la structure carbonatée du récif et elle est d'autre part indispensable au fonctionnement métabolique des récifs. L'activité biologique des récifs coralliens se limite à la partie sommitale de la structure, qui se situe dans la zone photique de l'océan, là où la lumière est suffisante pour la photosynthèse des algues qui vivent en symbiose avec les coraux. La zone photique de l'océan environnant est très pauvre en nutriments (les apports de nutriments des océans se font uniquement à proximité des continents au niveau de l'embouchure de grands fleuves ou par le biais de zones d'upwelling d'eau profonde en milieu côtier ou équatorial). La question est donc de savoir comment les polypiers des récifs coralliens arrivent à maintenir leur forte activité biologique dans un milieu aussi appauvri en nutriments.

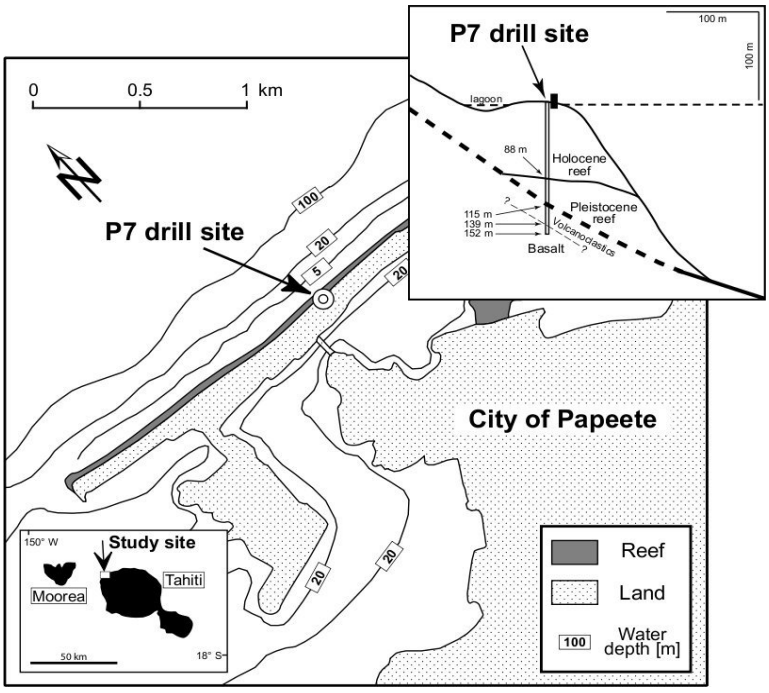

Fig. 22 : Carte et coupe avec la localisation du site de forage sur le récif barrière de Tahiti à Papeete (Fig. 1 de Steinmann et Dejardin, 2004).

Des données géothermiques et des modélisations thermohydrauliques, réalisées dans le cadre des études autour des essais nucléaires sur les atolls de l'océan Pacifique, ont fourni les premières indications pour la présence d'une circulation ascendante dans les récifs coralliens (ex. Swartz, 1958; Samaden *et al.*, 1985; Henry *et al.*, 1996; Jones *et al.*, 2000; Pfingsten *et al.*, 2001). Cette remontée serait avant tout contrôlée par le flux de chaleur résiduel dans le substratum volcanique du récif. L'hypothèse de "l'endoupwelling" formulée par Rougerie et Wauthy en 1986 (Rougerie et Wauthy, 1986 ;1993; Rougerie *et al.*, 1997), propose que cette remontée de fluides interstiels permette le transport d'élément minéraux nutritifs provenant de l'interaction eau-roche dans le socle basaltique et des eaux antarctiques intermédiaires (AIW). L'AIW est une couche d'eau riche en nutriments, qui apparaît dans le Pacifique austral à des profondeurs entre 200 à 500 m de profondeur. Ce processus de l'endoupwelling pourrait également expliquer des processus diagénétiques tels que la dolomitisation, qu'on observe dans certains atolls (Flood *et al.*, 1996; Jones *et al.*, 2000).

La présente étude avait pour objectif de vérifier cette hypothèse d'endoupwelling sur la base d'un suivi des eaux interstitielles sur 2 ans dans un forage réalisé par l'ORSTOM (aujourd'hui IRD) à travers la barrière récifale de Tahiti. L'étude est entièrement basée sur les données de la thèse de P. Déjardin (Déjardin, 1996), réalisé à l'ORSTOM de Tahiti et au Centre de Géochimie de la Surface de Strasbourg (CGS-CNRS) sous la direction de F. Rougerie (ORSTOM) et B. Fritz (CGS). J'ai encadré la partie isotopique de cette étude.

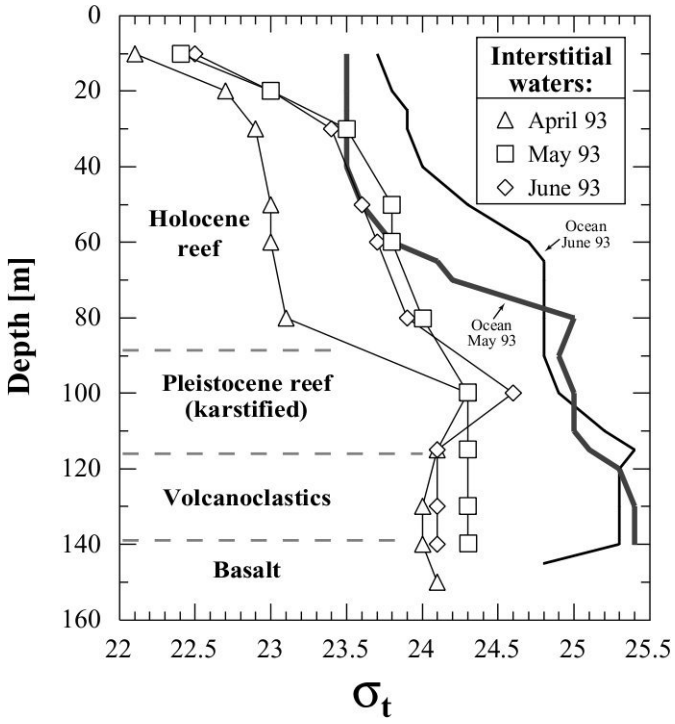

Fig. 23 : Comparaison de la densité de l'eau interstitielle avec celle de l'eau de mer au large du récif (σt = {densité - 1} * 1000). La densité de l'eau interstitielle est toujours plus faible que dans l'océan ouvert (Fig. 3 de Steinmann et Dejardin, 2004).

5.2 Principaux résultats

5.2.1 Les données de densité

L'étude a effectivement permis de mettre en évidence l'existence d'une remontée d'eau interstitielle à l'intérieur du récif. Cette remontée est contrairement aux prédictions des modèles thermohydrauliques pas directement due au réchauffement de l'eau par le socle volcanique, mais le résultat d'une chute de salinité (et donc de la densité) lors de l'interaction eau-roche dans le socle volcanique. Cette eau pénètre ensuite dans la structure récifale devenant ainsi une eau interstitielle. Sa densité au sein du récif diminue vers la surface, indiquant que la colonne de l'eau interstitielle est stable (Fig. 23). Mais la figure 23 montre aussi que l'eau interstitielle est toujours plus légère que l'eau dans l'océan ouvert à la même profondeur, avec lequel il existe des échanges à travers la porosité de la structure récifale. L'eau interstitielle forme ainsi une masse de densité plus faible que celle de l'océan environnant, ce qui peut expliquer sa remontée par poussée d'Archimède.

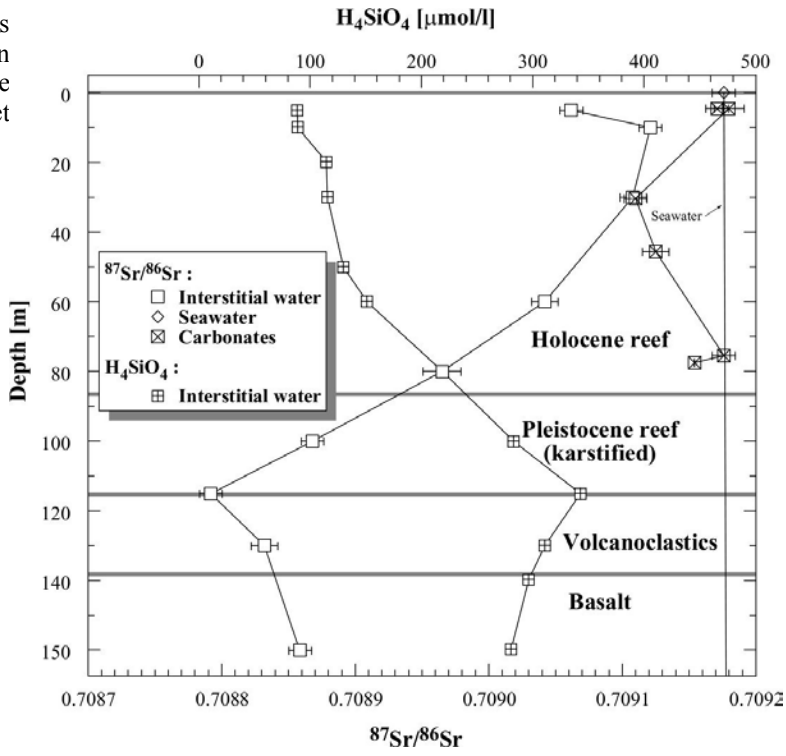

Fig. 24 : Comparaison entre les rapports 87Sr/86Sr et les teneurs en H4SiO4 de l'eau interstitielle (Fig. 5 de Steinmann et Dejardin, 2004).

5.2.2 Les données chimiques et isotopiques

L'étude est basée sur 16 profils d'eau interstitielle sur lesquels des paramètres physico-chimiques et des éléments majeurs et traces ont été analysés au laboratoire de l'ORSTOM à Tahiti. Une des 16 séries de dosages a été complétée par des analyses complémentaires d'éléments majeurs et traces par ICP-AES et ICP-MS au CGS de Strasbourg. Ces sur cette même série nous avons dosé le rapport $^{87}Sr/^{86}Sr$ par TIMS, au CGS. Le rapport isotopique du $^{87}Sr/^{86}Sr$ est un traceur particulièrement intéressant dans le

contexte de l'étude : En effet, le milieu est dominé par seulement 2 sources de Sr, qui sont l'eau de mer et le socle basaltique. Ces 2 pôles ayant des compositions isotopiques très différentes ($^{87}Sr/^{86}Sr$ basalte ≈ 0.704 ; $^{87}Sr/^{86}Sr$ eau de mer = 0.70916), cela permet de tracer les échanges avec beaucoup de précision.

Fig. 25 : Diagramme d'isochrone Rb-Sr avec les données d'eau interstitielle, d'eau de mer, de calcaires récifaux et de basalte. On peut distinguer dans le diagramme un mélange entre eau issue de l'interaction eau-roche et eau de mer (100 à 60 m), suivi dans la partie sommitale du récif par un mélange avec de l'eau de pluie. Les étiquettes des points de données en mètres indiquent la profondeur (Fig. 7 de Steinmann et Dejardin, 2004).

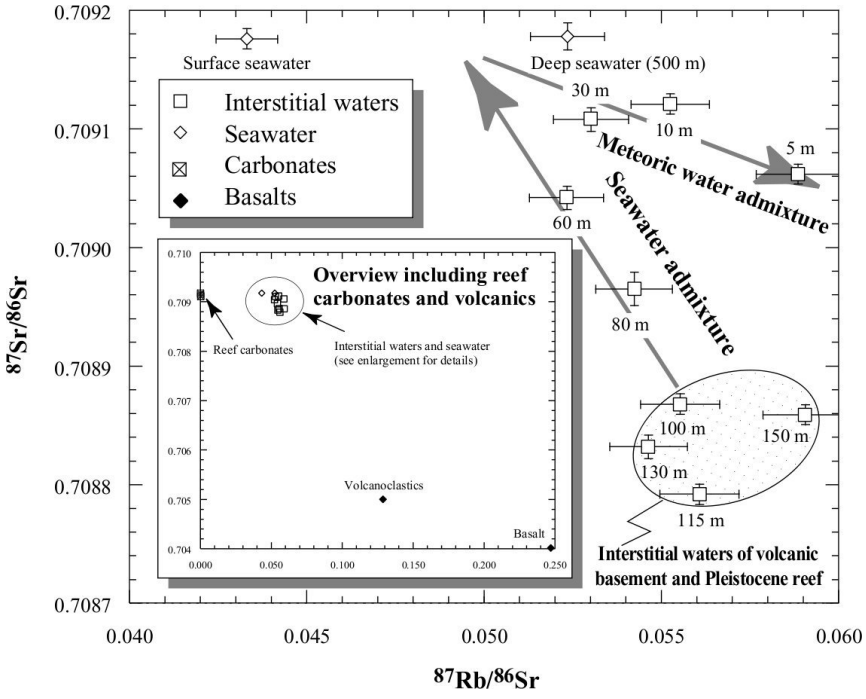

Fig. 26 : Diagramme de mélange 87Sr/86Sr vs. 1/Sr. Ce diagramme montre de façon plus détaillée les relations de mélange entre eau interstitielle, eau de mer et eau météorique (Fig. 8 de Steinmann et Dejardin, 2004).

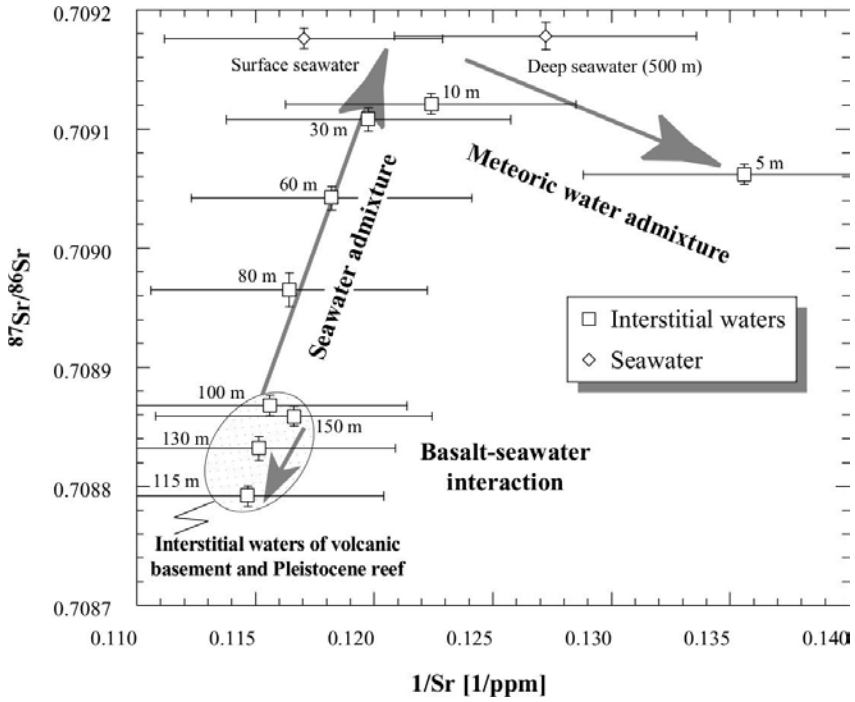

Les rapports $^{87}Sr/^{86}Sr$ des eaux interstitielles s'approchent de la composition du basalte lors du passage dans les coulées de basalte et dans les séries volcano-sédimentaires, ils retracent donc bien l'interaction eau-roche (Fig. 24). En remontant dans la structure récifale, les valeurs se rapprochent

progressivement de la composition de l'eau de mer. Les diagrammes d'isochrone (Fig. 25) et le diagramme de mélange (Fig. 26) montrent clairement, que cette évolution est due à un mélange binaire entre une eau issue de l'interaction eau-roche et de l'eau de l'océan ouvert. Les 2 diagrammes indiquent également une infiltration d'eau météorique à proximité de la surface. Des calculs de mélange basés sur les rapports $^{87}Sr/^{86}Sr$ et les teneurs en Sr mettent en évidence que le mélange entre l'eau issue de l'interaction eau-roche et l'eau de mer évolue de manière quasi linéaire avec la profondeur (Fig. 27). Ceci démontre que l'ajout d'eau de mer se fait par advection homogène sur toute la hauteur du récif holocène et non pas par injection ponctuelle à des niveaux précis.

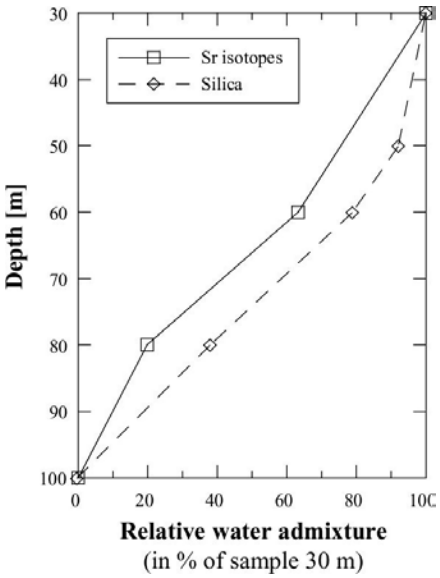

Fig. 27 : Mélange entre eau interstitielle et océan ouvert en fonction de la profondeur dans le récif calculé à partir des données isotopiques du Sr et des teneurs en H4SiO4 montrées dans la Fig. 24 (Fig. 9 de Steinmann et Dejardin, 2004).

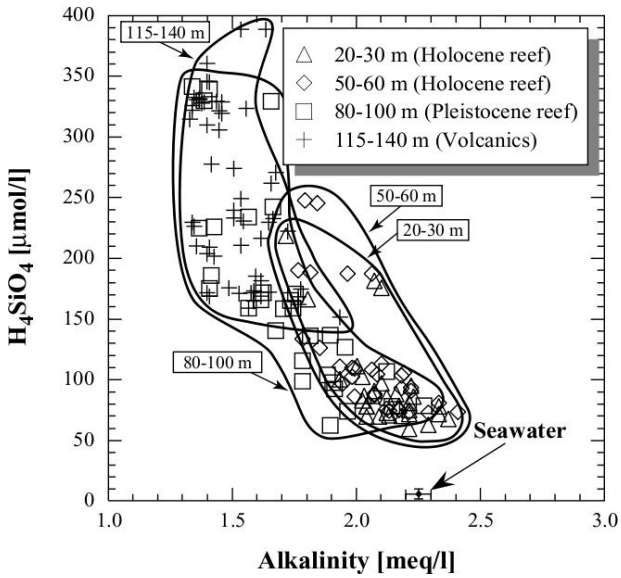

Fig. 28 : Comparaison entre les teneurs en silice et l'alcalinité de tous les échantillons d'eau interstitielle. On constate une corrélation négative entre les 2 paramètres et on peut observer un lien avec la profondeur : En s'approchant de la surface, les 2 paramètres évoluent progressivement vers des valeurs typiques pour une eau de mer (Fig. 6 de Steinmann et Dejardin, 2004).

Les données isotopiques du Sr se sont révélés particulièrement pertinentes pour tracer l'origine et les échanges des eaux interstitielles. Elles corroborent les résultats obtenus avec d'autres paramètres disponibles tels que la silice et l'alcalinité (Fig. 28) :

- ✗ Les teneurs en silice augmentent dans l'eau interstitielle lors de l'interaction eau-roche et les valeurs diminuent ensuite dans la structure récifale par dilution avec l'eau de mer caractérisée par des teneurs très faibles en silice (Fig. 24). Les calculs de mélange entre eaux interstitielles et eau de mer basée sur la silice indiquent une évolution similaire à ceux des isotopes du Sr (Fig. 27).
- ✗ L'alcalinité diminue lors de l'interaction eau roche dans le substratum basaltique, elle augmente

ensuite dans la structure récifale. L'alcalinité est dans un système carbonaté presque entièrement contrôlée par les teneurs en bicarbonates (Stumm et Morgan, 1996) et la précipitation de carbonates lors de l'interaction eau-roche induit une diminution de alcalinité de l'eau interstitielle. L'augmentation des valeurs dans la structure récifale s'explique directement par le mélange avec l'eau de mer, qui est caractérisée par une alcalinité élevée.

5.2.3 L'évolution de la circulation de l'eau interstitielle dans le temps

Dans le cadre de l'étude, les teneurs en silice et l'alcalinité peuvent donc être considérés, au même titre que les rapports isotopiques du Sr, comme des traceurs conservateurs. Ils tracent l'interaction eau-roche et le mélange entre eau interstitielle et eau de mer. Ceci permet d'intégrer dans l'étude les séries d'échantillons pour lesquels on ne dispose pas de données isotopiques et d'appréhender l'évolution de la circulation de l'eau interstitielle dans le temps. Trois types de profils de circulation on pu être distingués sur la base de l'évolution des teneurs en silice et de la salinité avec la profondeur (Fig. 29). Les résultats montrent, que le schéma de circulation de l'eau interstitielle évolue au cours des 2 ans du suivi (Fig. 30) : Pendant la première année (groupe 1 ; 6 séries d'échantillons entre 2/93 - 2/94), la circulation suit le schéma tel que décrit par les isotopes du Sr. A partir de la 2ème année (groupe 2 ; 5 séries d'échantillons entre 3/94 - 12/94) on constate une nouvelle zone d'alimentation en eau de mer profonde au niveau d'une surface de karstification située à la limite entre le recif pleistocène et holocène. Elle remplace en partie l'entrée d'eau de mer de la base du récif. Cette évolution générale est de temps en temps interrompue par des évènements ponctuels (groupe 3 ; 5 séries d'échantillons).

Les raisons pour ces changements de circulation n'ont pas pu être identifiées. Plusieurs pistes peuvent être proposées :

- Le flux de chaleur dans le socle volcanique dépend de la dynamique du panache mantellique dans le sous-sol du secteur d'étude. Un changement de flux de chaleur ferait varier l'intensité de l'interaction eau-roche et la dynamique d'alimentation en eau interstitielle à l'arrivée dans la zone récifale. Une diminution de l'apport serait substituée par une entrée latérale d'eau de mer plus importante, au niveau des surfaces karstifiées. Les données de flux de chaleur pour ces périodes, qui permettraient de tester cette hypothèse, ne sont pas disponibles.
- La porosité du récif peut varier dans le temps pour des raisons diagénétiques (dissolution et/ou précipitation de phases minérales) ou biologiques (colmatage temporaire par certains organismes) et ainsi faciliter ou empêcher l'infiltration d'eau de mer. Aucune donnée est disponible pour tester cette hypothèse.
- La circulation de l'eau interstitielle peut être sous l'influence directe de la circulation océanique. Un changement même léger de profondeur de la limite entre eau de surface et eaux antarctiques intermédiaires (AIW) (qui se trouve normalement à environ 200 m), pourrait avoir un impact direct sur la circulation interne du récif. On constate d'autre part que le passage de circulation du

groupe 1 au groupe 2 coïncide avec le début d'un évènement El Niño. Les changements des courants et des températures d'eau associés a un tel évènement pourraient expliquer les modifications observés. Mais la période d'observation effectuée est trop courte pour établir un lien précis.

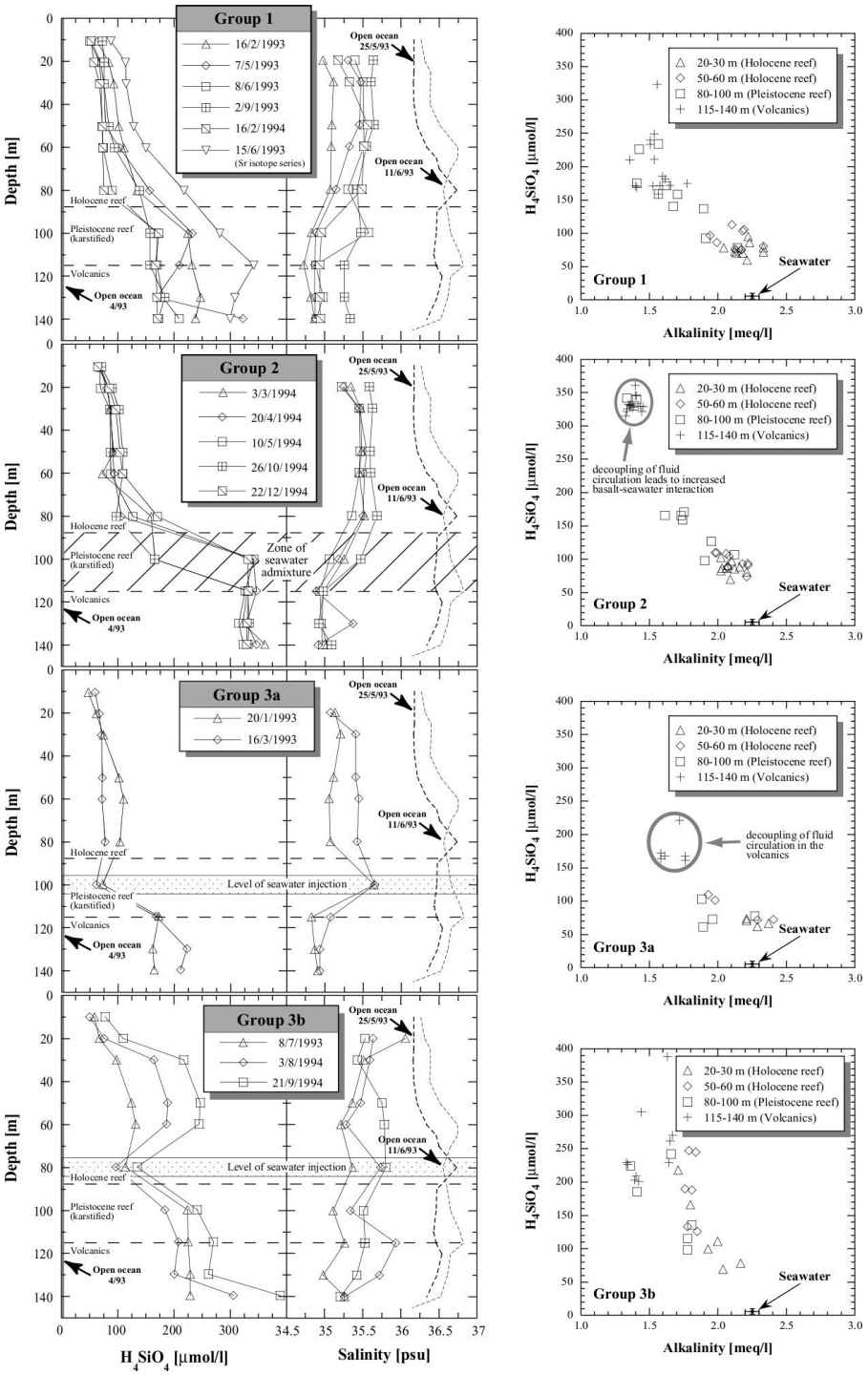

Fig. 29 : Évolution de la teneur en silice et de la salinitté des 16 séries d'eau interstitielle avec la profondeur. Sur la base de l'évolution de ces 2 paramètres, 3 groupes de circulation ont pu être distingués. Dans le diagramme H4SiO4 vs. alcalinité, les échantillons de chaque groupe définissent une répartition bien spécifique. L'évolution d'un groupe à l'autre peut être interprété en terme de changements de voies de circulation de l'eau interstitielle (Fig. 30) (Fig. 10 de Steinmann et Dejardin, 2004).

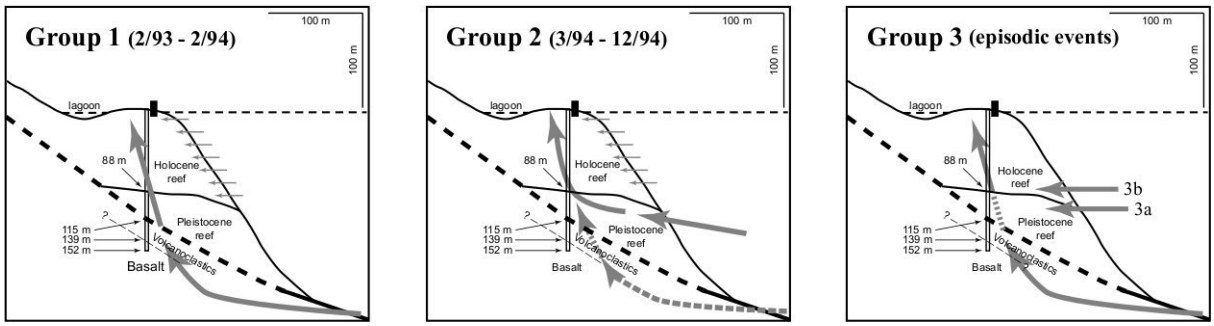

Fig. 30 : Différents schémas de circulation de l'eau interstitielle. Pendant la première année (groupe 1 ; 2/93 - 2/94), la circulation est alimentée par une infiltration d'eau de mer profonde à la limite basalte-récif, complétée par une infiltration diffuse dans la partie holocène du récif comme décrit par la Fig. 27. A partir de la 2ème année (groupe 2 ; 3/94 - 12/94) on constate une nouvelle alimentation d'eau de mer profonde au niveau d'une surface de karstification à la limite entre la partie pleistocène et holocène du récif, qui remplace en partie l'arrivée initiale à la base du récif. Cette évolution générale est de temps en temps interrompue par des évènements ponctuels (groupe 3). (Fig. 12 de Steinmann et Dejardin, 2004).

5.3 Perspectives de la thématique

Cette étude a clairement montré, que la migration des fluides interstitielles dans les récifs coralliens est un processus dynamique, qui évolue dans le temps. Plusieurs facteurs peuvent être à l'origine de ces variations et il est actuellement impossible de les hiérarchiser. Pourtant l'identification de l'origine de ces changements permettrait de savoir, si les circulations d'eau interstitielle sont contrôlées par des paramètres locaux (flux de chaleur) ou si elles sont sous l'influence de changements océanographiques ou climatiques plus globaux.

Les structures récifales sont aujourd'hui exposées à de nombreux changements imposés par l'homme. Qu'elles aient une origine locale (ex. installation de construction sur la structure récifale, contamination autour de zones portuaires) ou régionale (ex. changement climatique), ces perturbations vont avoir un impact sur la croissance et la conservation de la structure récifale et de l'intégralité de l'écosystème associé. Or, au delà de l'importante biodiversité qu'ils représentent, les récifs ont un rôle essentiel dans la protection de zones côtières, notamment contre la houle. Ils sont aussi le substratum de nombreuses îles et atolls océaniques. Une meilleure connaissance de la chimie des fluides interstitiels des récifs et de leur évolution dans le temps serait un moyen simple et efficace de suivre l'impact de l'homme et d'anticiper une éventuelle dégradation. Un suivi systématique de l'eau interstielle des récifs permettrait de mieux suivre et anticiper ces évolutions.

6 Origine et fractionnement des terres rares dans un contexte d'hydrothermalisme basse température

Publications associées :

- Bodeï, S., Buatier, M., **Steinmann, M.**, Adatte, T. & Wheat, C., 2008. Characterization of metalliferous sediment from a low-temperature hydrothermal environment on the Eastern Flank of the East Pacific Rise. Marine Geology 250, 128-141.
- Bodeï, S., **Steinmann, M.**, Buatier, M. Nd-Sr isotope and REY geochemistry of metalliferous sediments in a low-temperature off-axis hydrothermal environment (Costa Rica margin). en préparation.

Travaux de DEA et de thèse associés au projet :

- Bodeï, S., 2004. Transfert de matière et interactions eau-sédiment en environnement océanique (flanc de dorsale). DEA Environnement, Santé, Société . Université de Franche-Comté, Besançon, 30 pp.
- Bodeï, S., 2007. Étude minéralogique et géochimique de dépôts métallifères marins formés dans un contexte hydrothermal de basse température, sur le flanc Est de la dorsale Est-Pacifique. Thèse Université de Franche-Comté, Besançon, 264 pp.

6.1 Problématique

Les premières publications sur le comportement des TR en contexte hydrothermal étaient ciblées sur l'hydrothermalisme de haute température. Ces travaux ont montré une forte anomalie positive en Eu des eaux hydrothermales provenant de l'altération préférentielle des plagioclases dans la croûte océanique et indiquant ainsi que les spectres de TR dans l'eau hydrothermale reflètent au moins partiellement la minéralogie des phases altérées (Michard *et al.*, 1983; Klinkhammer *et al.*, 1994). Des travaux plus récents ont également mis en évidence un fractionnement des TR à la limite entre un panache d'eau hydrothermale et l'eau de mer environnante, par complexation en phase liquide avec des ligands de l'eau de mer et par précipitation de phases minérales secondaires (Bau et Dulski, 1999; Douville *et al.*, 1999; 2002; Humphris et Bach, 2005). Parmi ces dernières, la précipitation d'oxyhydroxydes Fe-Mn, semble extraire la quasi-totalité des TR de la solution. Ceci est confirmé par la composition isotopique du Nd de l'eau de mer, qui indique que les TR des océans du monde entier proviennent essentiellement de l'érosion continentale (Piepgras et Wasserburg, 1980; van de Flierdt *et al.*, 2004; 2007).

L'hydrothermalisme océanique de haute température montre une large gamme de températures (180-400 °C) et de pH (2.8-5). Ceci permet d'étudier la complexation en phase liquide et la co-précipitation des TR sous des conditions physico-chimiques très variables et plutôt insolites pour un milieu naturel. L'étude des systèmes hydrothermaux a donc un intérêt non seulement pour la compréhension des processus d'hydrothermalisme proprement dit, mais ces sites constituent aussi de grands laboratoires naturels pour l'étude du comportement physico-chimique des TR et d'autres éléments traces.

Les études du comportement des TR dans les systèmes hydrothermaux de basse température sont plutôt rares (ex. Usui *et al.*, 1997; Wheat *et al.*, 2002). Il s'agit de systèmes beaucoup plus diffus, moins spectaculaires et moins connus. Toutefois, la plus faible intensité des échanges est compensée par des superficies plus importantes à l'échelle du globe et on estime que la chimie des océans dépend plus fortement de l'hydrothermalisme de basse température que de celui de haute température (Jacobson, 1992; Mottl et Wheat, 1994; Wheat et MeDuff, 1994; Schultz et Elderfield, 1997; Wheat *et al.*, 2002). La circulation hydrothermale de basse température se localise principalement sur des hauts fonds marins ou "seamounts" caractérisés par une couverture sédimentaire de faible épaisseur, facilitant l'infiltration de l'eau de mer en entrée et son expulsion en sortie de circuit hydrothermal (Fisher *et al.*, 2003). L'eau s'infiltre dans le basalte fracturé, migre latéralement à l'intérieur de la croûte océanique en suivant le gradient thermique et ressort finalement dans des zones de remontées hydrothermales. Pendant ce trajet, la composition chimique de l'eau hydrothermale évolue (Wheat et MeDuff, 1994; Elderfield *et al.*, 1999; Wheat *et al.*, 2002). Dans les zones de résurgence d'eau hydrothermale, la composition chimique et minéralogique de la couverture sédimentaire est fortement modifiée, notamment par la précipitation de minéraux néoformés tels que des argiles et des oxyhydroxydes Fe-Mn (Honnorez *et al.*, 1983; Buatier *et al.*, 1995; 2001; Usui *et al.*, 1997).

Les données présentées ici proviennent de la thèse de Sabine Bodeï (Bodeï, 2007), dont j'ai été co-directeur avec M. Buatier. L'objectif des analyses géochimiques et isotopiques était à la fois de caractériser le comportement des TR en contexte hydrothermal de basse température et d'identifier les processus de formation des différentes phases minérales observées (Bodeï *et al.*, 2007; 2008). Une publication focalisée sur ces aspects géochimiques et isotopiques est en cours de rédaction (Bodeï *et al.*, in prep).

6.2 Contexte de l'étude

6.2.1 Origine et caractérisation des échantillons

Le site d'étude se trouve sur la plaque Cocos sur le flanc Est de la dorsale Est Pacifique (EPR, East Pacific Rise), au large du Costa Rica (Fig. 31). Les échantillons ont été récupérés lors de la mission "Ticoflux II" en 2001 au pied d'un seamount de 100 m de haut, nommé "Dorado" et situé à 3150 m de profondeur, sur une croûte océanique vielle de 18-24 Ma (Fisher *et al.*, 2003). L'étude est essentiellement basée sur la carotte 50GC, pour laquelle le flux de chaleur élevé et la chimie des eaux interstitielles indiquent la présence d'une zone active de remontée d'eaux hydrothermales. Afin de comparer les sédiments de la carotte 50 GC avec des sédiments non-altérés, nous avons intégré des échantillons de carottages voisins non atteints par une remontée hydrothermale, nous les appellerons "sédiments de référence" (Bodeï *et al.*, 2008).

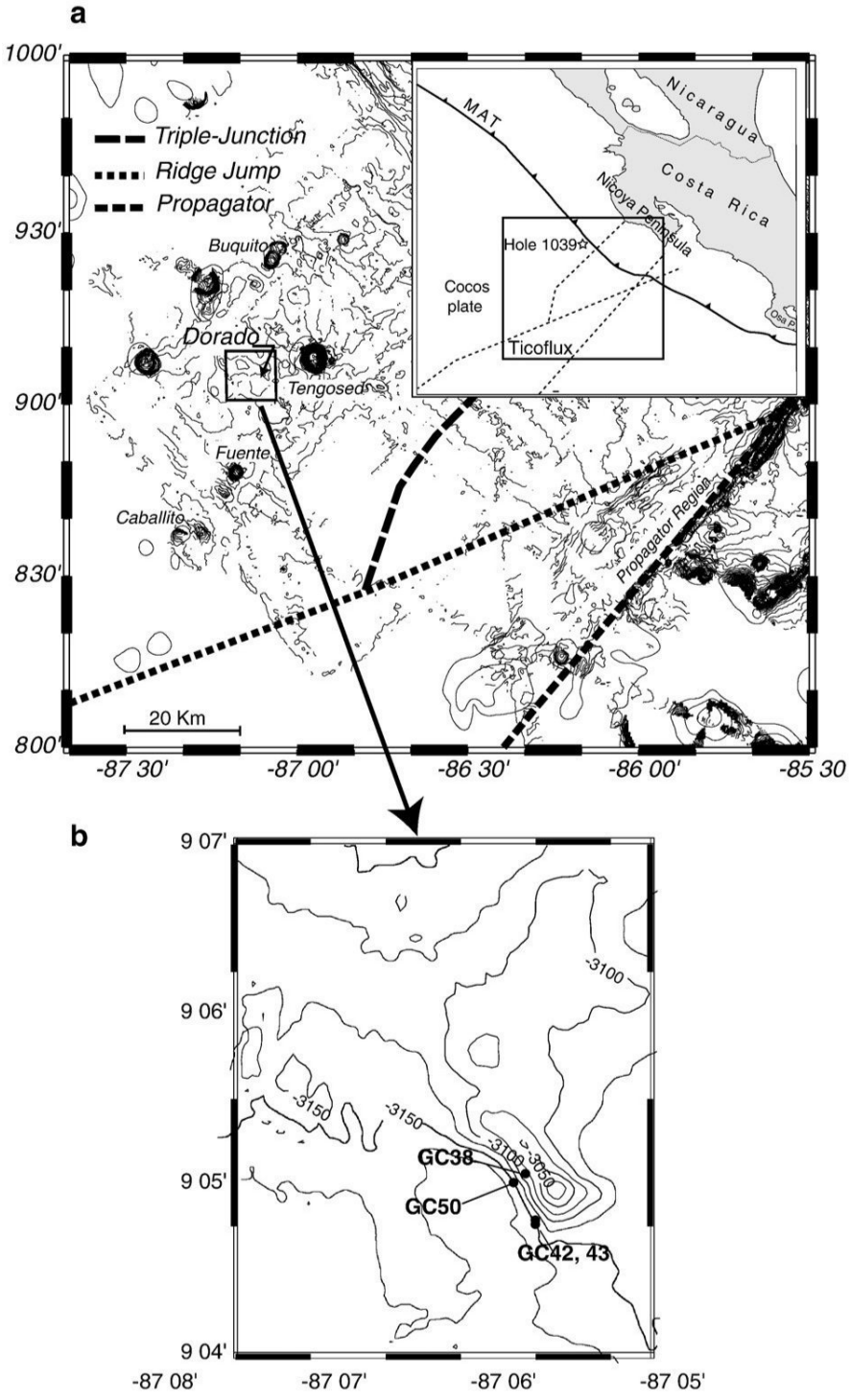

Fig. 31 : A) Situtation générale du site du seamount "Dorado" et B) carte détaillée de "Dorado" avec localisation de la carotte 50 GC et des sites voisins sans activité hydrothermale (Fig. 1 de Bodeï et al., 2008).

Les sédiments de la carotte 50 GC sont des séries hémi-pélagiques non-carbonatées, contenant du quartz, des feldspaths, des argiles, des verres volcaniques et des fragments d'organismes siliceux (radiolaires, diatomées, spicules d'éponge). Quantitativement, ces phases primaires sont minoritaires par rapport aux phases néoformées. Ces dernières se composent de zéolithes (phillipsite) et de barite ($BaSO_4$) entre 12 à 70 cm bsf ("below sea floor") et d'oxyhydroxides Fe-Mn et d'apatite en dessous de 100 cm bsf. Au MEB on constate que les oxyhydroxides Fe-Mn et l'apatite ont précipité sur des phillipsites déjà

néoformés. Pour les oxyhydroxides Fe-Mn, on observe une dominance du Fe entre 124 et 110 cm bsf, et une dominance du Mn à 100 cm bsf. Les oxydes de Mn se présentent sous forme de micro-concrétions zonées riches en vernadite au centre et en todorokite sur les bords (Bodeï *et al.*, 2007).

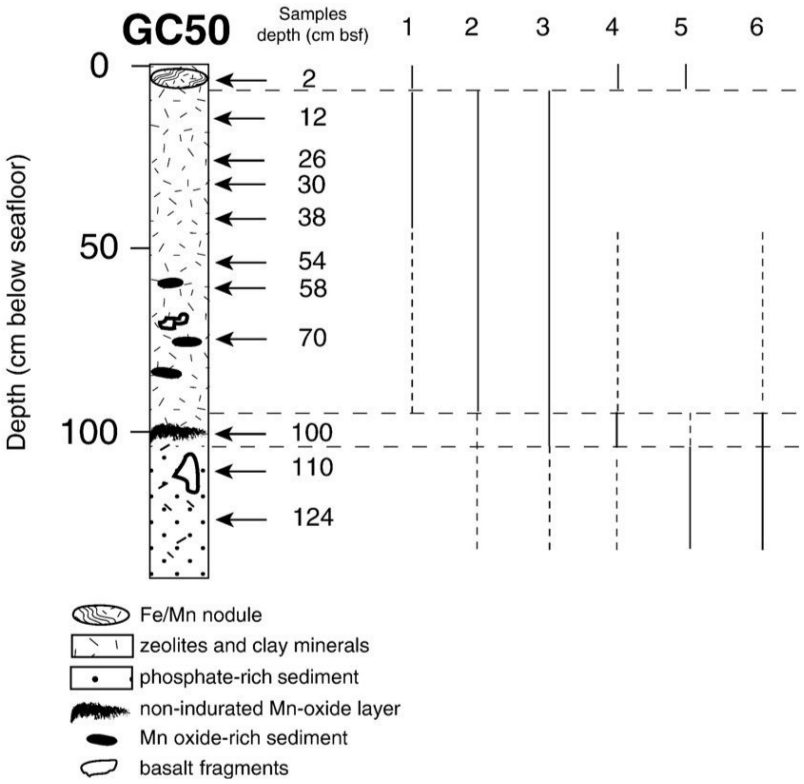

Fig. 32 : Log stratigraphique de la carotte 50 GC, localisation des échantillons et répartition des différentes composantes : 1 = particules de verres volcaniques et microfossiles siliceux ; 2 = argiles détritiques ; 3 = phillipsite ; 4 = oydes Mn ; 5 = oxydes Fe ; 6 = apatite (Fig. 2 de Bodeï et al., 2008).

La carotte 50 GC est caractérisée par l'abondance de phases néoformées par rapport aux sédiments de référence, dans lesquels on observe principalement des composantes primaires (quartz, feldspaths, argiles, verres volcaniques, fragments d'organismes siliceux). Les séries ne présentaient pas de micro-fossiles permettant de réaliser de datation, mais étant donné l'âge du substratum basaltique (de 18-24 Ma), il s'agit à priori pour l'essentiel de séries d'âge Miocène et Pliocène (Fig. 32 ; Bodeï *et al.*, 2008).

6.2.2 Approche méthodologique

Les spectres de TR des phases néoformées reflètent à la fois le spectre de leur source ainsi que les processus intervenus lors de leur mobilisation et leur transfert vers la phase néoformée. Les isotopes radiogéniques du Sr et du Nd reflètent uniquement la source et les processus de mélange (ex. Faure, 1986), ils permettent ainsi de distinguer ces 2 origines. L'utilisation des spectres de TR seul pourrait dans le contexte de l'étude mener à des interprétations erronées.

Les analyses chimiques et isotopiques ont été réalisées sur des échantillons de roche totale ainsi que sur la phase résiduelle et la phase lessivée issue d'une procédure de leaching à l'HCl 1 N (15 Min à température ambiante, Clauer *et al.*, 1993; Stille et Clauer, 1994; Innocent *et al.*, 1999). Cette procédure

a pour objectif de séparer les phases néoformées (leachates) de la phase détritique (résidue). La distinction entre leachate et résidue est définie de façon opérationnelle : Ces 2 fractions ne correspondent pas parfaitement aux phases respectivement authigènes et résiduelles. La procédure retenue est donc une extraction dite "trop faible", ne mobilisant qu'en partie la phase néoformée et permettant d'être sûre d'obtenir les phases néoformées pures, sans contamination notable par la phase détritique. La composition chimique et isotopique des phases néoformées permet de caractériser le fluide à partir duquel elles ont précipité. De son côté, le résidu représente un mélange entre phases détritiques et phases authigènes non-lessivées.

6.3 Principaux résultats et discussion

6.3.1 Caractérisation du leachate

Dans la Fig. 33 sont présentés des facteurs d'enrichissement E_i *. Ils permettent de comparer l'enrichissement en éléments majeurs de la carotte 50 GC par rapport aux sédiments de référence. Le diagramme montre que les sédiments à la base de la carotte 50 GC sont fortement enrichis en CaO, Fe_2O_3, MnO et P_2O_5 par rapport aux sédiments de référence et que cet enrichissement diminue ensuite vers la surface.

Fig. 33 : Comparaison de la composition en éléments majeurs entre la série de la carotte 50 GC et les sédiments de référence, par les facteurs d'enrichissement (voir texte). Les sédiments à la base de la carotte 50 GC sont fortement enrichis en CaO, Fe2O3, MnO et P2O5. Le niveau à 100 cm bsf est un encroûtement en oxyde de Mn (Fig. 8b de Bodeï et al., 2008).

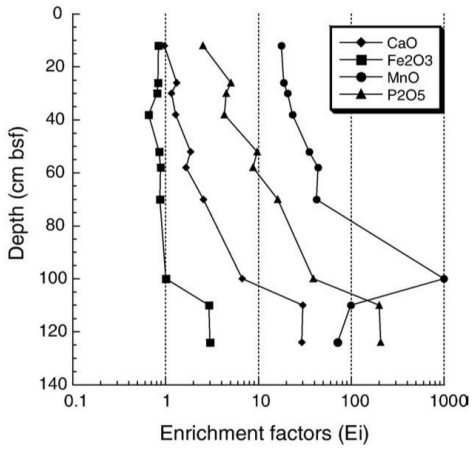

Les pourcentages d'éléments majeurs mobilisés par la procédure de leaching à l'HCl 1 N sont présentés dans la Fig. 34. Dans la carotte 50 GC on constate, que le leaching a mobilisé la quasi-totalité du P_2O_5 et du CaO, mais presque pas de Fe_2O_3, MnO et SiO_2. De plus les teneurs en P_2O_5 et CaO dans les leachates sont parfaitement corrélées (r = 0.999, n = 9). Pour les sédiments de référence les taux d'extraction sont plus faibles pour le P_2O_5 et CaO, mais quasiment identiques pour les autres éléments majeurs.

* $E_i = \{C_i/C_{Al}\}_{éch} / \{C_i/C_{Al}\}_{sédréf}$, avec "$C_i$" = concentration de l'élément "i" et "C_{Al}" = concentration an Al (Li, 1982)

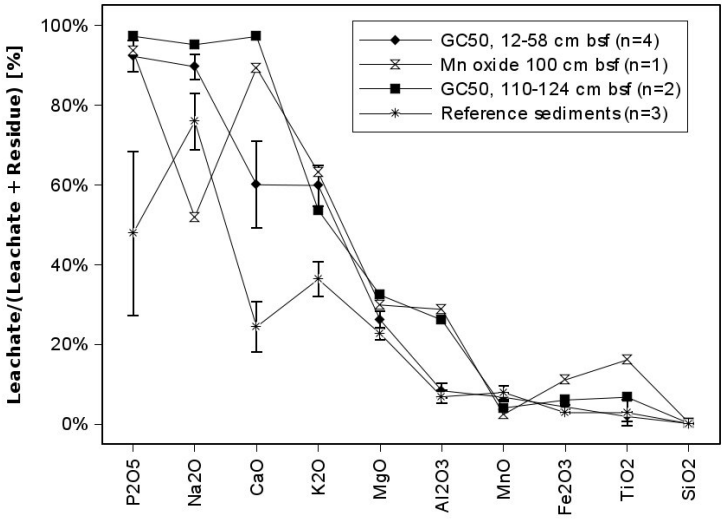

Fig. 34 : Pourcentages d'éléments majeurs mobilisés lors du leaching à l'HCl 1 N dans les sédiments de la carotte 50 GC et les sédiments de référence. Le leaching a mobilisé la quasi-totalité du P2O5, Na2O et CaO, quasiment pas de MnO, Fe2O3 et SiO2. Les barres d'erreurs désignent l'écart-type.

L'analyse minéralogique de la carotte 50 GC a permis d'identifier des phillipsites, des oxyhydroxides Fe-Mn et des apatites néoformées (Bodeï *et al.*, 2008). La répartition des oxyhydroxides Fe-Mn et des apatites est bien corrélée avec les enrichissements en Fe_2O_3, MnO, CaO et P_2O_5 présentés dans la Fig. 33. On peut donc émettre l'hypothèse, que ces enrichissements en éléments majeurs sont directement liés à l'authigenèse d'oxyhydroxides Fe-Mn et d'apatites. L'absence de lien entre la présence de phillipsites et l'évolution chimique suggère, que la phillipsite s'est formée in situ à partir d'une phase minérale primaire, sans apport d'éléments chimiques de l'extérieur.

Les pourcentages d'éléments majeurs mobilisés par le leaching montrent que, parmi les phases minérales authigènes, la procédure a avant tout mobilisé de l'apatite, éventuellement un peu d'oxyhydroxide Fe-Mn, mais pas de phillipsite. L'hypothèse de mise en solution de l'apatite est validée par l'excellente corrélation entre CaO et P_2O_5. Cette corrélation, qui s'étend sur l'intégralité de la carotte 50 GC, indique également, que l'apatite n'est pas uniquement présente à la base de la carotte, comme suggéré par les observations minéralogiques, mais également en plus faibles quantités dans la partie supérieure, au-dessus de 100 cm bsf. Les taux importants de leaching observés pour le Na_2O et K_2O sont probablement dues à la dissolution de cristaux de sels provenant de l'eau interstitielle actuelle.

6.3.2 Isotopes du Nd et du Sr

Les données isotopiques du Sr et du Nd de la carotte 50 GC sont présentées dans les figures 35 et 36. Pour comparaison, les diagrammes montrent également la composition de l'eau de mer, des basaltes océaniques et des sédiments de référence. Les rapports isotopiques de l'eau de mer sont les valeurs actuelles. Il faut préciser que le rapport $^{87}Sr/^{86}Sr$ de l'eau de mer était à 0.7085, il y a 20 Ma et qu'il a augmenté depuis de façon continue pour atteindre 0.709165 aujourd'hui (Hodell *et al.*, 1991). L'évolution du rapport isotopique du Nd de l'eau de mer est plus complexe, parce que sa valeur ne varie pas uniquement avec le temps, mais également avec la localisation géographique et la profondeur dans

l'océan (van de Flierdt *et al.*, 2004; Meynadier *et al.*, 2008). L'absence de données stratigraphiques ne nous permet pas de reconstruire de manière fiable l'évolution de la profondeur et de la position géographique de la carotte 50 GC, au cours de son histoire. Toutefois, les données disponibles dans la littérature suggèrent que le rapport $^{143}Nd/^{144}Nd$ a varié entre 0.51245 (ε_{Nd} = -3.7) et 0.51249 (ε_{Nd} = -2.9) dans le secteur d'étude pendant les derniers 20 Ma (van de Flierdt *et al.*, 2004), ce qui est inférieur ou égal aux plus faibles valeurs analysées dans la carotte 50 GC. En résumé, on peut dire que les compositions isotopiques du Sr et du Nd de la carotte 50 GC restent, au delà de l'âge réel des sédiments, toujours intermédiaires entre un pôle lithologique représenté par les sédiments de référence ou la croûte océanique et l'eau de mer. C'est la raison pour laquelle, nous utiliserons systématiquement dans la discussion la composition isotopique du Sr de du Nd de l'eau de mer actuelle, sachant que les conclusions seront extrapolables aux périodes antérieures.

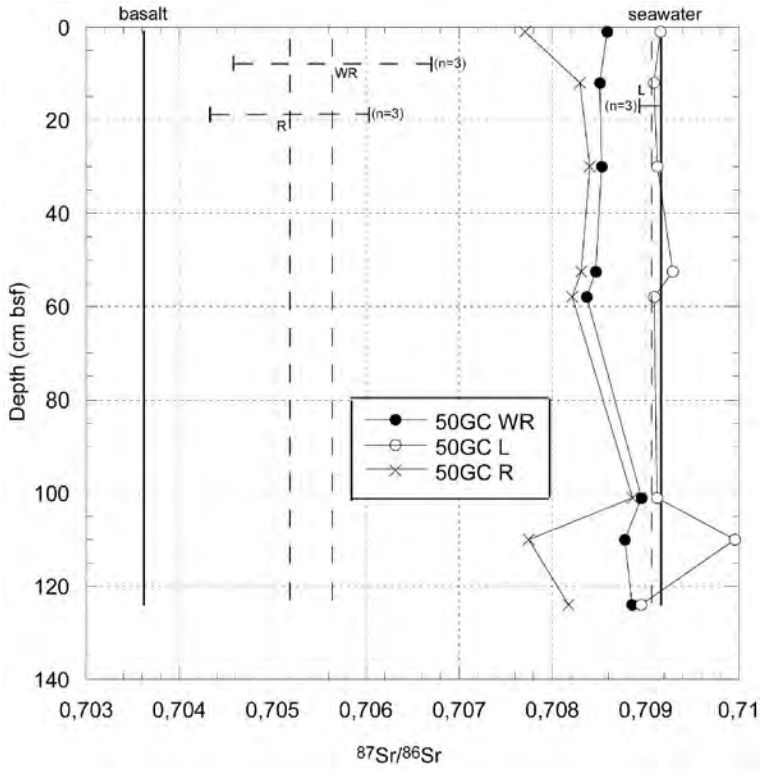

Fig. 35 : Composition isotopique du Sr des échantillons de roche totale (WR), des leachates (L) et des résidus (R) de la carotte 50 GC. Les compositions moyennes avec écart types des sédiments de référence (sites voisins sans activité hydrothermale), ainsi que celles du basalte océanique et de l'eau de mer actuelle (Palmer et Elderfield, 1985) sont données pour comparaison (Fig. 4 de Bodeï et al., in prep).

Dans la carotte 50 GC on n'observe pas d'évolution systématique de la composition isotopique du Sr avec la profondeur (Fig. 35). On constate que les compositions des leachates sont identiques à celles de l'eau de mer actuelle, tandis que les compositions des résidus et de la roche totale sont décalées vers les valeurs des sédiments de référence. Les rapports $^{87}Sr/^{86}Sr$ de la roche totale sont systématiquement intermédiaires entre leachate et résidu comme cela est exigé par le bilan de masse. Contrairement au Sr, les compositions isotopiques du Nd montrent une évolution avec la profondeur et on trouve des valeurs proches de l'eau de mer à la base de la carotte (Fig. 36). Les rapports $^{143}Nd/^{144}Nd$ des leachates s'approchent, comme pour les isotopes du Sr, de l'eau de mer et le faible écart part rapport à la roche

totale montre que le Nd des leachates domine également le rapport $^{143}Nd/^{144}Nd$ de la roche totale. Ces données isotopiques du Nd sont présentées de façon plus détaillée dans le diagramme d'isochrone Sm-Nd (Fig. 37). Les points définissent une droite de mélange entre les échantillons de référence et l'eau de mer. Entre ces 2 pôles; on constate comme dans la Fig. 36 une évolution progressive du sommet à la base de la carotte.

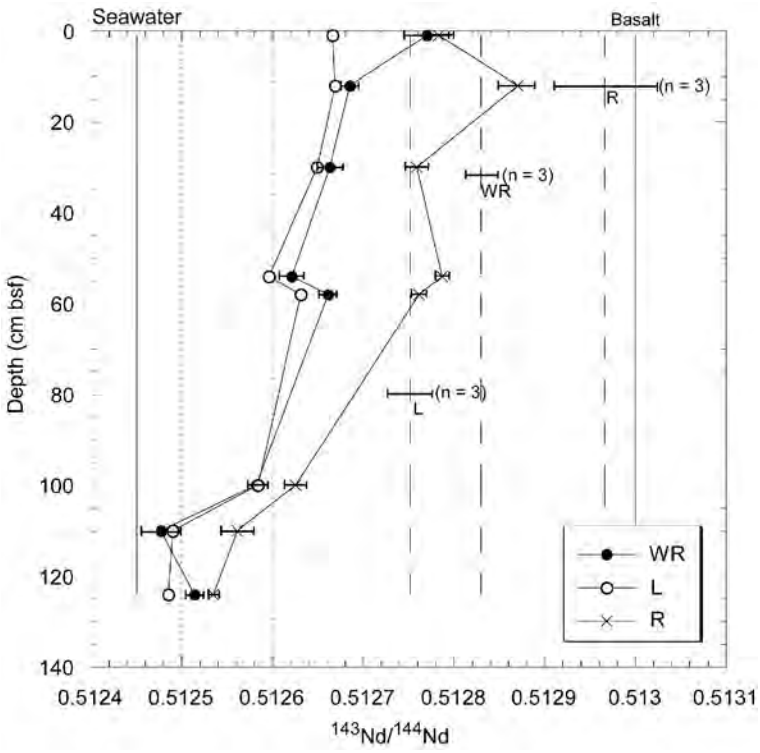

Fig. 36 : Composition isotopique du Nd des échantillons de roche totale (WR), des leachates (L) et des résidus (R) de la carotte 50 GC. Les compositions moyennes avec écart types des sédiments de référence, ainsi que celles du basalte océanique et de l'eau de mer actuelle du Pacifique à 2000 m (van de Flierdt et al., 2004) sont données pour comparaison (Fig. 5 de Bodeï et al., in prep).

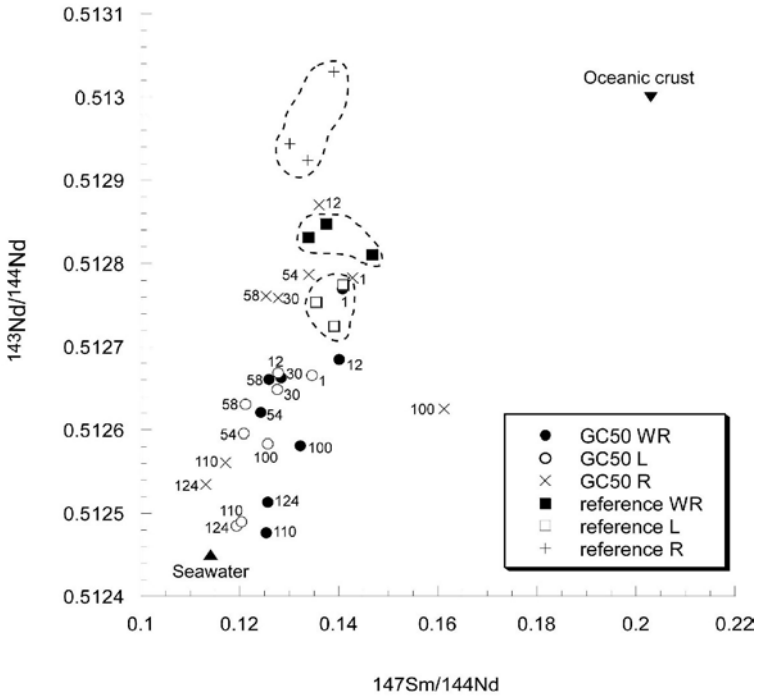

Fig. 37 : Diagramme d'isochrone Sm-Nd des données de la Fig. 36. Les données de la carotte 50 GC définissent une droite de mélange entre les échantillons de référence et l'eau de mer. Les chiffres à côté des points de données indiquent la profondeur dans la carotte 50 GC (Fig. 6 de Bodeï et al., in prep).

Les rapports isotopiques du Sr montrent clairement que nous avons, par la procédure de leaching, extrait une phase minérale qui était en équilibre avec un fluide de composition de l'eau de mer. Les données isotopiques du Nd indiquent en plus que la signature de l'eau de mer est la plus forte à la base de la carotte 50 GC et qu'elle diminue vers la surface. Les isotopes du Sr et du Nd ne suivent pas la même évolution avec la profondeur. La Fig. 38 présente les données des 2 systèmes isotopiques dans un diagramme classiquement utilisé pour quantifier les interactions eau-roche (Faure, 1986). Dans ce diagramme on compare les valeurs de la carotte 50 GC avec une courbe calculée pour un mélange entre eau de mer et sédiment de référence. On constate que les échantillons de la carotte 50 GC suivent assez bien la courbe de mélange et la comparaison avec les rapports eau/roche théoriques indiqués le long de la courbe suggèrent, qu'un rapport eau/roche entre 10 E6 et 10 E8 est nécessaire à expliquer les compositions isotopiques observées pour des échantillons de la carotte 50 GC. On constate également que le rapport eau/roche augmente avec la profondeur dans la carotte.

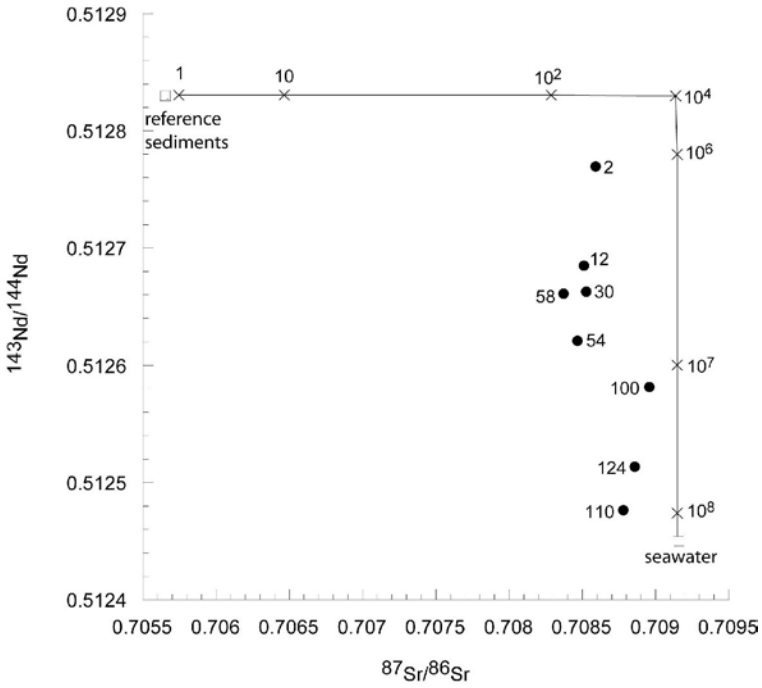

Fig. 38 : Diagramme 143Nd/144Nd vs. 87Sr/86Sr avec les données de roche totale de la carotte 50 GC. Les nombres à côté des points donnent la profondeur dans la carotte en cm. La ligne entre sédiments de référence et eau de mer est une courbe de mélange calculée d'après la procédure décrite dans Faure, 1986. Les valeurs indiquées le long de la courbe donnent le rapport eau/roche en L/kg nécessaire pour transformer le sédiment de référence en sédiment hydrothermal altéré avec une composition isotopique donnée. Le diagramme montre qu'un rapport eau/roche entre 10 E6 et 10 E8 est nécessaire pour expliquer les compositions isotopiques odes sédiments de la carotte 50 GC et qu'il augmente avec la profondeur (Fig. 12 de Bodeï et al., in prep).

La courbe de mélange de la Fig. 38 montre que le rapport $^{87}Sr/^{86}Sr$ est modifié le premier lors de l'interaction eau/roche et que le rapport $^{143}Nd/^{144}Nd$ change uniquement à partir d'un rapport eau/roche de 10 E4. Cette différence de comportement des 2 systèmes isotopiques en contexte hydrothermal est bien connue (Faure, 1986). Elle est due au rapport de concentration Sr/Nd, qui est beaucoup plus élevé dans l'eau de mer (Sr/Nd∼2.7 E6 avec Sr = 8 mg/L et Nd = 3 ng/L) que dans le sédiment (Sr/Nd∼15 avec Sr = 260 ppm et Nd = 17 ppm). Par conséquent, le rapport $^{87}Sr/^{86}Sr$ du sédiment de référence est beaucoup plus vite affecté par l'interaction eau/roche que le rapport $^{143}Nd/^{144}Nd$. Ceci explique pourquoi on observe partout dans la carotte 50 GC des rapports isotopiques du Sr proches de l'eau de mer (Fig. 35), tandis que

ceux du Nd s'approchent de la composition de l'eau de mer uniquement à la base de la carotte, là où les rapports eau/roche sont les plus élevés (Fig. 36).

En conclusion, les données isotopiques du Sr et du Nd nous indiquent, que les sédiments de la carotte 50 GC ont subi une forte interaction avec un fluide de composition d'eau de mer et que cette interaction a été la plus forte à la base de la carotte.

6.3.3 Les Terres Rares

Les teneurs en TR de la roche totale sont de 40 ppm environ pour le Nd à la base de la carotte 50 GC, elles atteignent un maximum d'environ 60 ppm de Nd à 60 cm bsf et redescendent à 35 ppm de Nd vers la surface (Fig. 39). Ces valeurs sont largement au-dessus de la valeur moyenne des sédiments de référence, qui est de 17 ± 1 ppm (±écart type, n = 3). Les teneurs sont quasi identiques dans les leachates (tout comme les données isotopiques du Nd), donc la quasi-totalité des TR de la roche totale se trouve dans la phase lessivable. Les teneurs en Nd de la roche totale des échantillons de 10 à 60 cm bsf sont corrélées avec les teneurs en P_2O_5 (Fig. 40), suggérant que les TR de ces échantillons sont fixées dans les apatites authigènes. Dans la chapitre 6.3.1 nous avons montré que ces apatites on presque entièrement été dissous lors du leaching. Cette hypothèse est confirmée par les données isotopiques du Nd et les données de TR. Les échantillons de la base de la carotte (110 et 124 cm bsf) et les niveaux riches en oxydes de Mn (à 2 et 100 cm bsf) ne rentrent pas dans la corrélation de la Fig. 40, la spéciation des TR semble être différente pour ces échantillons.

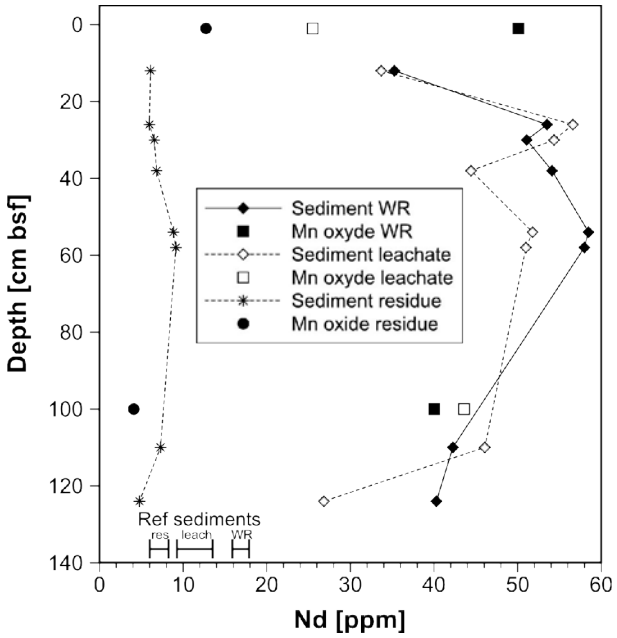

Fig. 39 : Log des teneurs en Nd avec la profondeur dans les échantillons de roche totale, les leachates et les résidus de la carotte 50 GC. Les niveaux essentiellement composés d'oxydes de Mn sont présentés séparément. La comparaison avec les teneurs moyennes des sédiments de référence montre que la roche totale et les leachates de la carotte 50 GC sont fortement enrichis en Nd, tandis que les concentrations des résidus sont similaires.

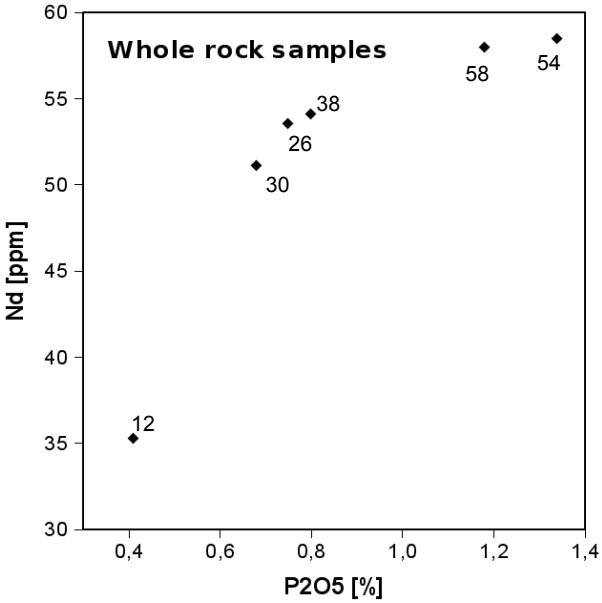

Fig. 40 : Corrélation entre les teneurs en Nd et P2O5 dans les échantillons de roche totale de la carotte 50 GC. Les niveaux riches en apatite et oxyhydroxydes de Fe à la base de la carotte (110 et 124 cm bsf), ainsi que les niveaux d'oxydes de Mn (2 et 100 cm bsf) ne rentrent pas dans la corrélation et ne sont pas présentés. Les étiquettes des points de données indiquent la profondeur dans la carotte en cm bsf.

Les spectres de TR normalisés par rapport au PAAS des échantillons de roche totale, des leachates et des résidus de la carotte 50 GC sont présentés dans la Fig. 41, avec les sédiments de référence et l'eau de mer actuelle du Pacifique à 2500 m (Alibo et Nozaki, 1999). L'échantillon 50GC2 est un nodule d'oxydes Mn provenant du sédiment superficiel, ses caractéristiques sont complètement différentes des autres échantillons. Pour ces derniers, on observe pour la roche totale une anomalie positive en Eu et une anomalie négative en Ce, qui évoluent régulièrement avec la profondeur (Fig. 42). L'anomalie positive en Eu disparaît presque entièrement dans les leachates, tandis que l'anomalie en Ce s'accentue (Fig. 41). Pour les résidus on observe inversement une anomalie positive en Eu plus prononcée et quasiment pas d'anomalie en Ce.

Cette répartition des anomalies en Ce et en Eu dans les différentes fractions indique que la phase porteuse de l'anomalie négative en Ce se trouve essentiellement dans les leachates et celle de l'anomalie en Eu dans la phase résiduelle. La similitude entre l'anomalie du Ce des leachates et l'eau de mer suggère que la procédure de leaching a permis de séparer une phase minérale précipitée en équilibre avec un solution de type eau de mer. Cette suggestion est confirmée par la corrélation entre les valeurs Ce/Ce* et $^{143}Nd/^{144}Nd$ des leachates et des échantillons de roche totale de la carotte 50 GC (Fig. 43). Les points sont alignés sur une droite de mélange entre sédiments de référence et eau de mer. Globalement, et à l'exception des 2 échantillons les plus profonds (110 et 124 cm bsf), les échantillons les plus profonds s'approchent d'avantage de la composition de l'eau de mer et les leachates sont, par rapport à leur roche totale, toujours décalés en direction de l'eau de mer. Ce diagramme confirme qu'il est possible d'interpréter la composition chimique et isotopique des sédiments de 21 à 100 cm bsf de la carotte 50 GC comme un sédiment de type sédiment de référence, qui a subi une forte interaction eau/roche avec un fluide de type eau de mer. L'anomalie en Ce trace donc, comme le rapport isotopique du Nd, l'interaction eau/roche.

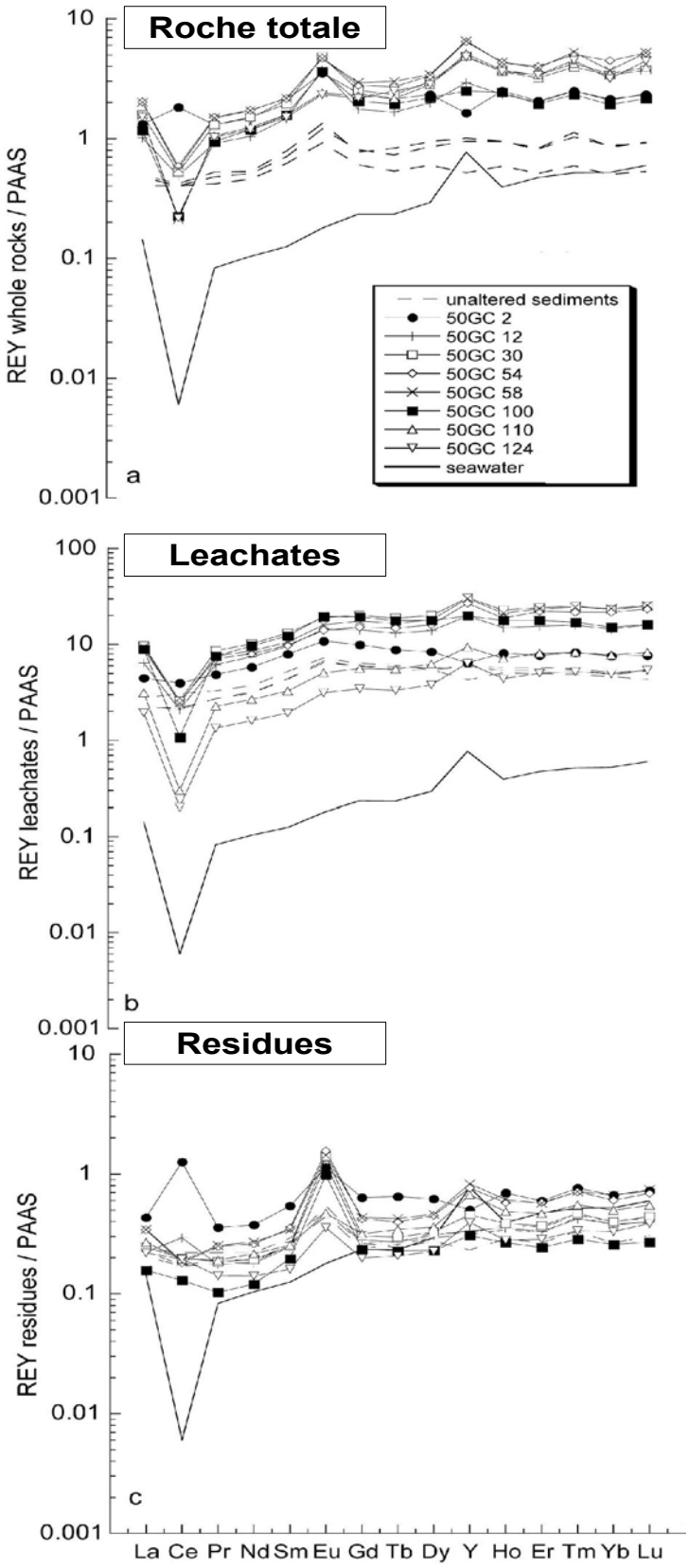

Fig. 41 : Spectres des TR des échantillons de roche totale (WR), des leachates (L) et des résidus (R) de la carotte 50 GC normalisés par rapport au PAAS (McLennan, 1989). Les spectres des sédiments de référence, ainsi que celui de l'eau de mer actuelle du Pacifique à 2500 m (Alibo et Nozaki, 1999) sont donnés pour comparaison. Le spectre de l'eau de mer a été multiplié d'un facteur de 1000 pour faciliter la comparaison (Fig. 7 de Bodeï et al., in prep).

La comparaison des différents spectres de TR (Fig. 41) suggère que l'anomalie en Eu est principalement portée par la phase résiduelle. Ceci est confirmé par la Fig. 42 : Les valeurs Eu/Eu*de la

roche totale et des résidus à la base de la carotte 50 GC sont similaires aux valeurs des sédiments de référence. Dans la partie supérieure de la carotte, l'anomalie positive en Eu s'accentue régulièrement et dépasse largement les valeurs du sédiment de référence, surtout dans les résidus. Cette évolution pourrait s'expliquer par l'altération d'une phase enrichie en Eu, par interaction eau/roche à la base de la carotte 50 GC, suivi de la précipitation d'une phase minérale secondaire non soluble à l'HCl et contenant l'Eu mobilisé plus en profondeur. La phase minérale typiquement enrichie en Eu est le plagioclase (McLennan, 1989) et on peut donc émettre l'hypothèse, que ce minéral a été altéré à la base de la carotte. La phillipsite, observée en quantités abondantes dans la partie supérieure de la série (Fig. 32), pourrait correspondre à la phase minérale secondaire porteuse de la forte anomalie positive en Eu. La quasi absence de phillipsites dans les sédiments de référence (Bodeï *et al.*, 2008) concorde avec cette hypothèse.

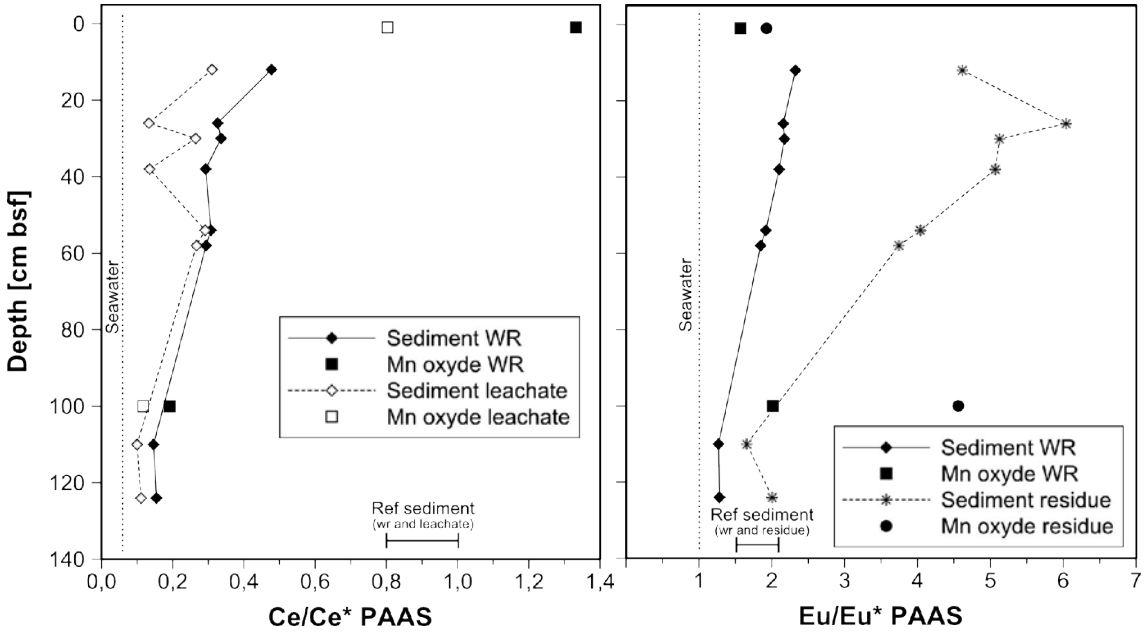

Fig. 42 : Évolution avec la profondeur de l'anomalie du Ce et de l'Eu dans les échantillons de roche totale de la carotte 50 GC. Les valeurs de l'eau de mer actuelle du Pacifique à 2500 m (Alibo et Nozaki, 1999) et du sédiment de référence sont données pour comparaison (Fig. 10 de Bodeï et al., 2008).

6.4 Interprétation

6.4.1 Les scénarios envisageables

Le scénario le plus simple, pour expliquer les données de la carotte 50 GC, est un scénario, qui débute loin de la dorsale Est Pacifique, avec le dépôt d'une série de sédiments hémipélagiques. Ces sédiments sont ensuite altérés lors de la remontée d'une eau hydrothermale de basse température, provoquant les variations minéralogiques, chimiques et isotopiques observées. Cette eau hydrothermale aurait conservée la signature chimique et isotopique de l'eau de mer lors de son passage dans la croûte

océanique. Ce premier scénario n'intègre pas le cadre géodynamique du secteur d'étude et c'est la raison pour laquelle je l'appellerai **scénario statique**.

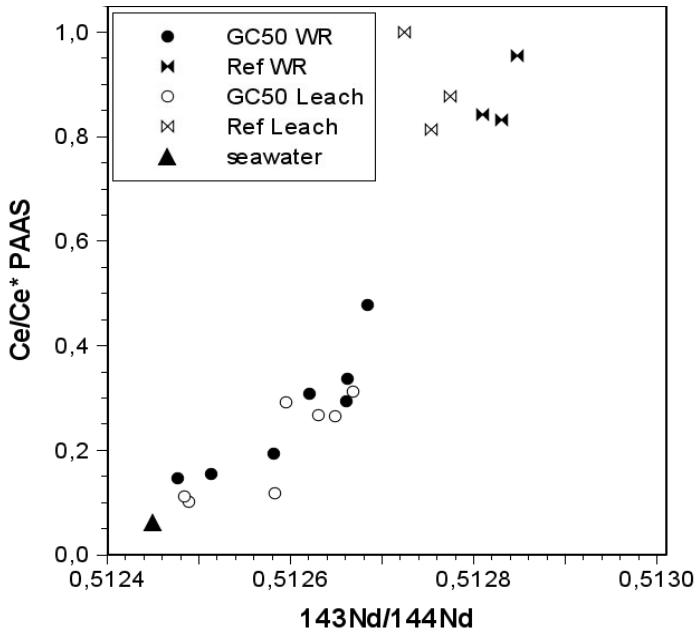

Fig. 43 : Corrélation entre anomalie du Ce et 143Nd/144Nd pour les leachates et les échantillons de roche totale de la carotte 50 GC et des sédiments de référence. Les échantillons de la carotte 50 GC occupent une position intermédiaire entre sédiment de référence et eau de mer. Les étiquettes à côté des points de la carotte 50 GC donnent la profondeur en cm bsf et montrent que l'influence du pôle eau de mer augmente avec la profondeur. On constate qu'à l'exception des échantillons de 110 et 124 cm bsf, les leachates sont par rapport à la roche totale systématiquement décalés en direction de l'eau de mer (Fig. 11 de Bodeï et al., in prep).

La seconde hypothèse intègre le contexte géodynamique, je l'appellerai **scénario dynamique**. Celui-ci se décompose en 2 étapes : la première phase "on-ridge", se déroule à proximité de la dorsale du Pacifique, suivi de la seconde phase "off-ridge" éloignée de la dorsale. Les dépôts de la phase "on-ridge" seraient des phases minérales ayant précipité à l'interface entre un panache d'eau hydrothermale à haute température et l'océan environnant (Feely *et al.*, 1990; 1994; Rudnicki et Elderfield, 1993). Avec l'éloignement de la ride, cette activité hydrothermale à haute température serait remplacée par une activité hydrothermale de basse température identique à celle du scénario statique. L'altération hydrothermale de la 2ème phase re-mobiliserait aussi les dépôts de la 1ère phase.

Dans la carotte 50 GC on observe un changement minéralogique et chimique assez marqué à 100 cm bsf (Fig. 32). Cette transition pourrait dans le contexte du scénario dynamique correspondre à la transition de la phase "on-ridge" vers la phase "off-ridge". Dans le contexte du scénario statique, ce changement lithologique s'intégrerait dans une séquence de précipitation de minéraux néoformées à partir d'un fluide hydrothermal de basse température. L'origine de l'apatite et des oxyhydroxides Fe-Mn présentes en dessus de 100 cm bsf est donc décisive pour distinguer les 2 scénarios. Nous allons donc discuter plus en détail l'origine possible de ces phases minérales.

6.4.2 L'origine des oxyhydroxydes Fe-Mn

Les oxyhydroxides Fe-Mn de la base de la carotte 50 GC, montrent un fort enrichissement en Fe à 124 et 110 cm bsf, suivi d'un enrichissement en Mn à 100 cm bsf (Fig. 33). Ceci suggère une

augmentation progressive du potentiel d'oxydoréduction (Eh), qui conduit à la précipitation successive des oxyhydroxydes de Fe, puis des oxyhydroxydes de Mn. Dans un contexte hydrothermal de basse température on pourrait rattacher cette augmentation du Eh à un mélange progressif, lors de la remontée dans le sédiment, entre un fluide hydrothermal réducteur et des fluides interstiels plus oxydants. En contexte hydrothermale de haute température, des transitions similaires ont été décrite dans la littérature en fonction de la distance du coeur d'un panache d'eau hydrothermale (German *et al.*, 1993; 2002; Chavagnac *et al.*, 2005). Cette succession est expliquée par un mélange progressif entre l'eau du panache sursaturée en Fe et Mn (provenant de l'interaction eau-roche dans la croûte océanique) et l'eau de mer. Ceci conduit également à une augmentation progressive du potentiel d'oxydoréduction et ainsi à la précipitation successive d'oxyhydroxides de Fe, puis d'oxyhydroxides de Mn. Avec l'éloignement de la plaque océanique du panache hydrothermale, cette succession latérale serait enregistrée comme une évolution verticale dans la série sédimentaire.

Par conséquent, les 2 scénarios pourraient expliquer la succession des enrichissements en Fe et en Mn, observée dans la carotte 50 GC. Les oxyhydroxides Fe-Mn ne permettent donc pas de les départager.

6.4.3 L'origine de l'apatite

Dans les échantillons de 110 et 124 cm bsf de profondeur, on observe un enrichissement en apatite, en plus de celui en oxydes de Fe. Les données isotopiques et de TR indiquent, que ces apatites ont précipité à partir d'un fluide de composition d'eau de mer. Dans le contexte hydrothermale à haute température, la formation d'apatite est liée à la précipitation des oxyhydroxides Fe-Mn en bordure du panache hydrothermal (Feely *et al.*, 1990; 1994). Le Fe et le Mn des oxyhydroxides provient de l'eau hydrothermale, tandis que la majorité des éléments associés sont issus de l'eau de mer (German *et al.*, 1990; 1991; Rudnicki et Elderfield, 1993; Wheat *et al.*, 1996; Cronan et Hodkinson, 1997; Kuhn *et al.*, 1998; Mills *et al.*, 2001). Ceci pourrait expliquer la signature d'eau de mer des apatites de la carotte 50 GC.

Toutefois, en contexte hydrothermal de haute température, les apatites sont finement dispersées sur les particules d'oxyhydroxides Fe-Mn, dont le diamètre est d'environ 0.1 µm (Feely *et al.*, 1990; 1994). La morphologie de ces apatites n'est pas comparable avec celle des apatites idiomorphes d'un diamètre d'environ 0.5 µm, observées à la base de la carotte 50 GC (Bodeï *et al.*, 2008). Par ailleurs, l'observation sous le MEB montre que les apatites et les oxyhydroxides ont précipité sur des phillipsites déjà néoformés. Cette association est incompatible avec une formation en contexte de panache, dans lequel les apatites coprécipitent avec les oxyhydroxides dans la colonne d'eau avant d'être mélangés au pied du panache avec des particules silicatées déjà présents. Enfin, l'enrichissement en CaO et P_2O_5 de la carotte 50 GC (Fig. 33), montre que la présence d'apatite ne se limite pas à la base de la série, mais qu'elles sont aussi présentes au -dessus de 100 cm bsf, avec une diminution graduelle vers la surface.

Ces arguments suggèrent une origine hydrothermale de basse température pour les apatites, dans un contexte global correspondant au **scénario statique.**

6.5 Conclusions

Le **scénario statique** semble plus cohérent pour expliquer l'origine des phases minérales authigènes de la carotte 50GC. Le scénario dynamique paraît certes plus adapté au contexte géodynamique du secteur d'étude, mais il n'est pas en accord avec les données minéralogiques et géochimiques.

La série sédimentaire, à priori d'âge Miocène, a subi une altération hydrothermale de basse température à partir d'une période non-précisée, qui pourrait avoir précédé directement l'activité hydrothermale actuelle. L'évolution de la l'anomalie en Eu suggère que cette circulation a mobilisé dans une première phase de l'Eu, probablement à partir de plagioclases dans la partie inférieure de la série, qui a ensuite été réintégré plus haut dans des minéraux néoformés, probablement des phillipsites. Ce scénario implique que les phillipsites ne sont pas d'origine diagénétique, mais hydrothermale. Ceci est en accord avec la plus faible quantité de phillipsites observée dans le sédiment de référence.

Les observations microscopiques montrent que les apatites et les oxyhydroxides Fe-Mn ont précipité après les phillipsites lors d'une seconde phase. Les apatites constituent la phase principale extraite par le leaching et elles contiennent l'essentiel des TR. Les compositions isotopiques du Nd et l'anomalie du Ce montrent que ces apatites ont précipité à partir d'un fluide, ayant conservé une composition d'eau de mer et traversant la série sédimentaire de bas en haut. L'eau hydrothermale n'a donc pas été en échange avec la croûte océanique, avant de remonter dans la colonne sédimentaire. Ceci implique un temps de résidence de l'eau de mer dans la croûte océanique court, probablement en lien avec un débit élevé, comme le suggèrent les rapports eau/roche très élevés (avec des valeurs allant jusqu'à 10 E8 à la base de la carotte suivi d'une diminution progressive vers la surface).

6.6 Perspectives de la thématique

L'étude de l'hydrothermalisme océanique a fait partie des sujets de recherches phares de la géologie dans la 2ème moitié du 20 siècle et un nombre important de missions en mer et de publications scientifiques ont été réalisés. Grâce à ces travaux, on a aujourd'hui des connaissances assez précises du processus de l'hydrothermalisme et de son impact sur les cycles géochimiques à l'échelle du globe. Ces études ont également mis en évidence l'existence de nombreux processus chimiques et biologiques, associés à des conditions uniques en milieu naturel. L'avenir de la recherche en contexte hydrothermal océanique est probablement tourné vers son utilisation en tant que laboratoire naturel d'étude de processus physico-chimiques et biologiques en absence de lumière et sous des conditions de P-T extrêmes.

7 Les processus de transport et de fractionnement des terres rares dans l'eau des ruisseaux

Publications associées :

- Tricca, A., Stille, P. & **Steinmann, M.**, Kiefel, B., Samuel, J. & Eikenberg, J. 1999: Rare earth elements and Sr and Nd isotopic compositions of dissolved and suspended loads from small river systems in the Vosges mountains (France), the river Rhine, and groundwater. Chem. Geol. 160, 139-158.
- **Steinmann, M.** & Stille P., 2006. Rare earth element transport and fractionation in small streams of a mixed basaltic-granitic catchment basin (Massif Central, France). J. Geochem. Exploration, 88(1-3), 336-340 (résumé étendu).
- **Steinmann, M.** et Stille, P. 2008. Controls on transport and fractionation of the Rare Earth Elements in stream water of a mixed basaltic-granitic catchment basin (Massif Central, France). Chem. Geol., 254, 1-18.

Travail de master associé au projet :

- Bontemps, S., 2006. Mobilisation et transfert des éments majeurs, en traces et terres rares au cours de l'altération dans le bassin versant de Malaval (Massif Central). Mémoire master recherche « Environnement, santé ,société ». Université de Franche-Comté, Besançon, 30 pp.

7.1 Problématique

Dans la chapitre 2.1.3 nous avons mentionné que les spectres de TR des eaux de de ruissellement et souterraines sont souvent fortement fractionnés par rapport aux spectres de la roche du bassin versant. Nous avons également dressé une liste de processus, qui sont potentiellement à l'origine de ce fractionnement.

La présente étude avait pour objectif d'appréhender dans le détail les processus de fractionnement des TR dans l'eau de petits ruisseaux à proximité de la source et en fonction de la distance de transport. Les ruisseaux et le bassin versant associé ont été recherchés et choisis de manière à présenter des caractéristiques lithologiques et géochimiques différentes de l'amont vers l'aval du bassin. Pour l'étude nous cherchions également un bassin avec des roches d'origine magmatique (afin de simplifier l'étude du comportement des TR lors de l'altération des roches du bassin versant) et des ruisseaux qui recoupent perpendiculairement les limites lithologiques (afin d'avoir une relation claire entre l'eau du ruisseau et les lithologies encaissantes).

Certains bassins versants de la chaîne du Devès, au SW du Puy-en-Velay (43) dans le Massif Central, correspondent bien à ces critères : Les sources des ruisseaux se trouvent sur des plateaux formés par des coulées basaltiques d'âge Villefranchien (début du Quaternaire) et les ruisseaux descendent ensuite dans des vallons abruptes situés dans des granites et orthogneiss d'âge Hercynien. Le relief plat de l'amont favorise l'altération de la roche et les profils d'altération sont par conséquent épais de plusieurs mètres. Par contre, sur les pentes raides dans les granites et orthogneiss à l'aval, la couche d'altération excède rarement 10 cm.

Les granites et orthogneiss d'une part et les basaltes d'autre part sont des roches avec des caractéristiques géochimiques et isotopiques très contrastées. Ceci permet dans la chaîne du Devès d'utiliser les isotopes du Sr et du Nd pour identifier avec précision l'origine de la charge chimique particulaire et dissoute de l'eau du ruisseau.

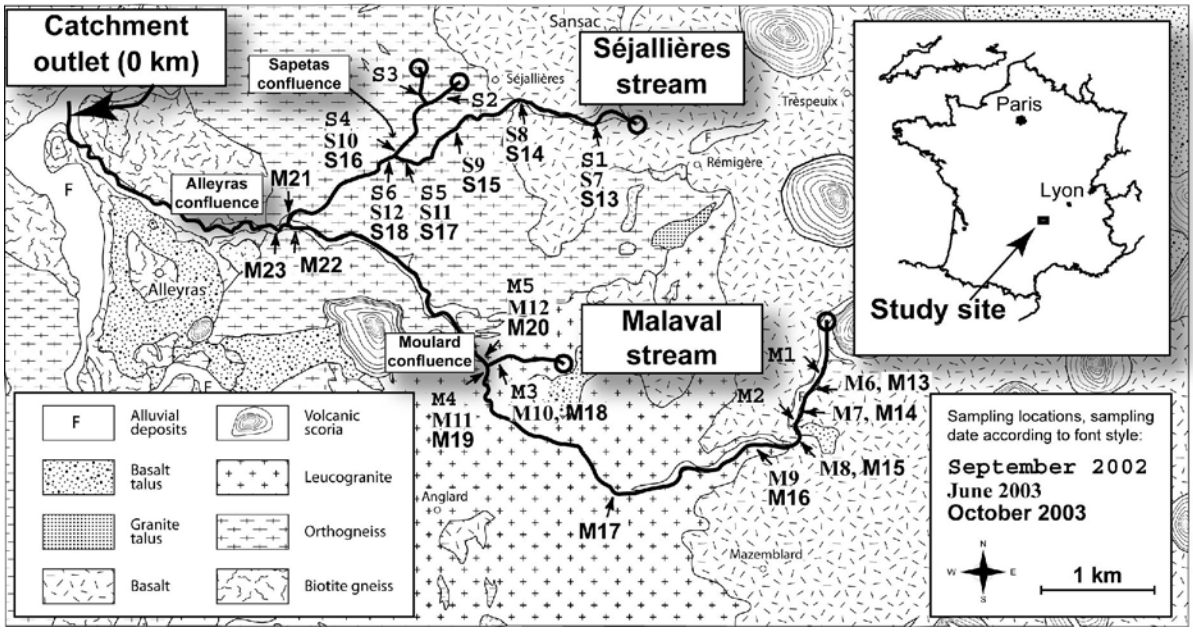

Fig. 44 : Carte géologique simplifiée du site d'étude du bassin versant du Malaval entre la chaîne du Devès et les gorges de l'Allier au SW du Puy-en-Velay (Fig. 1 de Steinmann et Stille, 2008).

7.2 Principaux résultats

Le bassin versant sélectionné pour cette étude est le bassin du Malaval dans la haute vallée de l'Allier à environ 25 km au SW du Puy-en-Velay (43, Fig. 44). Le ruisseau "Malaval" ainsi que son affluent principale, le ruisseau de "Séjallières", ont été échantillonnés à 3 reprises en septembre 2002, juin et octobre 2003. Sur ces échantillons, nous avons analysé séparément la fraction dissoute (< 0.45 µm), la fraction particulaire (> 0.45 µm) ainsi que des leachates à l'HCl 1N de la fraction particulaire. Afin d'identifier des processus de fractionnement des TR associés à l'altération de la roche mère, nous avons également étudié des profils d'altération sur les 3 principales lithologies du bassin versant. L' étude des profils d'altération a été réalisé dans le cadre du Master ESS de S. Bontemps (Bontemps, 2006), que j'ai co-encadré avec ma collègue A.V. Walter.

Les principaux résultats qui ressortent de l'étude des ruisseaux sont les suivants :

- La composition isotopique du Sr et du Nd de l'eau de rivière filtrée montre que le Sr et le Nd proviennent majoritairement de l'altération du basalte. La contribution de Sr et de Nd d'origine

granitique ou gneissique à l'aval reste inférieure à 20 % pour le Sr et inférieure à 40 % pour le Nd (Fig. 45). Ces données indiquent clairement que l'évolution des spectres des TR décrite ci-dessous n'est pas le résultat d'un mélange entre TR de différentes sources, mais qu'elle est liée à un processus de fractionnement.

- Dans la fraction dissoute des 2 ruisseaux, on observe un appauvrissement en TR légères, qui s'accentue de l'amont vers l'aval (Fig. 46). On constate parallèlement une diminution de l'anomalie positive en Ce dans les leachates de la phase particulaire.
- Les teneurs en Nd et le rapport Nd/Yb de la fraction dissoute, comme l'anomalie en Ce des leachates de la phase particulaire, suivent l'évolution des teneurs en Fe de la fraction dissoute (Fig. 47). Ces teneurs en Fe sont très élevées et l'indice de saturation de la goethite atteint des valeurs d'environ 8. Cette sursaturation s'estompe, comme le rapport Nd/Yb et l'anomalie du Ce, d'amont vers l'aval, après que les ruisseaux aient franchi le rebord du plateau de basalte (Fig. 48).

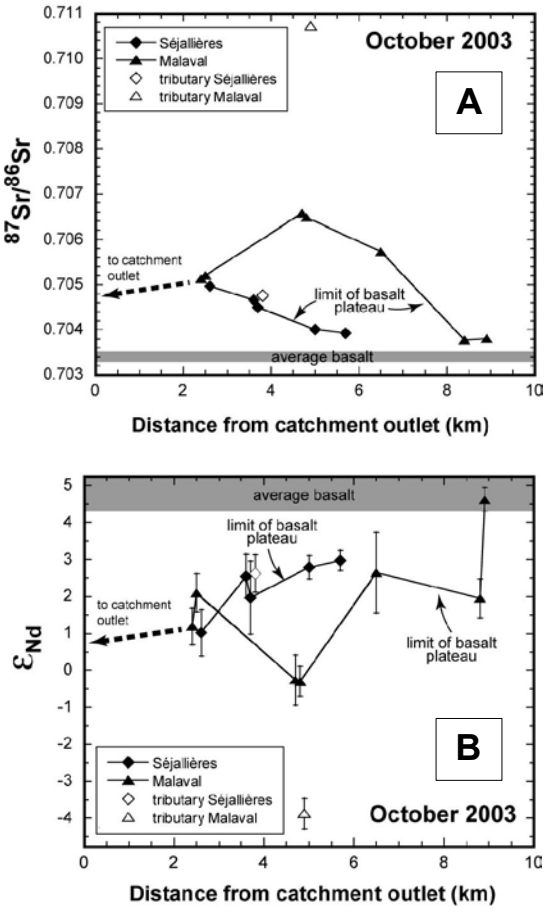

Fig. 45 : Évolution de la composition isotopique du Sr (A) et du Nd (B) dans l'eau filtrée à 0.45 µm des ruisseaux Malaval et Séjallières. Les compositions isotopiques de l'eau restent toujours proches du basalte. Les pourcentages de Sr et de Nd d'origine granitique ou orthogneissique restent même à l'aval inférieure à 20 % pour le Sr et à de 40 % pour le Nd.

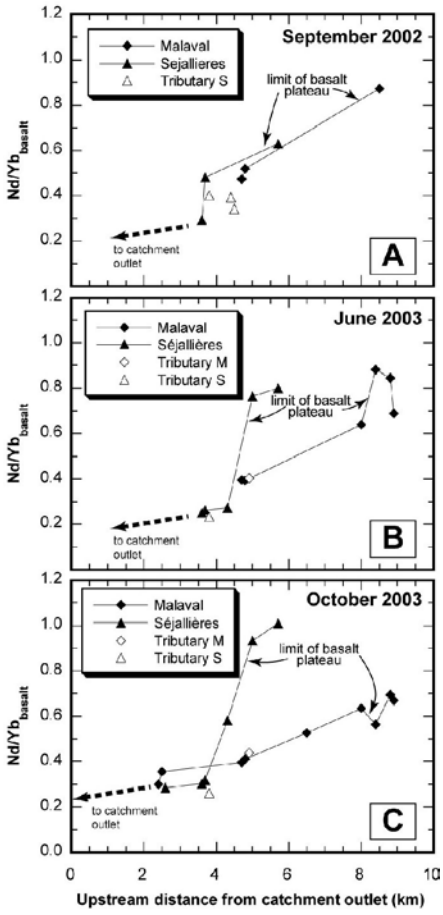

Fig. 46 : Évolution des rapports Nd/Yb dans l'eau filtrée à 0.45 µm des ruisseaux Malaval et Séjallières. Le rapport Nd/Yb permet, comme le rapport La/Yb, de quantifier un fractionnement entre TR légères et TR lourdes. Il montre que l'appauvrissement en TR légères s'accentue de l'amont vers l'aval (Fig. 4 de Steinmann et Stille, 2008).

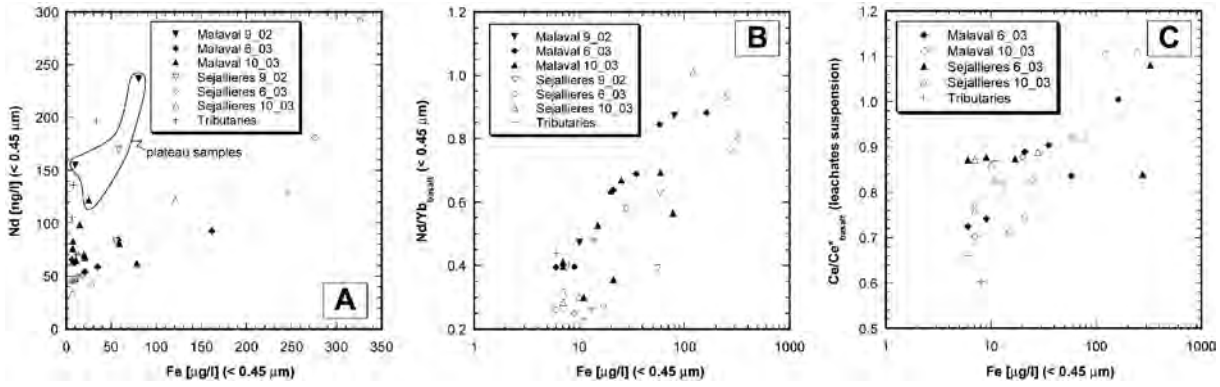

Fig. 47 : Les teneurs en Nd et les rapports Nd/Yb de la fraction <0.45 µm, ainsi que l'anomalie du Ce des leachates HCl 1M, de la phase particulaire dépendent des teneurs en Fe dans la fraction <0.45 µm (Fig. 5 de Steinmann et Stille, 2008).

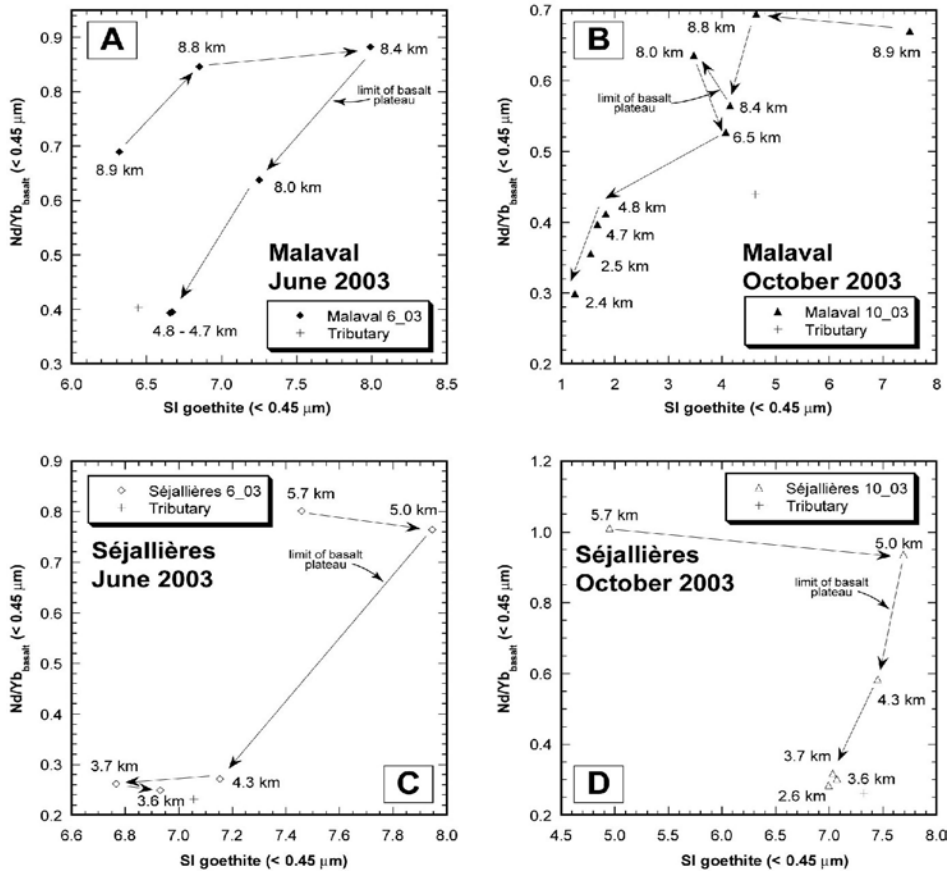

Fig. 48 : Variation de l'indice de saturation de la goethite et du rapport Nd/Yb de l'eau filtrée à 0.45 µm des ruisseaux Malaval et Séjallières avec la distance. On constate pour les 2 paramètres une diminution des valeurs à partir du moment où le ruisseau a franchi le rebord du plateau basaltique (Fig. 7 de Steinmann et Stille, 2008).

Nous interprétons ces données par la présence de colloïdes de Fe, qui sont les principaux porteurs des TR dans la fraction <0.45 µm (Fig. 47). Ces colloïdes augmentent de taille lorsque les ruisseaux

quittent le plateau basaltique pour traverser les pentes raides de granite et de gneiss. L'eau est plus agitée et le potentiel d'oxydoréduction augmente, ce qui accélère l'accroissement des particules colloïdales. Les colloïdes de Fe dépassent finalement la fraction de 0.45 µm et sont sédimentés sous forme de particules d'oxyhydroxydes de Fe. Ces particules sont enrichis en TR légères extraites de la fraction < 0.45 µm et en Ce désorbé de la phase particulaire. Ce modèle, illustré dans la Fig. 49, permet d'expliquer avec un seul processus l'évolution des différents paramètres décrits ci-dessus.

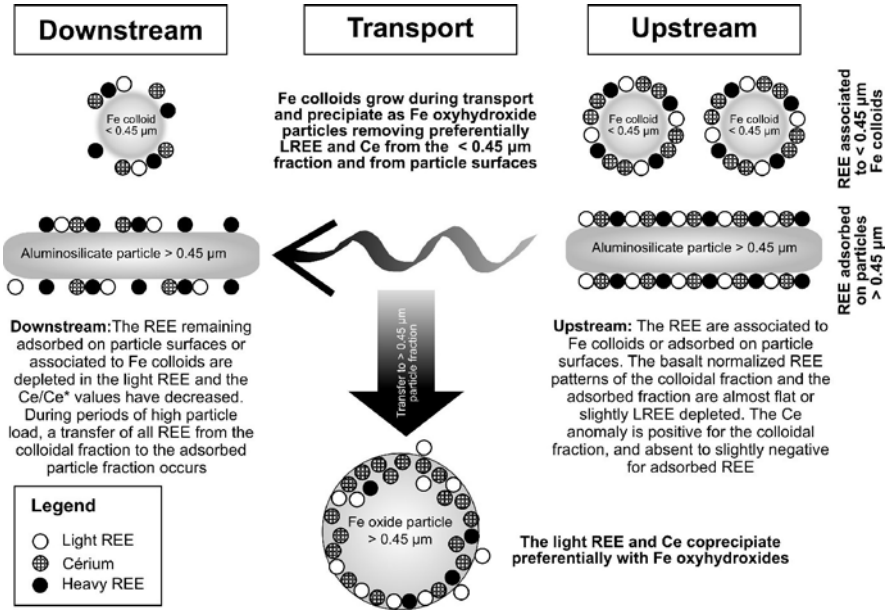

Fig. 49 : Schéma interprétatif des processus et paramètres contrôlant le transport et le fractionnement des TR dans les ruisseaux du Massif Central (Fig. 10 de Steinmann et Stille, 2008).

Au niveau de 3 confluences de ruisseaux, nous avons retrouvé une évolution des spectres de TR très similaire à celle que nous venons de décrire à l'échelle du bassin versant. Nous avons comparé pour chacun des ruisseaux et de leur affluent les spectres avant et après une confluence. On note une perte systématique en Ce et en TR légères après la confluence (Fig. 50). Cette dernière semble dépendre directement de la proportion d'eau provenant de l'affluent (Fig. 51). Cela signifie que lors du mélange entre l'eau d'un ruisseau et d'un affluent, les TR ne se comportent pas comme un traceur conservateur. Nous interprétons ces pertes à l'échelle de la 'confluence, comme à l'échelle du bassin versant, par la précipitation de particules d'oxyhydroxydes de Fe, aboutissant à une extraction préférentielle du Ce et des TR légères de la fraction <0.45 µm.

Contrairement à d'autres études de la littérature, nous ne constatons aucun lien entre le fractionnement des spectres des TR et la teneur en matière organique. Nous expliquons cette différence par le fait, que la quasi-totalité de ces études antérieures ait été menée sur de grands fleuves plus riches en matière organique et moins oxygénés que les ruisseaux du bassin du Malaval.

7.3 Perspectives de la thématique

L'importance de la phase colloïdale pour le transport des métaux traces dans les cours d'eaux naturels est de plus en plus reconnu. L'étude présentée ici montre, que la présence de colloïdes fractionne les spectres des TR, qui deviennent par le fait un outil simple et efficace pour identifier la présence de colloïdes et tracer leur évolution. Toutefois, il est maintenant nécessaire de pouvoir mettre clairement identifier ces phases colloïdales. Nous envisageons dans une seconde étape du projet l'analyse directe des TR de la phase colloïdale (chap. B10).

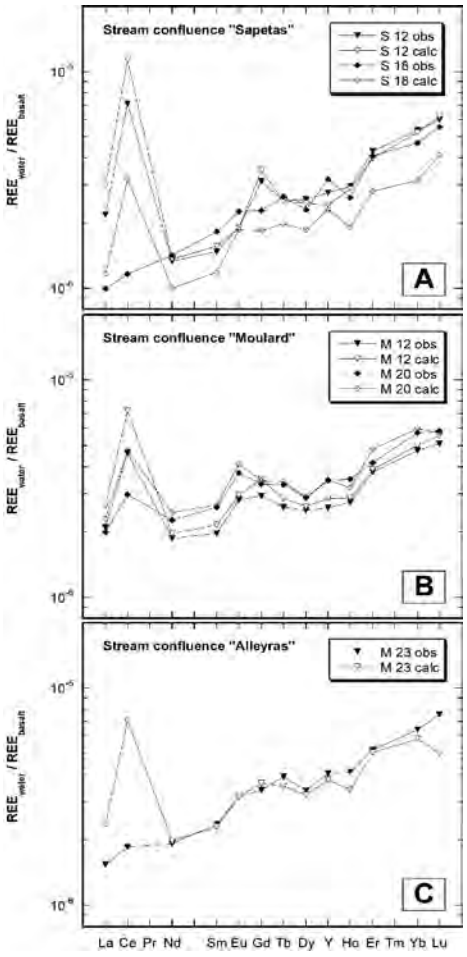

Fig. 50 : Évolution des spectres de TR de la fraction dissoute au niveau de 3 confluences de ruisseaux. Les spectres labélisé "obs" sont des spectres analysés après la confluence. Les spectres labélisé "calc" sont des spectres calculés pour le ruisseau après la confluence à partir des spectres des 2 affluents en utilisant les isotopes du Sr pour déterminer la fraction d'eau provenant de chacun des affluents. On constate que l'anomalie en Ce et le rapport La/Yb sont systématiquement plus élevés que ceux des spectres calculés (Fig. 8 de Steinmann et Stille, 2008).

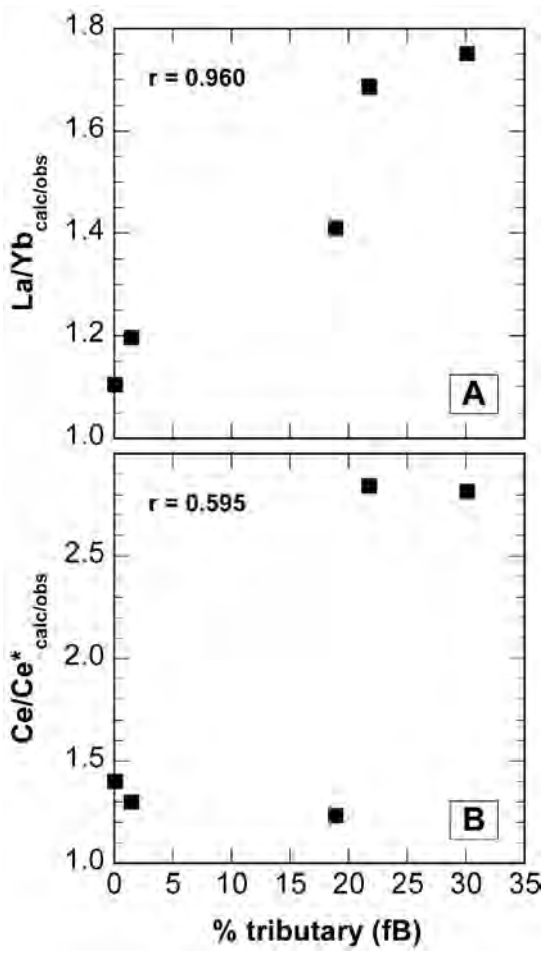

Fig. 51 : Les 2 diagrammes montrent un lien assez direct entre le pourcentage d'eau provenant de l'affluent et les écarts de l'anomalie du Ce et du rapport La/Yb présentés dans la Fig. 50. Ceci signifie, que les TR ne sont pas mélangées de façon homogène au niveau des confluences, mais qu'il y a systématiquement une perte de Ce et des TR légères, qui augmente en fonction de la taille relative de l'affluent (Fig. 9 de Steinmann et Stille, 2008).

8 Les transferts des terres rares à l'interface géosphère - biosphère

Publications associées :

- Stille, P., **Steinmann, M.**, Pierret, M.C., Gauthier-Lafaye, F., Aubert, D., Probst, A., Viville, D. & Chabaux, F., 2006. The impact of vegetation on fractionation of rare earth elements (REE) during water-rock interaction. J. Geochem. Exploration, 88(1-3), 341-344 (résumé étendu).
- Stille, P., **Steinmann, M.**, Pierret, M.C., Gauthier-Lafaye, F., Chabaux, F., Viville, D., Pourcelot, L., Matera, V., Aouad, G. and Aubert, D., 2006. The impact of vegetation on REE fractionation in stream waters of a small forested catchment (the Strengbach case). Geochim. Cosmochim. Acta, 70(13): 3217-3230.
- **Steinmann, M.**, Stille, P. & Pierret, M-C. 2007: Biogeochemical Cycling of Rare Earth Elements in Surface Soils . V.M. Goldschmidt Conference, August 20-24, 2007 Cologne, A972 (résumé).
- Brioschi, L. **Steinmann, M.**, Lucot, E., Badot, P.M. & Stille, P. 2008: Absorption and fractionation of REE by spruce and beech: a comparative study on specimens grown on brown acidic soils and calcareous soils. Réunion des Sciences de la Terre, Nancy – France, April 21-24 (résumé).

Travaux de master et de thèse associés au projet :

- Brioschi, L., 2007. Absorption et fractionnement des terres rares par la végétation, en fonction des conditions de sol. Mémoire master recherche « Environnement, santé , société ». Université de Franche-Comté, Besançon, 30 pp.
- Brioschi, L. Thèse en cours. Les transferts des terres rares à l'interface géosphère - biosphère . Bourse de thèse attribué par le Ministère de la recherche en septembre 2007

8.1 Problématique

Notre recherche sur la thématique du transfert des TR à l'interface géosphère – biosphère est actuellement en cours. Il s'agit d'un projet pluridisciplinaire, il regroupe des géochimistes, des pédologues et des physiologistes végétales du laboratoire de Chrono-environnement de Besançon (UMR 6249) et du Centre de Géochimie de la Surface (CGS, UMR 7517) de Strasbourg. Dans le cadre de ce projet, un stage de recherche de Master 2 "Environnement, Santé, Société" de l'université de Franche-Comté a été réalisé par Laure Brioschi en 2007 (Brioschi, 2007). Il a été suivi, en septembre 2007, par l'attribution d'une bourse de thèse par le Ministère de la recherche pour Laure Brioschi. Je suis à l'origine de ce projet de stage et de thèse et co-encadrant avec E. Lucot et P.M. Badot.

Le thématique "TR à l'interface géosphère – biosphère" a été lancée en 2005 en collaboration avec P. Stille et M.-C. Pierret du CGS de Strasbourg. L'idée, que la biosphère et notamment la végétation puisse jouer un rôle important dans le cycle des TR naturelles, vient de la nécessité de faire intervenir d'autres réservoirs que les réservoirs inorganiques pour pouvoir boucler les bilans des transferts et du fractionnement des TR sur le bassin versant du Strengbach dans le Vosges (http://ohge.u-strasbg.fr/index.html). Ces bilans ont montré que les processus et sources "classiques" (adsorption,

complexation, altération, retombés atmosphériques) ne pouvaient pas à eux seuls expliquer les spectres de TR observés dans le ruisseau à la sortie du bassin versant. Seule l'intégration du réservoir végétal a permis d'atteindre des bilans équilibrés (Stille *et al.*, 2006). Cette première étude a également mis en évidence que la quantité annuelle de TR absorbées par la végétation à l'échelle du bassin versant est comparable à celle exportées par l'écoulement de surface.

Nous avons montré, dans le chapitre 2.1.5, que les TR sont de plus en plus utilisées par l'homme et que le cycle externe des TR naturelles est de plus en plus perturbé par des TR anthropiques. L'intérêt d'étudier les transferts des TR à l'interface géosphère – biosphère est par conséquent double : Une telle étude contribue à la fois à une meilleure compréhension de l'impact de la végétation sur les cycles géochimiques de surface et elle donne aussi des informations sur l'absorption de TR d'origine anthropique par la biosphère et leur impact sanitaire et écologique. C'est la raison pour laquelle l'étude est d'une part focalisée sur le rôle de la végétation dans le cycle des TR naturelles, et d'autre part sur le transfert des TR anthropiques à l'interface géosphère-biosphère et leur impact sur le fonctionnement physiologique des végétaux. Les résultats de cette étude pourront également être précieux pour évaluer le comportement d'autres métaux traces ayant des caractéristiques chimiques comparables, notamment certains métaux lourds et certaines actinides.

8.2 Objectifs de l'étude et approche retenue

L'étude des transferts des TR à l'interface géosphère – biosphère permettra, à la fois, de mieux comprendre l'impact de la végétation (et du système sol-plante) sur les cycles géochimiques de surface, de documenter les mécanismes de transfert des TR naturelles et anthropiques vers la biosphère et de mieux évaluer les risques sanitaires et environnementaux associés à la dispersion de TR anthropiques. Nous avons fixé plus précisément 2 objectifs généraux :

- L'utilisation des TR comme traceur en géochimie externe est basée sur l'étude de l'évolution du fractionnement de leur spectre de distribution, c'est-à-dire l'enrichissement ou l'appauvrissement de certaines TR par rapport aux autres, dans les différents compartiments de la géosphère et de l'hydrosphère. La quasi-totalité des études présentées dans la littérature ne tiennent pas compte du compartiment végétal. Nous nous sommes donc fixé comme premier objectif de caractériser le rôle de la végétation dans le transfert et le fractionnement des TR naturelles à l'échelle d'un bassin versant.
- La littérature scientifique commence à faire état des premières traces de TR d'origine anthropique dans l'environnement (chap. 2.1.5). Le second objectif du projet est donc de réaliser une première évaluation du risque que représentent les TR anthropiques dans le milieu naturel, en identifiant les voies et mécanismes de transfert possibles au sein du système sol-plante et en déterminant les éventuels effets toxiques sur les végétaux.

Pour atteindre ces objectifs, nous avons choisi d'associer une étude de terrain à une étude en laboratoire, où l'absorption des TR par les végétaux sera étudiée sous conditions contrôlées, notamment pour évaluer leur impact écotoxicologique. Concrètement, le projet sera décliné en trois volets :

- ✗ Dans un premier volet du projet, nous envisageons de quantifier la capacité de la végétation à stocker les TR et à fractionner leurs spectres, ceci en fonction de espèces végétales. Ces données serviront de base pour intégrer la végétation dans des bilans quantitatifs des transferts des TR à l'échelle du bassin versant. L'objectif final de cette approche est de savoir, dans quelle mesure les spectres de TR mesurés dans l'écoulement de surface à la sortie d'un bassin versant, reflètent les échanges avec la végétation. Cette partie de l'étude sera entièrement basée sur des données de terrain.
- ✗ Le second volet se focalisera sur les mécanismes de transfert des TR à l'interface géosphère-biosphère et à l'intérieur des plantes. Ce volet a pour but de comprendre les variations des spectres de distribution que nous avons observées dans des végétaux issus de différents sites lors d'études antérieures (Stille *et al.*, 2006; Brioschi, 2007). Cette partie du projet sera à la fois basée sur des données acquises sur le terrain et sur des résultats expérimentaux obtenus en conditions contrôlées au laboratoire. Elle fournira une première caractérisation des paramètres susceptibles de favoriser l'accumulation des TR anthropiques dans la végétation.
- ✗ Le troisième volet a pour but d'évaluer l'effet des TR sur la physiologie de la plante et de déterminer des seuils de concentrations pouvant entraîner des modifications du fonctionnement physiologique. Cette partie de l'étude sera effectuée au laboratoire sous conditions contrôlées.

8.3 Sites de terrain

Trois sites d'études ont été choisis de manière à présenter des caractéristiques géochimiques et pédologiques contrastées. Ceci est illustré dans les figures 52 et 53, par la comparaison des spectres de TR des roches et des sols des 3 sites. L'objectif est de vérifier, si les spectres de TR dans les végétaux varient en fonction des conditions spécifiques de chaque site (ex. teneur et spectre des TR dans le sol et dans l'eau du sol, pH et teneur en matière organique du sol, disponibilité de ligands complexants dans l'eau du sol, compétition entre TR et certains éléments majeurs tels que le Ca, …). Ces données de terrain serviront également à intégrer la végétation dans des bilans quantitatifs des transferts des TR à l'échelle du bassin versant. Trois sites ont été retenus et sont brièvement décrits ci-dessous :

- ✗ **Le bassin versant de Cussey-sur-Lison (25)** situé sur des calcaires massifs du Jurassique supérieur (Rauracien). Nous avons mis en place ce site depuis 2005 et il est équipé de 3 stations d'échantillonnage de l'eau du sol (plaques lysimétriques). Dans le cadre d'un travail de master recherche (Brioschi, 2007), 3 profils de sol ainsi que 3 épicéas et 2 hêtres ont déjà été analysés.

Les sols sont majoritairement des sols bruns calciques d'une épaisseur inférieure à 30 cm avec un pH de 6 à 8. Localement apparaissent dans des dolines des sols bruns lessivés d'une épaisseur supérieure à 1 m avec un pH autour de 5. Les teneurs en TR des 2 sols sont d'environ 50 ppm pour le Nd.

- **Le bassin versant du Strengbach dans les Vosges du Sud (68)** situé sur des granites, micro-granites et gneiss. Il est depuis 1986 systématiquement étudié par le CGS de Strasbourg (Probst *et al.*, 1990; Probst *et al.*, 1992; Probst *et al.*, 1995) et équipé d'un dispositif de stations d'échantillonnage très complet (données météorologiques et hydrologiques, écoulement de surface, piézomètres, plaques lysimétriques, précipitations, pluviolessivats etc.). Le réservoir végétation et son impact sur la géochimie de l'ensemble du bassin versant a déjà fait l'objet de plusieurs études ayant développé des approches par les isotopes du Sr (Poszwa *et al.*, 2000; Aubert *et al.*, 2002a), par ceux du Ca (Schmitt et Stille, 2005), par les déséquilibres de l'U (Pierret *et al.*, 2004; Prunier *et al.*, 2007) et par les TR (Aubert *et al.*, 2002b; 2004; Stille *et al.*, 2006). Le site est reconnu comme Observatoire Hydro-Géochimique de l'Environnement (OHGE - http://ohge.u-strasbg.fr, responsable : Marie-Claire Pierret) de l'Ecole et Observatoire des Sciences de la Terre depuis 1997, il est labelisé comme service d'observation nationale par l'INSU depuis 2007. Il s'agit majoritairement de sols bruns acides ou sols ocres podzoliques avec un pH de 3.5 à 4, avec des teneurs en TR de 10-30 ppm pour le Nd.
- **Les carbonatites du volcan "Kaiserstuhl" (à proximité de Freiburg im Breisgau, Allemagne)**. Les carbonatites sont des roches carbonatées d'origine volcanique, présentant des teneurs en TR très élevées (jusqu'à 500 ppm pour le Nd) et des spectres fortement enrichis en TR légères (Hornig-Kjarsgaard, 1998). Ce site a été choisi afin de pouvoir déterminer si la végétation reflète les teneurs et les spectres très atypiques de la roche mère. Une plaque lysimétrique pour l'échantillonnage de l'eau du sol a été installée début juillet 2008 et les prélèvements vont démarrer en octobre 2008.

Sur les 3 sites nous étudions la végétation, les profils de sol et l'eau du sol. Des essais sont en cours afin de compléter les dispositifs actuels d'échantillonnage de l'eau du sol par plaques lysimétriques (1 prélèvement par saison) par un échantillonnage par bougie poreuse. L'intérêt de combiner les 2 méthodes est de vérifier, s'il y a une différence entre les spectres de TR de l'eau gravitaire échantillonnée par la plaque lysimétrique et de l'eau liée récupérée par la bougie poreuse. L'échantillonnage des végétaux est ciblé sur des hêtres, des chênes et des épicéas, au niveau des racines, des rondelles de tronc à différentes hauteurs du sols, des branches et des feuilles et aiguilles. Ponctuellement, ces analyses sont complétées par des analyses de sève, de retombées atmosphériques ainsi que d'eau souterraine et de surface. La biomasse autour des stations d'échantillonnage de chaque site a été quantifiée afin de comparer la quantité de TR stockée dans la végétation à celle dans les sols.

8.4 Résultats provisoires

Les expériences en laboratoire sur l'absorption des TR par les végétaux sont en cours et nous ne disposons pour l'instant que des premiers résultats des sites de terrain. Les données sur des épicéas, des hêtres et des chênes confirment les observations de Stille *et al.* (2006), qui ont montré que les teneurs en TR sont les plus élevées dans les racines des arbres, qu'elles diminuent dans les feuilles et épines et que les plus faibles teneurs observées sont au niveau du tronc. Parmi les racines, on trouve systématiquement les plus fortes teneurs dans les racines de petit diamètre (< 2 mm, Fig. 54). Contrairement à Stille *et al.* (2006), nous ne trouvons pas d'enrichissement systématique en TR légères par rapport à l'eau du sol local. Nous observons également des anomalies pour le Ce, l'Eu, le Gd et l'Y par rapport à l'eau du sol, mais pas d'évolution systématique entre les différentes parties des végétaux.

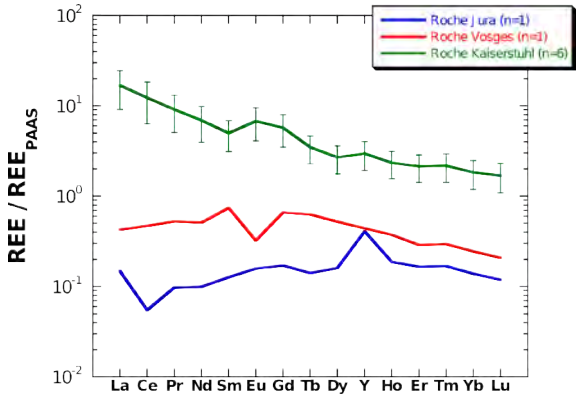

Fig. 52 : Spectres de TR (± écart type) du calcaire du site du massif du Jura (site Cussey-sur-Lison), du granite des Vosges (site du Strengbach) et des carbonatites du Kaiserstuhl. Les spectres de TR des trois sites sont clairement différents. Notamment les carbonatites ont des teneurs en TR très élevées et des spectres fortement enrichis en TR légères.

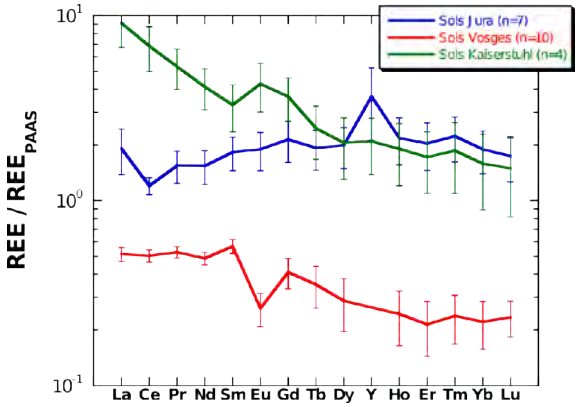

Fig. 53 : Spectres moyens de TR (± écart type) des sols du site du massif du Jura (site Cussey-sur-Lison sur calcaire), du massif des Vosges (site du Strengbach sur granite) et du Kaiserstuhl (carbonatites). La comparaison avec les spectres des roches correspondantes (Fig. 52) montre que les sols ont en grande partie hérité le spectre de la roche mère. Uniquement les sols du massif des Vosges montrent une évolution significative des spectres de TR par rapport à celui de leur roche mère.

La Fig. 52 montre que les spectres de TR du calcaire du massif du Jura (site Cussey-sur-Lison), du granite des Vosges (site du Strengbach) et des carbonatites du Kaiserstuhl sont différents. Les carbonatites ont notamment des teneurs en TR très élevées et les spectres sont fortement enrichis en TR légères. Les sols du massif du Jura et du Kaiserstuhl reflètent largement le spectre de TR de leur roche mère, tandis qu'une légère évolution des spectres apparaît dans le massif des Vosges (Fig. 53). D'autre part, on constate que les sols du massif du Jura sont plus riches en TR que ceux du massif des Vosges (environ 50 ppm de Nd dans les sols du Jura, contre 15 ppm dans les Vosges), malgré le fait que le calcaire soit moins riche en TR que le granite (environ 4 ppm dans le calcaire et 18 ppm de Nd dans le granite). Cette différence est, à priori, liée au pH du sol plus élevé dans le Jura, limitant le lessivage des

sols, et à la dissolution du calcaire lors de l'altération, cela permet d'expliquer l'enrichissement en TR du sol par rapport au calcaire d'un facteur d'environ de 10. Les sols du volcan du Kaiserstuhl, avec des teneurs en Nd allant jusqu'à 180 ppm, sont clairement plus riches en TR que les autres sites.

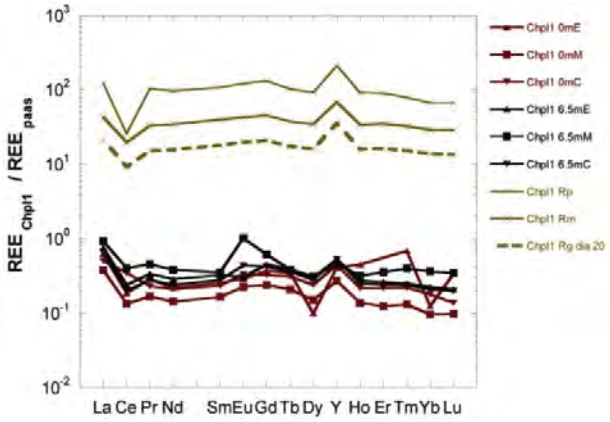

Fig. 54 : Exemple de spectres de TR d'un hêtre du massif du Jura (site Cussey-sur-Lison). Les teneurs en TR sont beaucoup plus élevés dans les racines (échantillons Rp, Rm, Rg) que dans le tronc (autres échantillons). La forme des spectres des racines reflète presque directement le spectre du sol local (Fig. 53). Rp = racines < 2 mm, Rm = racines 2-10 mm, Rg dia 20 = racine de 20 mm de diamètre. 0mC = centre de la rondelle de tronc à 0m de hauteur du sol, 0mM = milieu de la rondelle de tronc à 0m, 0mE = extérieur de la rondelle de tronc à 0m, idem pour la rondelle de tronc à 6.5 m de hauteur du sol (Thèse Brioschi en cours).

Les teneurs et spectres en TR dans les troncs d'épicéas et de hêtres dans le massif du Jura et dans le massif des Vosges sont comparables (Fig. 55, environ 6-8 ppb de Nd). La seule différence concerne l'anomalie en Ce, qui est négative dans le Jura et absente dans les Vosges. La comparaison avec les spectres des sols et des roches mères indique que cette disparité est directement héritée du substratum pédologique et géologique. Par contre, on observe pour les troncs d'arbres du Jura et des Vosges l'apparition d'une anomalie positive en Eu, qui est dans les 2 cas absente dans les sols. Les teneurs et spectres en TR des végétaux du Kaiserstuhl sont clairement différents des autres sites, mais reflètent eux aussi les spectres du sol.

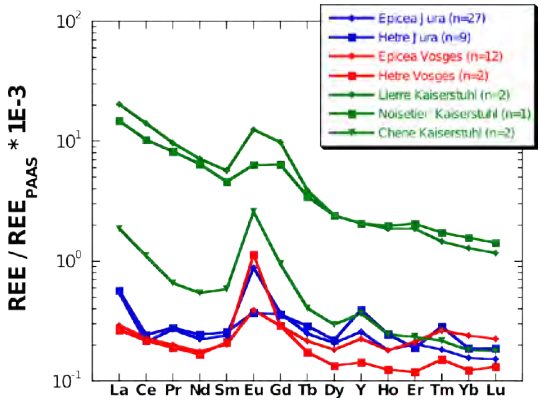

Fig. 55 : Spectres moyens de TR des troncs d'épicéa et de hêtre du massif du Jura et du massif des Vosges comparés avec les spectres de quelques échantillons préliminaires du Kaiserstuhl. On constate des spectres assez similaires pour le Jura et les Vosges. La seul différence concerne l'anomalie négative en Ce pour le Jura, qui est absente dans les Vosges et directement hérité du calcaire. On observe pour le Jura et les Vosges une anomalie positive en Eu, qui est absente dans la roche et les sols. Les spectres en TR des végétaux du Kaiserstuhl sont clairement différents des autres sites et reflètent assez directement les spectres du sol.

Ces résultats préliminaires indiquent donc un lien assez direct entre les spectres de TR de la roche mère, des sols et des végétaux. Toutefois, une analyse plus détaillée est en cours, pour retracer plus finement l'évolution des spectres entre les différents compartiments abiotiques et biotiques.

8.5 Perspectives de la thématique

L'étude des transferts des TR à l'interface géosphère-biosphère est encore à la phase de lancement et les perspectives sont multiples. Il s'agit toutefois d'une étape concrète d'intégration de la couverture végétale dans les cycles géochimiques externes. La majorité des travaux antérieurs a ignoré le rôle de la végétation dans les transferts géochimiques et en tant que réservoir d'éléments chimiques au sein des cycles exogènes.

De façon plus concrète, notre étude devrait contribuer à quantifier le rôle de la végétation en tant que réservoir de TR et à évaluer sa contribution au fractionnement des spectres de TR dans l'écoulement de surface. Cette approche sera dans un premier temps évidemment limitée à l'échelle kilométrique des petits bassins versants choisi pour notre étude, mais elle pourra dans un 2ème temps être étendue à des échelles plus vastes.

Les TR ont dans le passé fait preuve de leur efficacité en tant que traceur de nombreux processus géochimiques endogènes et exogènes. Nos premiers résultats suggèrent, que leur utilisation pourrait se révéler intéressante dans la connaissance des processus de transferts chimiques à l'interface sol-plante et du fonctionnement physiologique des végétaux.

Enfin, l'augmentation rapide de l'utilisation des TR par l'homme nécessite une évaluation du risque environnemental représenté par les TR anthropiques. Les tests écotoxicologiques en cours devraient permettre de déterminer, si les TR favorisent la croissance et le développement végétal, et à partir de quel seuil de concentration elles deviennent inhibitrices. Ces données devraient également fournir une base permettant de fixer les futurs objectifs de recherche sur l'éventuel risque écotoxicologique des TR d'origine anthropique.

9 Synthèse

Le dénominateur commun de mes travaux de recherche, réalisé depuis 1995, est l'étude des échanges et des transferts chimiques dans les enveloppes géologiques externes. Les mécanismes chimiques et minéralogiques à l'origine des ces processus sont systématiquement au cœur de mes préoccupations, sans jamais perdre de vue le contexte géologique général. Les terres rares et les isotopes radiogéniques sont mes principaux outils de traçage. Selon le contexte de l'étude, je complète ces outils de base par d'autres méthodes géochimiques ou minéralogiques. L'intégration récente du compartiment végétal aux bilans élémentaires montre le soucis de prendre en compte l'ensemble des compartiments et la recherche permanente d'une ouverture scientifique.

Les enveloppes géologiques externes constituent un ensemble complexe et hétérogène en perpétuelle évolution. Dans ce contexte, il est indispensable de savoir, d'une part si un traceur caractérise une évolution ancienne ou récente et d'autre part si l'évolution identifiée concerne l'intégralité de l'objet d'étude ou uniquement une sous-unité. Une première étape concrète pour répondre à ces questions consiste à déterminer la spéciation du traceur chimique ou isotopique employé, afin d'établir un lien entre l'évolution reflétée par le traceur et une phase précise de l'échantillon (comme une phase minérale néoformée). Cette identification permet, dans l'exemple d'un profil d'altération, de savoir si le traceur signale une inhomogénéité lithologique primaire ou un processus d'altération.

Cette détermination, de la spéciation du traceur utilisé, reste une étape critique de la réalisation technique. Pour un échantillon solide, les outils analytiques permettant une analyse ponctuelle in situ (microsonde, EDAX, ablation laser) n'ont pas encore la sensibilité suffisante pour réaliser un spectre complet de TR ou des analyses isotopiques du Sr et du Nd. Il faut donc avoir recours à des méthodes indirectes telles que le leaching, pour scinder un échantillon en plusieurs fractions et les analyser séparément. Ces approches indirectes restent délicates, tant dans leur mise en œuvre que dans les interprétations, elles ne sont à utiliser qu'en complément à des analyses de la fraction totale (bulk sample). Cette approche reste, pour le moment et dans beaucoup de situations, le seul moyen d'obtenir des informations inaccessibles par la seule analyse de la fraction totale. Dans la majorité de mes études, j'ai ainsi pu observer que les TR sont très souvent associées à des phases minérales accessoires et/ou secondaires, telles que l'apatite ou les oxyhydroxides Fe-Mn.

En ce qui concerne les échantillons d'eau, on peut constater que la distinction entre fraction "dissoute" (< 0.22 ou 0.45 µm) et fraction particulaire (> 0.22 ou 0.45 µm) reste insuffisante pour appréhender la spéciation des TR dans l'eau et une séparation de la fraction colloïdale s'impose en complément à des méthodes de modélisation. Cet aspect sera discuté de façon plus détaillée dans le chapitre "Perspectives" (chap. B10).

Au cours des projets successifs, j'ai systématiquement affiné les approches méthodologiques et les interprétations. Au delà des processus de contamination, j'ai progressivement abordé le traçage, plus général, des mécanismes d'échange et de transferts chimiques. Les milieux aquatiques ont pris de plus en plus de place dans mes projets, parce qu'ils représentent le vecteur principal des échanges et transferts chimiques dans les systèmes géochimiques exogènes. L'étude sur les ruisseaux du Massif Central correspond à un tournant important dans ce sens. L'intégration de la biosphère dans mes études marque, pour l'instant, la dernière étape dans l'évolution de mon approche scientifique. Cette évolution était avant tout motivée par le constat que la biosphère fait partie intégrante des cycles géochimiques externes, que l'on devrait appeler **cycles biogéochimiques**.

Les études présentées dans ce mémoire illustrent le grand potentiel de traçage des TR. L'interprétation des données de TR est avant tout basée sur l'évolution de la forme des spectres de TR d'un échantillon à un autre (enrichissement au appauvrissement en TR légères, TR intermédiaires ou TR lourdes) ou sur l'évolution d'une anomalie spécifique du spectre (Ce/Ce*, Eu/Eu*, Y/Ho). Toutes ces modifications peuvent à la fois être liées à un processus chimique (adsorption, complexation en phase liquide, interaction avec des phases colloïdales, coprécipitation avec des phases néoformées) ou à un mélange entre 2 ou plusieurs phases présentant des spectres différents. Il est donc nécessaire de distinguer d'abord avec certitude ces 2 origines possibles avant de passer à l'interprétation. C'est dans ce contexte, que la combinaison des spectres de TR avec des analyses isotopiques du Sr et du Nd trouve tout son intérêt. En effet, ces systèmes isotopiques reflètent uniquement des processus d'échange et de transfert et sont complètement indépendants de réactions chimiques ou processus biologiques. Les isotopes du Nd sont particulièrement intéressants, parce qu'ils permettent de disposer d'un traceur isotopique au sein même du groupe des TR. La combinaison avec des isotopes du Sr et du Nd est donc souvent indispensable pour exploiter correctement la richesse d'information des spectres de TR.

L'analyse des TR est aujourd'hui pour la majorité des échantillons devenue une procédure de routine, elle peut être effectuée en même temps que l'analyse des éléments majeurs et d'autres éléments traces sans sur coût. C'est un énorme avantage sur les méthodes isotopiques, pour lesquelles un aliquot additionnel doit être préparé et analysé, représentant un investissement en temps et en argent. C'est la raison pour laquelle je considère que l'analyse des TR devrait aujourd'hui être intégrée en routine dans toute analyse chimique.

Dans le cadre des projets de recherche résumés dans ce mémoire, j'ai eu l'opportunité d'encadrer ou de co-encadrer des étudiants et doctorants. A chacune de ces expériences d'encadrement est associée une avancée significative du projet en question. La recherche gagne, et c'est bien connu, en dynamique lorsqu'elle implique des étudiants et des doctorants. Ceci s'explique bien entendu par la présence d'un collaborateur disponible à 100 % pour la recherche, mais elle est aussi le résultat de la nécessaire remise

en question et ouverture, qu'impose le travail d'encadrement d'un jeune chercheur. Être disponible pour l'encadrement de jeunes chercheurs est aussi pour l'enseignant-chercheur un moyen efficace de lutter contre l'ensevelissement de son activité de recherche sous le poids des tâches administratives et techniques. Le maintien d'un équilibre sain entre enseignement et recherche est crucial pour l'avenir de la recherche universitaire et je présente ici mon habilitation à diriger des recherches pour maintenir cet équilibre.

10 Perspectives de recherche

Et l'avenir, ... Qui peut le dire ?

Alors restons raisonnable, mes projets de recherche à court et à moyen terme vont probablement se concentrer sur les 2 axes, que sont : les transferts des TR à l'interface géosphère – biosphère, ainsi que le transport et le fractionnement des TR dans l'eau par la phase colloïdale. La première thématique est actuellement en cours et décrite dans le chapitre B8. L'axe de recherche sur la phase colloïdale est la continuation directe du projet sur les TR dans les ruisseaux du Massif Central (chap. B7) et présenté ci-dessous :

10.1 Les TR de la phase colloïdale du bassin versant du Malaval : quantification du rôle de la fraction colloïdale et essai d'une modélisation des interactions

10.1.1 Contexte et objectifs

Dans le projet sur le transport et le fractionnement des TR dans le Massif Central (chap. B7) nous avons suggéré que le fractionnement des spectres de TR, observé dans l'eau des ruisseaux, était dû à la présence de colloïdes d'oxyhydroxides de Fe. Nous n'avons, pour l'instant, pas de preuve directe de la présence de ces colloïdes, qui sont des "microparticules" minérales ou organiques finement broyées ou des phases minérales ou organiques en cours de précipitation.

La méthode analytique donnant accès à la phase colloïdale est l'ultrafiltration, elle a été développée depuis les années 1990 (Gaillardet *et al.*, 2003 et réf. incluses). Le principe de cette méthode consiste à séparer, par filtration tangentielle, plusieurs fractions colloïdales jusqu'à environ 1 nm à partir d'une eau préfiltrée à 0.22 ou 0.45 µm. Les systèmes d'ultrafiltration ont beaucoup évolué ces dernières années en termes de performance, de facilité d'utilisation et de baisse de coût. Le laboratoire de chrono-environnement a récemment, sous l'impulsion de ma collègue Sophie Denimal, fait l'acquisition d'un système d'ultrafiltration Millipore Pellicon XL50. Nous sommes actuellement en train de tester le matériel et de mettre en place les protocoles analytiques, dans le cadre du projet de recherche de Master VTESS d'Elie Dhivert, dont je suis co-encadrant avec S. Denimal. Cet équipement sera utilisé pour l'étude de la phase colloïdale dans les ruisseaux du Massif Central.

10.1.2 État des connaissances

Des études récentes montrent que la phase colloïdale joue un rôle très important dans les transferts chimiques des ETM à l'échelle du bassin versant, notamment pour les ETM de charge 3+ (Viers *et al.*, 1997; Dupré *et al.*, 1999; Dia *et al.*, 2000; Ingri *et al.*, 2000; 2006; Andersson *et al.*, 2001; Lyven *et al.*,

2003; Tosiani *et al.*, 2004; Denimal *et al.*, 2005; Andersson *et al.*, 2006). Les colloïdes, sur lesquels les métaux peuvent être adsorbés ou coprécipités (colloïdes organiques ou colloïdes d'oxydes Fe-Mn), servent de vecteur de transport vers les eaux de surface, les eaux du sol et les eaux souterraines. Les quantités absolues d'ETM transportés à l'année par la phase particulaire et colloïdale de l'écoulement de surface sont, pour certains ETM, plus importantes que celles associées à la phase dissoute (Dahlqvist *et al.*, 2007). Ce contexte montre que l'étude des transferts des ETM dans l'eau doit aujourd'hui obligatoirement inclure une analyse de la phase colloïdale.

La séparation de la phase colloïdale est techniquement délicate et soumise à des artefacts analytiques (Viers *et al.*, 1997; Dupré *et al.*, 1999; Lyven *et al.*, 2003; Andersson *et al.*, 2006; Dahlqvist *et al.*, 2007). C'est la raison pour laquelle des efforts considérables ont été fait pour intégrer l'interaction entre éléments traces métalliques (ETM) et phase colloïdale dans des modèles numériques (Pourret *et al.*, 2007a,b; 2008). Ces modèles permettront d'affiner l'interprétation des données analytiques. Nous envisageons donc, dans un deuxième volet du projet, en collaboration avec Olivier Pourret de l'Institut Polytechnique LaSalle Beauvais, de modéliser l'interaction des TR avec la phase colloïdale et de comparer les résultats avec les données analytiques.

10.1.3 Approche envisagée

L'étude sera réalisée dans le bassin versant du Malaval décrit dans le chapitre B7 (Fig. 44). Le ruisseau principal sera dans un premier temps échantillonné à l'amont, au milieu et à l'aval sur une distance d'environ 10 km afin de vérifier l'hypothèse, que le fractionnement des spectres de TR est bien contrôlé par la phase colloïdale. Si les résultats sont concluants, nous envisageons d'étendre l'échantillonnage sur l'intégralité du bassin versant.

La plupart des études actuelles sur les colloïdes se concentrent sur des rivières et fleuves et décrivent l'évolution de la phase colloïdale sur une seule station au cours du temps (ex. Andersson *et al.*, 2006; Dahlqvist *et al.*, 2007). Le projet que nous proposons fournira des informations sur l'évolution des colloïdes, dans un petit ruisseau à un instant donné et en fonction de la distance de la source.

Les résultats des analyses de la phase colloïdale du bassin versant du Malaval serviront aussi de base pour des modélisations numériques. En effet, tandis que la modélisation de la spéciation chimique des ETM dans la phase dissoute est courante avec des logiciels tels que PHREEQC, très peu de codes de calcul prennent en charge la phase colloïdale. Cette partie du projet se déroulera en collaboration avec Olivier Pourret, qui a dans ses travaux antérieurs modélisé la spéciation des TR par des colloïdes organiques (Pourret *et al.*, 2007a,b; 2008) et il est actuellement en train d'inclure les colloïdes d'oxydes Fe-Mn dans ses modèles. Les analyses du présent projet permettront de confronter les résultats de la modélisation avec des données de terrain. Si ces premiers résultats se révèlent concluants, nous envisageons d'utiliser l'outil de modélisation pour quantifier le transport des TR et d'autres ETM par la phase colloïdale à l'échelle du bassin versant.

Liste des figures

des TR coprécipitées avec des apatites (Byrne *et al.*, 1996). Le facteur de fractionnement expérimentale λ_i est présenté en forme inverse afin de montrer le fractionnement dans la solution résiduelle (Fig. 11 de Steinmann *et al.*, 2001).

Fig. 22 : Carte et coupe avec la localisation du site de forage sur le récif barrière de Tahiti à Papeete (Fig. 1 de Steinmann et Dejardin, 2004).

Fig. 23 : Comparaison de la densité de l'eau interstitielle avec celle de l'eau de mer au large du récif (σ_t = {densité - 1} * 1000). La densité de l'eau interstitielle est toujours plus faible que dans l'océan ouvert (Fig. 3 de Steinmann et Dejardin, 2004).

Fig. 24 : Comparaison entre les rapports $^{87}Sr/^{86}Sr$ et les teneurs en H4SiO4 de l'eau interstitielle (Fig. 5 de Steinmann et Dejardin, 2004).

Fig. 25 : Diagramme d'isochrone Rb-Sr avec les données d'eau interstitielle, d'eau de mer, de calcaires récifaux et de basalte. On peut distinguer dans le diagramme un mélange entre eau issue de l'interaction eau-roche et eau de mer (100 à 60 m), suivi dans la partie sommitale du récif par un mélange avec de l'eau de pluie. Les étiquettes des points de données en mètres indiquent la profondeur (Fig. 7 de Steinmann et Dejardin, 2004).

Fig. 26 : Diagramme de mélange $^{87}Sr/^{86}Sr$ vs. 1/Sr. Ce diagramme montre de façon plus détaillée les relations de mélange entre eau interstitielle, eau de mer et eau météorique (Fig. 8 de Steinmann et Dejardin, 2004).

Fig. 27 : Mélange entre eau interstitielle et océan ouvert en fonction de la profondeur dans le récif calculé à partir des données isotopiques du Sr et des teneurs en H4SiO4 montrées dans la Fig. 24 (Fig. 9 de Steinmann et Dejardin, 2004).

Fig. 28 : Comparaison entre les teneurs en silice et l'alcalinité de tous les échantillons d'eau interstitielle. On constate une corrélation négative entre les 2 paramètres et on peut observer un lien avec la profondeur : En s'approchant de la surface, les 2 paramètres évoluent progressivement vers des valeurs typiques pour une eau de mer (Fig. 6 de Steinmann et Dejardin, 2004).

Fig. 29 : Évolution de la teneur en silice et de la salinitté des 16 séries d'eau interstitielle avec la profondeur. Sur la base de l'évolution de ces 2 paramètres, 3 groupes de circulation ont pu être distingués. Dans le diagramme H4SiO4 vs. alcalinité, les échantillons de chaque groupe définissent une répartition bien spécifique. L'évolution d'un groupe à l'autre peut être interprété en terme de changements de voies de circulation de l'eau interstitielle (Fig. 30) (Fig. 10 de Steinmann et Dejardin, 2004).

Fig. 30 : Différents schémas de circulation de l'eau interstitielle. Pendant la première année (groupe 1 ; 2/93 - 2/94), la circulation est alimentée par une infiltration d'eau de mer profonde à la limite basalte-récif, complétée par une infiltration diffuse dans la partie holocène du récif comme décrit par la Fig. 27. A partir de la 2ème année (groupe 2 ; 3/94 - 12/94) on constate une nouvelle alimentation d'eau de mer profonde au niveau d'une surface de karstification à la limite entre la partie pleistocène et holocène du récif, qui remplace en partie l'arrivée initiale à la base du récif. Cette évolution générale est de temps en temps interrompue par des évènements ponctuels (groupe 3). (Fig. 12 de Steinmann et Dejardin, 2004).

Fig. 31 : A) Situtation générale du site du seamount "Dorado" et B) carte détaillée de "Dorado" avec localisation de la carotte 50 GC et des sites voisins sans activité hydrothermale (Fig. 1 de Bodeï *et al.*, 2008).

Fig. 32 : Log stratigraphique de la carotte 50 GC, localisation des échantillons et répartition des différentes composantes : 1 = particules de verres volcaniques et microfossiles siliceux ; 2 = argiles détritiques ; 3 = phillipsite ; 4 = oydes Mn ; 5 = oxydes Fe ; 6 = apatite (Fig. 2 de Bodeï *et al.*, 2008).

Fig. 33 : Comparaison de la composition en éléments majeurs entre la série de la carotte 50 GC et les sédiments de référence, par les facteurs d'enrichissement (voir texte). Les sédiments à la base de la carotte 50 GC sont fortement enrichis en CaO, Fe_2O_3, MnO et P_2O_5. Le niveau à 100 cm bsf est un encroûtement en oxyde de Mn (Fig. 8b de Bodeï *et al.*, 2008).

Fig. 34 : Pourcentages d'éléments majeurs mobilisés lors du leaching à l'HCl 1 N dans les sédiments de la carotte 50 GC et les sédiments de référence. Le leaching a mobilisé la quasi-totalité du P_2O_5, Na_2O et CaO, quasiment pas de MnO, Fe_2O_3 et SiO_2. Les barres d'erreurs désignent l'écart-type.

Fig. 35 : Composition isotopique du Sr des échantillons de roche totale (WR), des leachates (L) et des résidus (R) de la carotte 50 GC. Les compositions moyennes avec écart types des sédiments de référence (sites voisins sans activité hydrothermale), ainsi que celles du basalte océanique et de l'eau de mer actuelle (Palmer et Elderfield, 1985) sont données pour comparaison (Fig. 4 de Bodeï *et al.*, in prep).

Fig. 36 : Composition isotopique du Nd des échantillons de roche totale (WR), des leachates (L) et des résidus (R) de la carotte 50 GC. Les compositions moyennes avec écart types des sédiments de référence, ainsi que celles du basalte océanique et de l'eau de mer actuelle du Pacifique à 2000 m (van de Flierdt *et al.*, 2004) sont données pour comparaison (Fig. 5 de Bodeï *et al.*, in prep).

Fig. 37 : Diagramme d'isochrone Sm-Nd des données de la Fig. 36. Les données de la carotte 50 GC définissent une droite de mélange entre les échantillons de référence et l'eau de mer. Les chiffres à côté des points de données indiquent la profondeur dans la carotte 50 GC (Fig. 6 de Bodeï *et al.*, in prep).

Fig. 38 : Diagramme $^{143}Nd/^{144}Nd$ vs. $^{87}Sr/^{86}Sr$ avec les données de roche totale de la carotte 50 GC. Les nombres à côté des points donnent la profondeur dans la carotte en cm. La ligne entre sédiments de référence et eau de mer est une courbe de mélange calculée d'après la procédure décrite dans Faure, 1986. Les valeurs indiquées le long de la courbe donnent le rapport eau/roche en L/kg nécessaire pour transformer le sédiment de référence en sédiment hydrothermal altéré avec une composition isotopique donnée. Le diagramme montre qu'un rapport eau/roche entre 10 E6 et 10 E8 est nécessaire pour expliquer les compositions isotopiques odes sédiments de la carotte 50 GC et qu'il augmente avec la profondeur (Fig. 12 de Bodeï *et al.*, in prep).

Fig. 39 : Log des teneurs en Nd avec la profondeur dans les échantillons de roche totale, les leachates et les résidus de la carotte 50 GC. Les niveaux essentiellement composés d'oxydes de Mn sont présentés séparément. La comparaison avec les teneurs moyennes des sédiments de référence montre que la roche totale et les leachates de la carotte 50 GC sont fortement enrichis en Nd, tandis que les concentrations des résidus sont similaires.

Fig. 40 : Corrélation entre les teneurs en Nd et P_2O_5 dans les échantillons de roche totale de la carotte 50 GC. Les niveaux riches en apatite et

oxyhydroxydes de Fe à la base de la carotte (110 et 124 cm bsf), ainsi que les niveaux d'oxydes de Mn (2 et 100 cm bsf) ne rentrent pas dans la corrélation et ne sont pas présentés. Les étiquettes des points de données indiquent la profondeur dans la carotte en cm bsf.

Fig. 41 : Spectres des TR des échantillons de roche totale (WR), des leachates (L) et des résidus (R) de la carotte 50 GC normalisés par rapport au PAAS (McLennan, 1989). Les spectres des sédiments de référence, ainsi que celui de l'eau de mer actuelle du Pacifique à 2500 m (Alibo et Nozaki, 1999) sont donnés pour comparaison. Le spectre de l'eau de mer a été multiplié d'un facteur de 1000 pour faciliter la comparaison (Fig. 7 de Bodeï *et al.*, in prep).

Fig. 42 : Évolution avec la profondeur de l'anomalie du Ce et de l'Eu dans les échantillons de roche totale de la carotte 50 GC. Les valeurs de l'eau de mer actuelle du Pacifique à 2500 m (Alibo et Nozaki, 1999) et du sédiment de référence sont données pour comparaison (Fig. 10 de Bodeï *et al.*, 2008).

Fig. 43 : Corrélation entre anomalie du Ce et $^{143}Nd/^{144}Nd$ pour les leachates et les échantillons de roche totale de la carotte 50 GC et des sédiments de référence. Les échantillons de la carotte 50 GC occupent une position intermédiaire entre sédiment de référence et eau de mer. Les étiquettes à côté des points de la carotte 50 GC donnent la profondeur en cm bsf et montrent que l'influence du pôle eau de mer augmente avec la profondeur. On constate qu'à l'exception des échantillons de 110 et 124 cm bsf, les leachates sont par rapport à la roche totale systématiquement décalés en direction de l'eau de mer (Fig. 11 de Bodeï *et al.*, in prep).

Fig. 44 : Carte géologique simplifiée du site d'étude du bassin versant du Malaval entre la chaîne du Devès et les gorges de l'Allier au SW du Puy-en-Velay (Fig. 1 de Steinmann et Stille, 2008).

Fig. 45 : Évolution de la composition isotopique du Sr (A) et du Nd (B) dans l'eau filtrée à 0.45 µm des ruisseaux Malaval et Séjallières. Les compositions isotopiques de l'eau restent toujours proches du basalte. Les pourcentages de Sr et de Nd d'origine granitique ou orthogneissique restent même à l'aval inférieure à 20 % pour le Sr et à de 40 % pour le Nd.

Fig. 46 : Évolution des rapports Nd/Yb dans l'eau filtrée à 0.45 µm des ruisseaux Malaval et Séjallières. Le rapport Nd/Yb permet, comme le rapport La/Yb, de quantifier un fractionnement entre TR légères et TR lourdes. Il montre que l'appauvrissement en TR légères s'accentue de l'amont vers l'aval (Fig. 4 de Steinmann et Stille, 2008).

Fig. 47 : Les teneurs en Nd et les rapports Nd/Yb de la fraction <0.45 µm, ainsi que l'anomalie du Ce des leachates HCl 1M, de la phase particulaire dépendent des teneurs en Fe dans la fraction <0.45 µm (Fig. 5 de Steinmann et Stille, 2008).

Fig. 48 : Variation de l'indice de saturation de la goethite et du rapport Nd/Yb de l'eau filtrée à 0.45 µm des ruisseaux Malaval et Séjallières avec la distance. On constate pour les 2 paramètres une diminution des valeurs à partir du moment où le ruisseau a franchi le rebord du plateau basaltique (Fig. 7 de Steinmann et Stille, 2008).

Fig. 49 : Schéma interprétatif des processus et paramètres contrôlant le transport et le fractionnement des TR dans les ruisseaux du Massif Central (Fig. 10 de Steinmann et Stille, 2008).

Fig. 50 : Évolution des spectres de TR de la fraction dissoute au niveau de 3 confluences de ruisseaux. Les spectres labélisé "obs" sont des spectres analysés après la confluence. Les spectres labélisé "calc" sont des spectres calculés pour le ruisseau après la confluence à partir des spectres des 2 affluents en utilisant les isotopes du Sr pour déterminer la fraction d'eau provenant de chacun des affluents. On constate que l'anomalie en Ce et le rapport La/Yb sont systématiquement plus élevés que ceux des spectres calculés (Fig. 8 de Steinmann et Stille, 2008).

Fig. 51 : Les 2 diagrammes montrent un lien assez direct entre le pourcentage d'eau provenant de l'affluent et les écarts de l'anomalie du Ce et du rapport La/Yb présentés dans la Fig. 50. Ceci signifie, que les TR ne sont pas mélangées de façon homogène au niveau des confluences, mais qu'il y a systématiquement une perte de Ce et des TR légères, qui augmente en fonction de la taille relative de l'affluent (Fig. 9 de Steinmann et Stille, 2008).

Fig. 52 : Spectres de TR (± écart type) du calcaire du site du massif du Jura (site Cussey-sur-Lison), du granite des Vosges (site du Strengbach) et des carbonatites du Kaiserstuhl. Les spectres de TR des trois sites sont clairement différents. Notamment les carbonatites ont des teneurs en TR très élevées et des spectres fortement enrichis en TR légères.

Fig. 53 : Spectres moyens de TR (± écart type) des sols du site du massif du Jura (site Cussey-sur-Lison sur calcaire), du massif des Vosges (site du Strengbach sur granite) et du Kaiserstuhl (carbonatites). La comparaison avec les spectres des roches correspondantes (Fig. 52) montre que les sols ont en grande partie hérité le spectre de la roche mère. Uniquement les sols du massif des Vosges montrent une évolution significative des spectres de TR par rapport à celui de leur roche mère.

Fig. 54 : Exemple de spectres de TR d'un hêtre du massif du Jura (site Cussey-sur-Lison). Les teneurs en TR sont beaucoup plus élevés dans les racines (échantillons Rp, Rm, Rg) que dans le tronc (autres échantillons). La forme des spectres des racines reflète presque directement le spectre du sol local (Fig. 53). Rp = racines < 2 mm, Rm = racines 2-10 mm, Rg dia 20 = racine de 20 mm de diamètre. 0mC = centre de la rondelle de tronc à 0m de hauteur du sol, 0mM = milieu de la rondelle de tronc à 0m, 0mE = extérieur de la rondelle de tronc à 0m, idem pour la rondelle de tronc à 6.5 m de hauteur du sol (Thèse Brioschi en cours).

Fig. 55 : Spectres moyens de TR des troncs d'épicéa et de hêtre du massif du Jura et du massif des Vosges comparés avec les spectres de quelques échantillons préliminaires du Kaiserstuhl. On constate des spectres assez similaires pour le Jura et les Vosges. La seul différence concerne l'anomalie négative en Ce pour le Jura, qui est absente dans les Vosges et directement hérité du calcaire. On observe pour le Jura et les Vosges une anomalie positive en Eu, qui est absente dans la roche et les sols. Les spectres en TR des végétaux du Kaiserstuhl sont clairement différents des autres sites et reflètent assez directement les spectres du sol.

Liste des tableaux

Bibliographie

Abdelouas, A., Crovisier, J.L., Lutze, W., Fritz, B., Mosser, A., Müller, R., 1994. Formation of hydrotalcite-like compounds during R7T7 nuclear waste glass and basaltic glass alteration. Clays and Clay Minerals 42, 526-533.

Advocat, T., Jollivet, P., Crovisier, J.L., del Nero, M., 2001. Long-term alteration mechanisms in water for SON68 radioactive borosilicate glass. Journal of Nuclear Materials 298, 55-62.

Albarède, F., Michard, A., 1987. Evidence for slowly changing 87Sr/86Sr in runoff from freshwater limestones of southern France. Chemical Geology 64, 55-65.

Alibo, D.S., Nozaki, Y., 1999. Rare earth elements in seawater: particle association, shale-normalization, and Ce oxidation. Geochimica et Cosmochimica Acta 63, 363-372.

Allègre, C., Dupré, B., Négrel, P., Gaillardet, J., 1996. Sr-Nd-Pb isotope systematics in Amazon and Congo River systems: Constraints about erosion processes. Chemical Geology 131, 93-112.

Andersson, K., Dahlqvist, R., Turner, D., Stolpe, B., Larsson, T., Ingri, J., Andersson, P., 2006. Colloidal rare earth elements in a boreal river: Changing sources and distributions during the spring flood. Geochimica et Cosmochimica Acta 70, 3261-3274.

Andersson, P.S., Dahlqvist, R., Ingri, J., Gustafsson, O., 2001. The isotopic composition of Nd in a boreal river: a reflection of selective weathering and colloidal transport. Geochimica et Cosmochimica Acta 65, 521-527.

Aouad, G., Stille, P., Crovisier, J., Geoffroy, V.A., Meyer, J., Lahd-Geagea, M., 2006. Influence of bacteria on lanthanide and actinide transfer from specific soil components (humus, soil minerals and vitrified municipal solid waste incinerator bottom ash) to corn plants: Sr-Nd isotope evidence. The Science of The Total Environment 370, 545-551.

Aubert, D., Probst, A., Stille, P., 2004. Distribution and origin of major and trace elements (particularly REE, U and Th) into labile and residual phases in an acid soil profile (Vosges Mountains, France). Applied Geochemistry 19, 899-916.

Aubert, D., Probst, A., Stille, P., Viville, D., 2002a. Evidence of hydrological control of Sr behavior in stream water (Strengbach catchment, Vosges mountains, France). Applied Geochemistry 17, 285-300.

Aubert, D., Stille, P., Probst, A., 2001. REE fractionation during granite weathering and removal by waters and suspended loads: Sr and Nd isotopic evidence. Geochimica et Cosmochimica Acta 65, 387-406.

Aubert, D., Stille, P., Probst, A., Gauthier-Lafaye, F., Pourcelot, L., Del Nero, M., 2002b. Characterization and migration of atmospheric REE in soils and surface waters. Geochimica et Cosmochimica Acta 66, 3339-3350.

Banner, J.L., 2004. Radiogenic isotopes: systematics and applications to earth surface processes and chemical stratigraphy. Earth-Science Reviews 65, 141-194.

Barry, M.J., Meehan, B.J., 2000. The acute and chronic toxicity of lanthanum to Daphnia carinata. Chemosphere 41, 1669-1674.

Bau, M., 1996. Controls on the fractionation of isovalent trace elements in magmatic and aqueous systems: evidence from Y/Ho, Zr/Hf, and lanthanide tetrad effect. Contributions to Mineralogy and Petrology 123, 323-333.

Bau, M., 1999. Scavenging of dissolved yttrium and rare earths by precipitating iron oxyhydroxide: experimental evidence for Ce oxidation, Y-Ho fractionation, and lanthanide tetrad effect. Geochimica et Cosmochimica Acta 63, 67-77.

Bau, M., Dulski, P., 1996. Anthropogenic origin of positive gadolinium anomalies in river waters. Earth and Planetary Science Letters 143, 245-255.

Bau, M., Dulski, P., 1999. Comparing yttrium and rare earths in hydrothermal fluids from the Mid-Atlantic Ridge: implications for Y and REE behaviour during near-vent mixing and for the Y/Ho ratio of Proterozoic seawater. Chemical Geology 155, 77-90.

Bau, M., Knappe, A., Dulski, P., 2006. Anthropogenic gadolinium as a micropollutant in river waters in Pennsylvania and in Lake Erie, northeastern United States. Chemie der Erde - Geochemistry 66, 143-152.

Bernard, L., Anthony, L., Daniel, A., Nadya, R., Natalie, M., Tilman, B.D., 2005. Chronic renal failure is associated with increase tissue depletion of lanthanum after 28-day oral administration. Kidney International 67, 1062–1069.

Blum, J., Erel, Y., Brown, K., 1994. 87Sr/86Sr ratios of Sierra Nevada stream waters: Implications for relative mineral weathering rates. Geochimica et Cosmochimica Acta 58, 5019-5025.

Blum, J.D., Erel, Y., 2003. Radiogenic isotopes in weathering and hydrology. In: Drever, J.A., Turekian, K.K. (Eds.), *Surface and ground water, weathering, and soils*. Elsevier, pp. 365-392.

Bodeï, S., 2004. Transfert de matière et interactions eau-sédiment en environnement océanique (flanc de dorsale). MS thesis, Unversité de Franche-Comté, Besançon, 30 pp.

Bodeï, S., 2007. Etude minéralogique et géochimique de dépôts métallifères marins formés dans un contexte hydrothermal de basse température, sur le flanc Est de la dorsale Est-Pacifique. PhD thesis, Université de Franche-Comté, Besançon, 264 pp.

Bodeï, S., Buatier, M., Steinmann, M., Adatte, T., Wheat, C., 2008. Characterization of metalliferous sediment from a low-temperature hydrothermal environment on the Eastern Flank of the East Pacific Rise. Marine Geology 250, 128-141.

Bodeï, S., Manceau, A., Geoffroy, N., Baronnet, A., Buatier, M., 2007. Formation of todorokite from vernadite in Ni-rich hemipelagic sediments. Geochimica et Cosmochimica Acta 71, 5698-5716.

Bodeï, S., Steinmann, M., Buatier, M., in prep. Nd-Sr isotope and REY geochemistry of metalliferous sediments in a low-temperature off-axis hydrothermal environment (Costa Rica margin). Chemical Geology , in prep.

Bonotto, D., Fujimori, K., Moreira-Nordemann, L., 2007. Determination of weathering rate of the Morro do Ferro Th-REEs deposit, Brazil using U-isotope method. Applied Radiation and Isotopes 65, 474-481.

Bontemps, S., 2006. Mobilisation et transfert des éléments majeurs, en traces et terres rares au cours de l'altération dans le bassin versant de Malaval (Massif Central). MS thesis, Unversité de Franche-Comté, Besançon, 30 pp.

Braitsch, O., 1971. *Salt deposits. their origin and composition*. Springer-Verlag, Berlin-Stuttgart-Heidelberg-New York, 297 pp.

Braun, J.J., Pagel, M., Muller, J.P., Bilong, P., Michard, A., Guillet, B., 1990. Ce anomalies in lateritic profiles. Geochimica et Cosmochimica Acta 54, 781-795.

Braun, J.J., Viers, J., Dupré, D., Polve, M., Ndam, J., Muller, J.P., 1998. Solid/liquid REE fractionation in the lateritic system of Goyoum, East Cameroon: The implication for the present dynamics of the soil covers of the humid tropical regions. Geochimica et Cosmochimica Acta 62, 273-299.

Briner, W., Rycek, R.F., Moellenberndt, A., Dannull, K., 2000. Neurodevelopmental effects of lanthanum in mice. Neurotoxicology and Teratology 22, 573-581.

Brioschi, L., 2007. Absorption et fractionnement des terres rares par la végétation, en fonction des conditions de sol. MS thesis, Unversité de Franche-Comté, Besançon, 30 pp.

Bros, R., Hidaka, H., Kamei, G., Ohnuki, T., 2003. Mobilization and mechanisms of retardation in the Oklo natural reactor zone 2 (Gabon) - inferences from U, REE, Zr, Mo and Se isotopes. Applied Geochemistry 18, 1807-1824.

Buatier, M.D., Früh-Green, G.L., Karpoff, A.M., 1995. Mechanisms of Mg-phyllosilicate formation in a hydrothermal system at a sedimented ridge (Middle Valley, Juan de Fuca). Contributions to Mineralogy and Petrology 122, 134-151.

Buatier, M.D., Monnin, C., Früh-Green, G.L., Karpoff, A., 2001. Fluid-sediment interactions related to hydrothermal circulation in the Eastern Flank of the Juan de Fuca Ridge. Chemical Geology 175, 343-360.

Byrne, R., Kim, K., 1993. Rare earth precipitation and coprecipitation behavior: The limiting role of PO43- on dissolved rare earth concentrations in seawater. Geochimica et Cosmochimica Acta 57, 519-526.

Byrne, R., Liu, X., Schijf, J., 1996. The influence of phosphate coprecipitation on rare earth distributions in natural waters. Geochimica et Cosmochimica Acta 60, 3341-3346.

Cantrell, K., Byrne, R., 1987. Rare earth element complexation by carbonate and oxalate ions. Geochimica et Cosmochimica Acta 51, 597-605.

Chavagnac, V., German, C.R., Milton, J.A., Palmer, M.R., 2005. Sources of REE in sediment cores from the Rainbow vent site (36°14'N, MAR). Chemical Geology 216, 329-352.

Choppin, G., 1983. Comparison of the solution chemistry of the actinides and the lanthanides. Journal of Less-Common Metals 93, 232-330.

Choppin, G., 1989. Soluble rare earth and actinide species in seawater. Marine Chemistry 28, 19-26.

Clauer, N., Chaudhuri, S., Kralik, M., Bonnot-Courtois, C., 1993. Effects of experimental leaching on Rb-Sr and K-Ar isotopic systems and REE contents of diagenetic illite. Chemical Geology 103, 1-16.

Cronan, D.S., Hodkinson, R.A., 1997. Geochemistry of hydrothermal sediments from ODP Sites 834 and 835 in the Lau Basin, southwest Pacific. Mar. Geol. 141, 237–268.

Crovisier, J., Advocat, T., Dussossoy, J., 2003. Nature and role of natural alteration gels formed on the surface of ancient volcanic glasses (Natural analogs of waste containment glasses). Journal of Nuclear Materials 321, 91-109.

Crovisier, J., Honnorez, J., Fritz, B., Petit, J., 1992. Dissolution of subglacial volcanic glasses from Iceland: laboratory study and modelling. Applied Geochemistry Suppl. Issue No. 1, 55-81.

Curti, E., Crovisier, J., Morvan, G., Karpoff, A., 2006. Long-term corrosion of two nuclear waste reference glasses (MW and SON68): A kinetic and mineral alteration study. Applied Geochemistry 21, 1152-1168.

D'Haese, P.C., Spasovski, G.B., Sikole, A., Hutchison, A., Freemont, T.J., Sulkova, S., Swanepoel, C., Pejanovic, S., Djukanovic, L., Balducci, A. et al., 2003. A multicenter study on the effects of lanthanum carbonate (Fosrenol) and calcium carbonate on renal bone disease in dialysis patients. Kidney International 64, 2327–2328.

Dahlqvist, R., Andersson, K., Ingri, J., Larsson, T., Stolpe, B., Turner, D., 2007. Temporal variations of colloidal carrier phases and associated trace elements in a boreal river. Geochimica et Cosmochimica Acta 71, 5339-5354.

Daux, V., Guy, C., Advocat, T., Crovisier, J., Stille, P., 1997. Kinetic aspects of basaltic glass dissolution at 90 °C: Role of aqueous silicon and aluminium. Chemical Geology 142, 109-126.

Davranche, M., Pourret, O., Gruau, G., Dia, A., Jin, D., Gaertner, D., 2008. Competitive binding of REE to humic acid and manganese oxide: Impact of reaction kinetics on development of cerium anomaly and REE adsorption. Chemical Geology 247, 154-170.

Davranche, M., Pourret, O., Gruau, G., Dia, A., Le Coz-Bouhnik, M., 2005. Adsorption of REE(III)-humate complexes onto MnO2: Experimental evidence for cerium anomaly and lanthanide tetrad effect suppression. Geochimica et Cosmochimica Acta 69, 4825-4835.

Degraaf, P., 2006. Investments off the beaten path: rare earth metals. Investor's digest 356, 12/06.

Déjardin, P., 1996. Etude d'un géosystème récifal insulaire (récif barrière de Tahiti, Polynésie Française). Caractérisation géochimique des différents compartiments et de leurs interactions. PhD thesis, Université Louis Pasteur de Strasbourg, 169 pp.

Denimal, S., Bertrand, C., Mudry, J., Paquette, Y., Hochart, M., Steinmann, M., 2005. Evolution of the aqueous geochemistry of mine pit lakes - Blanzy-Montceau-les-Mines coal basin (Massif Central, France): origin of sulfate contents; effects of stratification on water quality. Applied Geochemistry 20, 825-839.

Desaules, A., Sprengart, J., Wagner, G., Muntau, H., Theocharopoulos, S., 2001. Description of the test area and reference sampling at Dornach. The Science of The Total Environment 264, 17-26.

Dia, A., Gruau, G., Olivie-Lauquet, G., Riou, C., Molenat, J., Curmi, P., 2000. The distribution of rare earth elements in groundwaters: assessing the role of source-rock composition, redox changes and colloidal particles. Geochimica et Cosmochimica Acta 64, 4131-4151.

Diatloff, E., Smith, F.W., Asher, C.J., 2008. Effects of lanthanum and cerium on the growth and mineral nutrition of corn and mungbean. Annals of Botany 101, 971-982.

Ding, J.P., Pickard, B.G., 1993. Mechanosensory calcium-selective cation channels in epidermal cells. The Plant Journal 3, 83-110.

Douville, E., Bienvenu, P., Charlou, J.L., Donval, J.P., Fouquet, Y., Appriou, P., Gamo, T., 1999. Yttrium and rare earth elements in fluids from various deep-sea hydrothermal systems. Geochimica et Cosmochimica Acta 63, 627-643.

Douville, E., Charlou, J.L., Oelkers, E.H., Bienvenu, P., Jove Colon, C.F., Donval, J.P., Fouquet, Y., Prieur, D., Appriou, P., 2002. The rainbow vent fluids (36[deg]14′N, MAR): the influence of ultramafic rocks and phase separation on trace metal content in Mid-Atlantic Ridge hydrothermal fluids. Chemical Geology 184, 37-48.

Dupré, B., Gaillardet, J., Rousseau, D., Allègre, C.J., 1996. Major and trace elements of river-borne material: The Congo Basin. Geochimica et Cosmochimica Acta 60, 1301-1321.

Dupré, B., Viers, J., Dandurand, J., Polve, M., Benezeth, P., Vervier, P., Braun, J., 1999. Major and trace elements associated with colloids in organic-rich river waters: ultrafiltration of natural and spiked solutions. Chemical Geology 160, 63-80.

Elbaz-Poulichet, F., Seidel, J., Othoniel, C., 2002. Occurrence of an anthropogenic gadolinium anomaly in river and coastal waters of Southern France. Water Research 36, 1102-1105.

Elderfield, H., Wheat, C.G., Mottl, M.J., Monnin, C., Spiro, B., 1999. Fluid and geochemical transport through oceanic crust: a transect across the eastern flank of the Juan de Fuca Ridge. Earth and Planetary Science Letters 172, 151-165.

Ewing, R., 1979. Natural glasses: Analogues for radioactive waste forms. In: McCarthy, G. (Ed.), *Scientific basis for nuclear waste management*. Plenum Press, New York, pp. 57-68.

Faure, G., 1986. *Principles of isotope geology*. John Wiley & sons, New York, 589 pp.

Federer, P., 1993. Verteilung und Mobilität der Schwermetalle Cadmium, Kupfer und Zink in anthropogen belasteten, kalkreichen Böden. PhD thesis, ETH Zürich, 119 pp.

Federer, P., Sticher, H., 1991. Verhalten von Kupfer, Zink und Cadmium in einem stark belasteten Kalkboden. Chimia 45, 228-232.

Feely, R.A., Gendron, J.F., Baker, E.T., Lebon, G.T., 1994. Hydrothermal plumes along the East Pacific Rise, 8°40' to 11°50'N: Particle distribution and composition. Earth and Planetary Science Letters 128, 19-36.

Feely, R.A., Massoth, G.J., Baker, E.T., Cowen, J.P., Lamb, M.F., Krogslund, K.A., 1990. The effect of hydrothermal processes on midwater phosphorus distributions in the northeast Pacific. Earth and Planetary Science Letters 96, 305-318.

Feldhaus, A., 2006. Wirkung von Seltenen Erden auf den osteoporotisch veränderten Knochen im Tiermodell der ovariektomierten Ratte. PhD thesis, Tierärztliche Fakultät der Ludwig Maximilians-Universität München, 151 pp.

Feng, L., Xiao, H., He, X., Li, Z., Li, F., Liu, N., Zhao, Y., Huang, Y., Zhang, Z., Chai, Z., 2006. Neurotoxicological consequence of long-term exposure to lanthanum. Toxicology Letters 165, 112-120.

Fisher, A.T., Stein, C.A., Harris, R.N., Wang, K., Silver, E.A., Pfender, M., Hutnak, M., Cherkaoui, A., Bodzin, R., Villinger, H., 2003. Abrupt thermal transition reveals hydrothermal boundary and role of seamounts within the Cocos Plate. Geophysical Research Letters 30, 1550d oi:10.1029/2002GL016766.

Flood, P., Fagerstrom, J., Rougerie, F., 1996. Interpretation of the origin of massive replacive dolomite within atolls and sumerged carbonate platforms: strontium isotopic signature ODP Hole 866A, Resolution Guyot, Mid-Pacific Mountains. Sedimentary Geology 101, 9-13.

Gaillardet, J., Dupré, B., Allègre, C.J., Negrel, P., 1997. Chemical and physical denudation in the Amazon River Basin. Chemical Geology 142, 141-173.

Gaillardet, J., Viers, J., Dupré, B., 2003. Trace elements in river waters. In: Drever, J., Turekian, K. (Eds.), *Surface and ground water, weathering, and soils*. Elsevier, pp. 225-272.

Gauthier-Lafaye, F., Holliger, P., Blanc, P., 1996. Natural fission reactors in the Franceville basin, Gabon: A review of the conditions and results of a "critical event" in a geologic system. Geochimica et Cosmochimica Acta 60, 4831-4852.

Gauthier-Lafaye, F., Stille, P., Bros, R., 2004. The Gabon and Cigar lake U ore deposits. In: Gieré, R., Stille, P. (Eds.), *Energy, waste, and the environment: a geochemical perspective*. Geological Society, London, Special Publications, pp. 123-134.

German, C.R., Campbell, A.C., Edmond, J.M., 1991. Hydrothermal scavenging at the Mid-Atlantic Ridge: Modification of trace element dissolved fluxes. Earth and Planetary Science Letters 107, 101-114.

German, C.R., Colley, S., Palmer, M.R., Khripounoff, A., Klinkhammer, G.P., 2002. Hydrothermal plume-particle fluxes at 13°N on the East Pacific Rise. Deep-Sea Research I 49, 1921–1940.

German, C.R., Higgs, N.C., Thomson, J., Mills, R., Elderfield, H., Blusztajn, J., Fleer, A.P., Bacon, P., 1993. A geochemical study of metalliferous sediment from the TAG hydrothermal mound, 26°08' N, Mid-Atlantic Ridge. Journal of Geophysical Research 98, 9683–9692.

German, C.R., Klinkhammer, G.P., Edmond, J.E., Mitra, A., Elderfield, H., 1990. Hydrothermal scavenging of rare-earth elements in the ocean. Nature , 516–518.

Goldstein, S.J., Jacobsen, S.B., 1987. The Nd and Sr isotopic systematics of river-water dissolved material: Implications for the sources of Nd and Sr in seawater. Chemical Geology 66, 245-272.

Goldstein, S.J., Jacobsen, S.B., 1988. Rare earth elements in river waters. Earth and Planetary Science Letters 89, 35-47.

Gruau, G., Dia, A., Olivie-Lauquet, G., Davranche, M., Pinay, G., 2004. Controls on the distribution of rare earth elements in shallow groundwaters. Water Research 38, 3576-3586.

Guo, F.Q., Wang, Y.Q., Sun, J.X., Chen, H.M., 1996. REE bound proteins in natural plant fern Dicranopteris dichitoma. Journal of Radioanalytical and Nuclear Chemistry 209, 91-99.

Gutsche, A., 1988. Mineralreaktionen und Stofftransporte an einem Kontakt Basalt-Hartsalz in der Werra-Folge des Werkes Hattorf. MS thesis, Georg-August-Universität Göttingen, 118 pp.

Harlavan, Y., Erel, Y., 2002. The release of Pb and REE from granitoids by the dissolution of accessory phases. Geochimica et Cosmochimica Acta 66, 837-848.

Haxel, G.B., Hedrick, J.B., Orris, G.J., 2002. Rare Earth Elements: Critical Resources for High Technology. U.S. Geological Survey Fact Sheet 087-02, http://pubs.usgs.gov/fs/2002/fs087-02/.

He, M.L., Ranz, D., Rambeck, W.A., 2001. Study on the performance enhancing effect of rare earth elements in growing and fattening pigs. Journal of Animal Physiology and Animal Nutrition 85, 263-270.

He, M.L., Wang, Y.Z., Xu, Z.R., Chen, M.L., Rambeck, W.A., 2003. Effect of dietary rare earth elements on growth performance and blood parameters of rats. Journal of Animal Physiology and Animal Nutrition 87, 229-235.

Hedrick, J.B., 2008. Rare Earth. U.S. Geological Survey Mineral Commodity Summaries, January 2008, http://minerals.usgs.gov/minerals/pubs/commodity/rare_earths/mcs-2008-raree.pdf.

Hennebrüder, K., Wennrich, R., Mattusch, J., Stark, H., Engewald, W., 2004. Determination of gadolinium in river water by SPE preconcentration and ICP-MS. Talanta 63, 309-316.

Henry, P., Guy, C., Dudoignon, P., Sornein, J., Caristan, Y., 1996. A convective model of water flow in Muruora basalts. Geochimica et Cosmochimica Acta 60, 2087-2109.

Herrmann, A.G. & Knipping, B., 1993. *Waste disposal and evaporites. contributions to long-term safety*. Springer-Verlag, Berlin, 193 pp.

Hidaka, H., Gauthier-Lafaye, F., 2000. Redistribution of fissiogenic and non-fissiogenic REE, Th and U in and around natural fission reactors at Oklo and Bangombé, Gabon. Geochimica et Cosmochimica Acta 64, 2093-2108.

Hodell, P.J., Mueller, P.A., Garrido, J.R., 1991. Variations in the strontium isotopic composition of seawater during the Neogene. Geology 19, 24-27.

Honnorez, J., Karpoff, A.M., Trauth-Badaut, D., 1983. Sedimentology, mineralogy and geochemistry of green clay samples from the Galapagos

hydrothermal mounds, Holes 506, 506C and 507D Deep Sea Drilling Project Leg 70. Initial Reports DSDP 70, 221-224.

Hornig-Kjarsgaard, I., 1998. Rare Earth Elements in Sovitic carbonatites and their mineral phases. J. of Petrology 39, 2105-2121.

Humphris, S.E., Bach, W., 2005. On the Sr isotope and REE compositions of anhydrites from the TAG seafloor hydrothermal system. Geochimica et Cosmochimica Acta 69, 1511-1525.

Hutchison, A.J., Speake, M., Al-Baaj, F., 2004. Reducing high phosphate levels in patients with chronic renal failure undergoing dialysis: a 4-week, dose-finding, open-label study with lanthanum carbonate. Nephrology Dialysis Transplantation 19, 1902–1906.

Ingri, J., Malinovsky, D., Rodushkin, I., Baxter, D.C., Widerlund, A., Andersson, P., Gustafsson, O., Forsling, W., Ohlander, B., 2006. Iron isotope fractionation in river colloidal matter. Earth and Planetary Science Letters 245, 792-798.

Ingri, J., Widerlund, A., Land, M., Gustafsson, A., Andersson, P., Öhlander, B., 2000. Temporal variations in the fractionation of the rare earth elements in a boreal river; the role of colloidal particles. Chemical Geology 166, 23-45.

Innocent, C., Fagel, N., Stevenson, R., 1999. Do leaching experiments in deep-sea clays isolate a seawater component?. Canadian Journal of Earth Sciences 79, 707-713.

Jacobs, E., Steinmann, M., Stille, P., Pika-Biolzi, M., 1996. Sr isotope stratigraphy and variations in the Nd isotopic composition of foraminifera from the Lemme-Carosio section (northern Italy). Giornale di Geologia 58, 111-117.

Jacobson, R.S., 1992. Impact of Crustal Evolution on Changes of the Seismic Properties of the Uppermost Ocean Crust. Reviews in Geophysics 30, 23-42.

Jones, G., Whitaker, F., Smart, P., Sanford, W., 2000. Numerical modelling of geothermal and reflux circulation in Enewetak Atoll: implications for dolimitization. Journal of Geochemical Exploration 69-70, 71-75.

Kikuchi, M., Hidaka, H., Horie, K., Gauthier-Lafaye, F., 2007. Redistribution of REE, Pb and U by supergene weathering studied from in-situ isotopic analyses of the Bangombé natural reactor, Gabon. Geochimica et Cosmochimica Acta 71, 4716-4726.

Klinkhammer, G., Elderfield, H., Edmond, J., Mitra, A., 1994. Geochemical implications of rare earth element patterns in hydrothermal fluids from mid-ocean ridges. Geochimica et Cosmochimica Acta 58, 5105-5113.

Knappe, A., Möller, P., Dulski, P., Pekdeger, A., 2005. Positive gadolinium anomaly in surface water and ground water of the urban area Berlin, Germany. Chemie der Erde - Geochemistry 65, 167–189.

Knipping, B., 1989. *Basalt intrusions in evaporites*. Lecture Notes in Earth Sciences. Springer-Verlag, Berlin, 132 pp.

Knipping, B., Herrmann, A., 1985. Mineralreaktionen und Stofftransporte an einem Kontakt Basalt-Carnallitit im Kalisalzhorizont Thüringen der Werra-Serie des Zechsteins. Kali und Steinsalz 9, 111-124.

Koyama, M., Shirakawa, M., Takada, J., Katayama, Y., Matsubara, T., 1987. Trace elements in land plants: Concentration ranges and accumulators of rare earths, Ba, Ra, Mn, Fe, Co and heavy halogens. Journal of Radioanalytical and Nuclear Chemistry 112, 489-506.

Krauskopf, K., 1986. Thorium and rare-earth elements as analogues for actinide elements. Chemical Geology 55, 323-335.

Kuhn, T., Bau, M., Blum, N., Halbach, P., 1998. Origin of negative Ce anomalies in mixed hydrothermal-hydrogenetic Fe-Mn crusts from the Central Indian Ridge. Earth and Planetary Science Letters 163, 207-220.

Kulaksiz, S., Bau, M., 2007. Contrasting behaviour of anthropogenic gadolinium and natural rare earth elements in estuaries and the gadolinium input into the North Sea. Earth and Planetary Science Letters 260, 361-371.

Kümmerer, K., Helmers, E., 2000. Hospital Effluents as a Source of Gadolinium in the Aquatic Environment. Environmental Science and Technology 34, 573-577.

Land, M., Ohlander, B., Ingri, J., Thunberg, J., 1999. Solid speciation and fractionation of rare earth elements in a spodosol profile from northern Sweden as revealed by sequential extraction. Chemical Geology 160, 121-138.

Lee, J., Byrne, R., 1992. Examination of comparative rare earth element complexation behavior using linear free-energy relationships. Geochimica et Cosmochimica Acta 56, 1127-1138.

Li, Y.H., 1982. Interelement relationship in abyssal Pacific ferromanganese nodules and associated pelagic sediments. Geochimica et Cosmochimica Acta 46, 1053-1060.

Liang, T., Zhang, S., Wang, L., Kung, H., Wang, Y., Hu, A., Ding, S., 2005. Environmental biogeochemical behaviors of rare earth elements in soil-plant systems. Environmental Geochemistry and Health 27, 301-311.

Liu, Q., Wang, C., Huang, Y.X., Dong, K.H., Yang, W.Z., Wang, H., 2007. Effects of lanthanum on rumen fermentation, urinary excretion of purine derivatives and digestibility in steers. Animal Feed Science and Technology In Press, Corrected Proof, doi:10.1016/j.anifeedsci.2007.08.002.

Lunn, J., 2006. A 'rare' opportunity. Investment Briefing, Equity Research Great Western Minerals (GWG.V), Metals and Mining, http://www.gwmg.ca/pdf/Insinger_Report.pdf.

Lyven, B., Hassellov, M., Turner, D.R., Haraldsson, C., Andersson, K., 2003. Competition between iron- and carbon-based colloidal carriers for trace metals in a freshwater assessed using flow field-flow fractionation coupled to ICPMS. Geochimica et Cosmochimica Acta 67, 3791-3802.

Macfarlane, A., Danielson, A., Holland, H., Jacobsen, S., 1994. REE chemistry and Sm-Nd systematics of late Archean weathering profiles in the Fortescue Group, Western Australia. Geochimica et Cosmochimica Acta 58, 1777-1794.

Maheswaran, J., Meehan, B., Reddy, N., Peverill, K., Buckingham, S., 2001. Impact of rare earths elements on plant physiology and productivity. Rural Industries Research and Development Corporation (RIRDC) Publication 01, 145.

McLennan, S., 1989. Rare Earth Elements in sedimentary rocks: Influence of provenance and sedimentary processes. In: Lipin, B., McKay, G. (Eds.), *Geochemistry and mineralogy of rare earth elements*. Mineral. Soc. Am, Washington, D.C, pp. 169-225.

Meynadier, L., Allègre, C., O'Nions, R.K., 2008. Plate tectonics, radiogenic isotopic tracers and paleoceanography: The case of the manganese crusts in the Pacific. Earth and Planetary Science Letters 272, 513-522.

Michard, A., Albarède, F., Michard, G., Minster, J.F., Charlou, J.L., 1983. Rare earth elements and uranium in high-temperature solutions from East Pacific Rise hydrothermal vent field (13°N). Nature 303, 795–797.

Millero, F., 1992. Stability constants for the formation of rare earth inorganic complexes as a function of ionic strength. Geochimica et Cosmochimica Acta 56, 3123-3132.

Mills, R.A., Wells, D.M., Roberts, S., 2001. Genesis of ferromanganese crusts from the TAG hydrothermal field. Chemical Geology 176, 283-293.

Möller, P., Dulski, P., Bau, M., Knappe, A., Pekdeger, A., Sommer-von Jarmersted, C., 2000. Anthropogenic gadolinium as a conservative tracer in hydrology. Journal of Geochemical Exploration 69-70, 409-414.

Möller, P., Morteani, G., Dulski, P., 2003. Anomalous Gadolinium, Cerium, and Yttrium Contents in the Adige and Isarco River Waters and in the Water of Their Tributaries (Provinces Trento and Bolzano/Bozen, NE Italy). Acta Hydrochim. Hydrobiol. 31, 225–239.

Möller, P., Paces, T., Dulski, P., Morteani, G., 2002. Anthropogenic Gd in Surface Water, Drainage System, and the Water Supply of the City of Prague, Czech Republic. Environmental Science and Technology 36, 2387 - 2394.

Mottl, M.J., Wheat, C., 1994. Hydrothermal circulation through mid-ocean ridge flanks: Fluxes of heat and magnesium. Geochimica et Cosmochimica Acta 58, 2225-2237.

Munier, I., Crovisier, J.-., Grambow, B., Fritz, B., Clément, A., 2004. Modelling the alteration gel composition of simplified borosilicate glasses by precipitation of an ideal solid solution in equilibrium with the leachant. Journal of Nuclear Materials 324, 97-115.

Nesbitt, W., 1979. Mobility and fractionation of rare earth elements during weathering of a granodiorite. Nature 279, 206-210.

Nozaki, Y., Lerche, D., Alibo, D.S., Snidvongs, A., 2000a. The estuarine geochemistry of rare earth elements and indium in the Chao Phraya River, Thailand. Geochimica et Cosmochimica Acta 64, 3983-3994.

Nozaki, Y., Lerche, D., Alibo, D.S., Tsutsumi, M., 2000b. Dissolved indium and rare earth elements in three Japanese rivers and Tokyo Bay: Evidence for anthropogenic Gd and In. Geochimica et Cosmochimica Acta 64, 3975-3982.

Oelkers, E.H., Montel, J., 2008. Phosphates and Nuclear Waste Storage. Elements 4, 113-116.

Palmer, M.R., Elderfield, H., 1985. The Sr isotopic composition of seawater over the past 75 million years. Nature 314, 526-528.

Pfingsten, W., Hadermann, J., Perrochet, P., 2001. Radionuclide release and transport from nuclear underground tests performed at Mururoa and Fangataufa - predictions under uncertainty. Journal of Contaminant Hydrology 47, 349-363.

Piepgras, D., Wasserburg, G., 1980. Neodymium isotopic variations in seawater. Earth and Planetary Science Letters 50, 128-138.

Pierret, M.C., Chabaux, F., Huybrecht, F., Mergnac, L., Riotte, J., 2004. Sr and U isotopic variations in the water-soil-plant system: example of the Strengbach watershed. Goldschmidt Conference, Copenhagen 2004, 435.

Pokrovsky, O.S., Schott, J., Dupré, B., 2006. Trace element fractionation and transport in boreal rivers and soil porewaters of permafrost-dominated basaltic terrain in Central Siberia. Geochimica et Cosmochimica Acta 70, 3239-3260.

Poszwa, A., Dambrine, E., Pollier, B., Atteia, O., 2000. A comparison between Ca and Sr cycling in forest ecosystems. Plant and Soil 225, 299-310.

Pourret, O., Davranche, M., Gruau, G., Dia, A., 2007a. Organic complexation of rare earth elements in natural waters: Evaluating model calculations from ultrafiltration data. Geochimica et Cosmochimica Acta 71, 2718-2735.

Pourret, O., Davranche, M., Gruau, G., Dia, A., 2008. New insights into cerium anomalies in organic-rich alkaline waters. Chemical Geology 251, 120-127.

Pourret, O., Dia, A., Davranche, M., Gruau, G., Henin, O., Angee, M., 2007b. Organo-colloidal control on major- and trace-element partitioning in shallow groundwaters: Confronting ultrafiltration and modelling. Applied Geochemistry 22, 1568-1582.

Probst, A., Dambrine, E., Vivielle, D., Fritz, B., 1990. Influence of acid atmospheric input on surface water chemistry and mineral fluxes in a declining spruce stand within a small catchment (Vosges massif, France). Journal of Hydrology 116, 101-124.

Probst, A., Fritz, B., Vivielle, D., 1995. Mid-term trends in acid precipitation, streamwater chemistry and element budgets in the Strengbach catchment (Vosges mountains, France). Water, Air and Soil Poll 79, 39-59.

Probst, A., Viville, D., Fritz, B., Ambroise, B., Dambrine, E., 1992. Hydrochemical budgets of a small forested catchment exposed to acid deposition : the Strengbach catchment case study (Vosges massif, France). Water, Air, Soil Pollution 62, 337-347.

Prunier, J., Pierret, M.C., Chabaux, F., Trémolières, M., 2007. U-Th-Ra fractionation in soil horizons of forested ecosystem (Strengbach catchment, France). Goldschmidt conference, Cologne 2007, 811.

Quevauviller, P., Rauret, G., Muntau, H., Ure, A., Rubio, R., López-Sánchez, J., Fiedler, H., Griepink, B., 1994. Evaluation of a sequential extraction procedure for the determination of extractable trace metal contents in sediments. Fresenius' Journal of Analytical Chemistry 349, 808-814.

Rabiet, M., Brissaud, F., Seidel, J., Pistre, S., Elbaz-Poulichet, F., 2005. Deciphering the presence of wastewater in a medium-sized Mediterranean catchment using a multitracer approach. Applied Geochemistry 20, 1587-1596.

Rahn, M., Steinmann, M., Frey, M., 2002. Chloritoid composition and formation in the eastern Central Alps: a comparison between Penninic and Helvetic occurrences. Schweizerische mineralogisch-petrographische Mitteilungen 82, 409-426.

Redling, K., 2006. Rare Earth Elements in agriculture with emphasis on animal husbandry. PhD thesis, Tierärztliche Fakultät der Ludwig Maximilians-Universität München, 360 pp.

Rodot, S., 2006. Dispersion et dynamique des métaux traces d'origine anthropique dans le Lac de St. Point (Doubs). MS thesis, Master thesis, Université de Franche-Comté, Besançon, 30 pp.

Rougerie, F., Jehl, C., Trichet, J., 1997. Phosphorus pathways in atolls: interstitial nutrient pool, cyanobacterial accumulation and Carbonat-Fluoro-Apatite (CFA) precipitation. Marine Geology 139, 201-217.

Rougerie, R., Wauthy, B., 1986. Le concept d'endo-upwelling dans le fonctionnement des atolls-oasis. Oceanologica acta 9, 133-148.

Rougerie, R., Wauthy, B., 1993. The endo-upwelling concept: From geothermal convection to reef construction. Coral Reefs 12, 19-30.

Rudnicki, M., Elderfield, H., 1993. A chemical model of the buoyant and neutrally buoyant plume above the TAG vent field, 26 degrees N, Mid-Atlantic Ridge. Geochimica et Cosmochimica Acta 57, 2939-2957.

Samaden, G., Dallot, P., R, R., 1985. Atoll d'Eniwetok. Système géothermal insulaire à l'état naturel. La houille blanche 2, 143-151.

Schmitt, A., Stille, P., 2005. The source of calcium in wet atmospheric deposits: Ca-Sr isotope evidence. Geochimica et Cosmochimica Acta 69, 3463-3468.

Schultz, A., Elderfield, H., 1997. Controls on the physics and chemistry of seafloor hydrothermal circulation. Philosophical Transactions of the Royal Society A: Mathematical, Physical and Engineering Sciences 355, 387-425.

Seaborg, G., 1993. Overview of the actinide and lanthanide (the f) elements. Radiochimica Acta 61, 115-122.

Sholkovitz, E., 1995. The aquatic chemistry of rare earth elements in rivers and estuaries. Aquatic Geochemistry 1, 1-34.

Sholkovitz, E.R., Elderfield, H., Szymczak, R., Casey, K., 1999. Island weathering: river sources of rare earth elements to the Western Pacific Ocean. Marine Chemistry 68, 39-57.

Smellie, J.A.T., Karlsson, F., 1999. The use of natural analogues to assess radionuclide transport. Engineering Geology 52, 193-220.

Sonke, J.E., Salters, V.J.M., 2006. Lanthanide-humic substances complexation. I. Experimental evidence for a lanthanide contraction effect. Geochimica et Cosmochimica Acta 70, 1495-1506.

Spencer, A.J., Wilson, S.A., Batchelor, J., Reid, A., Rees, J., Harpur, E., 1997. Gadolinium chloride toxicity in the rat. Toxicologic pathology 25, 245-255.

Steinmann, M., Déjardin, P., 2004. The temporal evolution of fluid flow through the Tahiti barrier reef traced by Sr isotopes and pore water chemistry. Chemical Geology 203, 51-73.

Steinmann, M., Stille, P., 1997. Rare earth element behavior and Pb, Sr, Nd isotope systematics in a heavy metal contaminated soil. Applied Geochemistry 12, 607-623.

Steinmann, M., Stille, P., 1998. Strongly fractionated REE patterns in salts and their implications for REE migration in chloride-rich brines at elevated temperatures and pressures. Comptes Rendus de l'Académie des Sciences Paris, série II a 327, 173-180.

Steinmann, M., Stille, P., 1999. Geochemical evidence for the nature of the crust beneath the eastern North Penninic basin of the Mesozoic Tethys ocean. Geologische Rundschau 87, 633-643.

Steinmann, M., Stille, P., 2008. Controls on transport and fractionation of the rare earth elements in stream water of a mixed basaltic-granitic catchment basin (Massif Central, France). Chemical Geology 254, 1-18.

Steinmann, M., Stille, P., Bernotat, W., Knipping, B., 1999. The corrosion of basaltic dykes in evaporites: Ar-Sr-Nd isotope and rare earth elements evidence. Chemical Geology 153, 259.

Steinmann, M., Stille, P., Mengel, K., Kiefel, B., 2001. Trace element and isotopic evidence for REE migration and fractionation in salts next to a basalt dyke. Applied Geochemistry 16, 351.

Stern, J.C., Sonke, J.E., Salters, V.J.M., 2007. A capillary electrophoresis-ICP-MS study of rare earth element complexation by humic acids. Chemical Geology 246, 170-180.

Stille, P., Clauer, N., 1994. The process of Glauconitization. Chemical and isotopic evidence. Contributions to Mineralogy and Petrology 117, 253-262.

Stille, P., Gauthier-Lafaye, F., Jensen, K.A., Salah, S., Bracke, G., Ewing, R.C., Louvat, D., Million, D., 2003. REE mobility in groundwater proximate to the natural fission reactor at Bangombe (Gabon). Chemical Geology 198, 289-304.

Stille, P., Steinmann, M., Pierret, M.C., Gauthier-Lafaye, F., Chabaux, F., Viville, D., Pourcelot, L., Matera, V., Aouad, G., Aubert, D., 2006. The impact of vegetation on REE fractionation in stream waters of a small forested catchment (the Strengbach case). Geochimica et Cosmochimica Acta 70, 3217-3230.

Stille, P., Steinmann, M., Riggs, S., 1996. Nd isotope evidence for the evolution of the paleocurrents in the Atlantic and Tethys Oceans during the past 180 Ma. Earth and Planetary Science Letters 144, 9-20.

Stumm, W. & Morgan, J., 1996. *Aquatic chemistry*. John Wiley and sons, New York, 1022 pp.

Swartz, J., 1958. Bikini and nearby atolls, Marshall Islands. Geothermal measurements on Eniwetok and Bikini atolls. USGS Rept 260U, 711-715.

Tessier, A., Campbell, P., Bisson, M., 1979. Sequential extraction procedure for the speciation of particulate trace metals. Analytical Chemistry 51, 844-851.

Tosiani, T., Loubet, M., Viers, J., Valladon, M., Tapia, J., Marrero, S., Yanes, C., Ramirez, A., Dupre, B., 2004. Major and trace elements in river-borne materials from the Cuyuni basin (southern Venezuela): evidence for organo-colloidal control on the dissolved load and element redistribution between the suspended and dissolved load. Chemical Geology 211, 305.

Tricca, A., 1997. Transport mechanism of trace elements in surface and ground water: Sr, Nd, U isotope and REE evidence. PhD thesis, Université Louis Pasteur de Strasbourg, 234 pp.

Tricca, A., Stille, P., Steinmann, M., Kiefel, B., Samuel, J., Eikenberg, J., 1999. Rare earth elements and Sr and Nd isotopic compositions of dissolved and suspended loads from small river systems in the Vosges mountains (France), the river Rhine and groundwater. Chemical Geology 160, 139-158.

Ure, A., Quevauviller, P., Muntau, H., Griepink, P., 1993. Speciation of Heavy Metals in Soils and Sediments. An Account of the Improvement and Harmonization of Extraction Techniques Undertaken Under the Auspices of the BCR of the Commission of the European Communities. Int. J. Env. Anal. Chem. 51, 135-151.

Usui, A., Bau, M., Toshitsugu, Y., 1997. Manganese microchimneys buried in the Central Pacific pelagic sediments: evidence of intraplate water circulation?. Marine Geology 141, 269-285.

van de Flierdt, T., Frank, M., Lee, D., Halliday, A.N., Reynolds, B.C., Hein, J.R., 2004. New constraints on the sources and behavior of neodymium and hafnium in seawater from Pacific Ocean ferromanganese crusts. Geochimica et Cosmochimica Acta 68, 3827-3843.

van de Flierdt, T., Goldstein, S.L., Hemming, S.R., Roy, M., Frank, M., Halliday, A.N., 2007. Global neodymium-hafnium isotope systematics -- revisited. Earth and Planetary Science Letters 259, 432-441.

Verplanck, P.L., McCleskey, R.B., Roth, D.A., 2003. Inorganic Water Chemistry of the Boulder Creek Watershed, Colorado, During High-Flow and Low-Flow Conditions, 2000. In: Murphy, S.F., Verplanck, P.L., Barber, L.B. (Eds.), *Comprehensive water quality of the boulder creek watershed, colorado, during high-flow and low-flow conditions, 2000*. USGS Water-Resources Investigations, p. 71–102.

Viers, J., Dupre, B., Braun, J., Deberdt, S., Angeletti, B., Ngoupayou, J.N., Michard, A., 2000. Major and trace element abundances, and strontium isotopes in the Nyong basin rivers (Cameroon): constraints on chemical weathering processes and elements transport mechanisms in humid tropical environments. Chemical Geology 169, 211-241.

Viers, J., Dupré, B., Polve, M., Schott, J., Dandurand, J., Braun, J., 1997. Chemical weathering in the drainage basin of a tropical watershed (Nsimi-Zoetele site, Cameroon) : comparison between organic-poor and organic-rich waters. Chemical Geology 140, 181-206.

Waber, N., 1992. The supergene thorium and rare-earth element deposit at Morro do Ferro, Poços de Caldas, Minas Gerais, Brazil. Journal of Geochemical Exploration 45, 113-157.

Wagner, G., Mohr, M.-., Sprengart, J., Desaules, A., Muntau, H., Theocharopoulos, S., Quevauviller, P., 2001. Objectives, concept and design of the CEEM soil project. The Science of The Total Environment 264, 3-15.

Wheat, C.G., Feely, R.A., Mottl, M.J., 1996. Phosphate removal by oceanic hydrothermal processes: An update of the phosphorus budget in the oceans. Geochimica et Cosmochimica Acta 60, 3593-3608.

Wheat, C.G., MeDuff, R.E., 1994. Hydrothermal flow through the Mariana Mounds: Dissolution of amorphous silica and degradation of organic matter on a mid-ocean ridge flank. Geochimica et Cosmochimica Acta 58, 2461-2475.

Wheat, C.G., Mottl, M.J., Rudnicki, M., 2002. Trace element and REE composition of a low-temperature ridge-flank hydrothermal spring. Geochimica et Cosmochimica Acta 66, 3693-3705.

Wheeler, D.M., Power, I.L., 1995. Comparison of plant uptake and plant toxicity of various ions in wheat. Plant and Soil 172, .

Wilde, E.W., Berry, C.J., Goli, M.B., 2002. Toxicity of gadolinium to some aquatic microbes. Bulletin of environmental contamination and toxicology 68, 420-427.

Wyttenbach, A., Furrer, V., Schleppi, P., Tobler, L., 1998. Rare earth elements in soil and in soil-grown plants. Plant and Soil 199, 267-273.

Wyttenbach, A., Tobler, L., Furrer, V., 1996. The concentration of rare earth elements in plants and in the adjacent soils. Journal of Radioanalytical and Nuclear Chemistry 204, 401-413.

Zeng, F., Tian, H., Wang, Z., An, Y., Gao, F., Zhang, L., Li, F., Shan, L., 2003. Effect of rare earth element europium on amaranthin synthesis

in Amarathus caudatus seedlings. Biological Trace Element Research 93, 271-282.

Zhang, S., Shan, X., 2001. Speciation of rare earth elements in soil and accumulation by wheat with rare earth fertilizer application. Environmental Pollution 112, 395-405.

Zhang, Z.Y., Wang, Y.Q., Li, F.L., Xiao, H.Q., Chai, Z.F., 2002. Distribution characteristics of rare earth elements in plants from a rare earth ore area. Journal of Radioanalytical and Nuclear Chemistry 252, 461-465.

Zhu, W., Xu, S., Shao, P., Zhang, H., Wu, D., Yang, W., Feng, J., 1997. Bioelectrical activity of the central nervous system among populations in a rare earth element area. Biological Trace Element Research 57, 71.

C Sélection de publications

Thématique : "Le comportement des terres rares et des isotopes du Sr, du Nd et du Pb dans un sol contaminé"

Steinmann, M. & Stille, P. 1997: Rare earth element behavior and Pb, Sr, Nd isotope systematics in a heavy metal contaminated soil. Applied Geochem. 12, 607-624.

Thématique : "La mobilisation des terres rares lors de l'altération de filons de basalte en milieu salifère et leur migration dans le sel adjacent"

Steinmann, M. & Stille, P., 1998. Strongly fractionated REE patterns in salts and their implications for REE migration in chloride-rich brines at elevated temperatures and pressures. C.R. Acad. Sci. Paris, série II a, 327: 173-180.

Steinmann, M., Stille, P., Bernotat, W. & Knipping, B., 1999. The corrosion of basaltic dykes in evaporites: Ar-Sr-Nd isotope and REE evidence. Chem. Geol., 153, 259-279.

Steinmann, M., Stille, P., Mengel, K. & Kiefel, B, 2001. Trace element and isotopic evidence for REE migration and fractionation in salts next to a basalt dyke. Applied Geochem. 16, 351-361.

Steinmann, M.& Stille, P., 2004. Basaltic dykes in evaporites: a natural analogue. In: Gieré, R. and Stille P. (eds): Energy, waste, and the environment: a Geochemical Perspective. Geol. Soc. London Spec. Publ. 236, 135-141.

Thématique : "La migration des fluides interstitiels dans un récif corallien"

Steinmann, M. & Déjardin, P, 2004. Temporal evolution of fluid flow through the Tahiti barrier reef traced by Sr isotopes and pore water chemistry. Chem. Geol. 203, 51-73.

Thématique : "Origine et fractionnement des terres rares dans un contexte d'hydrothermalisme basse température"

Bodeï, S., Buatier, M., **Steinmann, M.**, Adatte, T. & Wheat, C., 2008. Characterization of metalliferous sediment from a low-temperature hydrothermal environment on the Eastern Flank of the East Pacific Rise. Marine Geology 250, 128-141.

Thématique : "Les processus de transport et de fractionnement des terres rares dans l'eau des ruisseaux"

Tricca, A., Stille, P. & **Steinmann, M**., Kiefel, B., Samuel, J. & Eikenberg, J. 1999: Rare earth elements and Sr and Nd isotopic compositions of dissolved and suspended loads from small river systems in the Vosges mountains (France), the river Rhine, and groundwater. Chem. Geol. 160, 139-158

Steinmann, M. & Stille, P., 2008. Controls on transport and fractionation of the Rare Earth Elements in stream water of a mixed basaltic-granitic catchment basin (Massif Central, France). Chem. Geol. 254, 1-18.

Thématique : "Les transferts des terres rares à l'interface géosphère – biosphère"

Stille, P., **Steinmann, M**., Pierret, M.C., Gauthier-Lafaye, F., Chabaux, F., Viville, D., Pourcelot, L., Matera, V., Aouad, G. and Aubert, D., 2006. The impact of vegetation on REE fractionation in stream waters of a small forested catchment (the Strengbach case). Geochim. Cosmochim. Acta, 70(13): 3217-3230.

Thématique : "Le comportement des terres rares et des isotopes du Sr, du Nd et du Pb dans un sol contaminé"

Steinmann, M. & Stille, P. 1997: Rare earth element behavior and Pb, Sr, Nd isotope systematics in a heavy metal contaminated soil. Applied Geochem. 12, 607-624.

Pergamon

PII: S0883-2927(97)00017-6

Applied Geochemistry, Vol. 12, pp. 607–623, 1997

0883-2927/97 $17.00 + 0.00

Rare earth element behavior and Pb, Sr, Nd isotope systematics in a heavy metal contaminated soil

Marc Steinmann* and Peter Stille

Centre de Géochimie de la Surface (CNRS), 1, rue Blessig, 67084 Strasbourg Cedex, France

(*Received* 1 *February* 1996; *accepted in revised form* 5 *January* 1997)

Abstract—The aim of this study is to characterize the processes and phases which control migration and retention of rare earth elements (REE) in a heavy metal contaminated soil. In addition to concentration data, we used Pb, Sr and Nd isotopic compositions in order to distinguish between natural and anthropogenic trace metals and to characterize the phases leached away during the sequential extraction procedure.

The samples were sequentially extracted in 3 steps with 1 N acetic acid (HAc), 1 N HCl and 1 N HNO_3. The Pb isotope data showed that anthropogenic Pb had mainly been retained in the uppermost 10 cm by the organic matter of the topsoil. The $^{87}Sr/^{86}Sr$ ratios of the HAc extracts are almost constant and indicate that soil carbonate is derived from regionally outcropping carbonate-rich sediments. Most HCl and HNO_3 extracts have more radiogenic Sr isotopic compositions, but it is unclear whether this reflects a growing influence of anthropogenic or silicate-derived Sr.

The depth distribution of the REE is mainly controlled by two different parameters: soil pH for the HAc extractable REE and Fe–Mn oxides for the REE in the HCl and HNO_3 extracts. A part of the HNO_3 extractable REE was also bound to the organic matter of the topsoil. The REE concentrations in the HAc extractable phase increase with depth and increasing soil pH, which indicates that they are derived from the surface and hence are of anthropogenic origin. This is confirmed by $^{143}Nd/^{144}Nd$ isotope ratios which show a mixing between a natural end-member at the top and an anthropogenic end-member at the base of the profile. We assume that the anthropogenic REE were transported in dissolved form as carbonate complexes and then precipitated during downward migration as soil pH increased. © 1997 Elsevier Science Ltd

INTRODUCTION

Various authors have used Pb isotopes to trace contamination in the environment. The Sr and Nd isotope systems have successfully been used to investigate exchange processes during diagenesis of sedimentary rocks, but applications in environmental studies are still scarce. In particular the isotopes of the rare earth element (REE) Nd have a great potential to illuminate the environmental behavior of REE.

REE appear as natural trace metals in the whole geosphere and have become important geochemical tracers during the last few decades. Some REE isotopes also occur as radionuclides in the decay series of nuclear fission and can therefore be found in nuclear waste or be released by nuclear accidents. Consequently, propagation of radioactive pollutants in the environment is to a considerable extent controlled by the migration behavior of the REE. In addition, analogies may be drawn between the behavior of trivalent actinides and the behavior of trivalent REE studied here (Choppin, 1983; Krauskopf, 1986).

In the following we will start with a general characterization of the soil and the different phases extracted in our sequential extraction procedure using X-ray diffractometry (XRD), transmission electron microscopy (TEM) and element concentration data. Then the Pb and Sr isotope data will be presented before we discuss the REE and Nd isotope data in the last part of the paper.

SETTING AND METHODOLOGY

Study site

We studied a profile in a 50-cm thick calcic fluvisol which is underlain by alluvial gravels. The site is located in close proximity to a brass foundry and has been contaminated by airborne particles from the foundry for more than 80 a. On a regional scale the heavy metal charge in the soils is clearly influenced by the dominant wind direction and decreases with distance from the brass foundry (Federer and Sticher, 1991). Figure 1 and Table 1 give a general characterization of the soil profile. The topsoil is mainly contaminated by Cu and Zn and to a lesser extent by Pb, Ni and Cd (Table 2). The behavior of Cd, Cu and Zn has already been studied by Federer and Sticher (1991) and Federer (1993) in the same profile.

The site is located in northern Switzerland in a wide river valley with a thick Quaternary gravel infill. The regionally outcropping rocks are essentially marine Jurassic carbonates, marine carbonate-rich siliciclastics of Tertiary age (molasse) and loess of Pleistocene age. Crystalline rocks do not outcrop in the immediate vicinity but have been brought in by glaciers during the Pleistocene.

* Corresponding author.

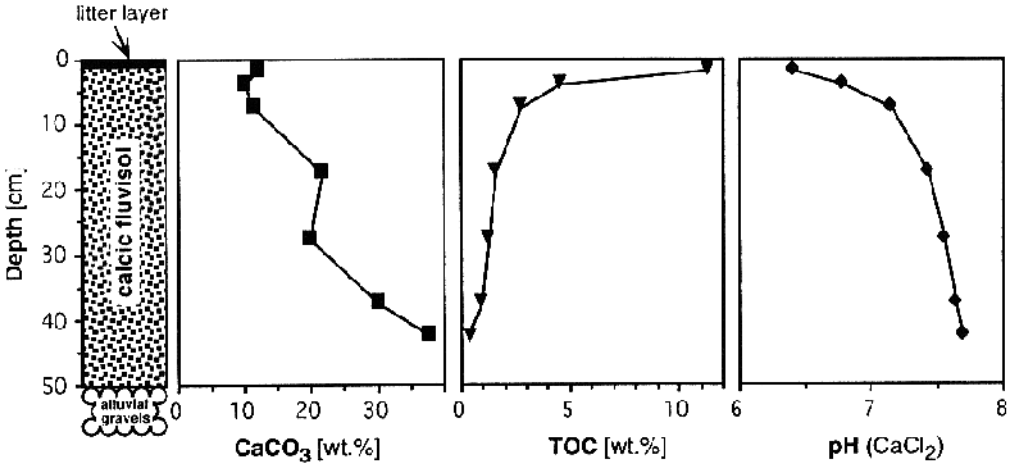

Fig. 1. General characterization of the soil profile (all data from Federer, 1993). TOC = Total Organic Carbon.

Sampling and experimental

Field sampling was done by Federer (1993) who removed the soil in a pit in layers of 5 cm thickness. The samples were dried at 40°C. Large stones were separated by hand before crushing and sieving through a nylon sieve (2 mm mesh width). All subsequent preparation and analytical work was done at the Centre de Géochimie de la Surface in Strasbourg. The samples were sequentially extracted in 3 steps with 1 N acetic acid (HAc), 1 N HCl and 1 N HNO_3. Often used eluents like hydroxylamine or H_2O_2 were not applied because they are not pure enough for isotope analysis. The reducing conditions during the hydroxylamine extraction would probably also have caused REE fractionation (e.g. Eu anomaly).

The extractions were conducted in centrifuge tubes (polypropylene, 15 ml). Bulk sample weight was 1 g at the beginning and the acid volume at the individual extraction steps 8 ml (Table 1). After the third step the residues were completely dissolved in a HF–HNO_3 mixture and likewise analyzed. In order to get information about the chemical and isotopic composition of the contamination we also studied an air filter sample from the chimney of the contaminating brass foundry. A detailed description of the preparation scheme is given below:

Extraction time was 45 min for HAc and 30 min for HCl and HNO_3 at room temperature. HAc was of suprapure quality whereas HCl and HNO_3 had, like H_2O, been distilled in our laboratory. During each step the samples were shaken every 5 min and then centrifuged for 15 min. The supernatant was decanted and filtered through a cellulose acetate filter (Millipore HA, 0.45 μm, 47 mm diameter) in order to remove floating particles. The recovered solutions were divided into two aliquots for concentration and isotope analysis and then evaporated. After each step the residues were washed with distilled water to remove acid derived ionic radicals using the same procedure as for the extractions. Then they were dried together with the filters at 40°C and weighed. The

Table 1. General characterization of the soil profile. The weights of the extracts are the weight differences of the sample before and after corresponding extraction steps. The residue weights are the weights after the extraction with HNO_3. $CaCO_3$ and TOC (Total Organic Carbon) are concentrations in the untreated bulk sample and like the soil pH are taken from Federer (1993)

Sample	Depth level (cm)	$CaCO_3$ (wt.%)	TOC (wt.%)	Soil pH[a]	Bulk sample (g)	HAc extract (g)	HCl extract (g)	HNO_3 extract (g)	Residue (g)	Weight difference[b] (%)
M2.2	1–3	12.14	11.37	6.42	1.0042	0.1310	0.0596	0.0352	0.7527	−3.42
M3.2	3–5	9.97	4.63	6.79	1.1059	0.1530	0.0559	0.0363	0.8589	−0.21
M4.1	5–10	11.31	2.76	7.16	1.0335	0.1700	0.0395	0.0173	0.8033	−0.42
M6.1	15–20	21.72	1.59	7.44	1.0456	0.1905	0.0609	0.0121	0.7780	−0.52
M8.1	25–30	19.81	1.32	7.56	1.0290	0.2041	0.0688	0.0098	0.7398	−0.88
M10.1	35–40	30.11	0.98	7.65	1.0445	0.2600	0.1061	0.0078	0.6602	−1.55
M11.2	40–45	37.83	0.36	7.70	0.9960	0.2777	0.0999	0.0213	0.5964	−0.12

[a]Soil pH measured in 0.01 M $CaCl_2$.

[b]Percentage weight difference $= \frac{\sum(\text{extracts}) - (\text{bulk sample} - \text{residue})}{(\text{bulk sample} - \text{residue})} \times 100$.

Table 2. Chemical composition of the extracts. All concentrations are normalized relative to bulk sample weight and given as μg/g bulk sample. For concentrations relative to leached sample weight the data have to be renormalized using the weights given in Table 1. Ni, Cu and Zn concentrations of the HAc extracts were closest to the detection limit but still at least 2.5 times above it

Sample	Rb (2)	Mg (1)	Ca (1)	Sr (2)	Ba (2)	Al (1)	Cr (1)	Mn (1)	Fe (1)	Co (2)	Ni (1)	Cu (1)	Zn (1)	Cd (2)	Pb (2)
HAc extracts															
M2.2 HAc	0.27	365.4	25 484	26.53	11.80	b.d.l.	0.96	204.2	15.6	1.37	18.09	920.5	1909.3	5.87	17.05
M3.2 HAc	0.22	266.2	29 748	30.24	9.37	b.d.l.	0.88	184.3	14.1	1.37	8.44	262.7	851.0	4.25	4.63
M4.1 HAc	0.26	276.0	43 994	39.30	11.22	b.d.l.	1.28	160.4	14.4	1.13	4.20	75.6	311.6	2.07	2.57
M6.1 HAc	0.18	271.9	48 259	41.21	10.01	b.d.l.	1.11	138.3	18.8	1.05	2.72	10.3	38.1	0.67	1.17
M8.1 HAc	0.14	285.6	56 025	48.61	8.53	b.d.l.	1.29	138.1	29.7	1.40	3.29	2.3	6.0	0.33	0.61
M10.1 HAc	0.13	317.3	66 547	98.71	8.90	b.d.l.	1.41	164.9	58.4	2.16	3.25	0.7	1.5	0.26	0.55
M11.2 HAc	0.05	356.0	52 628	68.11	6.98	b.d.l.	1.54	168.3	74.4	2.31	6.34	1.0	4.2	0.22	0.54
HCl extracts															
M2.2 HCl	0.51	183.9	9811	9.44	24.34	796	1.07	202.8	681.4	2.68	15.60	2635.4	1206.9	2.62	101.23
M3.2 HCl	0.52	168.3	9807	8.92	20.35	895	1.00	207.7	501.5	2.67	8.17	679.8	783.8	1.75	34.13
M4.1 HCl	0.77	181.8	8704	8.81	27.50	1010	0.89	232.9	808.5	2.56	3.60	198.1	367.1	1.29	30.97
M6.1 HCl	0.69	219.8	15 534	13.00	24.39	913	1.33	205.7	636.5	2.28	2.69	40.2	78.4	0.40	14.99
M8.1 HCl	0.67	231.4	17 885	17.12	24.43	867	1.26	171.8	541.2	2.15	3.06	10.6	15.3	0.24	9.40
M10.1 HCl	0.53	287.4	29 234	32.16	15.47	425	1.34	95.0	544.1	1.41	3.03	3.8	6.4	0.15	5.10
M11.2 HCl	0.37	255.9	26 056	28.81	12.13	911	1.23	83.9	345.3	1.28	4.36	4.0	5.7	0.08	2.96
HNO_3 extracts															
M2.2 HNO_3	0.61	197.2	1789	0.75	4.49	766	0.83	32.3	1043.4	0.76	9.12	722.0	248.0	0.09	17.18
M3.2 HNO_3	0.48	142.7	1342	0.59	3.39	564	0.78	28.5	711.9	0.61	3.74	127.5	211.7	0.13	6.14
M4.1 HNO_3	0.78	269.8	308	0.56	7.64	931	1.06	48.6	1033.8	0.99	5.32	57.4	411.2	0.18	6.00
M6.1 HNO_3	0.69	247.6	435	0.60	8.34	874	0.98	70.5	757.7	0.98	3.53	12.0	89.7	0.20	4.42
M8.1 HNO_3	0.68	238.6	575	0.72	7.84	775	0.94	73.9	653.4	0.98	3.17	3.1	14.9	0.16	3.29
M10.1 HNO_3	0.66	190.9	736	0.83	4.69	573	0.82	41.3	510.4	0.63	2.69	1.3	8.2	0.10	1.83
M11.2 HNO_3	0.79	161.4	3306	2.07	3.12	565	0.73	32.7	467.7	0.51	2.48	1.8	5.7	0.02	1.73

(1) ICP–AES; (2) ICP–MS; b.d.l. = below detection limit.

dissolved sample weights given in Table 1 are the weight differences of the residues before and after the corresponding extraction steps. The sample weight trapped by the filters was taken into account.

Four hundred milligrams of each residue was ignited at 800°C for 12 h to oxidize organic components. The ignited powder was then dissolved in a closed Savillex® Teflon vessel containing 12 ml of 40% HF and 400 μl of 65% HNO_3, both of suprapure quality. Digestion time was 7 days and the temperature 150°C. For the analysis of the air filter 200 mg of filter dust were dissolved in 14 ml suprapure HNO_3 in the same Teflon vessels and under the same conditions as the residues.

The element concentrations of all leachates, residues and the air filter were determined in 1 N HNO_3 solutions by ICP–AES (ARL 3500 C) and ICP–MS (VG Plasmaquad PQ2+). The analytical errors are better than ±10% for both instruments.

Isotope analysis

The $^{206}Pb/^{207}Pb$ isotope ratios of the leachates were directly measured by ICP–MS in 1 N HNO_3 solutions without preceding chemical separation. The ICP–MS had been calibrated in an earlier study for Pb isotope analysis (Fillion *et al.*, 1996). For our study we chose an integration mode yielding $^{206}Pb/^{207}Pb$ ratios reproducible in the second decimal.

For Sr and Nd isotope analysis, the evaporated leachates were treated with $HClO_4$ in order to destroy organic matter. The residues underwent the same digestion treatment as for the ICP analysis. For Sr and bulk REE separation 1 ml quartz columns with cation-exchange resin (AG 50W-X12, 200–400 mesh) and ammonium citrate, 1.5 N, 4 N and 6 N HCl were used as eluents. Neodymium was separated with the same type of resin and column and α-hydroxyisobutyric acid as eluent. The blanks at the time of analysis were <1.5 ng for Sr and <0.4 ng for Nd. Neodymium was measured using a Ta-Re-Ta triple filament assembly whereas Sr was deposited on W single filaments. The analyses were performed on a fully automatic VG Sector mass spectrometer with a 5-cup multicollector. The ratios $^{86}Sr/^{88}Sr = 0.1194$ and $^{146}Nd/^{144}Nd = 0.7219$ were used for fractionation correction. Typically, 100 ratios for Sr and Nd were collected to achieve adequate precision. During the measuring period the NBS 987 Sr standard yielded $^{87}Sr/^{86}Sr = 0.710264 \pm 13$ (2 standard deviations of the mean, $n = 8$) and the La Jolla Nd standard $^{143}Nd/^{144}Nd = 0.511856 \pm 7$ (2 standard deviations of the mean, $n = 6$).

XRD and TEM

In order to get detailed mineralogical and morphological information, additional sample aliquots were investigated with X-ray diffractometry (XRD) and transmission electron microscopy (TEM, Philips EM 300 and CM 12). The CM 12 is equipped with a supplementary scanning electron microscope (SEM) device and an energy dispersive X-ray analysis system (EDS) for spot chemical analysis. For both XRD and TEM investigations, the sample material was decalcified with 1 N HAc (the first step of the extraction procedure). The XRD investigations were done on decalcified bulk samples and oriented $<2\,\mu m$ clay fractions separated in an Atterberg cylinder according to Stokes' law. The $<2\,\mu m$ clay fractions were saturated with Ca in a $CaCl_2$ solution (110.9 g/l) and analyzed 4 times: (1) without additional treatment, (2) after 12 h in an ethylene glycol atmosphere for the identification of mixed-layer minerals, (3) after 4 h at 490°C to destroy all swelling layers in the mixed-layer minerals, and (4) after 12 h in a hydrazine atmosphere to differentiate kaolinite from chlorite.

Additional aliquots of $<2\,\mu m$ clay fractions of samples M4.1 and M6.1 were treated with sodium citrate (107 g/l) for 1 h at 80°C and analyzed like the untreated fractions in order to identify interlayer Al hydroxides in illite/smectites (Tamura, 1957). If present, interlayer Al hydroxides would be replaced by Na. The presence of interlayer Al hydroxides prevents illite/smectites from swelling during glycol treatment. Therefore citrate treated and glycolized samples have stronger XRD peaks at 16–18 Å than their untreated but glycolized counterparts (Tamura, 1957). The property of sodium citrate to exchange almost uniquely Al but almost no Fe and Si in interlayer positions has been demonstrated by El Gh'mari (1995).

Data normalization

The element concentrations of the leachates can be normalized relative to the weight of the untreated bulk sample before leaching or relative to the sample weight leached away during the extraction step. The first normalization is a measure of the absolute amount of an extracted element without giving specific information about its speciation. Concentrations relative to leached sample weight yield the composition of the extracted sample fraction. The occurrence of element–element correlations in leached sample weight normalized data indicates that the related elements are predominantly derived from the same phases. Consequently, correlations between specific elements can be used to identify certain trace metal carriers extracted during an extraction step.

For sequential extractions this information can only be furnished by leached sample weight but not by bulk sample weight normalized concentration data. Indeed, in the first extraction step the two normalizations yield the same correlations because the conversion between them is a constant factor for all elements of a single sample. But when in the subsequent steps chemically different carrier phases are leached, the conversion factor between the two normalizations is not constant because some elements have already been preferentially removed with other phases in the previous steps. In this case only leached sample weight normalized data can furnish the required information.

We present our data in Tables 2 and 3 and Table 4 as bulk sample normalized concentrations in order to give a picture of the absolute amounts extracted. However, most of our correlation analyses and most of the REE data shown in the figures are based on leached sample weight normalized concentrations. To get these numbers the data have to be renormalized using the weights given in Table 1.

RESULTS AND DISCUSSION

XRD and TEM observations

The XRD data show that the non-carbonate mineral fraction of the soil is dominated by quartz (ca. 70%), clay minerals (ca. 20%), K-feldspar and plagioclase (ca. 5% each). The percentages given are semi-quantitative and estimated from XRD peak heights. The proportion of clay minerals decreases with depth and is correlated with the total organic carbon (TOC) content ($r^2 = 0.896$, $n = 4$) whereas the percentages of the other minerals do not show significant depth variations. The $<2\,\mu m$ clay fractions have a depth-independent mineralogical composition which comprises illite/smectite (ca. 55%), kaolinite (ca. 20%) and some illite (ca. 15%) and illite/chlorite (ca. 10%). These percentages are less precise than for the non-carbonate mineral fractions because of diffuse XRD peak shapes. The smectite content in the illite/smectites is about 45%. Apart from these clay minerals, goethite was also detected in the $<2\,\mu m$ fractions. This hydroxide is the most frequent Fe mineral in soils of temperate regions (e.g. Schwertmann and Taylor, 1989).

The citrate treated and glycolized samples M6.1 and in particular M4.1 have stronger XRD peaks at 16–18 Å than the glycolized aliquots without citrate treatment. This indicates the presence of interlayer Al hydroxides in illite/smectites which is a widely known phenomenon in clay minerals of soils and weathered rocks (e.g. Rich, 1968; Barnhisel and Bertsch, 1989; Righi *et al.*, 1993).

The TEM investigations show that the illites and illite/smectites are much larger than the kaolinites and that they have a rugged morphology. Some of the kaolinites are associated with illites and illite/smectites and have an idiomorphous hexagonal shape (Fig. 2). These observations indicate a detrital origin for the

Table 3. REE concentrations of the extracts. All concentrations are normalized relative to bulk sample weight and given as μg/g bulk sample. For concentrations relative to leached sample weight the data have to be renormalized using the weights given in Table 1. The lowest concentrations were at least 15 times above the detection limit of the ICP–MS

Sample	La	Ce	Pr	Nd	Sm	Eu	Gd	Tb	Dy	Ho	Er	Tm	Yb	Lu	∑REE
HAc extracts															
M2.2 HAc	0.685	1.402	0.171	0.824	0.175	0.041	0.180	0.021	0.099	0.021	0.052	0.007	0.033	0.006	3.716
M3.2 HAc	1.131	2.210	0.273	1.340	0.291	0.066	0.282	0.034	0.164	0.031	0.081	0.009	0.047	0.009	5.968
M4.1 HAc	1.499	2.635	0.399	1.851	0.426	0.091	0.438	0.058	0.272	0.050	0.124	0.022	0.074	0.013	7.952
M6.1 HAc	2.446	3.998	0.622	2.721	0.610	0.146	0.674	0.084	0.369	0.079	0.176	0.023	0.122	0.024	12.094
M8.1 HAc	3.044	4.383	0.802	3.470	0.694	0.175	0.770	0.101	0.371	0.082	0.216	0.020	0.145	0.019	14.292
M10.1 HAc	4.939	6.286	1.119	5.119	1.040	0.231	1.163	0.131	0.643	0.118	0.314	0.037	0.205	0.031	21.377
M11.2 HAc	4.786	7.338	1.169	5.239	1.043	0.226	0.987	0.131	0.619	0.116	0.297	0.034	0.203	0.028	22.213
HCl extracts															
M2.2 HCl	6.466	12.885	1.443	6.124	1.152	0.263	1.282	0.190	1.007	0.197	0.539	0.062	0.383	0.057	32.049
M3.2 HCl	6.986	14.120	1.625	6.797	1.311	0.299	1.428	0.209	1.126	0.212	0.580	0.072	0.426	0.065	35.255
M4.1 HCl	7.865	15.196	2.050	7.989	1.750	0.377	1.932	0.254	1.188	0.248	0.720	0.084	0.480	0.069	40.202
M6.1 HCl	6.821	13.719	1.830	7.079	1.397	0.319	1.575	0.238	1.154	0.213	0.650	0.095	0.497	0.070	35.657
M8.1 HCl	7.045	14.028	1.855	7.132	1.500	0.339	1.779	0.241	1.185	0.229	0.634	0.082	0.494	0.077	36.619
M10.1 HCl	4.927	10.490	1.365	5.066	1.092	0.239	1.246	0.190	0.894	0.174	0.477	0.062	0.389	0.046	26.658
M11.2 HCl	4.253	9.655	1.115	4.686	0.970	0.218	1.000	0.151	0.786	0.151	0.409	0.054	0.307	0.044	23.799
HNO_3 extracts															
M2.2 HNO_3	2.711	6.372	0.813	3.677	0.809	0.175	0.715	0.104	0.517	0.096	0.278	0.035	0.216	0.030	16.548
M3.2 HNO_3	2.383	5.532	0.705	3.218	0.688	0.152	0.628	0.090	0.462	0.086	0.242	0.031	0.198	0.026	14.440
M4.1 HNO_3	2.319	4.973	0.700	2.929	0.730	0.148	0.673	0.092	0.432	0.084	0.220	0.035	0.190	0.033	13.558
M6.1 HNO_3	1.957	4.562	0.586	2.341	0.502	0.109	0.532	0.071	0.332	0.081	0.201	0.034	0.179	0.029	11.517
M8.1 HNO_3	1.996	4.729	0.594	2.395	0.577	0.108	0.537	0.077	0.369	0.076	0.218	0.032	0.183	0.033	11.923
M10.1 HNO_3	1.298	3.168	0.425	1.575	0.367	0.097	0.308	0.058	0.262	0.063	0.147	0.024	0.133	0.017	7.942
M11.2 HNO_3	1.802	4.884	0.536	2.391	0.535	0.114	0.498	0.077	0.374	0.075	0.205	0.028	0.178	0.028	11.724

illites and illite/smectites whereas the kaolinites are partly authigenic. Diffraction patterns taken with the TEM confirm the presence of goethite and in addition some hematite crystals were detected. Goethite was found to be associated with illite and illite/smectite. It occurs as small dots or continuous coatings on their surfaces or acts as a binding material in small clay mineral aggregates (Fig. 2). These observations demonstrate that goethite precipitation was triggered by adsorption on negatively charged clay mineral

Table 4. Chemical composition of the residues and the air filter. The concentrations of the residues are normalized to initial bulk sample weight and given as μg/g bulk sample. The concentrations of the air filter are given as μg/g air filter

Sample	M2.2R	M3.2R	M4.1R	M6.1R	M8.1R	M10.1R	M11.2R	Air filter
Rb (2)	55.7	69.1	54.5	70.0	70.2	57.0	57.0	2.74
Sr (2)	35.9	41.0	30.0	39.2	38.8	33.1	34.5	8.79
Al (1)	33 516	42 120	38 965	40 832	41 509	34 744	35 198	8859
Mn (1)	99.1	120.6	124.4	128.8	131.1	109.7	105.9	2725
Fe (1)	16 421	19 872	22 695	23 960	24 411	20 428	16 459	5440
REE (2)								
La	14.767	16.503	10.703	13.907	14.121	10.733	12.053	1.40
Ce	27.532	32.012	26.621	32.733	32.405	24.956	22.999	3.90
Pr	3.156	3.565	2.884	3.348	3.228	2.503	2.479	0.29
Nd	11.364	13.389	11.425	12.955	12.331	9.558	9.221	1.16
Sm	2.046	2.540	2.114	2.344	2.164	1.662	1.689	0.29
Eu	0.375	0.489	0.404	0.439	0.403	0.322	0.305	0.08
Gd	2.091	2.780	2.036	2.232	2.114	1.606	1.832	0.21
Tb	0.277	0.334	0.311	0.320	0.302	0.228	0.228	b.d.l.
Dy	1.582	1.965	1.858	1.875	1.704	1.315	1.389	0.17
Ho	0.345	0.412	0.389	0.394	0.352	0.278	0.287	b.d.l.
Er	1.034	1.289	1.181	1.220	1.100	0.866	0.892	0.11
Tm	0.165	0.186	0.171	0.179	0.158	0.133	0.132	b.d.l.
Yb	0.997	1.289	1.111	1.205	1.078	0.879	0.886	0.10
Lu	0.157	0.202	0.163	0.179	0.165	0.133	0.138	b.d.l.
∑REE	65.888	76.956	61.371	73.332	71.625	55.171	54.531	7.70

(1) ICP–AES, (2) ICP–MS; b.d.l. = below detection limit.

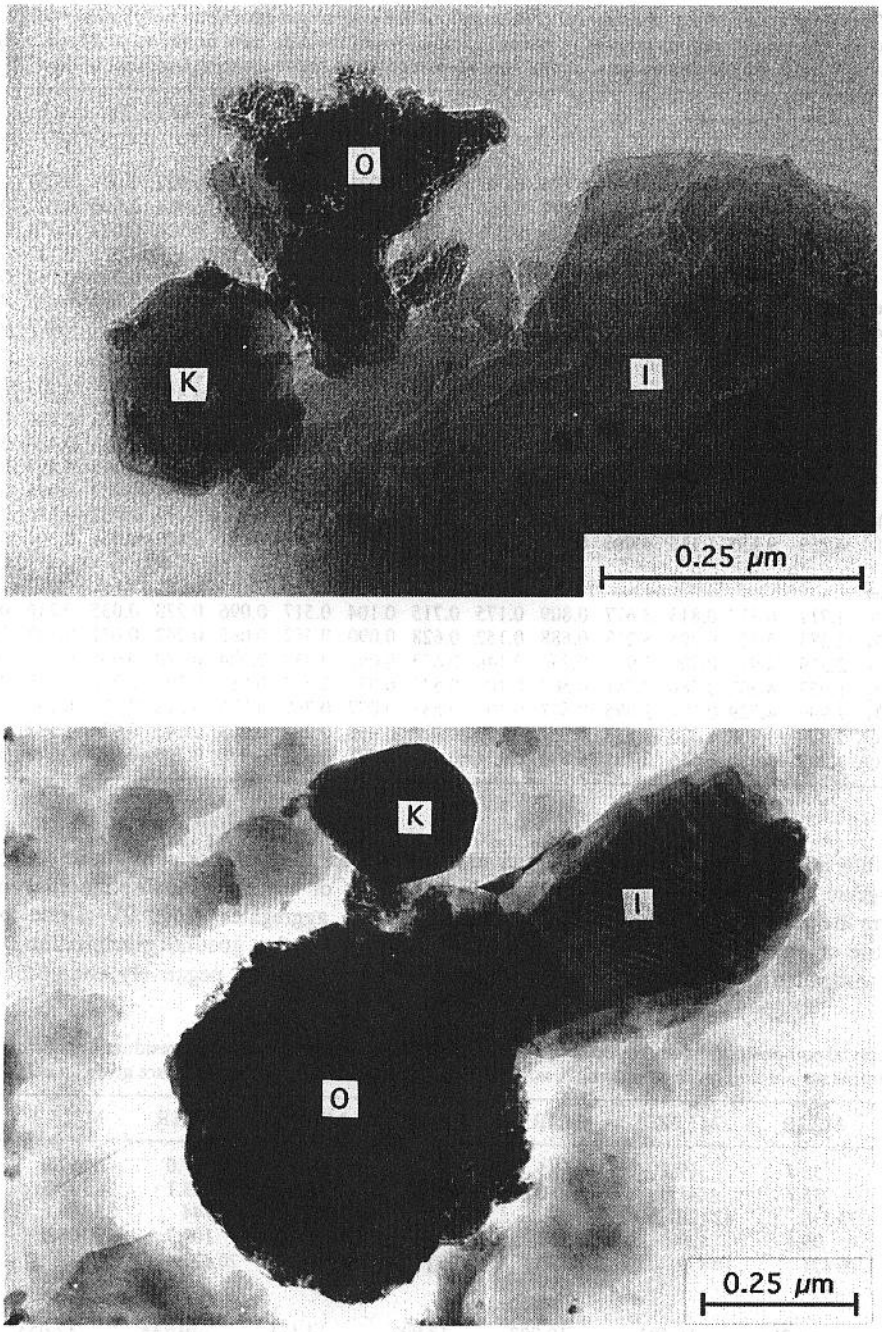

Fig. 2. TEM photographs of clay minerals (I = illite or illite/smectite, K = kaolinite) and associated Fe–Mn oxides (O) in decalcified bulk samples. Illites and illite/smectites are indistinguishable under the TEM. Note the idiomorphous hexagonal shape of the kaolinites which indicates an authigenic origin whereas the illites or illite/smectites with their rugged morphology are detrital (top: sample M4.1; bottom: sample M6.1).

surfaces. In particular, fine cracks in the clay minerals seem to have acted as nucleation points for goethite precipitation. EDS analysis on single goethite grains yielded Fe_2O_3 concentrations up to 90 wt.%. They also often contain up to 30 wt.% Al_2O_3 and up to 50 wt.% SiO_2 which can be related to the intimate association with illites and illite/smectites.

Characterization of the extracts

Acetic acid (1 N) dissolves mainly carbonate and removes trace metals adsorbed as outerspheric complexes on soil particles (Filipek *et al.*, 1981; Robinson, 1984; Sposito, 1989). The second extraction step with 1 N HCl was applied in order to remove remaining

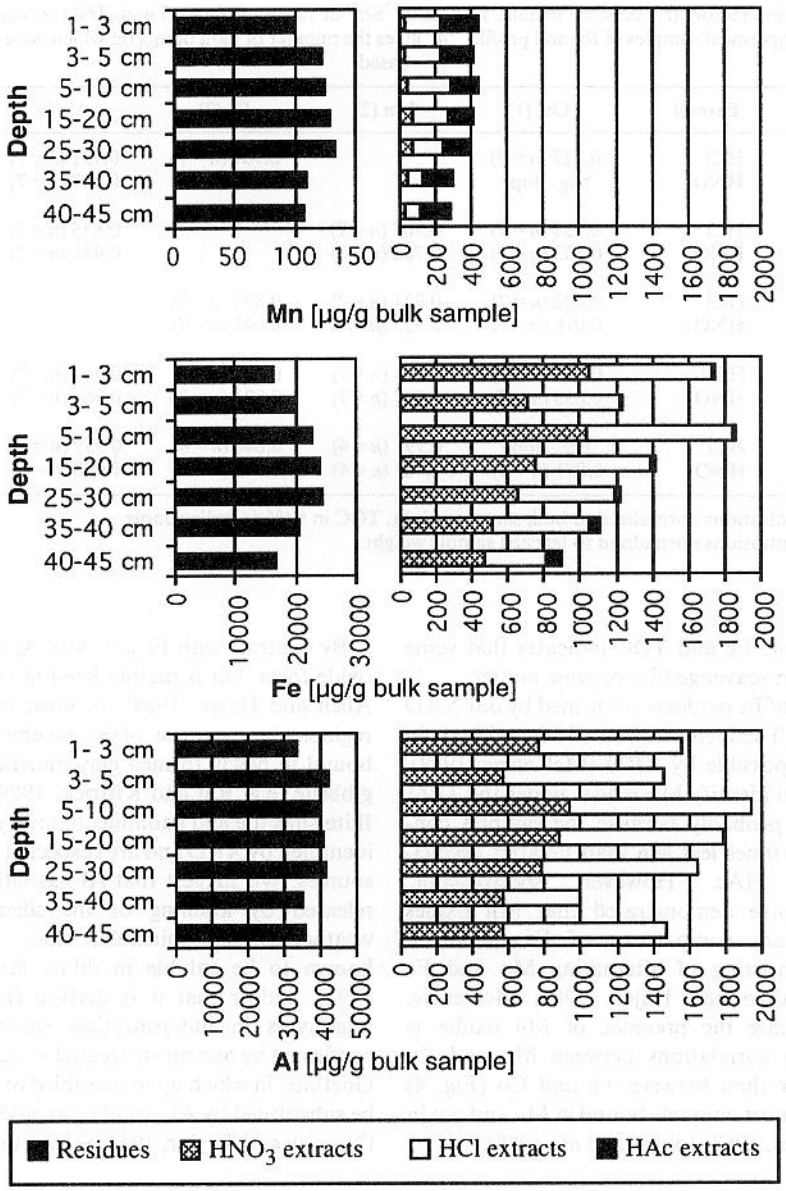

Fig. 3. Mn, Fe and Al concentrations in the extracts and the residues. All concentrations are normalized to initial bulk sample weight in order to illustrate the total amounts extracted in the different steps and to compare them with the concentrations remaining in the residues.

carbonate and to dissolve Fe–Mn oxides and hydroxides. For brevity the term oxide will be used hereafter as a group name for oxides and hydroxides. The third step with 1 N HNO_3 should also attack organic matter. Extractions with 1 N HNO_3 have been applied by different authors in order to characterize the "labile reservoir" in soils and sediments because 1 N HNO_3 removes all relatively mobile cations (Chow *et al.*, 1973; Shirahata *et al.*, 1980; Ng and Patterson, 1982; Erel *et al.*, 1990).

The sample weights extracted with HAc and the $CaCO_3$ content of untreated samples are highly correlated ($r^2 = 0.937$, $n = 7$) which demonstrates that HAc dissolved carbonate almost exclusively. It also extracted significant amounts of Cr, Mn, Zn and Cd (Table 2). Figure 3 shows a marked concentration increase for Fe and Al in the HCl and HNO_3 extracts over the HAc extracts. HCl and HNO_3 extractable Fe, Al and also Mn are highly correlated and there is furthermore a slight correlation between HNO_3 extractable Fe and TOC (Table 5).

The rise in Fe and the correlation with Mn observed in the HCl and HNO_3 extracts can be directly related to the dissolution of Fe–Mn oxides. Mn bound in Fe–Mn oxides has mainly a tetravalent oxidation state (Manceau *et al.*, 1992). In contrast, we suggest that the Mn removed by HAc was bound as Mn(II) in carbonate. The correlation between

Table 5. Correlation factors (r^2) between metals, TOC and $^{87}Sr/^{86}Sr$ ratios of the HCl and HNO_3 extracts. "$\sum$REE top 4" represents the 4 uppermost samples of the soil profile. "n" gives the number of data points on which each correlation factor is based

	Extract	TOC (1)	Mn (2)	Fe (2)	Al (2)	$^{87}Sr/^{86}Sr$ (2)
Mn	HCl	0.227 ($n=7$)		0.907 ($n=7$)	0.931 ($n=7$)	0.708 ($n=6$)
	HNO_3	neg. slope		0.788 ($n=7$)	0.927 ($n=7$)	0.543 ($n=6$)
Fe	HCl	0.158 ($n=7$)	0.907 ($n=7$)		0.835 ($n=7$)	0.502 ($n=6$)
	HNO_3	0.503 ($n=7$)	0.788 ($n=7$)		0.941 ($n=7$)	0.805 ($n=6$)
Al	HCl	0.002 ($n=7$)	0.931 ($n=7$)	0.835 ($n=7$)		0.598 ($n=6$)
	HNO_3	0.018 ($n=7$)	0.927 ($n=7$)	0.941 ($n=7$)		0.696 ($n=6$)
$\sum$REE	HCl	0.026 ($n=7$)	0.974 ($n=7$)	0.909 ($n=7$)	0.945 ($n=7$)	0.560 ($n=6$)
	HNO_3	0.655 ($n=7$)	0.967 ($n=7$)	0.871 ($n=7$)	0.964 ($n=7$)	0.625 ($n=6$)
$\sum$REE top 4	HCl	neg. slope	0.991 ($n=4$)	0.840 ($n=4$)	0.999 ($n=4$)	
	HNO_3	0.871 ($n=4$)	0.927 ($n=4$)	0.945 ($n=4$)	1.000 ($n=4$)	

(1) Metal concentrations normalized to bulk sample weight, TOC in wt% in bulk sample.
(2) Metal concentrations normalized to leached sample weight.

HNO_3 extractable Fe and TOC indicates that some Fe had also been scavenged by organic matter.

The presence of Fe oxides is confirmed by our XRD and TEM data. The identification of Mn oxides is in most cases not possible by XRD (McKenzie, 1989). We also failed to identify Mn oxides under the TEM using the EDS probably because the samples contained about 60 times less Mn than Fe after decalcification with HAc. However, spectroscopic investigations have demonstrated that Mn oxides occur as constant companions of Fe oxides in associations consisting of alternating Mn and Fe oxide layers (Allen and Hajek, 1989; McKenzie, 1989). In our case the presence of Mn oxides is strengthened by correlations between Mn and Co which are better than between Fe and Co (Fig. 4) because Co is almost uniquely bound in Mn and not in Fe oxides (Taylor, 1968; Johnson *et al.*, 1988).

By contrast with Fe and Mn, Al does not occur in oxide form, but is mainly fixed in clay minerals (e.g. Allen and Hajek, 1989). In most soils of temperate regions the presence of Si ensures that Al will be bound in newly formed clay minerals rather than in gibbsite (e.g. Rai and Kittrick, 1989; Schulze, 1989). Illite/smectite and kaolinite, but not gibbsite, could be identified by XRD and are suspected to be the main Al sources. We suggest that Al has either been directly released by leaching of the silicate structure of weathered clay minerals, since illite/smectite is known to be soluble in dilute acids (Deer *et al.*, 1992), and/or that it is derived from Al hydroxy-interlayers in illite/smectites whose occurrence is confirmed by our citrate treated <2 μm clay fractions. Goethite, in which up to one-third of the Fe atoms can be substituted by Al, could be an additional Al carrier (Norrish and Taylor, 1961; Schwertmann and Taylor,

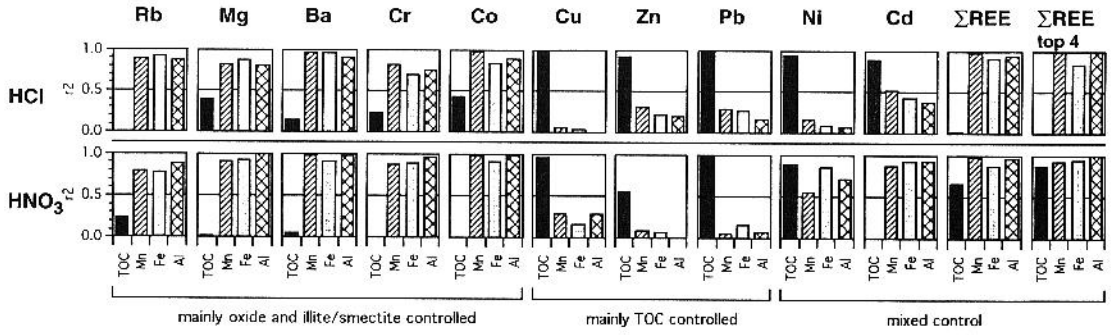

Fig. 4. Correlation factors (r^2) between TOC, Mn, Fe, Al and different trace metals of the HCl and HNO_3 extracts. The r^2 values are based on 7 data points except for "ΣREE top 4" where the 4 uppermost samples were taken. For the correlations with Mn, Fe and Al all concentrations were normalized relative to the leached sample weight in order to characterize the extracted phase. For the correlations with TOC, the metal concentrations were normalized relative to the untreated bulk sample weight and the TOC values of the untreated bulk samples were taken. This is because the extractions essentially leached out TOC bound trace metals without completely destroying the organic matter itself.

1989) but molar concentrations of Al in the leachates are about twice as high as Fe, so goethite cannot be the main leachable Al phase. The strong correlations between oxide bound Fe–Mn and silicate derived Al can be explained by the intimate association of oxides and illite/smectites observed under the TEM.

HCl extractable Cu, Zn, Pb, Ni and to a smaller extent Cd are correlated with the TOC content and therefore predominantly bound to the organic matter of the topsoil (Fig. 4). As a result, these metals, which in this situation are almost uniquely of anthropogenic origin, only have elevated concentrations above 30 cm depth. HCl extractable Rb, Mg, Ba, Cr and Co are well correlated with Mn, Fe and Al (Fig. 4) and thus are mainly derived from oxides and/or illite/smectite. The trace metal speciation of the HNO_3 extracts is similar to that for the HCl extracts. However, Cd is no longer fixed on organic matter but correlated with Fe, Mn and Al. Nickel seems now to be bound to organics, oxides and illite/smectite (Fig. 4).

In summary: HAc extracted carbonate and trace metals adsorbed on particles; 1 N HCl removed remaining carbonate and, together with 1 N HNO_3, dissolved Fe–Mn oxides and associated trace metals; 1 N HCl and 1 N HNO_3 also attacked illite/smectite and/or extracted Al hydroxy-interlayers from illite/smectites which led to the release of Al. HCl and HNO_3 furthermore removed some heavy metals bound to organic matter. A weak correlation ($r^2 = 0.617$, $n = 7$) between HNO_3 extracted sample weight and TOC content indicates that HNO_3 also attacked the organic matter itself.

Lead isotopes

$^{206}Pb/^{207}Pb$ isotope ratios are well suited to distinguish between natural and industrial Pb and can be analyzed with sufficient precision by ICP–MS (e.g. Sturges and Barrie, 1987). The $^{206}Pb/^{207}Pb$ composition of a rock is a function of its age and its initial U/Pb ratio. In general it can be stated that the older the rock the lower its $^{206}Pb/^{207}Pb$ ratio. The oldest rocks around the studied site are Variscan granites outcropping in the Vosges and Black Forest area. Variscan granites are about 300 Ma old and form the oldest geological units of central Western Europe. Their $^{206}Pb/^{207}Pb$ ratios range between 1.18 and 1.20 (Michard-Vitrac *et al.*, 1981). Most non-metamorphic sediments in central Western Europe are post-Variscan and have $^{206}Pb/^{207}Pb$ ratios from 1.18 to 1.22 indicating that their Pb content is derived from erosion of Variscan or younger rocks (Elbaz-Poulichet *et al.*, 1986; Monna *et al.*, 1995). Based on these data the range from 1.18 to 1.22 can be regarded as the natural $^{206}Pb/^{207}Pb$ range for central Western Europe as shown in Fig. 5. The ores presently used for industrial manufacturing and automotive fuel originate from mines outside central Western Europe and are characterized by $^{206}Pb/^{207}Pb$ compositions lower than 1.16 (Elbaz-Poulichet *et al.*, 1986; Monna *et al.*, 1995).

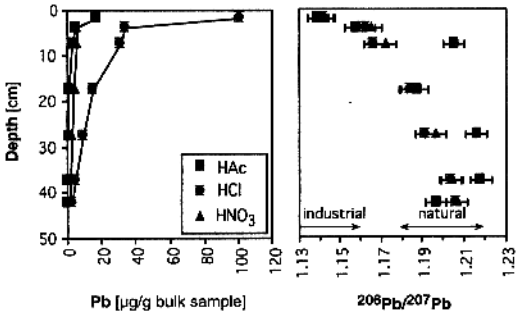

Fig. 5. The $^{206}Pb/^{207}Pb$ isotope ratios demonstrate the retention of anthropogenic Pb in the uppermost 30 cm. Pb concentrations are bulk sample normalized in order to illustrate the absolute amounts of Pb extracted. The limits of the industrial and natural $^{206}Pb/^{207}Pb$ ranges are discussed in the text.

In all extractions, our uppermost surface sample yields a $^{206}Pb/^{207}Pb$ ratio of 1.14 which is clearly below the natural and within the range for industrial Pb (Table 6, Fig. 5). With increasing depth the $^{206}Pb/^{207}Pb$ ratios shift continuously towards the natural range with only small variations in the $^{206}Pb/^{207}Pb$ ratios of the different extracts at any depth (Fig. 5).

The increase in Pb isotope ratios with depth confirms that industrial Pb had mainly been retained in the topsoil by the organic matter. The small variations in $^{206}Pb/^{207}Pb$ ratios at a specific depth level indicate that Pb migration was mainly a depth-dependant process without preferential scavenging of industrial Pb by particular phases. However, the compositions of 3 HAc extracts are shifted towards higher values. They range from 1.20 to 1.22 which is typical for a natural sedimentary source and in agreement with the finding that HAc extracted dominantly carbonate. In these cases we suggest that the carbonate extracted with HAc could preserve its natural Pb isotopic composition and that it was the HCl and HNO_3 extractable phases which scavenged the contaminants.

Strontium isotopes

The Sr isotopic compositions were determined in the leachates, in the residues, and in the air filter sample from the brass foundry (Table 6). The HAc extracts yielded an almost constant Sr isotopic composition ($^{87}Sr/^{86}Sr \approx 0.70775$). Only in the topsoil can a trend to slightly higher values be recognized (Fig. 6). In contrast, significant variations occur in the HCl and HNO_3 extracts ($^{87}Sr/^{86}Sr = 0.7077$–0.7091). The HCl extracts of the 4 uppermost samples have somewhat higher and those of the two lowermost samples somewhat lower Sr isotopic compositions

Table 6. Nd, Sr and Pb isotopic compositions of extracts, residues and air filter. The errors given for the Nd and Sr isotopic compositions are 2 sigma mean values and refer to the last digits. The Pb isotope ratios were determined by ICP–MS and are reproducible on the second decimal

Sample	$^{143}Nd/^{144}Nd$	$^{87}Sr/^{86}Sr$	$^{206}Pb/^{207}Pb$
HAc extracts			
M2.2 HAc	0.512195 (42)	0.707844 (6)	1.14
M3.2 HAc	0.512165 (19)	0.707762 (7)	1.16
M4.1 HAc	0.512195 (20)	0.707741 (6)	1.21
M6.1 HAc	0.512118 (15)	0.707745 (8)	1.19
M8.1 HAc	0.512176 (11)	0.707765 (7)	1.22
M10.1 HAc	0.512115 (10)	0.707746 (6)	1.22
M11.2 HAc	n.d.	n.d.	1.20
HCl extracts			
M2.2 HCl	0.512184 (18)	0.707895 (6)	1.14
M3.2 HCl	0.512128 (8)	0.707948 (8)	1.16
M4.1 HCl	0.512192 (9)	0.707944 (6)	1.17
M6.1 HCl	0.512146 (6)	0.707790 (6)	1.18
M8.1 HCl	0.512182 (8)	0.707696 (6)	1.19
M10.1 HCl	0.512115 (17)	0.707682 (7)	1.20
M11.2 HCl	n.d.	n.d.	1.21
HNO_3 extracts			
M2.2 HNO_3	0.512192 (22)	0.707940 (12)	1.14
M3.2 HNO_3	0.512140 (6)	0.707893 (10)	1.17
M4.1 HNO_3	0.512179 (17)	0.709096 (10)	1.17
M6.1 HNO_3	0.512148 (6)	0.708961 (7)	1.18
M8.1 HNO_3	0.512190 (16)	0.708949 (8)	1.20
M10.1HNO_3	0.512139 (12)	0.708533 (8)	1.20
M11.2HNO_3	n.d.	n.d.	1.21
Residues			
M3.2 R	0.512079 (22)	0.719201 (8)	n.d.
M4.1 R	0.512387 (9)	0.720768 (7)	n.d.
M6.1 R	0.512158 (10)	0.721063 (8)	n.d.
M10.1 R	0.512336 (6)	0.721787 (6)	n.d.
Air filter	0.511923 (50)	0.710819 (8)	n.d.

n.d. = not determined.

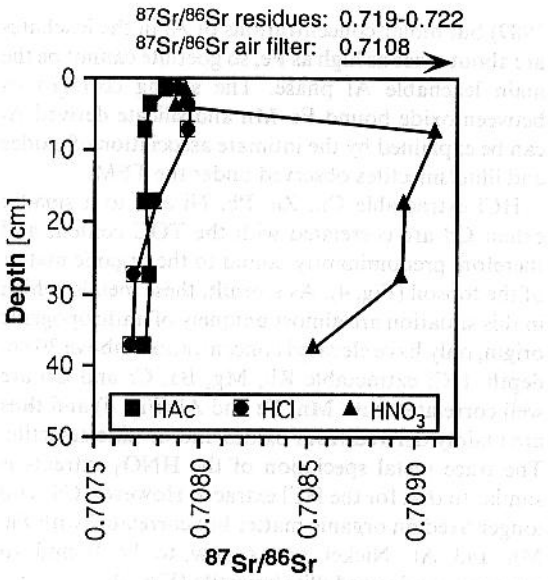

Fig. 6. Depth distribution of the Sr isotopic compositions of the leachates. Analytical errors are smaller than symbol widths.

than the corresponding HAc extracts. The $^{87}Sr/^{86}Sr$ ratios of the HNO_3 extracts are clearly higher than in the HAc and HCl extracts. The air filter ($^{87}Sr/^{86}Sr = 0.7108$) and in particular the residues ($^{87}Sr/^{86}Sr = 0.719$–0.722) have distinctly elevated Sr isotopic compositions. In the HCl and HNO_3 extracts, the $^{87}Sr/^{86}Sr$ ratios are correlated with concentrations of Mn, Fe, Al and associated elements (Table 5).

The constant Sr compositions of the HAc extracts indicate a common Sr source which is, as demonstrated by a correlation between the $CaCO_3$ content of the untreated bulk sample and the leached Sr ($r^2 = 0.869$, $n = 7$), the carbonate extracted during the first extraction step. Its isotopic composition is in the range of Tertiary marine sediments (Burke *et al.*, 1982) and, therefore, the regionally outcropping Tertiary carbonate-rich siliciclastics are the most probable initial carbonate source. This carbonate-derived Sr almost completely swamps Sr contributed from other phases with different isotopic compositions. Only the slight rise in $^{87}Sr/^{86}Sr$ ratios found near the topsoil with its lower carbonate content could reflect another Sr source.

The higher Sr isotopic compositions found in the 4 uppermost HCl and in all HNO_3 extracts could be due to leaching of silicate minerals, pollution or an influence of natural rainwater which has Sr isotopic compositions ranging from 0.7096 to 0.7114 (Probst *et al.*, 1992). Studies in the acidic soils of the adjoining Vosges mountains have shown that rainwater takes up the Sr isotopic composition of the soil minerals immediately after precipitation (Probst *et al.*, 1992; El Gh'mari, 1995). For the carbonate rich soil of our study an even faster assimilation of the rainwaters' isotopic composition can be expected. Therefore it is improbable that it was rainwater which caused the elevated $^{87}Sr/^{86}Sr$ ratios found in the HCl and HNO_3 extracts.

A distinction between anthropogenic and silicate-derived Sr is not possible on the basis of Sr isotopic compositions because both air filter and residues have higher $^{87}Sr/^{86}Sr$ ratios than the HNO_3 extracts. The correlations between Sr isotopic compositions and Al concentrations found in the HCl and HNO_3 extracts indicate that at least part of the Sr with elevated isotopic compositions is derived from silicate minerals. However, the correlations with Mn and Fe also show that some Sr with elevated isotopic compositions has been bound in Mn–Fe oxides which in turn could have incorporated anthropogenic or silicate-derived Sr. The Sr isotopic compositions of the two lowermost HCl extracts which are lower than in the corresponding HAc extracts might be due to leaching of carbonate with lower isotopic composition, e.g. gravels consisting of marine Jurassic limestones.

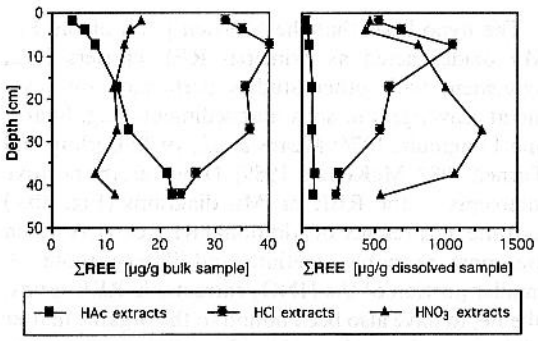

Fig. 7. Depth distribution of REE concentrations. The difference between the two diagrams is the different normalizations. The diagram on the left describes the total amount of REE extracted in each step whereas the diagram on the right shows the concentrations in the extracted phases.

REE speciation

The REE data of the leachates and residues are given in Tables 3 and 4. The bulk sample normalized REE concentrations of the HAc extracts increase almost linearly with depth, whereas the HCl and HNO_3 extractable REEs show no clear depth trends (Fig. 7). In the leachate normalization, two concentration peaks appear in the HCl and HNO_3 extracts and a correlation with soil pH can be observed for the HAc extractable REE (Fig. 8a). The REE of the HCl and HNO_3 extracts are, like Rb, Mg, Ba, Cr and Co, positively correlated with Mn, Fe and Al (Figs 4 and 8b,c) and there is also a weak correlation between REE and Sr isotopic compositions, as for Mn, Fe and Al (Table 5). In the HCl extracts no correlation can be

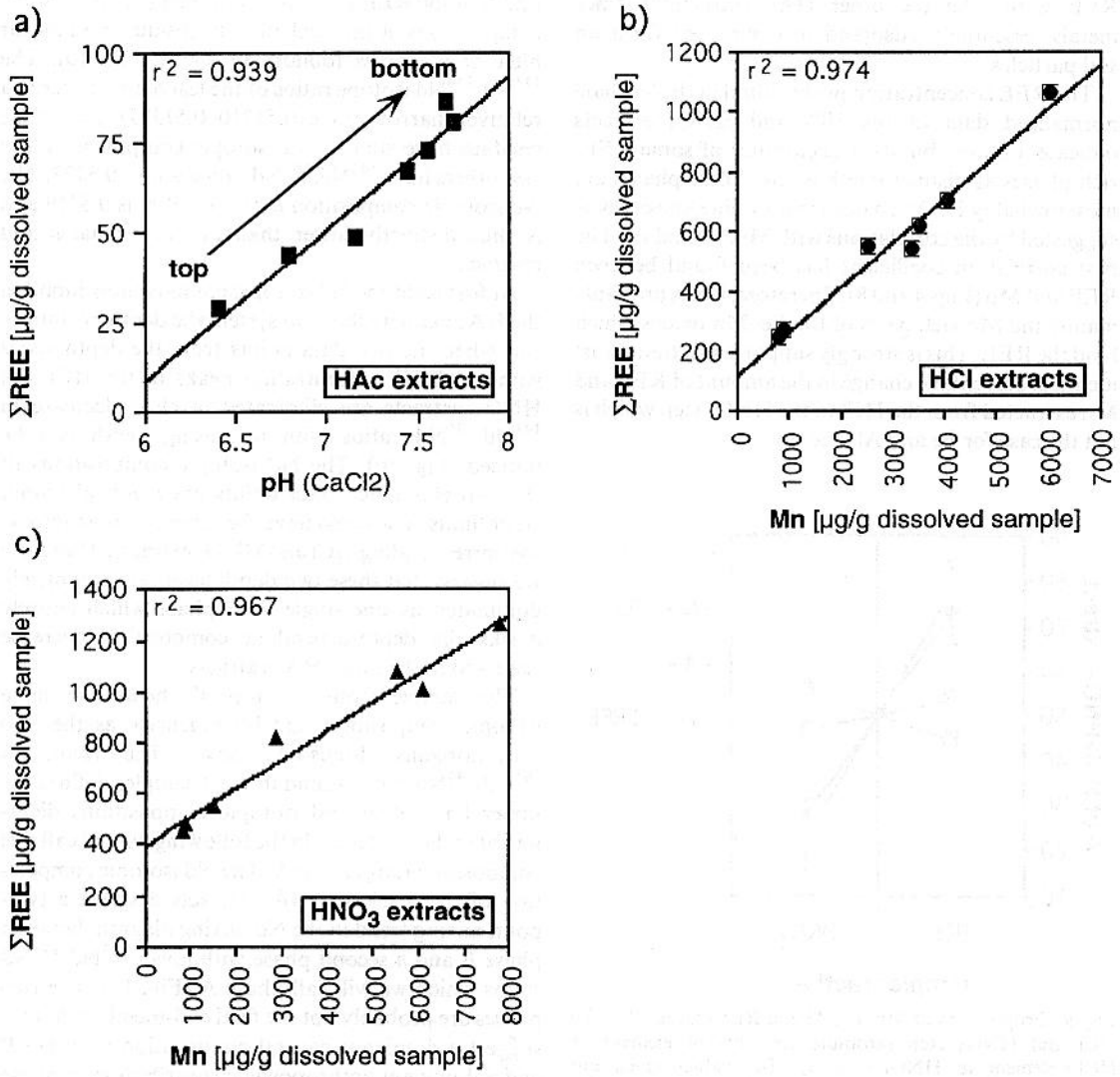

Fig. 8. The HAc extractable REE are correlated with soil pH whereas the REE of the HCl and HNO_3 extracts are correlated with Mn.

found between REE and TOC. However, for the HNO_3 extractable REE a weak correlation with TOC exists (Fig. 4, Table 5) which is similar to the correlation between Fe and TOC. The correlation between REE and TOC is even better when only the 4 uppermost samples with TOC > 1.5 wt.% are considered (Fig. 4, Table 5).

The relation between REE concentrations in the HAc extractable phase and soil pH indicates that the REE of this fraction were dissolved at the surface and then, during their transport downwards with increasing pH, were continuously precipitated from soil solution. This implies REE input from the surface and hence probably an anthropogenic origin of the HAc extractable REE.

The binding sites of the HAc extractable REE are difficult to characterize. A direct integration of REE into carbonate is improbable because their charge and size are incompatible with the lattice structure of calcite. Therefore we assume that the HAc extractable REE were, like the other HAc extractable trace metals, essentially adsorbed in complexed form on soil particles.

The REE concentration peaks found in the leachate normalized data of the HCl and HNO_3 extracts indicate a more abundant occurrence of some REE-rich phases at distinct depth levels. These phases are most probably Fe–Mn oxides and/or illite/smectites as suggested by the correlations with Mn, Fe and Al. The best correlation coefficient has been found between REE and Mn (Figs 4 and 8). Therefore, it was probably mainly the Mn-rich parts of the Fe–Mn oxides which bind the REE. This is strongly supported by the almost identical percentage change in the amount of REE and Mn extracted from the HCl to the HNO_3 step which is not the case for Fe and Al (Fig. 9).

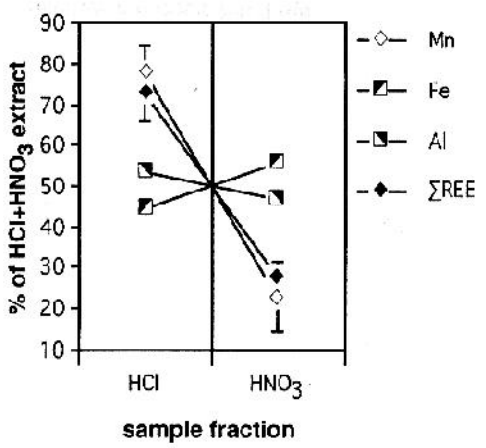

Fig. 9. Proportions of Mn, Fe, Al and REE extracted in the HCl and HNO_3 step (absolute amounts of element in HCl + element in HNO_3 = 100%). The values given are averages of all samples with standard deviations. Only Mn shows a similar percentage change between the two extraction steps as the REE.

The hypothesis that the Mn-rich parts of the Fe–Mn oxides acted as principal REE carriers is in agreement with other studies performed on trace metal scavengers in soils and sediments (e.g. Suarez and Langmuir, 1976; Means *et al.*, 1978; Cerling and Turner, 1982; McKenzie, 1989). However, the positive intercepts in the REE vs. Mn diagrams (Fig. 8b,c) indicate the presence of additional REE carriers which are most probably goethite and illite/smectite. A smaller portion of the HNO_3 extractable REE seems, like Fe, to have also been bound to the organic matter of the topsoil as indicated by the correlation between HNO_3 extractable REE and TOC and confirmed by the better correlation factor found for the 4 uppermost samples.

Neodymium isotopes

In order to get more precise information about the origin of the REE we also determined the Nd isotopic compositions of the leachates, the residues and the air filter of the brass foundry (Table 6, Fig. 10). The $^{143}Nd/^{144}Nd$ isotope ratios of the leachates scatter in a relatively narrow range (0.51210–0.51222). Two of the residues have similar Nd isotopic compositions and two others have $^{143}Nd/^{144}Nd$ ratios above 0.5123. The Nd isotopic composition of the air filter is 0.5119 and is thus distinctly lower than in the leachates and residues.

At first sight the Nd isotopic compositions found in the HAc extracts show no systematic depth evolution. But when the two data points from the depth levels with the REE concentration peaks in the HCl and HNO_3 extracts are eliminated, a clear decrease in $^{143}Nd/^{144}Nd$ ratios with increasing depth can be noticed (Fig. 10). The Nd isotopic compositions of the two eliminated data points are identical within error limits. They also have the same compositions as the corresponding HCl and HNO_3 extracts. Therefore we suggest that these two depth levels are completely dominated by one single REE phase which entirely masks the depth-dependant composition decrease observed in the other HAc extracts.

The sample from the topsoil shows the same isotopic composition and homogeneity as the two soil horizons discussed above. The range in $^{143}Nd/^{144}Nd$ ratios found in the 3 samples defines the upper limit of all Nd isotopic compositions determined in the leachates. In the following we will call this composition range phase B. The Nd isotopic composition of the 4 selected HAc extracts describe a two-point mixing trend in the Nd mixing diagram between phase B and a second phase with lower $^{143}Nd/^{144}Nd$ ratios which we will call phase A (Fig. 11). The two phases are probably not the final end-members but we suggest a dominant natural contribution in phase B and a dominant anthropogenic contribution in phase A. The low Nd isotopic composition of phase A is in agreement with the low composition found in the air

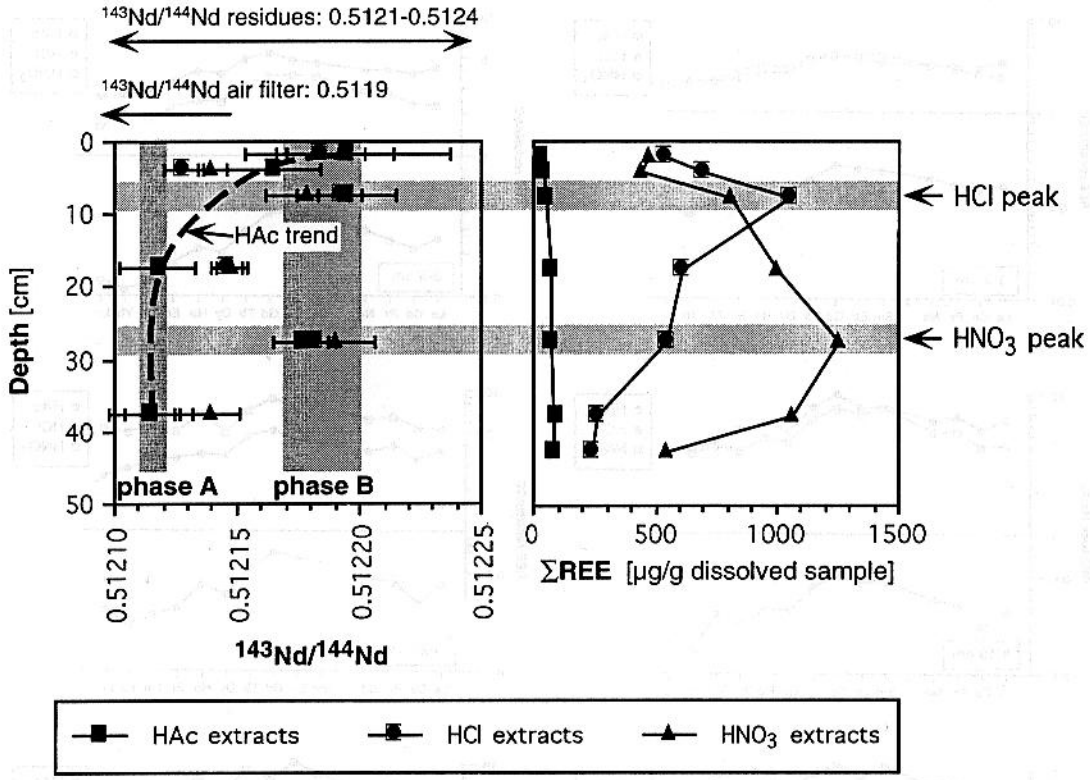

Fig. 10. Nd isotopic compositions of the leachates. The $^{143}Nd/^{144}Nd$ ratios of the HAc extracts decrease from a composition "phase B" at the surface to a composition "phase A" at the bottom of the profile. Only the samples from the depth levels with concentration peaks in the HCl and HNO_3 extracts do not follow this trend.

filter of the brass foundry. Consequently, the anthropogenic Nd has migrated through the soil and then accumulated in the lower part of the profile. This is consistent with the relationship between HAc-extractable REE and soil pH.

The Nd isotopic compositions of the HCl and HNO_3 leachates cover the same range as the HAc extracts but show no significant depth trends. We suggest that this is simply due to variations in soil mineralogy because a similarly large variation in Nd isotopic compositions also occurs in the residues.

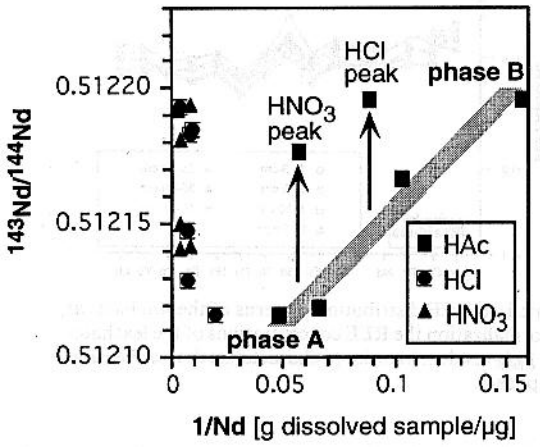

Fig. 11. Nd mixing diagram. The HAc extracts describe a mixing line between phase A and phase B. The two samples from the depth levels with concentration peaks in the HCl and HNO_3 extracts are shifted towards higher Nd isotopic compositions. We suggest that phase A is dominated by anthropogenic and phase B by natural Nd.

REE fractionation

The NASC (North American Shale Composite; Haskin *et al.*, 1968; Gromet *et al.*, 1984) normalized REE distribution patterns are shown in Fig. 12. In the 3 uppermost samples the patterns of the HCl and HNO_3 extracts are almost identical and can clearly be distinguished from the HAc patterns. From depth level 15–20 cm and downwards the HCl patterns are intermediate between the HAc and HNO_3 patterns.

The patterns of the HAc extracts show enrichment in the light rare earth elements (LREE = La, Pr, Nd, Sm) with respect to the heavy rare earth elements (HREE = Dy-Lu). This LREE enrichment, monitored by La/Yb ratios, is strongest in the HAc extracts, then decreases in the HCl and finally disappears in the HNO_3 extracts (Fig. 13). A negative Ce anomaly is present in the HAc extracts which becomes more accentuated with increasing depth and which is absent in the HCl and HNO_3 extracts (Fig. 13). Eu-anomalies are lacking in all extracts.

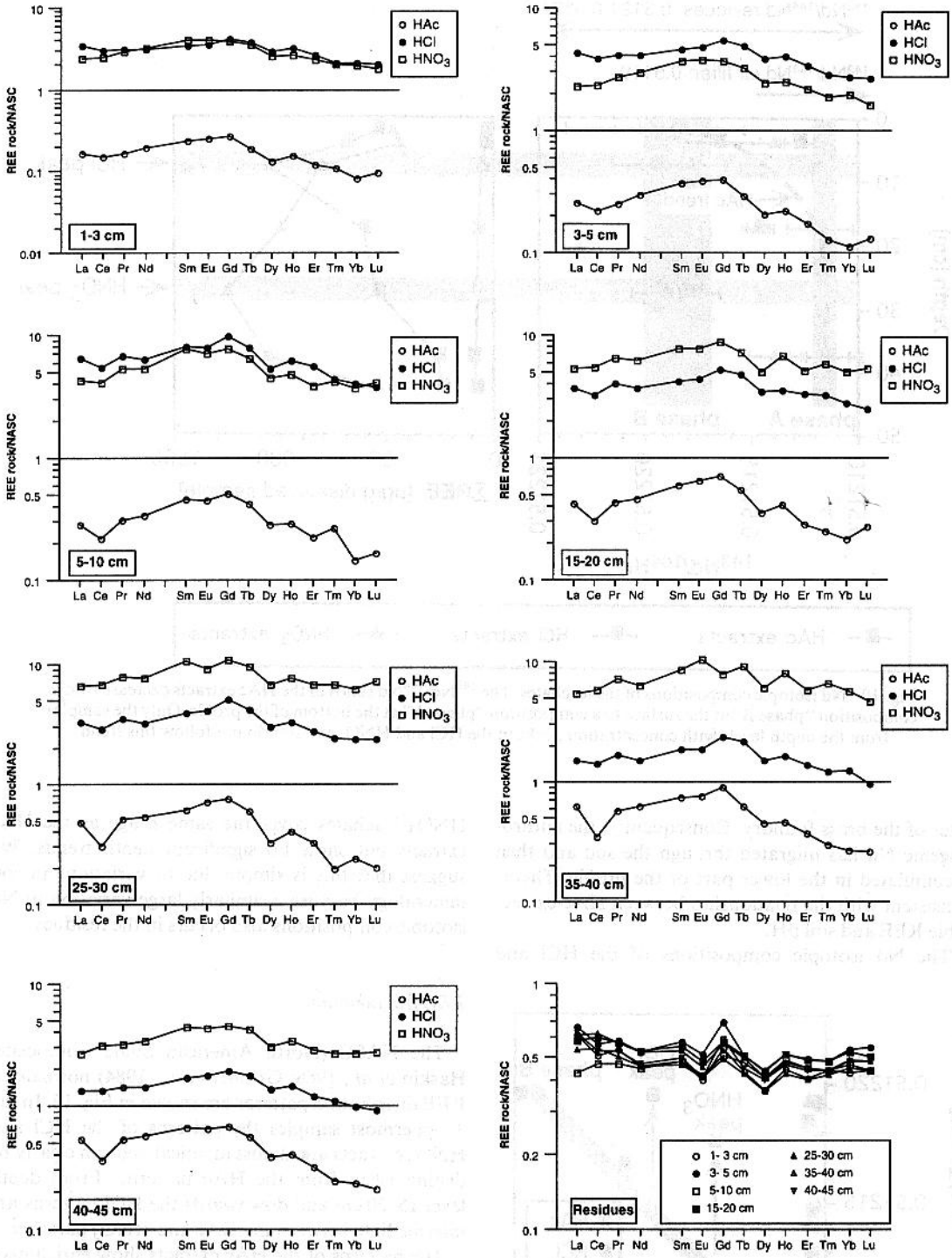

Fig. 12. NASC (North American Shale Composite) normalized REE distribution patterns of the leachates at different depth levels and the residues. Before the NASC normalization the REE concentrations of the leachates were in μg/g dissolved sample, and those of the residues in μg/g residue, in order to characterize the leached and the residual phases.

In the HNO_3 extracts a slight enrichment in the intermediate REE (IREE, Sm–Tb), which can be quantified with Sm/La ratios, is observable (Fig. 14). Within the HREE of the HNO_3 extracts, where a LREE enrichment is absent (i.e. La/Yb = 1), an additional fractionation is present which can be monitored with Er/Yb ratios (Fig. 14). The Er/Yb ratios of the HAc and HCl extracts are biased by LREE enrichment and thus do not yield information about HREE fractionation. The Er/Yb ratios of the

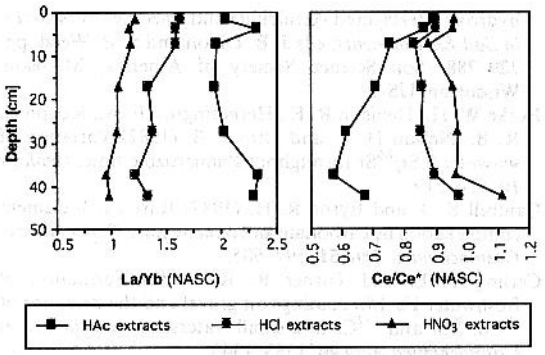

Fig. 13. NASC normalized La/Yb and Ce/Ce* ratios illustrating LREE enrichment and Ce anomaly. $Ce/Ce* = \frac{3Ce_{NASC}}{2La_{NASC}+Nd_{NASC}}$, whereas the subscript NASC signifies NASC normalized concentrations.

HNO_3 extracts are correlated with the TOC content of the untreated bulk samples ($r^2 = 0.792$, $n = 7$) and the correlation is even more pronounced when only the 4 uppermost samples with TOC > 1.5 wt.% are considered ($r^2 = 0.904$). The Er/Yb and Sm/La ratios of the HNO_3 extracts are not correlated among one another which indicates that they are two independent phenomena. All patterns of the residues are very similar and reveal NASC-like distributions.

The intermediate position of the HCl patterns found below 15–20 cm depth is probably a leaching artefact, because in the carbonate-rich deeper soil levels HCl had first to dissolve the remaining carbonate before it can begin to extract the same phase as the subsequent HNO_3 step. This is confirmed by the 3 topsoil samples with low carbonate content where the HCl and HNO_3 patterns are almost identical.

The LREE enrichment of the HAc extracts has probably been produced by two processes which are favoured retention of HREE by organic matter and higher solubility of HREE in soil water, e.g. caused by soluble carbonate complexes or organic complexes

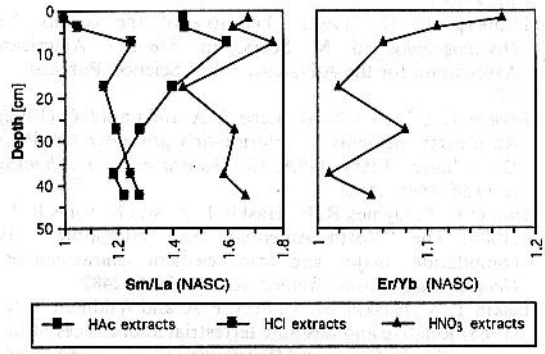

Fig. 14. NASC normalized Sm/La and Er/Yb ratios. The Sm/La ratios show that IREE enrichment is strongest in the HNO_3 extracts. The Er/Yb ratios of the 4 uppermost HNO_3 extracts decrease with decreasing TOC content which indicates HREE fractionation by organic matter. The Er/Yb ratios of the HAc and HCl extracts are biased by LREE enrichment and therefore not shown.

(Nesbitt, 1979; Cantrell and Byrne, 1987; Millero, 1992; Lee and Byrne, 1993). The stronger adsorption of HREE on organics postulated in the first process is generally known (e.g. Cantrell and Byrne, 1987) and used in the laboratory for REE separations. In our case the HREE were preferentially retained by the organic matter of the topsoil which caused a relative LREE enrichment in the deeper portions of the profile. The second process implies that the REE were transported as carbonate complexes and that it was mainly the LREE which precipitated during downward migration whereas the more soluble HREE were washed out into the underlying alluvial gravels. The importance of REE-carbonate complexes in circumneutral pH groundwaters has recently been pointed out by Johannesson *et al.* (1996).

The negative Ce anomaly of the HAc extracts can be explained by the redox behavior of Ce which, by contrast with the other REE, occurs in both trivalent and tetravalent states. The pH dependant depth distribution and the Nd isotope data have demonstrated that the HAc extractable REE are derived from the surface and are of anthropogenic origin. The industrial contamination was introduced as oxide particles and therefore Ce appears at the surface as Ce(IV) in CeO_2. This oxide is less soluble than the other REE oxides and consequently, Ce will be depleted with respect to the other REE in the deeper parts of the soil profile. Preferential scavenging of Ce by Fe–Mn oxides, as suggested by Goldberg (1961) and shown experimentally by Koeppenkastrop and DeCarlo (1992), could be an alternative explanation for the negative Ce anomaly. But since no positive Ce anomaly is present in the HCl and HNO_3 extracts we favour the first explanation. The lack of a distinct Ce anomaly in the HCl and HNO_3 extracts also underlines that these REE originated from another source than the HAc extractable REE.

Because HNO_3 essentially extracted Fe–Mn oxide bound REE in the lower part of the soil profile, the IREE enrichment observed in these extracts seems to be typical for such oxides. This is in agreement with data compiled by Gosselin *et al.* (1992) which show that secondary minerals and in particular Fe–Mn oxides have IREE enriched REE patterns. In our case, the IREE enrichment could be due to preferential removal of IREE from primary minerals during weathering. A similar preferential removal of IREE from its initial carrier phase has also been reported by Palmer and Elderfield (1986) for diagenetic processes.

The correlation between Er/Yb ratios of the HNO_3 extracts and the TOC of the untreated bulk sample indicates that the organic matter of the topsoil preferentially retained Yb during leaching with HNO_3. This can be related to the known property of organics to scavenge REE more effectively the heavier they are and demonstrates that a part of the HNO_3 extractable REE was bound to the organic matter of the topsoil. This finding is consistent with the earlier mentioned correlation between HNO_3 extractable

REE and TOC and supports the suggestion that HREE retention on organic matter was one of the processes which led to the LREE enrichment observed in the HAc extracts.

The NASC-like distribution patterns of the residues indicate that these REE mainly originated from clay minerals. It is not clear whether the positive Gd anomaly is real or due to a mass interference on the ICP–MS.

CONCLUSIONS

Pb isotopes allow the differentiation of anthropogenic and natural Pb. With Sr isotopes the Sr source of the HAc extracts could be characterized but in the HCl and HNO_3 extracts it was not possible to distinguish between anthropogenic and silicate-derived Sr. In contrast, our approach has allowed the distinction of natural and anthropogenic REE. A large part of the REE is of natural origin, in spite of the strong anthropogenic heavy metal influence. The natural REE are immobile and mainly fixed in Fe–Mn oxides. In contrast, the anthropogenic REE were mobile even under the present intermediate to alkaline pH conditions and have migrated through the soil. We suggest that they were dissolved as carbonate complexes and that considerable amounts, in particular the heavy REE, were washed out into the underlying alluvial gravels. Despite their well-known affinity for organics, the anthropogenic REE have, in contrast to other anthropogenic heavy metals, only partly been retained by the organic matter of the topsoil. We speculate that the high concentrations of Cu in the topsoil, where it forms very stable organic complexes, have led to a competitive process resulting in the displacement of the REE from the topsoil. This REE mobility is of particular importance for the propagation of accidentally released radioactive REE.

Acknowledgements—Peter Federer furnished sample material and unpublished data from his PhD thesis done at the ETH Zürich. Many thanks to the staff in Strasbourg with J. L. Cézard, B. Kiefel, Ph. Larqué, G. Morvan, R. Rouault, J. Samuel, D. Tisserant and Robert Wendling for technical assistance and help provided throughout this study. The critical reviews of S. Bottrell and an anonymous reviewer helped to improve an earlier version of the manuscript. MS profited from a fellowship of the Schweizerischer Nationalfonds zur Förderung der wissenschaftlichen Forschung, which is kindly acknowledged.

Editorial handling: R. Fuge.

REFERENCES

Allen, B. L. and Hajek, B. F. (1989) Mineral occurrence in soil environment. In *Minerals in Soil Environments*, eds J. B. Dixon and S. B. Weed, pp. 199–278. Soil Science Society of America, Madison, Wisconsin, USA.

Barnhisel, R. I. and Bertsch, P. M. (1989) Chlorites and hydroxy interlayered vermiculite and smectite. In *Minerals in Soil Environments*, eds J. B. Dixon and S. B. Weed, pp. 729–788. Soil Science Society of America, Madison, Wisconsin, USA.

Burke W. H., Denison R. E., Hetherington E. A., Koepnick R. B., Nelson H. F. and Otto J. B. (1982) Variation of seawater $^{87}Sr/^{86}Sr$ throughout Phanerozoic time. *Geology* **10**, 516–519.

Cantrell K. J. and Byrne R. H. (1987) Rare earth element complexation by carbonate and oxalate ions. *Geochimica et Cosmochimica Acta* **51**, 597–605.

Cerling T. E. and Turner R. R. (1982) Formation of freshwater Fe–Mn coatings on gravel and the behavior of ^{60}Co, ^{90}Sr and ^{137}Cs in a small watershed. *Geochimica et Cosmochimica Acta* **46**, 1333–1343.

Choppin G. R. (1983) Comparison of the solution chemistry of the actinides and the lanthanides. *Journal of the Less-Common Metals* **93**, 232–330.

Chow T. J., Bruland K. W., Bertine K. K., Soutar A., Koide M. and Goldberg E. D. (1973) Records in Southern California coastal sediments. *Science* **181**, 551–552.

Deer, W. A., Howie, R. A. and Zussman, J. (1992) *An Introduction to the Rock-forming Minerals*. Longman Scientific and Technical, London.

El Gh'mari, A. (1995) Étude miméralogique, pétrophysique et géochimique de la dynamique d'altération d'un granite soumis aux dépôts atmosphériques acides (bassin versant du Strengbach, Vosges, France): Mécanismes, bilans et modélisations. PhD thesis, Université Louis Pasteur de Strasbourg.

Elbaz-Poulichet F., Holliger P., Martin J. M. and Petit D. (1986) Stable lead isotopes ratios in major French rivers and estuaries. *The Science of the Total Environment* **54**, 61–76.

Erel Y., Patterson C. C., Scott M. J. and Morgan J. J. (1990) Transport of industrial lead through soil to stream water and groundwater. *Chemical Geology* **85**, 383–392.

Federer, P. (1993) Verteilung und Mobilität der Schwermetalle Cadmium, Kupfer und Zink in anthropogen belasteten, kalkreichen Böden. PhD thesis, ETH Zürich.

Federer P. and Sticher H. (1991) Verhalten von Kupfer, Zink und Cadmium in einem stark belasteten Kalkboden. *Chimia* **45**, 228–232.

Filipek L. H., Chao T. T. and Carpenter R. H. (1981) Factors affecting the partitioning of Cu, Zn and Pb in boulder coatings and stream sediments in the vicinity of a polymetallic sulfide deposit. *Chemical Geology* **33**, 45–64.

Fillion N., Clauer N., Samuel J., Verdoux P., Monna F. and Lancelot J. R. (1996) Dosage isotopique à l'ICP–MS du Sr d'eaux et du Pb de sédiments et de cendres d'un incinérateur urbain. *Comptes Rendus Academie des Sciences, Paris* **322**, 1029–1038.

Goldberg, E. D. (1961) Chemistry of the oceans. In *Oceanography*, ed. M. Sears, pp. 538–597. American Association for the Advancement of Science, Publication 67.

Gosselin D. C., Smith M. R., Lepel E. A. and Laul J. C. (1992) Rare earth elements in chloride-rich groundwater, Palo Duro Basin, Texas, USA. *Geochimica et Cosmochimica Acta* **56**, 1495–1505.

Gromet L. P., Dymek R. F., Haskin L. A. and Korotev R. L. (1984) The "North American shale composite": Its compilation, major and trace element characteristics. *Geochimica et Cosmochimica Acta* **48**, 2469–2482.

Haskin, L. A., Haskin, M. A., Frey, F. A. and Wildman, T. R. (1968) Relative and absolute terrestrial abundances of the rare earths. In *Origin and Distribution of the Elements*, ed. L. H. Ahrens, pp. 889–912. Pergamon Press, New York.

Johannesson K. H., Stetzenbach K. J., Hodge V. F. and Lyons W. B. (1996) Rare earth element complexation behavior in circumneutral pH groundwaters: Assessing the role of carbonate and phosphate ions. *Earth and Planetary Science Letters* **139**, 305–319.

Johnson K. S., Stout P. M., Berelson W. M. and Sakamoto-Arnold C. M. (1988) Cobalt and copper distributions in the waters of Santa Monica Basin, California. *Nature* **332**, 527–530.

Koeppenkastrop D. and DeCarlo E. H. (1992) Sorption of rare-earth elements from seawater onto synthetic mineral particles: An experimental approach. *Chemical Geology* **95**, 251–263.

Krauskopf K. B. (1986) Thorium and rare-earth elements as analogues for actinide elements. *Chemical Geology* **55**, 323–335.

Lee J. H. and Byrne R. H. (1993) Complexation of the trivalent rare earth elements (Ce, Eu, Gd, Tb, Yb) by carbonate ions. *Geochimica et Cosmochimica Acta* **57**, 295–302.

Manceau A., Gorshkov A. I. and Drits V. A. (1992) Structural chemistry of Mn, Fe, Co and Ni in manganese hydrous oxides: Part I. Information from XANES spectroscopy. *American Mineralogist* **77**, 1133–1143.

McKenzie, R. M. (1989) Manganese oxides and hydroxides. In *Minerals in Soil Environments*, eds J. B. Dixon and S. B. Weed, pp. 439–465. Soil Science Society of America, Madison, Wisconsin, USA.

Means J. L., Crerar D. A. and Borsik M. P. (1978) Adsorption of Co and selected actinides by Mn and Fe oxides in soils and sediments. *Geochimica et Cosmochimica Acta* **42**, 1763–1773.

Michard-Vitrac A., Albarède F. and Allègre C. J. (1981) Isotopic composition of Hercynian granitic K-feldspars constrains continental genesis. *Nature* **291**, 460–464.

Millero F. J. (1992) Stability constants for the formation of rare earth inorganic complexes as a function of ionic strength. *Geochimica et Cosmochimica Acta* **56**, 3123–3132.

Monna F., Ben Othman D. and Luck J. M. (1995) Pb isotopes and Pb, Zn and Cd concentrations in the rivers feeding a coastal pond (Thau, southern France): constraints on the origin(s) and flux(es) of metals. *The Science of the Total Environment* **166**, 19–34.

Nesbitt H. W. (1979) Mobility and fractionation of rare earth elements during weathering of a granodiorite. *Nature* **279**, 206–210.

Ng A. C. and Patterson C. C. (1982) Changes of lead and barium with time in California off-shore basin sediments. *Geochimica et Cosmochimica Acta* **46**, 2307–2321.

Norrish K. and Taylor R. M. (1961) The isomorphous replacement of iron by aluminium in soil goethites. *Journal of Soil Science* **14**, 179–187.

Palmer M. R. and Elderfield H. (1986) Rare earth elements and neodymium isotopes in ferromanganese oxide coatings of Cenozoic foraminifera from the Atlantic Ocean. *Geochimica et Cosmochimica Acta* **50**, 409–417.

Probst, A., Fritz, B. and Stille, P. (1992) Consequence of acid deposition on natural weathering processes: Field studies and modelling. In *Proceedings of the 7th International Symposium on Water Rock Interaction — WRI-7/Park City/Utah/USA/13–18 July 1992*, eds Y. K. Kharaka and A. S. Maest, pp. 581–584. A.A. Balkema, Rotterdam.

Rai, D. and Kittrick, J. A. (1989) Mineral equilibria and the soil system. In *Minerals in Soil Environments*, eds J. B. Dixon and S. B. Weed, pp. 161–198. Soil Science Society of America, Madison, Wisconsin, USA.

Rich C. I. (1968) Hydroxy interlayers in expansible layer silicates. *Clays and Clay Minerals* **16**, 15–30.

Righi D., Petit S. and Bouchet A. (1993) Characterization of hydroxy-interlayered vermiculite and illite/smectite interstratified minerals from the weathering of chlorite in a cryorthod. *Clays and Clay Minerals* **41**, 484–495.

Robinson G. D. (1984) Sequential chemical extractions and metal partitioning in hydrous Mn-Fe-oxide coatings: Reagent choice and substrate composition affect results. *Chemical Geology* **47**, 97–112.

Schulze, D. G. (1989) An introduction to soil mineralogy. In *Minerals in Soil Environments*, eds J. B. Dixon and S. B. Weed, pp. 1–34. Soil Science Society of America, Madison, Wisconsin, USA.

Schwertmann, U. and Taylor, R. M. (1989) Iron oxides. In *Minerals in Soil Environments*, eds J. B. Dixon and S. B. Weed, pp. 379–438. Soil Science Society of America, Madison, Wisconsin, USA.

Shirahata H., Elias R., Patterson C. C. and Koide M. (1980) Chronological variation in concentrations and isotopic compositions of anthropogenic atmospheric lead in sediments of a remote subalpine pond. *Geochimica et Cosmochimica Acta* **44**, 149–162.

Sposito, G. (1989) *The Chemistry of Soils*. Oxford University Press, New York.

Sturges W. T. and Barrie L. A. (1987) Lead 206/207 isotope ratios in the atmosphere of North America as tracers of US and Canadian emissions. *Nature* **329**, 144–146.

Suarez D. L. and Langmuir D. (1976) Heavy metal relationships in a Pennsylvania soil. *Geochimica et Cosmochimica Acta* **40**, 589–598.

Tamura T. (1957) Identification of the 14 Å clay mineral component. *American Mineralogist* **42**, 107–110.

Taylor R. M. (1968) The association of Mn and Co in soils — Further observations. *Journal of Soil Science* **19**, 77–80.

Thématique : "La mobilisation des terres rares lors de l'altération de filons de basalte en milieu salifère et leur migration dans le sel adjacent"

Steinmann, M. & Stille, P., 1998. Strongly fractionated REE patterns in salts and their implications for REE migration in chloride-rich brines at elevated temperatures and pressures. C.R. Acad. Sci. Paris, série II a, 327: 173-180.

Steinmann, M., Stille, P., Bernotat, W. & Knipping, B., 1999. The corrosion of basaltic dykes in evaporites: Ar-Sr-Nd isotope and REE evidence. Chem. Geol., 153, 259-279.

Steinmann, M., Stille, P., Mengel, K. & Kiefel, B, 2001. Trace element and isotopic evidence for REE migration and fractionation in salts next to a basalt dyke. Applied Geochem. 16, 351-361.

Steinmann, M.& Stille, P., 2004. Basaltic dykes in evaporites: a natural analogue. In: Gieré, R. and Stille P. (eds): Energy, waste, and the environnement: a Geochemical Perspective. Geol. Soc. London Spec. Publ. 236, 135-141.

Geochemistry / *Géochimie*
(Isotopic Geochemistry / *Géochimie isotopique*)

Strongly fractionated REE patterns in salts and their implications for REE migration in chloride-rich brines at elevated temperatures and pressures

Mise en évidence d'un important fractionnement des terres rares dans les sels. Implications dans les processus de migration des terres rares dans des saumures riches en chlorures à température et pression élevées

Marc Steinmann*, Peter Stille

ULP–EOST–CNRS,Centre de géochimie de la surface, UMR 7517, 1, rue Blessig, 67084 Strasbourg cedex, France

Abstract—Rare earth element (REE) distribution patterns have been determined in a salt profile adjacent to a basaltic intrusion. The REE concentrations in the salts are in the ppb range, which required an enrichment prior to ICP-MS analysis. The results document a strong REE fractionation with increasing distance from the basalt contact which could be due to REE-chloride solution complexation. The observed fractionation occurred at elevated temperatures and pressures and indicates a higher mobility of Ce, Pr, Nd, Sm and Eu. This finding is of interest for basic research and for the disposal of nuclear waste in salt formations. (© Académie des sciences / Elsevier, Paris.)

REE fractionation / salts / chloride solution complexation / liquid–liquid extraction

Résumé — Les diagrammes de répartition des terres rares (TR), réalisés sur un profil salifère au contact d'une intrusion basaltique, mettent en évidence un important fractionnement. Ce dernier est directement proportionnel à la distance par rapport au basalte et pourrait être dû à une complexation solution chlorurée – terres rares. Le fractionnement se produit à des températures et pressions élevées et indique une plus grande mobilité de Ce, Pr, Nd, Sm et Eu par rapport aux autres TR. Ce résultat est important, aussi bien pour la recherche fondamentale que pour le stockage des déchets nucléaires dans les sels. (© Académie des sciences / Elsevier, Paris.)

fractionnement des terres rares / sels / complexation de solution chlorurée / extraction liquide–liquide

Version abrégée (voir p. 179)

1. Introduction

The migration and fractionation of the rare earth elements (REE) in the natural environment is of interest for a better understanding of the chemical processes controlling the mobility of the REE. In this study we investigate REE migration and fractionation in a salt deposit. The REE, derived from a basaltic dike cross-cutting the salts, have, together with chloride-rich fluids, migrated in the salts. The scope of the study is to gather information about the processes which control REE migration in a chloride-rich brine at elevated temperatures and pressures.

Salt deposits are potential host rocks for the disposal of high level radioactive waste. Fission products released from a leaking repository will most probably be transported in chloride-rich brines at elevated temperatures and pressures (up to 200 °C [Lutze and Grambow, 1992] and about 250 to 300 bar at 1 000 m depth). The behav-

Note présentée par Ghislain de Marsily.
Note remise le 23 mars, acceptée le 2 juin 1998.

* E-Mail: ms@illite.u-strasbg.fr

iour of the rare earths is of importance in such a scenario because some REE isotopes occur as fission-derived long-lived radionuclides in nuclear waste and because the trivalent REE are considered as good analogues for the trivalent actinides (Choppin, 1983; Krauskopf, 1986). In this view, our study site is, furthermore, a natural analogue for a leaking salt repository.

2. Analytical procedures

2.1. REE enrichment

The REE concentrations in salts are, like in water samples, below the detection limit of present-day ICP-MS. To enrich them, we applied a modified liquid–liquid extraction procedure currently used for water samples (Shabani et al., 1990; Tricca, 1997).

Typically, 10 g of salt were dissolved overnight in 1 L polypropylene bottles containing 400 mL of bi-distilled water acidified with HCl to pH 2 in order to prevent REE adsorption on the bottle walls. After dissolution, the samples were filtered (Millipore GSWP 0.22 µm, 47 mm diameter) and poured into a Teflon funnel containing a mixture of bis-(2-ethylhexyl) hydrogen phosphate (HDEHP) and 2-ethylhexyl dihydrogen phosphate (H_2MEHP) in heptane, and shaken. During the subsequent settling the two phases became unmixed, which led to a quantitative transfer of the REE from the aqueous phase into the organic extractant. The REE were then back-extracted from the organic phase with a small volume of 9 M HCl (Peppard, 1966), evaporated and redissolved in 10 mL of 1 M HNO_3 for ICP analysis (VG Plasmaquad PQ 2+, analytical error < ± 5 %). The REE concentrations determined with this procedure were within the 5 % error range of the ICP-MS reproducible for concentrations above 1 ppb. The chemical products used for the extraction are listed in *table I*. The total blanks of the whole extraction procedure and the blank contributions in the salt samples are given in *table II*.

2.2. Control of the extraction yield

Basically, the light REE (LREE, La-Nd) are less extracted from the aqueous phase than the heavy REE (HREE, Dy-Lu) because they form less stable organic complexes (Peppard et al., 1957; Cantrell and Byrne, 1987). However, for the liquid–liquid extraction of sample solutions acidified with HCl to pH 2, this fractionation is not observed because the high ratio of organic phase over sample REE leads to the complete complexation of all REE (Tricca, 1997). In contrast, during the back extraction of the REE from the organic phase with 9 M HCl, the HREE are less back-extracted than the LREE resulting in lower yields for the HREE for the total extraction procedure.

Table I. The reagents used in the REE liquid–liquid extraction.

Réactifs utilisés pour l'extraction liquide-liquide des terres rares.

Reagents	Origin
HCl bi-distilled	Isotope geochemistry lab.
HNO_3 bi-distilled	Isotope geochemistry lab.
HDEHP/H_2MEHP 55/45	Merck Art. 821943
Oxalic acid > 99 %	Sigma 0-0376
1-Octanol extrapure	Merck Art. 1.00991
n-Heptane p. a.	Merck Art. 1.04379

Table II. Total blanks for the REE liquid–liquid extraction and average blank contributions in the salt samples. The average blank values are based on five blanks. Only La and Ce were present in detectable amounts in all blanks. Nd could only be detected twice. The blank contributions in the samples are based on the average blank values.

Valeur moyenne des blancs, réalisée à partir de 5 blancs, pour l'extraction liquide-liquide des terres rares. Contributions de ces blancs moyens aux échantillons de sel. Seuls La et Ce ont été détectés dans tous les blancs. Nd n'a été détecté que deux fois.

	La	Ce	Nd
Average blank [ng] (n = 5, ± s):	0.33 (± 0.10)	0.37 (± 0.31)	0.10 (± 0.05)
Blank contributions [%]:			
R 4250	0.11	0.06	0.03
R 4251	0.28	0.31	0.26
R 4252	0.23	0.31	0.29
R 4253	1.07	0.89	0.33
R 4254	1.61	2.22	1.48

To quantify the yield percentages, a spike solution containing known concentrations of La, Nd, Eu, Dy, Er and Lu was added to aliquots of salt samples whose REE concentrations had previously been determined. The solution had approximately a NASC (North American Shale Composite) distribution in order to get an almost constant over-spiking factor and to hold the total REE load as low as possible. However, Eu and Lu were, respectively, two and three times enriched with respect to the NASC distribution. This, together with the appropriate dilutions, made it possible to keep all REE in the measuring solutions within a range of 1–50 µg/L in which our ICP-MS has shown to be most precise (Tricca, 1997). The quantity of spike solution added to the samples was calculated in such a way that the samples contained at least 50 times more spike REE than natural REE. Since the analytical error of the ICP-MS is ± 5 % on the 1 sigma level, the REE measured in a spiked sample can be considered to be only spike REE. The advantage of using spiked salt samples over pure standard solutions to control the extraction yield is that modifications of the REEs distribution coefficients due to the salt matrix are also taken into account.

The average extraction yields were 91–93 % for the HREE and the MREE and the decrease within the HREE group was down to 78 % for Lu (*table III*). From these average yields correction factors defined as '100/average

Table III. Average extraction yields of the liquid–liquid extraction, correction factors and Y and REE concentrations of the salt samples and the average basalt. The average basalt data are based on six samples. The stability data for $Ln(III)Cl^{2+}$ complexes are infinite dilution values from Millero (1992) and plotted in *figure 4*.

Taux d'extraction moyens de l'extraction liquide-liquide, facteurs de correction et concentrations en Y et en terres rares des échantillons de sel et du basalte moyen. Les données moyennes obtenues pour le basalte sont établies à partir de six échantillons. Les données de stabilité pour les complexes $Ln(III)Cl^{2+}$ sont des valeurs infinies de dilution, issues de Millero (1992) et reportées sur la *figure 4*.

		Y	La	Ce	Pr	Nd	Sm	Eu	Gd	Tb	Dy	Ho	Er	Tm	Yb	Lu
Average extraction yield (n = 5):																
	[%]		91.6			93.0		92.2			91.0		87.4			78.2
	±s		5.82			4.82		4.98			5.05		5.14			2.29
Correction factors *(interpolated values in italic)*:																
			1.09	*1.09*	*1.08*	1.08	*1.08*	1.08	*1.09*	*1.09*	1.10	*1.12*	1.14	*1.19*	*1.23*	1.28
REE concentrations (yield corrected):																
R 4250	[ppb]	14.7	32.8	66.8	8.0	33.3	6.1	2.0	6.3	0.79	3.4	0.61	1.5	0.17	0.93	0.12
R 4251	[ppb]	4.3	12.8	13.0	1.1	4.0	0.7	0.2	0.9	0.12	0.6	0.14	0.4	0.06	0.39	0.07
R 4252	[ppb]	7.8	15.6	12.7	0.9	3.6	0.6	0.2	0.9	0.13	0.8	0.21	0.7	0.11	0.66	0.10
R 4253	[ppb]	9.1	3.4	4.5	0.6	3.2	1.4	0.7	2.4	0.39	2.1	0.36	0.9	0.11	0.60	0.09
R 4254	[ppb]	4.2	2.1	1.7	0.1	0.6	0.3	0.1	0.6	0.13	0.8	0.16	0.4	0.07	0.33	0.06
av. basalt	[ppm]	29.03	65.44	131.21	15.35	58.59	10.41	3.18	8.53	1.22	5.96	1.11	2.69	0.38	2.03	0.31
Complex stabilities (25 °C, 1 bar)																
$Ln(III)Cl^{2+}$	log ß		0.29	0.31	0.32	0.32	0.30	0.28	0.28	0.27	0.27	0.27	0.28	0.27	0.16	-0.03

yield in %' have been calculated for each REE which were used to correct the REE concentrations of unspiked salt samples. For REE not contained in the spike solution interpolated values were taken. The REE concentrations of the unspiked salt samples presented in *table III* are all yield corrected.

3. Geological setting

The sampling site is situated in an underground mine in central Germany where Permian evaporites are cross-cut by Miocene basaltic dikes. The evaporite series has a total thickness of up to 400 m and is dominated by halites (NaCl) containing some intercalations of potash salts and anhydrites ($CaSO_4$). The basalt–salt contact investigated in this study is located in a potash salt level (*figure 1*) originally consisting of essentially carnallite ($KMgCl_3$, $6H_2O$). During basalt intrusion, these carnallites have been transformed mainly into halite and sylvite (KCl) by fluids saturated in NaCl originating from the partial dissolution of an underlying 150-m thick halite formation (Knipping and Herrmann, 1985; Gutsche, 1988; Knipping, 1989). This salt metamorphism was strongest near the basalt contact and decreases regularly with distance (Gutsche, 1988). An estimation of the ionic strength of the penetrating brine yields a value of about 5 when referring to the solubility limit of NaCl in water at 90 °C (Braitsch, 1971). The chemical composition of the brine can be estimated by a quantitative analysis of the observed mineral reactions (Herrmann et al., 1978; Gutsche, 1988). The results show that the major anion composition of the brine remained

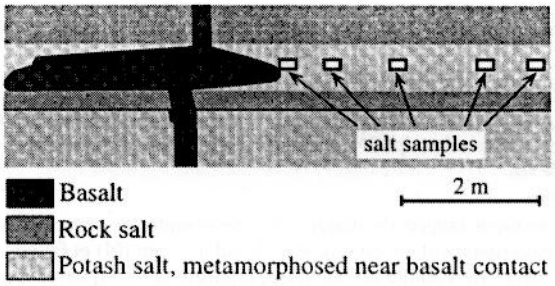

Figure 1. The salt profile studied here is situated in a underground mine next to a basalt dyke which is locally enlarged to an apophysis.

Le profil de sel étudié se trouve dans une mine souterraine, à proximité d'un filon basaltique localement élargi en une apophyse.

almost unchanged during the penetration of the salts. The brine contained in particular Cl^- which dominated more than 95 % of the total anion charge and some SO_4^{2-}. The dominant cations were Na, K and Mg (Gutsche, 1988).

No direct temperature data are available for the brines. Directly at the basalt contact they may have reached a few hundred °C since the temperature of the basaltic melt was around 1 150 °C (Knipping, 1989). However, already less than 1 m from the contact the temperatures might locally have been much lower as indicated by relicts of primary carnallite (Knipping and Herrmann, 1985; Knipping, 1989) whose upper thermal stability limit is 167.5 °C (Braitsch, 1971). The pH of the penetrating brines was, in analogy to carbonate-free recent brines occurring in salt pans (6.5–7, Herrmann et al., 1973), groundwaters (4.5–6.5, Fisher and Kreitler, 1987) and deep-sea basins of the Red Sea (5.5–6.5, Hartmann, 1969), probably below 7.

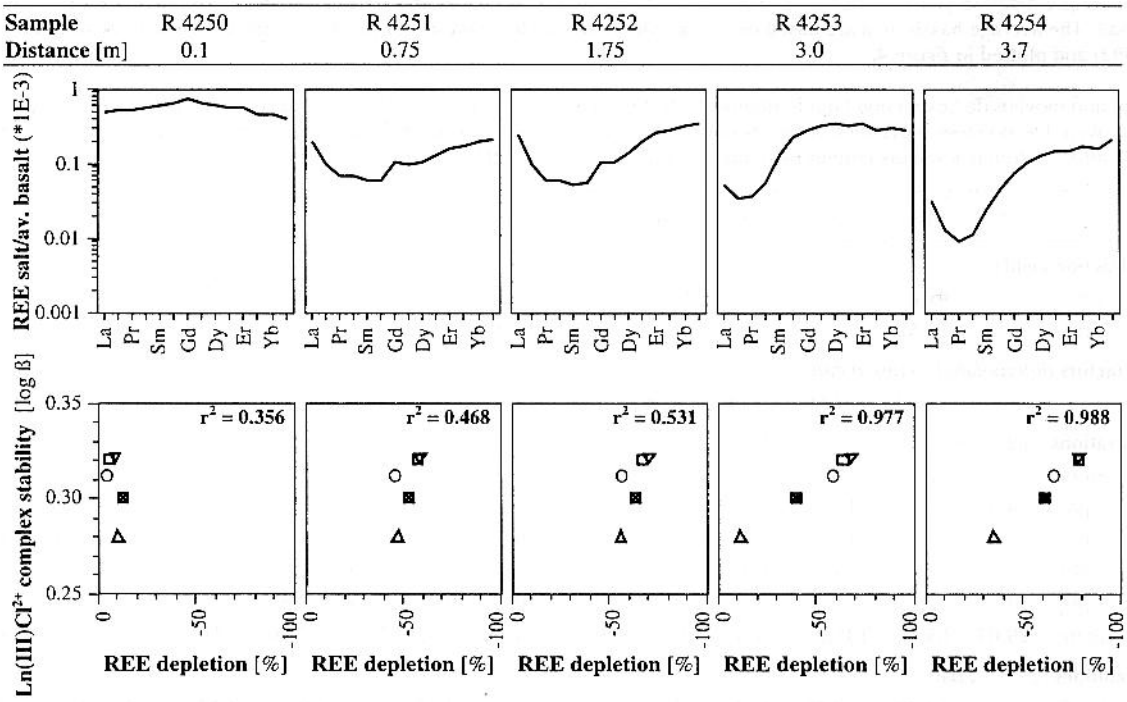

Figure 2. The diagrams in the first row show the average basalt normalised REE distribution patterns of the salts. Note the evolving depletion of Ce (○), Pr (▽), Nd (□), Sm (⊠) and Eu (△) with distance. In the second row, the chloride complex stability constants of the five depleted REE are plotted against their relative depletions. The correlations between the two parameters increase with distance. This suggests that the REE were transported as chloride complexes and that the observed depletion of Ce, Pr, Nd, Sm and Eu in the salts is due to their higher solubility in the brine. The relative REE depletion is defined as rel. Ln depletion $[\%] = \left(\frac{Ln - Ln_{int}}{Ln_{int}}\right)$, **whereas** $Ln_{int} = La_{BN} + \left\{ (z_{Ln} - 57)^* \left(\frac{Gd_{BN} - La_{BN}}{7}\right) \right\}$.

Ln_{int} signifies the interpolated value of the corresponding lanthanide and z_{Ln} its atomic number. The interpolation is based on La_{BN} and Gd_{BN}, whereas the subscript BN stands for average basalt normalised concentrations. The complex stability data are from Millero (1992) and given in *table III*.

La première rangée de diagrammes représente les répartitions des terres rares des sels, normalisées par rapport au basalte moyen. À noter l'appauvrissement en Ce (○), Pr (▽), Nd (□), Sm (⊠) et Eu (△), avec l'augmentation de la distance. Dans la seconde rangée, sont reportées les constantes de stabilité du complexe chloruré des cinq terres rares appauvries, en regard de leurs appauvrissements relatifs. Les corrélations entre les deux paramètres augmentent avec la distance. Ceci suggère que les terres rares ont été transportées sous forme de complexes chlorurés et que l'appauvrissement observé en Ce, Pr, Nd, Sm et Eu est dû à leur plus grande solubilité dans la saumure. L'appauvrissement relatif en terres rares est défini par la relation appauvrissement rel. $[\%] = \left(\frac{Ln - Ln_{int}}{Ln_{int}}\right)$, avec $Ln_{int} = La_{BN} + \left\{ (z_{Ln} - 57)^* \left(\frac{Gd_{BN} - La_{BN}}{7}\right) \right\}$.

Ln_{int} est la valeur interpolée du lanthanide correspondant et z_{LN} son numéro atomique. L'interpolation est basée sur La_{BN} et Gd_{BN}, sachant que l'indice BN représente les concentrations normalisées par rapport au basalte moyen. Les constantes de stabilité des complexes sont issues de Millero (1992) et fournies dans le *tableau III*.

4. Results

The total REE concentrations decrease with increasing distance from the basalt (*table IV*). The average basalt normalised REE distribution patterns of the salts are flat, i.e. basalt-like, near the contact (*figure 2*). Then a depletion in Ce, Pr, Nd, Sm and Eu can be observed, which becomes more pronounced with increasing distance. This fractionation cannot be an analytical artefact of the liquid–liquid extraction because we controlled the extraction yield of sample R 4250 (without anomaly) and R 4254 (with anomaly) by using spiked sample aliquots and found almost identical values.

The observed fractionation can be quantified with La/Pr ratios. The La/Pr ratios are correlated with the Y/Ho ratios (*figure 3*). Both ratios have basalt-like values near the contact and evolve with distance (*table IV*). An additional distance-dependant REE fractionation parameter is La/Yb, which decreases regularly with distance (r^2 La/Yb versus distance: 0.950; *table IV*).

5. Discussion

The almost basalt-like distribution pattern at the contact and the with distance evolving depletion of Ce, Pr, Nd, Sm, and Eu indicate that the REE are basalt-derived and that their

Table IV. Distance from the basalt contact, total REE concentrations and REE fractionation parameters of the salt samples. The subscript BN stands for average basalt normalised concentrations.

Distance par rapport au contact du basalte, concentrations totales en terres rares et paramètres de fractionnement des terres rares des échantillons de sel. L'indice BN représente les concentrations normalisées par rapport au basalte moyen.

Sample	Distance [m]	ΣREE [ppb]	Y/Ho_{BN}	La/Pr_{BN}	La/Yb_{BN}
R 4250	0.10	177.6	0.92	0.96	1.10
R 4251	0.75	38.9	1.16	2.77	1.01
R 4252	1.75	45.0	1.38	3.98	0.73
R 4253	3.00	29.7	0.97	1.36	0.17
R 4254	3.70	11.7	1.00	3.40	0.20

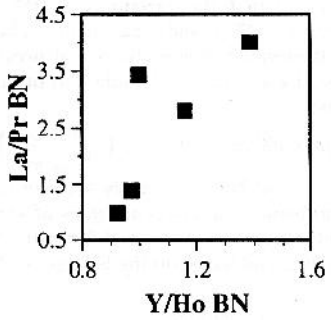

Figure 3. Average basalt normalised La/Pr and Y/Ho ratios. The data point deviating from the linear trend is the most distant sample R 4254.

Rapports La/ Pr et Y/Ho normalisés par rapport au basalte moyen. Le point situé hors de la tendance linéaire correspond à l'échantillon R 4254, le plus éloigné du contact avec le basalte.

distributions have been modified during migration. This hypothesis is supportec by Nd isotopic compositions which are basalt-like for all samples and which do not indicate any mixing relations (Steinmann et al., submitted).

Y and Ho are both trivalent in magmatic and aqueous systems and have almost identical ionic radii (Brookins, 1989). The only process able to fractionate them is complexation because of slight differences in their electron structure. Varying Y/Ho ratios are therefore indicative for Y and REE transport as dissolved complexes or for their retention on particles by surface complexes (Bau, 1996). Accordingly, the correlation between La/Pr and Y/Ho ratios indicates that the observed fractionation is due to complexation-controlled differential REE solubility or adsorption.

In the case of solubility control, the depleted REE would have been more soluble and been transported out of the profile. In the case of adsorption control, the depleted REE would have been less adsorbed by surface complexes during migration. This selective adsorption must have occurred within the salts since the salt sample at the basalt contact still shows a basalt-like REE distribution pattern. In this latter case one would furthermore expect a positive correlation between La/Pr and ΣREE because an adsorption process able to fractionate the REE is also expected to scavenge them. However, no such correlation can be observed; in contrast, the ΣREE concentrations decrease with increasing La/Pr ratios. Therefore, we favour a solubility-induced REE fractionation due to differential stabilities of dissolved REE complexes.

Chloride is a potential ligand to cause such a fractionation because it made up more than 95 % of the total anion charge and because experimental data have demonstrated strongly increasing stabilities for Nd chloride complexes at temperatures above 50 °C (Gammons et al., 1996). Because the pH of the brines was probably slightly acidic, a part of the REE may also have been transported as free ions which, however, is not expected to cause REE fractionation. A plot of the stability constants given by Millero (1992) for $Ln(III)Cl^{2+}$ lanthanide complexes for 25 °C and 1 bar effective y yields an inverse mirror image of the REE patterns found for the two most distant salt samples (*figure 4*). The constants of Mironov et al. (1982; see also Wood, 1990a) for $Ln(III)Cl^{2+}$ lanthanide complexes basically show, like Millero's data, higher stabilities for the light rare earths than for the heavy ones, but in detail, the fit with the observed distribution patterns is less convincing. The stability constants for other potential complex ligands at 25 °C and 1 bar such as $Ln(III)SO_4^+$ or, in the case of alkalic pH, $Ln(III)(OH)_3$, show no distributions comparable with our REE patterns even when the constants of various ligands are combined. For this comparison the stability constants compiled by Haas et al. (1995) were taken.

In *figure 2* the chloride complex stability constants of Millero (1992) for Pr, Nd, Sm and Eu are plotted against the relative depletions of these elements. With increasing distance the two parameters become increasingly more correlated. The complexes with higher stabilities are more depleted in the salts. This indicates that the observed fractionation could in fact be caused by soluble chloride complexes and that the stronger depletion in the more distant samples is similar to a chromatographic separation due to the longer continuation of the complexation-related fractionation. This hypothesis is also supported by the decreasing La/Yb ratios with distance because $LaCl^{2+}$ is more stable than $YbCl^{2+}$ and La thus more soluble than Yb.

The observed REE fractionation (and our finding that it could have been complexation with chloride which caused it) is not in agreement with REE model speciations calculated for comparable chloride-rich hypersaline brines at 25 °C and 1 bar (Millero, 1992; Johannesson et al., 1996). In these studies REE chloride complexes were estimated to be of minor importance and no preferential complexation of specific rare earths which could result in fractionated distribution patterns was found. This discrepancy is most probably due to the temperatures, which were higher in our case, and the herewith strongly increasing stabilities of chloride complexes (Gammons et al., 1996).

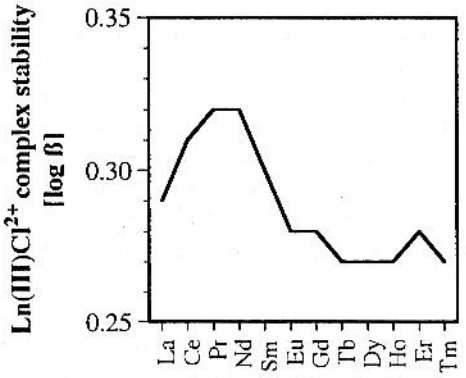

Figure 4. Plot of the complex stability constants of $Ln(III)Cl^{2+}$ complexes. They give, except for Yb and Lu, an inverse mirror image of the REE distribution patterns of the samples R 4253 and R 4254 shown in *figure 2*. The stability constants are infinite dilution values from Millero (1992) and given in *table III*. The values for Yb and Lu are below 0.25 and not shown to limit the scale of the figure (Yb = 0.16; Lu = –0.03).

Représentation des constantes de stabilité des complexes Ln $(III)Cl^{2+}$. À l'exception de l'Yb et du Lu, elles fournissent une image inverse de celle des diagrammes de répartition des terres rares, obtenus pour les échantillons R 4253 et 4254 représentés sur la *figure 2*. Les valeurs pour Yb et Lu sont inférieures à 0,25, et n'ont pas été représentées pour limiter la taille de la figure (Yb = 0,16 ; Lu = 0,03).

Experimentally determined stability constants for chloride complexes at elevated temperatures exist only for Nd (Gammons et al., 1996). It is therefore, at present, not possible to predict chloride complexation-related REE fractionation at elevated temperatures based on experimental data. Haas et al. (1995) calculated the stability constants of all potential inorganic REE complexes at temperatures and pressures up to 700 °C and 5 kbar, respectively. However, the distributions of these constants, even those for chloride complexes, do not show any similarities with the REE patterns of our salts, although the estimations are based on the values of Millero (1992) which are correlated with our data. The higher relative stabilities of Ce, Pr, Nd, Sm and Eu chloride complexes of Millero's data set have disappeared in the high *P–T* estimations of Haas et al. (1995). This is not in agreement with our data, which rather indicate that small variations in complex stabilities at 25 °C and 1 bar do not completely disappear but are magnified at elevated *P–T* conditions (*figure 5*) as already suggested by Wood (1990b). An additional point might be the ionic strength of the solution which is not considered in the estimations of Haas et al. (1995), but which could have a strong influence on the speciation of the rare earths in concentrated brines (Johannesson et al., 1996).

6. Conclusion

The salt profile studied here presents a unique opportunity to investigate REE transport and fractionation in a chloride-rich brine under natural conditions. The REE

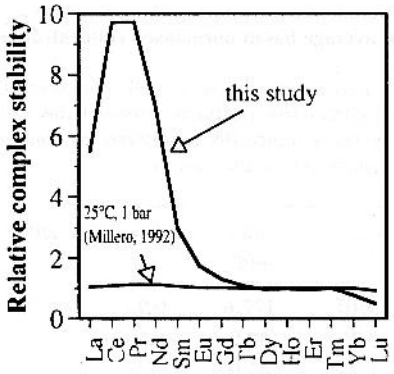

Figure 5. Relative stabilities of the suggested REE chloride complexes derived from the observed fractionated REE patterns compared with the relative stabilities at 25 °C and 1 bar. Note that the stabilities of each curve are normalised to the corresponding value for Tm and that the two curves are not proportional to each other. Our data indicate that the variations in REE chloride complex stabilities existing at 25 °C and 1 bar (*figure 4*) become much more accentuated at elevated temperatures and pressures. The relative stability value of a specific lanthanide (Ln) of our data was calculated as follows:

$$\text{Relative complex stability (Ln)} = 1/\left(\frac{Ln_{av,\,BN}}{Tm_{av,\,BN}}\right)$$

whereas $Ln_{av,\,BN}$ and $Tm_{av,\,BN}$ signify average values of the basalt normalised lanthanide Tm concentrations of samples R 4253 and R 4254, respectively. The relative stabilities at 25 °C and 1 bar are defined as $ß_{Ln}/ß_{Tm}$ and based on the ß values of Millero (1992).

Comparaison entre les stabilités relatives des complexes chlorure - terres rares tirées des diagrammes de fractionnement des terres rares, et les stabilités relatives à 25 °C et 1 bar. À noter que, pour chaque courbe, les stabilités sont normalisées par rapport à la valeur correspondante de Tm et qu'il n'est pas possible d'établir de proportionnalité entre les deux courbes. Nos données indiquent que les variations de stabilité des complexes chlorure – terres rares à des températures et pressions élevées sont beaucoup plus accentuées que celles observées à 25 °C et 1 bar (*figure 4*). La stabilité relative de chaque lanthanide (Ln) provenant de nos données a été calculé de la façon suivante :

$$\text{Stabilité relative des complexes (Ln)} = 1/\left(\frac{Ln_{av,\,BN}}{Tm_{av,\,BN}}\right)$$

pour laquelle : $Ln_{av,\,BN}$ et $Tm_{av,\,BN}$ représentent les valeurs moyennes des concentrations en lanthanide et en Tm, dans les échantillons R 4253 et R 4254, normalisées par rapport au basalte. Les stabilités relatives, 25 °C et 1 bar sont définies par le rapport $ß_{Ln}/ß_{Tm}$, pour lequel les valeurs ß sont issues de Millero (1992).

analysed in the salt profile have probably been accumulated over at least several days or weeks and the observed fractionated patterns thus represent strongly amplified variations of the mobility of the individual REE. This makes the salts a highly sensitive monitor of relative REE mobilities in a natural, chloride-rich salt brine under elevated temperatures and pressures.

The observed fractionation of the rare earths could have been caused by complexation with chloride. In this case, the REE depletion observed in the most distant samples can be translated into relative REE chloride complex stabilities and be compared with the complex stabilities of Millero (1992). This comparison shows that the small

variations in relative complex stabilities occurring at 25 °C and 1 bar are up to nine times magnified in our case (*figure 5*). This finding is not in agreement with REE complex stability estimations for comparable conditions, but the discrepancies cannot be resolved at present. In particular, new experimental data are needed which take, in addition to elevated *P–T* conditions, elevated ionic strengths into account.

For the REE and actinides leaving a leaking high level waste repository in salt rocks, a similar transport as chloride complexes can be expected. In this perspective, the higher mobility of Ce, Pr, Nd, Sm and Eu with respect to the other rare earths is not only of importance for the migration behaviour of fission-derived long-lived radionuclides such as ^{144}Ce, ^{144}Pr and ^{147}Pm. It could also have implications for the mobility of trivalent Am and Cm, which are major constituents of spent nuclear fuel and for which, due to their almost identical ionic radii, an almost analogous behaviour in natural solutions is expected as for Sm and Nd (Choppin, 1983, 1986; Krauskopf, 1986).

Acknowledgements. We thank M. de Boisseson, B. Klefel, J. Paumard, J. Samuel, D. Tisserant, and A. Tricca for their assistance in the laboratory. The salt samples were kindly supplied by K. Mengel from the Technical University of Clausthal (Germany). M. Steinmann benefitted from a fellowship of the Swiss National Science Foundation, which is highly acknowledged.

Version abrégée

Introduction

Cette étude concerne la migration et le fractionnement des terres rares dans des formations salifères. Les terres rares, issues d'un filon basaltique qui traverse ces formations, ont migré avec des solutions chlorurées. Le but de cette étude est d'obtenir des informations sur les mécanismes qui contrôlent la migration des terres rares dans une saumure riche en chlorures, à température et pression élevées. D'autre part, le site d'étude est considéré comme un analogue naturel de site de stockage de déchets radioactifs de haute activité dans les sels.

Le site échantillonné est localisé dans une mine souterraine d'Allemagne centrale, où des évaporites d'âge Permien sont recoupées par des filons basaltiques miocènes. Le contact basalte-sel étudié est situé dans un niveau de sel de potasse (*figure 1*), qui était composé principalement de carnallite ($KMgCl_3$,6 H_2O) avant l'intrusion basaltique. Lors de l'intrusion, les carnallites ont été transformées essentiellement en halite (NaCl) et sylvite (KCl) par des fluides saturés en NaCl. Ce métamorphisme des sels est plus intense au contact du basalte et décroît avec la distance. Dans la saumure qui a pénétré le basalte, Cl est l'anion majeur et les principaux cations sont Na, K et Mg (Gutsche, 1986).

Résultats

Les concentrations totales en terres rares dans les sels diminuent en fonction de l'augmentation de la distance par rapport au basalte (*tableau IV*). A proximité du contact, les diagrammes de répartition des terres rares des sels, normalisés par rapport au basalte moyen, sont plats, c'est-à-dire semblables à ceux du basalte (*figure 2*). Ensuite, un appauvrissement en Ce, Pr, Nd, Sm, et Eu, est observé ; il s'accentue avec l'augmentation de la distance par rapport au basalte.

Le rapport La/Pr permet de quantifier le fractionnement observé. Ce rapport La/Pr est corrélé avec le rapport Y/Ho (*figure 3*). Les valeurs de ces deux rapports sont proches de celles des basaltes près du contact et évoluent ensuite avec la distance (*tableau IV*).

Discussion

Au contact du basalte, la répartition des terres rares est pratiquement identique à celle de ce dernier. Puis au fur et à mesure que la distance augmente, un appauvrissement progressif en Ce, Pr, Nd, Sm et Eu apparaît. Ceci indique que les terres rares dérivent du basalte et que leurs répartitions sont modifiées au cours de leur migration. Cette hypothèse est confirmée par les compositions isotopiques de Nd, qui sont proches de celles du basalte pour l'ensemble des échantillons et qui ne signalent aucun mélange (Steinmann et al., soumis).

Une variation des rapports Y/Ho peut être attribuée à un transport de Y et des terres rares sous forme de complexes dissous, ou à leur rétention sur des particules sous la forme de complexes de surface (Bau, 1996). La corrélation entre les rapports La/Pr et Y/Ho indique par conséquent que le fractionnement observé est dû à un processus de solubilisation ou d'adsorption différentielle des terres rares, contrôlé par la complexation. Dans le cas présent, nous suggérons qu'il s'agisse plutôt d'une solubilisation différentielle.

Un ligand susceptible de provoquer un tel fractionnement est le chlorure, et ceci pour deux raisons : (i) le chlorure représente plus de 95 % de la charge anionique totale ; (ii) les données expérimentales ont montré une forte augmentation des stabilités au-dessus de 50 °C pour les complexes chlorure-Nd (Gammons et al., 1996).

Les constantes de stabilité, fournies par Millero (1992), pour des complexes $Ln(III)Cl^{2+}$ à 25 °C et 1 bar, donnent une image inverse de celle des diagrammes de terres rares des deux échantillons de sel les plus éloignés du basalte (*figure 4*). Aucun autre ligand potentiel ne montre de répartition comparable.

Dans la *figure 2*, les constantes de stabilité du complexe chloruré pour Pr, Nd, Sm et Eu sont reportées en fonction des appauvrissements relatifs en ces éléments. La corrélation entre ces deux paramètres augmente avec la distance. Ceci indique que le fractionnement observé peut effectivement être provoqué par des complexes chlorurés solubles. L'appauvrissement croissant observé est semblable à une séparation chromatogra-

phique, pour laquelle la séparation est d'autant plus efficace que la distance par rapport à la source des terres rares est importante.

Conclusions

Le profil salifère présenté ici fournit l'opportunité unique d'étudier le transport et le fractionnement des terres rares dans une saumure riche en chlorures, à des températures et pressions élevées. L'appauvrissement en terres rares, observé dans les échantillons les plus éloignés du contact du basalte, permet de calculer des stabilités relatives de complexes chlorure-terres rares, qui peuvent ensuite être comparées aux stabilités de complexes de Millero (1992), à 25 °C et 1 bar (*figure 5*). Cette comparaison montre que les faibles variations des stabilités relatives des complexes, observées dans les conditions de surface, sont multipliées par 9 dans les conditions de l'étude. Ce résultat n'est pas en accord avec les estimations numériques des stabilités des complexes de terres rares, actuellement disponibles pour des températures et pressions élevées (Haas et al., 1995). Toutefois, ces divergences ne peuvent pas être expliquées sans l'acquisition de nouvelles données expérimentales, qui prennent en compte, non seulement les conditions de température et de pression importantes, mais aussi les forces ioniques élevées.

Dans un site de stockage de déchets radioactifs de haute activité dans des sels, un transport similaire des éléments de type complexe chloruré peut être attendu. Dans cette perspective, la plus grande mobilité de Ce, Pr, Nd, Sm et Eu, par rapport aux autres terres rares, est importante pour la migration de certains actinides et terres rares radio-actifs.

7. References

Bau M. 1996. Controls on the fractionation of isovalent trace elements in magmatic and aqueous systems: evidence from Y/Ho, Zr/Hf, and lanthanide tetrad effect, *Contrib. Mineral. Petr.*, 123, 323–333

Braitsch O. 1971. *Salt Deposits. Their Origin and Composition*, Springer-Verlag, Berlin-Stuttgart-Heidelberg-New York, 297 p.

Brookins D.G. 1989. Aqueous geochemistry of the rare earth elements, *in:* Lipin B.R. and McKay G.A. (Eds.), *Geochemistry and Mineralogy of Rare Earth Elements, Reviews in Mineralogy*, vol. 21. Mineral. Soc. Am., 201–225

Cantrell K.J. and Byrne R.H. 1987. Rare earth element complexation by carbonate and oxalate ions, *Geochim. Cosmochim. Acta*, 51, 597–605

Choppin G.R. 1983. Comparison of the solution chemistry of the actinides and the lanthanides, *J. Less-Common Met.*, 93, 232–330

Choppin G.R. 1986. Speciation of trivalent f elements in natural waters, *J. Less-Common Met.*, 126, 307–313

Fisher R.S. and Kreitler C.W. 1987. Geochemistry and hydrodynamics of deep-basin brines, Palo Duro Basin Texas, USA, *Applied Geochem.*, 2, 459–476

Gammons C.H., Wood S.A. and Williams-Jones A.E. 1996. The aqueous geochemistry of the rare earth elements and yttrium: VI. Stability of neodymium chloride complexes from 25 to 300 °C, *Geochim. Cosmochim. Acta*, 60, 4615–4630

Gutsche A. 1988. Mineralreaktionen und Stofftransporte an einem Kontakt Basalt-Hartsalz in der Werra-Folge des Werkes Hattorf, *Thesis*, Georg-August-Universität Göttingen

Haas J.R., Shock E.L. and Sassani D.C. 1995. Rare earth elements in hydrothermal systems: estimates of standard partial molal thermodynamic properties of aqueous complexes of the rare earth elements at high pressures and temperatures, *Geochim. Cosmochim. Acta*, 59, 4329–4250

Hartmann H. 1969. Investigations of Atlantis II deep samples taken by the FS Meteor, *in:* Degens E.T. and Ross D.A. (Eds.), *Hot Brines and Recent Metal Deposits in the Red Sea*, Springer, 204–207

Herrmann A.G., Knake D., Schneider J. and Peters H. 1973. Geochemistry of modern seawater and brines from salt pans: main components and bromine distribution, *Contrib. Mineral. Petr.*, 40, 1–24

Herrmann A.G., Siebrasse G. and Könnecke K. 1978. Computerprogramme zur Berechnung von Mineral- und Gesteinsumbildungen bei der Einwirkung von Lösungen auf Kali- und Steinsalzlagerstätten (Lösungsmetamorphose), *Kali u. Steinsalz*, 7, 288–299

Johannesson K.H., Lyons W.B., Yelken M.A., Gaudette H.E. and Stetzenbach K.J. 1996. Geochemistry of the rare-earth elements in hypersaline and dilute acidic natural terrestrial waters: complexation behavior and middle rare-earth element enrichments, *Chem. Geol.*, 133, 125–144

Knipping B. 1989. Basalt intrusions in evaporites, *Lecture Notes in Earth Sciences*, vol. 24, Springer-Verlag, Berlin, 132 p.

Knipping B. and Herrmann A.G. 1985. Mineralreaktionen und Stofftransporte an einem Kontakt Basalt-Carnallitit im Kalisalzhorizont Thüringen der Werra-Serie des Zechsteins, *Kali u. Steinsalz*, 9, 111–124

Krauskopf K.B. 1986. Thorium and rare-earth elements as analogues for actinide elements, *Chem. Geol.*, 55, 323–335

Lutze W. and Grambow B. 1992. The effect of glass corrosion on near field chemistry, *Radiochim. Acta*, 58/59, 3–7

Millero F.J. 1992. Stability constants for the formation of rare earth inorganic complexes as a function of ionic strength, *Geochim. Cosmochim. Acta*, 56, 3123–3132

Mironov V.E., Avramenko N.I., Koperin A.A., Blokhin V.V., Eike M.Y. and Isayev I.D. 1982. Thermodynamics of the formation reaction of the monochloride complexes of the rare earth metals in aqueous solutions, *Koord. Khim.*, 8, 636–638

Peppard D.F. 1966. Liquid–liquid extraction of metal ions, *in:* Emeleus H.J. and Sharpe A.G. (Eds.), *Advances in Inorganic Chemistry and Radiochemistry*, Academic Press, 1–80

Peppard D.F., Mason G.W., Maier J.L. and Driscoll W.J. 1957. Fractional extraction of the lanthanides as their di-alkyl orthophosphates, *J. Inorg. Nucl. Chem.*, 4, 334–343

Shabani M.B., Akagi T., Shimizu H. and Masuda A. 1990. Determination of trace lanthanides and yttrium in seawater by inductively coupled plasma mass spectrometry after preconcentration with solvent extraction and back-extraction, *Anal. Chem.*, 62, 2709–2714

Steinmann M., Stille P., Mengel K. and Kiefel B. Trace element and isotopic evidence for REE migration and fractionation in salts at elevated *T* and *P*, *Chem. Geol.* (submitted for publication)

Tricca A. 1997. Transport mechanism of trace elements in surface and ground water: Sr, Nd, U isotope and REE evidence, *Thesis*, Université Louis-Pasteur, Strasbourg

Wood S.A. 1990a. The aqueous geochemistry of the rare-earth elements and yttrium. 1. Review of available low-temperature data for inorganic complexes and the inorganic REE speciation of natural waters, *Chem. Geol.*, 82, 159–185

Wood S.A. 1990b. The aqueous geochemistry of the rare-earth elements and yttrium. 2. Theoretical predictions of speciation in hydrothermal solutions to 350 °C at saturation water vapor pressure, *Chem. Geol.*, 88, 99–125

ELSEVIER

Chemical Geology 153 (1999) 259–279

CHEMICAL GEOLOGY
INCLUDING
ISOTOPE GEOSCIENCE

The corrosion of basaltic dykes in evaporites: Ar–Sr–Nd isotope and rare earth elements evidence

Marc Steinmann [a,*], Peter Stille [a], Walter Bernotat [b], Bernhard Knipping [c,1]

[a] *ULP-EOST-CNRS, Centre de Géochimie de la Surface, UMR 7517, 1 rue Blessig, F-67084 Strasbourg Cedex, France*
[b] *INE, Forschungszentrum Karlsruhe, Postfach 3640, D-76021 Karlsruhe, Germany*
[c] *Institut für Mineralogie und Mineralogische Rostoffe, Technische Universität Clausthal, Adolph-Roemer-Str. 2A, D-38670 Clausthal-Zellerfeld, Germany*

Received 3 December 1997; accepted 16 September 1998

Abstract

The corrosion of basaltic dykes from central Germany which intruded during the Tertiary into rock and potash salts of Upper Permian age (Zechstein) has been studied. The corrosion behavior of these glassy basalts can serve as a natural analogue for the long-term corrosion expected for nuclear waste glasses in a salt repository. Our data demonstrate mobility and fractionation of the rare earth elements (REE) during a postintrusive circulation of salt brines. The processes controlling this behavior of the REE were dissolution and reprecipitation of phosphates. The K–Ar data document the synintrusive assimilation of a salt phase followed by a postintrusive fluid circulation in the peripheral parts. This circulation removed the assimilated salt and imported highly radiogenic salt Ar which was integrated into newly formed sheet silicates. The central part of the dyke was not affected by this circulation and could retain a mantle gas phase. The Sr isotope data document a synintrusive assimilation of salt Sr and a strong exchange with salt fluids during the postintrusive corrosion which was strongest in a zone next to the chilled dyke margins. This locally stronger alteration is probably due to different cooling and shrinking rates of the basalt at the margins and in the core of the dyke which led to the formation of a highly permeable fractured zone.

Keywords: Basalt glass alteration; Natural analogue study; Radioactive waste; Rare earth element mobility; Phosphate

1. Introduction

High Level Radioactive Waste (HLW) has to be isolated from the biosphere over geological time scales. Technical and geological barriers are presently employed to prevent the possible long-term release of radionuclides into surface waters. Nevertheless, laboratory experiments and long-term mathematical modelling alone do not provide a conclusive long-term safety assessment for such barriers. In order to improve or validate geochemical models of the long-term behavior of vitrified HLW in a geological environment, analogues in nature have to be studied.

Ewing (1979) proposed the study of volcanic glassy rocks as natural analogue of HLW glass to quantify processes like corrosion and trace element redistribution over geological decades and to test

* Corresponding author. Geosciences, Université de Franche-Comté, 16 route de Gray, 25030 Besançon Cedex, France. Fax: +33-381-66-62-67; E-mail: marc.steinmann@univ-fcomte.fr
[1] Deceased.

0009-2541/99/$ - see front matter
PII: S0009-2541(98)00164-8

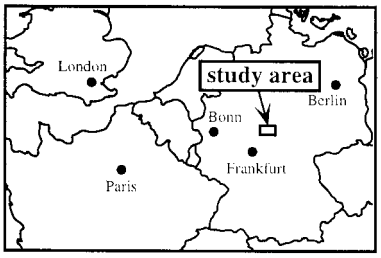

Fig. 1. The basalt dykes originate from the Werra–Fulda salt mining district in Central Germany.

long-term predictions of the mathematical models for pertinence (Chapman et al., 1984; Petit, 1992). Despite some differences in the chemical composition between natural basalt glasses and synthetic HLW borosilicate glasses, several authors could show that similar alteration products can form on both natural and nuclear waste glasses (Malow et al., 1984; Byers et al., 1985; Crovisier et al., 1992; Lutze and Grambow, 1992; Abdelouas et al., 1994; Daux et al., 1997). However, this chemical difference between basaltic and HLW glasses remains, together with only limited control over the alteration conditions, a major drawback of the natural analogue approach (Crovisier et al., 1992). But keeping these limitations in mind, valuable information can be drawn from natural analogues because it is the only way to study alteration and corrosion processes over geological time scales and under natural conditions (Petit, 1992).

The aim of the present study is to trace alteration and corrosion of basaltic dykes in evaporites as a natural analogue for the long-term stability of HLW glass in a salt repository. Such basaltic intrusions in evaporites occur in only a few localities around the world. The Werra–Fulda salt mining district of Germany (Fig. 1) is most suitable for such studies because of the multitude and variability of basaltic glass–salt contacts and the excellent outcrop conditions in underground mines (Knipping, 1989).

2. Geological setting and repository analogy

The evaporites of the Werra–Fulda potash district were deposited about 250 Ma ago during the Upper Permian (Zechstein). The series contains two important potash salt horizons actually being mined at depths of about 800 m. The thickness of these horizons varies between 2 and 10 m. The total evaporite series has a thickness of up to 400 m and is dominated by halite (NaCl).

In the Tertiary, basaltic melts intruded the evaporites, but only a few reached the Earth's surface. Basaltic melt production can be related to regional volcanic activity some 10 to 25 Ma ago (Lippolt, 1982; Wedepohl, 1982). Their genesis has been extensively discussed by Wedepohl (1985). In the underground mines, they are exposed as subvertical dykes which can be followed horizontally over several kilometers. However, correlations of the dykes between different mines and between surface and subsurface outcrops often remain uncertain. The basalts are phonolitic tephrites, limburgites, basanites and olivine nephelinites. The dyke margins are usually vitrified and especially in limburgites microlitic glass is very abundant (Knipping, 1989).

All basalt–salt contacts discussed here are located in the two potash salt horizons mentioned above which consist essentially of carnallite ($KMgCl_3 \cdot 6H_2O$). Near the basalt contacts, in a zone of less than 3 m width, these salts have been transformed mainly into halite and sylvite (KCl) by fluids saturated in NaCl. These fluids, originating from the partial dissolution of underlying halite formations, had accompanied the basaltic melts (Knipping and Herrmann, 1985; Gutsche, 1988; Knipping, 1989).

During salt metamorphism, the NaCl-fluids were mixed with fluids originating from the potash salts. This brine mixture altered, as will be shown later on, the basalts during postintrusive cooling. Numerical models suggest that this cooling was quite rapid (Knipping, 1989): a dyke of less than 0.5 m thickness reached within 14 days temperatures below 200°C which is about the maximum temperature expected for a HLW salt repository (Lutze and Grambow, 1992; McMenamin, 1997).

We regard this alteration of the basalts during the postintrusive cooling by hot brines as a natural analogue for the processes expected for the corrosion of vitrified HLW in a leaking salt repository. We will in particular focus on the behavior of the REE and Sr, because these elements have some isotopes which occur as fission-derived radionuclides in high level waste. The trivalent REE are furthermore good analogues for trivalent actinides (Choppin, 1983;

Krauskopf, 1986; Seaborg, 1993). The Ar isotopes were studied to gather information on the mobility of gases during waste glass corrosion.

3. Samples and methods

3.1. Sample material

All samples originate from the collection of the Technical University of Clausthal. In order to recognize alteration of the basaltic rocks due to exchange with salts, dyke samples from underground mines and surface outcrops have been analyzed and compared. In addition, samples from a detailed cross-section through a 45 cm thick basaltic dyke were studied (Hattorf dyke; Fig. 2). This dyke outcrop is located in an underground mine and in direct contact with potash salts mainly consisting of carnallite ($KMgCl_3 \cdot 6H_2O$). The profile has been previously described by Knipping and Herrmann (1985). The average major element composition for the Hattorf samples is given in Table 1. All basalt samples were very fine-grained. It was therefore not possible to separate and enrich the basaltic glass-fraction in sufficient quantities.

3.2. Light microscopic and SEM observations

A detailed petrographic description is given by Knipping (1989) for the basaltic dykes of the Werra–Fulda area in general and by Knipping and Herrmann (1985) for the Hattorf dyke profile in particular. The data of this latter profile will be of importance for the discussion later on. Therefore, the microscopic observations are summarized below.

Olivine and augite occur as the main xenocrysts together with some peridotitic inclusions. The olivine aggregates and the augite generally do not exceed 3 mm in size, whereas the peridotite xenoliths reach up to 2.5 cm in diameter. The basalt matrix has a hemicrystalline-porphyric texture with Ti-rich augite as the main acicular mineral. The rest of the matrix consists of granular magnetite, small flakes of biotite, xenomorphic nepheline and some acicular ap-

Table 1
Average major element composition for the five samples of the Hattorf dyke profile with standard deviations

	Average ($n = 5$)	± S.D.
SiO_2	41.0	0.2
TiO_2	2.4	0.0
Al_2O_3	11.7	0.1
Fe_2O_3	3.9	0.3
FeO	7.1	0.3
CaO	11.6	0.2
MgO	12.6	0.2
MnO	0.19	0.00
Na_2O	2.3	0.5
K_2O	2.3	0.6
H_2O	3.5	0.2
K_2O	0.64	0.00
C (as CO_2)	0.39	0.30
SUM	99.6	0.2

The concentrations are in %.
Data from Knipping and Herrmann (1985).

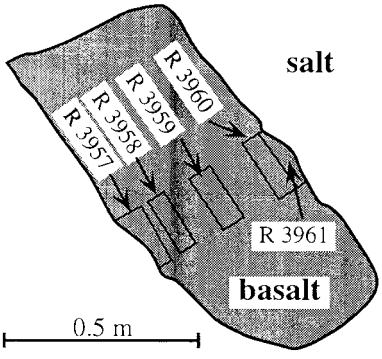

Fig. 2. Detailed dyke cross-section in the Hattorf mine with sampling points. The dyke is conserved as an isolated tectonic boudin embedded in potash salts.

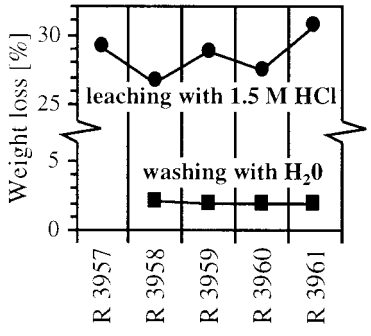

Fig. 3. Weight loss for the Hattorf samples during washing with H_2O and leaching with 1.5 M HCl. See Table 2 for raw data.

Table 2
Weight losses during washing with H_2O and leaching with 1.5 M HCl in wt.% relative to untreated bulk sample

	H_2O washing	HCl leaching
R 3957		29.04
R 3958	2.10	26.58
R 3959	1.86	28.73
R 3960	1.92	27.45
R 3961	1.89	30.70

The percentages refer to initial bulk sample weight.

atite. These matrix minerals are generally < 0.2 mm. The remaining matrix space is filled with a yellowish microlitic glass phase which becomes more important towards the dyke margins. Near the salt contact the basalt becomes more and more fractured and directly at the contact also small salt inclusions and some vesicles can be observed. The fractures are always filled with halite or less frequently with sylvite. Aggregates of hematite accompany this fractured marginal zone. Small flakes of newly formed clay minerals cover the basalt surface at the contact with the evaporites.

The salt inclusions were investigated in considerable detail under the SEM. Their diameter ranges from a few tenths to maximally 1 mm. The dominant mineral of the inclusions is NaCl followed by $CaSO_4$ and $CaCO_3$. Carnallite has not been observed. The inclusions are isolated and not connected by joints with the adjacent salts. The contact between the inclusions and the basalt matrix is characterized by a rim of sheet silicates: most of these consist of biotite associated with smectite/chlorite, but some consist of saponite.

3.3. Methods

3.3.1. Washing with H_2O and leaching with 1.5 M HCl

All analyses are based on powders (< 125 mm) which were washed in bidistilled water in order to remove salt minerals. For the K–Ar analyses, an additional sample series was analysed without previous washing in water in order to evaluate the influence of the salts.

In order to get additional information about the exchange processes between the basalts and the salts, leaching experiments with 1.5 M HCl were performed on the H_2O-washed Hattorf samples. The leachings were conducted in 50 ml polypropylene centrifuge tubes. Bulk sample weight was 1.5 g and the acid volume 30 ml. Extraction time was 30 min at room temperature. After leaching, the samples were centrifuged, the supernatant separated by a pipette and evaporated. The residues were washed with bidistilled water in order to remove acid derived ionic radicals and dried.

Table 3
Selected major and trace element concentrations for the HCl-leachates and residues of the Hattorf dyke profile

HCl-leachates	Al_2O_3	CaO	Fe_2O_3	P_2O_5	SiO_2	Mn_3O_4	S
R 3957	5.3	1.47	1.09	0.66	0.1018	0.0354	0.1022
R 3958	5.3	1.79	1.41	0.81	0.1100	0.0387	0.2033
R 3959	5.6	1.57	1.27	0.79	0.1026	0.0344	0.0526
R 3960	5.8	1.62	1.46	0.83	0.0962	0.0394	0.0520
R 3961	5.8	1.65	1.31	0.68	0.1098	0.0420	0.0257

HCl-residues	Al_2O_3	CaO	Fe_2O_3	P_2O_5	SiO_2	Mn_3O_4	MgO
R 3957	7.6	13.9	14.8	0.31	43.8	0.237	13.56
R 3958	8.0	13.5	14.2	0.23	44.2	0.241	13.02
R 3959	7.8	13.9	14.9	0.21	42.7	0.247	13.83
R 3960	7.7	13.7	14.1	0.25	44.5	0.231	12.91
R 3961	7.5	13.5	15.1	0.34	40.1	0.230	14.60

The leachate concentrations are normalized to bulk sample weight before leaching.
All concentrations are in %.
Fe_2O_3 stands for total Fe concentrations.
Sulphur was analyzed by UV-spectrophotometry, all other elements by ICP-AES.

This leaching removed about 30% of the total sample weight (Fig. 3, Table 2). The distribution of the weight loss throughout the dyke section shows a typical w-shaped pattern which in this or inverse form will also be characteristic for a whole series of other leachate and residue parameters. This is in contrast to the washing with H_2O. Here, the weight loss was almost homogenous over the profile and represented only about 2% of the bulk sample weight. The HCl leachates had a yellow colour after evaporation and subsequent S analyses showed elevated sulphur contents (Table 3). However, the S concentrations did not show any relations with other parameters and are therefore not discussed further.

Table 4
REE data for the basalts

	La	Ce	Pr	Nd	Sm	Eu	Gd	Tb	Dy	Ho	Er	Tm	Yb	Lu
Surface Samples														
H_2O-washed whole rocks														
R 3781	55	115	13	61	11	3.0	8.5	1.4	5.9	1.2	2.6	0.40	2.1	0.29
R 3782	50	93	10	44	8	2.2	6.0	1.1	4.4	0.9	2.0	0.33	1.7	0.25
R 3783	77	149	15	72	12	3.3	8.9	1.6	5.9	1.2	2.6	0.43	2.0	0.31
R 3784	77	151	16	73	12	3.3	8.9	1.6	6.0	1.2	2.6	0.42	2.0	0.27
R 3785	55	103	11	49	9	2.4	6.5	1.2	4.6	0.9	2.1	0.34	1.7	0.24
R 3786	48	93	10	46	9	2.4	6.6	1.2	4.7	0.9	2.0	0.30	1.5	0.22
R 3787	45	89	10	38	7	2.3	5.7	0.8	4.1	0.7	1.7	0.24	1.3	0.18
Subsurface Samples														
H_2O-washed whole rocks														
R1 3950	41.1	88.3	11.0	45.6	9.0	2.83	7.03	1.00	5.04	0.90	2.03	0.30	1.56	0.21
R1 3951	48.9	110.1	14.0	58.6	11.6	3.65	9.10	1.31	6.67	1.17	2.73	0.39	2.10	0.28
R1 3952	42.4	94.8	12.0	49.8	9.8	3.16	7.73	1.09	5.67	1.00	2.29	0.33	1.77	0.24
R1 3953	64.5	124.4	14.1	53.1	9.5	2.97	7.53	1.05	5.42	0.96	2.29	0.33	1.83	0.24
R1 3954	58.4	115.0	13.0	49.0	8.6	2.63	6.79	0.95	4.75	0.84	1.97	0.29	1.55	0.21
R2 3955	36.9	72.4	8.2	31.5	5.8	1.81	4.68	0.66	3.43	0.61	1.44	0.21	1.11	0.15
R2 3956	54.7	105.6	11.9	45.3	8.2	2.64	6.58	0.93	4.79	0.85	2.01	0.29	1.58	0.22
Hattorf Dyke Profile														
H_2O-washed whole rocks														
R 3957	77.3	144.0	16.0	59.8	10.1	3.20	8.07	1.13	5.91	1.09	2.54	0.37	2.05	0.28
R 3958	77.1	143.9	15.9	59.8	10.2	3.22	8.17	1.14	5.96	1.08	2.56	0.36	2.07	0.29
R 3959	75.5	141.2	15.7	59.0	10.0	3.19	8.08	1.13	5.86	1.07	2.55	0.37	2.04	0.29
R 3960	75.7	141.3	15.6	59.0	10.0	3.21	8.07	1.13	5.91	1.06	2.52	0.37	2.05	0.28
R 3961	74.8	140.5	15.6	58.5	9.9	3.17	7.93	1.12	5.87	1.06	2.51	0.36	2.03	0.28
HCl leachates														
R 3957	37.9	66.6	5.9	20.2	2.8	0.83	3.06	0.32	1.40	0.26	0.72	0.09	0.51	0.07
R 3958	42.3	75.6	6.7	23.3	3.1	0.93	3.43	0.34	1.45	0.26	0.70	0.08	0.45	0.06
R 3959	40.7	73.3	6.5	22.6	3.0	0.87	3.26	0.32	1.36	0.24	0.66	0.07	0.40	0.05
R 3960	40.3	71.5	6.3	21.7	2.9	0.87	3.18	0.32	1.38	0.25	0.68	0.08	0.46	0.06
R 3961	35.6	62.5	5.5	18.7	2.6	0.77	2.85	0.29	1.31	0.24	0.67	0.08	0.49	0.06
HCl residues														
R 3957	32.4	78.0	10.2	43.3	8.3	2.58	6.74	0.99	5.11	0.94	2.26	0.35	1.81	0.25
R 3958	27.3	68.5	9.1	39.7	7.9	2.53	6.64	1.00	5.13	0.97	2.31	0.36	1.90	0.28
R 3959	26.6	65.8	9.0	38.8	7.9	2.53	6.60	1.00	5.25	0.98	2.38	0.35	1.85	0.28
R 3960	29.2	72.7	9.7	41.7	8.4	2.59	6.76	1.00	5.30	0.97	2.36	0.34	1.89	0.27
R 3961	35.5	81.6	10.7	45.3	8.8	2.72	7.18	1.02	5.22	0.97	2.28	0.32	1.83	0.25

The surface samples except R 3787 were analyzed by ICP-AES at the Technical University in Clausthal, all other samples by ICP-MS at the CNRS in Strasbourg.
All concentrations are in ppm.
The HCl leachate concentrations are normalized to bulk sample weight before leaching.

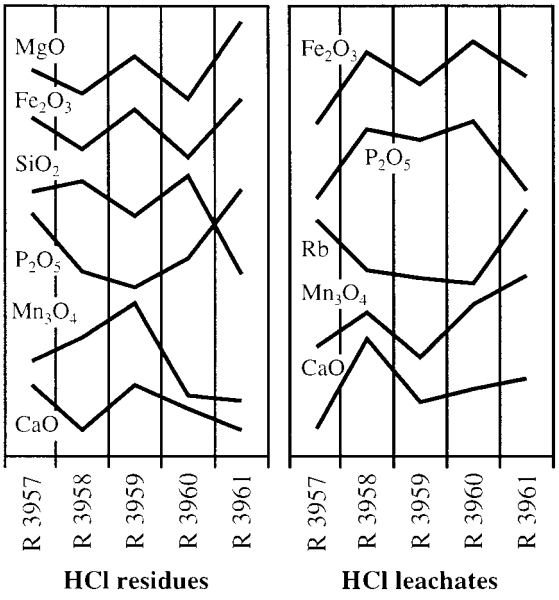

Fig. 4. Distribution of some major and trace elements for the HCl leachates and residues of the Hattorf dyke profile. See Table 3 for absolute values.

A mass balance between the REE concentrations of the HCl leachates and residues and those of the H_2O-washed whole rock samples shows that 10–20% of the REE are lost during the leaching procedure with HCl (Table 4). This is greater than normal

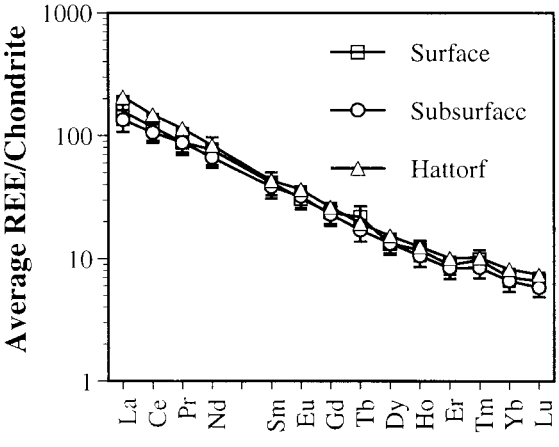

Fig. 5. Chondrite-normalized REE distribution patterns for the surface and subsurface basalts including the Hattorf samples. The values are average values with standard deviations of H_2O-washed whole rock samples. See Table 4 for raw data.

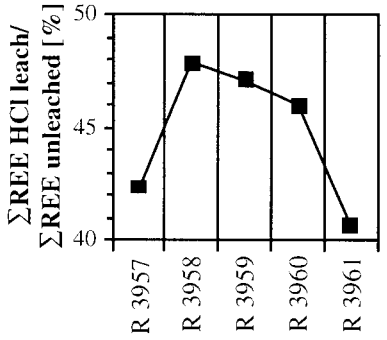

Fig. 6. Rare earths removed in the Hattorf dyke profile by leaching with 1.5 M HCl relative to the REE content in the H_2O-washed whole rock samples.

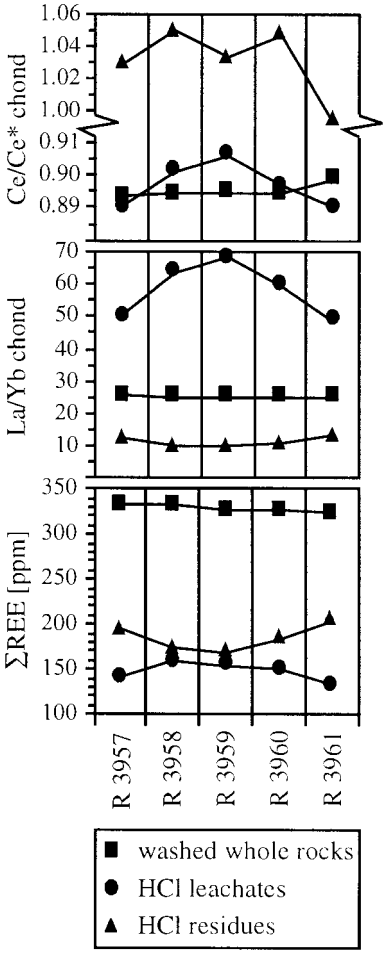

Fig. 7. ΣREE, La/Yb, and Ce/Ce∗ for the H_2O-washed whole rocks, and HCl leachates and residues of the Hattorf dyke profile. See Table 5 for raw data.

losses which are < 10% when the same procedure is applied to basalts not in contact to evaporites (Steinmann, unpublished data). We suggest that the losses occurred during the rinsing of the residues with H_2O after leaching with 1.5 M HCl owing to the presence of water soluble REE complexes.

3.3.2. Analytical

Sulphur concentrations were determined by UV-spectrophotometry (Leco CS 125), all other elements by ICP-AES (ARL 3500 C) and ICP-MS (VG Plasmaquad PQ2 +). The analytical precision is < ±10% for the ICP-AES and < ±5% for the ICP-MS on the first sigma level. For the analyses, 300 mg of the H_2O-washed whole rocks and the residues were dried at 110°C, ignited at 1000°C, fused with Li_2BO_4 and then dissolved in 20 ml of a HNO_3–glycerine solution for measurement. The HCl leachates were evaporated and directly redissolved in 1 M HNO_3 for analysis.

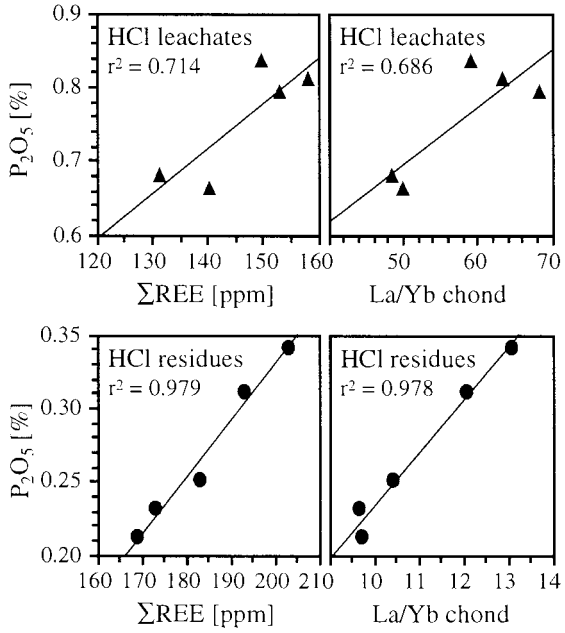

Fig. 8. Correlations of ΣREE and La/Yb with P_2O_5 for the HCl leachates and residues of the Hattorf samples.

Table 5
ΣREE and REE fractionation parameters for the H_2O-washed whole rocks and the HCl leachates and residues of the Hattorf dyke profile

	ΣREE	La/Yb_{chond}	Eu/Eu_{chond} *	Ce/Ce_{chond} *
H_2O-washed whole rocks				
R 3957	331.7	25.46	1.084	0.893
R 3958	331.7	25.17	1.079	0.894
R 3959	325.9	25.02	1.086	0.895
R 3960	326.2	24.94	1.092	0.894
R 3961	323.5	24.90	1.093	0.899
HCl leachates				
R 3957	140.6	50.33	0.869	0.890
R 3958	158.7	63.54	0.864	0.901
R 3959	153.4	68.40	0.851	0.906
R 3960	150.0	59.54	0.869	0.897
R 3961	131.5	48.95	0.861	0.890
HCl residues				
R 3957	193.2	12.11	1.056	1.029
R 3958	173.6	9.73	1.069	1.049
R 3959	169.2	9.76	1.073	1.032
R 3960	183.2	10.44	1.047	1.047
R 3961	203.7	13.14	1.046	0.994

The values are based on the data given in Table 4.
The chondrite values used for normalization are those of Taylor and McLennan (1985).

For Sr and Nd isotope analyses of the H_2O-washed whole rocks and the residues, 50 mg of sample powder were dissolved in closed Savillex teflon vials containing 12 ml of HF 40% and 400 μl of HNO_3 65%, both of suprapure quality. Digestion time was 7 days and the temperature 150°C. The same digestion treatment, but with only half of the sample and

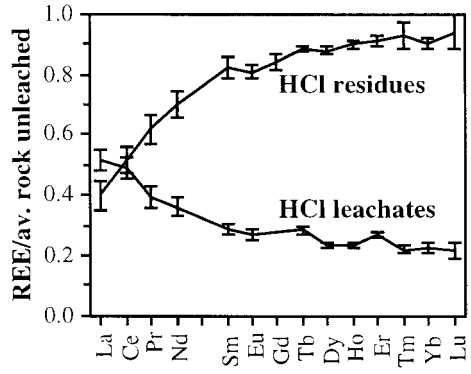

Fig. 9. Average REE concentrations for the HCl leachates and residues of the Hattorf dyke profile normalized to the average concentrations of the H_2O-washed whole rocks. The error bars represent ±s of the average values.

Table 6
K–Ar data for the basalts

	K_2O	Ar total	$^{40}K/^{36}Ar$	$^{40}Ar/^{36}Ar$
Surface samples				
H_2O-washed whole rocks				
R1 3781	1.78	0.000219	81246	404
R1 3782	0.93	0.000212	36098	332
R2 3782	0.68	0.000144	40385	345
R1 3783	1.69	0.000188	80053	360
R2 3783	1.38	0.000196	61685	354
R1 3784	0.86	0.000173	41170	334
R2 3784	1.45	0.000083	203310	469
R1 3785	1.08	0.000187	56022	391
R1 3786	0.76	0.000139	46473	343
R2 3786	0.41	0.000098	35090	340
R 3787	2.21	0.000489	65555	586
Subsurface samples				
H_2O-washed whole rocks				
R1 3950	4.61	0.000821	63745	457
R2 3950	4.59	0.000719	79241	500
R1 3951	3.12	0.002294	10719	317
R2 3951	3.33	0.002123	12512	321
R1 3952	1.83	0.001224	13556	365
R1 3953	2.22	0.000632	45443	521
R1 3954	1.56	0.000547	31107	439
R2 3955	3.14	0.000665	46801	399
R2 3956	3.76	0.000576	76330	471
Hattorf dyke profile				
Unwashed whole rocks				
R 3957	2.72	0.000539	113477	907
R 3958	1.89	0.000599	77469	990
R 3959	1.97	0.003740	5532	423
R 3960	2.01	0.000937	29761	559
R 3961	2.82	0.000557	114904	914
H_2O-washed whole rocks				
R 3957	2.32	0.000536	99667	928
R 3958	1.55	0.000604	60948	958
R 3959	1.43	0.001368	12320	476
R 3960	1.99	0.001024	24466	507
R 3961	2.82	0.000497	119822	853

The K_2O concentrations are in %.
The total Ar concentrations in μmol/g.

acid quantities, was used to measure the K concentrations for the K–Ar isotope analyses by AAS (Perkin-Elmer 400). The $^{40}Ar/^{36}Ar$ ratios were determined on a VG 1200 and an upgraded AEI 20 mass spectrometer.

For Sr and bulk REE separation, 1 ml quartz columns with cation-exchange resin (AG 50W-X12, 200–400 mesh) and ammonium citrate, HCl 1.5 M, 4 M and 6 M as eluents were used. Neodymium was separated with the same type of resin and column and α-hydroxyisobutyric acid as eluent. The blanks at the time of analysis were < 1.5 ng for Sr and < 0.4 ng for Nd. Neodymium was measured using a Ta–Re–Ta triple and Ta–Re double filament assemblies whereas Sr was deposited on W single filaments. The analyses were performed on a fully automatic VG Sector mass spectrometer with a 5 cup multicollector. The ratios $^{86}Sr/^{88}Sr = 0.1194$ and $^{143}Nd/^{144}Nd = 0.7219$ were used for fractionation correction. Typically, 100 ratios for Sr and Nd were collected to achieve adequate precision. During the measuring period, the NBS 987 Sr standard yielded $^{87}Sr/^{86}Sr = 0.710264 \pm 13$ ($\pm$s of the mean, $n = 8$) and the La Jolla Nd standard $^{143}Nd/^{144}Nd = 0.511856 \pm 7$ ($\pm$s of the mean, $n = 6$).

The scanning electron microscope used is a field emission SEM of Camscan at the Research Centre Karlsruhe. Microanalysis and element mapping were performed with the Voyager program of Noran Instruments.

4. Results

4.1. Major and trace elements

The concentrations of some major and trace elements show a zigzag-shaped distribution over the dyke profile (Fig. 4). The zigzag line can have the shape of 'm' or, as the weight losses during leaching

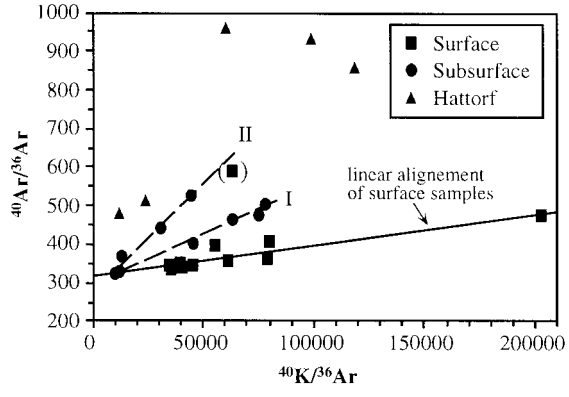

Fig. 10. K–Ar isochron diagram with all surface and subsurface samples including the Hattorf dyke. Note the lower $^{40}Ar/^{36}Ar$ values for the surface samples and their linear alignment. See text for the alignments labelled I and II.

(Fig. 3), the shape of 'w'. Such m- or w-shaped concentration distributions can be observed for MgO, Fe_2O_3 and SiO_2 in the residues and for Fe_2O_3 and P_2O_5 in the leachates. The leachate concentrations are normalized relative to bulk sample weight before leaching and therefore not biased by the w-shaped weight distribution of the leached phase. Another series of elements show a u-shaped concentration distribution. These are P_2O_5 in the residues, Rb in the leachates (Fig. 4), and K_2O in the H_2O-washed whole rocks (Fig. 11). No clear trends can be observed for the distributions of CaO and Mn_3O_4 in the leachates and residues (Fig. 4). The concentration distributions of P_2O_5, Fe_2O_3, CaO and Mn_3O_4 are complementary in the HCl leachates and residues.

4.2. Rare earth elements (REE)

The chondrite-normalized REE distribution patterns are strongly enriched in the light rare earths (LREE, La–Nd) and show distribution patterns typical for alkali-basaltic melts (Fig. 5). Significant differences in the patterns of the H_2O-washed whole rock samples from the surface and subsurface do not exist.

Leaching with HCl removed almost up to 50% of the REE in the samples of the Hattorf dyke profile (Fig. 6). It is important to note that most of the REE have been leached out of the dyke core although the total REE concentrations (ΣREE) in the H_2O-washed whole rocks are almost constant throughout the profile (Fig. 7, Table 5).

The total REE concentrations, and the La/Yb and Ce/Ce* ratios of the Hattorf samples are shown in Fig. 7 for the H_2O-washed whole rocks, and the HCl leachates and residues. The parameters of the H_2O-washed whole rocks seem to have almost constant values. Looking in more detail, however, the distributions throughout the profile are slightly asymmetric (Table 5). The REE parameters of the leachates and residues show much larger variations than the H_2O-washed whole rocks. ΣREE, and the La/Yb and Ce/Ce* ratios of the leachates and residues are symmetrically distributed from the core to the border (Fig. 7).

The total REE concentrations, and La/Yb are correlated with P_2O_5 in the leachates and the residues (Fig. 8). A plot of the average REE distribution patterns of the leachates and residues shows that they have complementary patterns when normalized to

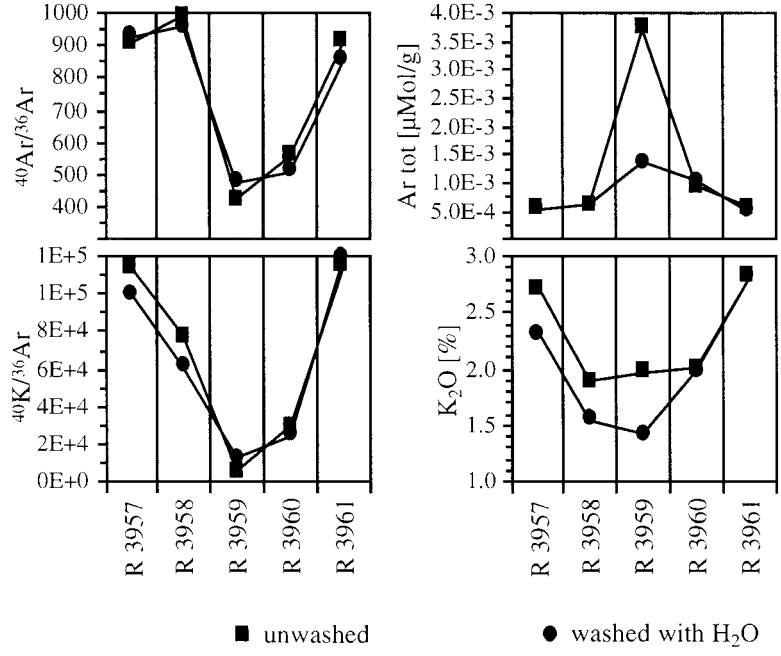

Fig. 11. K–Ar data for the Hattorf dyke. The samples were analyzed without washing and after washing with H_2O.

Table 7
Rb–Sr isotope data for the basalts

	Rb [ppm]	Sr [ppm]	$^{87}Rb/^{86}Sr$	$^{87}Sr/^{86}Sr$
Surface samples				
H_2O-washed whole rocks				
R 3787	24.1	670.3	0.1039	0.703507(8)
Subsurface samples				
H_2O-washed whole rocks				
R1 3950	96.2	743.8	0.3742	0.704066(7)
R2 3950	121.4	915.5	0.3834	0.704066(6)
R1 3951	87.7	550.7	0.4605	0.703900(6)
R2 3951	89.1	555.4	0.4641	0.703886(6)
R1 3952	9.9	647.1	0.0445	0.703783(6)
R1 3953	23.1	1020.9	0.0654	0.705599(6)
R1 3954	12.8	724.1	0.0511	0.703581(7)
R2 3955	25.1	610.8	0.1189	0.706239(7)
R2 3956	32.5	809.2	0.1160	0.703699(8)
Hattorf dyke profile				
H_2O-washed whole rocks				
R 3957	50.9	887.5	0.1658	0.703544(6)
R 3958	46.1	874.6	0.1526	0.703563(6)
R 3959	32.6	840.2	0.1121	0.703514(6)
R 3960	49.7	884.7	0.1625	0.703551(7)
R 3961	54.1	860.1	0.1819	0.703519(6)
HCl leachates				
R 3957	47.2	584.6	0.2337	0.703529(7)
R 3958	24.8	562.8	0.1276	0.703578(6)
R 3959	21.6	407.4	0.1535	0.703526(6)
R 3960	18.4	285.3	0.1868	0.703573(5)
R 3961	52.0	695.1	0.2163	0.703498(6)
HCl residues				
R 3957	28.8	380.6	0.2187	0.703456(6)
R 3958	31.7	468.0	0.1961	0.703427(6)
R 3959	23.6	428.3	0.1591	0.703435(6)
R 3960	26.7	407.5	0.1894	0.703435(7)
R 3961	26.7	323.3	0.2389	0.703496(7)

The Rb and Sr concentrations are ICP-MS data.
The HCl leachate concentrations are normalized to bulk sample weight before leaching.
The errors given for the $^{87}Sr/^{86}Sr$ ratios are ± 2 sigma mean values and refer to the last digits.

the H_2O-washed whole rock (Fig. 9). The diagram furthermore shows that La is mainly contained in the leachable phase although the sum of the rare earths is predominantly located in the residues (Fig. 7).

The chondrite-normalized Eu anomalies of the leachates are biased by a positive Gd anomaly and therefore not evident. This Gd anomaly in the leachates could be due to a mass interference on the ICP-MS (e.g., $^{140}CeOH$ instead of ^{157}Gd, Dulsky, 1994) or to preferential mobilization of Gd during leaching owing to its half filled f-orbitals (Kawabe, 1992; Akagi et al., 1993). However, we are at present not able to distinguish between these two possibilities and the origin of the anomaly thus remains unclear. The Gd concentrations of the leachates are therefore only given in Table 4 but omitted in the figures.

The $Eu/Eu*$ values of the H_2O-washed whole rocks and the residues are slightly positive and somewhat higher in the whole rocks, but no clear trends can be observed (Table 5). The chondrite-normalized Ce anomalies are slightly positive in the residues and slightly negative in the H_2O-washed whole rocks and the leachates. The distribution of the values is m-shaped in the residues and n-shaped in the leachates (Fig. 7).

4.3. Ar isotopes

The K–Ar data are listed in Table 6. A comparison of the K–Ar isotope data of the underground and surface samples is given in Fig. 10. The basalts from the surface show the lowest $^{40}Ar/^{36}Ar$ ratios and, with the exception of one sample (R 3787), define a regression line intercepting the $^{40}Ar/^{36}Ar$ axis at a value of 313. The intercept value decreases to 299 if the sample with the highest $^{40}Ar/^{36}Ar$ and $^{40}K/^{36}Ar$ ratios is omitted (R2 3784). This initial $^{40}Ar/^{36}Ar$ value corresponds closely to the atmospheric isotopic composition of 295.5 which indicates that the surface basalts had completely equilibrated with atmospheric argon. In the Ar mixing-diagram ($^{40}Ar/^{36}Ar$ vs. $1/Ar$, not shown) the points of the surface samples are scattered which excludes two-component mixing. Therefore, the slope of the observed linear alignment might yield an approximate intrusion age. Using the slope of the regression line in Fig. 10, we calculated an age of 13.5 Ma which falls into the range of 25–10 Ma found for regional volcanic activity (Lippolt, 1982; Wedepohl, 1982).

The K–Ar isotope data for the underground samples are strongly scattered and show considerable ^{40}Ar overpressure (i.e., $^{40}Ar/^{36}Ar > 400$). The subsurface samples from outside the Hattorf profile can be subdivided into a group I with a more gentle, and a group II with a steeper slope in the K–Ar isochron diagram (Fig. 10). The slopes of both groups are

Table 8
Sm–Nd isotope data for the basalts

	Sm [ppm]	Nd [ppm]	$^{147}Sm/^{144}Nd$	$^{143}Nd/^{144}Nd$	ε_{Nd}
Subsurface samples					
H_2O-washed whole rocks					
R1 3950	8.95	45.56	0.1189	0.512919(26)	5.48
R2 3950	11.19	56.58	0.1196	0.512857(16)	4.27
R1 3951	11.63	58.64	0.1200	0.512877(11)	4.66
R2 3951	11.58	58.79	0.1192	0.512855(10)	4.23
R1 3952	9.85	49.84	0.1195	0.512879(12)	4.70
R1 3953	9.50	53.12	0.1082	0.512863(13)	4.39
R2 3955	5.80	31.55	0.1112	0.512889(5)	4.90
R2 3956	8.20	45.28	0.1096	0.512869(4)	4.51
Hattorf dyke profile					
H_2O-washed whole rocks					
R 3957	10.09	59.84	0.1020	0.512847(12)	4.08
R 3958	10.18	59.78	0.1030	0.512856(4)	4.25
R 3959	9.97	58.97	0.1023	0.512855(4)	4.23
R 3960	10.00	59.03	0.1025	0.512852(2)	4.17
R 3961	9.91	58.45	0.1026	0.512856(8)	4.25

The Sm and Nd concentrations are ICP-MS data.
The errors given for the $^{143}Nd/^{144}Nd$ ratios are ± 2 sigma mean values and refer to the last digits.
The ε_{Nd} CHUR values are chondrite normalized $^{143}Nd/^{144}Nd$ ratios and calculated using the formula: ε_{Nd} CHUR = 1E 4 * (($^{143}Nd/^{144}$ Nd—0.512638)/0.512638).

steeper than the surface samples. Group I corresponds to samples with K_2O concentrations of 3.12 to 4.61%, and group II to samples having K_2O concentrations of 1.56 to 2.22% (Table 6). The two groups are not related to a specific geographic or stratigraphic position.

In the Hattorf dyke section, the $^{40}Ar/^{36}Ar$ ratios are highest at the border and lowest in the core of the dyke (Fig. 11). The values do not change significantly when the $^{40}Ar/^{36}Ar$ ratios are corrected for postintrusive in situ formation of ^{40}Ar by the decay of K. This indicates that the elevated ratios near the margins are due to the admixture of highly radiogenic Ar. The Ar concentrations are in contrast to the isotopic compositions highest in the dyke centre whereas the K_2O concentrations show an opposite distribution. Washing with H_2O reduced the concentrations of Ar and K_2O but did not significantly affect the $^{40}Ar/^{36}Ar$ and $^{40}K/^{36}Ar$ ratios.

4.4. Sr and Nd isotopes

The Sr and Nd isotope data are given in Tables 7 and 8. The Sr and Nd isotope data of the H_2O-washed whole rock samples of basalts from the subsurface are compiled in Fig. 12. They show rather homogeneous Nd isotopic compositions with ε_{Nd} values between +4 and +5. The $^{87}Sr/^{86}Sr$ ratios, how-

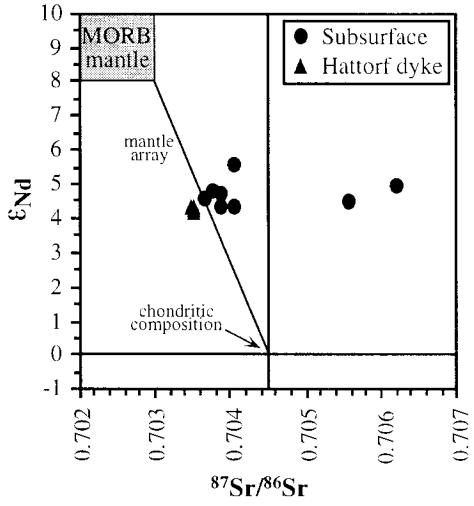

Fig. 12. Nd–Sr isotopic compositions for the subsurface samples including the Hattorf dyke.

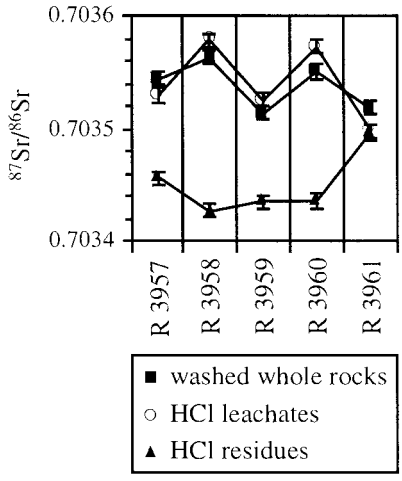

Fig. 13. Sr isotope data for the H_2O-washed whole rocks, and the HCl leachates and residues of the Hattorf dyke profile.

ever, are much more scattered ranging between 0.7035 and 0.7065. Nevertheless, most of the samples plot on or close to the mantle array between the chondritic and the depleted MORB-type mantle reservoirs. They are similar to those recently discussed for the Central European subcontinental mantle (Stille and Schaltegger, 1996) and comparable with other alkali-basalts of Tertiary intraplate volcanism in western Germany (Wedepohl et al., 1994).

The H_2O-washed whole rocks of the Hattorf dyke plot in Fig. 12 together with regional samples with low Sr isotope ratios. A detailed look at the Sr isotopic compositions of the H_2O-washed whole rocks of the Hattorf profile reveals significant variations throughout the profile (Fig. 13), whereas the Nd isotopic compositions remain constant (Table 8).

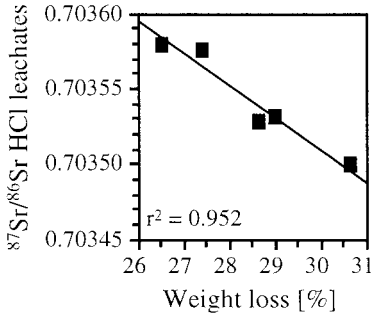

Fig. 14. Negative correlation between the $^{87}Sr/^{86}Sr$ ratios for the HCl leachates and the sample weight removed during leaching with 1.5 M HCl in the Hattorf samples.

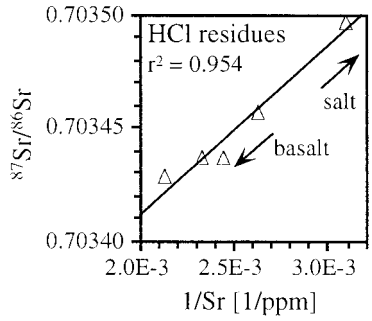

Fig. 15. Sr mixing diagram for the Hattorf HCl residues indicating a mixing between a salt and a basalt end-member.

The $^{87}Sr/^{86}Sr$ ratios of the HCl leachates and the H_2O-washed whole rocks of the Hattorf profile show the symmetrical m-shaped pattern already encountered for other parameters throughout the section (Fig. 13). The Sr isotopic compositions of the HCl leachates are furthermore negatively correlated with the loss of sample weight during leaching with HCl (Fig. 14).

The $^{87}Sr/^{86}Sr$ ratios of the residues show a completely different pattern with highest values at the dyke margin (Fig. 13). In the Sr mixing diagram, a mixing trend can be observed between an end-member with low composition and high concentration and an end-member with high composition and low concentration (Fig. 15).

5. Discussion

5.1. Major and trace elements

In the residues of the Hattorf dyke profile, MgO and SiO_2 are negatively correlated ($r^2 = 0.935$). This is typical for a cogenetic basaltic rock suite related by fractional crystallisation of olivine, clinopyroxene and magnetite (e.g., Wilson, 1989). The fractionation path starts with high MgO and low SiO_2 and ends up with low MgO and high SiO_2. In the case of the Hattorf profile, this correlation points to a chemical fractionation within the only 0.5 m large dyke transect. A detailed look at the MgO and SiO_2 data of the residues shows that the concentrations are less

evolved at the dyke margins and in the core of the dyke and most evolved in the intermediate samples R 3958 and R 3960 (Fig. 4). These two latter samples are closer to the dyke margins than to the core (Fig. 2). We suggest that their more evolved chemical composition is due to a differentiation-related zoning triggered by the chilling at the dyke margins. This chilling has led to an enrichment of the most compatible elements in the marginal zone resulting in a depletion in the adjacent intermediate zone. The dyke centre was not influenced by this marginal differentiation as shown by the MgO and SiO_2 concentrations which are less evolved in the dyke centre than in the intermediate samples.

5.2. Weight loss during leaching

The weight loss of about 30% during leaching with 1.5 M HCl is much higher than usual values, which are normally $< 2\%$, and even $< 10\%$ for carbonate-bearing oceanic basalts (Steinmann, unpublished data). This is therefore an indication of alteration of the basalt. The weight loss is also elevated in the core of the dyke which shows that the basalt is not only altered near the margins but throughout the whole profile. We suggest that these elevated losses are essentially due to the presence of altered or newly formed minerals leachable by HCl.

The characteristic w-shaped distribution of the weight loss (Fig. 3) is similar to that of the fractionation-controlled MgO concentrations in the residues (Fig. 4). This suggests that the corrosion behavior of the basalt is related to the degree of fractionation. But the negative correlation between the HCl leachate weights and the $^{87}Sr/^{86}Sr$ ratios of the HCl leachates (Fig. 14) demonstrates that fractionation was not the primary controlling mechanism because Sr isotopic compositions, like $^{40}Ar/^{36}Ar$ and $^{143}Nd/^{144}Nd$ isotope ratios, can only be changed by mixing and exchange processes but not by magmatic fractionation.

The negative correlation between the leachate weights and the $^{87}Sr/^{86}Sr$ ratios shows that the weight loss was lowest when alteration was strongest, since increasing Sr isotope ratios indicate increasing degree of alteration as will be discussed in Section 5.5. A possible explanation for this is that potentially leachable phases had already been removed during basalt alteration and were hence not more available for leaching. The alteration of the basalt was thus strongest in the two intermediate samples R 3958 and R 3960 where leaching loss was smallest.

5.3. Rare earth elements (REE)

The positive correlations of ΣREE with P_2O_5 in the leachates and the residues indicate that a phosphate phase is an important REE carrier in both cases (Fig. 8). This is ascertained by the positive correlations between La/Yb ratios and P_2O_5 concentrations in the leachates and residues (Fig. 8) because phosphates are generally characterized by LREE enrichment (e.g., Taylor and McLennan, 1988).

The dependence of the La/Yb ratios on the phosphate content is outlined in more detail in the REE distribution diagrams in Fig. 16. In these diagrams, the REE of the HCl leachates and residues are normalized to the leachate and residue values, respectively of sample R 3959 from the core of the dyke. Keep in mind that the leachates are more enriched in the LREE than the residues when normalized to the same reference data set (Fig. 9). The leachate and residue distribution patterns in Fig. 16 show a direct relation between the slope of the pattern and the P content as already indicated by the correlations between La/Yb and P_2O_5 (Fig. 8). The two P-poor leachates of the marginal samples R 3957 and R 3961 are depleted in the LREE and enriched in the HREE (heavy rare earth elements, Dy–Lu) with respect to the P-rich sample R 3959 from the core. It is important to note that the HREE concentrations of these marginal samples are even higher than in the dyke core. This shows that at the margins, where only little phosphate was leached, the REE were partly derived from a carrier phase which preferentially integrated the HREE such as clinopyroxene and magnetite (Lemarchand et al., 1987). The same trend can be observed for the residues where the LREE-enriched end-member is in contrast located at the dyke margins because of the complementary distribution of P_2O_5 in the leachates and residues. From these observations, it can be concluded that in phosphate-poor leachates and residues a part of the REE is derived from a HREE-enriched non-phosphatic carrier phase which is lacking when phosphate is dominant.

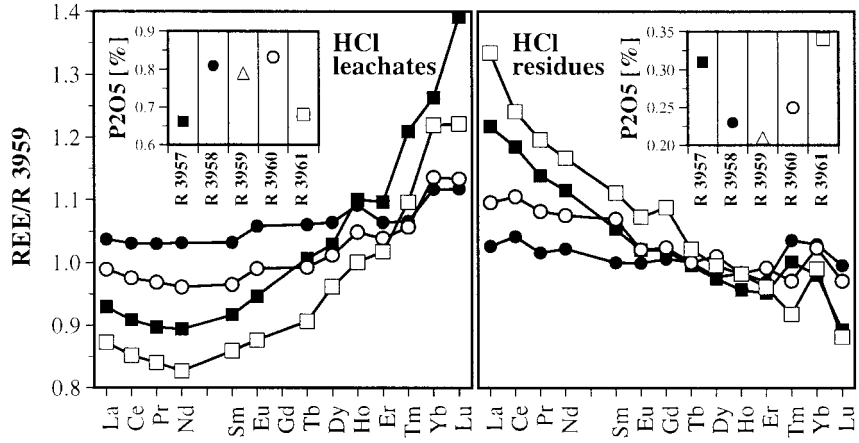

Fig. 16. Detailed REE patterns for the Hattorf HCl leachates and residues and their dependence on the P_2O_5 content. The REE are normalized to sample R 3959 from the core of the dyke in order to show the symmetric evolution of the patterns. See inserts for sample identification.

However, phosphate remains the most important REE carrier in the leachable and the residual phase. The leachable phosphate is more enriched in the LREE than the residual one. Such an enrichment of the light rare earths is typical for secondary phosphate such as florencite or rhabdophane and has been described in several weathering profiles (Duddy, 1980; Tazaki et al., 1987; Banfield and Eggleton, 1989; Braun et al., 1990, 1993; Prudêncio et al., 1993; Macfarlane et al., 1994). A comparative study of weathered and unweathered phosphates by Tazaki et al. (1987) has shown that weathered phosphates are characterized by a less ordered lattice structure. This could in our case explain why leaching with HCl removed in a very selective way essentially the secondary and not the primary magmatic phosphates.

The LREE-enrichment of secondary phosphate can be caused by two processes: (1) REE-removal from the primary minerals without fractionation followed by a preferential integration of the LREE into secondary phosphate whereas the better soluble HREE were transported out of the system (Braun et al., 1990) or (2) higher availability of the LREE in the weathering system owing to their preferential removal from primary minerals (Macfarlane et al., 1994). Which of these possibilities finally controls the system essentially depends on the pH and the chemistry of the circulating fluid (Macfarlane et al., 1994).

The first process would in our case signify that an important quantity of HREE had left the dyke during weathering. But our data of the H_2O-washed whole rocks show that the concentrations of all rare earths are almost constant throughout the profile (Table 4) which is not in agreement with an important HREE loss. In contrast, the concentration of the light rare earth La is higher in the leachates than in the residues (Fig. 9). This can better be explained by the second process, i.e., that the LREE were preferentially removed from primary phoshate during weathering. This implies that weathering has essentially led to a in situ fractionation and redistribution of the REE into a leachable and non-leachable reservoir and not to their removal. The complementary distributions of P_2O_5, Fe_2O_3, CaO and Mn_3O_4 in the leachates and residues throughout the dyke profile (Fig. 4) confirm such a process because the complementary aspect would have been obliterated by strong element migrations. This is also confirmed by the complementary REE distribution patterns of the leachates and residues.

The discussion of the weight losses during leaching has shown that alteration was strongest in the two intermediate samples R 3958 and R 3960. This is in agreement with the elevated P_2O_5 and Fe_2O_3 concentrations observed in the HCl leachates of these samples (Fig. 4) because it indicates a locally higher abundance of secondary phosphate and Fe-oxide.

The occurrence of hematite in this part of the dyke is confirmed by the microscopic investigations. The $Ce/Ce*$ ratios are not only distinctly higher in the residues than in the leachates but they also show, similar P_2O_5 and Fe_2O_3, elevated values for the intermediate samples R 3958 and R 3960 (Fig. 7). We interpret this in the way that Ce, which normally occurs as Ce(III) in magmatic systems, has partly been oxidized to poorly soluble Ce(IV) during basalt alteration. The stronger alteration in the intermediate samples has led to greater oxidation and thus higher $Ce/Ce*$ values. Leaching with HCl essentially removed the more soluble Ce(III) which explains the lower $Ce/Ce*$ ratios of the leachates. The symmetric distribution of $Ce/Ce*$ in the leachates is probably due to the LREE enrichment in the secondary phosphate as indicated by a good correlation between $Ce/Ce*$ and La/Yb ($r^2 = 0.983$).

We have tried to speciate the primary and secondary phosphatic REE carriers in more detail. The idiomorphic acicular apatites observed in the basaltic groundmass under the light-microscope (cf. Section 3.2) are the only primary phosphate minerals of importance. Therefore, we regard them as the most probable primary REE carrier. However, their REE concentrations were below the detection limit of the EDS device of our SEM.

In contrast, in the alteration rims around the salt inclusions mentioned in Section 3.2, we found, associated with secondary sheet silicates, numerous grains of a secondary phosphate phase with high REE concentrations (Fig. 17). It could be identified as REE-chlorapatite with an average formula $(Ca_{2.2}La_{0.5}CeNd_{0.5})(PO_4)_3$. The thin crystals allowed only a semi-quantitative concentration analysis. The high REE content of these secondary apatite is illustrated by the element maps of Fig. 18. These SEM observations thus confirm the existence of a secondary, REE-rich apatite phase as suggested by our chemical data.

The secondary apatite is by comparison with the primary apatite rather isometric in shape and much smaller. Its diameter is mostly around 1 μm and always smaller than 10 μm. In contrast, the primary acicular apatites can reach 200 μm in length. This larger size of the primary apatite might explain why

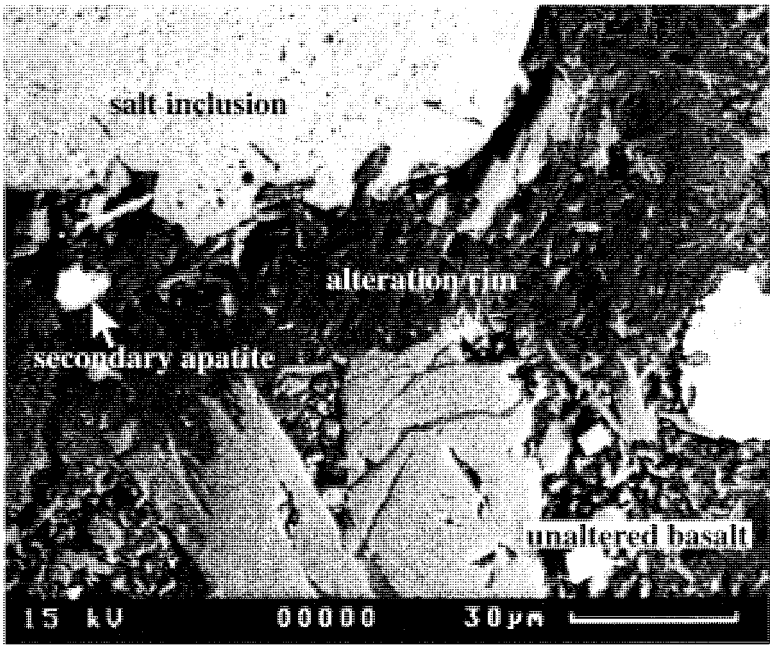

Fig. 17. SEM photograph showing a secondary apatite crystal within a rim of altered basalt around a salt inclusion. The other minerals contained in the rim are sheet silicates and hematite.

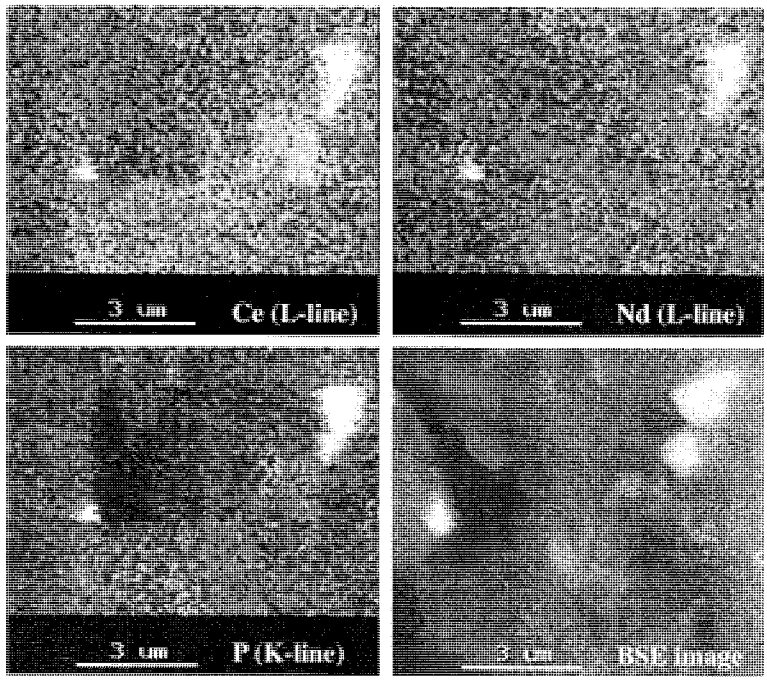

Fig. 18. Element maps of Ce, Nd, and P demonstrating the high REE content of the secondary apatite. The elevated REE concentrations lead to the high contrast of the apatite in the backscattered electron (BSE) image.

no rare earths could be detected by EDS. The secondary REE-apatite is in many places intimately associated with a SO_4-phase.

5.4. Ar isotopes

The subdivision of the subsurface samples from outside the Hattorf profile into two groups can be related to syn- or postintrusive K-uptake of the basalts. This led to an increase of the $^{40}K/^{36}Ar$ ratios at constant $^{40}Ar/^{36}Ar$ compositions and thus to a more gentle slope of the group I samples in the K–Ar isochron diagram.

The much stronger ^{40}Ar overpressure of the subsurface samples with respect to the surface samples indicates that the former retained considerable amounts of mantle Ar. However, the observed $^{40}Ar/^{36}Ar$ ratios of 400–1000 are still much lower than typical mantle compositions which can achieve values up to 17,000 for the subcontinental mantle (Dunai and Baur, 1994) and 28,000 for the MORB mantle (Staudacher et al., 1989). This suggests that the mantle Ar contained in the basaltic melt was mixed with atmospheric Ar during magma ascent. Probable sources for this atmospheric Ar are paragneisses of the upper crust or sedimentary units such as the Rotliegend sandstones situated below the Zechstein evaporites.

The high Ar concentrations in the core of the Hattorf dyke section and the rapid concentration decrease at the margins point to synintrusive outgassing or postintrusive removal by a process like hydrothermalism. However, the $^{40}Ar/^{36}Ar$ ratios are higher at the margins than in the core which points to the presence of an additional Ar source with higher $^{40}Ar/^{36}Ar$ compositions. This additional Ar source are most probably the potash salts since they can have highly radiogenic Ar isotopic compositions as demonstrated by $^{40}Ar/^{36}Ar$ ratios of up to 5000 determined in mineral separates of langbeinites ($K_2Mg_2(SO_4)_3$) from the same mining district (Oesterle and Lippolt, 1975). The migration of this salt Ar into the peripheral parts of the dyke would have taken place in a second phase after the outgassing or removal of the mantle–atmospheric Ar mixture.

The results of the washing with H_2O indicate for the core of the dyke the presence of a water-soluble phase containing considerable amounts of Ar and K. The solubility in H_2O and the release of K suggest that it was a salt phase. This salt must have had identical $^{40}Ar/^{36}Ar$ and $^{40}K/^{36}Ar$ ratios to those of the H_2O-washed whole rock because its removal did not lead to a shift in the residues. This isotopic homogeneity and the elevated Ar concentrations with respect to the margins indicate that the salt and the insoluble residue of the dyke core had simultaneously been precipitated during intrusion under Ar overpressure. Alternatively, both phases could have reequilibrated after intrusion under closed system conditions. In both cases, however, the salt phase must have been assimilated during intrusion. Postintrusive migration of salt fluids into the dyke core can be excluded because it would have led to an opening of the system.

A possible source for this synitrusively assimilated salt could be the NaCl-rich fluids which accompanied the basaltic melt (Section 2). We suggest that this assimilated salt has been finely dispersed within the basaltic matrix. The salt inclusions observed under the microscope (Section 3.2) cannot correspond to this assimilated salt, because they occur near the margins and not in the dyke core.

The identical concentrations and compositions found in the washed and unwashed marginal and intermediate samples show that the K and Ar content of these samples is entirely contained in the insoluble phase. The presence of a synintrusively assimilated K and Ar bearing salt in the dyke core and its lacking in the marginal and intermediate samples suggests that it has been removed from the margins after intrusion, most probably by circulating fluids. At the same time, these fluids imported highly radiogenic Ar from the salts which was then integrated into newly formed minerals, most probably into the sheet silicates observed under the microscope.

5.5. Sr and Nd isotopes

The Sr and Nd isotope data for all samples preclude significant contamination of the basaltic magma by continental crust because such contamination would at the same time have modified both isotopic compositions. The observed Nd–Sr isotopic compositions are comparable with those of oceanic basalts that have been altered by seawater (e.g., Jacobsen and Wasserburg, 1979). The decoupled behavior of the Nd and Sr isotope systems is due to the relatively high Sr but very low Nd concentrations in seawater. Rock and potash salts have Sr/Nd concentration ratios similar to seawater and in particular, K-salts can have strongly elevated $^{87}Sr/^{86}Sr$ ratios. Therefore, we attribute the partly elevated Sr isotopic compositions of the basalts to the presence of salt-derived Sr. It is now of major importance to know whether this occurrence of salt Sr is due to synintrusive salt assimilation or to postintrusive basalt alteration. This will be discussed in the following on the basis of the Hattorf data.

The low $^{87}Sr/^{86}Sr$ ratios of the basalt residues in the centre of the Hattorf dyke possibly reflect the original isotopic signature of the unaltered basalt. The increase of the values at the dyke margins points to the presence of a HCl unleachable secondary mineral phase which has integrated more radiogenic Sr. This radiogenic Sr is, as discussed above, probably salt derived Sr. The higher Sr isotopic compositions of the H_2O-washed whole rocks and the HCl leachates indicate as well the presence of salt Sr. The almost identical $^{87}Sr/^{86}Sr$ ratios of the whole rocks and leachates show that the leachable phase is an important Sr carrier (300–700 ppm, Table 7) that strongly influences the Sr isotopic composition of the whole rocks. This Sr carrier could be phosphate as indicated by a correlation between $^{87}Sr/^{86}Sr$ and P_2O_5 in the leachates ($r^2 = 0.616$).

The discussion of the major and trace element data has shown that the chemical composition of the residues is to a large extent controlled by fractional crystallisation. In Fig. 19, the $^{87}Sr/^{86}Sr$ ratios of the HCl leachates and residues are plotted against the degree of this fractionation represented by Al_2O_3/MgO ratios of the HCl residues which are increasing with increasing fractionation. The Sr isotopic compositions of the residues increase with decreasing fractionation. In contrast, in the leachates the Sr isotope ratios increase with increasing fractionation. Note that the fractionation succession does not correspond to a simple dyke section from the core to the margins. The most fractionated samples are, as discussed in Section 5.1, the two intermediate samples R 3958 and R 3960, and fractionation is

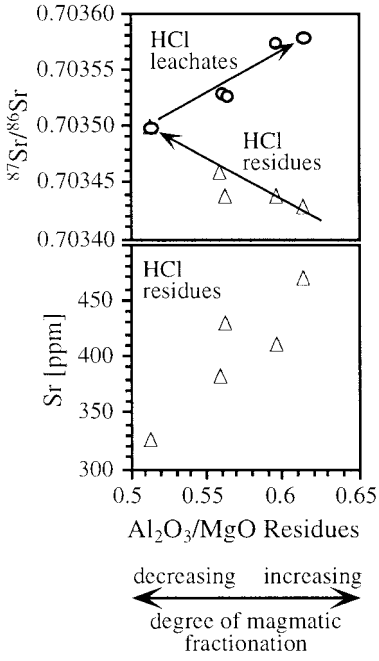

Fig. 19. Sr concentrations for the HCl residues and Sr isotopic compositions for the HCl leachates and residues of the Hattorf dyke profile plotted against the Al_2O_3/MgO ratios for the HCl residues. These ratios increase with increasing degree of magmatic of fractionation.

lowest in the border samples R 3961 and R 3957. Using SiO_2/MgO instead of Al_2O_3/MgO yields an almost identical picture. The classical $(Na_2O + K_2O)/SiO_2$ index was not taken because Na and K could be influenced by the salts.

The Sr concentrations of the residues increase in contrast to the evolution of the $^{87}Sr/^{86}Sr$ ratios not with decreasing but with increasing fractionation (Fig. 19). This shows that the Sr concentrations of the residues is directly controlled by fractionation. In the Sr mixing diagram, the residues define a mixing trend between a basalt and a salt end-member (Fig. 15). The most fractionated intermediate sample R 3958 is closest to the basalt and the less fractionated sample R 3961 from the dyke margin closest to the salt end-member. The salt contamination is thus strongest where the Sr concentration of the basalts are lowest and no salt contamination seems to be present in the highly fractionated samples with high Sr content. Accordingly, the admixture of the salt Sr must have occurred after fractionation controlled distribution of the basaltic Sr. However, the homogeneity of the mixture indicates that the mixing still occurred during the presence of a melt phase. Therefore, we suggest that the basaltic Sr was in a first phase distributed as a function of the degree of fractionation. In a second, but still synintrusive phase salt Sr was assimilated and admixed to a magma in which crystallisation and fractionation had already started. Like in the discussion of the K–Ar data, we suggest that this assimilated salt phase is derived from the NaCl-rich fluids which accompanied the basaltic melt. The admixture of salt–Sr is thus not best visible in the marginal samples because of the immediate vicinity to the salts, but because the basalt contained at its margins, as a consequence of magmatic fractionation, least Sr prior to salt assimilation.

In contrast to the residues, no Sr mixing relation can be observed in the leachates. Therefore, the increase of the $^{87}Sr/^{86}Sr$ ratios of the leachates with increasing degree of fractionation cannot be related to a simple mixing caused by synintrusive salt assimilation. The trend is rather due to postintrusive alteration and exchange with salt-derived fluids. This alteration has also directly influenced the resistance of the basalts to HCl leaching as demonstrated by the discussed negative correlation of the leachate weights and the $^{87}Sr/^{86}Sr$ ratios of the leachates (Fig. 14).

A possible mechanism to link the $^{87}Sr/^{86}Sr$ ratios of the leachates with the degree of fractionation is over a fractionation-induced zoning of the mechanical properties of the dyke. Samples R 3957 and R 3961 from the chilled dyke margin remained, like the slowly cooled sample R 3959 from the dyke core, almost unfractured compact rock bodies. The different cooling speed and the different shrinking rates between the margins and the core of the dyke may have led to a mechanical fracturing of the intermediate zone. Together with the thermal gradient between the core and the margins this might have led to the evolution of a strong circulation of salt-derived fluids resulting in stronger alteration of the basalts in this part of the dyke.

In contrast to the Sr isotope system, which clearly responds to exchange processes at the basalt interface, the almost constant Nd isotopic compositions throughout the whole dyke profile indicate that the Nd isotopes of the basalts have not been significantly modified during salt corrosion. However, this does

not exclude migration of Nd or of all REE out of the basaltic dyke into the salts.

6. Alteration model

In the following, we will integrate the major results of the individual data sets into a coherent alteration model.

The synintrusive chilling of the dyke margins has led to zoned fractionation with a locally more evolved major element composition in the intermediate samples R 3958 and R 3960. The intruding melt contained an Ar-bearing gas phase which has been preserved in the central part of the dyke. Its disappearance towards the margins may be due to synintrusive outgassing or removal by postintrusive alteration. The melt also assimilated some salts during intrusion as indicated by the Ar and Sr isotope data. These salts are preserved as a H_2O-soluble phase only in the dyke core. A possible source for this assimilated salt are NaCl-rich salt fluids which accompanied the basaltic melts. The influence of the assimilated salt is best visible in the Sr isotopic compositions of the HCl-residues from the dyke margins because they had, as a consequence of magmatic fractionation, primarily lower Sr concentrations. The REE of the basalts were probably mainly contained in the acicular apatites occurring in the groundmass. Cerium was in trivalent form as is typical for fresh basalts.

The different cooling speeds and shrinking rates at the margins and in the core of the dyke led to mechanical fracturing of the intermediate zone around samples R 3958 and R 3960. This in turn resulted in stronger alteration by the subsequent postintrusive fluid circulation. The alteration fluids were salt brines containing among others K and highly radiogenic salt Ar and Sr. These fluids leached the primary basalt minerals and removed preferentially LREE from the acicular magmatic apatite. At the same time, Ce(III) was oxidized to poorly soluble Ce(IV). Subsequently, it came to an almost in situ precipitation of secondary minerals, such as Fe-oxide, sheet silicates and small grains of strongly LREE-enriched apatite. These secondary minerals essentially formed in alteration rims around small salt inclusions near the dyke margins. The K and Ar contained in the fluids was integrated into the secondary sheet silicates whereas salt Sr was probably, like the REE, mainly contained in secondary apatite. Leaching with HCl essentially affected these secondary minerals because of their better solubility. The postintrusive fluid circulation removed in the most altered samples the weathered basaltic material not rebound in secondary phases which explains the observed decrease in leaching losses with increasing Sr isotopic composition. The alteration fluids also led to the removal of the synintrusively assimilated salts except in the dyke core where the Ar-bearing salt phase was probably finely dispersed and located in small grains not affected by the fluids.

7. Conclusions

Our study documents alteration of basaltic dykes during postintrusive circulation of salt derived fluids. The alteration fluids were salt brines that leached the primary basaltic minerals. This led to the formation of secondary minerals such as secondary apatite, hematite, and sheet silicates, in particular smectite/chlorite and saponite. These secondary phases have been shown to be clearly less resistant to leaching with HCl than the primary basaltic minerals.

The REE were mobile during this alteration. The higher mobility of the LREE has led to fractionated REE distributions. The most important REE carrier phases before and after alteration were primary magmatic and secondary apatite, respectively. The small grains of secondary apatite were precipitated almost in situ around small salt inclusions after dissolution of the acicular magmatic apatite. This led to refixation of the mobilized rare earths which shows that the scavenging capacity of the precipitating apatite was stronger than complexation of the rare earths in the circulating brine. This suggests for a leaking HLW salt repository that outgoing rare earths and actinides would probably also be retained when phosphate minerals are present in the backfill material. Such a retention of fission products by phosphate has also been documented in the natural fission reactor of Oklo, Gabon (Gauthier-Lafaye et al., 1996; Dymlov et al., 1997).

Despite the strong alteration of the basalt, a primary gas phase was preserved in the dyke core. This demonstrates that gas loss by diffusion is limited even over millions of years and that the alteration fluids did not homogeneously penetrate and alter the basalt which remained locally unaffected. This finding is of importance for the retention of fission derived gas phases within a repository.

Acknowledgements

This study has been initiated by Bernd Knipping. With his unexpected death, we have lost an initiative colleague who knew how to bring researchers from different disciplines together in order to advance in the research of basalt–salt contacts as a natural analogue for radwaste disposal. We thank B. Kiefel, Ph. Larqué, R. Rouault, J. Samuel and D. Tisserant for their technical assistance in the laboratory. The constructive reviews by S.A. Wood and M. Pagel helped to improve an earlier version of the manuscript. MS profited from a fellowship of the Swiss National Science Foundation, which is kindly acknowledged.

References

Abdelouas, A., Crovisier, J.L., Lutze, W., Fritz, B., Mosser, A., Müller, R., 1994. Formation of hydrotalcite-like compounds during R7T7 nuclear waste glass and basaltic glass alteration. Clays and Clay Minerals 42, 526–533.

Akagi, T., Shabani, M., Masuda, A., 1993. Lanthanide tetrad effect in kimuraite [$CaY_2(CO_3)_4 \cdot 6H_2O$]: implication for a new geochemical index. Geochim. Cosmochim. Acta 57, 2899–2905.

Banfield, J.P., Eggleton, R.A., 1989. Apatite replacement and rare earth mobilization, fractionation, and fixation during weathering. Clays Clay Miner. 37, 113–127.

Braun, J.J., Pagel, M., Herbillon, A., Rosin, C., 1993. Mobilization and redistribution of REEs and thorium in a syenitic lateritic profile: a mass balance study. Geochim. Cosmochim. Acta 57, 4419–4434.

Braun, J.J., Pagel, M., Muller, J.P., Bilong, P., Michard, A., Guillet, B., 1990. Ce anomalies in lateritic profiles. Geochim. Cosmochim. Acta 54, 781–795.

Byers, C.D., Byers, M.J., Byers, J., Ewing, R.C., Keil, K., 1985. Basalt glass: an analogue for the evaluation of the long-term stability of nuclear waste form borosilicate glasses. In: Jantzen, C.M., Stone, J.A., Ewing, R.C. (Eds.), Scientific Basis for Nuclear Waste Management VIII. Mat. Res. Soc. Symp. Proc., Pittsburgh, PA, p. 44.

Chapman, N.A., McKinley, I.G., Smellie, I., 1984. The potential of natural analogues in assessing systems for deep disposal of high-level radioactive waste. NAGRA Tech. Rept., NTB, pp. 84–41.

Choppin, G.R., 1983. Comparison of the solution chemistry of the actinides and the lanthanides. J. Less-Common Met. 93, 232–330.

Crovisier, J.-L., Honnorez, J., Fritz, B., Petit, J.-C., 1992. Dissolution of subglacial volcanic glasses from Iceland: laboratory study and modelling. Appl. Geochem. 1, 55–81, Suppl. Issue.

Daux, V., Guy, C., Advocat, T., Crovisier, J.-L., Stille, P., 1997. Kinetic aspects of basaltic glass dissolution at 90°C: role of aqueous silicon and aluminium. Chem. Geol. 142, 109–126.

Duddy, I.R., 1980. Redistribution and fractionation of rare earth and other elements in a weathering profile. Chem. Geol. 30, 363–381.

Dulsky, P., 1994. Interferences of oxide, hydroxide and chloride analyte species in the determination of rare earth elements in geological samples by inductively coupled plasma-mass spectrometry. Fresenius J. Anal. Chem. 350, 194–203.

Dunai, T.J., Baur, H., 1994. Helium, neon, and argon systematics of the European subcontinental mantle: implications for its geochemical evolution. Geochim. Cosmochim. Acta 59, 2767–2783.

Dymlov, Y., Holliger, P., Pagel, M., Gorshkov, A., Artyukhina, A., 1997. Characterization of a La–Ce–Sr–Ca aluminous hydroxy phosphate in nuclear zone 13 in the Oklo uranium deposit (Gabon). Mineralium Deposita 32, 617–620.

Ewing, R.C., 1979. Natural glasses: analogues for radioactive waste forms. In: McCarthy, G. (Ed.), Scientific Basis for Nuclear Waste Management. Plenum, New York, pp. 57–68.

Gauthier-Lafaye, F., Holliger, P., Blanc, P.-L., 1996. Natural fission reactors in the Franceville basin, Gabon: a review of the conditions and results of a 'critical event' in a geologic system. Geochim. Cosmochim. Acta 60, 4831–4852.

Gutsche, A. 1988. Mineralreaktionen und Stofftransporte an einem Kontakt Basalt-Hartsalz in der Werra-Folge des Werkes Hattorf. Unpubl. Diploma Thesis, Georg-August-Universität Göttingen.

Jacobsen, S.B., Wasserburg, G.J., 1979. Nd and Sr isotopic study of the Bay of Islands ophiolite complex and the evolution of the source of mid-ocean ridge basalts. J. Geophys. Res. 84, 7429–7445.

Kawabe, I., 1992. Lanthanide tetrad effect in the Ln^{3+} ionic radii and refined spin-pairing energy theory. Geochem. J. 26, 309–335.

Knipping, B., 1989. Basalt intrusions in evaporites. Lecture Notes in Earth Sciences 24. Springer, Berlin, 132 pp.

Knipping, B., Herrmann, A.G., 1985. Mineralreaktionen und Stofftransporte an einem Kontakt Basalt-Carnallitit im Kalisalzhorizont Thüringen der Werra-Serie des Zechsteins. Kali und Steinsalz 9, 111–124.

Krauskopf, K.B., 1986. Thorium and rare-earth elements as analogues for actinide elements. Chem. Geol. 55, 323–335.

Lemarchand, F., Villemant, B., Calas, G., 1987. Trace element

distribution coefficients in alkaline series. Geochim. Cosmochim. Acta 51, 1071–1081.

Lippolt, H.J., 1982. K/Ar age determinations and the correlation of Tertiary volcanic activity in Central Europe. Geol. Jb. D52, 113–135.

Lutze, W., Grambow, B., 1992. The effect of glass corrosion on near field chemistry. Radiochim. Acta 58–59, 3–7.

Macfarlane, A.W., Danielson, A., Holland, H.D., Jacobsen, S.B., 1994. REE chemistry and Sm–Nd systematics of late Archean weathering profiles in the Fortescue Group, Western Australia. Geochim. Cosmochim. Acta 58, 1777–1794.

Malow, G., Lutze, W., Ewing, R.C., 1984. Alteration effects and leach rates of basaltic glasses: implications for the long-term stability of nuclear waste form borosilicate glasses. J. Noncryst. Solids 67, 305–321.

McMenamin, T. (Ed.), 1997. Fourth European Conference on Management and Disposal of Radioactive Waste. Office for Official Publications of the European Communities, Luxembourg.

Oesterle, F.P., Lippolt, H.J., 1975. Isotopische Datierung der Langbeinitbildung in der Kalisalzlagerstätte des Fuldabeckens. Kali und Steinsalz 11, 391–398.

Petit, J.C., 1992. Reasoning by analogy: rational foundation of natural analogue studies. Appl. Geochem. 1, 9–11, Suppl. Issue.

Prudêncio, M.I., Braga, M.A.S., Gouveia, M.A., 1993. REE mobilization, fractionation and precipitation during weathering of basalts. Chem. Geol. 107, 251–254.

Seaborg, G.T., 1993. Overview of the actinide and lanthanide (the f) elements. Radiochim. Acta 61, 115–122.

Staudacher, T., Sarda, P., Richardson, S.H., Allègre, C.J., Sagna, I., Dmitriev, L.V., 1989. Noble gases in basalt from a Mid-Atlantic Ridge topographic high at 14°N: geodynamic consequences. Earth Planet. Sci. Lett. 96, 119–133.

Stille, P., Schaltegger, U., 1996. The lithospheric mantle beneath Central Europe: Nd isotopic constraints for its Late Proterozoic enrichment and implications for early crustal evolution. Geophys. Monogr. 95, 269–276.

Taylor, S.R., McLennan, S.M., 1985. The Continental Crust: Its Composition and Evolution. Blackwell, Oxford, 312 pp.

Taylor, S.R., McLennan, S.M., 1988. The significance of the rare earths in geochemistry and cosmochemistry. In: Gschneidner, Jr., K.A., Eyring, L. (Eds.), Handbook on the Physics and Chemistry of the Rare Earths. Elsevier, Amsterdam, pp. 485–578.

Tazaki, K., Fyfe, W.S., Dissanayake, C.B., 1987. Weathering of apatite under extreme conditions of leaching. Chem. Geol. 60, 151–162.

Wedepohl, K.H., 1982. K–Ar-Altersbestimmungen an basaltischen Vulkaniten der nördlichen Hessischen Senke und ihr Beitrag zur Diskussion der Magmengenese. N. Jb. Mineral. Abh. 144, 172–196.

Wedepohl, K.H., 1985. Origin of the Tertiary basaltic volcanism in the northern Hessian Depression. Contrib. Mineral. Petrol. 89, 122–143.

Wedepohl, K.H., Gohn, E., Hartmann, G., 1994. Cenozoic alkali basaltic magmas of western Germany and their products of differentiation. Contrib. Mineral. Petrol. 115, 253–278.

Wilson, M., 1989. Igneous petrogenesis: a global tectonic approach. Unwin Hyman, London, 466 pp.

PERGAMON

Applied Geochemistry 16 (2001) 351–361

Applied Geochemistry

www.elsevier.com/locate/apgeochem

Trace element and isotopic evidence for REE migration and fractionation in salts next to a basalt dyke

Marc Steinmann[a,*], Peter Stille[a], Kurt Mengel[b], Bernard Kiefel[a]

[a] *ULP-EOST-CNRS, Centre de Géochimie de la Surface UMR 7517, 1 rue Blessig, F-67084, Strasbourg, Cedex, France*
[b] *IMMR, Technische Universität Clausthal, Adolph-Roemer-Strasse 2 A, D-38670, Clausthal-Zellerfeld, Germany*

Received 20 July 1999; accepted 22 February 2000
Editorial handling by R. Fuge

Abstract

Neodymium and Sr isotopic compositions and the rare earth elements (REE) distribution patterns have been determined in salts adjacent to a basaltic dyke along 2 parallel horizontal profiles. The salts, originally consisting of carnallite ($KMgCl_3 \cdot 6H_2O$), have been transformed during basalt intrusion mainly into halite (NaCl) and sylvite (KCl) by fluids saturated in NaCl. The Sr isotope data suggests that much more fluid penetrated the upper than the lower horizon. The Nd isotope data shows that in the upper horizon, where fluid flow was stronger, Nd is essentially derived from the basalt. In contrast, in the lower horizon a strong salt Nd component is present.

The REE data document in both horizons is a strong depletion of Ce, Pr, Nd, Sm and Eu with increasing distance from the basalt. This depletion of the light rare earths (LREE) is stronger in the upper horizon where fluid flow was stronger. The authors suggest that this REE fractionation is more likely due to precipitation of LREE-enriched accessory minerals such as apatite, than to differential REE solubility caused by selective REE complexation. This finding is of interest for REE behaviour in brines in general, and for the behaviour of radioactive REE and actinides in a salt repository for high-level nuclear waste in particular.

1. Introduction

Considerable efforts have been made during the past few years towards a better understanding of the chemical processes controlling mobility and fractionation of the rare earth elements (REE) in aqueous solutions. This paper focuses on REE behaviour in brines. Earlier studies on this topic have mainly been based on numerical models and experimental data (e.g., Millero, 1992; Haas et al., 1995; Gammons et al., 1996; Johannesson et al., 1996). In contrast, this study directly relies on a natural environment and presents the first Sr and Nd isotope and REE concentration data for salts sampled close to a basalt dyke crosscutting the salts. The REE, derived from the dyke, have migrated with Cl^--rich fluids through the salts. Temperature and pressure conditions during migration are not well constrained. However, heat flow calculations and relict primary carnallite suggest temperatures below 170°C (Knipping and Herrmann, 1985; Knipping, 1989).

The scope of the study is to gather information

* Corresponding author: Département de Géosciences, Université de Franche-Comté, 16 route de Gray, 25030 Besançon Cedex, France. Fax: +33-381-66-65-58.

E-mail address: marc.steinmann@univ-fcomte.fr (M. Steinmann).

0883-2927/01/$ - see front matter
PII: S0883-2927(00)00039-1

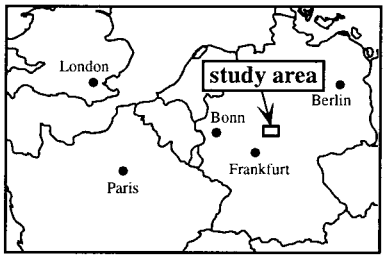

Fig. 1. The study site is located in underground mines of the Werra-Fulda salt mining district in Central Germany.

about fluids and processes, which control REE transport and fractionation in salts. In addition to REE concentration data, Sr and Nd isotopic compositions are used in order to identify the origin of the rare earths and to trace brine migration. The study is complementary to an earlier investigation on REE mobilization during corrosion of the basalt dykes at the same site (Steinmann et al., 1999).

Salt deposits are potential host rocks for the disposal of high-level radioactive waste. Fission products released from a leaking repository may be transported under similar conditions as the REE studied here. In this view, the study site is furthermore a natural analogue for a leaking salt repository.

2. Setting and methods

2.1. Geological setting

The sampling site is situated in an underground mine in central Germany where Permian evaporites (Zechstein) are crosscut by Miocene basalt dykes (Fig. 1). The evaporite series has a total thickness of up to 400 m. The most important salt is halite (NaCl), followed by thinner horizons of potash salt and anhydrite ($CaSO_4$). The basalt–salt contact investigated here is located in a potash salt level (Fig. 2) originally consisting of carnallite ($KMgCl_3 \cdot 6H_2O$). During basalt intrusion, the carnallite was transformed mainly into halite and sylvite (KCl) by fluids saturated with respect to NaCl originating from the partial dissolution of an underlying, 150 m thick halite formation (Knipping and Herrmann, 1985; Gutsche, 1988; Knipping, 1989). The present-day mineralogy of the salts and its evolution with distance are shown in Fig. 3.

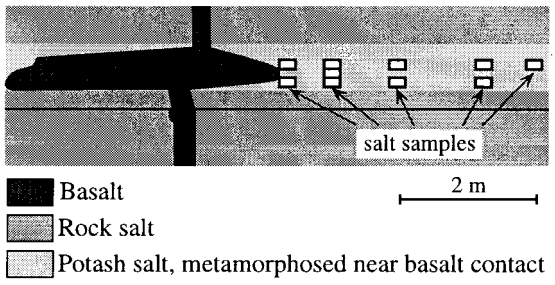

Fig. 2. The salt profiles studied here are situated in an underground mine next to a basalt dyke which is locally enlarged to an apophysis. The sample numbers and the exact distances from the basalt contact are given in Table 1. No vertical exaggeration.

The metamorphosed potash salt level studied here has been sampled by Gutsche (1988). It can be subdivided into 3 horizontal layers characterized by different colours: a rose upper, a reddish brown middle, and a white lower layer. This differentiation is clear up to 1 m away from the basalt and can vaguely be traced up to 3 m. Afterwards, the entire potash salt level has a greyish white colour. This suggests that the primary salt level was homogeneous and that the occurrence of 3 distinct horizons is due to basalt intrusion.

No direct temperature data are available for the brines. At the basalt contact they may have reached a

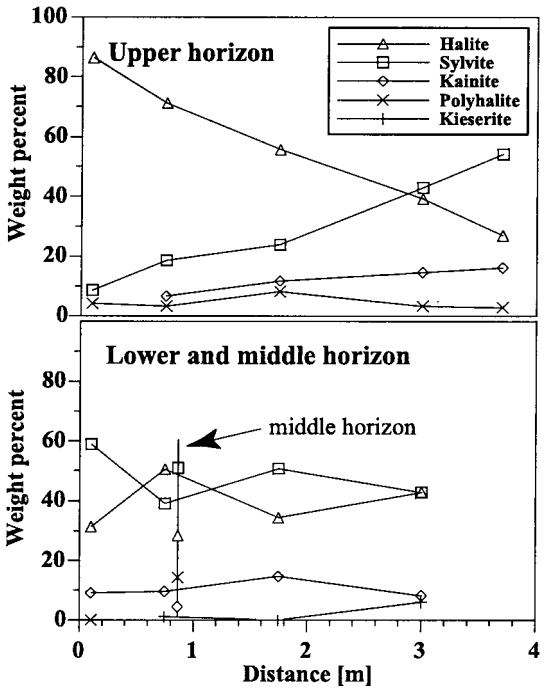

Fig. 3. Present-day mineralogical composition of the salt profiles. The subdivision into 3 horizons is based on their distinct colours in the field (see text for details). The minerals have been newly formed during basalt intrusion from carnallite ($KMgCl_3 \cdot 6H_2O$) which reacted with fluids saturated with respect to NaCl. Halite = NaCl, Sylvite = KCl, Kainite = $KMgClSO_4 \cdot 11/4\ H_2O$, Polyhalite = $K_2MgCa_2(SO_4)_4 \cdot 2\ H_2O$, Kieserite = $MgSO_4 \cdot H_2O$. Data from Gutsche (1988).

few hundred °C because the temperature of the basaltic melt was around 1150°C (Knipping, 1989). However, model calculations based on conductive heat transport suggest that the salts at 3 m distance from a basaltic dyke of 1 m thickness never attained 200°C (Knipping, 1989). This is supported by the occurrence of relicts of primary carnallite, whose upper thermal stability limit is 167.5°C (Braitsch, 1971), in salts less than 1 m from basalt contacts (Knipping and Herrmann, 1985; Knipping, 1989).

An estimation of the ionic strength of the fluids yields a value of about 5 when referring to the solubility limit of NaCl in water at 90°C (Braitsch, 1971). The chemical composition of the brine has been estimated by a quantitative analysis of the observed mineral reactions (Herrmann et al., 1978; Gutsche, 1988). The results show that it contained as the major anion Cl^- which dominated more than 95% of the total anion charge and some SO_4^{2-}. This anion composition remained almost unchanged during the migration of the brine. The dominant cations were Na, K and Mg.

Paleo-pH indicators such as mineral equilibria to estimate pH are unfortunately lacking. However, in analogy to carbonate-free recent brines occurring in salt pans (6.5–7, Herrmann et al., 1973), groundwaters (4.5–6.5, Fisher and Kreitler, 1987) and deep-sea basins of the Red Sea (5.5–6.5, Hartmann, 1969), the pH was probably below 7.

2.2. Analytical methods

Yttrium and the rare earths were analysed by ICP-MS (VG Plasmaquad PQ2+) after preconcentration with a liquid–liquid extraction procedure currently used for water samples (Shabani et al., 1990; Tricca et al., 1999) which was subsequently modified for salts (Steinmann and Stille, 1998). A major advantage of liquid–liquid extractions over chromatographic enrichment methods is that the rare earths are well separated from major elements such as Ba or Fe. Barium would cause interferences on the ICP-MS (^{138}Ba "bleeds" over the ^{139}La-peak, mass interference of $^{135}Ba^{16}O$ with ^{151}Eu), whereas Fe would hamper emission for the Nd isotope analyses by thermoionization mass spectrometry (TIMS).

Typically 10 g of salt was dissolved overnight in 400 ml of bidistilled water which was acidified with Quartex® distilled HCl to pH 2 to avoid readsorption of the REE on particles and on the bottle walls. The solutions were filtered through 0.22 μm filters (Millipore GSWP, 47 mm diameter) prior to preconcentration. The Y and REE concentrations determined with this method were within the 5% error range of the ICP-MS reproducible for concentrations above 1 ppb. For each sample run Ba concentration was checked, but its concentration was below the detection limit.

For Nd isotope analysis the same liquid–liquid extraction procedure was used for a first preconcentration step. To achieve the required minimum quantity of 20 ng Nd necessary for measurement by TIMS, up to 80 g of salt were dissolved in 3.2 l of water and extracted. The resulting bulk REE fractions were purified from organic traces and remaining salts using 1 ml quartz columns with cation-exchange resin (AG 50W-X8, 200–400 mesh) and distilled HCl 1.5 M, 4 M and 6 M as eluents. Neodymium was separated from the purified bulk REE fractions using the same type of column and resin and α-hydroxyisobutyric acid as eluent. The total procedure blank of the liquid–liquid extraction and the subsequent column separation was <0.7 ng for Nd.

For Sr isotope analysis, 200 mg of salt were dissolved in 40 ml of bidistilled water, centrifuged and evaporated. Afterwards the samples underwent standard column separation procedures using 1 ml quartz columns with cation-exchange resin (AG 50W-X8, 200–400 mesh) and ammonium citrate, distilled HCl 1.5 M, 4 M and 6 M as eluents. The total Sr blank was <1.5 ng.

The Nd and Sr isotope analyses were performed on a fully automatic VG Sector mass spectrometer with a 5 cup multicollector. Neodymium was measured using a Ta-Re double filament assembly whereas Sr was deposited on W single filaments. The ratios $^{146}Nd/^{144}Nd = 0.7219$ and $^{86}Sr/^{88}Sr = 0.1194$ were used for fractionation correction. For Nd 40 to 100 ratios

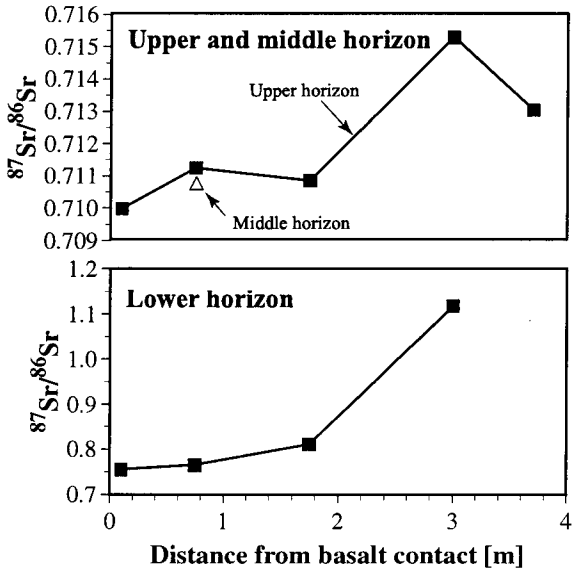

Fig. 4. The evolution of the Sr isotopic compositions with distance in the 3 salt horizons. Note the different *y*-axis scale in the diagram of the lower horizon.

were collected depending on the sample quantity available. For Sr typically 100 ratios were measured to achieve adequate precision. During the measuring period the NBS 987 Sr standard yielded $^{87}Sr/^{86}Sr = 0.710258 \pm 5$ ($\pm$s of the mean, $n = 9$) and the La Jolla Nd standard $^{143}Nd/^{144}Nd = 0.511871 \pm 5$ ($\pm$s of the mean, $n = 14$).

3. Results

3.1. Sr isotopes

The Sr isotope data are given in Table 1 and shown in Fig. 4. The 3 samples R 4250, R 4255 and R 4256 collected directly at the basalt contact have clearly higher Sr isotopic compositions than the basalt itself ($^{87}Sr/^{86}Sr = 0.704$). The values significantly increase in both upper and lower horizons with distance from the basalt contact. This trend is more regular in the lower horizon where the isotopic compositions reach more elevated values ($^{87}Sr/^{86}Sr = 1.12$ vs 0.715 in the upper horizon). The $^{87}Rb/^{86}Sr$ ratios show basically the same evolution as the Sr isotopic compositions (Table 1). The Sr concentrations show no systematic variations in the upper horizon, whereas they decrease with distance from the dyke in the lower horizon (Table 1).

The samples from the lower horizon appear at a glance to be aligned in the Sr mixing and the Rb–Sr isochron diagrams (Fig. 5a, b). However, this is in both cases essentially due to the extreme values of the most distant sample R 4259 (3.0 m). The remaining points are not aligned, which indicates that there is no simple mixing between 2 end-members. The samples from the upper horizon are somewhat aligned in the isochron diagram, whereas no alignment is observable in the mixing diagram (Fig. 5c, d). Thus, similar to the lower horizon, the data exclude a complete mixing between a basaltic and a salt Sr component for the upper horizon.

3.2. Rare earth elements (REE) and Nd isotopes

The REE and Nd isotope data are presented in Tables 2 and 3, respectively. The basalt-normalized REE distribution patterns of the 3 samples closest to the basalt are almost flat (Fig. 6). In the upper horizon, the REE distribution patterns show with increasing distance from the basalt contact a depletion of Ce, Pr, Nd, Sm, and Eu. The same kind of depletion, although less accentuated, can be observed in the lower horizon.

The Nd isotopic compositions of the 3 samples close to the basalt contact are, in contrast to their Sr isotopic compositions, almost basalt-like (Fig. 7). In the upper horizon, the ϵ_{Nd} values decrease slightly with distance. Only the most distant sample R 4254 has a clearly negative ϵ_{Nd} value of -1.37 which, however, still remains above values typical for continental crust or Permian seawater (Stille et al., 1996, and citations therein). In contrast, in the lower horizon the ϵ_{Nd} values decrease much faster and the 2 most distant samples approach seawater or crust-like values ($\epsilon_{Nd} = -7.37$ and -7.14). The data points of both levels are aligned neither in the Sm–Nd isochron nor in the Nd mixing diagrams (Fig. 8). However, a general decrease of the Nd isotopic compositions and concentrations with distance can be observed for both horizons. Simi-

Table 1
Rb–Sr isotope data of the salts and average values for the basalt. The errors given in parentheses for the $^{87}Sr/^{86}Sr$ ratios are ± 2 sigma mean values and refer to the last digits. The Rb and Sr concentrations are ICP-MS data

	Distance [m]	Rb [ppm]	Sr [ppm]	$^{87}Rb/^{86}Sr$	$^{87}Sr/^{86}Sr$
Upper horizon					
R 4250	0.10	7.91	117.01	0.1957	0.709990(10)
R 4251	0.75	26.76	168.19	0.4605	0.711253(11)
R 4252	1.75	46.95	535.83	0.2536	0.710857(11)
R 4253	3.00	83.12	178.26	1.3501	0.715297(13)
R 4254	3.70	88.10	173.72	1.4681	0.713052(10)
Middle horizon					
R 4255	0.75	59.92	624.65	0.2776	0.710738(10)
Lower horizon					
R 4256	0.10	57.38	3.09	53.8892	0.755478(10)
R 4257	0.75	46.61	2.85	47.5912	0.765613(27)
R 4258	1.75	70.25	2.76	74.2946	0.811169(12)
R 4259	3.00	57.27	0.94	183.8220	1.117723(14)
Average basalt ($n = 4$)					
		54.36	845.39	0.1860	0.703980

lar to the Sr isotope data, the Sm–Nd isotope data thus exclude simple mixing between a basalt and a salt component.

4. Discussion

4.1. Sr isotopes

The basalt has a Sr isotopic composition of about 0.704. The Sr isotopic compositions of the salts are clearly elevated with respect to this, even at the basalt contact ($^{87}Sr/^{86}Sr = 0.7099$). However, with distance the $^{87}Sr/^{86}Sr$ ratios of the salts increase, which shows that the compositions near the contact had been lowered during basalt intrusion. This implies that the fluids penetrating the salts contained, in spite of their elevated composition values, a basaltic Sr-component. The Sr isotope data thus trace the fluids, which accompanied the basaltic intrusion and demonstrate an exchange with the salts. A possible explanation for the relatively elevated $^{87}Sr/^{86}Sr$ ratio at the basalt contact could be that the basalt fluids had previously assimilated Sr with elevated isotopic compositions during the partial dissolution of an underlying halite formation.

The $^{87}Sr/^{86}Sr$ ratios are clearly lower and the Sr con-

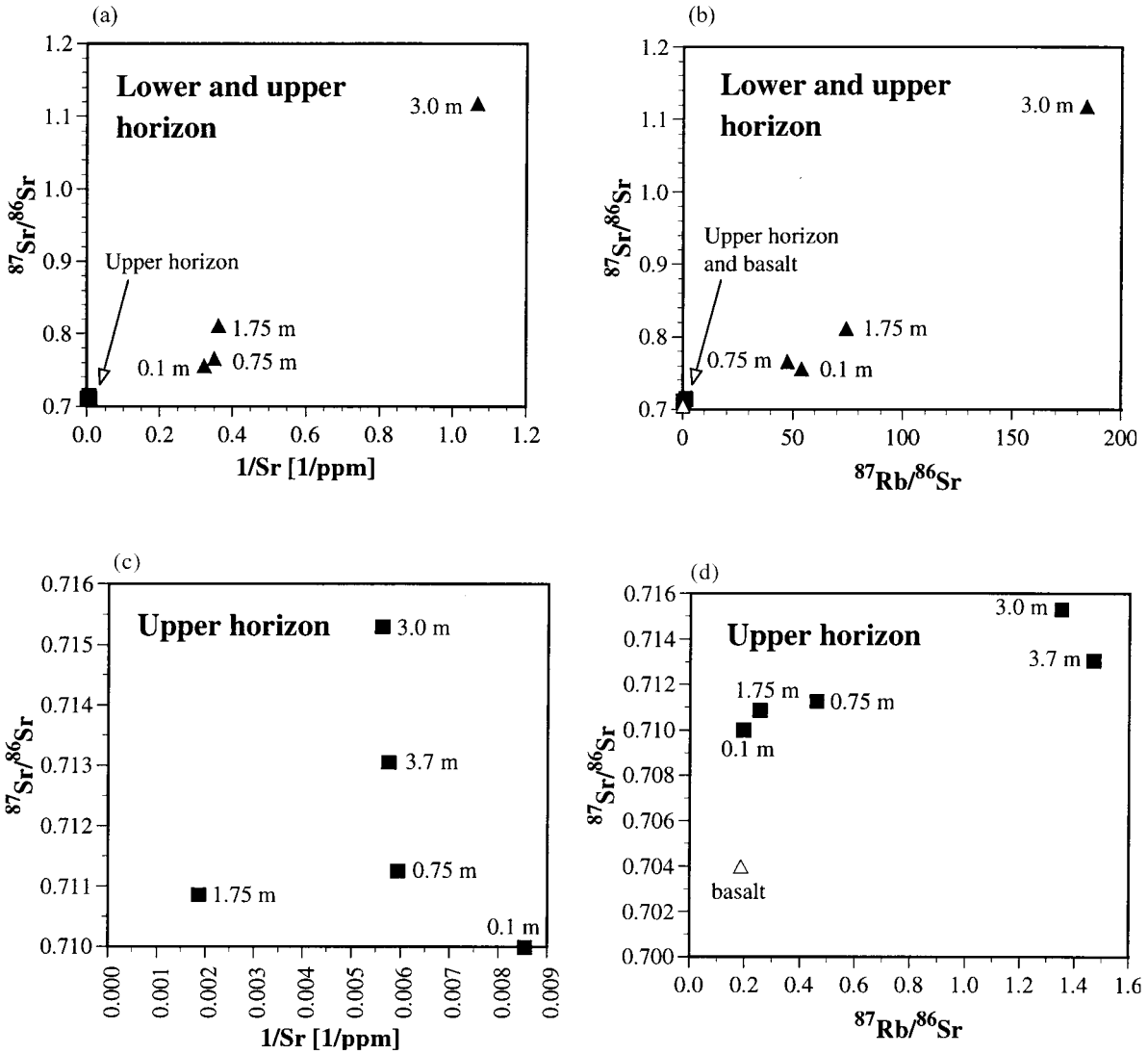

Fig. 5. Sr-mixing (a, c) and Rb–Sr isochron (b, d) diagrams of the salt samples of the lower (triangles) and upper (squares) horizon. In the isochron diagrams also the average basalt is shown (open triangle). The labels next to the sample symbols give the distance from the basalt contact.

Table 2
Y and REE concentrations of the salt samples and the average basalt. b.d.l. = below detection limit

	Y	La	Ce	Pr	Nd	Sm	Eu	Gd	Tb	Dy	Ho	Er	Tm	Yb	Lu
Upper horizon [ppb]															
R 4250	14.67	32.79	66.77	7.98	33.33	6.12	2.01	6.30	0.79	3.44	0.61	1.55	0.17	0.93	0.12
R 4251	4.34	12.84	13.03	1.09	4.00	0.65	0.20	0.89	0.12	0.63	0.14	0.42	0.06	0.39	0.07
R 4252	7.78	15.61	12.73	0.92	3.60	0.56	0.18	0.90	0.13	0.85	0.21	0.71	0.11	0.66	0.10
R 4253	9.12	3.36	4.50	0.58	3.21	1.36	0.70	2.39	0.39	2.05	0.36	0.89	0.11	0.60	0.09
R 4254	4.17	2.11	1.70	0.15	0.64	0.25	0.14	0.62	0.13	0.75	0.16	0.41	0.07	0.33	0.06
Middle horizon [ppb]															
R 4255	36.72	89.20	183.24	21.20	83.08	14.69	4.95	14.10	1.77	8.26	1.47	4.03	0.50	3.04	0.44
Lower horizon [ppb]															
R 4256	1.71	5.25	10.46	1.22	4.82	0.83	0.28	0.79	0.10	0.43	0.07	0.20	0.03	0.13	0.02
R 4257	0.77	2.66	4.33	0.43	1.55	0.24	0.08	0.26	0.04	0.18	0.03	0.09	b.d.l.	0.06	b.d.l.
R 4258	0.49	0.50	0.56	0.06	0.31	0.06	0.02	0.11	0.02	0.11	0.02	0.05	b.d.l.	0.03	b.d.l.
R 4259	0.49	0.58	0.83	0.10	0.44	0.09	0.03	0.11	0.02	0.11	0.02	0.06	b.d.l.	0.04	b.d.l.
Average basalt (n = 6) [ppm]	29.03	65.44	131.21	15.35	58.59	10.41	3.18	8.53	1.22	5.96	1.11	2.69	0.38	2.03	0.31

centrations higher in the upper than in the lower horizon. This indicates that fluid flow was more important in the upper than in the lower horizon, which is also in agreement with the more advanced salt metamorphism of the upper layer (Fig. 3). However, a quantitative comparison of the fluid flow in the 2 layers is not possible because a clear mixing relation is lacking in the Sr mixing diagram. The lack of such a relation furthermore suggests that the exchange between the fluids and the salts was irregular and excludes complete melting or dissolution of the salts during fluid penetration.

4.2. Rare earth elements (REE) and Nd isotopes

The basalt-like REE distribution patterns and the almost basaltic Nd isotopic compositions of the 3 salt samples collected at the basalt-salt contact point to a basaltic origin of the rare earths. The subsequent modification of the patterns with increasing distance from the contact must have occurred during migration of the rare earths in the salt because of the basalt-like patterns of the contact samples. The process controlling this evolution of the patterns could be mixing between a basalt and a salt end-member or fractionation of the rare earths during migration. In order to test which of these 2 possibilities is true, the observed REE patterns of the upper and lower horizon have been compared with calculated mixing patterns.

The calculation of the mixing patterns is based on the assumption that the samples of each salt horizon

Table 3
Sm–Nd isotope data of the salts and average values for the basalt. The errors given in parentheses for the $^{143}Nd/^{144}Nd$ ratios are ± 2 sigma mean values and refer to the last digits. The ϵ_{Nd} values are chondrite normalized $^{143}Nd/^{144}Nd$ ratios and calculated according to the relation $\epsilon_{Nd} = 10^4 \cdot ((^{143}Nd/^{144}Nd\text{-}0.512638)/0.512638)$. See Table 2 for Sm and Nd concentration data

	$^{147}Sm/^{144}Nd$	$^{143}Nd/^{144}Nd$	ϵ_{Nd}
Upper horizon			
R 4250	0.1111	0.512778(6)	2.73
R 4251	0.0984	0.512644(10)	0.12
R 4252	0.0943	0.512624(19)	−0.27
R 4253	0.2556	0.512717(13)	1.54
R 4254	0.2367	0.512568(13)	−1.37
Middle horizon			
R 4255	0.1070	0.512807(4)	3.30
Lower horizon			
R 4256	0.1045	0.512794(6)	3.04
R 4257	0.0951	0.512683(6)	0.88
R 4258	0.1128	0.512260(31)	−7.37
R 4259	0.1193	0.512272(9)	−7.14
Average basalt (n = 3)			
	0.1071	0.512845	4.04

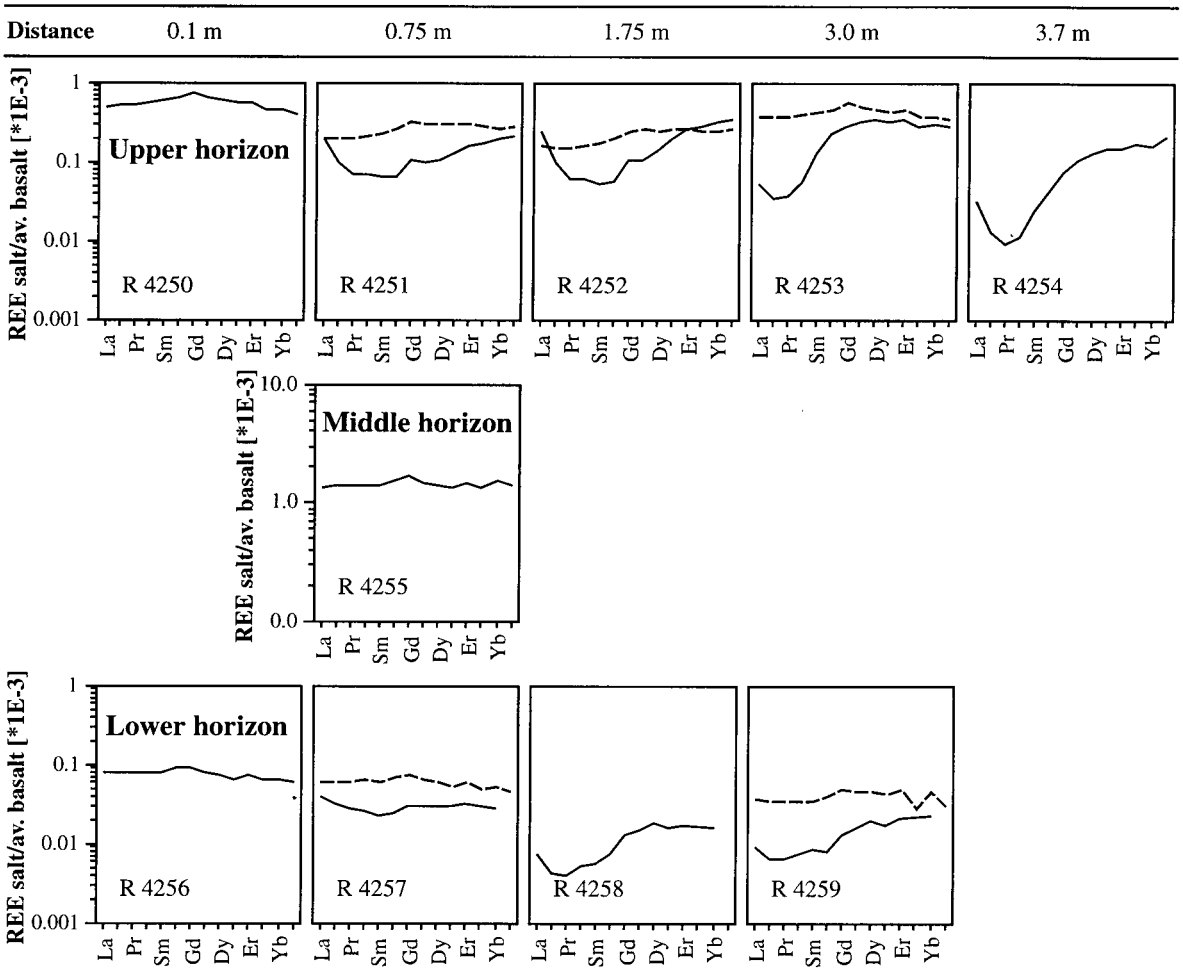

Fig. 6. Basalt-normalized REE distributions of the salt samples (black lines). Note the depletion of Ce, Pr, Nd, Sm, and Eu appearing with distance in the upper and the lower horizon. The dashed lines are calculated patterns discussed in Section 4.2. Rare earth elements (REE) and Nd isotopes.

represent binary mixtures between the sample with the highest and the lowest ϵ_{Nd} values and that the REE behaved conservatively during mixing, as has been demonstrated in several studies (e.g., Westerlund and Ohman, 1992; Zhang and Nozaki, 1996). The end-members with the highest and the lowest ϵ_{Nd} values, respectively, are the contact and the most distant sample in the upper horizon, and the contact sample and sample R 4258 at 1.75 m in the lower horizon. The portion of the 2 end-members contained in each mixture has been calculated from the Nd isotopic compositions by the formula:

$$\%\ \text{REE of sample with } \epsilon_{Nd}\ \text{max} = 100^{*}\left(\frac{^{143}Nd/^{144}Nd_{sample} - ^{143}Nd/^{144}Nd_{min}}{^{143}Nd/^{144}Nd_{max} - ^{143}Nd/^{144}Nd_{min}}\right)$$

Taking these percentages and the patterns of the 2 extreme samples, the synthetic patterns shown in Fig. 6 have been calculated by the simple mixing formula:

$$\{\%\ \text{REE}_{\epsilon_{Nd}\ \text{max}} \times \text{REE pattern}_{\epsilon_{Nd}\ \text{max}}\} + \{(100 - \%\ \text{REE}_{\epsilon_{Nd}\ \text{max}}) \times \text{REE pattern}_{\epsilon_{Nd}\ \text{min}}\}.$$

The calculated patterns are in most cases almost flat and show no similarities with the observed patterns. Therefore it can be concluded that the observed evolution of the REE distributions cannot be attributed to mixing but must be due to a fractionation process as already indicated by the lack of a clear linear alignment in the Nd mixing diagram (Fig. 5). An additional argument against mixing is that the samples with strongest depletions of the light rare earths (LREE) do not have the lowest ϵ_{Nd} values.

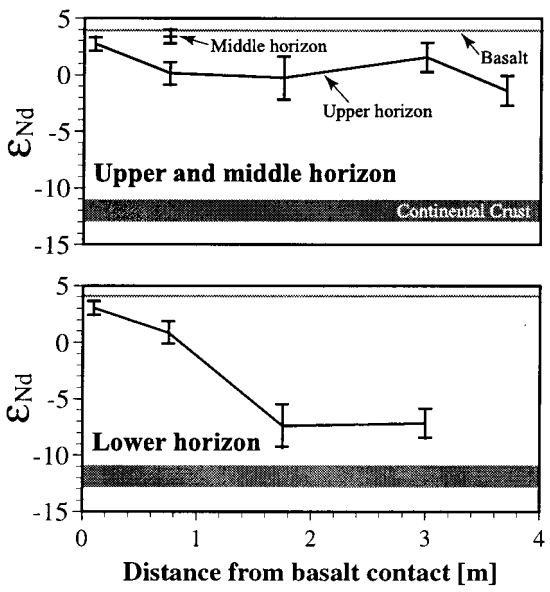

Fig. 7. The evolution of the Nd isotopic compositions with distance in the three salt horizons together with the compositions of average basalt and average continental crust. The error bars represent ±2 sigma mean values of the individual measurements. Continental crust data are from Stille et al. (1996).

Consequently, the calculations indicate that it was fractionation during REE transport that led to the observed evolution of the REE distribution patterns, and not mixing. For this fractionation basically 2 mechanisms can be envisaged: (a) greater solubility of the LREE in the fluid; or (b) preferential scavenging of the LREE by an accessory phase which remained unaffected when the salt samples were dissolved in water acidified to pH 2 (see Section 2.2. Analytical methods). In case "a", it would have been solution complexation which led to increased solubility of the LREE in the fluid. As a consequence, LREEs could be leached from the salts and transported out of the profile. Alternatively, the solubility of a REE scavenging mineral phase may have varied as a function of the atomic number of the coprecipitated rare earths and been greater for the LREE end-member. In case "b", it would have been surface complexation or coprecipitation that preferentially bound the LREE to an accessory phase. This process would have led to a repartitioning of the REE with an enrichment of the LREE in the water-insoluble accessory phase. In this case, the LREE depleted in the salts would have remained within the profile.

It has been proposed earlier (Steinmann and Stille, 1998) that complexation of the rare earths with Cl^- could be a possible process to explain the observed fractionation of the rare earths by option "a". One of the main arguments was, besides the high Cl^- concentrations of the brines, a plot of the stability constants of REE–Cl^- complexes, which yields an inverse mirror image of the REE patterns found for the most fractionated samples (Fig. 9).

In a first step, such a process could in fact produce a depletion of the LREE in the solid phase because the LREE would preferentially remain in the fluid. However, the residual fluid would be enriched in LREE which would, after repeated precipitation steps, probably compensate the better solubility of the LREE. The more distant salt samples should consequently be characterized by LREE-enrichment rather than depletion. Therefore, differential complexation with Cl^- cannot explain the increasing fractionation of the rare earths with distance from the basalt dyke. An additional argument against Cl^- solution complexation is the small variation of the log β_{Cl} values which only vary by 0.1 log units (Fig. 9).

Therefore, the authors prefer an interpretation in which the REE have been fractionated by a "b"-type mechanism, i.e., by preferential scavenging of the LREE by an accessory phase. In a previous study on REE mobilization during corrosion of the adjacent basalts, it could be shown that the REE had been mobilized in the basalts by dissolution of REE-bearing magmatic apatites (Steinmann et al., 1999). These rare earths were almost re-immobilized in situ by precipitation of secondary apatites strongly enriched in light rare earths (Fig. 10).

Similarly to this, precipitation of LREE-enriched phosphate minerals in the salt could explain the observed fractionation of the rare earths. The increase of REE-fractionation with distance would in this model be due to increasing precipitation of phosphate triggered by decreasing fluid temperature.

The Sr isotope data have shown that fluid flow was stronger in the upper than in the lower salt horizon. This is in agreement with the observation that REE concentrations are higher and fractionation stronger in the upper than in the lower horizon, simply because more rare earths and P of basaltic origin entered with the fluids the upper horizon. The larger amount of P in the upper horizon led to the precipitation of larger quantities of phosphate and thus to a stronger fractionation of the REE patterns.

The hypothesis that the observed fractionation of the REE is essentially due to coprecipitation of phosphate minerals is in agreement with the in situ observation and modeling of Byrne and Kim (1993) and Johannesson et al. (1995), and with an experimental study of Byrne et al. (1996). The experimental data of Byrne et al. (1996) show that phosphate coprecipitation leads, in the presence of a high degree of solution complexation, to HREE and La-enrichment in

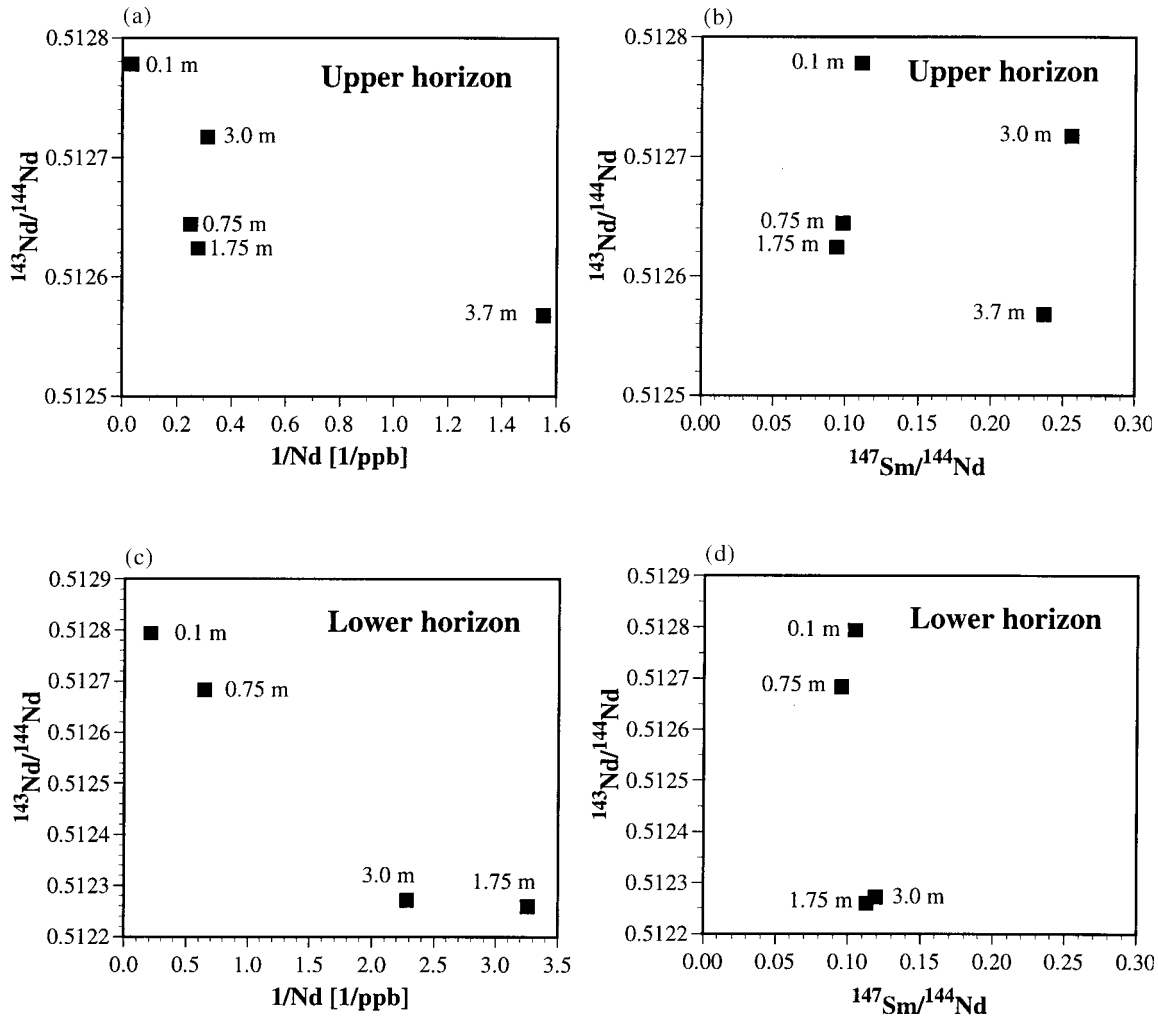

Fig. 8. Nd-mixing (a, c) and Sm–Nd isochron (b, d) diagrams of the salt samples. The labels next to the sample symbols give the distances from the basalt contact.

the remaining solution, a signature that is in the present case preserved in the salt samples. The fractionated REE patterns of the salt samples are compared with the experimental data of Byrne et al. (1996) in Fig. 11 and one can observe a general agreement of the data. In order to verify this hypothesis of phosphate coprecipitation, an attempt was made to analyze REE and P concentrations in the water-insoluble salt residues of the samples. This was, however, not possible because of the small quantities of solid phases extracted from the salts.

5. Summary and conclusions

The Sr isotope data show that brine flow was more important in the upper than in the lower horizon and exclude melting or complete dissolution of the salts during fluid penetration.

The ϵ_{Nd} values of the salts in the upper and lower horizon close to the dyke contact are high (+3.3) and close to those of the basaltic melt (+4). This demonstrates together with the basalt-like REE patterns of the contact samples that the REE contained in the salts have directly been mobilized in the adjacent basalt and then been transported into the salts by migrating brines.

The REE data document a strong depletion of the light rare earths during migration in the salt. The REE concentration and Nd isotope data exclude that this evolution is due to mixing between a basalt and a salt end-member or due to selective

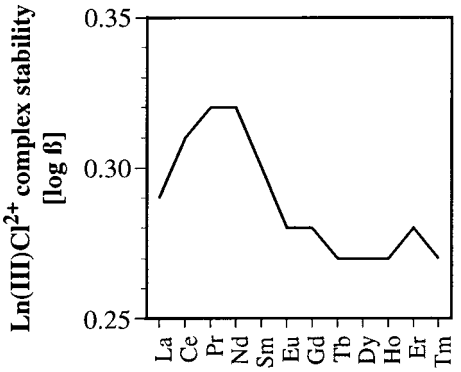

Fig. 9. Plot of the complex stability constants of $Ln(III)Cl^{2+}$ lanthanide complexes. The constants are infinite dilution values from Millero (1992). The values for Yb and Lu are below 0.25 and not shown to limit the scale of the figure (Yb = 0.16; Lu = −0.03).

solution complexation. Most probably it was precipitation of LREE-enriched phosphate minerals during migration of the brine, which fractionated the rare earths.

The salt-study therefore suggests that coprecipitation of the rare earths with accessory minerals such as phosphates, might be an important process to remove rare earths from brines and to fractionate their distribution patterns. This is in agreement with earlier studies based on in situ observation and modeling (Byrne and Kim, 1993; Johannesson et al., 1995), and on experimental data (Byrne et al., 1996). Coprecipitation with phosphates seems to remove Ce, Pr, Nd, Sm and Eu more easily from the brine than the other rare earths. This finding could be of interest for the mobility of trivalent Am and Cm in a radioactive waste salt repository, because for these elements owing to their

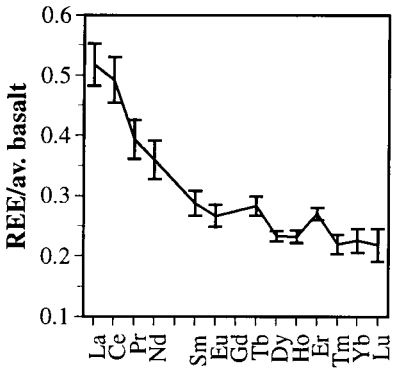

Fig. 10. REE distribution pattern of secondary apatites of an adjacent basalt dyke (data from Steinmann et al., 1999).

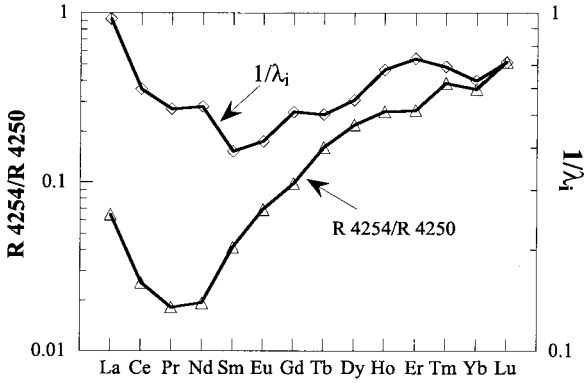

Fig. 11. Comparison of REE fractionation in the salts with fractionation factors λ_i determined by Byrne et al. (1996) from experimental data for REE coprecipitation with phosphate. REE fractionation in the salts is illustrated by the ratio of samples R 4254/R 4250, which are the 2 extreme samples of the upper salt horizon. The λ_i values are plotted in reciprocal form in order to show REE fractionation in the remaining solution from which phosphate has precipitated.

almost identical ionic radii, an almost analogous geochemical behaviour is expected as for Sm and Nd (Choppin, 1983; Krauskopf, 1986).

Acknowledgements

We thank M. de Boisseson, J. Paumard, J. Samuel and D. Tisserant for their assistance in the laboratory. We are especially grateful to A. Tricca for support and helpful discussions during the development of the analytical methods. S. Wood and K. Johannesson are thanked for their constructive reviews. MS profited from a fellowship of the Swiss National Science Foundation, which is highly acknowledged.

References

Braitsch, O., 1971. Salt deposits. Their Origin and Composition. Springer-Verlag, Berlin–Stuttgart–Heidelberg–New York.

Byrne, R.H., Kim, K.-H., 1993. Rare earth precipitation and coprecipitation behavior: The limiting role of PO_4^{3-} on dissolved rare earth concentrations in seawater. Geochim. Cosmochim. Acta 57, 519–526.

Byrne, R.H., Liu, X., Schijf, J., 1996. The influence of phosphate coprecipitation on rare earth distributions in natural waters. Geochim. Cosmochim. Acta 60, 3341–3346.

Choppin, G.R., 1983. Comparison of the solution chemistry of the actinides and the lanthanides. J. Less-Common Met. 93, 232–330.

Fisher, R.S., Kreitler, C.W., 1987. Geochemistry and hydro-

dynamics of deep-basin brines, Palo Duro Basin Texas, USA. Applied Geochem. 2, 459–476.

Gammons, C.H., Wood, S.A., Williams-Jones, A.E., 1996. The aqueous geochemistry of the rare earth elements and yttrium: VI. Stability of neodymium chloride complexes from 25 to 300°C. Geochim. Cosmochim. Acta 60, 4615–4630.

Gutsche, A., 1988. Mineralreaktionen und Stofftransporte an einem Kontakt Basalt-Hartsalz in der Werra-Folge des Werkes Hattorf. Unpubl. diploma thesis, Georg-August-Universität Göttingen.

Haas, J.R., Shock, E.L., Sassani, D.C., 1995. Rare earth elements in hydrothermal systems: Estimates of standard partial molal thermodynamic properties of aqueous complexes of the rare earth elements at high pressures and temperatures. Geochim. Cosmochim. Acta 59, 4329–4350.

Hartmann, H., 1969. Investigations of Atlantis II Deep samples taken by the FS Meteor. In: Degens, E.T., Ross, D.A. (Eds.), Hot Brines and Recent Metal Deposits in the Red Sea. Springer, New York, pp. 204–207.

Herrmann, A.G., Knake, D., Schneider, J., Peters, H., 1973. Geochemistry of modern seawater and brines from salt pans: Main components and bromine distribution. Contr. Mineral. Petrol. 40, 1–24.

Herrmann, A.G., Siebrasse, G., Könnecke, K., 1978. Computerprogramme zur Berechnung von Mineral- und Gesteinsumbildungen bei der Einwirkung von Lösungen auf Kali- und Steinsalzlagerstätten (Lösungsmetamorphose). Kali u. Steinsalz 7, 288–299.

Johannesson, K.H., Lyons, W.B., Stetzenbach, K.J., Byrne, R.H., 1995. The solubility control of rare earth elements in natural terrestrial waters and the significance of PO_4^{3-} and CO_3^{2-} in limiting dissolved concentrations: A review of recent information. Aquat. Geochem. 1, 157–173.

Johannesson, K.H., Lyons, W.B., Yelken, M.A., Gaudette, H.E., Stetzenbach, K.J., 1996. Geochemistry of the rare-earth elements in hypersaline and dilute acidic natural terrestrial waters: Complexation behavior and middle rare-earth element enrichments. Chem. Geol. 133, 125–144.

Knipping, B., 1989. Basalt Intrusions in Evaporites. Springer-Verlag, Berlin.

Knipping, B., Herrmann, A.G., 1985. Mineralreaktionen und Stofftransporte an einem Kontakt Basalt-Carnallitit im Kalisalzhorizont Thüringen der Werra-Serie des Zechsteins. Kali u. Steinsalz 9, 111–124.

Krauskopf, K.B., 1986. Thorium and rare-earth elements as analogues for actinide elements. Chem. Geol. 55, 323–335.

Millero, F.J., 1992. Stability constants for the formation of rare earth inorganic complexes as a function of ionic strength. Geochim. Cosmochim. Acta 56, 3123–3132.

Shabani, M.B., Akagi, T., Shimizu, H., Masuda, A., 1990. Determination of trace lanthanides and yttrium in seawater by inductively coupled plasma mass spectrometry after preconcentration with solvent extraction and back-extraction. Anal. Chem. 62, 2709–2714.

Steinmann, M., Stille, P., 1998. Strongly fractionated REE patterns in salts and their implications for REE migration in chloride-rich brines at elevated temperatures and pressures. C.R. Acad. Sci. Paris, série II a 327, 173–180.

Steinmann, M., Stille, P., Bernotat, W., Knipping, B., 1999. The corrosion of basaltic dykes in evaporites: Ar–Sr–Nd isotope and REE evidence. Chem. Geol. 153, 259–279.

Stille, P., Steinmann, M., Riggs, S.R., 1996. Nd isotope evidence for the evolution of the paleocurrents in the Atlantic and Tethys Oceans during the past 180 Ma. Earth Planet. Sci. Lett. 144, 9–20.

Tricca, A., Stille, P., Steinmann, M., Kiefel, B., Samuel, J., Eikenberg, J., 1999. Rare earth elements and Sr and Nd isotopic compositions of dissolved and suspended loads from small river systems in the Vosges mountains (France), the river Rhine and groundwater. Chem. Geol. 16, 139–158.

Westerlund, S., Ohman, P., 1992. Rare earth elements in the Arctic Ocean. Deep Sea Research 39, 1613–1626.

Zhang, J., Nozaki, Y., 1996. Rare earth elements and yttrium in seawater: ICP-MS determinations in the East Caroline, Coral Sea, and Fiji basins of the South Pacific Ocean. Geochim. Cosmochim. Acta 60, 4631–4644.

Basaltic dykes in evaporites: a natural analogue

Marc Steinmann and Peter Stille

Geological Society, London, Special Publications 2004; v. 236; p. 135-142
doi:10.1144/GSL.SP.2004.236.01.09

Basaltic dykes in evaporites: a natural analogue

MARC STEINMANN[1] & PETER STILLE[2]
[1]*Département de Géosciences, Université de Franche-Comté, Besançon, France*
(e-mail: marc.steinmann@univ-fcomte.fr)
[2]*ULP-EOST-CNRS, Centre de Géochimie de la Surface UMR 7517, Strasbourg, France*
(e-mail: pstille@illite.u-strasbg.fr)

Abstract: We present rare earth element (REE) data of basalt and salt samples from central Germany where basaltic dykes of Tertiary age crosscut Upper Permian rock and potash salt. The glassy rims of the dykes can be considered as a natural analogue for the corrosion of nuclear waste glass in a salt repository, whereas the REE data from the salt can serve as an analogue for radionuclide migration in salt next to a leaking nuclear waste repository because the light rare earths (LREE) have a geochemical behavior similar to that of some actinides.

Our basalt data demonstrate mobility and fractionation of the REE during postintrusive circulation of salt brines. The processes controlling this behavior of the REE were dissolution and reprecipitation of phosphate minerals. The salt data show that a small portion of the REE has left the basalt during postintrusive fluid circulation and migrated into the salt where a strong depletion of the LREE can be observed with increasing distance from the basalt contact. This fractionation is most probably due to precipitation of LREE-enriched accessory minerals such as apatite. In analogy to this, a similar behavior might be expected from actinides such as Am and Cm, which would in the case of a leaking salt nuclear waste repository probably be immobilized when phosphate minerals are present in the backfill material.

The repository analogy

Salt deposits are potential host rocks for the disposal of high-level radioactive waste. In this chapter we will present data from the Werra–Fulda district (northern Germany) where Upper Permian (Zechstein) salt is crosscut by numerous basalt dykes of Miocene age.

The chilled margins of the dykes are glassy and can therefore, as proposed by Ewing (1979), be used as a natural analogue for the long-term behaviour of vitrified high-level radioactive waste (HLW) glass in a salt environment. Several studies have shown that similar alteration products form on both nuclear waste and natural glasses in spite of differences in the chemical composition between natural basalt and synthetic HLW borosilicate glass (Malow *et al.* 1984; Byers *et al.* 1985; Crovisier *et al.* 1992; Lutze & Grambow 1992; Petit 1992; Abdelouas *et al.* 1994; Daux *et al.* 1997).

The unique setting of the Werra–Fulda district allows not only the study of basalt alteration, but also the ability to trace basalt-derived elements within the salt. The study site is thus, on one hand, a natural analogue for the long-term corrosion expected for nuclear waste glass in contact with salt brines, and on the other hand, a natural analogue for radionuclide migration in salt next to a leaking salt repository. We will focus mainly on the behaviour of the rare earth elements (REE) during basalt alteration and fluid migration in the salt. The REE are of particular interest for natural analogue studies because they are considered to be chemical analogues for the actinides Am and Cm (Choppin 1983; Krauskopf 1986; Seaborg 1993; Silva & Nitsche 1995). The basalt–salt reaction zones have been studied in detail previously (Steinmann & Stille 1998; Steinmann *et al.* 1999, 2001) and the reader is referred to these earlier publications for analytical details and raw data. The aim of the present article is to give an overview on REE behaviour at basalt–salt contacts and to contribute to radionuclide behaviour during HLW glass corrosion and radionuclide migration in salt formations.

The study site

The evaporites of the Werra–Fulda potash district were deposited during the Upper Permian (Zechstein). The series has a total thickness of

From: GIERÉ, R. & STILLE, P. (eds) 2004. *Energy, Waste, and the Environment: a Geochemical Perspective*. Geological Society, London, Special Publications, **236**, 135–141.
0305-8719/04/$15

up to 400 m. The most important salt is halite (NaCl), followed by thinner horizons of potash salt and anhydrite ($CaSO_4$). The series contains two important potash salt horizons, mainly consisting of carnallite ($KMgCl_3 \cdot 6H_2O$), which are mined at depths of about 800 m. The thickness of these horizons varies between 2 and 10 m.

In the Tertiary, basaltic dykes intruded the evaporite. Small flakes of newly formed clay minerals cover the basalt surface at the contact with the evaporite. In the underground mines, the basalt is exposed as subvertical dykes, which can be followed horizontally over several kilometres. All basalt–salt contacts discussed here are located in underground mines in the two potash salt horizons mentioned above.

Near the basalt contacts, in a zone of less than 3 m width, the potash salt has been transformed mainly into halite and sylvite (KCl) by fluids saturated in NaCl. These fluids accompanied the basaltic melt and became saturated in NaCl during upward migration by the partial dissolution of an underlying, up to 100 m thick, halite formation (Knipping & Herrmann 1985; Gutsche 1988; Knipping 1989). During the metamorphism of the potash salt, the NaCl-fluids were mixed with fluids originating from the potash salt and the resulting mixture subsequently altered the basalt and transported basalt-derived trace elements such as Sr and REE into the salt (Steinmann *et al.* 1999, 2001). The study of the alteration of the basalt presented here is based on a detailed profile across a dyke of about 50 cm width (Fig. 1), whereas trace element migration in the salt has been studied in another outcrop in a 4 m long horizontal salt profile (Fig. 2).

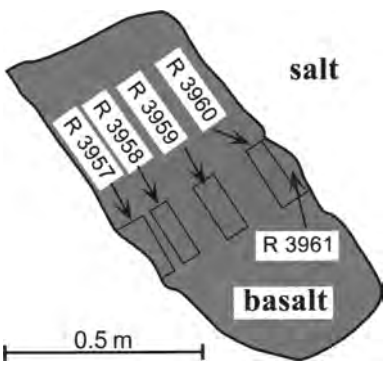

Fig. 1. Detailed cross-section of the basalt dyke with sampling points of samples R 3957 to R 3960. The dyke is conserved as an isolated tectonic boudin embedded in potash salt.

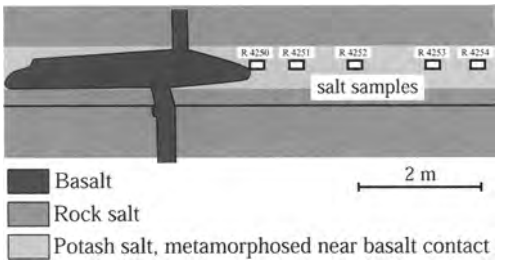

Fig. 2. The salt profile studied here is situated next to a basalt dyke, which is locally enlarged to an apophysis. The sampling points in the salt are indicated by the small rectangles numbered R 4250 to R 4254.

Mobility of the REE during basalt corrosion

In order to obtain information about the exchange processes between the basalt and the salt, leaching experiments were performed with 1.5 M HCl on basalt powder samples that had previously been washed in bi-distilled water in order to remove salt minerals. The H_2O-washed whole rock samples, as well as the resulting leachate and residue fractions have been analysed for major elements, REE, and for Sr isotopes.

A key problem in the present natural analogue study is the distinction between chemical variations related to trace element migration during basalt alteration and variations due to magmatic fractionation and other syn-intrusive processes. The detailed evaluation of the available data has shown that the chemical and isotopic composition of the HCl residues is largely controlled by fractional crystallization and syn-intrusive assimilation of salt. In contrast, the chemical composition of the leachates is strongly modified by post-intrusive alteration (Steinmann *et al.* 1999).

For both HCl leachates and HCl residues, a positive correlation between ΣREE and P_2O_5 has been found suggesting that phosphate is an important REE carrier in both cases (Fig. 3). The positive correlation between La/Yb and P_2O_5 furthermore indicates that the REE carrier phase is enriched in the light REE (LREE, La–Nd). Such an LREE enrichment is characteristic for phosphate minerals such as apatite, which is in agreement with the suggestion that phosphate is the principal REE carrier in the leachable phase and in the residues.

A plot of the average REE distribution patterns of the leachates and residues normalized to the H_2O-washed whole rock data shows that they have complementary patterns (Fig. 4). Furthermore the data show that leaching removed

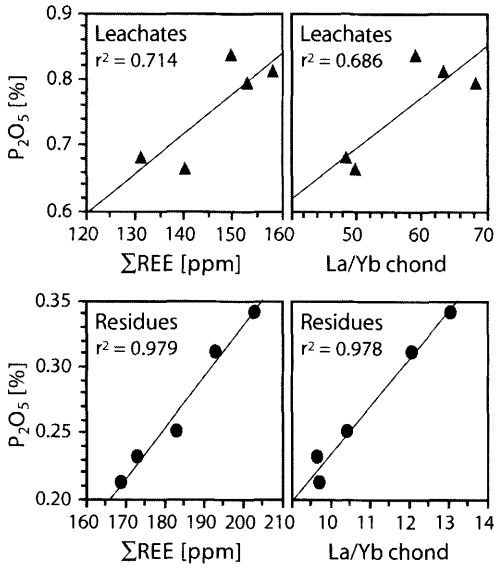

Fig. 3. Correlations of ∑REE and chondrite normalized La/Yb ratios with P_2O_5 for the HCl leachates and residues of the basalt samples.

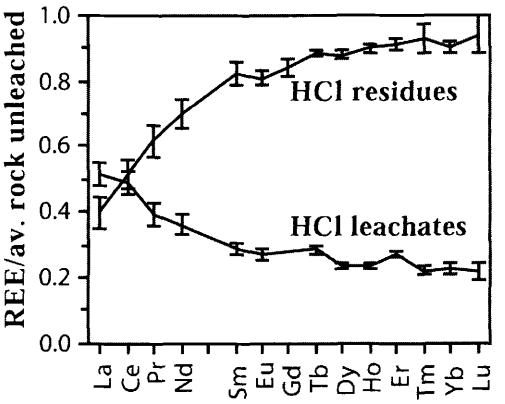

Fig. 4. Average REE concentrations with standard deviations of the 5 HCl leachates and residues normalized to the average concentrations of the H_2O-washed whole rock.

almost 50% of the total REE content, in the case of La even more. The leachable phosphate is more enriched in the LREE than the residual one. Such an enrichment of the LREE is typical for a secondary Al-phosphate such as florencite or rhabdophane and has been described in several weathering profiles (Duddy 1980; Tazaki *et al.* 1987; Banfield & Eggleton 1989; Braun *et al.* 1990, 1993; Prudêncio *et al.* 1993; Macfarlane *et al.* 1994) and in hydrothermal deposits (Nasraoui *et al.* 2000). A comparative study of weathered and unweathered phosphate by Tazaki *et al.* (1987) has shown that weathered phosphate is characterized by a less ordered lattice structure. This could in our case explain why leaching with HCl removed in a very selective way essentially secondary and not primary phosphate.

The only primary phosphate mineral in the basaltic groundmass is an idiomorphic acicular apatite, which we therefore regard as the most probable primary REE carrier in the residues. However, the REE concentrations of this apatite were below the detection limit of the EDS device of our SEM.

The secondary phase that contained the leachable REE was identified in alteration rims around small salt inclusions in the peripheral parts of the dyke where numerous phosphate grains with high REE concentrations occur in association with secondary sheet silicates (Fig. 5). This secondary phosphate could be identified as REE–chlorapatite [$Ca_2La_{0.5}CeNd_{0.5}(PO_4)_3Cl$] and its high REE content is demonstrated by EDS element maps (Fig. 6).

In summary, the study of the basalt dykes shows that the REE of the primary basalt have been mobilized during basalt alteration, most probably by dissolution of primary apatite. This mobilization was strongest in the intermediate samples R 3958 and R 3960 (Fig. 1) and the mobilized REE were subsequently immobilized by precipitation of secondary apatite.

Migration of the REE in the salts

In order to trace the migration of basalt-derived REE in the salt, REE distribution patterns (Fig. 7) and Nd isotopic compositions (Fig. 8) have been determined in a salt horizon adjacent to a basalt dyke (Fig. 2). The flat REE distribution patterns and the almost basaltic Nd isotopic composition of the salt samples collected at the basalt–salt contact point to a basaltic origin of the REE for this sample. With increasing distance from the contact, the patterns are more and more depleted in Ce, Pr, Nd, Sm, and Eu and the Nd isotopic compositions are slightly shifted towards lower ε_{Nd} values, which, however, still remain above values typical for continental crust or Permian seawater (Stille *et al.* 1996, and citations therein). This evolution of the REE distribution patterns and the Nd isotopic compositions could basically be due to mixing between a basalt and a salt end member or, alternatively, it could have been fractionation of the REE during migration in the salt that modified the REE patterns.

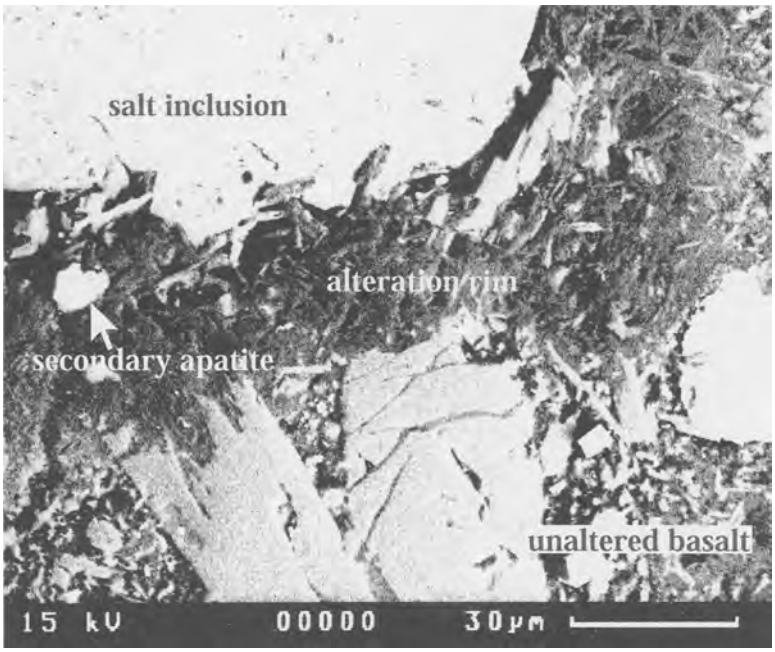

Fig. 5. SEM photograph showing a secondary apatite crystal within a rim of altered basalt around a salt inclusion. The other minerals contained in the rim are sheet silicates and hematite.

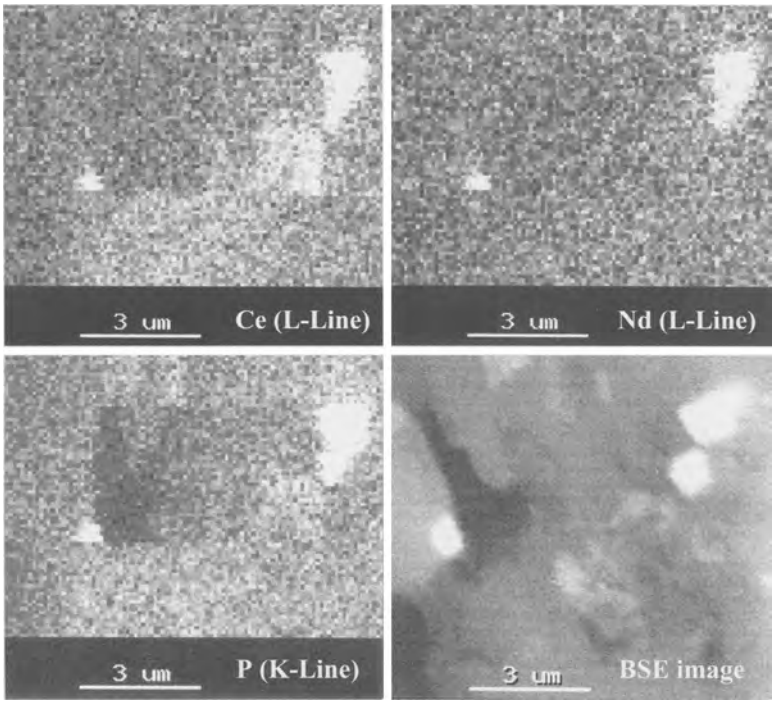

Fig. 6. Element maps of Ce, Nd, and P demonstrating the high REE content of the secondary apatite. The elevated REE concentrations lead to the high contrast of the apatite in the backscattered electron (BSE) image.

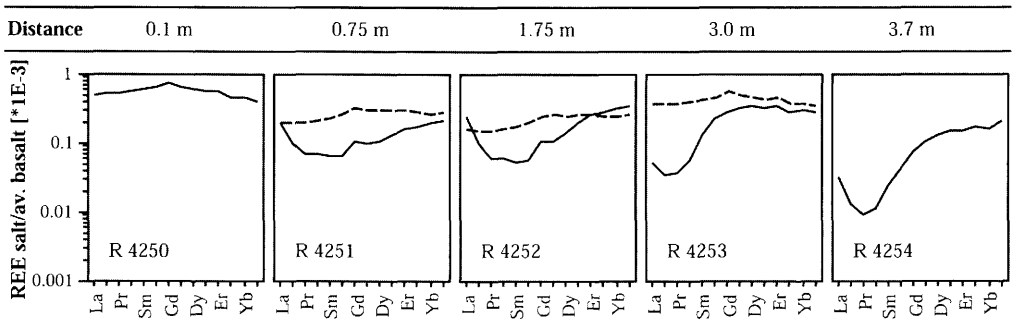

Fig. 7. Basalt normalized REE distributions of the salt samples R 4250 to R 4254 from 0.1 to 4.7 m from the basalt contact. The solid lines show the measured REE distributions. Note the depletion of Ce, Pr, Sm, and Eu appearing with distance. The dashed lines are calculated mixing patterns discussed in the text. See Fig. 2 for sample locations.

The Nd isotopic compositions of the salt give valuable information to test these two hypotheses. The lack of an alignment in the Nd-mixing diagram (not shown) is a first indication that the observed modification of the REE patterns cannot be due to mixing (Steinmann *et al.* 2001). In addition, hypothetical REE patterns have been calculated for the three intermediate samples R 4251, R 4252, and R 4253 by using a binary mixing model and the sample R 4250 from the basalt contact and the most distant sample R 4254 as end members. First, the percentage of REE derived from the contact sample R 4250 has been calculated for each of the three intermediate samples on the basis of their Nd isotopic compositions and the Nd isotopic compositions of the two end members from equation (1):

$$\%\ \mathrm{REE}_{\mathrm{R\,4250}} = 100 \times \left(\frac{^{143}\mathrm{Nd}/^{144}\mathrm{Nd}_{\mathrm{sample}} - {}^{143}\mathrm{Nd}/^{144}\mathrm{Nd}_{\mathrm{R\,4254}}}{^{143}\mathrm{Nd}/^{144}\mathrm{Nd}_{\mathrm{R\,4250}} - {}^{143}\mathrm{Nd}/^{144}\mathrm{Nd}_{\mathrm{R\,4254}}} \right) \quad (1)$$

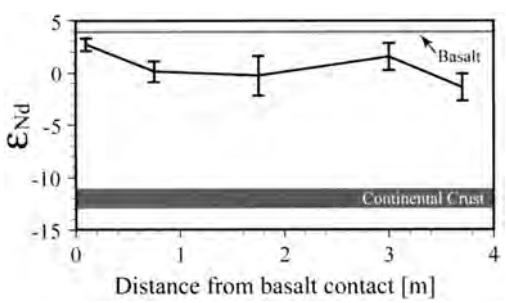

Fig. 8. The evolution of the Nd isotopic compositions with distance in the salt profile together with the compositions of average basalt and average continental crust. The error bars represent ±2 sigma mean values of the individual measurements.

Afterwards, the percentage calculated in equation (1) has been used together with the REE patterns of the two end members to calculate a hypothetical REE mixing pattern for each of the three intermediate samples according to equation (2):

$$\mathrm{REE}_{\mathrm{sample}} = \{\%\ \mathrm{REE}_{\mathrm{equation\ (1)}} \times \mathrm{REE}_{\mathrm{R\,4250}}\} + \{(100 - \%\ \mathrm{REE}_{\mathrm{equation\ (1)}}) \times \mathrm{REE}_{\mathrm{R\,4254}}\} \quad (2)$$

The hypothetical REE mixing patterns calculated for the three intermediate samples are shown as dashed lines in Fig. 7. They are almost flat and show no similarities with the observed patterns. We therefore conclude that the observed evolution of the REE distributions cannot be attributed to mixing, but must be due to a fractionation process.

This with distance increasing fractionation of the salt patterns is probably due to preferential immobilization of the REE by coprecipitation with a secondary mineral phase rather than to better solubility in the fluid by solution complexation (Steinmann *et al.* 2001). This secondary mineral phase could, in analogy to the finding in the previous section on REE immobilization during basalt corrosion, be apatite. This hypothesis is ascertained by a comparison with experimental data on REE fractionation by phosphate precipitation (Fig. 9, Byrne *et al.* 1996). The experimental data in fact show that apatite precipitation preferentially immobilizes Ce, Pr, Nd, Sm, and Eu, which is in agreement with our traverse in the salt. This finding is also in agreement with *in situ* observation and modelling of Byrne and Kim (1993) and Johannesson *et al.* (1995), who found that phosphate precipitation is an important process leading to fractionation of the rare earths in surface water and groundwater.

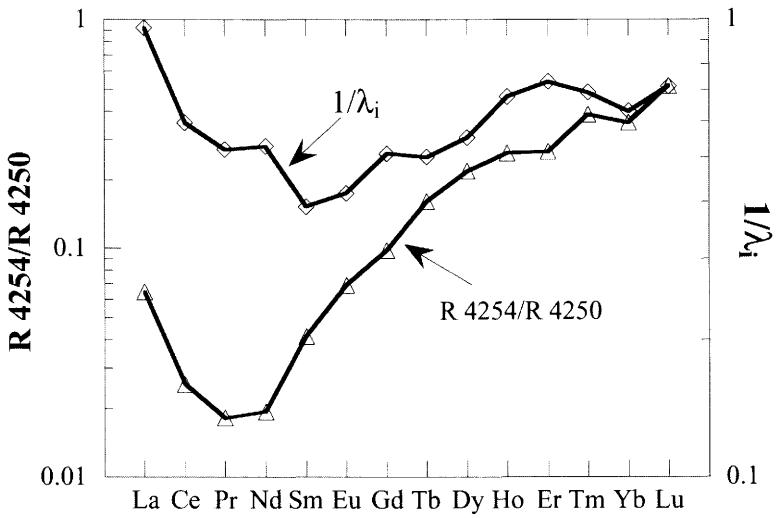

Fig. 9. Comparison of REE fractionation in the salt with fractionation factors λ_i determined by Byrne *et al.* (1996) from experimental data for REE coprecipitation with phosphate. REE fractionation in the salt is illustrated by the ratio of samples R 4254/R 4250, which are the two extreme samples of the salt profile. The λ_i values are plotted in reciprocal form in order to show REE fractionation in the remaining solution from which phosphate has precipitated.

A key question for the present natural analogue is the temperature at which REE migration and fractionation occurred in the salt. The temperature of the basaltic melt was around 1150 °C (Knipping 1989). However, model calculations based on conductive heat transport suggest that the temperatures in the salt never exceeded 800 °C, even directly at the basalt contact, and that they never attained 200 °C at 3 m distance from a basalt dyke of 1–1.8 m thickness (Knipping 1989). This is also supported by the presence of relicts of primary carnallite, for which the thermal stability limit is 167.5 °C (Braitsch 1971), in salt less than 1 m from basalt contacts (Knipping & Herrmann 1985; Knipping 1989). All these data suggest that REE migration in the salt occurred only in close proximity to the basalt at temperatures above 200 °C, whereas temperatures were already lower at 1–3 m from the contact. These temperatures can be regarded as maximum temperatures because the study of the basalt has shown that mobilization of the REE occurred after intrusion, at a moment when cooling of the basalt and the adjacent salt had already started. This decrease of temperature with distance might, together with increasing pH, have been one of the key parameters that triggered apatite precipitation within the salt, which in turn led to immobilization and fractionation of the REE.

Concluding remarks

The study of the basaltic dykes in evaporites demonstrates that dissolution and precipitation of phosphate minerals is a key process for the control of REE mobility and REE fractionation. In the present case, all REE found in secondary apatite in the basalt and in the salt are derived from the dissolution of primary magmatic apatite during basalt corrosion. This loss of REE from the basalt to the salt was not sufficient to lower significantly the REE concentrations of the basalt and it could only be detected by the analysis of the salt. The absolute quantity of REE transferred from the basalt into the salt, however, cannot be quantified because we have no three-dimensional control on the REE concentrations around the basalt apophysis.

Our results show that coprecipitation of the REE with phosphate removed Ce, Pr, Nd, Sm, and Eu more easily from the brine than other REE. This finding might be of importance for the mobility of trivalent Am and Cm in a radioactive waste salt repository, because for these elements, owing to their almost identical ionic radii, an almost analogous geochemical behaviour is expected as for Sm and Nd (Choppin 1983; Krauskopf 1986). These radionuclides would, in the case of a leaking HLW salt repository, probably be retained when phosphate minerals are present in the backfill material.

M. Cuney and S. Church are thanked for their constructive reviews. This is EOST/CGS contribution no. 2004.602-UMR7517.

References

ABDELOUAS, A., CROVISIER, J. L., LUTZE, W., FRITZ, B., MOSSER, A. & MÜLLER, R. 1994. Formation of hydrotalcite-like compounds during R7T7 nuclear waste glass and basaltic glass alteration. *Clays and Clay Minerals*, **42**, 526–533.

BANFIELD, J. F. & EGGLETON, R. A. 1989. Apatite replacement and rare earth mobilization, fractionation, and fixation during weathering. *Clays and Clay Minerals*, **37**, 113–127.

BRAITSCH, O. 1971. *Salt Deposits. Their Origin and Composition*. Springer-Verlag, Berlin-Stuttgart-Heidelberg-New York, 297 pp.

BRAUN, J. J., PAGEL, M., HERBILLON, A. & ROSIN, C. 1993. Mobilization and redistribution of REEs and thorium in a syenitic lateritic profile: A mass balance study. *Geochimica et Cosmochimica Acta*, **57**, 4419–4434.

BRAUN, J. J., PAGEL, M., MULLER, J. P., BILONG, P., MICHARD, A. & GUILLET, B. 1990. Ce anomalies in lateritic profiles. *Geochimica et Cosmochimica Acta*, **54**, 781–795.

BYERS, C. D., EWING, R. C. & KEIL, K. 1985. Basalt glass: an analogue for the evaluation of the long-term stability of nuclear waste form borosilicate glasses. *In*: JANTZEN, C. M., STONE, J. A. & EWING, R. C. (eds) *Scientific Basis for Nuclear Waste Management VIII. Mat. Res. Soc. Symp. Proc.*, Pittsburgh, Pennsylvania, 44.

BYRNE, R. H. & KIM, K.-H. 1993. Rare earth precipitation and coprecipitation behavior: The limiting role of PO_4^{3-} on dissolved rare earth concentrations in seawater. *Geochimica et Cosmochimica Acta*, **57**, 519–526.

BYRNE, R. H., LIU, X. & SCHIJF, J. 1996. The influence of phosphate coprecipitation on rare earth distributions in natural waters. *Geochimica et Cosmochimica Acta*, **60**, 3341–3346.

CHOPPIN, G. R. 1983. Comparison of the solution chemistry of the actinides and the lanthanides. *Journal of the Less-Common Metals*, **93**, 232–330.

CROVISIER, J.-L., HONNOREZ, J., FRITZ, B. & PETIT, J.-C. 1992. Dissolution of subglacial volcanic glasses from Iceland: laboratory study and modelling. *Applied Geochemistry*, **Suppl. Issue No. 1**, 55–81.

DAUX, V., GUY, C., ADVOCAT, T., CROVISIER, J.-L. & STILLE, P. 1997. Kinetic aspects of basaltic glass dissolution at 90 °C: Role of aqueous silicon and aluminium. *Chemical Geology*, **142**, 109–126.

DUDDY, I. R. 1980. Redistribution and fractionation of rare earth and other elements in a weathering profile. *Chemical Geology*, **30**, 363–381.

EWING, R. C. 1979. Natural glasses: Analogues for radioactive waste forms. *In*: MCCARTHY, G. (ed) *Scientific Basis for Nuclear Waste Management*. Plenum Press, New York, 57–68.

GUTSCHE, A. 1988. *Mineralreaktionen und Stofftransporte an einem Kontakt Basalt-Hartsalz in der Werra-Folge des Werkes Hattorf*. Unpubl. Diploma Thesis, Georg-August-Universität Göttingen.

JOHANNESSON, K. H., LYONS, W. B., STETZENBACH, K. J. & BYRNE, R. H. 1995. The solubility control of rare earth elements in natural terrestrial waters and the significance of PO43- and CO32- in limiting dissolved concentrations: A review of recent information. *Aquatic Geochemistry*, **1**, 157–173.

KNIPPING, B. 1989. *Basalt Intrusions in Evaporites. Lecture Notes in Earth Sciences 24*. Springer-Verlag, Berlin, 132 pp.

KNIPPING, B. & HERRMANN, A. G. 1985. Mineralreaktionen und Stofftransporte an einem Kontakt Basalt-Carnallitit im Kalisalzhorizont Thüringen der Werra-Serie des Zechsteins. *Kali und Steinsalz*, **9**, 111–124.

KRAUSKOPF, K. B. 1986. Thorium and rare-earth elements as analogues for actinide elements. *Chemical Geology*, **55**, 323–335.

LUTZE, W. & GRAMBOW, B. 1992. The effect of glass corrosion on near field chemistry. *Radiochimica Acta*, **58/59**, 3–7.

MACFARLANE, A. W., DANIELSON, A., HOLLAND, H. D. & JACOBSEN, S. B. 1994. REE chemistry and Sm–Nd systematics of late Archean weathering profiles in the Fortescue Group, Western Australia. *Geochimica et Cosmochimica Acta*, **58**, 1777–1794.

MALOW, G., LUTZE, W. & EWING, R. C. 1984. Alteration effects and leach rates of basaltic glasses: implications for the long-term stability of nuclear waste form borosilicate glasses. *Journal of Non-Crystalline Solids*, **67**, 305–321.

NASRAOUI, M., TOULKERIDIS, T., CLAUER, N. & BILAL, E. 2000. Differentiated hydrothermal and meteoric alterations in the Lueshe carbonatite complex (Democratic Republic of Congo) identified by a REE study combined with a sequential acid-leaching experiment. *Chemical Geology*, **165**, 109–132.

PETIT, J. C. 1992. Reasoning by analogy: rational foundation of natural analogue studies. *Applied Geochemistry*, **Suppl. Issue 1**, 9–11.

Prudêncio, M. I., BRAGA, M. A. S. & GOUVEIA, M. A. 1993. REE mobilization, fractionation and precipitation during weathering of basalts. *Chemical Geology*, **107**, 251–254.

SEABORG, G. T. 1993. Overview of the actinide and lanthanide (the f) elements. *Radiochimica Acta*, **61**, 115–122.

SILVA, R. J. & NITSCHE, H. 1995. Actinide environmental chemistry. *Radiochimica Acta*, **70/71**, 377–396.

STEINMANN, M. & STILLE, P. 1998. Strongly fractionated REE patterns in salts and their implications for REE migration in chloride-rich brines at elevated temperatures and pressures. *Comptes Rendus de l'Académie des Sciences Paris, Série II a*, **327**, 173–180.

STEINMANN, M., STILLE, P., BERNOTAT, W. & KNIPPING, B. 1999. The corrosion of basaltic dykes in evaporites: Ar–Sr–Nd isotope and REE evidence. *Chemical Geology*, **153**, 259–279.

STEINMANN, M., STILLE, P., MENGEL, K. & KIEFEL, B. 2001. Trace element and isotopic evidence for REE migration and fractionation in salts next to a basalt dyke. *Applied Geochemistry*, **16**, 351–361.

STILLE, P., STEINMANN, M. & RIGGS, S. R. 1996. Nd isotope evidence for the evolution of the paleocurrents in the Atlantic and Tethys Oceans during the past 180 Ma. *Earth and Planetary Science Letters*, **144**, 9–20.

TAZAKI, K., FYFE, W. S. & DISSANAYAKE, C. B. 1987. Weathering of apatite under extreme conditions of leaching. *Chemical Geology*, **60**, 151–162.

Thématique : "La migration des fluides interstitiels dans un récif corallien"

Steinmann, M. & Déjardin, P, 2004. Temporal evolution of fluid flow through the Tahiti barrier reef traced by Sr isotopes and pore water chemistry. Chem. Geol. 203, 51-73.

ELSEVIER

Chemical Geology 203 (2004) 51–73

CHEMICAL GEOLOGY
INCLUDING
ISOTOPE GEOSCIENCE

www.elsevier.com/locate/chemgeo

The temporal evolution of fluid flow through the Tahiti barrier reef traced by Sr isotopes and pore water chemistry

Marc Steinmann[a,*], Pascale Déjardin[b]

[a] *Département de Géosciences, Université de Franche-Comté, 16 route de Gray, F-25030 Besançon Cedex, France*
[b] *ULP-EOST-CNRS, Centre de Géochimie de la Surface UMR 7517, 1 rue Blessig, F-67084 Strasbourg Cedex, France*

Received 27 March 2002; received in revised form 5 September 2003; accepted 8 September 2003

Abstract

The internal fluid circulation of the Tahiti barrier reef has been studied with Sr isotopes and pore water chemistry. The study is based on 15 sample series recovered over 2 years from a 150-m deep core drilled through the entire barrier reef down to the volcanic basement.

Temperature data suggest that the interstitial fluids originate from seawater that penetrated the volcanic basement to at least 200 m depth on the ocean-sided slope below the barrier reef. Subsequently, the fluids migrated upward driven by buoyancy through the entire reef.

Chemical evolution of the interstitial fluids is mainly controlled by basalt–seawater interaction and by admixture of seawater from the open ocean during upward migration. These processes are monitored with $^{87}Sr/^{86}Sr$ isotope ratios, H_4SiO_4 concentrations and alkalinity to give a picture of the evolution of interstitial fluid flow over 2 years. The results indicate that the internal circulation patterns change through time. The modifications concern mainly the residence time of the fluids within the volcanics and the intensity and localization of lateral seawater admixture within the karstified Pleistocene reef.

Keywords: Coral reef; Interstitial fluid migration; Endo-upwelling; Circulation changes; Sr isotopes

1. Introduction

Migration pathways and chemical evolution of interstitial fluids in reefs of coral atolls are important controls on reef metabolism, carbonate diagenesis and carbonate preservation. In particular, the significance of interstitial fluids as a nutrient source for corals was ignored until studies based on temperature data and thermohydraulic modeling demonstrated geothermal upward migration of fluids within coral reefs (e.g. Swartz, 1958; Samaden et al., 1985; Henry et al., 1996; Jones et al., 2000; Pfingsten et al., 2001). Based on these data, Rougerie and Wauthy (1986, 1993) and Rougerie et al. (1997) proposed in their endo-upwelling model that ascending fluid circulation driven by thermal convection may pump nutrient-rich intermediate and deep waters to the surface where they become a principal nutrient source for the corals. The nutrients available from surface water alone would not be sufficient to explain the high productivity observed for algo-coral com-

* Corresponding author. Tel.: +33-381-66-65-46; fax: +33-381-66-65-58.
E-mail address: marc.steinmann@univ-fcomte.fr (M. Steinmann).

0009-2541/$ - see front matter © 2003 Elsevier B.V. All rights reserved.
doi:10.1016/j.chemgeo.2003.09.003

munities in barrier reefs and adjacent lagoons (Rougerie et al., 1997). Endo-upwelling can furthermore explain diagenetic processes such as dolomitization observed in recent atolls (Flood et al., 1996; Jones et al., 2000).

It is evident that the interstitial fluids originate from the ocean and migrate upward, but little is known about the depth of seawater intrusion and about the path and speed of upward migration within the reef. We furthermore have only imperfect knowledge about changes in these parameters through time.

The present study traces fluid migration within the barrier reef of the mid-Pacific island of Tahiti (French Polynesia) over time and identifies exchange and mixing processes between interstitial fluids, reef carbonates and the open ocean. The study is based on a vertical sequence of 12 samples of interstitial fluids

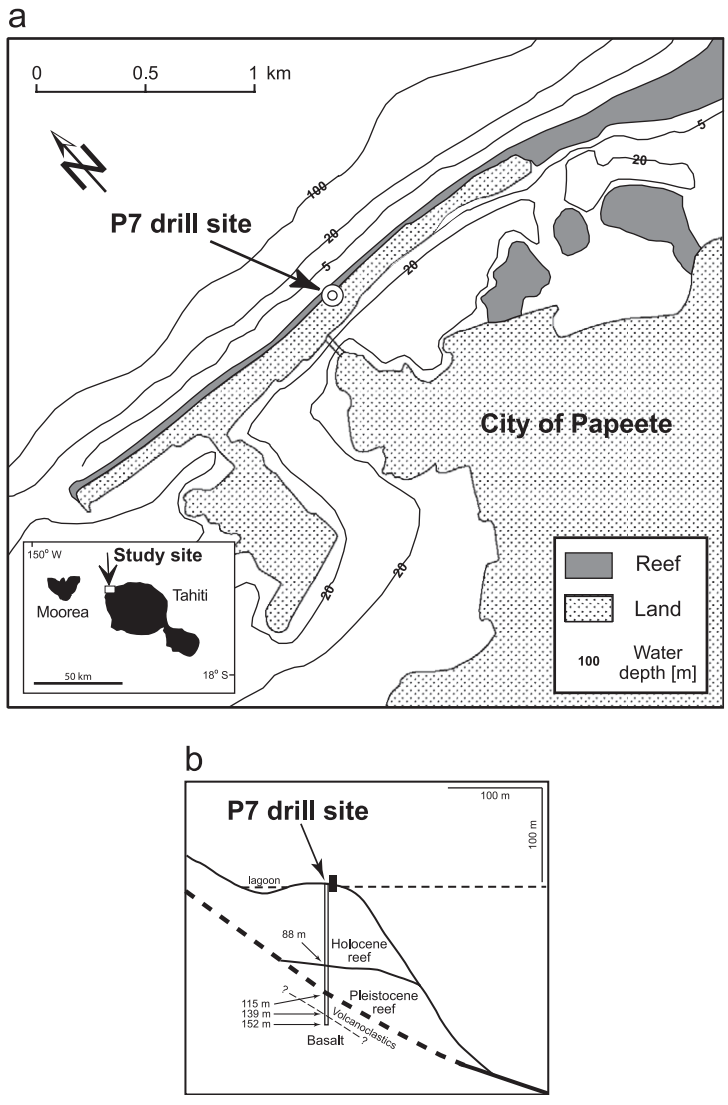

Fig. 1. Location of drilling P7 on the edge of the barrier reef that faces Papeete harbor, Tahiti (a) and schematic vertical cross-section of the drilling site (b).

recovered at 15 time intervals over 2 years from a 150-m deep core drilled through the entire barrier reef down to the volcanic basement. As tracers, we use major and trace element data as well as Sr isotopic compositions. Our work is complementary to an earlier study of Andrié et al. (1998), who investigated pore waters of a single sample series from the same drilling locality, but using anthropogenic tracers (chlorofluorocarbon [CFC] and tritium), oxygen isotopes and helium isotopes.

2. Setting and methods

2.1. Geology and oceanography

Our study is based on a bore hole, referenced as P7, situated on the crest of the Tahiti barrier reef, north of Papeete harbor (Fig. 1). The drill site is located on an artificial dam constructed on the island-sided part of the reef crest. The hole was drilled in October 1992 and penetrates the whole reef buildup. Its total length is 152 m and it reaches the volcanic basement at 139 m depth. The principal lithological units are shown in Figs. 1 and 2. Major limits are the upper limit of the volcanic basement consisting of submarine lava flows at 139 m, the contact between a volcano-sedimentary unit and the reef carbonates at 115 m, and at 88 m an unconformity within the reef which separates a probably Pleistocene from a Holocene reef complex. For brevity, the general term "volcanics" will be used thereafter as a group name for the volcanic basement and the volcanoclastics. The Pleistocene reef carbonates located from 115 to 88 m in depth have undergone subaerial alteration, probably during glacial sea-level lowstands, which led to a strong karstification of the buildup (Déjardin, 1996). In contrast, the reef complex located above the 88 m unconformity represents a continuous record from about 14,000 years up to the present (Bard et al.,

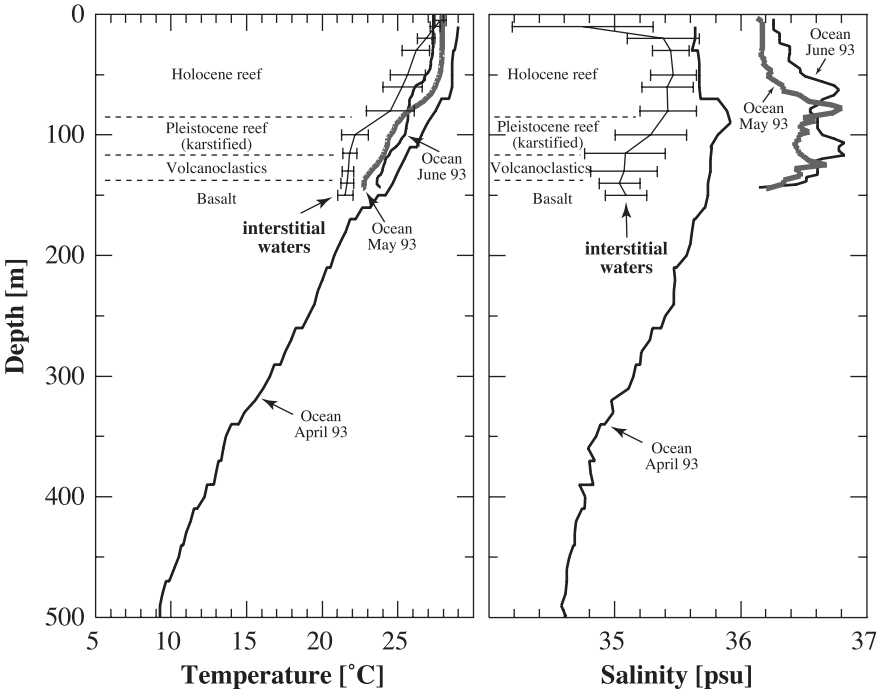

Fig. 2. Average temperature and salinity values with standard deviations for the interstitial fluids in comparison with seawater values. The average data for the interstitial fluids are those given in Table 1. The seawater data for the profiles from May and June 1993 are from the immediate vicinity of P7 (Table 3), whereas the data from April 1993 are from a few kilometers offshore P7 (Déjardin, 1996).

1996; Déjardin, 1996; Montaggioni et al., 1997; Camoin et al., 1999). The limits between the different lithological units are of importance for the interpretation of the pore water data and, therefore, are indicated in the depth logs.

The drill site is exposed to NE and SE tradewind-generated swells and low-range spring tides. This general pattern may be modified during southern winter by SW derived swells originating from the Antarctic depression zone. Short periods with N-derived swells triggered by winter storms in the north Pacific may occur during southern summer. Tropical surface waters extend to 200 m depth and are characterized by temperatures above 20 °C and salinities higher than 35.5‰ (Fig. 2). Below follows the thermocline, which extends to about 500 m. It is the transition zone between surface water and Antarctic intermediate water (AIW). Low temperatures (5–10 °C) and salinities (34.5–35‰) characterize the AIW that are located at 500–1000 m depth (ORSTOM, 1993; Déjardin, 1996). The AIW form by subsidence of cold surface water at about 60°S, next to the Antarctic continent, and they are, in contrast to surface water, rich in nutrients. Upward transport of these waters within reefs by processes such as endo-upwelling makes of them an important nutrient source for biological activity.

2.2. Sampling and analytical

The P7 drill hole is completely cored (63 mm diameter) and lined with a PVC open casing with 2 mm slots and a specific porosity of about 15%. This installation allows study of the interstitial fluids in an open borehole without disturbing the internal fluid circulation of the reef. In situ measurements and sampling began 3 months after drilling when the salinities of the interstitial fluids indicated that the system had recovered from freshwater injected during drilling.

An automatic multi-sampler with an integrated peristaltic pump was used to sample the interstitial fluids simultaneously at 12 fixed depths (5, 10, 20, 30, 50, 60, 80, 100, 115, 130, 140 and 150 m). The sampler was kept immobile for at least 30 min prior to sampling to avoid turbulence related to the movement of the sampler. Sampled fluids were pumped to the surface and recovered in polyamide tubes (250 ml),

Table 1
Average values and standard deviations of temperature ($n=10$), pH ($n=15$), salinity ($n=14$), alkalinity, Eh, oxygen, silica, NO_2+NO_3, NH_4, and PO_4 (all $n=15$, except for 150 m where $n=12$) for the interstitial fluids

Depth (m)	Temperature (°C)		pH		Eh (mV)		Salinity (psu)		Alkalinity (meq/l)		O_2 (mg/l)		H_4SiO_4 (μmol/l)		NO_2+NO_3 (μmol/l)		NH_4 (μmol/l)		PO_4 (μmol/l)	
	Mean	S.D.	Mean	S.D.	Mean	S.D.	Mean	S.D.	Mean	S.D.	Mean	S.D.	Mean	S.D.	Mean	S.D.	Mean	S.D.	Mean	S.D.
5	27.82	0.38	7.91	0.27	65	116	31.41	1.18	2.02	0.59	1.25	0.59	83.1	21.5	0.60	1.05	15.45	9.05	0.67	0.31
10	27.49	0.33	7.72	0.06	132	96	34.75	0.56	2.30	0.19	1.21	0.68	61.8	9.2	0.59	0.82	6.05	3.28	0.79	0.12
20	26.88	0.56	7.72	0.05	146	76	35.38	0.28	2.15	0.12	1.39	0.59	76.2	13.1	0.28	0.53	8.42	3.44	1.03	0.06
30	26.22	0.90	7.73	0.05	141	75	35.45	0.14	2.07	0.16	1.36	0.81	97.8	40.8	1.04	1.65	8.69	6.76	1.12	0.09
50	25.65	1.16	7.72	0.05	148	78	35.47	0.18	2.08	0.19	1.29	0.57	108.4	48.3	1.49	1.78	8.49	7.89	1.14	0.19
60	25.31	1.31	7.72	0.05	153	70	35.42	0.20	2.05	0.16	1.31	0.61	111.5	47.4	2.00	2.16	6.80	7.31	1.22	0.36
80	24.50	1.57	7.71	0.06	160	67	35.43	0.23	1.89	0.17	1.42	0.54	118.8	29.8	3.27	2.15	4.06	6.43	1.01	0.26
100	22.18	0.87	7.61	0.12	159	65	35.29	0.28	1.55	0.19	1.55	0.60	205.9	85.4	1.41	1.27	1.19	2.92	1.24	0.67
115	21.83	0.46	7.53	0.08	163	64	35.08	0.32	1.48	0.13	1.66	0.64	243.4	72.1	0.86	0.87	0.61	0.83	1.40	0.55
130	21.72	0.38	7.51	0.11	171	67	35.07	0.26	1.50	0.14	1.43	0.48	244.0	66.4	0.87	0.84	0.83	1.26	1.35	0.61
140	21.66	0.42	7.49	0.14	170	64	35.04	0.16	1.50	0.14	1.41	0.48	273.8	76.6	0.44	0.28	0.49	0.39	1.45	0.56
150	21.53	0.52	7.52	0.19	167	68	35.09	0.16	1.54	0.15	1.56	0.53	245.6	70.9	0.91	1.10	0.47	0.48	1.22	0.48
Open ocean water (April 1993)																				
0	28.99		8.30				35.64		2.20				2							
500	9.05		7.90				34.56		2.20				16							

The data given for seawater are single sample analyses.

Table 2
Detailed chemical parameters and compositions for the interstitial fluids of the individual time series

Date	Depth (m)												
	5	10	20	30	50	60	80	100	115	130	140	150	Group
Temperature (°C), 10 time series													
18/02/1993	27.61	27.39	26.78	25.82	24.97	24.45	23.89	21.58	21.43	21.43	21.38	21.18	
19/03/1993	27.85	27.58	27.42	27.14	26.88	26.86	26.71	23.86	22.76	22.54	22.54	22.52	
05/04/1993	28.06	27.65	27.44	27.16	26.88	26.78	26.43	23.42	22.34	21.88	21.88	21.66	
15/04/1993	27.99	27.67	26.87	25.76	24.87	24.48	23.39	21.43	21.41	21.38	21.36	21.26	
17/06/1993	27.78	27.70	27.09	26.32	25.71	25.33	24.12	22.42	22.14	22.08	22.05	21.98	
28/07/1993	27.72	27.44	26.25	24.47	23.44	23.06	22.42	21.70	21.63	21.60	21.55		
24/01/1994	27.76	27.19	25.97	25.54	24.90	24.25	23.02	21.63	21.50	21.40	21.10	21.03	
10/02/1994	27.19	26.83	26.43	26.02	25.56	25.21	24.15	21.58	21.58	21.53	21.38	21.13	
21/02/1994	27.60	27.34	26.83	26.48	26.15	25.61	24.13	21.55	21.53	21.48	21.48	21.08	
24/05/1994	28.65	28.06	27.73	27.44	27.18	27.08	26.74	22.59	21.98	21.92	21.87	21.91	
pH, 15 time series													
20/01/1993	8.72	7.81	7.77	7.76	7.80	7.81	7.83	7.79	7.54	7.49	7.48	7.55	3a
16/02/1993	8.13	7.66	7.68	7.68	7.66	7.67	7.70	7.56	7.41	7.40	7.39	7.40	1
16/03/1993	8.07	7.63	7.64	7.65	7.67	7.67	7.67	7.62	7.49	7.49	7.48	7.49	3a
07/05/1993	7.95	7.67	7.69	7.69	7.69	7.69	7.70	7.61	7.56	7.57	7.58		1
08/06/1993	8.06	7.76	7.75	7.75	7.76	7.76	7.76	7.75	7.60	7.34	7.39		1
08/07/1993	7.85	7.66	7.69	7.70	7.68	7.64	7.59	7.46	7.50	7.52	7.51	7.52	3b
02/09/1993	8.00	7.76	7.70	7.70	7.69	7.67	7.66	7.32	7.32	7.22	7.06	7.03	1
16/02/1994	7.68	7.73	7.75	7.75	7.72	7.70	7.71	7.59	7.58	7.59	7.58	7.59	1
03/03/1994	7.69	7.74	7.76	7.78	7.74	7.73	7.67	7.67	7.54	7.57	7.57	7.66	2
20/04/1994	7.73	7.78	7.78	7.80	7.80	7.78	7.77	7.77	7.61	7.64	7.64	7.75	2
10/05/1994	7.68	7.68	7.67	7.69	7.70	7.70	7.71	7.59	7.57	7.54	7.51	7.43	2
03/08/1994	7.75	7.70	7.70	7.70	7.68	7.66	7.64	7.52	7.51	7.50	7.42		3b
21/09/1994	7.68	7.68	7.67	7.69	7.70	7.70	7.71	7.59	7.57	7.54	7.51	7.43	3b
26/10/1994	7.85	7.78	7.77	7.79	7.79	7.79	7.78	7.70	7.64	7.63	7.62	7.70	2
22/12/1994	7.83	7.77	7.78	7.78	7.78	7.78	7.74	7.59	7.58	7.57	7.57	7.65	2
Eh (mV), 15 time series													
20/01/1993	175	194	195	195	195	195	207	219	219	221	211	207	3a
16/02/1993	168	179	179	176	175	174	173	175	178	179	192	192	1
16/03/1993	188	191	195	158	188	190	191	194	198	205	206	198	3a
07/05/1993	110	197	183	109	180	158	197	211	219	223	226		1
08/06/1993	89	114	93	66	63	61	90	90	117	121	121		1
08/07/1993	179	208	209	215	207	204	201	203	207	215	210	218	3b
02/09/1993	10	36	42	42	74	73	72	76	76	80	82	84	1
16/02/1994	164	161	156	153	151	150	152	151	149	148	147	146	1
03/03/1994	188	220	212	218	209	205	203	202	203	201	200	198	2
20/04/1994	− 23	− 50	− 42	0	18	50	50	51	53	53	55	55	2
10/05/1994	− 121	− 67	50	17	− 29	5	24	25	32	39	43	43	2
03/08/1994	83	35	145	175	207	235	235	190	156	242	218		3b
21/09/1994	− 32	190	190	190	183	184	193	192	217	218	221	224	3b
26/10/1994	− 114	181	185	195	200	202	203	205	208	212	215	220	2
22/12/1994	− 88	196	198	202	203	205	206	207	208	209	210	213	2
Salinity (psu), 14 time series													
20/01/1993	30.05	34.43	35.14	35.21	35.12	35.06	35.08	35.65	34.83	34.87	34.91	34.90	3a
16/02/1993	28.76	33.72	34.98	35.12	35.10	35.09	35.08	34.83	34.73	34.82	34.87	34.86	1
16/03/1993	29.90	34.67	35.08	35.41	35.41	35.45	35.43	35.66	35.08	34.94	34.94	34.98	3a
07/05/1993	30.51	34.91	35.31	35.48	35.46	35.33	35.15	34.89	34.87	34.87	34.88		1

(continued on next page)

Table 2 (*continued*)

Date	Depth (m)												
	5	10	20	30	50	60	80	100	115	130	140	150	Group
Salinity (psu), 14 time series													
08/06/1993	31.10	35.09	35.40	35.51	35.52	35.52	35.31	35.58	34.89	34.98	34.90		1
08/07/1993	32.02	35.58	36.06	35.51	35.36	35.21	35.36	35.11	35.26	34.98	35.26	35.26	3b
02/09/1993	32.57	35.37	35.64	35.61	35.65	35.55	35.43	35.48	35.26	35.26	35.34	35.17	1
16/02/1994	31.49	34.05	35.18	35.33	35.57	35.52	35.49	34.96	34.94	34.94	34.95		1
03/03/1994	31.88	34.36	35.35	35.48	35.49	35.46	35.53	35.26	34.99	34.97	35.03	35.37	2
20/04/1994	32.42	34.37	35.25	35.46	35.56	35.53	35.51	35.19	34.90	35.38	34.92	35.02	2
10/05/1994	32.23	34.25	35.23	35.46	35.47	35.46	35.36	35.07	34.95	34.96	34.98	35.03	2
03/08/1994	32.04	35.06	35.63	35.59	35.47	35.28	35.73	35.34	35.93	35.72	35.26		3b
21/09/1994	32.53	35.28	35.53	35.43	35.75	35.78	35.80	35.51	35.53	35.42	35.20	35.08	3b
26/10/1994	32.28	35.3	35.59	35.63	35.6	35.61	35.69	35.48	34.99	34.93	35.1	35.23	2
Alkalinity (meq/l), 15 time series													
20/01/1993	1.02	2.41	2.29	2.21	1.98	1.93	1.88	1.96	1.58	1.76	1.58	1.61	3a
16/02/1993	1.54	2.41	2.23	2.22	2.18	2.10	1.89	1.42	1.50	1.53	1.50	1.54	1
16/03/1993	1.54	2.66	2.37	2.21	2.41	2.29	2.27	1.89	1.76	1.72		1.61	3a
07/05/1993	1.93	2.37	2.33	2.33	2.33	2.19	1.70	1.56	1.53	1.52	1.55		1
08/06/1993	1.36	2.14	2.13	2.12	2.13	2.12	1.91	1.62	1.57	1.61	1.35		1
08/07/1993	1.45	2.08	2.04	1.93	1.85	1.78	1.78	1.36	1.34	1.33	1.64	1.39	3b
02/09/1993	1.30	2.08	2.04	2.04	1.99	1.94	1.67	1.56	1.56	1.59	1.77	1.48	1
16/02/1994	2.53	2.38	2.21	2.18	2.17	2.17	2.14	1.40	1.40	1.39	1.64	1.93	1
03/03/1994	2.58	2.66	2.02	2.03	2.18	2.21	1.74	1.61	1.43	1.44	1.39	1.66	2
20/04/1994	2.64	2.36	2.21	2.16	2.22	2.22	2.12	1.40	1.40	1.45	1.39	1.45	2
10/05/1994	2.54	2.22	2.09	2.06	2.07	2.07	1.95	1.33	1.33	1.32	1.33	1.39	2
03/08/1994	2.51	2.24	2.17	1.80	1.76	1.81	1.78	1.41	1.40	1.42	1.44		3b
21/09/1994	2.30	2.13	2.00	1.71	1.79	1.84	1.81	1.66	1.67	1.65	1.63	1.53	3b
26/10/1994	2.43	2.16	2.07	2.02	1.99	1.98	1.90	1.73	1.36	1.34	1.35	1.50	2
22/12/1994	2.69	2.25	2.12	2.10	2.08	2.06	1.75	1.38	1.36	1.38	1.37	1.41	2
O_2 (mg/l), 15 time series													
20/01/1993	1.13	0.94	0.76	0.75	1.59	1.67	1.91	2.38	2.43	1.61	1.70	1.90	3a
16/02/1993	1.05	1.29	1.13	1.21	1.23	1.43	1.99	1.60	2.83	2.44	2.08	2.07	1
16/03/1993	1.49	1.25	1.52	1.14	1.55	1.55	1.45	1.70	2.11	1.62	1.83	1.98	3a
07/05/1993	1.62	1.38	1.35	1.27	1.21	1.26	1.64	1.44	1.89	1.88	2.13		1
08/06/1993	1.36	1.22	1.16	0.99	1.21	1.16	1.59	1.29	2.22	1.69	1.77		1
08/07/1993	1.54	1.49	1.59	1.79	1.34	1.13	1.28	1.21	1.31	1.38	1.18	1.35	3b
02/09/1993	1.87	1.91	1.91	1.91	1.55	1.17	1.06	1.69	1.69	1.60	1.43	1.59	1
16/02/1994	1.30	1.94	2.02	1.35	1.27	1.24	0.84	1.13	0.78	0.88	0.78	1.83	1
03/03/1994	2.16	2.79	2.57	3.26	2.28	2.61	2.17	1.99	1.11	1.29	1.34	2.60	2
20/04/1994	0.02	0.32	0.69	0.00	0.26	0.21	0.53	0.22	0.80	0.61	0.62	0.97	2
10/05/1994	0.24	0.35	0.71	0.31	0.57	0.46	0.78	1.69	1.32	1.10	1.08	0.82	2
03/08/1994	1.93	1.42	1.99	2.38	1.28	1.36	2.24	2.30	1.28	1.99	1.98		3b
21/09/1994	1.36	0.86	1.83	1.86	2.38	2.39	1.69	1.75	2.13	1.39	1.06	0.92	3b
26/10/1994	0.85	0.61	1.14	1.27	1.14	0.96	1.44	2.24	2.12	0.87	1.12	1.29	2
22/12/1994	0.89	0.42	0.55	0.87	0.53	1.09	0.70	0.64	0.91	1.13	1.03	1.45	2
H_4SiO_4 (μmol/l), 15 time series													
20/01/1993	37.0	47.0	61.0	73.5	101.4	109.5	102.9	72.2	172.5	161.2	164.1	168.0	3a
16/02/1993	79.7	64.7	84.5	93.9	102.3	111.8	135.7	225.6	233.1	248.8	239.6	230.6	1
16/03/1993	72.0	59.0	66.0	70.3	71.8	71.6	77.0	60.9	167.7	222.1	211.0	215.9	3a
07/05/1993	75.5	54.3	70.2	76.6	79.1	104.5	157.6	233.7	210.3	170.3	324.0		1
08/06/1993	66.9	51.0	69.0	71.6	73.0	74.7	91.2	170.7	170.7	180.8	209.6		1
08/07/1993	60.8	59.5	68.2	99.0	125.3	132.4	114.2	224.5	225.9	229.3	229.3	203.5	3b

Table 2 (*continued*)

Date	Depth (m)												
	5	10	20	30	50	60	80	100	115	130	140	150	Group
H_4SiO_4 (μmol/l), 15 time series													
02/09/1993	71.1	73.4	76.7	76.7	84.7	95.2	139.3	158.1	158.1	184.5	173.9	175.2	1
16/02/1994	70.6	53.2	58.3	68.8	73.5	74.1	76.4	174.5	168.1	170.6	171.2	150.5	1
03/03/1994	102.7	69.0	81.5	85.2	91.5	71.9	158.2	165.1	329.7	322.0	361.1	232.3	2
20/04/1994	105.8	67.3	79.4	86.5	89.4	91.9	105.3	339.9	345.7	329.1	346.4	319.7	2
10/05/1994	103.0	66.4	68.0	84.9	85.7	86.7	125.7	342.1	326.1	315.1	322.6	310.2	2
03/08/1994	84.9	51.0	77.1	165.4	189.5	187.9	97.6	185.0	208.8	201.3	305.9		3b
21/09/1994	119.9	78.6	110.4	218.1	247.5	245.5	135.4	241.9	270.9	261.8	389.3	389.3	3b
26/10/1994	98.5	69.9	89.3	101.3	108.0	108.4	96.5	164.4	330.9	333.3	330.9	274.1	2
22/12/1994	97.7	63.0	83.9	95.7	103.2	107.2	169.8	330.6	331.8	329.4	328.2	277.8	2
$NO_2 + NO_3$ (μmol/l), 15 time series													
20/01/1993	0.07	0.31	0.30	5.62	4.65	3.48	2.76	3.16	0.26	0.13	0.18	0.08	3a
16/02/1993	0.06	2.44	0.07	0.38	2.67	4.74	3.97	0.20	0.15	0.12	0.12	0.11	1
16/03/1993	0.08	0.32	0.08	0.09	0.09	0.08	0.16	3.44	1.75	1.82	0.57	0.12	3a
07/05/1993	0.07	1.57	0.06	0.07	0.65	6.14	4.79	0.58	0.60	0.51	0.39		1
08/06/1993	0.11	2.33	0.09	0.10	0.10	0.13	5.72	2.61	0.76	1.82	0.68		1
08/07/1993	0.06	0.13	0.08	1.37	4.60	4.64	5.17	0.29	0.64	0.29	0.28	1.45	3b
02/09/1993	0.16	0.05	0.06	0.25	1.55	3.41	3.08	2.40	1.60	1.56	0.33	3.60	1
16/02/1994	1.06	0.08	0.12	0.15	0.15	0.05	0.14	0.42	0.39	0.45	1.02	0.56	1
03/03/1994	0.53	0.32	0.32	0.41	0.21	0.25	3.01	0.47	0.52	0.56	0.97	2.33	2
20/04/1994	0.49	0.16	0.11	0.13	0.14	0.17	8.04	0.11	0.23	0.48	0.22	0.14	2
10/05/1994	0.50	0.15	0.15	0.16	0.17	0.15	0.33	0.21	0.38	0.24	0.33	0.20	2
03/08/1994	4.25	0.19	0.22	3.47	2.80	2.50	3.47	2.64	3.21	2.38	0.34		3b
21/09/1994	0.58	0.44	2.16	2.89	4.10	3.59	2.96	1.90	1.85	2.26	0.66	1.01	3b
26/10/1994	0.64	0.25	0.27	0.20	0.22	0.39	3.02	2.51	0.33	0.26	0.36	1.06	2
22/12/1994	0.30	0.10	0.16	0.35	0.29	0.21	2.41	0.18	0.19	0.13	0.15	0.24	2
NH_4 (μmol/l), 15 time series													
20/01/1993	6.26	3.33	5.79	3.15	0.89	0.34	0.87	0.25	2.76	0.48	0.44	0.10	3a
16/02/1993	6.15	1.45	4.94	4.93	2.36	0.44	0.22	0.15	0.19	0.09	0.18	0.08	1
16/03/1993	6.84	5.00	10.17	14.04	13.78	10.33	9.90	0.16	0.18	0.12	0.09	0.12	3a
07/05/1993	9.76	2.10	10.84	12.86	12.67	5.87	0.25	0.10	0.05	0.03	0.04		1
08/06/1993	9.42	1.61	12.77	12.97	13.31	9.64	1.73	0.10	0.36	0.20	0.83		1
08/07/1993	6.72	6.57	6.68	2.78	0.37	0.21	0.24	0.24	0.11	0.09	0.09	0.09	3b
02/09/1993	3.41	5.75	3.11	2.76	1.43	0.42	0.06	0.07	0.07	0.48	0.48	0.91	1
16/02/1994	20.96	9.14	5.28	9.53	15.20	14.13	12.66	1.08	0.92	0.84	0.78	1.32	1
03/03/1994	17.09	6.55	7.13	10.35	11.27	9.98	1.02	1.31	0.78	0.76	0.75	0.47	2
20/04/1994	28.74	10.45	15.47	21.10	23.94	23.39	19.26	0.54	0.74	1.28	0.55	1.39	2
10/05/1994	27.58	7.06	8.51	21.03	20.75	17.90	13.87	0.24	− 0.02	0.00	0.10	0.57	2
03/08/1994	22.74	4.46	11.87	0.34	0.32	0.36	0.22	0.28	2.25	4.10	0.54		3b
21/09/1994	16.46	5.43	6.67	0.15	0.56	0.30	0.12	11.61	0.10	0.31	0.16	0.18	3b
26/10/1994	21.15	12.46	10.88	8.59	5.22	3.56	0.27	1.46	0.23	0.18	0.83	0.17	2
22/12/1994	28.44	9.39	6.14	5.77	5.35	5.08	0.26	0.27	0.40	3.51	1.43	0.19	2
PO_4 (μmol/l), 15 time series													
20/01/1993	0.24	0.73	0.94	0.95	1.04	1.06	1.05	0.52	1.17	0.53	1.28	1.11	3a
16/02/1993	0.50	0.79	1.06	1.15	1.24	1.21	1.16	2.07	1.79	1.72	1.77	1.44	1
16/03/1993	0.42	0.87	1.02	1.12	1.13	1.11	1.09	0.56	0.93	1.43	1.58	1.19	3a
07/05/1993	0.55	0.76	1.05	1.19	1.25	1.25	1.38	2.04	2.04	2.02	2.04		1
08/06/1993	0.37	0.82	1.07	1.17	1.12	1.17	0.92	1.40	1.19	0.74	0.86		1
08/07/1993	0.45	0.88	1.00	1.12	1.21	1.22	1.06	1.92	1.90	1.96	1.94	1.62	3b

(continued on next page)

Table 2 (*continued*)

Date	Depth (m)												
	5	10	20	30	50	60	80	100	115	130	140	150	Group
PO_4 (μmol/l), 15 time series													
02/09/1993	0.50	1.06	1.19	1.19	1.13	1.15	1.12	1.03	1.03	1.03	0.65	0.54	1
16/02/1994	0.84	0.66	0.98	1.09	1.24	1.24	1.22	2.06	2.00	2.19	2.26	1.25	1
03/03/1994	0.86	0.83	1.01	0.94	1.18	1.11	1.17	1.33	1.71	1.72	1.71	1.97	2
20/04/1994	1.23	0.81	1.08	1.29	1.39	1.35	1.12	1.44	1.68	1.22	1.56	1.26	2
10/05/1994	1.06	0.74	0.99	1.20	1.26	1.11	0.91	0.83	0.70	0.34	0.30	0.17	2
03/08/1994	0.33	0.52	0.96	1.15	1.24	1.20	0.75	0.91	0.31	0.49	1.72		3b
21/09/1994	0.71	0.72	1.00	1.07	0.53	0.61	0.30	0.15	0.86	1.28	1.15	1.02	3b
26/10/1994	0.83	0.84	1.07	1.07	1.06	2.36	0.72	0.42	1.68	1.66	0.95	1.46	2
22/12/1994	1.10	0.84	1.06	1.14	1.13	1.13	1.21	1.96	1.98	1.97	1.95	1.59	2

which had previously been flushed with the sample fluid.

From January 1993 to December 1994, pH, salinity, alkalinity, NO_2, NO_3, NH_4, PO_4 and H_4SiO_4 of the interstitial fluids were monitored in 15 sampling campaigns. Temperature was measured in situ 10 times from February 1993 to February 1994 by an Aanderaa temperature–pressure probe with a precision of ± 0.1 °C. A WTW 539 pH-meter was used to measure pH on site directly after sampling with a precision of ± 0.02 pH units. All other parameters were determined immediately after sampling in the laboratory of ORSTOM Tahiti.

Salinity was measured by an Auto-Lab induction salinometer (precision ± 0.002 ‰) and alkalinity by potentiometry (precision ± 0.02 meq/l; Bradshaw et al., 1981; Almgren et al., 1983). NO_2, NO_3, NH_4, PO_4 and H_4SiO_4 were analyzed by spectrophotometry (precision ± 5%; Aminot and Chaussepied, 1983). An oxymeter with a precision of ± 0.01 mg/l was used to measure the dissolved oxygen content and the redox potential was determined with a voltmeter and a Pt-electrode (Ingold Pt-4805-S7, precision ± 0.05 mV).

Some major (Na, K, Mg, Ca, Cl, SO_4, H_4SiO_4) and trace elements (Rb, Sr, Al, Mn) as well as the Sr isotopic compositions were analyzed on an additional, single sample series at the CNRS laboratory in Strasbourg (sampling date: 15th June 1993). The samples were stored and transported in acid cleaned polypropylene bottles. Aliquots for the trace element and Sr isotope analysis were filtered on site through 0.45-μm filters (Millipore HA, 47 mm diameter) and acidified by nitric acid (Merck suprapur) to pH 1–2 immediately after sampling. The major cations Na, K, Mg and Ca were determined by atomic adsorption spectrometry (AAS, Perkin Elmer 400), the anions Cl and SO_4 by ion chromatography (Dionex), and H_4SiO_4 by colorimetry (Technicon chain). The trace elements Rb, Sr, Al and Mn were analyzed by ICP-AES (ARL 3500 °C). The precision of all these analyses is ± 5%.

For Sr isotope analysis, 2 ml of fluid was evaporated after addition of 50 μl of concentrated $HClO_4$ (Merck suprapur) to disintegrate organic matter. After evaporation, the samples were redissolved in 0.5 ml of bidistilled 4 M HCl, centrifuged and the supernatants were directly loaded on cation exchange columns (AG 50W-X8, 200–400 mesh). The basalt rock samples were digested in HF and HNO_3 for 4 days in closed Savillex vials at 150 °C. Carbonate rock samples were dissolved in 6 M HCl.

We used 1-ml quartz columns and ammonium citrate, HCl 1.5, 4 and 6 M as eluents. The total Sr blank was < 1.5 ng. The Sr isotope analyses were performed on a fully automatic VG Sector mass spectrometer with a five-cup multicollector. The samples were deposited on W single filaments for analysis. The ratio $^{86}Sr/^{88}Sr = 0.1194$ was used for fractionation correction and typically 100 ratios were measured to achieve adequate precision. During the measuring period, the NBS 987 Sr standard yielded $^{87}Sr/^{86}Sr = 0.710264 \pm 13$ (± standard deviation of the mean, $n = 8$).

Three depth profiles were made offshore P7 from April to June 1993 to compare temperature, salinity

Table 3
Temperature and salinity profiles from the open ocean directly offshore P7

Depth (m)	T ocean (°C)	Salinity ocean (psu)	T ocean (°C)	Salinity ocean (psu)
	Date: 25/05/1993		Date: 11/06/1993	
10	27.94	36.17	27.36	36.26
20	27.95	36.17	27.34	36.31
25	27.93	36.17	27.37	36.39
30	27.90	36.16	27.32	36.39
40	27.88	36.17	27.20	36.38
50	27.75	36.21	26.80	36.51
60	27.49	36.34	26.23	36.74
65	27.18	36.46	25.94	36.74
70	26.92	36.50	25.77	36.65
80	25.58	36.73	25.66	36.55
90	24.86	36.47	25.66	36.61
100	24.49	36.46	25.46	36.65
110	24.32	36.43	24.92	36.78
115	24.10	36.46	24.43	36.82
120	23.78	36.54	24.20	36.65
130	23.18	36.47	23.97	36.61
140	22.81	36.34	23.63	36.52
145			23.83	36.15

and chemistry of the interstitial fluids with the open ocean. In a first profile from April 1993, temperature and salinity were measured at depths down to 500 m and water samples for chemical analyses were taken at the surface, at 200 m and at 500 m depth. In May and June 1993, two additional temperature and salinity profiles were made in the immediate vicinity of the reef at depths down to 150 m. However, no chemical analyses were made on these two latter profiles.

3. Results

Average values of the chemical parameters analyzed for the interstitial fluids during the 15 sampling campaigns are presented in Table 1, and the complete data set is reported in Table 2. The salinity and temperature data of the two ocean profiles taken in May and June 1993 from the immediate vicinity of the reef are given in Table 3. The chemical compositions of three seawater samples taken in April 1993 are given in Tables 1 and 4, respectively. Table 4 also presents the major (Na, K, Mg, Ca, Cl, SO_4) and trace elements (Rb, Sr, H_4SiO_4, Al, Mn) as well as the Sr isotopic compositions of the sample series taken 15th June 1993. Finally, the Rb–Sr isotope data for the reef carbonates and the volcanics are given in Table 5.

Table 4
Major and trace elements, and Rb–Sr isotopic compositions for the interstitial fluids of the Sr isotope sample series sampled on 15th June 1993 and seawater

Depth (m)	Na (mmol/l)	K (mmol/l)	Mg (mmol/l)	Ca (mmol/l)	Cl (mmol/l)	SO_4 (mmol/l)	Rb (μmol/l)	Sr (μmol/l)	H_4SiO_4 (μmol/l)	Al (μmol/l)	Mn (μmol/l)	$^{87}Sr/^{86}Sr$	$^{87}Rb/^{86}Sr$
5	420	9.5	44.5	10.8	515	25.2	1.71	82.9	89	29.0	7.03	0.709062 (9)	0.0589
10	473	10.6	52.0	10.4	565	28.6	1.77	91.8	89	29.9	3.60	0.709121 (9)	0.0553
20	470	10.6	52.5	10.4	565	28.6	1.77	90.8	115	28.5	2.55		
30	475	10.7	52.0	10.6	580	28.8	1.74	93.8	116		2.11	0.709108 (10)	0.0530
50	473	10.7	52.0	10.6	570	28.8	1.76	94.7	129	27.2	1.23		
60	468	10.7	51.5	10.6	570	28.6	1.74	95.1	151	26.3	0.40	0.709042 (10)	0.0523
80	468	10.7	52.0	10.7	570	28.4	1.83	96.5	219	27.0	0.30	0.708965 (14)	0.0542
100	465	10.7	51.5	10.6	565	28.3	1.89	97.2	283	27.0	0.37	0.708868 (9)	0.0555
115	465	10.5	50.5	10.5	565	28.2	1.92	98.0	343	27.6	0.37	0.708792 (9)	0.0561
130	468	10.5	51.0	10.5	570	28.4	1.86	97.6	310	25.9	0.37	0.708832 (10)	0.0546
140	468	10.5	50.0	10.6	570	28.5	1.90	96.8	301	25.6	0.40		
150	473	10.5	51.0	10.8	560	28.4	1.99	96.3	280	24.7	0.79	0.708859 (9)	0.0591
Open ocean water (April 1993)													
0	478	10.7	53.5	10.8	595	29.1	1.45	96.0	2			0.709176 (9)	0.0433
200	478	10.8	54.0	10.8	580	29.0	1.59	94.4	2				
500	460	10.4	53.0	10.3	555	28.0	1.62	88.3	16			0.709178 (11)	0.0524

The errors given for the $^{87}Sr/^{86}Sr$ ratios are 2σ mean values and refer to the last digits.

Table 5
Rb–Sr isotope data for reef carbonates and volcanics

Depth (m)	$^{87}Sr/^{86}Sr$	$^{87}Rb/^{86}Sr$	Rb (ppm)	Sr (ppm)
Carbonates				
5	0.709171 (9)			
5	0.709180 (11)	0.0002	0.19	2862
30	0.709110 (9)	0.0002	0.08	1390
46	0.709125 (10)	0.0003	0.15	1294
76	0.709176 (9)			
78	0.709154 (9)	0.0002	0.09	1704
Basalt (144 m) and volcanoclastics (116 m)				
116	0.704999 (12)	0.1288	13.40	301
144	0.704014 (7)	0.2470	77.30	905

The errors given for the $^{87}Sr/^{86}Sr$ ratios are 2σ mean values and refer to the last digits.

3.1. Temperature, salinity, alkalinity and pH

The temperature profile is characterized by slowly increasing values in the volcanics and at the base of the Pleistocene reef, followed by a rapid upward increase at 100–90 m directly beneath the boundary between the Pleistocene and the Holocene reef (Fig. 2). The temperatures increase again slowly in the lower part of the Holocene reef followed by a final rise at about 20 m depth in the uppermost part of the Holocene reef. The temperature of the interstitial waters is always below that measured in the open ocean. The lowest values are in most cases at least 2 °C colder than seawater in the open ocean at the same depth. However, the interstitial water temperatures converge towards seawater values within the uppermost part of the Holocene reef.

Salinity values are relatively low in the volcanics and increase in the Pleistocene reef (Fig. 2). Within the Holocene reef, the values remain almost constant but drop abruptly next to the surface. The salinity values of the pore waters are, like temperature, always distinctly lower than in the open ocean at same depth.

Temperature and salinity data have been used to determine σ_t density values. These values are reported in Fig. 3 and compared with seawater. The interstitial fluids are, in spite of the lower temperatures, systematically lighter than seawater because of their low salinities. However, the σ_t values decrease towards the surface indicating that the water column within the reef is stable.

The pH and alkalinity values are low in the volcanics and increase in the Pleistocene reef (Fig. 4). Within the Holocene reef, pH remains constant whereas alkalinity continues to increase slowly. As for salinity, a strong offset can be observed next to the surface. This overall similar evolution of pH and alkalinity is not surprising because both parameters are located in carbonate-rich natural environments and are thus mainly controlled by these carbonates (Stumm and Morgan, 1996).

3.2. Major and trace elements, and saturation indexes

A distinct positive peak at the bottom of the Holocene reef characterizes the depth profile of NO_2+NO_3. NH_4 increases within the lower part of the Holocene reef and shows a negative peak at 10 m depth. PO_4 generally decreases from the volcanic basement to the surface and shows, in contrast to NO_2+NO_3, a slight negative peak at the base of the Holocene reef (Table 1).

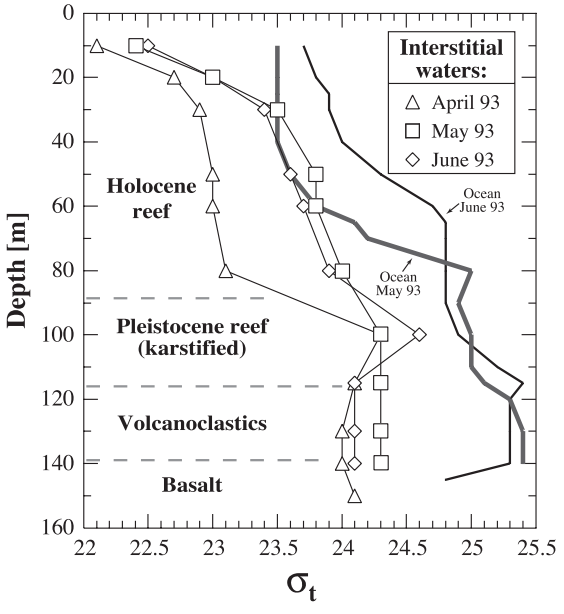

Fig. 3. σ_t values for the interstitial fluids of April to June 1993 in comparison with seawater values from the immediate vicinity of P7 (σ_t={density − 1}∗1000). The interstitial fluids are, in particular below 60 m, systematically lighter than seawater. The σ_t values have been determined with a T–S diagram and are based on the temperature and salinity data given in Tables 2 and 3.

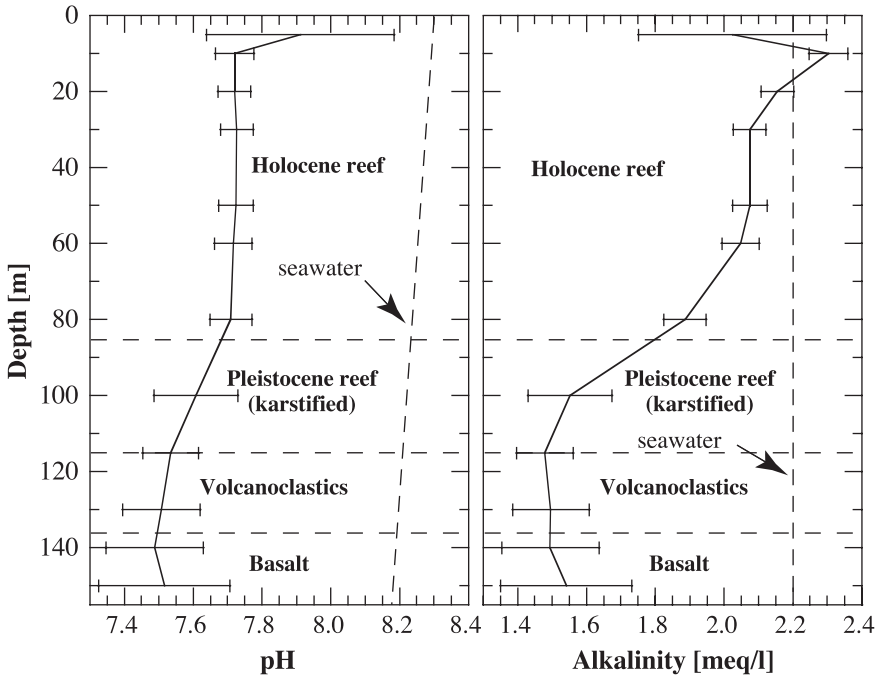

Fig. 4. Average pH and alkalinity values for the interstitial fluids of the 15 time series with standard deviations. The seawater values given for comparison are based on the data points from 0 and 500 m. The data are those given in Table 1.

Na, Mg, Cl and SO_4 of the Sr isotope series show no significant depth variations; only near the surface an abrupt drop can be observed (Table 4). K concentrations are almost constant in the volcanics; they increase slightly in the Pleistocene reef and remain almost constant in the Holocene reef. The concentrations drop next to the surface like for the other major elements. Ca increases systematically with depth within the volcanics and no systematic variations can be observed within the reef (Table 4). All these major element concentrations are not significantly different from seawater except for Mg and SO_4^- where a significant depletion can be recognized (Table 4).

Aluminium increases within the volcanics, then remains constant in the lower part of the reef up to 60 m depth, followed by a regular increase up to the surface (Table 4). Mn remains almost constant from the bottom of the hole up to 60 m depth and then increases like Al towards the surface. The Sr concentrations increase like Al within the volcanics and then diminish. Rb shows an irregular decrease from the bottom of the whole upward.

Average silica concentrations are relatively high in the volcanics and then regularly decrease towards the surface (Table 1). The concentrations are about 40 to 140 times higher than in the adjacent open ocean. This general evolution can also be observed for the silica concentrations of the Sr isotope samples series (Fig. 5, Table 4). Silica data of each sample series have been compared with all other chemical parameters available. A compilation of the results of this correlation analysis is given in Table 6 for the samples from the volcanics and the carbonate reef. In the discussion below, the term "correlated" will be used for correlations with $r^2>0.7$. Within the volcanics, H_4SiO_4 is negatively correlated with pH and salinity in 5 of the 15 sample series, and with alkalinity in 6 of the 15 sample series. However, the correlation with alkalinity is complicated by one positive correlation. Finally, H_4SiO_4 is positively correlated with PO_4 in 5 of the 15 sample series, but again, one negative correlation complicates the picture. Within the carbonate reef, H_4SiO_4 is like in the volcanics negatively correlated with pH (7 of 15 series) and salinity (3 of 15 series), and positively correlated with PO_4 (5 of 15 series).

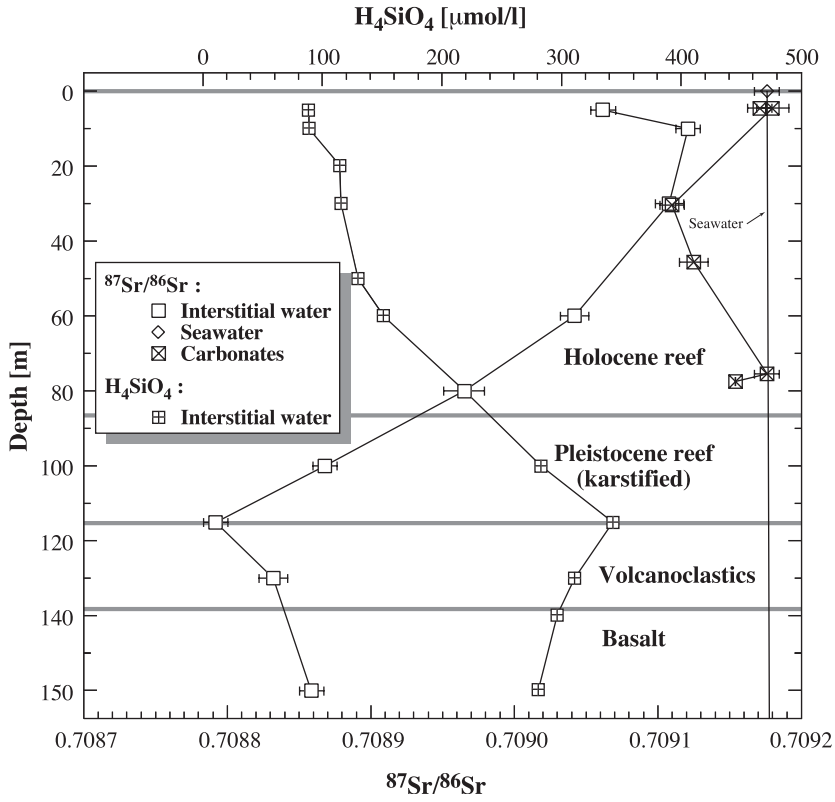

Fig. 5. Depth profiles of dissolved silica and $^{87}Sr/^{86}Sr$ of interstitial fluids, and $^{87}Sr/^{86}Sr$ of seawater and reef carbonates. The interstitial fluids have been sampled on 15th June 1993. Note the opposite depth evolutions of silica and $^{87}Sr/^{86}Sr$ for the interstitial fluids. The $^{87}Sr/^{86}Sr$ seawater values are based on the data points from 0 and 500 m. See Table 4 for raw data.

Again, the picture is complicated by one correlation with an opposite slope for the correlations with pH and with PO_4. However, the most coherent picture is found for the correlations between silica and alkalinity, where negative correlations can be found for 11 of the 15 sample series with r^2 better than 0.9 in 9 cases.

This coherency between silica concentrations and alkalinity is also shown in the scatter diagram of Fig. 6. The data points are aligned and grouped for the different depth levels. The samples from the volcanics define a wide range in the upper left of the diagram, whereas seawater plots in the lower right. Samples from the Pleistocene reef are most scattered and cover the whole range defined by all other sample groups. In contrast, the scatter of the data points from the overlying young reef is clearly smaller and the points are with decreasing depth more and more shifted towards seawater composition.

The data of the interstitial fluids of the Sr isotope series (Table 4) have been used to calculate saturation indexes for calcite, aragonite and dolomite using the computer code EQUIL (Fritz, 1975, 1981). Unfortunately, no pH and alkalinity data were available for these samples and therefore the average values given in Table 1 have been used. The resulting log Q/K values are presented in Table 7. The results show upward increasing saturation indexes for calcite, aragonite and dolomite. The fluids are oversaturated with respect to dolomite above 60 m, but the values remain, as for calcite and aragonite, systematically below the log Q/K values calculated for seawater.

3.3. Sr isotopes

The Sr isotopic compositions vary in a range of 0.7088–0.7091. This is significantly above the com-

Table 6
Correlation factors r^2 and slopes of silica with different parameters for the interstitial fluids within the volcanics and the carbonate reef

Date	H_4SiO_4 vs. pH		H_4SiO_4 vs. salinity		H_4SiO_4 vs. alkalinity		H_4SiO_4 vs. PO_4	
	r^2	Slope	r^2	Slope	r^2	Slope	r^2	Slope
Volcanics (n = 4, 115–150 m)								
20/01/1993								
16/02/1993								
16/03/1993			0.894	–				
07/05/1993*			**0.937**	+	**0.994**	+		
08/06/1993*					0.851	–		
08/07/1993							**0.997**	+
02/09/1993								
16/02/1994					0.712	–	**0.990**	+
03/03/1994	0.790	–	0.817	–	**0.983**	–	**0.919**	–
20/04/1994	0.701	–			**0.902**	–	0.817	+
10/05/1994								
03/08/1994	**0.973**	–	0.865	–			**0.967**	+
21/09/1994			0.870	–				
26/10/1994	**0.947**	–	0.742	–	**0.994**	–		
22/12/1994	**0.969**	–	**no salinity data**		0.880	–	**0.999**	+
Carbonate reef (n = 6, 20–100 m)								
20/01/1993								
16/02/1993	0.741	–			**0.989**	–	**0.906**	+
16/03/1993	0.860	+						
07/05/1993			**0.906**	–	**0.932**	–	**0.909**	+
08/06/1993					**0.945**	–		
08/07/1993	0.804	–			**0.972**	–	**0.936**	+
02/09/1993			0.807	–	**1.000**	–	0.799	–
16/02/1994	**0.940**	–			**0.992**	–	**0.982**	+
03/03/1994	0.800	–			0.884	–		
20/04/1994					**0.992**	–		
10/05/1994	0.793	–			**0.998**	–		
03/08/1994								
21/09/1994								
26/10/1994	0.778	–	0.711	–	0.794	–		
22/12/1994	**0.983**	–	**no salinity data**		**0.973**	–	**0.958**	+

Only r^2 values >0.7 are shown, values >0.9 in bold.
* Three data points for all correlations.

position of the basalt (0.704014, Table 5), but only slightly below seawater composition (0.70918, Fig. 5). The $^{87}Sr/^{86}Sr$ ratios of the interstitial fluids decrease upward within the volcanics and are lowest at the contact between the volcanoclastics and the Pleistocene reef. Above this minimum, the values constantly increase towards the surface and almost reach seawater values in the upper part of the young reef. The surface samples from 5 and 10 m depth are offset from this trend towards lower values. This whole evolution of the $^{87}Sr/^{86}Sr$ ratios is negatively correlated with H_4SiO_4 (Fig. 5). The correlation is particularly well defined for the samples from the carbonate reef.

The Sr isotopic compositions of the carbonate samples are identical with seawater for the surface samples and at 75 m depth (Fig. 5). This seawater composition is identical to the global average value of 0.709165 ± 0.000020 when normalized to the commonly reported value for NBS standard 987

of 0.710250. The $^{87}Sr/^{86}Sr$ values of some subsurface carbonates are shifted towards the composition of the interstitial fluids; the values are even identical at 30 m depth, probably due to diagenetic exchange processes.

The Rb–Sr isochron diagram (Fig. 7) shows a point cluster for the samples from the volcanics (150, 130 and 115 m), followed by a linear decrease for the reef samples from 100 to 60 m. This alignment defines a mixing line between the pore waters from the volcanics and seawater. Note the regular organization of the 3 sample points on this mixing line with decreasing depth. At 30 m depth, the sample point start to deviate from the mixing line towards more elevated $^{87}Rb/^{86}Sr$ ratios and the surface sample from 5 m plots completely off the other data points.

Both fluid and rock chemistry can be compared in the Rb–Sr isochron diagram shown in the insert of Fig. 7. This diagram demonstrates that the pore waters have a Rb–Sr isotopic composition similar to seawater. However, the compositions have slightly been modified by the interaction with the volcanic basement. The carbonate samples have $^{87}Sr/^{86}Sr$ ratios identical to seawater. The points are offset towards lower $^{87}Rb/^{86}Sr$ ratios due to chemical fractionation between Rb and Sr during biogenic precipitation of carbonate.

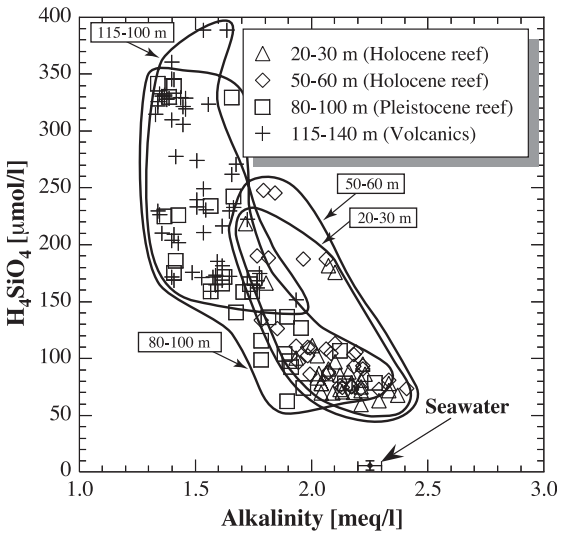

Fig. 6. Silica and alkalinity data of all samples of the 15 sample series plotted as 4 distinct depth sets. A general, depth-dependent evolution can be recognized with low alkalinity and high silica values in the volcanics followed by a shift in the carbonate reef towards seawater values with high alkalinity and low silica. The data are those given in Table 1 for seawater and in Table 2 for the interstitial fluids.

Table 7
Log *Q*/*K* saturation indexes for interstitial waters and seawater

Depth (m)	Calcite	Aragonite	Dolomite
20	0.202	0.032	1.501
60	0.138	−0.032	1.348
100	−0.115	−0.285	0.825
115	−0.197	−0.367	0.659
Open ocean water			
0	0.695	0.525	2.491
500	0.326	0.156	1.730

The calculations are based on the concentration data of the Sr isotope series presented in Table 4. For pH and alkalinity, the average values given in Table 1 have been used because these parameters are not available for the Sr isotope series.

The Sr mixing diagram (Fig. 8) shows the same trends as the Rb–Sr isochron diagram. However, some additional details are evident. Samples from the volcanics are, in contrast to the isochron diagram, aligned and their $^{87}Sr/^{86}Sr$ ratios decrease with decreasing depth. As in the isochron diagram, the samples from the carbonate reef define a mixing line between the samples from the volcanics and seawater. However, the trend is better defined because the sample from 30 m also plots on the line. The sample from 10 m slightly deviates from this trend whereas the shallowest sample from 5 m is offset towards lower Sr concentrations and Sr isotopic compositions.

4. Discussion

4.1. Origin of the pore waters

The temperature data give valuable information on the origin of the pore waters. A study in a comparable context from the adjacent Muruora atoll shows that pore waters reach minimum temperatures of 16–19 °C at the reef-basalt contact (at about 300 m depth in Muruora) followed by a continuous increase within the basaltic basement reaching 32–33 °C at 1000 m depth (Henry et al., 1996). This clearly demonstrates that the volcanic basement is not a heat sink but a heat source.

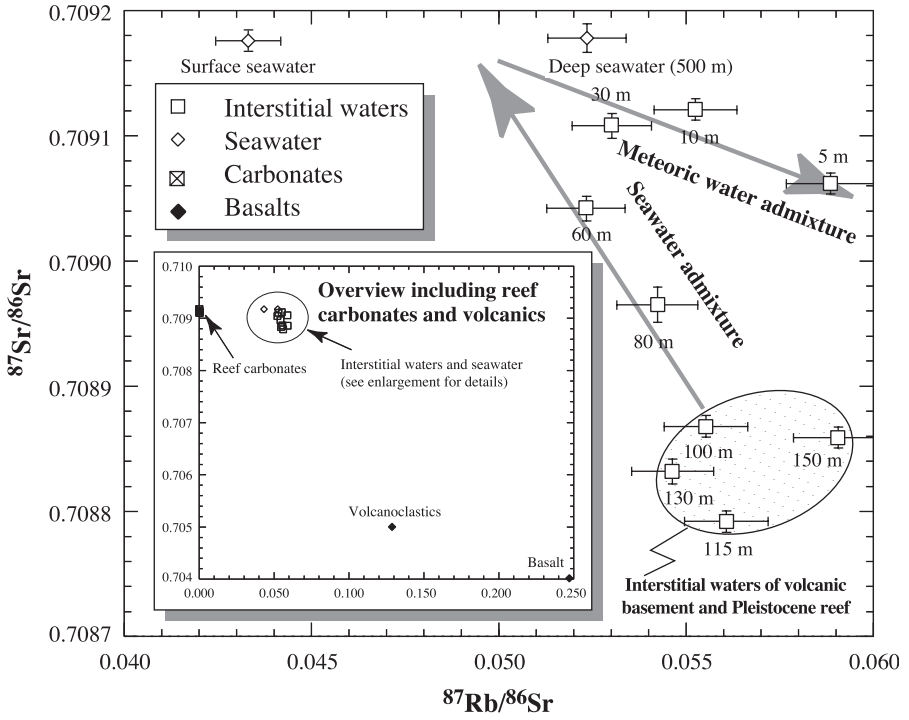

Fig. 7. Rb–Sr isochron diagram showing the mixing relation between deep interstitial waters from the volcanic basement and seawater. The insert shows furthermore the values for the basalts and the reef carbonates in order to give an overview on the entire system.

In the present case, the pore waters are always colder than seawater at the same depth in spite of the fact that no heat sinks are present in the direct vicinity (Fig. 2). Therefore, the pore waters must originate from a depth in the ocean where water temperatures are colder or at least equivalent to those within the reef. The temperature of the interstitial fluids can thus be used to make a minimum depth estimate for their origin. Our data indicate in this case an origin of at least 200 m depth (Fig. 2). The only place where seawater infiltration can take place at that depth is the volcanic basement on the ocean-sided slope below the carbonate reef (Fig. 1b). Such a deep water origin for the interstitial fluids has also been proposed by Andrié et al. (1998) based on $\delta^{18}O$ data. The temperature data are furthermore a clear indication that the pore waters are not derived from the adjacent lagoon because in that case they could not be colder than seawater from the open ocean.

However, within the reef, the σ_t values decrease towards the surface showing that the pore water column is stable and that upward migration of the fluids cannot be controlled by a simple buoyancy effect between lighter fluids at the base and heavier ones on the top of the pore water column. In Section 4.3, it will be shown that the pore fluids are not completely isolated from the ocean, but that the reef structure is porous, which results in a continuous exchange between seawater and interstitial fluids. Consequently, the pore fluids can be regarded as a light water mass embedded within the heavier seawater. It is this density contrast that creates buoyancy, which controls the upward migration of the interstitial fluids within the reef.

4.2. Fluid evolution within the volcanics

The shift of volcanic pore water $^{87}Sr/^{86}Sr$ ratios to values below that of normal seawater is a clear indication of basalt–seawater interaction (Fig. 5). Furthermore, the isotope ratios within the volcanics become lower upward, suggesting further basalt–seawater interaction during upward migration (Fig. 8). Silica concentrations increase upward consistent with progressive basalt–seawater interaction (Fig. 5).

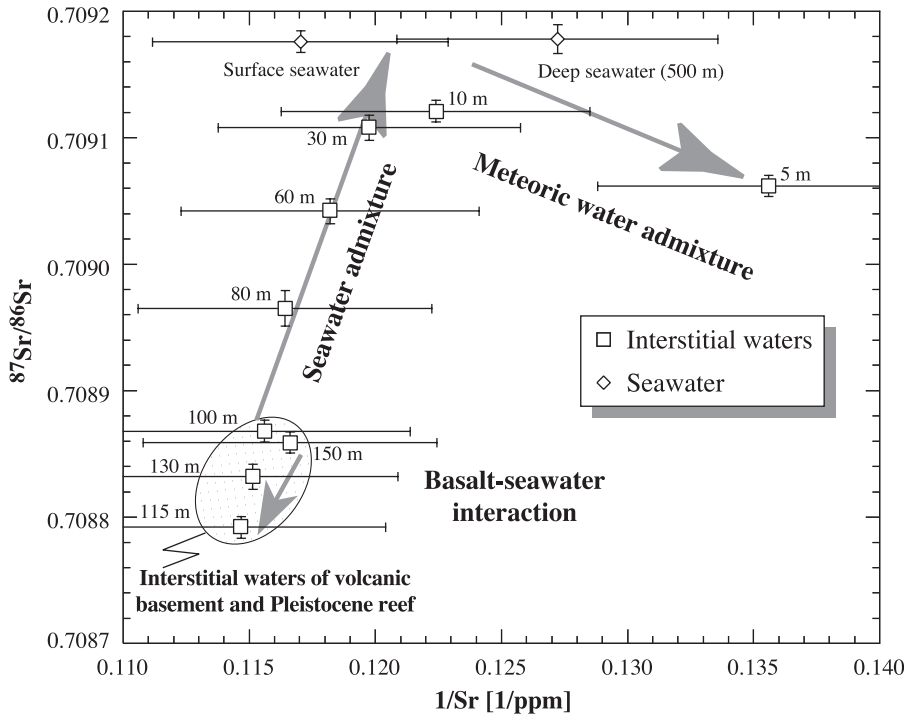

Fig. 8. Sr-mixing diagram for the interstitial fluids and seawater. It shows in detail growing basalt–seawater interaction in the volcanics and seawater admixture in the carbonate reef. The trend for seawater admixture indicates that open ocean water is not derived from the surface but from deeper depth levels.

The origin of silica from basalt–seawater interaction can also explain why the silica concentrations of the interstitial fluids are 40–150 times above normal seawater values (Table 1). Other potential silica sources such as silica-bearing organisms within the reef are lacking (Déjardin, 1996).

In Section 3.2, it has been shown that silica is negatively correlated with pH in 5 of the 15 sample series (Table 6). A link between silica and pH is in agreement with laboratory experiments by Seyfried and Bischoff (1979) on basalt–seawater interaction. This study demonstrated that Ca and H_4SiO_4 concentrations in seawater increase with progressing alteration, whereas Mg, Na, K and pH decrease. The chemical processes triggering these changes in fluid composition are mainly hydration of basalt minerals, and precipitation of calcite and secondary clay minerals such as saponite and zeolite (Dudoignon et al., 1989; Guy et al., 1992, 1999). Thermodynamic models demonstrate that pH will decrease at low rock/water ratios (<1 g/l) due to calcite precipitation, whereas zeolite precipitation at higher rock/water ratios would yield pH values above that of normal seawater (Guy et al., 1992). In the present case, the pH values of the interstitial fluids of the volcanics are always below that of the ocean (Fig. 4), which suggests low rock/water ratios.

The precipitation of carbonate may not only explain the lower pH values within the volcanics but also account for the simultaneously low alkalinity values (Fig. 6) because the alkalinity of carbonate-rich natural waters is mainly controlled by the carbonate system (Stumm and Morgan, 1996): carbonate precipitation removes bicarbonate and CO_3^{2-} from solution, which lowers alkalinity.

Basalt–seawater interaction and associated precipitation of carbonate leads to high silica concentrations and low alkalinity values for the pore waters. This explains why the pore waters from the volcanics mainly plot in the upper left of the H_4SiO_4 vs. alkalinity diagram (Fig. 6). The position on these data points may even provide a qualitative indication of the

intensity and/or duration of basalt–seawater interaction. Pore waters having undergone strong basalt–seawater interaction will plot on the upper left of the point cluster defined by the samples from the volcanics, whereas less intensive basalt–seawater interaction will yield data points shifted towards the lower right. The rather large dispersion of the point cluster suggests that the intensity of basalt–seawater interaction has varied with time, an aspect that will be discussed in detail in Section 4.4.

4.3. Pore water migration within the reef

The alignment of the pore water samples in the Rb–Sr isochron and the Sr-mixing diagram demonstrates mixing between pore waters originating from the volcanics and seawater (Figs. 7 and 8). The two diagrams also show that seawater has constant $^{87}Sr/^{86}Sr$ ratios, but various $^{87}Rb/^{86}Sr$ ratios and Sr concentrations at the surface and at 500 m depth. Both diagrams suggest that the seawater, which has been admixed to the pore waters, has had intermediate $^{87}Rb/^{86}Sr$ ratios and Sr concentrations. The seawater thus originates from depths below the surface.

Mixing calculations based on the Sr isotopic compositions and the Sr concentrations of those samples, which are aligned in the Sr mixing diagram (100–30 m), allows quantification of pore water/seawater mixing. The results are shown in Fig. 9. The diagram presents the percentage of 100 and 30 m depth water that was mixed to create the 60–80 m depth waters. The contribution of sample 30 m increases almost linearly suggesting an almost continuous mixing of seawater with the pore waters during upward migration. For comparison, the same mixing calculations based on silica concentrations are also shown. The results are similar but note that mixing calculations based on Sr isotopic compositions and Sr concentrations are more reliable. The finding that seawater admixture was a continuous process indicates for the Sr isotope series that there were no local injections of seawater at specific depths but that mixing was controlled by diffuse advective seawater infiltration from the open ocean through the walls of the entire Holocene reef. This is in agreement with the saturation indexes, which show that the interstitial fluids approach progressively seawater values during upward migration. Andrié et al. (1998) came to the same

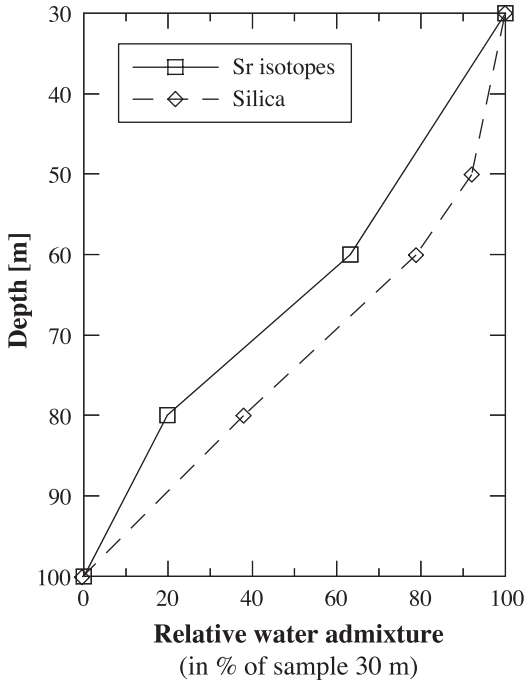

Fig. 9. Depth evolution of interstitial water mixing for samples 100, 80, 60 and 30 m from the Holocene reef, which have shown a linear trend in Fig. 8. The samples from 80 and 60 m are displayed as binary mixtures issued from mixing between samples 100 and 30 m. The mixing ratios are based on $^{87}Sr/^{86}Sr$ isotope ratios and Sr concentrations for the data points labeled "Sr isotopes" and on silica concentrations of the same samples for the data points labeled "Silica". Both data sets indicate continuous seawater admixture towards the surface.

conclusion based on the study of the anthropogenic tracers CFC and tritium.

The offset of the surficial samples from 5 and 10 m from the general mixing trend in the Rb–Sr isochron and the Sr mixing diagram coincides with anomalies observed for several other chemical parameters (Sections 3.1 and 3.2). In particular the salinity and major elements concentration decreases indicate rainwater infiltration derived from the artificial dam of the drill site. Elevated tritium concentrations found at the same depth confirm this hypothesis (Andrié et al., 1998).

At depths from 100 to 30 m, silica is almost perfectly negatively correlated with the $^{87}Sr/^{86}Sr$ ratios ($r^2 = 0.994$, $n = 4$). This indicates that the vertical evolution of the silica concentrations also results from pore water/seawater mixing (see Table 4). There is no indication that precipitation and/or biogeochemical

processes significantly affect silica concentrations. Within the carbonate reef, silica thus behaves conservatively and reflects seawater dilution.

The depth evolutions of pH, salinity, PO_4 and alkalinity also seem to be controlled by seawater dilution, at least in those sample series where they are correlated with H_4SiO_4 (Section 3.1, Table 6). In particular, alkalinity, which is correlated with silica in 11 of the 15 series, appears to reflect pore water/seawater mixing like $^{87}Sr/^{86}Sr$ and silica. The silica vs. alkalinity plot confirms this, because the data points are progressively shifted towards seawater composition with decreasing depth (Fig. 6). Accordingly, the silica vs. alkalinity plot can not only be used to qualify the intensity of basalt–seawater exchange in the volcanics, but also to trace fluid mixing within the reef.

4.4. Temporal variation of circulation patterns

The above discussion has shown that seawater penetrates the basaltic basement at depths below 200 m. Within the basement, this water is heated and basalt–seawater interaction modifies its chemical composition and lowers its salinity. The increased temperature and the lowered salinity leads to a lower density fluid, which results in buoyancy driven upward migration. Within the reef, the chemical composition of the pore waters is again modified, this time by fluid mixing with seawater.

This global picture is mainly based on the single sample series for which Sr isotope data are available. However, the correlation analysis presented in Section 3.2 did not show the same correlations for all 15 sample series, suggesting that the general circulation pattern may vary with time. This is confirmed by a detailed analysis of the parameters available for all sample series. In particular, salinity, alkalinity and silica content show some temporal variations, which will be discussed below.

Based on the depth evolution of silica, the 15 sample series and the Sr isotope series can be subdivided into three groups. Using alkalinity as a criterion for classification yields basically the same groups. A first group consisting of six sample series including the Sr isotope series is characterized by continuously upward decreasing H_4SiO_4 concentrations (Fig. 10). At the same time, the salinity values increase towards seawater values. This evolution of silica is attributed to the continuous admixture of seawater within the Holocene reef. In the silica vs. alkalinity plot (Fig. 10), a strong overlap for the samples from the volcanics and from the Pleistocene reef is observed suggesting that the fluids derived from the volcanics have not been significantly modified within the Pleistocene reef. In contrast, the samples from the Holocene reef are clearly shifted towards seawater values.

A second group of five sample series differs from the group 1 samples by a drop in silica by at least 150 μmol/l either within the Pleistocene reef or at the base of the Holocene reef (Fig. 10). We attribute this shift to seawater admixture from the open ocean within the karstified Pleistocene reef because the salinity values shift at the same time towards seawater values. In the H_4SiO_4 vs. alkalinity diagram (Fig. 10), the group 2 volcanic samples have higher H_4SiO_4 and slightly lower alkalinity values than the group 1 samples. This indicates, as discussed in Section 4.2, that basalt–seawater exchange within the volcanics has been more intensive or longer lasting than for the group 1 samples.

Fig. 10. Depth evolutions of silica and salinity for the sample groups 1, 2, 3a and 3b. The silica concentrations given for seawater are based on the data points from 0 and 200 m given in Table 4. The salinity profiles for seawater are those given in Table 3. The subdivision of the interstitial fluids into individual sample groups is based on the silica data. Group 1 profiles are characterized continuously upward decreasing silica concentrations. The Sr isotope series (15th June 1993) belongs to this first group. Group 2 profiles are characterized by an abrupt decrease of H_4SiO_4 concentrations of at least 150 μmol/l within the Pleistocene reef or at the base of the Holocene reef, which coincides with a salinity shift towards seawater. The sample series of groups 3a and 3b show distinct negative silica and positive salinity peaks at 100 m (group 3a) or 80 m (group 3b), which can be related to local seawater injections. Note the increasing silica concentrations above the injection level for group 3b.The scatter diagrams to the right of the depth profiles show the silica and alkalinity data of the individual sample groups plotted as four distinct depth sets together with seawater. A general, depth-dependent evolution can be recognized for group 1. Note the coincidence between samples from the volcanics and the Pleistocene reef. The group 2 samples have higher silica and lower alkalinity values in the volcanics than the group 1 samples. The samples from the volcanics are, with two exceptions, completely detached from the reef samples. Group 3a shows similarly to group 2 a decoupling of interstitial water circulation in the volcanics and in the reef. The group 3b samples show a strong dispersion for the individual data sets.

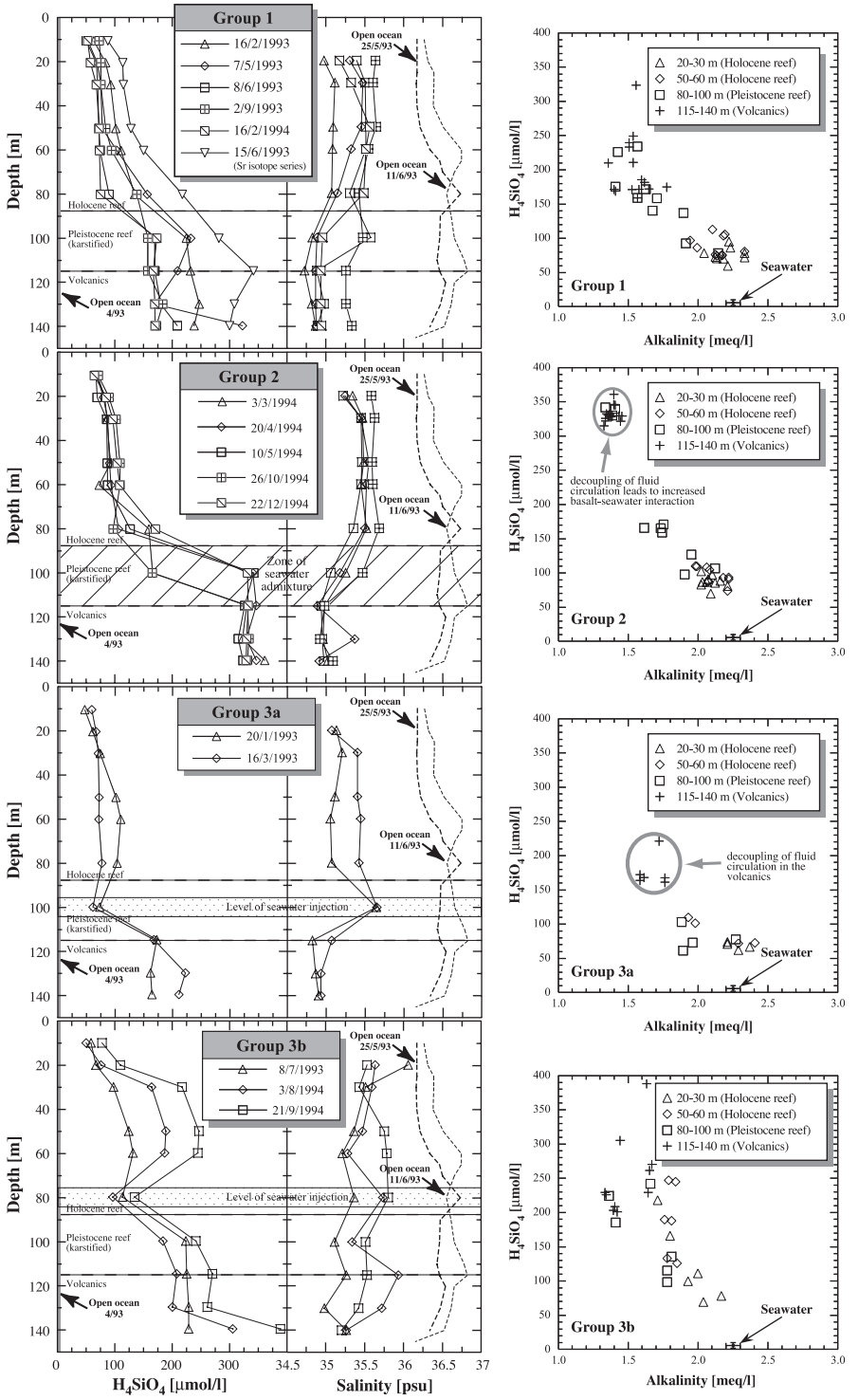
Group 1
16/2/1993
7/5/1993
8/6/1993
2/9/1993
16/2/1994
15/6/1993
(Sr isotope series)
Group 2
3/3/1994
20/4/1994
10/5/1994
26/10/1994
22/12/1994
Group 3a
20/1/1993
16/3/1993
Group 3b
8/7/1993
3/8/1994
21/9/1994
Open ocean 25/5/93
Open ocean 11/6/93
Open ocean 4/93
Holocene reef
Pleistocene reef (karstified)
Volcanics
Zone of seawater admixture
Level of seawater injection
Depth [m]
H4SiO4 [µmol/l]
Salinity [psu]
20-30 m (Holocene reef)
50-60 m (Holocene reef)
80-100 m (Pleistocene reef)
115-140 m (Volcanics)
Seawater
decoupling of fluid circulation leads to increased basalt-seawater interaction
decoupling of fluid circulation in the volcanics
Alkalinity [meq/l]

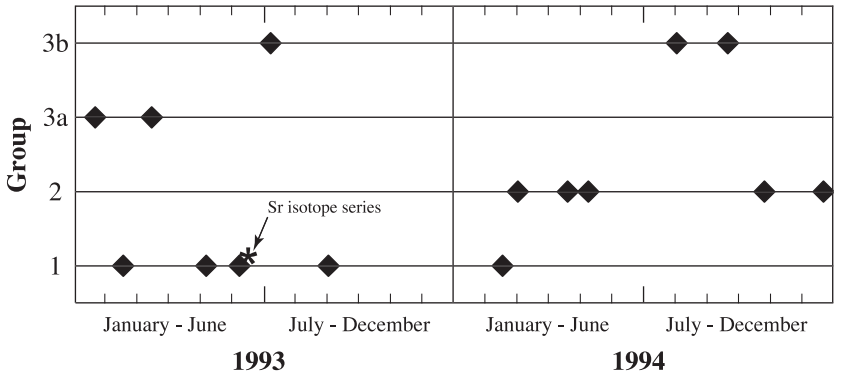

Fig. 11. Temporal distribution of the different circulation groups.

The group 3 sample series show punctuated negative H_4SiO_4 and positive salinity peaks at 100 m water depth for two series (group 3a) and at 80 m depth for three series (group 3b). Both parameters are shifted towards seawater values indicating that the peaks are due to local injection of seawater from the open ocean. However, in contrast to groups 1 and 2, the silica concentrations of group 3a and in particular group 3b increase above the injection level despite the absence of a silica source. Within the Holocene reef, the group 3b samples reach silica concentrations clearly higher than that for the other groups. In the silica vs. alkalinity plot, the group 3a volcanic samples from the plot away from the other data points. In contrast, no similar separation can be observed for group 3b samples (Fig. 10).

The increase in silica concentrations above the injection level for groups 3a and 3b can be explained by a short duration injection event, which was too short to affect the fluids 20 m above the injection level. This punctuated nature of seawater injection is ascertained by the analysis of the temporal distribution of the different circulation groups (Fig. 11), which will be discussed below. In the case of group 3a, seawater injection seems to have led to a decoupling of the circulation in the volcanics. The elevated silica concentrations in the Holocene reef for group 3b indicate reduced seawater admixture during upward migration of the interstitial fluids. The data thus suggest that local seawater injection for the group 3b samples occurred as punctuated events during periods of reduced diffuse seawater admixture.

Fig. 11 shows the occurrence of the three types of circulation patterns through time. The diagram shows that type 1 circulation prevailed until February 1994; afterwards, type 2 circulation became dominant. These two circulation patterns have episodically been interrupted by type 3a events until March 93 and type 3b events afterwards.

The long duration of types 1 and 2 circulations excludes short-term meteoric or seasonal variations as a triggering mechanism. In contrast, the episodic character of the type 3 injection events suggests that they are controlled by short-term phenomena such as storms.

A possible explanation for the change from types 1 to 2 circulation may be lowered heat flow in the volcanic basement. Tahiti is located on top of a mantle plume (Searle et al., 1995) and a decrease in heat flow in the volcanic basement would mainly reflect changing mantle convection (Courtillot et al., 2003). A lower heat flow would slow upward migration of the interstitial fluids and prolong basalt–seawater interaction in the volcanics. This would finally lead, as observed for the group 2 samples, to high silica concentrations and low alkalinities in the fluids. In contrast, the interstitial fluids in the Holocene reef would not immediately be affected by the lowered heat flow in the basement because their upward migration is driven by density differences originating from basalt–seawater interaction during the preceding type 1 period. However, the reduced fluid input from the volcanics and the continuing upward migration of the fluids in the Holocene reef would create a "void" at the

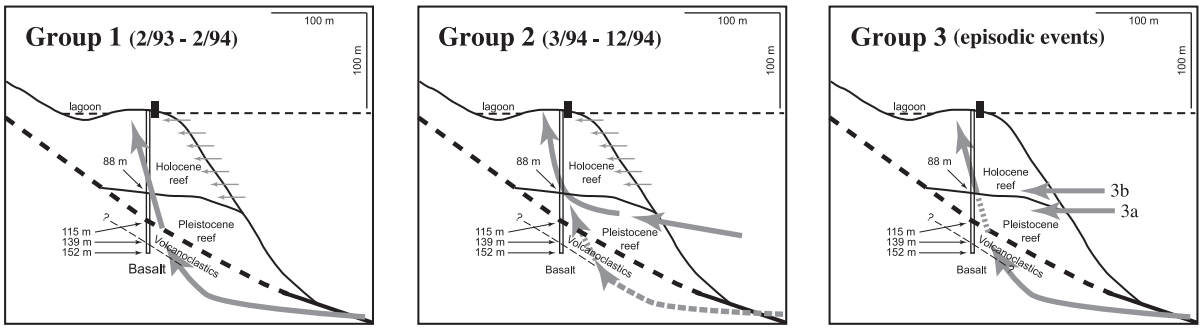

Fig. 12. Sketches of the circulation patterns of the three groups.

base of the Holocene reef, which will necessary be filled with seawater from the open ocean. This could explain the enhanced lateral admixture of seawater in the Pleistocene reef observed for the group 2 circulation. This enhanced lateral admixture of seawater would reduce the density contrast between interstitial fluids and seawater, and consequently slow or stop upward migration of the interstitial fluids within the Holocene reef. Unfortunately, insufficient density and heat flow data are available to test this hypothesis. Alternatively, the change from type 1 to type 2 circulation may be triggered by increased permeability of the karstified Pleistocene reef due to diagenetic or biologic processes. In that scenario, enhanced seawater admixture in the Pleistocene reef would have led to a decrease of pore water input from the volcanics. Finally, the change from types 1 to 2 circulation occurs shortly after the onset of the 1994 El Niño event. The elevated seawater temperatures in the central and eastern Pacific Ocean during an El Niño event are known to damage coral reefs (Spencer et al., 2000; Douglas, 2003), which in turn could affect the porosity of the reef and hence modify internal fluid circulation. However, we have at present no data to establish such a link and additional studies are needed.

5. Conclusions

Our data demonstrate that fluid flow through the Tahiti barrier reef starts in the volcanic basement followed by upward migration driven by buoyancy. The data thus confirm an internally ascending fluid circulation as proposed in the endo-upwelling model of Rougerie and Wauthy (1986, 1993) and Rougerie et al. (1997). Our results are likewise in agreement with those of Andrié et al. (1998).

Chemical evolution of the interstitial fluids is mainly controlled by basalt–seawater interaction in the volcanics and by admixture of seawater from the open ocean during upward migration. These processes could be monitored with $^{87}Sr/^{86}Sr$ isotope ratios, H_4SiO_4 concentrations and alkalinity. These results show that the Holocene reef is not a laterally confined system, but that there is a constant advection of seawater on the ocean-sided face of the reef.

Earlier studies on fluid flow in barrier reefs have been based on either a single series or only a small number of sample series. Consequently, they could only yield a snapshot of a complex and continuously evolving process. In contrast, the data of the present study show how fluid flow evolves over 2 years. These results demonstrate that the internal circulation patterns change through time (Fig. 12). The modifications concern mainly the residence time of the fluids within the volcanics and the intensity and localization of lateral seawater admixture within the karstified Pleistocene reef. Possible processes able to control these changes are either heat flow variations within the volcanic basement or permeability changes within the Pleistocene reef. There could also be a link with the 1994 El Niño event.

Such changes in circulation patterns may have consequences for the availability of nutrients in the living upper part of the reef. For future studies, it

will therefore be important to compare the evolution of fluid flow in the reef with heat flow variations in the basement on one hand, and temperature and salinity changes in the adjacent ocean on the other hand.

Acknowledgements

We thank P. Dudoignon, B. Fritz and F. Rougerie for their interest and support during the study. C. Destrigneville is thanked for the calculations of the saturation indexes. The constructive reviews of J. Humphrey and F. Whitaker, and the helpful comments of the editor E. Oelkers helped to improve a previous version of the manuscript. We are especially indebted to our deceased colleague J.L. Crémoux for his help during field sampling and for the chemical analyses in the ORSTOM laboratory in Tahiti. P.D. was financially supported by ORSTOM (now IRD), which is kindly acknowledged. **[EO]**

References

Almgren, T., Dryssen, D., Fonselius, S., 1983. Determination of alkalinity and total carbonate. In: Grasshoff, K., Ehrhardt, M., Kremlin, K. (Eds.), Methods in Seawater Analysis. Verlag Chemie, Weinheim, pp. 99–123.

Aminot, A., Chaussepied, M., 1983. Manuel des analyses chimiques en milieu marin CNEXO, Brest. 395 pp.

Andrié, C., Jean-Baptiste, P., Pierre, C., Déjardin, P., Fichez, R., Poupeau, J.J., Rougerie, F., 1998. Pore water geochemistry and mixing processes within the Tahiti barrier reef. Geochim. Cosmochim. Acta 62, 2809–2822.

Bard, E., Hamelin, B., Arnold, M., Montaggioni, L., Cabioch, G., Faure, G., Rougerie, F., 1996. Deglacial sea-level record from Tahiti corals and the timing of global meltwater discharge. Nature 382, 241–244.

Bradshaw, A.L., Brewer, P.G., Shafer, O., Williams, R.T., 1981. Measurements of total dioxide and alkalinity by potentiometric titration. Earth Planet. Sci. Lett. 55, 99–115.

Camoin, G.F., Gautret, P., Montaggioni, L.F., Cabioch, G., 1999. Nature and environmental signifcance of microbialites in Quarternary reefs: the Tahiti paradox. Sediment. Geol. 126, 271–304.

Courtillot, V., Davaille, A., Besse, J., Stock, J., 2003. Three distinct types of hotspots in the Earth's mantle. Earth Planet. Sci. Lett. 205, 295–308.

Déjardin, P., 1996. Etude d'un géosystème récifal insulaire (récif barrière de Tahiti, Polynésie Française). Caractérisation géochimique des différents compartiments et de leurs interactions. Unpubl. PhD thesis, Université Louis Pasteur de Strasbourg.

Douglas, A.E., 2003. Coral bleaching—how and why? Mar. Pollut. Bull. 46, 385–392.

Dudoignon, P., Meunier, A., Beaufort, D., Gachon, A., Buigues, D., 1989. Hydrothermal alteration at Mururoa Atoll (French Polynesia). Chem. Geol. 76, 385–401.

Flood, P.G., Fagerstrom, J.A., Rougerie, F., 1996. Interpretation of the origin of massive replacive dolomite within atolls and sumerged carbonate platforms: strontium isotopic signature ODP Hole 866A, resolution Guyot, mid-Pacific Mountains. Sediment. Geol. 101, 9–13.

Fritz, B., 1975. Etude thermodynamique et simulation des réactions entre minéraux et solutions—application à la géochimie des altérations et des eaux continentalesSci. Géol., Mém., vol. 41. Université Louis Pasteur, Strasbourg. 152 pp.

Fritz, B., 1981. Etude thermodynamique et modélisation des réactions hydrothermales et diagénétiques. Sci. Géol., Mém., vol. 65. Strasbourg, 198 pp.

Guy, C., Schott, J., Destrigneville, C., Chiappini, R., 1992. Low temperature alteration of basalt by interstitial seawater, Mururoa, French Polynesia. Geochim. Cosmochim. Acta 56, 4169–4189.

Guy, C., Daux, V., Schott, J., 1999. Behaviour of rare earth elements during seawater/basalt interactions in the Mururoa Massif. Chem. Geol. 158, 21–35.

Henry, P., Guy, C., Dudoignon, P., Sornein, J.F., Caristan, Y., 1996. A convective model of water flow in Muruora basalts. Geochim. Cosmochim. Acta 60, 2087–2109.

Jones, G., Whitaker, F., Smart, P., Sanford, W., 2000. Numerical modelling of geothermal and reflux circulation in Enewetak Atoll: implications for dolimitization. J. Geochem. Explor. 69–70, 71–75.

Montaggioni, L.F., Cabioch, G., Camoinau, G.F., Bard, E., Ribaud-Laurenti, A., Faure, G., Déjardin, P., Récy, J., 1997. Continuous record of reef growth over the past 14 k.y. on the mid-Pacific island of Tahiti. Geology 25, 555–558.

ORSTOM, 1993. Atlas de la Polynésie française. ORSTOM Editions, Paris. 112 pp.

Pfingsten, W., Hadermann, J., Perrochet, P., 2001. Radionuclide release and transport from nuclear underground tests performed at Mururoa and Fangataufa—predictions under uncertainty. J. Contam. Hydrol. 47, 349–363.

Rougerie, R., Wauthy, B., 1986. Le concept d'endo-upwelling dans le fonctionnement des atolls-oasis. Oceanol. Acta 9, 133–148.

Rougerie, R., Wauthy, B., 1993. The endo-upwelling concept: from geothermal convection to reef construction. Coral Reefs 12, 19–30.

Rougerie, F., Jehl, C., Trichet, J., 1997. Phosphorus pathways in atolls: interstitial nutrient pool, cyanobacterial accumulation and carbonat-fluoro-apatite (CFA) precipitation. Mar. Geol. 139, 201–217.

Samaden, G., Dallot, P., Roche, R., 1985. Atoll d'Eniwetok. Système géothermal insulaire à l'état naturel. Houille Blanche 2, 143–151.

Searle, R.C., Francheteau, J., Cornaglia, B., 1995. New observations on mid-plate volcanism and the tectonic history of the Pacific plate, Tahiti to Easter microplate. Earth Planet. Sci. Lett. 131, 395–421.

Seyfried, W.E., Bischoff, J.L., 1979. Low temperature basalt alteration by seawater: an experimental study at 70 °C and 150 °C. Geochim. Cosmochim. Acta 43, 1937–1947.

Spencer, T., Teleki, K.A.C.B., Spalding, M.D., 2000. Coral bleaching in the southern Seychelles during the 1997–1998 Indian Ocean warm event. Mar. Pollut. Bull. 40, 569–586.

Stumm, W., Morgan, J.J., 1996. Aquatic Chemistry. Wiley, New York. 1022 pp.

Swartz, J.H., 1958. Bikini and nearby atolls, Marshall Islands. Geothermal measurements on Eniwetok and Bikini atolls. USGS Rept. 260U, 711–715.

Thématique : "Origine et fractionnement des terres rares dans un contexte d'hydrothermalisme basse température"

Bodeï, S., Buatier, M., **Steinmann, M.**, Adatte, T. & Wheat, C., 2008. Characterization of metalliferous sediment from a low-temperature hydrothermal environment on the Eastern Flank of the East Pacific Rise. Marine Geology 250, 128-141.

ELSEVIER

Marine Geology 250 (2008) 128 – 141

MARINE GEOLOGY
INTERNATIONAL JOURNAL OF MARINE GEOLOGY, GEOCHEMISTRY AND GEOPHYSICS

www.elsevier.com/locate/margeo

Characterization of metalliferous sediment from a low-temperature hydrothermal environment on the Eastern Flank of the East Pacific Rise

S. Bodeï [a,*], M. Buatier [a], M. Steinmann [a], T. Adatte [b], C.G. Wheat [c]

[a] *Département des Géosciences, EA2642, UFR Sciences et Techniques, Université de Franche Comté, 16 Route de Gray, 25030 Besançon, France*
[b] *University of Neuchâtel, Institute of Geology, Emile-Argand 11, CH-2007 Neuchâtel, Switzerland*
[c] *Global Undersea Research Unit, Univ. of Alaska Fairbanks, P.O Box 757 220 Fairbanks, Alaska 99775, USA*

Received 5 February 2007; received in revised form 21 December 2007; accepted 20 January 2008

Abstract

Metalliferous deposits are described from the eastern flank of the East Pacific Rise (EPR) offshore Costa Rica, close to a basaltic seamount called "Dorado high". Based on heat-flow data and porewater profiles, the site is an area of active low-temperature hydrothermal discharge. We focus on the mineralogical and chemical analysis from a 124 cm long gravity core (GC50), located on the northwestern slope of the 100 m high Dorado. In this core, the sediments consist of detrital clay minerals as well as authigenic minerals such as zeolites, apatites, and Fe/Mn-rich oxyhydroxides. In contrast, the reference sediments from adjacent areas without hydrothermal activity are olive gray hemipelagic muds composed of volcanic glass particles, clay minerals, siliceous microfossils, and some detrital quartz and feldspar.

Bulk sediment chemistry and chemical enrichment factors calculated with respect to the reference sediment indicate that the most important chemical changes occurred at the base of the core from 100 to 124 cm bsf, with strong enrichments in MnO, CaO, P_2O_5, and Fe_2O_3. These enrichments are correlated with the occurrence of authigenic Fe-oxyhydroxide (goethite) and Mn oxide (todorokite and vernadite, at 100 cm bsf), and hydrothermal apatite (110–124 cm bsf). In the upper section of the core from 12 to 70 cm, the sediment is composed of abundant smectite and authigenic phillipsite, and only minor chemical changes can be observed with respect to the reference sediments.

The ubiquitous presence of phillipsite suggests that the entire sedimentary column of core GC50 was first affected by diagenesis. However, below 70 cm bsf, these phillipsites are partially dissolved and Fe oxides occur from 110 to 124 cm, followed upward by Mn oxides at 100 cm. This transition from Fe to Mn-rich sediments can be interpreted in terms of an upward increasing redox potential. PAAS-normalized REY patterns of GC50 sediments present clearly negative Ce and positive Y anomalies inherited from seawater at the base of core GC50. These anomalies decrease upward, which we interpret together with the transition from Fe to Mn-rich sediments by an upward migrating low-temperature hydrothermal fluid. Thus, after a first stage of diagenesis, the discharge of a low-temperature hydrothermal fluid occurred through the sedimentary column, leading to the precipitation of hydrothermal compounds that are lacking towards the surface.

Keywords: East Pacific Rise; ridge flank; hydrothermalism; alteration; metalliferous deposits; rare-earth elements

1. Introduction

Oceanic metalliferous deposits consisting of assemblages of Fe–Mn oxyhydroxides, zeolites, and clay minerals are efficient scavengers for trace elements such as Ni, Co, Cu, and rare-earth elements and yttrium (REY; Hein et al., 1997; Kuhn et al., 1998). Such deposits result from the precipitation of dissolved metals from seawater, porewater, or hydrothermal fluids and have been classified into three general categories based on their mechanisms of formation (Boles, 1977; Kastner, 1981). The first category of metalliferous deposits is called hydrogenetic and results from basalt alteration by seawater occurring directly after crust accretion followed by oxide precipitation from seawater (Cann, 1979; Humphris et al., 1980; Honnorez, 1981).

* Corresponding author. Tel.: +33 3 81 66 64 31; fax: +33 3 81 66 65 58.
E-mail addresses: sabine.bodei@univ-fcomte.fr (S. Bodeï), martine.buatier@univfcomte.fr (M. Buatier), marc.steinmann@univ-fcomte.fr (M. Steinmann), thierry.adatte@unine.ch (T. Adatte), wheat@mbari.org (C.G. Wheat).

0025-3227/$ - see front matter © 2008 Elsevier B.V. All rights reserved.
doi:10.1016/j.margeo.2008.01.003

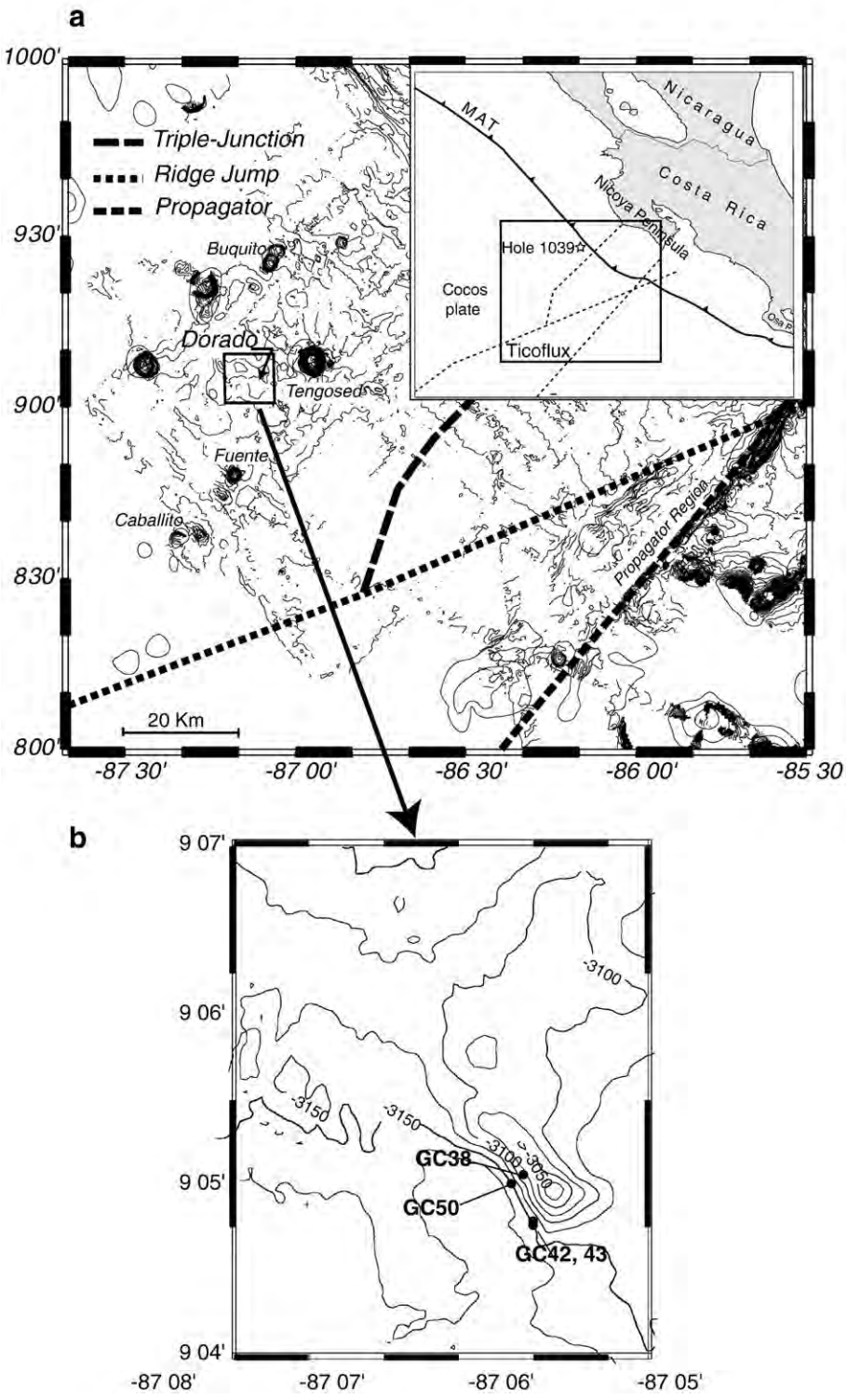

Fig. 1. a) General map of the Ticoflux field area with location of the Dorado outcrop and the ODP hole 1039 (modified from Fisher et al., 2003). b) Location of the studied cores on the southwest side of the Dorado outcrop.

The second category forms during early diagenetic processes, typically within volcanoclastic deposits as well as in deep-sea red clays (Karpoff, 1989; Karpoff et al., 1992; Aoki and Kohyama, 1998). These deposits usually form at redox boundaries within the sediment or at the sediment–water interface. The third category of deposits precipitates from discharging hydrothermal fluids close to the ridge-axis, or on ridge flanks with a thin sedimentary cover (Honnorez et al., 1983; Buatier et al., 1995, 2000). These hydrothermal deposits generally occur in volcanically active areas mainly at plate boundaries (spreading centers, fracture zones), while hydrogenetic and diagenetic deposits are formed in tectonically stable areas on old oceanic

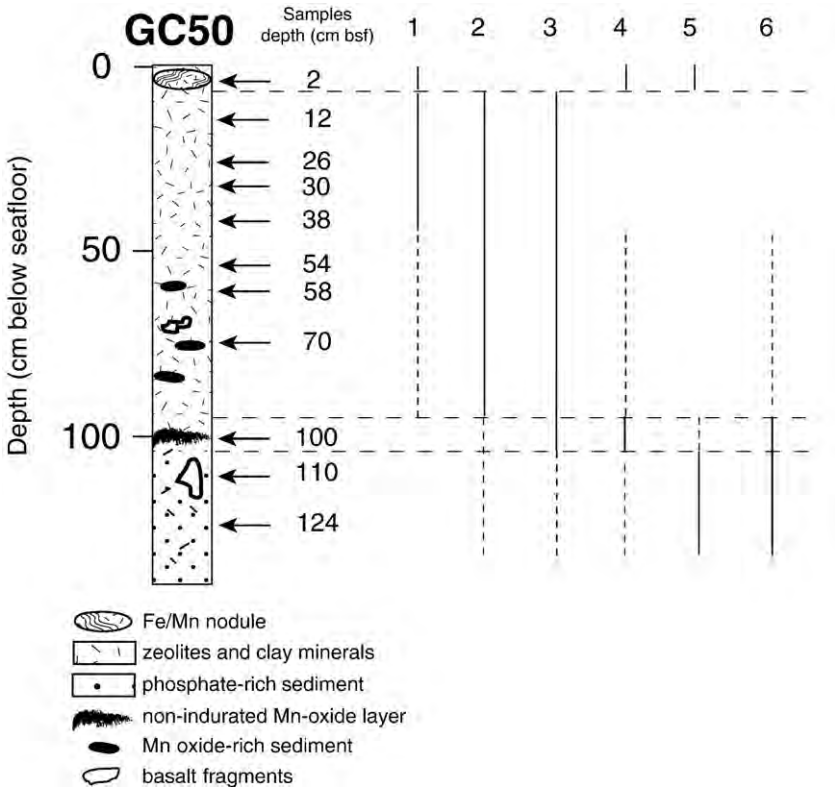

Fig. 2. Sedimentary sequence of gravity core GC50 and location of the studied samples (depth below sea floor (bsf) are indicated). The relative abundance of various sedimentary components in the core is shown, estimated from smear slides and SEM observations. Continuous line: dominant; dashed line: minor and no line: not detected. 1=volcanic glass particles and siliceous microfossils; 2=clay minerals; 3=phillipsite; 4=Mn oxides; 5=Fe oxides; 6=apatite.

crust (Usui et al., 1997). The nature and the chemical composition of newly formed minerals related to fluid–sediment interactions reflect the nature of the fluids from which they precipitated (hydrothermal fluids, seawater or mixtures) and local physicochemical parameters such as redox conditions.

We studied metalliferous hemipelagic sediments that were sampled near a off axis basaltic outcrop, on the eastern flank of the East Pacific Rise (EPR, Fig. 1a). The purpose of this paper is to determine the mineralogical and chemical characteristics of the secondary mineral phases in order to elucidate their mechanism of formation. Special attention will be paid to Fe/Mn ratios, trace metal content, and REY patterns, commonly used to trace the origin of metalliferous deposits (Usui et al., 1997).

2. Regional setting

Metalliferous and hemipelagic sediments were collected by gravity coring during the Ticoflux II expedition in 2002, west of the Nicoya Peninsula, Costa Rica (Fig. 1a). The aim of this expedition was to study the impact of low-temperature ridge-flank hydrothermal activity on the cooling rate of the Cocos plate consisting of a 18–24 Ma-old crust (Fisher et al., 2003). The Cocos plate has a complex tectonic history in the Ticoflux area, comprising basalt crust generated at the EPR (East Pacific Rise) at fast spreading rates and at the CNS (Cocos-Nasca Spreading Center) at intermediate spreading rates. The heat flow measured on EPR generated crust is typically 90% below theoretical heat flow predicted by the conductive lithosphere model, suggesting that cooling has been strongly accelerated by the circulation of hydrothermal fluids (Von Herzen and Uyeda, 1963; Vacquier and Sclater, 1967; Fisher et al., 2003). In contrast, the heat flow of CNS generated crust is in good agreement with calculated conductive heat-flow values. The Ticoflux cruises focused on the hydrologic processes that determine heat-flow distribution using heat-flow measurements, coring, and seismic surveys. Plate boundaries, seamounts, and basaltic outcrops were the primary targets for sampling, because they are fundamental structures for fluid circulations (Harris et al., 2004).

The results from ODP Hole 1039, drilled in close vicinity (Fig. 1a), document that the sedimentary cover of the Cocos plate is ~450 m thick. The upper 150 m is composed of Pleistocene to Pliocene hemipelagic muds, followed below by Miocene pelagic nanofossil oozes. The sedimentation rate is ~46 m/m.y. for the Pleistocene and 6 m/m.y. for the Pliocene and late Miocene (Silver et al., 1997). However, in the Ticoflux area the nature and the thickness of the sediments vary laterally with seafloor topography, bottom currents, and distance from the continent. In general, the total sediment thickness does not exceed 200 m and the overlying hemipelagic sediment section is thin or absent on the top of seamounts (Spinelli and Underwood, 2004).

The gravity cores studied are from the Dorado outcrop, a 100 m high basaltic seamount from 3150 m water depth (Fig. 1a). Heat flow along the SW slope reached values up to 389 mW m^{-2}, which is much higher than the theoretical range of 95 to 120 mW m^{-2} calculated for an 18–24 Ma-old seafloor (Fisher et al., 2002). Fourteen gravity cores were taken on and

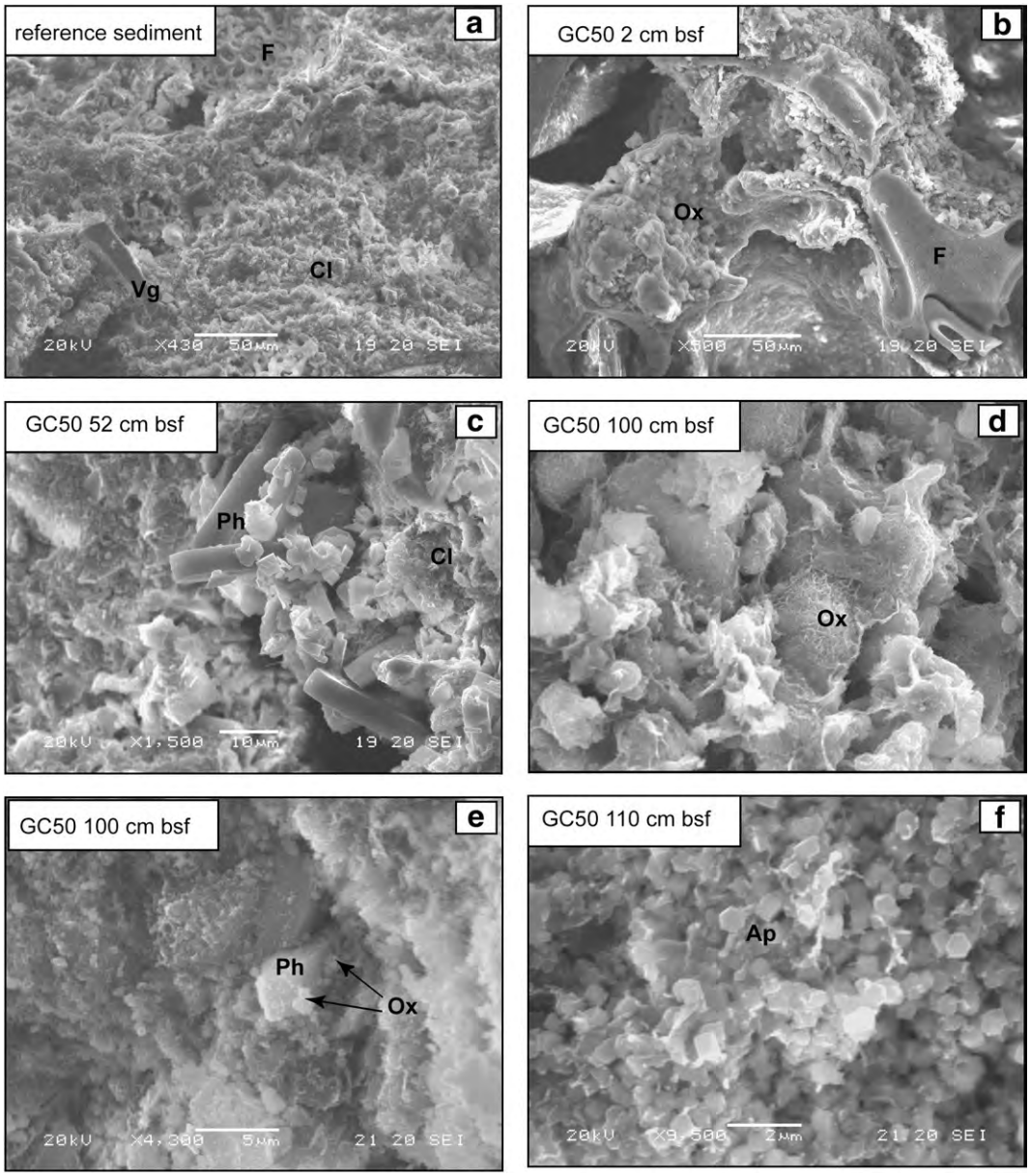

Fig. 3. SEM images of reference sediment and GC50 samples (a) hemipelagic mud from the reference sediment. (b) Mn–Fe oxides encrusting siliceous fossils in sample GC50 at 2 cm bsf. (c) Void filling by authigenic phillipsite in clay-rich sediment at 52 cm bsf. (d) Mn oxides with honeycomb structure in the non-indurated Mn crust at 100 cm bsf. (e) Mn oxides encrusting authigenic phillipsite (100 cm bsf). (f) Authigenic euhedral crystals of apatite at 120 cm bsf. Abbreviations: Cl = detrital smectite; Ap = apatite; F = siliceous microfossils; Ox = oxides; Ph = phillipsite and Vg = volcanic glass.

around the Dorado outcrop (GC 33 to 43 and GC 49 to 51). The sediments of the area consist of hemipelagic mud in the core collected at the base of the seamount and on its southwestern slope, whereas highly altered yellowish brown muds (locally zeolitic) and Mn oxides occur on its northwestern side (Fisher et al., 2002). Phosphate concentrations and alkalinity values of pore water decrease with depth in some of the cores, consistent with upward flowing fluids with low phosphate concentrations and alkalinity values issued from basalt–seawater interaction (Wheat et al., 1996). This suggests, together with the heat-flow data, that the Dorado Outcrop is a site of active discharge of low-temperature hydrothermal fluid (<65 °C).

The location for gravity core GC50 on the northwestern slope of the Dorado outcrop, at 3142 m water depth, was chosen because of the highest heat flow in this area (Fig. 1b, at 9°05.044 °N–87°05.929 °W). This 138 cm long core consists of a mottled mixture of dark yellowish brown zeolitic clay and yellowish brown mud from 12 to 70 cm below seafloor (bsf), some up to 6 cm thick layers and patches of oxides with phosphates and altered zeolites from 70 to 124 cm bsf. Scattered fragments of glassy basalt at the base of the core indicate the proximity to the basalt–sediment interface (Fig. 2). Our study is focused on core GC50 and for comparison we present data from the adjacent cores GC38, GC42, and GC43 (Fig. 1b). These latter cores are composed of hemipelagic mud with no metalliferous deposits. In the following, we consider that these samples, called “reference sediments”, represent the unmineralized sediment of core GC50.

3. Materials and methods

Five samples of bulk sediments from core GC50 (at 2, 30, 52, 100 and 110 cm bsf) representative of each lithologic level, and two bulk reference sediments from neighboring cores (GC42 114 cm bsf and GC38 90 cm bsf) were analyzed by X-ray diffraction (XRD) and observed by scanning and transmission electron microscopy (SEM and TEM).

XRD analysis of bulk sediment samples were conducted at the Geological Institute of the University of Neuchâtel with a Sintag 2000 diffractometer using Cu Kα radiation with 2θ slit varying between 0 and 60° at a scan speed of 0.5°/min, 45 kV/18 mA, 0.1°–1° slits. Samples were prepared following the procedure of Kübler (1987). About 800 mg of sediment was ground to powder, pressed at 20 MPa in a powder holder, covered with a blotting paper, and analyzed. The relative abundances of minerals were

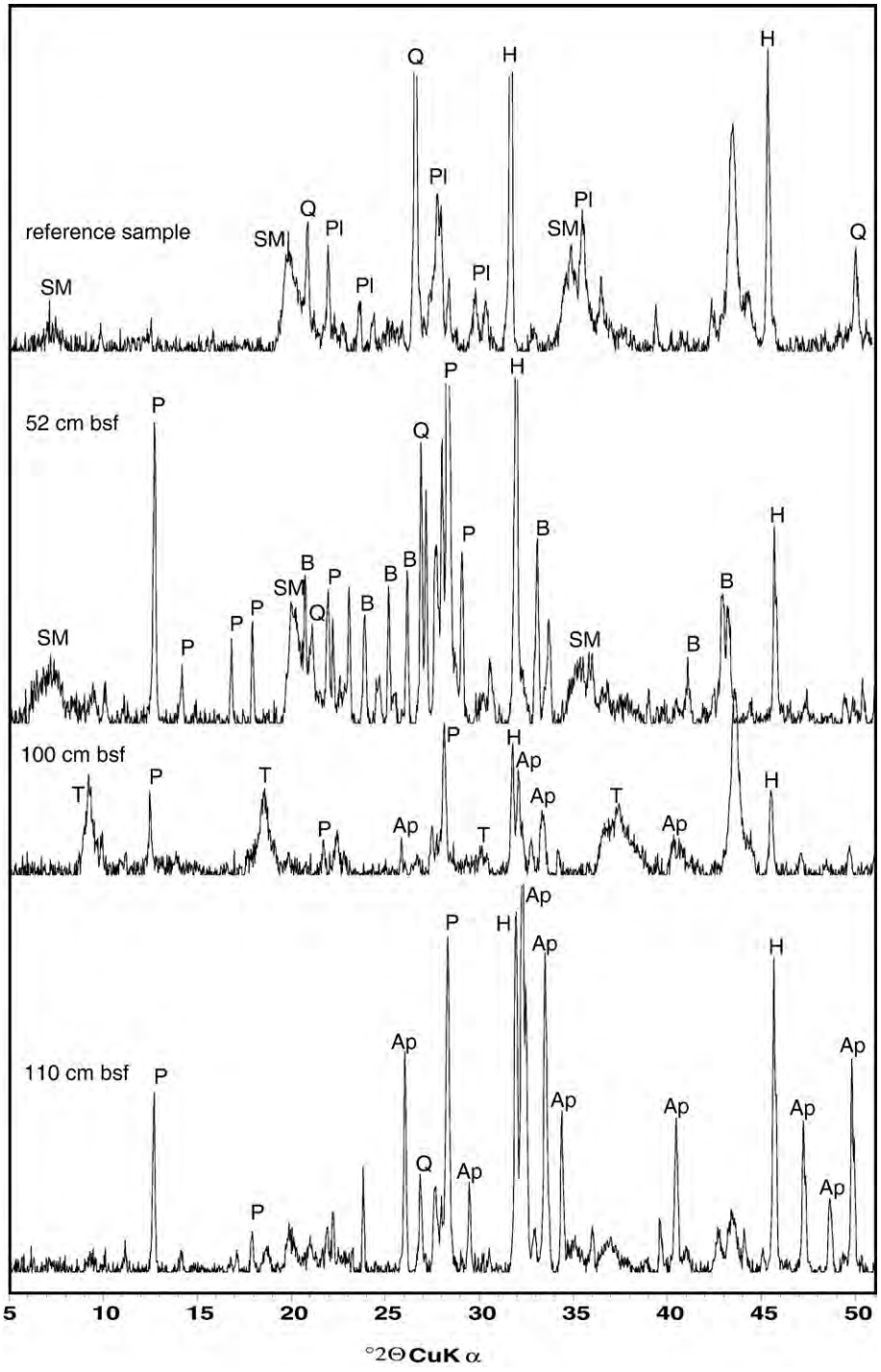

Fig. 4. XRD patterns of the reference sediment and three GC50 samples showing the mineralogical changes with depth. Peak labels: B = barite, Ap = apatite, H = halite, P = phillipsite, Pl = plagioclase, Q = quartz, SM = smectite, T = todorokite.

estimated qualitatively, based on peak heights without interference. A semi-quantitative evaluation of the X-ray diffraction data was not possible because of the abundance of amorphous siliceous fossils and volcanic glass. The clay minerals were identified on oriented samples of <2 μm and 2–16 μm fractions collected on glass slides, after air-drying, and again after ethylene–glycol treatment. To identify more precisely the diffraction peak positions, XRD patterns were decomposed into elementary Gaussian curves using the McDiff program.

Detailed petrographic observations of freshly broken and carbon-coated sample surfaces were performed using a scanning electron microscope (SEM Jeol 5600 operating at 20 kV) equipped with a X-ray EDX Fondis detector (Centre Commun de Microscopie, Université de Franche Comté, Besançon). EDX analysis provided qualitative chemical compositions. For TEM analysis, sediments were stored at 5 °C immediately after sampling. Selected samples were then impregnated in a Spurr resin according to the method of Tessier (1984) and Elsass et al. (1998), cut with a diamond knife on an ultramicrotome, and collected on carbon-coated Cu grids. We used a Jeol 1260 at 120 kV (CCME, Université de Franche Comté, Besançon) and a Philips CM30 at 300 kV equipped with a EDAX detector (CCM, Université de Lille 1).

Chemical analysis were performed on 11 bulk samples from core GC50 and four reference sediments (38GC90, 38GC225, 42GC114 and 43GC89 cm bsf), at the Centre de Géochimie de la Surface at CNRS Strasbourg (France). The samples were ground in an agate mill, dried at 110 °C, calcinated at 1000 °C, melted with a mixture of lithium tetraborate, and dissolved in a glycolated solvent for analysis (Samuel et al., 1985). Major element contents (in wt.% oxides), and trace and rare-earth element contents (in ppm) were determined with a precision of ±5% by ICP-AES (Jobin Yvon) and ICP-MS (VG Plasmaquad PG2+).

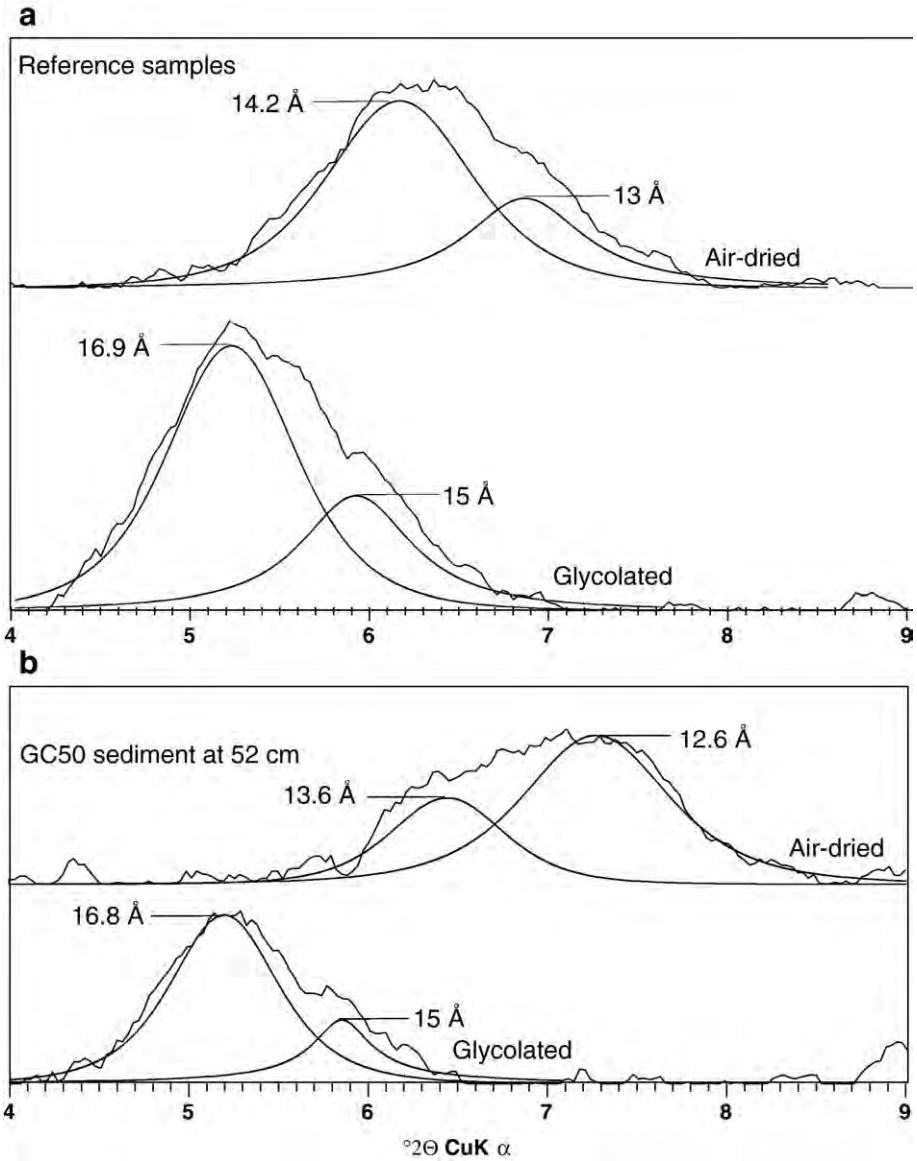

Fig. 5. Fitting of the 4–9°2θ XRD reflections band of the air-dried and glycolated preparations for the reference sediment (a) and sample at 52 cm bsf (b).

4. Results

4.1. Sedimentology and mineralogy

The reference sediments are olive gray hemipelagic muds mainly composed of siliceous microfossils (radiolarians, diatoms, sponge spicules), clay minerals, and volcanic glass particles, according to SEM observations (Fig. 3a). XRD patterns (Fig. 4) show that the clay minerals are smectites, and also reveal the presence of halite, quartz, and feldspar.

At the top of the core (2 cm bsf), a nodule of about 5 cm in diameter was collected (Fig. 2). According to SEM observations, it consists of siliceous microfossils encrusted by black oxides (Fig. 3b). Microfossils seem to have served as a framework for cementation by oxides rich in Mn and Fe as confirmed by the chemical data (Table EA-1).

Sediment samples from mid-core (12–70 cm bsf) are composed of yellowish brown mud containing a mottled mixture of zeolites and clay minerals (Fig. 3c). All samples between 12 and 70 cm bsf present similar XRD patterns. A typical example from 52 cm bsf is shown in Fig. 4. The XRD data allowed to identify the zeolites as phillipsite (major reflections at 3.19 Å and 7.17 Å). This is in agreement with qualitative EDX data from individual crystals, yielding peaks for Si, Al, Na, and K. SEM images of bulk sediment show euhedral prismatic crystals with a size of 20 μm to 1 mm (Fig. 3c), often concentrated in clusters that fill cavities and voids in the sediment. The XRD data furthermore reveal the presence of barite ($BaSO_4$) (Fig. 4). Phillipsite and barite represent the dominant mineral phases in this part of core GC50 and they are accompanied by minor portions of quartz, halite and clay minerals.

The diffraction pattern of the oriented <2 μm fraction displays a large and asymmetric peak between 5 and 9 °2θ (Fig. 5b), in the air-dried sample at 52 cm bsf. A simulated XRD pattern reproduces a comparable asymmetric peak by superposition of two Gaussian curves at respectively 7.3° 2θ (12.6 Å, the most intense) and 6.4° 2θ (13.6 Å, Fig. 5b). After glycolation, the observed peaks are shifted towards lower 2θ angles: the most intense peak is at 5.2° 2θ (16.8 Å) and the second peak at 5.9° 2θ (15 Å). The shift of the 001 reflection from 12.6 Å for air-dried sample to 16.8 Å after glycolation is characteristic for smectite having one water layer in the interlayer position (Deer et al., 1992). The second reflection at 13.6 Å shifted to 15 Å after glycolation corresponds to less expandable clay minerals and can be attributed to irregular mixed-layer chlorite-smectite (Holtzapffel, 1985). The diffraction pattern of the oriented <2 μm fraction of the reference sediment shows a similar asymmetric peak between 5 and 9 °2θ (Fig. 5a). As for the GC50 sediment, this asymmetric peak can be reproduced by superposition of two Gaussian curves which are shifted to 16.9 Å and 15 Å when glycolated. The <2 μm fraction of the reference sediment is thus similar to the upper part of core GC50, mainly composed of smectite and mixed-layer chlorite–smectite.

At 100 cm bsf, a black layer is mainly composed of Fe–Mn oxyhydroxide, phosphate and phillipsite (Fig. 4). XRD analysis of this sample (GC50 100 cm) show large peaks at 9.68 Å and 4.80 Å characteristic of todorokite and/or 10 Å-vernadite (Fig. 4). Todorokite is a manganate with a tunneled-structure and an octahedral sheet of about 10 Å with a cross row octahedral chain running along the *b* axis. 10 Å-vernadite is a disordered phyllomanganate with a 10 Å-thick octahedral sheet layer related to the presence of water and cations within the interlayer (Manceau et al., 2007; Bodeï et al., 2007). These oxyhydroxides show micro-hemispheroidal structures or filament textures under the SEM (Fig. 3d). The spheroids are 10 to 30 μm in diameter and have a honeycomb structure formed by the aggregation of flaky particles of about 2 μm in size. These aggregates seem to have grown on zeolite surfaces (Fig. 3e). Under the TEM, the diameter of the spheroids varies from 5 to 25 μm with a systematic mineralogical zonation (Fig. 6a). The size and morphology of the individual oxide particles vary from the center to the edge: the center is composed of poorly crystallized nanometric particles of phyllomanganate embedded within better crystallized flakes of 10 Å-vernadite, whereas elongated laths of todorokite occur towards the edge of the microconcretions.

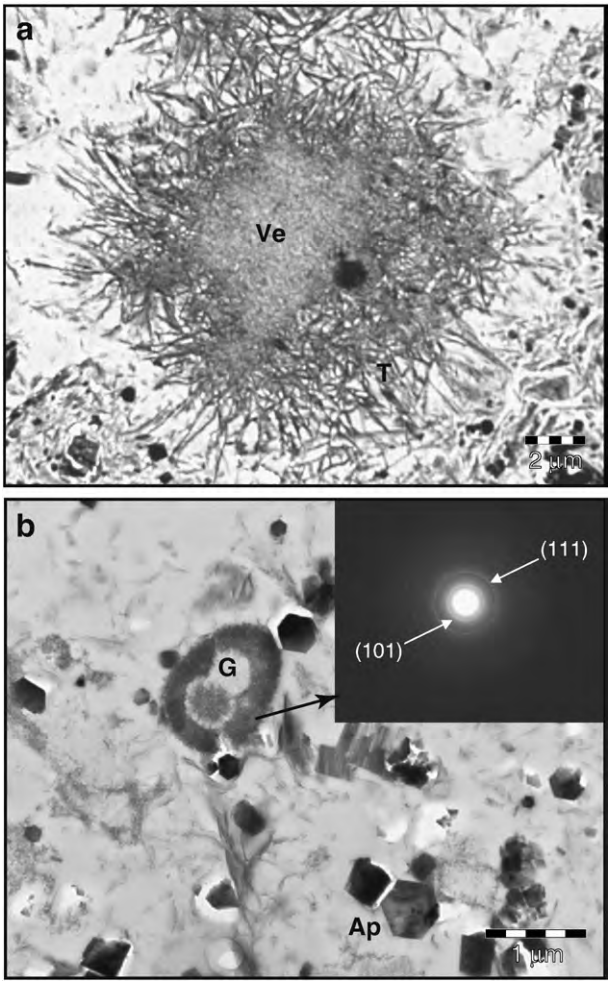

Fig. 6. TEM images of impregnated samples at 100 cm (a) and 124 cm (b). (a) Mn concretions with concentric zonation, showing 10 Å-vernadite (Ve) in the center and todorokite (T) with lath like morphology on the edge. (b) Apatite (Ap) and Fe oxide (G, goethite) with associated SAED (selected area diffraction electron) pattern.

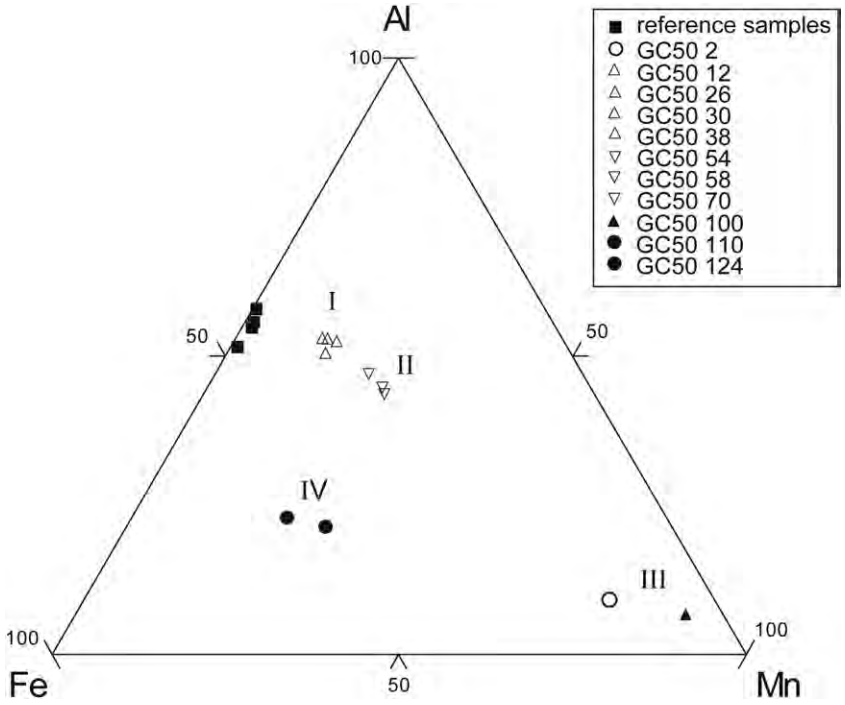

Fig. 7. Al–Fe–Mn ternary diagram for GC50 sediment samples and reference sediments.

Fig. 4 shows the XRD pattern from 110 cm bsf as a typical example of the GC50 sediments below 100 cm bsf. The pattern displays major reflections at 2.80 Å and 2.71 Å corresponding to the major reflections of fluorapatite and hydroxyapatite. Phillipsite is also present in this section as well as quartz and halite. SEM observations confirm the presence of well crystallized authigenic phosphates occurring as aggregates of small euhedral crystals of about 0.7 μm (Fig. 3f). On TEM images, these euhedral crystals display the typical hexagonal morphology of apatite when observed along the 001 zone axis (Fig. 6b). In this part of the core, Fe oxides are also present often on phillipsite surfaces. Their poor crystallinity did not allow their characterization by XRD. However, TEM images show that aggregates of Fe-rich nanoparticles, with common cellular texture, display electron diffraction diagrams with two broad circular reflections at 4.19 Å and 2.44 Å, which could correspond to the (101) and (111) reflections of goethite (Fig. 6b).

Associated to these major phases, XRD diffractograms indicate the presence of quartz and halite in all core GC50 samples (Fig. 4). The occurrence of halite is certainly related to precipitation during sample drying.

4.2. Chemical data

4.2.1. Major and trace elements

The bulk chemistry of the reference sediment (GC38, GC42, and GC43) is characterized by about 55% SiO_2, 15% Al_2O_3, and low contents of CaO (~2%), P_2O_5 (~0.2%), and MnO (~0.13%) (Table EA-1). The altered sediments from core GC50 contain lower Al_2O_3 and SiO_2 concentrations, but relatively high CaO, MnO, and P_2O_5 contents, especially below 70 cm bsf. Compared with the reference sediment, GC50 samples also present high Ba, Ni, Co and Cu contents. In the non-indurated Mn-rich horizon from 100 cm bsf, the Ni and Cu contents are higher than those in hydrothermal crusts from the Valu Fa ridge and approach concentrations typical for Mean Pacific hydrogenous crusts (Hein et al., 1997). The metalliferous surface nodule from 2 cm bsf presents a relatively high Mn concentration. However, its Mn/Fe ratio (4.30) is lower than in the non-indurated Mn horizon at 100 cm bsf (16.73) (Table EA-1).

In a ternary Al–Fe–Mn diagram (Dymond and Corliss, 1973; Toth, 1980), all reference samples are almost Mn-free with an Al/Fe mass ratio of about 1.32 (Fig. 7). In contrast, samples from core GC50 are shifted towards the Mn apex with increasing depth. Four groups can be distinguished. The first group (I) consists of samples from 12 to 38 cm bsf and is characterized by weak Mn enrichment. A second group (II) with a slightly greater Mn enrichment consists of samples from 52 to 70 cm bsf. The third group (III) is defined by the samples from 2 and 100 cm bsf, which are characterized by a strong Mn enrichment and low Fe concentrations. Finally, the fourth group (IV) includes the basal sediments from 110 and 124 cm bsf. This latter group does not follow the general trend and has Mn concentrations similar to the second group, but shifted towards the Fe apex (Fig. 7).

To permit a more direct comparison, we have calculated enrichment factors for all elements in GC50 samples, with respect to the reference sediment.

4.2.2. Enrichment factors

The enrichment factor E_i, used to quantify the chemical variations within core GC50, is defined as (Li, 1982)

$$E_i = (C_i/C_{Al})\ \text{sample}/(C_i/C_{Al})\ \text{reference sediment}$$

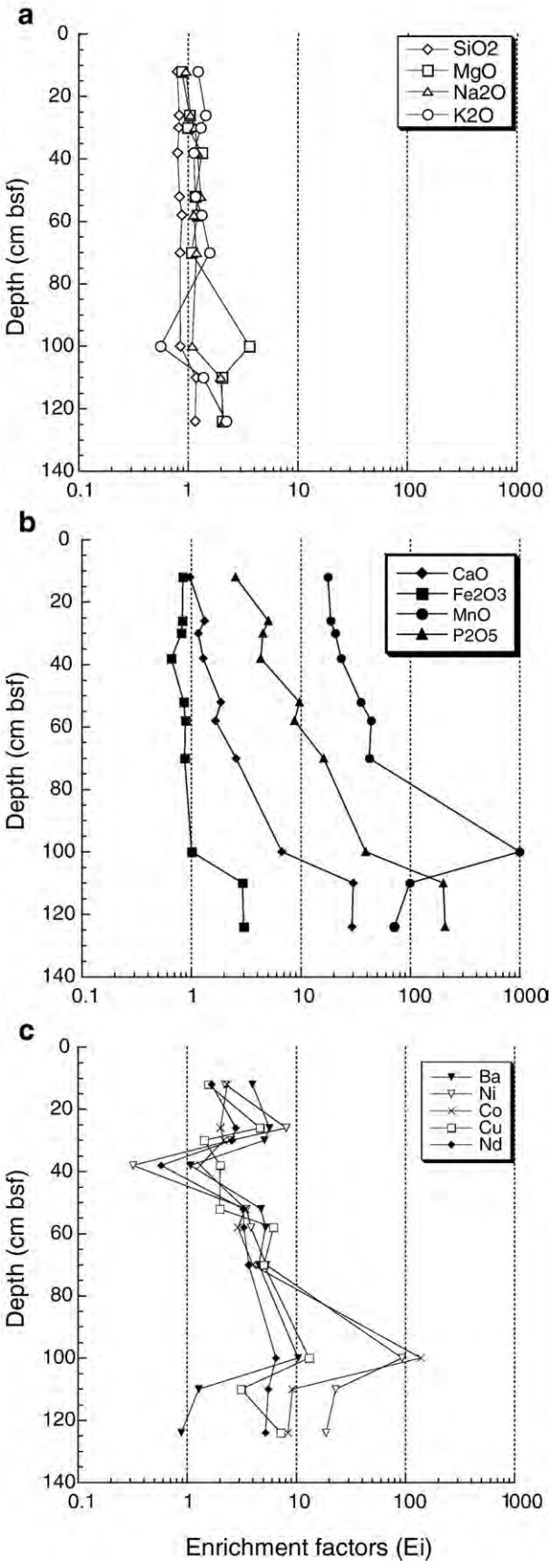

Fig. 8. Depth plots of elemental enrichment factors (E_i), on a log-scale, for GC50 samples (except for the surface nodule at 2 cm bsf) relative to average reference sediment. For major elements (a and b) and trace elements (c).

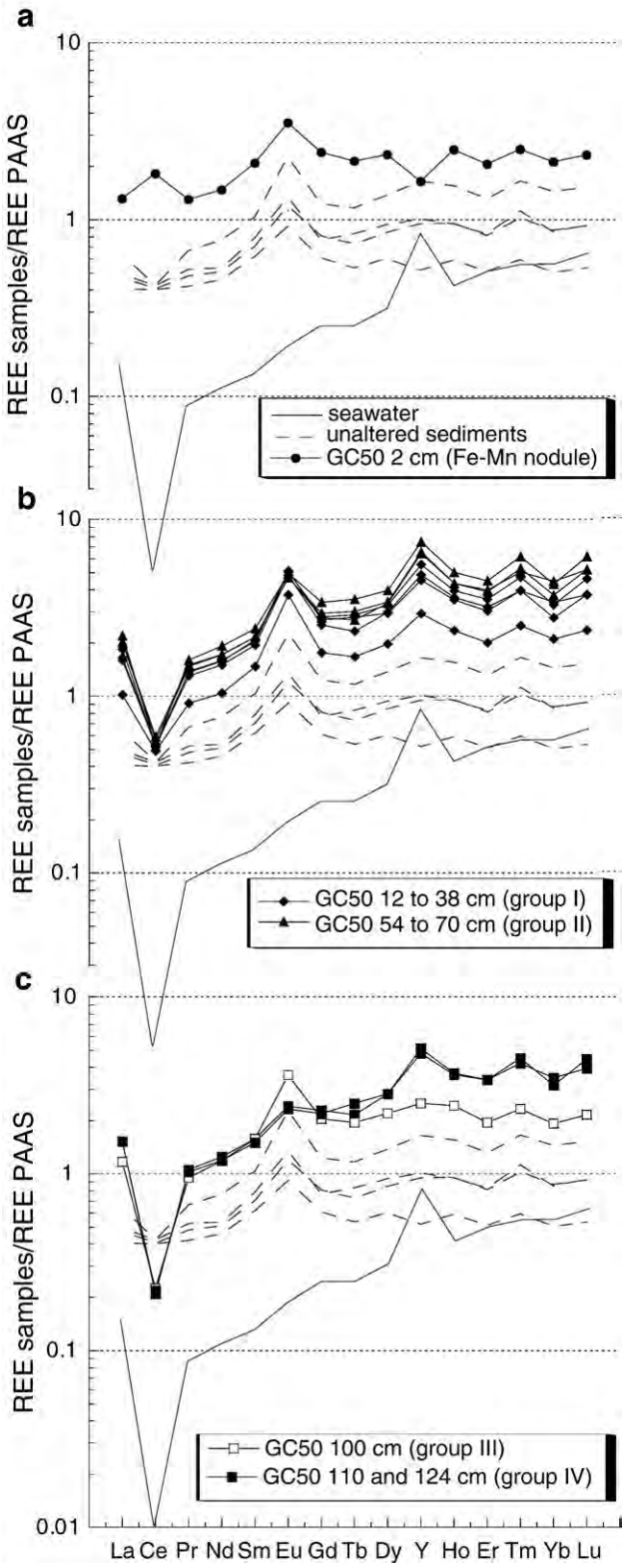

Fig. 9. REE patterns normalized to PAAS (Post-Archean Australian Shale, McLennan, 1989). For comparison, we included patterns for Pacific seawater from 2576 m depth (Alibo and Nozaki, 1999). Seawater values were multiplied by factor 10^6 for comparison.

whereas C_i stands for the concentration of an element i and C_{Al} to the concentration of Al. The normalization with respect to Al is used because Al is considered to be the most immobile major

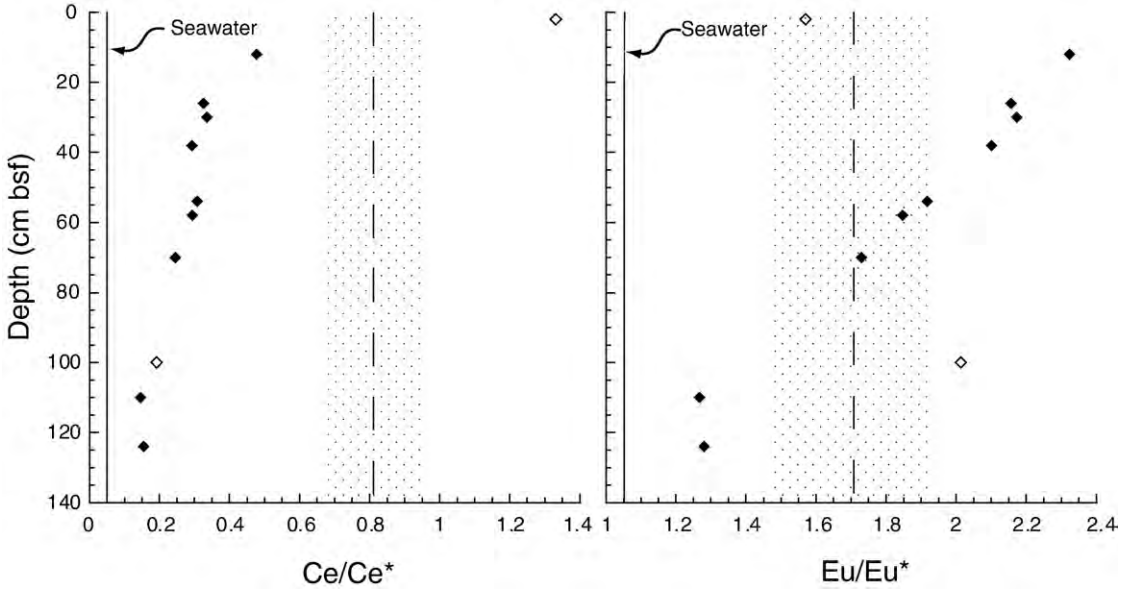

Fig. 10. Ce/Ce* and Eu/Eu* changes with depth for all GC50 samples. The solid lines = seawater values; dotted lines = average of the reference samples with the standard deviation. Open filled = surface nodule at 2 cm bsf and non-indurated Mn oxide layer at 100 cm bsf.

element. As reference sediment we use as previously the average of the four samples from cores GC38, GC42, and GC43.

E_i is close to 1 for SiO_2, K_2O, Na_2O, and MgO, suggesting that these elements remained almost unchanged during alteration (Fig. 8a). For sediments above 100 cm bsf, the enrichment factor for Fe_2O_3 is also around 1, whereas the values for CaO, P_2O_5 and MnO are bigger than 1 and increase with depth (Fig. 8b). Trace elements (Ba, Ni, Co and Cu) are also slightly enriched in this section above 100 cm (Fig. 8c). The highest E_i value of about 1000 is found for MnO in the non-indurated Mn layer at 100 cm bsf (Fig. 8b). The E_i values for Ni and Co have similar depth evolution as MnO and reach values of about 100 at 100 cm bsf (Fig. 8c). The E_i values for P_2O_5, Fe_2O_3, and CaO evolve similarly with depth reaching, in contrast to MnO, their maximum values not at 100 cm bsf but in the two deepest samples at 110 and 124 cm bsf.

4.2.3. Rare-earth elements and yttrium (REY)

The PAAS-normalized REY patterns of the reference samples are almost flat except for the distinct positive Eu anomaly and a slight enrichment of the heavy rare-earth elements (HREE, Gd-Lu) (Fig. 9). Reference samples REY concentrations are distinctly lower than those in GC50 sediments. This is confirmed by the calculated enrichment factor for neodymium, showing a slight increase with depth in the core from 2 to 6 (Fig. 8c). Except for a positive Eu anomaly, the patterns from core GC50 are very similar to seawater, with negative Ce and positive Y anomalies, and a HREE enrichment (Fig. 9b,c). Negative Ce anomaly values ($Ce/Ce^* = 3Ce_N/[2La_N + Nd_N]$) are between 0 and 1, whereas positive Eu anomaly values ($Eu/Eu^* = Eu_N/[\sqrt{(Sm_N * Gd_N}]$) are above 1 (Table EA-2). In core GC50, Eu/Eu* and Ce/Ce* values decrease regularly from the top to bottom achieving almost seawater-like values at the base of the core (Fig. 10, Table EA-2). In contrast, the surface nodule is characterized by a REY pattern that differs from the other samples by having a positive Ce anomaly, a negative Y anomaly, and lack of a HREE enrichment (Fig. 9a).

5. Discussion

5.1. Origin of the authigenic components

Mineralogical observations demonstrate the presence of authigenic minerals in core GC50 suggesting that the pristine sediment has been modified by fluid–sediment interaction. The authigenic phases include phillipsite and barite especially from 12 to 70 cm bsf, then apatite, and Mn and/or Fe oxides from 100 to 124 cm bsf.

The surface nodule, composed of a mixture of Mn oxides and fragments of microfossils, is chemically distinct from the underlying sediment. Its PAAS-normalized REY pattern precludes, together with the enrichment in Ni and Cu, a hydrothermal origin (Usui et al., 1997; Dekov et al., 2003). In contrast, in particular the positive Ce anomaly is rather indicative for hydrogenetic Mn nodules (Usui et al., 1997). However, the Co concentration is below values typical for Mean Pacific hydrogenetic crusts (Hein et al., 1997; Table EA-1). Diagenetic nodules formed in oxic sediments usually have high concentrations in Mn, Cu, and Ni, and are particularly enriched in Cu and Ni. Such diagenetic nodules are furthermore characterized by Mn/Fe ratios between 2.5 and 5 (Dymond et al., 1984; Takematsu et al., 1989). The Mn/Fe ratio of our surface nodule of 4.3 falls within this range. However, this surface nodule is exposed to the water column and may therefore also include a weak hydrogenetic component as suggested by its Co and Fe concentrations that are higher than in typical diagenetic nodules, and by the positive Ce anomaly (Usui et al., 1997; Verlaan et al., 2004).

The sediment from 12 to 70 cm bsf is only slightly different from the reference sediment (Fig. 7). The clay fraction is in both

cases composed of smectite associated with some chlorite/smectite mixed layers. Smectite is a common detrital mineral in deep-sea sediments, but it has also been described as an alteration product of volcanic glass (Chamley, 1989). According to Spinelli and Underwood (2004), smectite is ubiquitous in hemipelagic mud and olive brown clay off the Nicoya Peninsula. These authors described a sediment mainly composed of smectite including probably some illite in a disordered mixed-layer structure, and concluded from this a detrital rather than a diagenetic origin from the alteration of volcanic glass. SEM and TEM investigations did not show textural evidence for the presence of authigenic smectite. Furthermore, smectite is present in both reference and GC50 sediments. For all these reasons we conclude that smectite in core GC50 is of detrital origin.

The barite content found in core GC50 is much higher than in the reference samples and also much higher than can be anticipated from regional organic matter fluxes (Dymond and Corliss, 1996). Therefore it is unlikely to be of biogenic origin. The barite from 12 to 70 cm in core GC50 may therefore be of hydrothermal origin (Bonatti et al., 1972; Dymond et al., 1992). Immediately below this interval, the highest Ba concentration of core GC50 occurs in the Mn oxides rich layer at 100 cm. However, no barite could be identified in this sample (Figs. 4 and 8). Beneath this level no other enrichments of Ba or barite occur. In conclusion, the occurrence of hydrothermal barite above the large Ba enrichment of the Mn oxides layer reflects a more complex origin of the GC50 sediment.

The major mineralogical difference between the sediment from the upper part of core GC50 and the reference sediment is the abundance of phillipsite. Phillipsite is a zeolite group mineral that forms in marine sediments mainly by alteration of volcanic glass (Hay, 1964; Sheppard and Fitzpatrick, 1989). On SEM images, phillipsite fills cavities and voids within the sediment underlining that this mineral is of authigenic origin, and can be interpreted as progressive dissolution and replacement of volcanic glass particles (Burns and Burns, 1978). An additional contribution of silica from siliceous tests is probable. The dissolution of siliceous organisms, leading to a strong Si enrichment, normally promotes the formation of clinoptilolite rather than phillipsite (Stonecipher, 1976; Petzing and Chester, 1979). However, even if SEM observations show that siliceous microfossils present in the reference sediment have disappeared in core GC50, the enrichment factors (E_i) for SiO_2 always remain close to 1 all along the sedimentary column (Fig. 8). Moreover, clinoptilolite is often associated with calcareous sediments and high sedimentation rates, whereas in this study zeolites are formed in volcanic and siliceous sediments with a low sedimentation rate. These environmental factors are generally associated to the formation of phillipsite (Stonecipher, 1976). We can thus suggest that in this particular environmental context the dissolution of volcanic glass particles and probably siliceous microfossils leads to the formation of phillipsite rather than clinoptilolite.

In summary, in the upper part of core GC50 authigenic phillipsite is probably related to early diagenetic processes whereas most of the smectite, also present in the reference samples, is probably of detrital origin.

Below 70 cm bsf, the most important modifications that affected the sediment are strong enrichments in MnO, CaO, P_2O_5, and Fe_2O_3 (Fig. 8b), leading to the precipitation of Fe oxide (goethite), Mn oxide (todorokite and 10 Å-vernadite), and apatite. SEM observations show that Mn and Fe oxides encrust zeolite crystals suggesting that their precipitation postdates that of phillipsite. Moreover, TEM observations of the Mn oxides at 100 cm bsf revealed the presence of Mn microconcretions with a particular structure suggesting that the phyllomanganates of the vernadite family precipitated first on zeolites, followed by todorokite (Fig. 6a). Such a coexistence of todorokite and 10 Å-vernadite is common for marine low-temperature hydrothermal deposits (Usui et al., 1986; Hein et al., 1997; Koschinsky and Hein, 2003). The high concentrations of Ni, Co, and Cu in this sample can be explained by scavenging of these elements by the Mn oxides (Marchig et al., 1999). Dissolution of biogenic siliceous components is a possible source of Ni, Co, and Cu (Burns and Burns, 1978).

Apatite has only been detected in the deepest part of the core, where the enrichment factors (E_i) for CaO and P_2O_5 are highest (Fig. 8). However, the strong correlation between the E_i values of CaO and P_2O_5 over the entire core ($r^2=0.99$) suggests that small amounts of apatite, not detected by X-ray diffraction and microscopy, may also be present at smaller depth. The apatite observed in the deepest part of the core occurs as aggregates of idiomorphous euhedral crystals of about 0.7 μm (Figs. 3f and 6b) and is thus of authigenic origin. Phosphorous in marine sediments is mainly derived from the decomposition of organic matter, a process that is controlled by biologic activity and the availability of oxygen within the sediment. The released phosphorous can directly precipitate as authigenic P-bearing minerals or be integrated into Fe oxyhydroxides (Froelich et al., 1982; Berner et al., 1993). Therefore, the phosphorus cycle can be closely related to the stability of Fe oxyhydroxides, which is directly redox controlled (Krom and Berner, 1980). Consequently, dissolved P can be scavenged by Fe oxyhydroxides under oxic conditions, then be remobilized by the reductive dissolution of Fe oxyhydroxides during burial. The released P may return to the ocean or remain within the sediment and contribute to the formation of authigenic phosphate minerals (Cha et al., 2005). Hydrothermal processes, especially low-temperature systems, are considered to be a major sink for P in the oceans (Froelich et al., 1982; Wheat et al., 1996). In such systems, the relative apatite enrichment can be of organogenic origin (fish bone debris) or result from precipitation of hydrothermal apatite as described by Marchig et al. (1999) for sediments from the Peru basin. These authors found that P_2O_5/Y ratios were higher in hydrothermal apatite than in adjacent biogenic apatite. They explained this difference by the absence of a complete reequilibration of hydrothermal apatite with seawater. In the samples from the deeper part of core GC50, P_2O_5 reaches 12%, and Y 130 ppm (Tables EA-1 and EA-2), yielding a P_2O_5/Y ratio that is highly above the regression line of biogenic apatite, whereas the sample from above 100 cm bsf plots together with the reference samples on the regression line (Fig. 11). We thus conclude that apatite observed at the base of core GC50 is likely of hydrothermal origin. The precipitation of authigenic phosphate minerals rather than

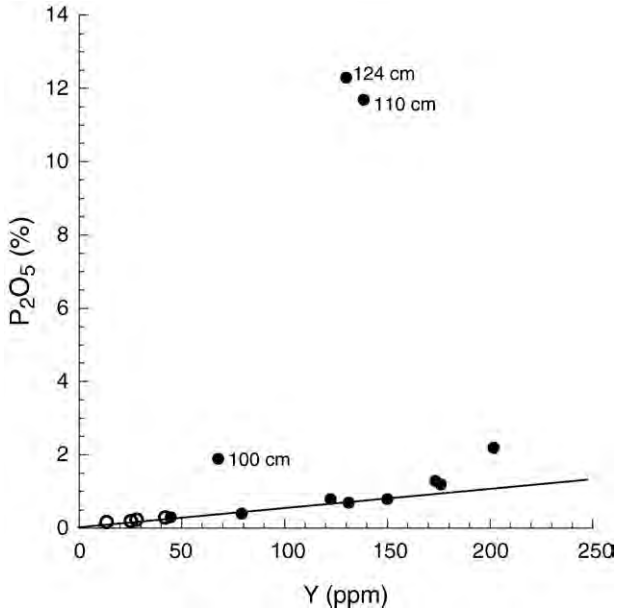

Fig. 11. Plot of Y vs. P_2O_5 for GC50 and reference samples. The ratio valid for organogenic apatite is shown as a line (Marchig et al., 1999). Filled circles are GC50 samples, and open circles are reference samples.

incorporation of P in iron oxyhydroxides occurs, probably because of the high hydrothermal P flux under the reducing conditions at the base of the core.

5.2. Indications for an upward fluid flow

The chemical enrichment factors presented in Section 4.2.2 show that the highest E_i values in core GC50 occur below 70 cm with enrichment factor up to 1000 for MnO at 100 cm (Fig. 8). By comparison, the enrichment factors remain close to 1 in the upper part of the core, suggesting that authigenic phillipsite occurring above 70 cm bsf is of early diagenetic origin and derived from volcanic glass particles and possibly biogenic tests. These data show that the strongest chemical changes occurred in the deepest sediments, below 70 cm bsf.

The enrichment factors for MnO, CaO and P_2O_5 are >1 above 70 cm bsf, and continually increase up to their maximum values below 70 cm. The slight enrichment from 12 to 70 cm suggests that small amounts of phosphate and Mn oxides are also present in the upper part of the core. The Nd content follows the same trend in this section (Fig. 8c), and is better correlated with P_2O_5 ($r^2=0.724$) than with MnO ($r^2=0.502$), suggesting that the phosphate is the main REY carrier phase above 100 cm bsf.

Apatite, Fe oxides and Mn oxides are the major authigenic phases in the basal part of the sedimentary column. The E_i values for P_2O_5 and Fe_2O_3 are highest for the samples at 110 and 124 cm bsf, whereas MnO reaches its maximum value at 100 cm bsf. This succession between Fe_2O_3 and MnO can be explained by an upward increasing redox potential where the oxidation of Fe^{2+} to Fe^{3+} occurs at an Eh of about 0 mV and Mn^{2+} oxidizes to Mn^{4+} above 400 mV. Such an upward increasing redox potential is typical for hydrothermal systems and can be explained by the progressive mixing of a reduced ascending fluid with a more oxygenated porewater towards the sediment–seawater interface (Hein et al., 1994).

To confirm the probable occurrence of an ascending hydrothermal fluid, we focus on REY distribution patterns commonly used to determine the origin of metalliferous deposits (Elderfield and Greaves, 1982). All GC50 samples, excluding the surface nodule, show PAAS-normalized REY patterns characteristic for seawater, except for a strong positive Eu anomaly (Fig. 9b and c). The strong negative Ce anomaly in seawater is due to its quadrivalent oxidation state leading to a preferential removal of Ce from seawater with respect to the other REY which are all trivalent. The pronounced enrichment of the heavy REEs relative to the light REEs is due to the greater stability of HREE complexes in seawater (Elderfield and Greaves, 1982). The REY patterns of low-temperature hydrothermal fluids strongly resemble seawater patterns (Alt, 1988), because they result from the infiltration and the migration of seawater through fractured oceanic basalts with only limited seawater–basalt interaction due to the low temperatures and short residence times (Wheat et al., 1996). The positive Eu anomaly observed in GC50 samples is also present in the reference sediment. Europium commonly substitutes for Sr in feldspars, notably Ca-plagioclases (McLennan, 1989). The positive Eu anomaly of the reference sediment can thus be explained by the presence of plagioclase identified by XRD (Fig. 4) and commonly associated to volcanic glass (Marchig et al., 1999). However, feldspar is rare or absent in GC50 sediment. Alternatively, zeolites, which are the dominant mineral phase in the upper part of core GC50, could be the Eu carrier since they probably derive from the alteration of volcanic glass particles and the breakdown of plagioclase (Laverne et al., 1996). Consequently, the downward decreasing Eu/Eu* anomaly in GC50 core could be explained by the progressive alteration of zeolites and/or plagioclase with depth.

The seawater-like REY distribution patterns of the GC50 sediments confirm an exchange with a low-temperature hydrothermal fluid. The upward decreasing negative Ce and positive Eu anomalies demonstrate furthermore that this hydrothermal influence was strongest at the base and decreased upward.

6. Summary and conclusions

Mineralogical and chemical data define depth-related trends of sediment alteration in gravity core GC50 recovered from the western edge of a seamount east of the East Pacific Rise, at about 9°N. The sedimentary sequence of the core can be subdivided into three units:

– The surface nodule (GC50 2 cm) is mineralogically and chemically distinct from the sediment of the core. This Mn–Fe oxide nodule shows a REY pattern with a positive Ce anomaly precluding a hydrothermal origin. Its high Ni and Cu contents and a Mn/Fe ratio between 2.5 and 5 suggest a diagenetic origin. However, a weak hydrogenetic contribution from the overlying seawater leads to a low enrichment in Co and Fe.

– In the middle part of the sedimentary column (from 12 to 70 cm bsf), chemical exchanges were limited to the formation of diagenetic phillipsite. However, these sediments show a negative Ce anomaly (weaker than in the basal sediments) and a REY pattern similar to sediments of low-temperature hydrothermal origin, suggesting a hydrothermal overprint with a low enrichment in phosphate and Mn oxides.
– In the basal sediments (below 70 cm bsf), the Fe/Mn fractionation and the REYs with a seawater pattern are typical of alteration produced by a reduced ascending fluid of low temperature. The resulting hydrothermal precipitates correspond to authigenic apatite, Fe oxide (goethite), and a mixture of todorokite and 10 Å-vernadite enriched in Ni and Cu probably due to the dissolution of the biogenic siliceous components.

This mineralogical and chemical study of the GC50 core suggests the occurrence of an ascending hydrothermal fluid of low temperature on "Dorado high". This discharge started after a early stage of diagenesis that affected the entire sedimentary column, and lead to the precipitation of hydrothermal minerals that decrease upcore.

Acknowledgements

The authors thank Nicolas Rouge (CCME, Besançon) who helped with SEM analysis, and René Boutin (Centre de Géochimie de la Surface, CNRS Strabourg) for ICP-AES and ICP-MS analysis. This research was financially supported by the GDR Transmet (MB) and the NSF grant OCE 98-19454 (GW).

Appendix A. Supplementary data

Supplementary data associated with this article can be found, in the online version, at doi:10.1016/j.margeo.2008.01.003.

References

Alibo, D.S., Nozaki, Y., 1999. Rare earth elements in seawater: particle association, shale-normalization, and Ce oxidation. Geochim. Cosmochim. Acta 63, 363–372.

Alt, J.C., 1988. Hydrothermal oxide and nontronite deposits on seamounts in the Eastern Pacific. Mar. Geol. 81, 227–239.

Aoki, S., Kohyama, N., 1998. Cenozoic sedimentation and clay mineralogy in the Northern part of the Megallen Trough, Central Pacific basin. Mar. Geol. 148, 21–37.

Berner, R.A., Ruttenberg, K.C., Ingall, E.D., Rao, J.L., 1993. The nature of phosphorus burial in modern marine sediments. In: Wollast, R., Mackenzie, F.T., Chou, L. (Eds.), Interactions of C, N, P and S Biogeochemical Cycles and Global Change. Springer-Verlag, New York, pp. 365–378.

Bodeï, S., Manceau, M., Geoffroy, N., Baronnet, M., Buatier, M., 2007. Formation of todorokite from vernadite in Ni-rich hemipelagic sediments. Geochim. Cosmochim. Acta 71, 5698–5716.

Boles, J.R., 1977. Zeolites in deep-sea sediments. Mineralogy and geochemistry of natural zeolites. Mineral. Soc. Am. Short Course Notes 4, 137–163.

Bonatti, E., Kraemer, T., Rydell, H.S., 1972. Classification and genesis of submarine iron–manganese deposits. Ferromanganese deposits on the Ocean Floor: palisades, N.Y. (Lamont-Doherty Geol. Observ. Columbia Univ.), pp. 149–166.

Buatier, M., Früh-Green, G.L., Karpoff, A.M., 1995. Mechanisms of Mg-phyllosilicate formation in a hydrothermal system at a sedimented ridge (Middle Valley, Juan de Fuca). Contr. Mineral. Petrol. 122, 134–151.

Buatier, M., Monnin, C., Frü-Green, G., Karpoff, A.M., 2000. Fluid–sediment interactions related to hydrothermal circulation in the Eastern Flank of the Juan de Fuca Ridge. Chem. Geol. 175, 343–360.

Burns, V.M., Burns, R.G., 1978. Authigenic todorokite and phillipsite inside deep-sea manganese nodules. Am. Mineral. 63, 827–831.

Cann, J.R., 1979. Metamorphism in the ocean crust, Deep Drilling Results in the Atlantic Ocean: Ocean Crust. American Geophysical Union, Washington, D.C.

Cha, H.J., Lee, C.B., Kim, B.S., Choi, M.S., Ruttenberg, K.C., 2005. Early diagenetic redistribution and burial of phosphorus in the sediments of the southwestern East Sea (Japan Sea). Mar. Geol. 216, 127–143.

Chamley, H., 1989. Clay Sedimentology, ed. Springer-Verlag, Berlin Heidelderg, pp. 291–329.

Deer, D.A., Howie, R.A., Zussman, J., 1992. An Introduction to the Rock-forming Minerals, 2nd edition. Longman Scientific & Technical, London. (696 pp.).

Dekov, V.M., Marchig, V., Rajta, I., Uzonyi, I., 2003. Fe–Mn micronodules born in the metalliferous sediments of two spreading centers: the East Pacific Rise and Mid-Atlantic Ridge. Mar. Geol. 199, 101–121.

Dymond, J., Corliss, J.B., 1973. Origin of metalliferous sediments from the Pacific. Ocean. Geol. Soc. Amer. Bull. 84, 3355–3372.

Dymond, J., Lyle, M., Finney, B., Piper, D.Z., Murphy, K., Conard, R., Pisias, N., 1984. Ferromanganese nodules from MANOP sites H, S and R-control of mineralogical and chemical composition by multiple accretionary processes. Geochim. Cosmochim. Acta 48, 931–949.

Dymond, E., Suess, E., Lyle, M., 1992. Barium in deep sea sediments: a geochemical proxy for paleoproductivity. Paleoceanography 7, 163–181.

Dymond, J., Corliss, J.B., 1996. Particulate barium fluxes and their relationships to biological productivity. Deep-sea Res. II 43, 1283–1308.

Elderfield, H., Greaves, M.J., 1982. The rare earth elements in sea water. Nature 296, 214–219.

Elsass, F., Beaumont, A., Pernes, M., Jaunet, A.M., Tessier, D., 1998. Changes in layer organization of Na and Ca exchanged smectite during solvent exchange for embedment in resin. Can. Mineral. 36, 1325–1333.

Fisher, A., Buatier, M., Costa, P., Ellsworth, C., Friedmann, P., Harris, R., Hasterok, D., Hernandez, B., Hutnak, M., Jones, M., MacKnight, B., Moser, C., Parsons, W., Silver, E., Spinelli, G., Stein, C., Underwood, M., Wheat, G., 2002. The thermal state of 20–25 Ma lithosphere subducting at the Costa Rica Margin: implications for hydrogeology, fluxes and seismogenic zone. Preliminary Cruise Report, Ticoflux 2 Expedition (28 pp.).

Fisher, A.T., Stein, C.A., Harris, R.N., Wang, K., Silver, E.A., Pfender, M., Hutnak, M., Cherkaoui, A., Bodzin, R., Villinger, H., 2003. Abrupt thermal transition reveals hydrothermal boundary and role of seamounts within the Cocos Plate. Geophys. Res. Lett. 30, 1–4.

Froelich, P.N., Bender, M.L., Luedtke, N.A., Heath, G.R., DeVries, T., 1982. The marine phosphorus cycle. Am. J. Sci. 282, 474–511.

Harris, R.N., Fisher, A.T., Chapman, D., 2004. Fluid flow through seamounts and implications for global mass fluxes. Geology 32 (8), 725–728.

Hay, R.L., 1964. Phillipsite of saline lakes and soils. Am. Mineral. 49, 1366–1387.

Hein, J.R., Hsueh-Wen, Y., Gunn, S.H., Gibbs, A.E., Chung-Ho, W., 1994. Composition and origin of hydrothermal ironstones from central Pacific seamounts. Geochim. Cosmochim. Acta 58, 179–189.

Hein, J.R., Koschinsky, A., Halbach, P., Manaheim, F.T., Kang, J.K., Lubick, N., 1997. Iron and manganese oxide mineralization in the Pacific. In: Nicholson, K., Hein, J.R., Bühn, B., Dasgupta, S. (Eds.), Manganese Mineralization: Geochemistry and Mineralogy of Terrestrial and Marine Deposits. Geol. Soc. London Spec. Publ., vol. 119, pp. 123–138.

Holtzapffel, T., 1985. Les minéraux argileux. Préparation, analyse diffractométrique et détermination. Soc. géol. du nord 12, 67–91.

Honnorez, J., 1981. The aging of the oceanic crust at low temperature. In: Emiliani, C. (Ed.), The oceanic lithosphere. Wiley and Sons, New York, pp. 525–597.

Honnorez, J., Karpoff, A.M., Trauth-Badaut, D., 1983. Sedimentology, mineralogy and geochemistry of green clay samples from the Galapagos hydrothermal mounds, Holes 506, 506C and 507D Deep Sea Drilling Project

Leg 70. Initial Reports DSDP, US Gov. Print. Office, Washington, D.C., pp. 221–224.
Humphris, S.E., Thompson, R.N., Marriner, G.F., 1980. The mineralogy and geochemistry of basalt weathering, Holes 417A and 418A. Initial Reports DSDP, US Gov. Print. Office, Washington, D.C. , pp. 1201–1218.
Karpoff, A.M., 1989. Les faciès pélagiques condensés des Océans Pacifique et Atlantique: témoins des grandes crises géodynamiques. DOc. Es Sci. Thesis, ULP, Strasbourg, France.
Karpoff, A.M., France-Larnord, C., Lothe, F., Karcher, P., 1992. Miocene tuff from Mariana Basin, Leg 129, Site 802: a first deep-sea occurrence of thaumasite. In: Larson, R.L., Lancelot, Y., et al. (Eds.), Proceeding ODP. Sci. Results, vol. 129. College Station, Texas, pp. 119–135.
Kastner, M., 1981. Authigenic silicates in deep-sea sediments: formation and diagenesis. In: W.a. Sons (Ed.), The Oceanic Lithosphere. The Sea. Wiley F.A. Mumpton, New York, pp. 915–980.
Koschinsky, A., Hein, J.R., 2003. Uptake of elements from seawater by ferromanganese crusts: solid-phase associations and seawater speciation. Mar. Geol. 198 (3–4), 331–351.
Krom, M.D., Berner, R.A., 1980. The diffusion coefficients of sulfate, ammonium, and phosphate ions in anoxic marine sediments. Limnol. Oceanogr. 25, 327–337.
Kübler, B., 1987. Cristallinité de l'illite, méthodes normalisées de préparations, méthodes normalisées de mesures. Cahier de l'institut de Géologie de Neuchâtel, Ser. ADX 1, p. 13.
Kuhn, T., Bau, M., Blum, N., Halbach, P., 1998. Origin of negative Ce anomalies in mixed hydrothermal–hydrogenetic Fe–Mn crusts from the Central Indian Ridge. Earth Planet. Sci. Lett. 163, 208.
Laverne, C., Belarouchi, A., Honnorez, J., 1996. Alteration mineralogy and chemistry of the upper oceanic crust from Hole 896A, Costa Rica Rift. Proc. Ocean Drill. Prog., Sci. Results 148, 151–170.
Li, Y.H., 1982. Interelement relationship in abyssal Pacific ferromanganese nodules and associated pelagic sediments. Geochim. Cosmochim. Acta 46, 1053–1060.
Manceau, A., Lanson, M., Geoffroy, N., 2007. Natural speciation of Ni, Zn, Ba, and As in ferromanganese coatings on quartz using X-ray fluorescence, absorption, and diffraction. Geochim. Cosmochim. Acta 71, 95–128.
Marchig, V., Von Stackelberg, U., Wiedicke, M., Durn, G., Milovanovic, D., 1999. Hydrothermal activity associated with off-axis volcanism in Peru Basin. Mar. Geol. 159, 179–203.
McLennan, S.M., 1989. Rare earth elements in sedimentary rocks: influence of provenance and sedimentary processes, geochemistry and mineralogy of rare earth elements. Reviews in Mineralogy, Mineral. Soc. Am., Washington, D.C., pp. 169–225.
Petzing, J., Chester, B., 1979. Authigenic marine zeolites and their relationship to global volcanism. Mar. Geol. 29, 253–271.
Samuel, J., Rouault, R., Besnus, Y., 1985. Analyse multiélémentaire standardisée des matériaux géologiques en spectrométrie d'émission par plasma par couplage inductif. Analusis 13, 312–317.
Sheppard, R.A., Fitzpatrick, J.J., 1989. Phillipsite from silicic tuffs in saline, alkaline-lake deposits. Clays Clay Miner. 37, 243–247.
Silver, E., Kimura, G., Blum, P., 1997. Costa Rica Accretionary wedge, Sites 1039–1043. Proceedings ODP. Preliminary Report, vol. 170, pp. 11–16 (College station, Texas).
Spinelli, G.A., Underwood, M.B., 2004. Character of sediments entering the Costa Rica subduction zone: implications for partitioning of water along the plate interface. The island Arc 13, 432–451.
Stonecipher, S.A., 1976. Origin, distribution and diagenesis of phillipsite and clinoptilolite in deep-sea sediments. Chem. Geol. 17, 307–318.
Takematsu, N., Sato, Y., Okabe, S., 1989. Factors controlling the chemical composition of marine manganese nodules and crusts. Mar. Chem. 26, 41–56.
Tessier, D., 1984. Hydratation, gonflement et structuration des matériaux argileux au cours de la dessication et la réhumectation. Doc. Ès Sci. Thesis, Univ. Paris & INRA Versailles, France.
Toth, J.R., 1980. Deposition of submarine crusts rich in manganese and iron. Bull. Geol. Soc. Am. 91, 44–54.
Usui, A., Yuasa, M., Yokota, M., Nishimura, A., Murakami, M.F., 1986. Submarine hydrothermal manganese deposits from the Ogasawara (Bonin) Arc, off the Japan Islands. Mar. Geol. 73, 311–322.
Usui, A., Bau, M., Yamazaki, T., 1997. Manganese microchimneys buried in the Central Pacific pelagic sediments: evidence of intraplate water circulation. Mar. Geol. 141, 269–285.
Vacquier, V., Sclater, J.G., 1967. Studies in the thermal state of the earth, the 21st paper: heat flow, Eastern Pacific. Bull. Earthq. Res. Inst. 45, 375–393.
Verlaan, P.A., Cronan, D.S., Morgan, C.L., 2004. A comparative analysis of compositional variations in and between marine ferromanganese nodules and crusts in the South Pacific and their environmental controls. Prog. Oceanogr. 63, 125–158.
Von Herzen, R.P., Uyeda, S., 1963. Heat flow through the Eastern Pacific floor. J. Geophys. Res. 68, 4219–4250.
Wheat, C.G., Feely, R.A., Mottl, M.J., 1996. Phosphate removal by oceanic hydrothermal processes. An update of the phosphorus budget in the oceans. Geochim. Cosmochim. Acta 60, 3593–3608.

Thématique : "Les processus de transport et de fractionnement des terres rares dans l'eau des ruisseaux"

Tricca, A., Stille, P. & **Steinmann, M**., Kiefel, B., Samuel, J. & Eikenberg, J. 1999: Rare earth elements and Sr and Nd isotopic compositions of dissolved and suspended loads from small river systems in the Vosges mountains (France), the river Rhine, and groundwater. Chem. Geol. 160, 139-158

Steinmann, M. & Stille, P., 2008. Controls on transport and fractionation of the Rare Earth Elements in stream water of a mixed basaltic-granitic catchment basin (Massif Central, France). Chem. Geol. 254, 1-18.

ELSEVIER

Chemical Geology 160 (1999) 139–158

CHEMICAL GEOLOGY
INCLUDING
ISOTOPE GEOSCIENCE

Rare earth elements and Sr and Nd isotopic compositions of dissolved and suspended loads from small river systems in the Vosges mountains (France), the river Rhine and groundwater

Aude Tricca [a,1], Peter Stille [a,*], Marc Steinmann [a], Bernard Kiefel [a], Jean Samuel [a], Jost Eikenberg [b]

[a] *ULP-Ecole et Observatoire des Sciences de la Terre-CNRS, Centre de Géochimie de la Surface, UMR7517, 1 rue Blessig, 67084 Strasbourg, France*

[b] *Paul Scherrer Institute CH-5232 Villigen PSI, Switzerland*

Received 26 March 1998; received in revised form 31 March 1999; accepted 31 March 1999

Abstract

The aim of this study is to characterize the evolution of the rare earth elements (REE) in non-mature streams from small catchment areas in the Vosges mountains downstream to more mature plain rivers including the river Rhine. The dissolved load REE distribution patterns of the low-pH Vosges streams are very different from those of high-pH plain rivers indicating that different physico-chemical parameters control REE transport in these different water systems. The plain rivers and groundwater show similar REE distribution patterns with a strong negative Ce anomaly and heavy rare earth element (HREE) enrichment. In addition, the river Rhine has a positive Gd anomaly which is of anthropogenic origin. Similar to the world's major rivers the light rare earth element (LREE) enrichment in the plain rivers is mainly pH controlled. Their Sm/Nd and $^{143}Nd/^{144}Nd$ isotope ratios are close to average continental crust values. This is not the case for the less evolved, non-mature and low pH Vosges streams. Their high Sm/Nd and $^{143}Nd/^{144}Nd$ ratios but low $^{87}Sr/^{86}Sr$ ratios suggest that chemical alteration of accessory middle rare earth element (MREE) enriched minerals such as apatites from rocks in the catchment area control the REE abundances of these waters. A comparison of the dissolved load REE distribution patterns with those of the principal lithologies in the corresponding drainage basins illustrates that especially the Eu anomalies of the Vosges streamlets are strongly lithology dependent. Leaching experiments indicate that the suspended load is isotopically very inhomogeneous. The REE distribution patterns of the suspended load leachates have no similarities with those of the corresponding dissolved load indicating that the leachable reservoir not only contains adsorbed REE but also REE from leachable mineral phases. Their $^{143}Nd/^{144}Nd$, Sm/Nd and $^{87}Sr/^{86}Sr$ ratios support this suggestion being always higher and lower, respectively, than those of their corresponding dissolved loads. They rather point to the presence of relic primary apatite in the leachable portion of the suspended load. The flat PAAS normalized REE distribution patterns, the high $^{87}Sr/^{86}Sr$ and low $^{143}Nd/^{144}Nd$ isotopic ratios of the corresponding residues suggest secondary silicate phases such as clay minerals in the residual phase of the suspended load. Leachates and corresponding residual phases define alignments in

* Corresponding author. Fax: +33-0388-367235; E-mail: pstille@illite.u-strasbg.fr

[1] Present address: Division of Geological and Planetary Sciences, Mail stop #170-25, California Institute of Technology, Pasadena, CA 91125, USA.

PII: S0009-2541(99)00065-0

the Sm/Nd isochron diagram whose slopes define ages ranging between 200 and 390 Ma indicating that the mineral phases in the suspended load retain some memory of their primary precursor minerals in the Hercynian granitic source rocks.

Keywords: Rhine River; Groundwater; Suspended load; Dissolved load; REE; Sr and Nd isotopes

1. Introduction

Processes controlling the chemical composition of natural waters are of major interest for geochemists because they are the main pathways for the transport of elements and particles at the surface and subsurface of the earth to the oceans. Major river systems have been studied to estimate the fluxes of continent derived material to the oceans, to elucidate erosion processes on a global scale and to elucidate weathering and physical erosion rates (Martin and Meybeck, 1979; Stallard and Edmond, 1983; Meybeck, 1987; Négrel et al., 1993; Blum et al., 1994; Probst et al., 1994; Gaillardet et al., 1995, 1997). Studies of major river systems are of importance because they integrate the great lithological and chemical variety of the earth surface and, therefore, allow estimations about the average chemical composition of the earth's continental crust (Goldstein et al., 1984; Taylor and McLennan, 1985).

Chemical and mechanical alteration of the continental crust leads to the disaggregation of rocks and minerals, the formation of soil systems and also allows the removal of chemical elements as well as of larger and smaller particles from altered rocks and soils by rain, pore, spring and river water. Chemical alteration supplies the dissolved load to the rivers whereas the rivers' suspended loads predominantly contain residual alteration products as well as secondary mineral phases which formed during alteration, such as clay minerals and oxyhydroxides. However, the suspended load may also contain other authigenic minerals which formed directly in the water such as Fe–Mn oxyhydroxides (Andersson et al., 1994).

Several geochemical and isotopic studies focused especially on suspended particulate and dissolved river loads in order to provide information about their origin and to examine elemental fractionation between colloidal and solution phases. Rare earth elements (REE) as well as Sr and Nd isotopic ratios have become most important geochemical tracers in this field of research and, today, dissolved and suspended load data are available for several major river systems (Keasler and Loveland, 1982; Goldstein et al., 1984; Stordal and Wasserburg, 1986; Goldstein and Jacobsen, 1987, 1988a,b; Elderfield et al., 1990; Sholkovitz, 1992; Négrel et al., 1993; Douglas et al., 1995; Allègre et al., 1996; Henry et al., 1996). However, no data exist for smaller rivers and streams with more distinct drainage basin lithology and water chemistry.

The aim of the present study was to elucidate the origin and behavior of REE in river waters from small catchment areas and determine the evolution of their REE distribution patterns downstream to the groundwater in the Rhine valley and to the river Rhine. In this view, it is a complement to studies dealing with large river systems on a continental scale. Another aim was to provide additional information on a number of factors controlling REE concentrations in river waters and distributions such as stabilization by organic matter, pH and adsorption–precipitation processes. Of special interest was also to elucidate the relationship of the dissolved load REE patterns of the small river systems with those of the surrounding sedimentary and granitic rock types. Sr and Nd isotope ratios have been used as additional tracers to determine the origin of the various suspended and dissolved load fractions. Differences between isotopic compositions of suspended and dissolved loads have been previously attributed to differences in weathering susceptibility between minerals (Goldstein and Jacobsen, 1987).

2. The studied area

The Upper Rhine Valley belongs to a large scale geological graben structure, the Rhine graben, which extends from Basel (Switzerland) in the south to

Mainz (Germany) in the north (Fig. 1). The Rhine graben is over 300 km long and 40 km wide. It is bordered by two horst zones which are the French Vosges mountains to the West and the German Black Forest mountains to the East. The Alsatian part of the Upper Rhine valley (France) represents about two thirds of the graben-width and is bordered to the East by the river Rhine.

The southern part of the Vosges mountains consist mainly of Paleozoic granitic and metamorphic rocks. The topographic and geologic transition from the geologic horst structure of the Vosges mountains to the graben structure of the Rhine valley is represented by a series of tilted tectonic blocks containing sandstones, evaporites and carbonates of mainly Triassic and Jurassic age. The plain itself consists of

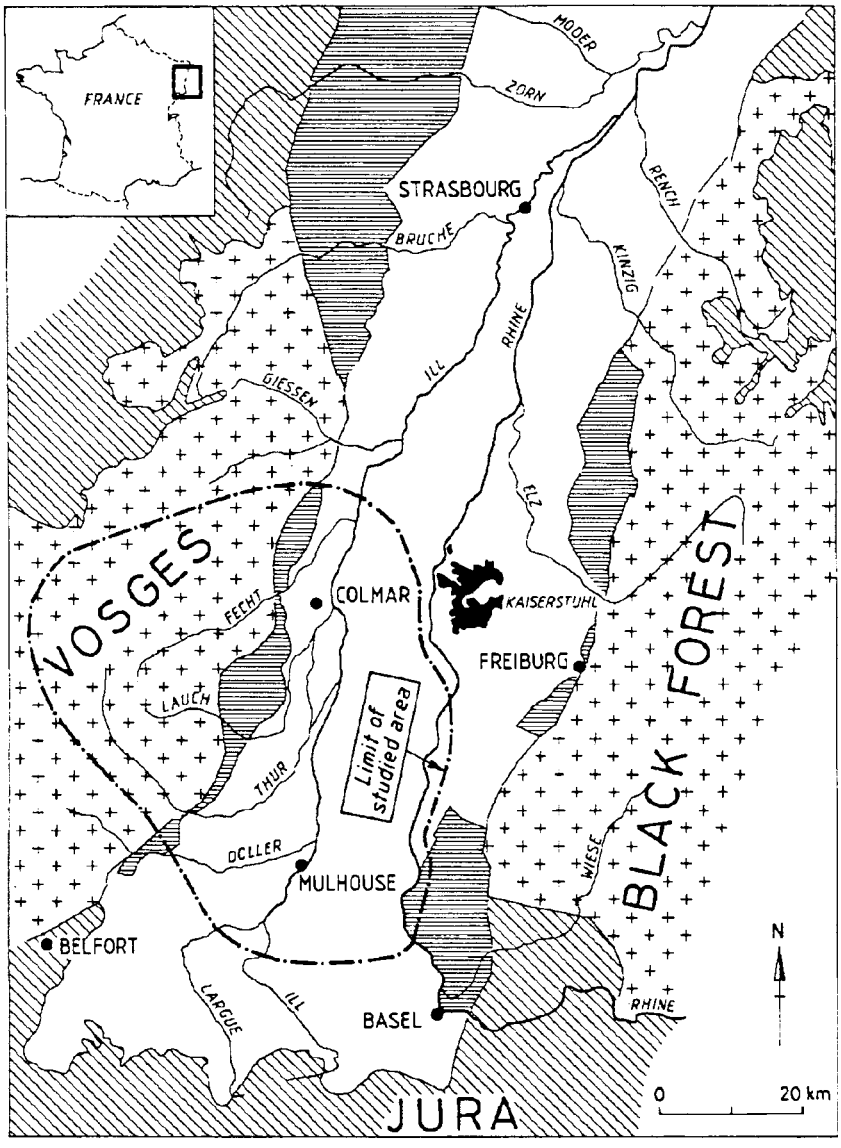

Fig. 1. Upper Rhine Valley with sampling sites.

Tertiary marls and Pliocene and Quaternary alluvial deposits and loess, which represent the groundwater reservoir.

The superficial hydrography of the Rhine valley is dominated by two main rivers, the Ill and the Rhine. The Ill originates from the Jura mountains and flows North, parallel to the Rhine until their confluence located 200 km downstream the source. It receives successively from the west tributaries which derive from small drainage basins in the Vosges mountains (Probst et al., 1992). Groundwater, river Rhine and some of the plain rivers are strongly polluted by fertilizers and by discharge of waste waters from the Alsatian salt mines (KCl, NaCl) near Mulhouse.

The different components of the Alsatian hydrosystem (Rhine, groundwater, plain rivers, Vosges rivers) have been sampled and analysed for their Sr and Nd isotope ratios and REE. One of the Vosges rivers, the Strengbach, has been studied in more detail from its source downstream until the confluence with the plain rivers.

3. Analytical methods

The water samples were filtered on site through 0.45 μm pore size Millipore filters. The solution which passed this filter is called the dissolved load. It consists of dissolved ions and < 0.45 μm colloids. The filtered samples were acidified with HCl to reach a pH between 1 and 2. A non-acidified aliquot was kept to determine major elements, alkalinity, conductivity and dissolved organic carbon (DOC) in the laboratory. pH was measured on site using a pH meter Knick (651) with a combined electrode and in the laboratory using the Mettler DL40GP memotitrator. The DOC was measured in a Shimadzu TOC 5000. No salinity correction was necessary for the DOC measurement. Each value represents the mean of 6 to 10 measurements performed on two aliquots (standard deviation $< 2\%$; reproducibility $< 5\%$). Al has been determined by Inductively Coupled Plasma Atomic-Emission (ICP-AES) with an ARL 3500 spectrometer. The error is $< 10\%$. For the determination of cations, anions and alkalinity (Table 1), see Tricca (1997).

The REE were determined by Inductively Coupled Plasma Spectrometry (ICP-MS, VG PlasmaQuad PQ2 +). The detection limit is 0.01 μg/l and the error of measurement $< 5\%$. The REE concentrations of our samples, however, are below the detection limit of the ICP-MS and, therefore, a specific enrichment method was required. A liquid–liquid extraction technique using HDEHP as organic solvent has been applied to enrich the REE by a factor of at least 100 (Shabani et al., 1992; Tricca,

Table 1
Average chemical compositions, pH and $^{87}Sr/^{86}Sr$ ratios of 0.45 μm filtered water samples[a]

	Groundwater ($n = 14$)	Plain rivers ($n = 48$)	Rhine ($n = 19$)	Vosges streams ($n = 25$)
pH	7.47 (0.14)	7.77 (0.26)	8.01 (0.26)	7.18 (1.00)
Ca^{2+} (mmol/l)	2.47 (0.54)	0.99 (0.65)	1.39 (0.15)	0.24 (0.31)
Na^{+} (mmol/l)	2.18 (0.62)	1.40 (0.95)	1.12 (1.0)	0.24 (0.25)
Mg^{2+} (mmol/l)	0.34 (0.08)	0.20 (0.10)	0.31 (0.04)	0.11 (0.10)
K^{+} (mmol/l)	0.16 (0.11)	0.21 (0.26)	0.08 (0.08)	0.04 (0.03)
HCO_3^{-} (mmol/l)	3.40 (0.48)	1.74 (1.11)	2.75 (0.24)	0.51 (0.77)
SO_4^{2-} (mmol/l)	0.43 (0.10)	0.33 (0.21)	0.32 (0.05)	0.11 (0.09)
Cl^{-} (mmol/l)	3.59 (1.36)	1.33 (0.90)	1.08 (1.00)	0.21 (0.17)
NO^{3-} (mmol/l)	0.34 (0.15)	0.19 (0.10)	0.12 (0.03)	0.05 (0.04)
Σcations (meq/l)	7.94 (1.50)	3.99 (2.04)	4.61 (1.81)	0.97 (1.04)
Σanions (meq/l)	8.19 (1.64)	3.84 (1.95)	4.57 (1.80)	0.96 (1.04)
$^{87}Sr/^{86}Sr$	0.70870 (7)	0.7097 (11)	0.70847 (9)	0.7167 (43)
Sr (μg/l)	349 (81)	135 (83)	355 (59)	28 (25)

Values in parentheses: ± std.dev.; for Sr isotopic composition, std.dev. refers to the last digits.
[a] For single analysis, see Tricca (1997).

1997). Some 0.5 to 2 l of samples was necessary to achieve concentrations above detection limit. The same extraction technique has been used to obtain sufficient Nd (at least 20 ng) for isotope determinations using thermal ionization mass spectrometry. All Sr and Nd isotope analyses were performed on a fully automatic VG Sector mass spectrometer with a 5-cup multicollector after enrichment and separation of Sr and Nd from the bulk sample using cation-exchange resin.

The solid sample material (suspended load, bottom sediments) was considered to consist of two major phases: the unleachable detritus and the leachable pool (Sholkovitz et al., 1994). This is an operational definition because there is always a continuum between leachable and residual phases (Stille and Clauer, 1994; Steinmann and Stille, 1997). The REE from the leachable pool itself were considered to originate from two different reservoirs: the leachable detrital one and the labile reservoir which includes all REE participating in solid–liquid interaction such as adsorption–desorption, surface complexation, coprecipitation and leaching reactions. To separate the two major phases we performed leaching experiments on the suspended load with 1 N HCl at room temperature for 15 min. In order to avoid readsorption (Sholkovitz, 1989) and to prevent buffering effects by dissolution of carbonate, the leaching experiments have been performed using a high acid/solid weight ratio of about 1000. Leachates, residues and corresponding untreated, total suspended loads have been analysed for REE, Sr and Nd isotopes. The unsoluble residual phases were digested for 7 days in closed Savilex vessels containing a HF, HNO_3 and $HClO_4$ mixture. For Sr and bulk REE separation, 1 ml quartz columns with cation-exchange resin and ammonium citrate and HCl as eluents were used. Nd was separated from the remaining REE fraction using the same type of columns and cation-exchange resin and α-hydroxyisobutyric acid as eluent.

For Sr and Nd isotope analysis standard techniques were applied (Steinmann and Stille, 1997). Sr was loaded with nitric acid and Ta_2O_5 as activator on W single filaments. The ratio $^{86}Sr/^{88}Sr = 0.1194$ was used for fractionation correction. Typically, 100 ratios were collected to achieve adequate precision. During the measuring period the NBS 987 Sr standard yielded $^{87}Sr/^{86}Sr = 0.710258 \pm 13$ (± 2 standard deviations of the mean, $n = 9$). Nd was measured using Ta–Re double filament assemblies. The ratio $^{146}Nd/^{144}Nd = 0.7219$ was used for fractionation correction. During the period of measurement the $^{143}Nd/^{144}Nd$ ratio of the La Jolla standard was 0.511856 ± 7 (± 2 standard deviations of the means, $n = 6$).

4. Results and discussion

4.1. Major element and Sr isotopic characteristics of 'dissolved' and corresponding suspended load.

On the basis of their chemical compositions, two types of water samples can be distinguished (Table 1). The first type corresponds to water samples with high alkalinity, thus a neutral to basic pH. The river Rhine, the groundwater and the plain rivers belong to this type of water. Their alkalinity ranges between 0.454 and 4.42 meq/l and the pH between 7.1 and 8.5. The second group represents rivers that are acid or only slightly basic with a pH ranging from 5 to 7.8. These rivers contain low concentrations of bicarbonates and are generally very dilute. This group is represented by the Vosges rivers.

Below Mulhouse the river Rhine and the groundwater show very similar Sr isotopic ratios scattering around 0.7087 (Fig. 2), which points to extensive exchange between the two hydrological systems. The $^{87}Sr/^{86}Sr$ ratio of 0.7087 is slightly higher than the isotopic ratios of 0.7083 and 0.7085 found in the Upper Rhine above Mulhouse and in the Grisons (Switzerland) before entering the Lake of Constance (Buhl et al., 1991). The increase of the $^{87}Sr/^{86}Sr$ ratio is of anthropogenic origin and appears only downstream of waste water discharge from the Alsatian salt mines near Mulhouse with a $^{87}Sr/^{86}Sr$ ratio of 0.7094 and a Ca/Sr ratio of about 100 (Buhl et al., 1991; Tricca, 1997). The slightly lower $^{87}Sr/^{86}Sr$ ratios of 0.7083 to 0.7085 are not only typical of the Upper Rhine above Mulhouse but also of other non-polluted river systems draining marine calcareous sediments of the Alpine molasse. It has therefore been suggested that the Upper Rhine's Sr was derived from carbonates of Tertiary molasse sediments (Buhl et al., 1991; Tricca, 1997). Consequently, the

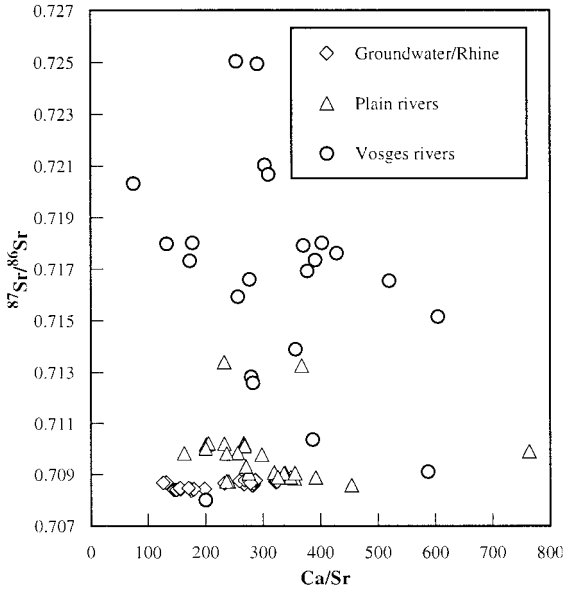

Fig. 2. Mixing diagram showing $^{87}Sr/^{86}Sr$ vs. Ca/Sr molar ratios of water samples.

Ca/Sr ratios of the groundwater and the river Rhine, ranging between 120 and 320, might be the result of mixing between an evaporite end-member with a Ca/Sr ratio of 100 and marine carbonate end-member with Ca/Sr ratios greater than 700. However, two additional and isotopically very similar Sr sources might have been of importance for the plain rivers, the river Rhine and the groundwater: fertilizers and magmatic apatites. The waters are strongly polluted by agricultural activities especially due to the addition of fertilizers. However, their $^{87}Sr/^{86}Sr$ ratios range between 0.707 and 0.7085 (Négrel and Deschamps, 1996) and, therefore, are indistinguishable from the isotope ratios of the marine calcareous sediments of the Alpine molasse.

The reservoir with the high Ca/Sr ratio (>700) and a $^{87}Sr/^{86}Sr$ isotopic ratio of about 0.709 is possibly not only controlled by dissolution of marine carbonates but also of magmatic apatites which, as shown later on, also occur in the leachable portion of the suspended load. Apatites from the catchment area of the Vosges rivers (Strengbach) have Ca/Sr ratios of about 700 and $^{87}Sr/^{86}Sr$ isotopic ratios scattering around 0.709 (El Gh'mari, 1995; Probst et al., submitted). Thus, apatite dissolution might have been of importance in addition to carbonate dissolution at least for the Vosges streams with low $^{87}Sr/^{86}Sr$ isotopic ratios and high Ca/Sr ratios.

The important lithological units in the source region of the investigated Vosges streams are granitic rocks (e.g., the Brezouard granite in the Strengbach catchment with an initial $^{87}Sr/^{86}Sr$ isotopic composition of 0.795; Bonhomme, 1967). Thus, the high $^{87}Sr/^{86}Sr$ isotopic ratio of 0.725 at the sources of the Vosges streams is controlled by a silicate end-member. This ratio decreases rapidly after passing sandstones and Triassic evaporitic carbonate complexes (Tricca, 1997; Riotte and Chabaux, 1999). After entering the Rhine valley, the Vosges streams partly exchanged with the plain rivers causing an increase in the $^{87}Sr/^{86}Sr$ isotopic composition values of some of the plain rivers.

The $^{87}Sr/^{86}Sr$ isotope ratios of the dissolved and corresponding suspended loads of the river Rhine and most of the Vosges streams are very different (Table 2) and suggest that the Sr of the suspended load originates from sources that are more radiogenic than those of the dissolved load. This finding is in agreement with an earlier study on river waters (Goldstein and Jacobsen, 1987). The Sr isotopic composition of the suspended load from the Vosges rivers is much more radiogenic and scattered than those of the more mature river Rhine. The leached fraction of the suspended load of the river Rhine shows significantly lower Sr isotopic ratios than the corresponding residual phase and is even significantly less radiogenic than the dissolved load (Fig. 3). Therefore, it does not exclusively consist of adsorbed dissolved strontium but another low radiogenic component must contribute to the composition of the leachable reservoir. As shown in the following chapters the same leachates are characterized by high $^{143}Nd/^{144}Nd$ and Sm/Nd ratios pointing to the presence of relic primary mineral phases such as apatite in the leachable portion of the suspended load.

4.2. The Sm–Nd isotopic characteristics of the 'dissolved' load

The Sm–Nd isotope data of the 'dissolved' load are compiled in Table 3. The Nd and Sr isotopic ratios of river water have been considered to reflect the isotopic characteristics and ages of the lithological units of the corresponding drainage basins (Gold-

Table 2
$^{87}Sr/^{86}Sr$ of dissolved and suspended loads, suspended load leachates and residues

Sample	$^{87}Sr/^{86}Sr$ suspended load	$^{87}Sr/^{86}Sr$ dissolved load	$^{87}Sr/^{86}Sr$ suspended leach	$^{87}Sr/^{86}Sr$ suspended residue
4107/41:Vosges streams	0.716944 (8)	0.717072 (7)	0.715830 (12)	n.d.
4108/33:Vosges streams	0.745444 (8)	0.721043 (7)	0.720225 (5)	n.d.
4110/42:Vosges streams	0.748259 (7)	0.715940 (7)	0.715961 (9)	n.d.
4111/43:Vosges streams	0.729790 (6)	0.716932 (7)	0.719178 (11)	n.d.
4112/35:Vosges streams	0.744573 (7)	0.720680 (7)	0.720211 (6)	n.d.
4113/44:Vosges streams	0.726185 (8)	0.715154 (6)	0.714927 (6)	n.d.
4114/46:Vosges streams	0.731944 (7)	0.716608 (8)	0.716545 (7)	n.d.
Cleurie/48:Vosges streams	n.d.	0.717329 (17)	n.d.	n.d.
Strengb/32:Vosges streams	n.d.	0.724473 (7)	n.d.	n.d.
8:Rhine	n.d.	0.708463 (8)	n.d.	n.d.
3569:Rhine	0.711718 (7)	0.708438 (7)	0.708213 (7)	0.720226 (7)
3570:Rhine	0.711193 (6)	0.708421 (6)	0.708198 (7)	0.720159 (7)
3571:Rhine	0.711089 (7)	0.708433 (8)	0.708187 (8)	0.720136 (8)
3572:Rhine	0.711365 (7)	0.708466 (7)	0.708162 (7)	0.720264 (7)
3573:Rhine	0.710267 (6)	0.708430 (7)	0.708238 (7)	0.719376 (6)
3575:Rhine	0.709928 (7)	0.708462 (8)	0.708325 (6)	0.719667 (7)
31:Groundwater	n.d.	0.708733 (7)	n.d.	n.d.

The errors given for the Sr isotopic compositions are two sigma mean values and refer to the last digits.
n.d. = not determined.

stein and Jacobsen, 1987; Andersson et al., 1992). Generally, two end-members control the dissolved ε_{Nd} of the world rivers: one end-member corresponds to waters of high pH draining carbonate rocks with $\varepsilon_{Nd} = -8.5$ and a $^{87}Sr/^{86}Sr$ ratio of about 0.7095 and the other one represents waters of low pH draining Precambrian silicate rocks with lower ε_{Nd} and higher Sr isotopic composition values. Therefore, the large river systems show an overall inverse correlation trend between $^{87}Sr/^{86}Sr$ and ε_{Nd} (Fig. 4). Our samples, however, do not show this trend. On the contrary, they are positively correlated indicating that the Sr–Nd isotopes are controlled by a silicate end-member (Vosges streams: $\varepsilon_{Nd} = -7$ and $^{87}Sr/^{86}Sr = 0.725$) and another end-member with less radiogenic Nd and Sr isotopic compositions (groundwater and Rhine: $\varepsilon_{Nd} = -10$; $^{87}Sr/^{86}Sr = 0.709$). The silicate end-member is different from the world average because the drainage basin consists only of younger Hercynian granites while the silicate end-member defined earlier from the world's major river systems reflects Precambrian rocks (Goldstein and Jacobsen, 1988a,b).

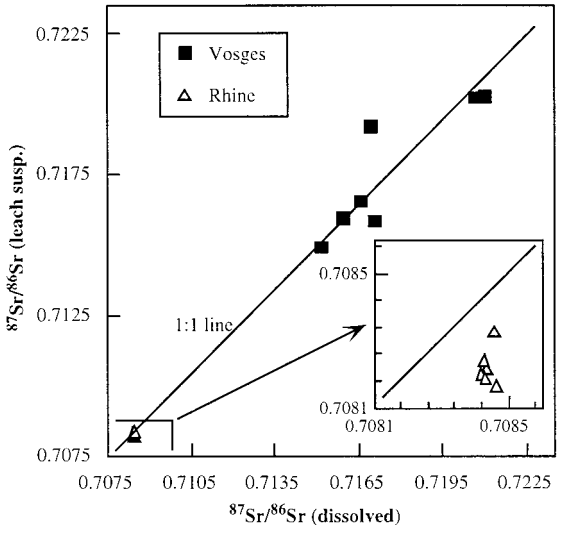

Fig. 3. Comparison of $^{87}Sr/^{86}Sr$ in dissolved load and leachate of suspended load.

The second end-member with less radiogenic Nd and Sr isotope compositions is more difficult to characterize. The Sr and Nd isotopic compositions of especially the Rhine and groundwater are geochemically decoupled. Their Sr isotopic compositions are strongly carbonate controlled. The average $^{87}Sr/^{86}Sr$ ratio of 0.708436 for the carbonate-rich Rhine can be

Table 3
$^{147}Sm/^{144}Nd$ and $^{143}Nd/^{144}Nd$ isotope ratios, ε_{Nd} values and Nd model ages (T_{DM}) of dissolved and suspended loads, of suspended load leachates and residues and of bottom sediments

Sample	$^{147}Sm/^{144}Nd$	$^{143}Nd/^{144}Nd$	ε_{Nd}	T_{DM} (By)
Diss/Cleurie/48: Vosges stream	0.161	0.512190 (20)	−8.78	2.8
Diss/Strengb/32: Vosges stream	0.247	0.512258 (7)	−7.41	−4.2
Diss/Rhine 8	0.146	0.512140 (10)	−9.75	2.3
Diss/Groundwater 31	0.147	0.512130 (10)	−9.95	2.4
LEACH/Susp/4029/4/Rhine	0.148	0.512264 (13)	−7.34	2.1
LEACH/Susp/4108/33/Vosges stream	0.227	0.512244 (8)	−7.73	−11.3
LEACH/Susp/4110/42/Vosges stream	0.182	0.512248 (7)	−7.65	4.3
LEACH/Susp/4107/41/Vosges stream	0.179	0.512198 (12)	−8.62	4.2
LEACH/Bot.sed/4109/32/Vosges stream	0.243	0.512131 (10)	−9.93	−5.6
LEACH/Bot.sed/4021/39/Vosges stream	0.175	0.512282 (7)	−6.98	3.5
LEACH/Bot.sed/4110/42/Vosges stream	0.200	0.512356 (10)	−5.54	8.9
RES/SED4109/32/Vosges stream	0.142	0.512311 (8)	−6.42	1.8
RES/SED4108/33/Vosges stream	0.124	0.512155 (4)	−9.46	1.7
RES/SED4021/39/Vosges stream	0.137	0.512132 (5)	−9.91	2.0
RES/SED4110/42/Vosges stream	0.148	0.512169 (5)	−9.19	2.3
RES/SED4107/41/Vosges stream	0.116	0.512247 (6)	−7.67	1.4
RES/Susp4029/4/Rhine	0.108	0.512162 (13)	−9.32	1.6
RES/Susp4108/33/Vosges stream	0.110	0.512102 (8)	−10.50	1.6
RES/Susp4110/42/Vosges stream	0.110	0.512152 (7)	−9.52	1.5
Tot/Susp4029/4/Rhine	0.124	0.512218 (8)	−8.23	1.6
Tot/Susp4108/33/Vosges stream	0.162	0.512164 (8)	−9.29	2.9

The errors given for the Nd isotopic compositions are two sigma mean values and refer to the last digits.

observed in marine carbonates of Tertiary age (Hodell et al., 1991). Therefore, an important component of the Rhine's Sr probably originates from carbonates of Tertiary molasse sediments which represent one of the most important lithological units of the Rhine's drainage basin after it left the Alpine domain. This, however, is not the case for the REE. The corresponding ε_{Nd} values for Tertiary marine sediments (phosphates) range between −7 and −9.8 (Stille et al., 1996) which is higher than the ε_{Nd} values observed for the river Rhine and the groundwater.

Comparison of the ε_{Nd} values with the corresponding Sm/Nd ratios yields more information about the origin of the REE in the dissolved load (Fig. 5A). They are positively correlated with low $^{147}Sm/^{144}Nd$ ratios for the river Rhine and groundwater (0.14) and rather high ratios for the Vosges rivers (0.16–0.25). These ratios are significantly higher than the average continental crust value of 0.105 (Allègre and Lewin, 1989). At low Sm/Nd and ε_{Nd} values, the correlation line passes through the average continental crust value derived from terrigeneous Mesozoic schists (so-called Bündnerschiefer) of the Central Alps (Grisons, Switzerland) which form a dominant part of the Rhine's catchment basin. These schists represent best the average isotopic composition of the continental crust for the studied area. Its average Nd isotopic composition corresponds to an ε_{Nd} value of −10.3 and its $^{147}Sm/^{144}Nd$ ratio is 0.127 (Steinmann, 1994a; Steinmann and Stille, 1999). The ε_{Nd} value is similar to that postulated earlier for the average continental crust in the South Alpine domain (Stille and Buletti, 1987). Thus, the Sm–Nd and Sr isotope data of the dissolved loads taken together reflect mixing between a carbonate-rich continental crust end-member represented by the large water masses of the mature river Rhine and the groundwater and a very radiogenic end-member represented by a small stream from the Vosges mountains with a very distinct granitic drainage basin lithology.

The rather similar Sr and Nd isotopic composition values for the river Rhine and the groundwater suggest similar sources. Undoubtedly, the river Rhine was always the most important hydrologic system feeding the groundwater. On the other side the

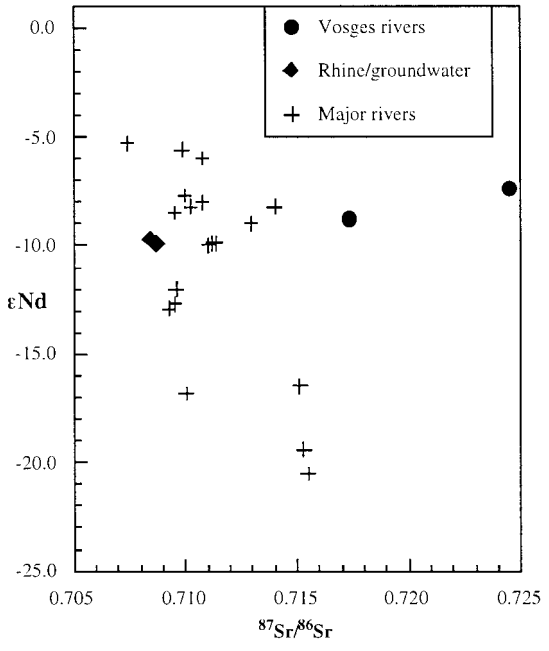

Fig. 4. Comparison of ε_{Nd} and $^{87}Sr/^{86}Sr$ in dissolved loads of Voges Rivers, river Rhine and groundwater with data of the world's major river systems (Goldstein and Jacobsen, 1988a,b).

groundwater is situated in alluvial deposits which contain most rock types of the Rhine's catchment area. Therefore, the isotopic similarity between the two hydrological systems might also simply be due to exchange with similar lithologies.

4.3. Nd isotopic and REE characteristics of the suspended load

The Sm–Nd isotope data of suspended loads and their corresponding leachates and residues (Table 2) are shown in Fig. 5B and compared with those of the dissolved loads. For all suspended loads [(1) Rhine; (2,3) Vosges rivers], the leachates always show much higher Sm/Nd ratios than the corresponding residues. The untreated total suspended loads plot as required from mass balance considerations between the values of corresponding leachates and residues. Most striking in this diagram are the ε_{Nd} values and Sm/Nd ratios for the leachates which are always much higher than those of the corresponding residues or untreated fractions. The leachates and dissolved loads show a large variation in their $^{147}Sm/^{144}Nd$ ratios compared to the corresponding solid phases ranging between 0.12 and 0.25. This may point to the preferential leaching of middle rare earth element (MREE) enriched mineral phases during experimental leaching of the suspended load and/or during weathering of the granitic source rocks.

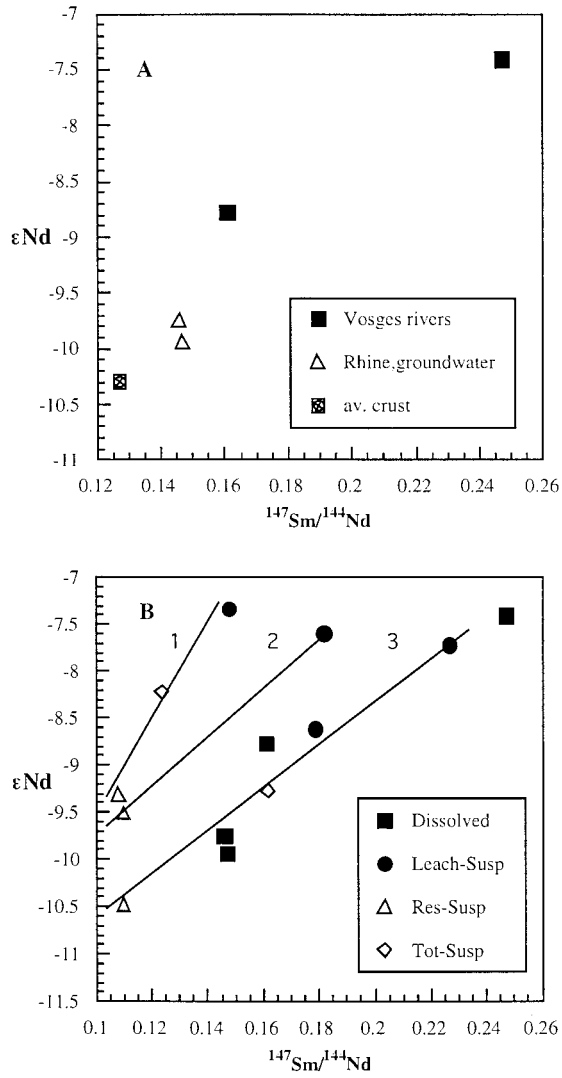

Fig. 5. (A) ε_{Nd} vs. $^{147}Sm/^{144}Nd$ of dissolved loads compared to average crust. River Rhine and groundwater with low $^{147}Sm/^{144}Nd$ (0.145) and Vosges rivers with high ratios (0.16–0.25). (B) ε_{Nd} vs. $^{147}Sm/^{144}Nd$ of dissolved loads compared to suspended loads, leachates and corresponding residues. Suspended loads: (1) river Rhine; (2 and 3) Vosges rivers.

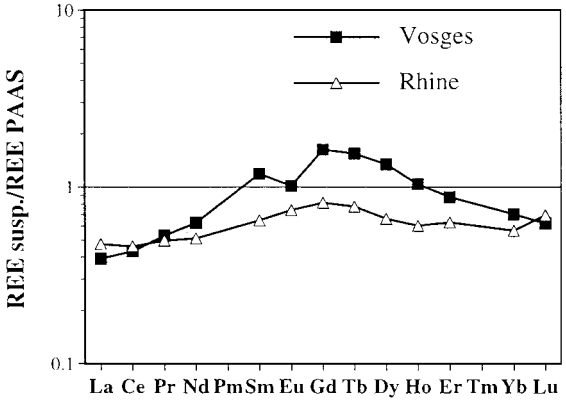

Fig. 6. PAAS normalized REE patterns of suspended loads from catchment lithologies with positive and negative Eu anomalies.

The large differences in isotopic composition between leachable and residual phase (up to three epsilon units) indicates that the suspended load is isotopically very inhomogeneous and that the leachable reservoir contains a mineral phase with high $^{143}Nd/^{144}Nd$ and $^{147}Sm/^{144}Nd$ ratios. Thus, the Sm/Nd ratio is not a leaching artefact as discussed earlier (Sholkovitz, 1989). The same leachates are characterized by very low $^{87}Sr/^{86}Sr$ ratios, much lower than those of the corresponding residues and even lower than the corresponding dissolved load (Fig. 3). Similarly, their REE distribution patterns are different from those of the corresponding dissolved loads (see Section 4.4). They are humpshaped and can be found in argillaceous carbonates, clay minerals, authigenic Fe–Mn coatings, iron oxide-clay-rich dolomites and magmatic or diagenetic apatite (Banner et al., 1988; Banfield and Eggleton, 1989; Gosselin et al., 1992; Schaltegger et al., 1994; Stille and Clauer, 1994; Johannesson et al., 1996; Steinmann and Stille, 1997).

Most probably, the high Sm/Nd ratios together with high ε_{Nd} and low $^{87}Sr/^{86}Sr$ isotopic composition values reflect relic primary mineral phases such as apatite in the leachable portion of the suspended load. This is supported by the following observation: leachate–residue pairs in the Sm–Nd isochron diagram describe similar alignments whose slopes correspond to ages ranging between 200 and 390 Ma (Fig. 5B). This might indicate that the leachable phases and corresponding residues retained some memory of their primary precursor minerals within the Hercynian granitic rocks.

The PAAS normalized REE distribution patterns of untreated total suspended loads are plotted in Fig. 6 for suspended matter of the river Rhine and Vosges rivers, respectively. The absolute REE concentrations and distributions of both types of river systems are very similar with the exception of the strong negative Eu anomaly (Eu^*) (McLennan, 1989) for the Vosges rivers (Table 4). The strong Eu anomaly might indicate that feldspar is not an important mineral phase in the Vosges rivers suspended load. As

Table 4
REE concentrations in ppm of suspended loads, leachates and residues

Sample	La	Ce	Pr	Nd	Sm	Eu	Gd	Tb	Dy	Ho	Er	Tm	Yb	Lu
8Rhine/4029/4Leach	5.0	12.0	1.5	6.9	1.7	0.41	1.7	0.27	1.4	0.26	0.7		0.50	0.08
Rhine/4032/7Leach	7.0	14.0	2.0	9.0	2.2	0.5	2.3	0.34	1.7	0.33	0.8		0.60	0.09
Rhine/4033/8Leach	9.0	23.0	3.2	14.3	3.3	0.74	3.2	0.44	2.2	0.40	1.0		0.70	0.10
Vosges/4108/33Leach	4.6	11.3	1.8	9.0	3.4	0.55	4.3	0.73	3.8	0.63	1.5	0.19	1.20	0.15
Vosges/4109/32Leach	5.2	11.6	2.2	11.5	4.8	0.82	5.9	1.00	5.1	0.80	1.9	0.23	1.30	0.16
Vosges/4112/35Leach	3.4	8.1	1.4	7.1	2.5	0.45	3.2	0.55	2.8	0.49	1.2	0.15	0.94	0.13
4029/4residue	13.0	26.2	3.0	11.1	2.0	0.37	2.2	0.38	2.2	0.47	1.4		1.39	0.25
4032/7residue	11.2	21.7	2.2	7.9	1.3	0.29	1.4	0.22	1.3	0.29	0.9		0.90	0.17
4033/8residue	7.1	14.2	1.5	5.6	1.0	0.22	1.0	0.16	0.8	0.18	0.5		0.60	0.10
4029/4/tot. Susp.	19.6	40.3	4.8	19.4	4.0	0.9	4.3	0.70	3.9	0.80	2.2		2.00	0.40
4032/7/tot. Susp.	18.2	36.8	4.4	17.4	3.6	0.8	3.8	0.60	3.1	0.60	1.8		1.60	0.30
4033/8/tot. Susp.	16.8	38.7	4.9	20.7	4.5	1.0	4.4	0.60	3.2	0.60	1.6		1.30	0.20
4108/33/tot. Susp.	16.4	38.9	4.8	20.5	5.5	0.9	6.2	1.00	5.2	0.88	2.3	0.30	1.86	0.27
4109/32/tot. Susp.	15.0	34.5	4.7	21.3	6.6	1.1	7.6	1.20	6.3	1.03	2.5	0.32	1.98	0.27
4112/35/tot. Susp.	15.5	37.1	4.6	19.8	5.1	0.8	5.6	0.90	4.5	0.81	2.1	0.28	1.83	0.27

discussed below this anomaly is characteristic of the lithologies of the drainage basin itself. All samples are slightly depleted in heavy rare earth element (HREE) and light rare earth element (LREE) relative to PAAS, which is typical of phosphates (Weber et al., 1998). The slight upward convexity of the patterns has also been observed for other much larger river systems such as the Congo, Amazon, Mississippi and Ohio rivers (Goldstein and Jacobsen, 1988a,b; Dupré et al., 1996). The REE patterns of the untreated suspended loads are similar to the corresponding leachates (Fig. 7). However, their Sr isotope ratios and those of the residues are much higher (0.720–0.745) than those of the corresponding leachates (0.7082; Table 2). Similarly, the ε_{Nd} values and $^{147}Sm/^{144}Nd$ ratios of the corresponding residues are much lower than those of the leachates and close to average crust values. In addition, the PAAS normalized REE patterns of the residues (not shown) are flat. This indicates that the residues consist of mineral phases which do not occur in the leachable portion of the suspended load. Most probably, these residues with high $^{87}Sr/^{86}Sr$ isotope ratios consist of secondary silicate phases such as clay minerals.

In Fig. 8, the Sm–Nd depleted mantle model ages (DePaolo et al., 1982) are compared with the corresponding $^{147}Sm/^{144}Nd$ and La/Yb ratios. Model ages allow to estimate the average crustal residences age of Nd in the source lithologies of the suspended loads. The ages range between 1.5 and 2.5 Ga which is similar to the crustal residence ages found in basement rocks from the Alpine domain (Stille and Buletti, 1987; Steinmann, 1994; Henry et al., 1997). It appears that suspended loads derived from rocks with young model ages tend to have lower $^{147}Sm/^{144}Nd$ and higher La/Yb ratios than loads derived from rock units with older model ages. Larger river systems, however, show decreasing Sm/Nd ratios and increasing La/Yb ratios of the suspended load as the depleted mantle model ages increase (Goldstein and Jacobsen, 1987; Dupré et al., 1996; Gaillardet et al., 1997). This is in contrast to our study dealing with younger lithologies, less mature and much smaller river systems. Thus, in the present study, the Nd model ages are directly controlled by the corresponding Sm/Nd ratios and do not reflect

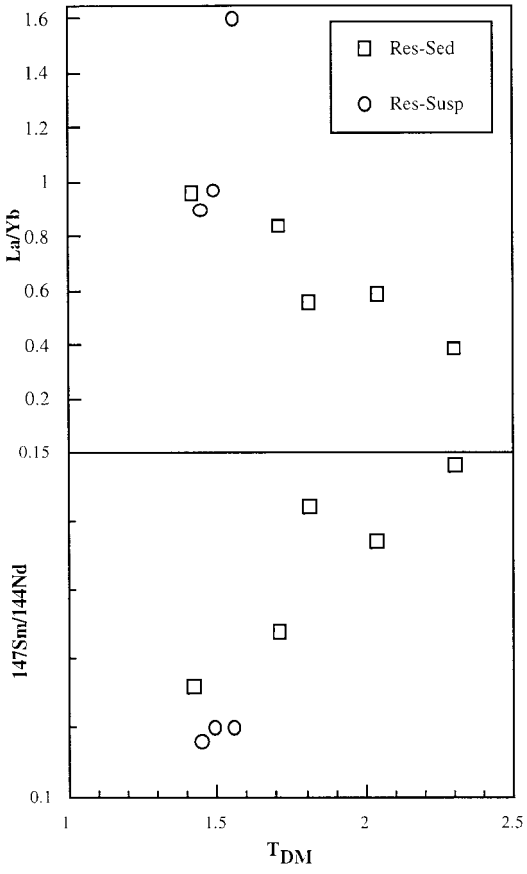

Fig. 8. Sm–Nd model ages in function of $^{147}Sm/^{144}Nd$ and La/Yb for residues of bottom sediments and suspended loads.

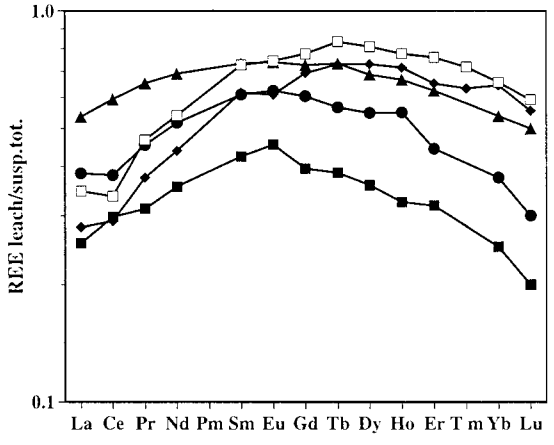

Fig. 7. REE patterns of leachates normalized to untreated suspended load.

variable ages of the different lithologies in the drainage area.

4.4. The REE characteristics of the 'dissolved' load

The PAAS normalized REE patterns of groundwater, river Rhine, plain rivers and some Vosges rivers are shown in Fig. 9 and Table 5. Plain rivers, river Rhine and the groundwater show very similar REE distribution patterns with strong negative Ce anomalies (Ce^*: 0.6–0.12; Table 6) (Elderfield et al., 1990) and HREE enrichment (La/Yb: 0.1–0.8). In addition, the Rhine water is characterized by an important Gd anomaly of 2.2 ± 0.1. The positive Gd anomaly is of anthropogenic origin (Bau and Dulski, 1996). It has not been observed in the leachates of the corresponding suspended loads suggesting that, unlike the other REE, Gd is almost completely related to the 'dissolved' REE fraction ($< 0.45\ \mu m$) of the water samples. It is difficult at present to decide to what extent the REE characteristics of the plain rivers, river Rhine and the groundwater have also been modified by agricultural activities, especially the addition of fertilizers. We do not yet know the REE distribution patterns of these fertilizers. If they are similar to phosphates and characterized by a MREE enrichment, then such a pollution is not visible for the river Rhine and the groundwater. Their distribution patterns are similar to those of non-polluted rivers draining marine carbonate-rich sediments of the Alpine molasse (Tricca, 1997). Some of the plain and Vosges streamlets, however, are characterized by a slight MREE enrichment which might be due to fertilizer pollution and/or phosphate dissolution (Fig. 9). The Ce^* varies widely from one stream to another and some of them show no Ce^* at all.

The suspended load normalized REE patterns of the dissolved load manifest the huge differences in the REE distributions between the dissolved and corresponding suspended load (Fig. 10). The dissolved load is much more HREE-enriched and shows compared to the suspended load a strong negative Ce^*. The REE characteristics of the dissolved load are not only controlled by physico-chemical parameters such as pH and DOC-concentrations but also by

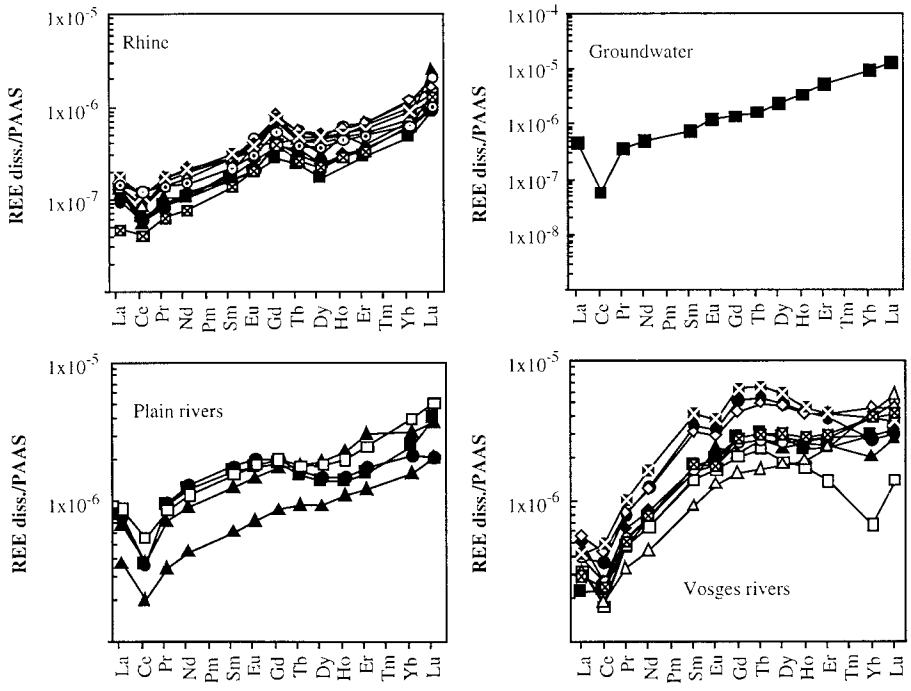

Fig. 9. PAAS normalized REE patterns for dissolved loads.

Table 5
REE concentrations (ng/l) of the 0.45 μm filtered water samples

	La	Ce	Pr	Nd	Sm	Eu	Gd	Tb	Dy	Ho	Er	Yb	Lu
Rhine													
E3945;4	4.8	5.1	0.74	3.6	0.9	0.21	1.3	0.18	0.8	0.12	0.83	1.35	0.4
E3948;7	3.6	4.7	0.72	4.0	0.9	0.22	1.9	0.24	1.1	0.29	1.0	1.7	0.4
E3949;8	4.4	4.4	0.91	3.6	1.1	0.42	1.9	0.35	1.4	0.49	1.1	2.0	1.1
E3947;6	4.4	5.2	0.81	3.9	1.0	0.28	1.7	0.27	1.1	0.30	1.0	1.7	0.6
E4029;4	6.0	9.1	1.37	6.7	1.5	0.37	3.3	0.33	2.1	0.49	1.8	2.7	0.6
E4030;5	5.1	6.8	1.38	6.5	1.5	0.49	3.5	0.43	2.2	0.62	1.9	3.2	0.9
E4031;6	5.0	6.6	1.20	5.8	1.5	0.40	3.4	0.33	1.9	0.47	1.5	2.1	0.5
E4032;7	6.0	8.5	1.52	7.4	1.5	0.43	3.8	0.42	2.4	0.57	1.9	3.3	0.7
E4033;8	6.5	8.7	1.53	7.0	1.7	0.41	3.5	0.37	2.2	0.51	1.6	2.5	0.5
E4062;2	1.8	3.2	0.56	2.6	0.75	0.22	1.8	0.2	1.03	0.28	0.94	1.76	0.6
E4063;3	5.4	9.6	1.20	5.0	1.2	0.32	2.5	0.29	1.7	0.43	1.4	1.77	0.4
Groundwater													
E3733;31	17.6	4.6	3.12	16.7	4.1	1.27	6.4	1.24	10.6	3.31	14.9	26.1	5.6
Plain rivers													
3889;14	31	29	8.4	42	9.3	1.9	8.7	1.2	6.5	1.4	4.6	7.1	1.7
3890;15	30	28	8.7	45	10	2.2	9.4	1.3	7	1.5	5	6	0.9
3891;16	34	43	9.4	46	10	2.2	10.4	1.6	9	2	6	4.5	0.6
3892;17	38	50	9.8	50	12	2.7	12	2	12	3	10	12	2.6
3893;13	54	55	13.0	60	13	2.8	15	2.6	16	4.3	15	14	2.5
3894;18	14	16	3.0	15	3.4	0.8	4.1	0.73	4.4	1.1	3.5	4.5	0.9
3895;19	26	30	6.4	31	7.1	1.6	8.1	1.4	9.1	2.3	8.7	9	1.6
3896;20	23	25	5.4	26	6.1	1.4	7	1.2	7.5	2	7.5	15	3.3
3898;27	23	29	6.3	31	6.2	1.6	7.6	1	6.1	1.4	3.7	1.1	0.2
3897;21	34	44	7.7	38	8.7	2	9.4	1.4	8.6	2	7.1	11.1	2.2
Vosges rivers													
3915;47	121	383	43	284	61	13	65	13	53	11	36	33	6.62
3916;48	140	319	50	272	73	15	81	13	72	15	45	31	4.18
3917;49	108	337	38	195	49	11	54	8.1	47	10	32	31	4.49
3918;50	139	378		260	69	11	75		66		34	17	3.28
3919;51	153	93	49	245	50	8.7	37	4.6	20	4.1	12	7.8	1.44
3920;52	23	47	6.4	38	7.5	2.1	8.2	1.4	7.3	1.5	3.6	1.5	0.21
3921;53	18	8.5	4.4	25	4.7	1.3	5.1	0.8	3.9	0.85	2	1.1	0.18
4018;45	11	12	3.7	20	7.5	1.4	9.5	1.8	10.2	2.2	6.1	5	0.91
4107;41	13	17	2.5	29	3.6	1.1	4.3	0.8	4.7	1.1	4	5.9	1.2
4110;42	10	16	2.6	15	4.6	2	5.4	0.98	6.2	1.2	4.1	6.1	1.1
4111;43	7.9	12	2.6	16	4.0	1.5	5	0.85	4.7	0.92	3.8	4.5	0.92
4113;44	7.4	13	2.2	16	4.5	0.61	5.4	0.98	5.9	1.3	4.1	3.3	0.47
3999;32	8.4	18.2	4.2	25	10	2.1	13	2.3	13	2.3	6.8	8.3	1.4
4015;32	15	29	7.0	42	19	3.5	24	4.2	23	4.3	11	7.7	1.3
4016;34	12	15	4.1	22	8	2.6	10	2.1	11	2.5	7	5.8	1.2
4017;36	19	21	5.5	29	9.7	2.2	13	2.3	13	2.6	8.1	8.3	1.4
4019;37	12	14	4.2	22	7.8	1.8	9.6	1.8	8.8	1.7	3.9	1.9	0.6
4020;38	15	21	4.8	26	9	1.9	12	2.1	12	2.7	8.1	11	2.2
4022;40	12	15	2.9	15	5.1	1.4	7.3	1.3	8.4	1.9	6.9	12	2.5
4108;33	21	34	7.2	41	17	3.1	20	3.8	22	4.1	12	13	2
4109;32	16	39	8.8	56	23	4.1	29	5	27	4.6	12	11	1.6
4112;35	11	19	4.5	26	10	1.9	13	2.3	14	2.8	8.5	11	1.8

Table 6
Ce, Eu and Gd anomalies, pH, DOC and Al concentrations of the filtered water samples

	pH	DOC (mg/l)	Ce*	Eu*	Gd*	Al (mg/l)
Rhine						
E3945;4	7.96	1.79	0.51	0.97	1.57	< 50
E3948;7	8.00	1.78	0.56	0.83	1.93	< 50
E3949;8	8.10	1.79	0.47	1.39	1.53	< 50
E3947;6	8.19	1.97	0.54	1.07	1.60	< 50
E4029;4	7.92	2.11	0.64	0.82	2.24	< 50
E4030;5	8.00	2.45	0.54	1.06	2.06	< 50
E4031;6	7.89	2.86	0.56	0.86	2.21	< 50
E4032;7	7.98	2.64	0.58	0.87	2.32	< 50
E4033;8	8.04	2.30	0.58	0.82	2.05	< 50
E4062;2	8.16	1.67	0.68	0.94	2.26	< 50
E4063;3	8.21	1.95	0.81	0.9	1.92	< 50
Groundwater						< 50
E3733;31	7.16	1.02	0.12	1.21	1.39	< 50
Plain rivers						< 50
3889;14	7.50	1.20	0.37	1.05	1.06	< 50
3890;15	7.46	1.26	0.36	1.11	1.04	< 50
3891;16	7.40	1.51	0.51	1.04	1.1	< 50
3892;17	7.58	2.72	0.53	1.11	1.1	60
3893;13	7.58	1.66	0.43	0.99	1.15	50
3894;18	8.03	2.38	0.5	1.07	1.18	144
3895;19	8.08	2.07	0.47	1.03	1.17	112
3896;20	8.10	2.17	0.46	1.03	1.18	112
3898;27	7.78	3.43	0.5	1.12	1.32	137
3897;21	7.68	2.18	0.55	1.06	1.16	72
Vosges rivers						
3915;47	5.04	3.69	0.97	1.04	1.07	411
3916;48	6.73	6.83	0.77	0.92	1.17	197
3917;49	5.72	5.08	1.08	1.01	1.16	265
3918;50	5.57	3.13	0.93	0.76		285
3919;51	7.80	2.03	0.22	0.99	0.88	76
3920;52	8.05	1.78	0.73	1.29	1.13	58
3921;53	8.28	1.01	0.19	1.27	1.14	< 50
4018;45	7.74	2.06	0.38	0.81	1.23	< 50
4107;41	6.89	0.99	0.41	1.38	1.18	< 50
4110;42	7.22	1.31	0.62	2	1.18	< 50
4111;43	7.75	1.34	0.52	1.67	1.25	< 50
4113;44	7.69	1.61	0.57	0.6	1.18	< 50
3999;32	6.20	1.27	0.57	0.88	1.28	< 50
4015;32	6.40	1.23	0.54	0.81	1.25	< 50
4016;34	7.40	1.43	0.43	1.37	1.2	< 50
4017;36	7.36	1.60	0.4	0.98	1.26	< 50
4019;37	7.56	1.79	0.41	1.03	1.2	< 50
4020;38	7.47	1.88	0.48	0.93	1.27	< 50
4022;40	8.14	3.31	0.5	1.1	1.34	< 50
4108;33	6.82	2.05	0.53	0.81	1.2	< 50
4109;32	6.20	1.44	0.56	0.79	1.25	< 50
4112;35	7.25	2.77	0.51	0.82	1.26	< 50

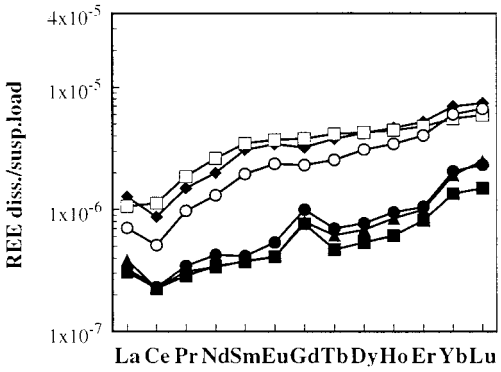

Fig. 10. Suspended load normalized REE patterns of dissolved loads.

the REE characteristics of the source rocks in the drainage basin itself. This is especially true for the waters of the less evolved and mature Vosges streamlets. A comparison of the dissolved load REE distribution patterns with those of principal lithologies in the corresponding drainage basins illustrates the similarities and the close relationship between them (Fig. 11). Especially the Eu* is strongly lithology dependent. Thus, waters originating from source rocks with positive Eu anomalies have similarly positive anomalies whereas waters from source rocks with negative anomalies have also negative Eu*. This is also true for the corresponding suspended loads as shown in Fig. 6. These suspended loads originate from Vosges streams whose basin lithologies are characterized by negative Eu anomalies. The negative Ce*, however, is pH controlled and not by the characteristics of the granitic source rocks (Fig. 12). At high pH (8.5), the samples show a strong negative Ce* (0.2), whereas it disappears at a pH of 5. This behavior can be explained by the redox behavior of Ce which, by contrast with the other REE, occurs in both trivalent and tetravalent states. Ce(III) is the dominant form at low pH whereas Ce(IV) removal as CeO_2 from the other trivalent lanthanides occurs at higher pH. Precipitation of Ce as Cerianite might be responsible for the Ce deple-

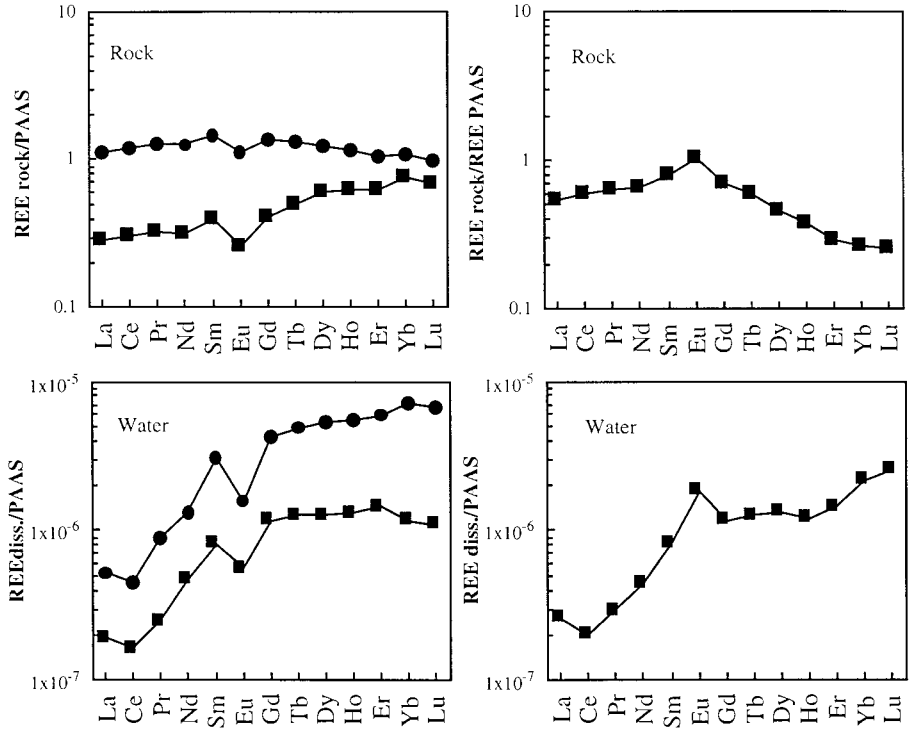

Fig. 11. Comparison of PAAS normalized REE patterns of dissolved load with those from the corresponding catchment lithologies having negative or positive Eu anomalies.

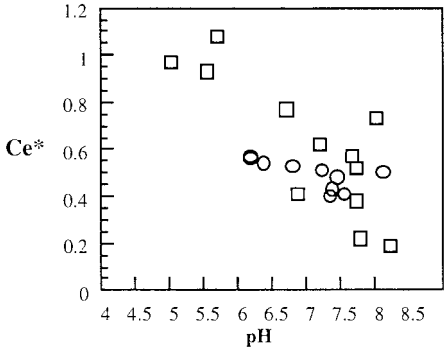

Fig. 12. Ce anomaly of dissolved load vs. pH.

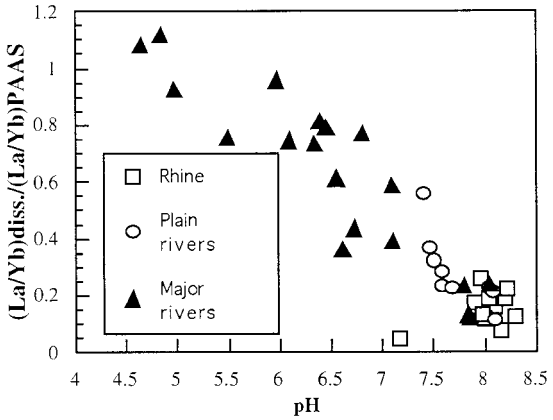

Fig. 13. PAAS normalized La/Yb of dissolved load in function of pH. Comparison with data from the literature (Goldstein and Jacobsen, 1988a,b; Dupré et al., 1996; Gaillardet et al., 1997).

tion in groundwaters (Braun et al., 1998; Stille et al., submitted). However, the Ce anomaly in the plain rivers and the Vosges streams might be caused by oxidative scavenging from the dissolved phase of the river water (Goldberg et al., 1963) or by exchange of the stream and source waters with soil components (Braun et al., 1998). The latter case, however, is only possible if the stream waters have been in physico-chemical equilibrium with corresponding Ce depleted interstitial waters of the soil.

On the other hand, earlier studies pointed to the importance of pH as a controlling factor of the REE concentrations in the dissolved load (Keasler and Loveland, 1982; Goldstein and Jacobsen, 1988a,b; Michard, 1989; Elderfield et al., 1990). Similar observations have been made for the plain rivers, the groundwater and the river Rhine. La concentrations and pH are inversely correlated with high La concentrations at low pH and low La concentrations at high pH (not shown). The REE concentrations of the Vosges streams, however, are not that strongly controlled by pH and show at various pH values (5 to 7.5) similar La concentrations (ca. 100 ppt; not shown). This might be due to the strong influence of the source rocks in the drainage basins on the REE composition of the immature Vosges streamlets. The pH might be in a range which is not critical for La solubility. Therefore, the LREE enrichment expressed by the La/Yb ratios is not pH-controlled for the Vosges streams whereas the PAAS normalized La/Yb ratios of plain rivers, groundwater and Rhine river are strongly correlated with pH (Fig. 13). Compared with the world's major rivers our samples plot at the low end of the correlation line with high pH and low La/Yb ratios. The plain waters LREE enrichment is similar to the world's major rivers in being strongly pH-controlled. Therefore, our observations are in agreement with those of earlier studies suggesting that the pH is a major factor controlling the REE abundances and the shape of the REE distribution patterns in the dissolved load (Goldstein and Jacobsen, 1988a,b; Elderfield et al., 1990; Gaillardet et al., 1997). The less mature Vosges streams, however, are an exception to this relation because they still directly reflect the REE distribution of their source area and because the low pH is not critical for REE solubility.

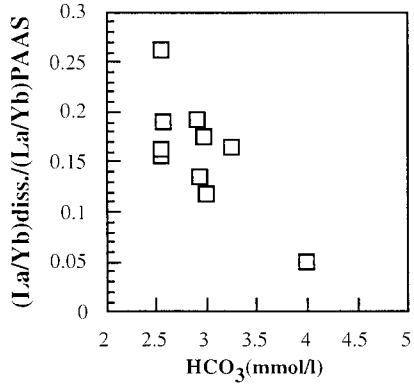

Fig. 14. PAAS normalized La/Yb of dissolved load in function of alkalinity.

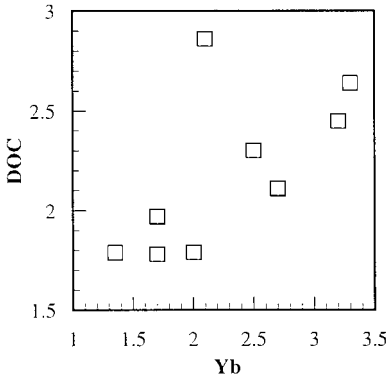

Fig. 15. Yb concentrations (ng/l) of dissolved loads in function of DOC (mg/l).

The HREE enrichment for rivers with low REE concentrations and high pH has generally been thought to be controlled by alkalinity and DOC contents (Cantrell and Byrne, 1987; Goldstein and Jacobsen, 1988a,b; Stanley and Byrne, 1990; Elderfield et al., 1990; Lee and Byrne, 1993; Byrne and Li, 1995). Our high pH-samples such as those from the river Rhine support this suggestion as shown by the correlations between PAAS normalized La/Yb ratios and alkalinity (Fig. 14) as well as by the positive correlation between DOC and Yb concentration (Fig. 15). Thus, alkalinity and DOC contents are additional major factors controlling HREE/LREE fractionation in the solution.

5. Summary and conclusions

This study provides new Sr and Nd isotope and REE data of groundwater and plain rivers from the Upper Rhine valley, of the river Rhine and of several small tributaries originating from different small drainage basins in the Vosges mountains, in both dissolved and suspended loads. It therefore allows us to shed some light onto the evolution of the REE in immature streams from small catchment areas downstream to the more mature plain rivers and the river Rhine. Several major conclusions can be drawn:

The dissolved load REE distribution patterns of the high pH samples from the plain rivers, the river Rhine and groundwater are very similar showing a strong negative Ce anomaly and HREE enrichment. Only the river Rhine has a strong positive Gd anomaly which is of anthropogenic origin. The dissolved load REE distribution patterns of the low-pH Vosges streamlets including the Strengbach are very different from those of the plain rivers and much more scattered. A comparison of the dissolved load REE distribution patterns with those of the principal lithologies in the corresponding drainage basins illustrates some similarities and close relationships between both of them. The Eu anomaly, especially, is strongly lithology dependent.

Different physico-chemical parameters control the LREE enrichment in the low pH Vosges and high pH plain rivers. Only the plain rivers including the river Rhine and groundwater show a pH-controlled LREE enrichment similar to the world's major rivers. Therefore, also the shape of the REE distribution patterns of these solutions are pH dependent. An additional parameter controlling the HREE/LREE fractionation is the DOC concentration in the solution. However, the Sm/Nd ratios of these evolved and mature water systems did not significantly fractionate with respect to average continental crust as documented by the correlation between ε_{Nd} and Sm/Nd.

The Sm/Nd ratios and corresponding ε_{Nd} values of the dissolved load of the river Rhine and the groundwater are low and close to values of the terrigeneous clay-rich Mesozoic schists from the Rhine's catchment basin. These schists are thought to represent best the average isotopic composition of the continental crust in the studied area and therefore also of the alluvial deposits in the Rhine valley. This, however, is not the case for the less evolved, nonmature and low-pH Vosges streams. Chemical alteration of accessory probably LREE-depleted minerals in the catchment area control the REE abundances of these waters. The high Sm/Nd ratios and the associated and compared to average crust significantly higher ε_{Nd} values but lower Sr isotopic composition values of these dissolved loads support this suggestion.

Thus, the mature water systems like the river Rhine and the groundwater integrated the Sm–Nd isotope characteristics of average continental crust whereas the less evolved and mature Vosges rivers integrated the isotope characteristics of REE carrying

minerals from the different lithologies in the different catchment areas. Thus, the least mature streams provide most important information about chemical alteration especially about differences in weathering susceptibility between minerals and about fractionation of their REE patterns during weathering.

The negative Ce^* in the dissolved load of the non-mature Vosges streams and of the evolved plain rivers including the Rhine and groundwater, however, is not controlled by the source rock characteristics but the pH. The pH dependence can be explained by the redox behavior of Ce, which, by contrast with other REE, occurs in both trivalent and tetravalent states. Ce(IV) removal as Ce_2O_2 from the other trivalent lanthanides at higher pH leads to the negative Ce^* in the waters.

The REE distribution patterns of the suspended load leachates have no similarities with those of the corresponding dissolved load indicating that they contain not only REE adsorbed on the suspended particles but also REE deriving from minerals at least partly leachable in 1 N HCl. The Sr and Nd isotope data support this suggestion. Their $^{143}Nd/^{144}Nd$ and $^{87}Sr/^{86}Sr$ isotope ratios are always higher and lower, respectively, than those of their corresponding 'dissolved' loads. The leachates show MREE enriched distribution patterns very similar to those of the corresponding residual phases but are more strongly depleted in light and heavy REE. Leachable and residual phases show very different Sr and Nd isotopic composition values indicating that both of them contain very different mineral phases. The humpshaped REE distribution patterns of the leachates are typical of diagenetically altered apatite. With the exception of the Eu anomaly the REE distribution patterns of the suspended loads do not mirror the characteristics of the basin lithologies. The patterns are, however, similar to those of alteration products like clay-minerals which is supported by the very high $^{87}Sr/^{86}Sr$ and low $^{143}Nd/^{144}Nd$ isotopic composition values and Sm/Nd ratios. Leachates and corresponding residual phases define alignments in the Sm/Nd isochron diagram whose slopes define ages ranging between 200 and 390 Ma indicating that the mineral phases in the suspended load retained some memory of their primary precursor minerals originating from the Hercynian granitic rocks.

Acknowledgements

We sincerely thank B. Dupré and two anonymous reviewers for their comments and Dr. J.I. Drever for editorial handling. AT profited from a BDI fellowship which is kindly acknowledged. The technical assistance of D. Tisserant, R. Rouault, G. Krempp and D. Million of the Centre de Géochimie de la Surface at Strasbourg is acknowledged. *[JD]*

References

Allègre, C.J., Lewin, E., 1989. Chemical structure and history of the Earth: evidence from global non-linear inversion of isotopic data in a three-box-model. Earth Planet. Sci. Lett. 96, 61–88.

Allègre, C.J., Dupré, B., Négrel, P., Gaillardet, J., 1996. Sr–Nd–Pb isotope systematics in Amazon and Congo river systems: constraints about erosion processes. Chem. Geol. 131, 93–112.

Andersson, P.S., Wasserburg, G.J., Ingri, J., 1992. The sources and transport of Sr and Nd isotopes in the Baltic sea. Earth Planet. Sci. Lett. 113, 459–472.

Andersson, P.S., Wasserburg, G.J., Ingri, J., Stordal, M.C., 1994. Strontium, dissolved and particulate loads in fresh and brackish water: the Baltic Sea and Mississippi Delta. Earth Planet. Sci. Lett. 124, 195–210.

Banfield, J.F., Eggleton, R.A., 1989. Apatite replacement and rare earth mobilization, fractionation, and fixation during weathering. Clays Clay Miner. 37, 113–127.

Banner, J.L., Hanson, G.N., Meyers, W.J., 1988. Rare earth element and Nd isotopic variations in regionally extensive dolomites from the Burlington–Keokuk formation (Mississippian): implications for REE mobility during carbonate diagenesis. J. Sediment. Petrol. 58, 415–432.

Bau, M., Dulski, P., 1996. Anthropogenic origin of positive gadolinium anomalies in river waters. Earth Planet. Sci. Lett. 143, 245–255.

Blum, J.D., Erel, Y., Brown, K., 1994. $^{87}Sr/^{86}Sr$ ratios of Sierra Nevada stream waters implications for relative mineral weathering rates. Geochim. Cosmochim. Acta 58, 5019–5025.

Bonhomme, M., 1967. Ages radiométriques de quelques granites des Vosges moyennes. Bull. Serv. Carte Geol. Alsace Lorraine 20, 101–106.

Braun, J.-J., Viers, J., Dupré, B., Polvé, M., Ndam, J., Muller, J.-P., 1998. Solid/liquid REE fractionation in the lateritic system of Goyoum, East Cameroon: the implication for the present dynamics of the soil covers of the humid tropical regions. Geochim. Cosmochim. Acta 62, 273–299.

Buhl, D., Neuser, R.D., Richter, D.K., Riedel, D., Roberts, B., Strauss, H., Veizer, J., 1991. Nature and nurture: environmental isotope story of the river Rhine. Naturwissenschaften 78, 337–346.

Byrne, R.H., Li, B., 1995. Comparative complexation behavior of the rare earths. Geochim. Cosmochim. Acta 59, 4575–4589.

Cantrell, K.J., Byrne, R.H., 1987. Rare earth element complexation by carbonate and oxalate ions. Geochim. Cosmochim. Acta 51, 597–605.

DePaolo, D.J., Manton, W.I., Grew, E.S., Halpern, M., 1982. Sm–Nd, Rb–Sr and U–Th–Pb systematics of granulite facies rocks from Fyfe Hills Enderby Land, Antarctica. Nature 298, 614–618.

Douglas, G.B., Gray, C.M., Hart, B.T., Beckett, R., 1995. A strontium isotopic investigation of the origin of suspended particulate matter (SPM) in the Murray–Darling river system, Australia. Geochim. Cosmochim. Acta 59, 3799–3815.

Dupré, B., Gaillardet, J., Rousseau, D., Allègre, C.J., 1996. Major and trace elements of river-borne material: the Congo basin. Geochim. Cosmochim. Acta 60, 1301–1321.

Elderfield, H., Upstill-Goddard, R., Sholkovitz, E.R., 1990. The rare earth elements in rivers, estuaries, and coastal seas and their significance to the composition of ocean waters. Geochim. Cosmochim. Acta 54, 971–991.

El Gh'mari, 1995.

Gaillardet, J., Dupré, B., Allègre, C.J., 1995. A global geochemical mass budget applied to the Congo Basin rivers: erosion rates and continental crust composition. Geochim. Cosmochim. Acta 59, 3469–3485.

Gaillardet, J., Dupré, B., Allègre, C.J., Négrel, P., 1997. Chemical and physical denudation in the Amazon river basin. Chem. Geol. 142, 141–173.

Goldberg, E.D., Koide, M., Schmitt, R.A., Smith, R.H., 1963. Rare earth distributions in the marine environment. J. Geophys. Res. 68, 4209–4217.

Goldstein, S.J., Jacobsen, S.B., 1987. The Nd and Sr isotopic systematics of river-water dissolved material: implications for the sources of Nd and Sr in seawater. Chem. Geol. 66, 245–272.

Goldstein, S.J., Jacobsen, S.B., 1988a. Rare earth elements in river waters. Earth Planet. Sci. Lett. 89, 35–47.

Goldstein, S.L., Jacobsen, S.B., 1988b. Nd and Sr isotopic systematics of river water suspended material: implications for crustal evolution. Earth Planet. Sci. Lett. 87, 249–265.

Goldstein, S.L., O'Nions, R.K., Hamilton, P.J., 1984. A Sm–Nd isotopic study of atmospheric dusts and particulates from major river systems. Earth Planet. Sci. Lett. 70, 221–236.

Gosselin, D.C., Smith, M.R., Lepel, E.A., Laul, J.C., 1992. Rare earth elements in chloride-rich groundwater, Palo Duro Basin, TX, USA. Geochim. Cosmochim. Acta 56, 1495–1505.

Henry, F., Probst, J.-L., Thouron, D., Depetris, P., V, G., 1996. Nd–Sr isotopic compositions of dissolved and particulate material transported by the Parana and Uruguay rivers during high and low water periods. Sci. Geol., Bull. 49, 1–3.

Henry, P., Deloule, E., Michard, A., 1997. The erosion of the Alps: Nd isotopic and geochemical constraints on the sources of the peri-Alpine molasse sediments. Earth Planet. Sci. Lett. 146, 627–644.

Hodell, P.J., Mueller, P.A., Garrido, J.R., 1991. Variations in the strontium isotopic composition of seawater during the Neogene. Geology 19, 24–27.

Johannesson, K.H., Lyons, W.B., Yelken, M.A., Gaudette, H.E., Stetzenbach, K.J., 1996. Geochemistry of the rare-earth elements in hypersaline and dilute acidic natural terrestrial waters: complexation behavior and middle rare-earth element enrichments. Chem. Geol. 133, 125–144.

Keasler, K.M., Loveland, W.D., 1982. Rare earth elemental concentrations in some Pacific Northwest rivers. Earth Planet. Sci. Lett. 61, 68–72.

Lee, J.H., Byrne, R.H., 1993. Complexation of the trivalent rare earth elements (Ce, Eu, Gd, Tb, Yb) by carbonate ions. Geochim. Cosmochim. Acta 57, 295–302.

Martin, J.M., Meybeck, M., 1979. Element mass-balance of material carried by major world rivers. Mar. Chem. 7, 173–206.

McLennan, S.M., 1989. Rare earth elements in sedimentary rocks: influence of provenance and sedimentary processes. In: B.R. Lippin, G.A. McKay (Eds.), Reviews in Mineralogy. Geochemistry and Mineralogy of Rare Earth Elements. Mineral. Soc. Am., pp. 169–200.

Meybeck, M., 1987. Global chemical weathering from surficial rocks estimated from river dissolved loads. Am. J. Sci. 287, 401–428.

Michard, A., 1989. Rare earth elements systematics in hydrothermal fluids. Geochim. Cosmochim. Acta 53, 745–750.

Négrel, P., Deschamps, P., 1996. Natural and anthropogenic budgets of a small watershed in the Massif Central (France): chemical and strontium isotopic characterization of water and sediments. Aquat. Geochem. 2, 1–27.

Négrel, P., Allègre, C.J., Dupré, B., Lewin, E., 1993. Erosion sources determined by inversion of major and trace element ratios in river water: the Congo basin case. Earth Planet. Sci. Lett. 120, 59–76.

Probst, A., Viville, D., Fritz, B., Ambroise, B., Dambrine, E., 1992. Hydrochemical budgets of a small forested granitic catchment exposed to acid deposition: the Strengbach catchment case study (Vosges Massif, France). Water Air Soil Pollut. 62, 337–347.

Probst, J.L., Mortatti, J., Tardy, Y., 1994. Carbon river fluxes and weathering CO_2 consumption in the Congo and Amazon river basins. Appl. Geochem. 9, 1–13.

Probst, A., El Gh'mari, A., Aubert, D., Fritz, B., Stille, P., McNutt, R., submitted. Strontium as a tracer of weathering processes in an acid atmospheric polluted catchment: the Strengbach catchment case study, Vosges mountains, France. Chem. Geol.

Riotte, J., Chabaux, F., 1999. ($^{243}U/^{238}U$) activity ratios in freshwaters as tracers of hydrological processes: the Strengbach watershed, Vosges, France. Geochim. Cosmochim. Acta (in press).

Schaltegger, U., Stille, P., Rais, N., Piqué, A., Clauer, N., 1994. Neodymium and strontium isotopic dating of diagenesis and low-grade metamorphism of argillaceous sediments. Geochim. Cosmochim. Acta 58, 1471–1481.

Shabani, M.B., Agaki, T., Masuda, A., 1992. Preconcentration of trace rare earth elements in seawater by complexation with HDEHP and H2MEHP adsorbed on a C18 cartridge and determination by inductively coupled plasma mass spectrometry. Anal. Chem. 64, 737–743.

Sholkovitz, E.R., 1989. Artifacts associated with the chemical leaching of sediments for rare-earth elements. Chem. Geol. 77, 47–51.

Sholkovitz, E.R., 1992. Chemical evolution of rare earth elements: fractionation between colloidal and solution phases of filtered river water. Earth Planet. Sci. Lett. 114, 77–84.

Sholkovitz, E.R., Landing, W.M., Lewis, B.L., 1994. Ocean particle chemistry: the fractionation of rare earth elements between suspended particles and seawater. Geochim. Cosmochim. Acta 58, 1567–1579.

Stallard, R.F., Edmond, J.M., 1983. Geochemistry of the Amazon 2. The influence of geology and weathering environment on the dissolved load. J. Geophys. Res. 88, 9671–9688.

Stanley, J.K., Byrne, R.H., 1990. The influence of solution chemistry on REE uptake by *Ulva lactuca* L. in seawater. Geochim. Cosmochim. Acta 54, 1587–1595.

Steinmann, M., 1994. Die nordpenninischen Bündnerschiefer der Zentralalpen Graubündens: Tektonik, Stratigraphie und Beckenentwicklung. Unpubl. PhD Thesis, ETH Zürich No. 10668.

Steinmann, M., Stille, P., 1997. Rare earth element behavior and Pb, Sr, Nd isotope systematics in a heavy metal contaminated soil. Appl. Geochem. 12, 607–624.

Steinmann, M., Stille, P., 1999. Geochemical evidence for the nature of the crust beneath the North Penninic basin of the Mesozoic Tethys ocean. Geol. Rundsch (in press).

Stille, P., Buletti, M., 1987. Nd–Sr Isotopic characteristics of the Lugano volcanic rocks and constraints on the continental crust formation in the South Alpine domain (N-Italy–Switzerland). Contrib. Mineral. Petrol. 96, 140–150.

Stille, P., Clauer, N., 1994. The process of glauconitization: chemical and isotopic evidence. Contrib. Mineral. Petrol. 117, 253–262.

Stille, P., Steinmann, M., Riggs, S.R., 1996. Nd isotope evidence for the evolution of the paleocurrents in the Atlantic and Tethys Oceans during the past 180 Ma. Earth Planet. Sci. Lett. 144, 9–20.

Stille, P., Jensen, K.A., Gomez, P., Gauthier-Lafaye, F., Ewing, R., Louvat, D., submitted. REE migration in groundwaters close to the natural fission reactor of Bangombé (Gabon). Geochim. Cosmochim. Acta.

Stordal, M.C., Wasserburg, G.J., 1986. Neodymium isotopic study of Baffin Bay water: sources of REE from very old terranes. Earth Planet. Sci. Lett. 77, 259–272.

Taylor, S.R., McLennan, S.M., 1985. The Continental Crust: Its Composition and Evolution. Blackwell, Oxford.

Tricca, A., 1997. Transport mechanism of trace elements in surface and ground water: Sr, Nd, U isotope and REE evidence. Unpubl. PhD Thesis, Université Louis Pasteur de Strasbourg.

Weber, E.T., Owen, R.M., Dickens, G.R., Rea, D.K., 1998. Causes and implications of the middle rare earth element depletion in the eolian component of North Pacific sediment. Geochim. Cosmochim. Acta 62, 1735–1744.

Chemical Geology 254 (2008) 1–18

Contents lists available at ScienceDirect

Chemical Geology

journal homepage: www.elsevier.com/locate/chemgeo

Controls on transport and fractionation of the rare earth elements in stream water of a mixed basaltic–granitic catchment basin (Massif Central, France)

M. Steinmann [a,*], P. Stille [b]

[a] UMR 6249 Chrono-Environnement, Université de Franche-Comté, F-25030 Besançon, France
[b] Centre de Géochimie de la Surface, CNRS, UMR 7517, EOST, F-67084 Strasbourg, France

ARTICLE INFO

Article history:
Received 25 July 2007
Received in revised form 4 February 2008
Accepted 9 April 2008

Editor: B. Bourdon

Keywords:
REE fractionation
Fe colloids
Nd–Sr isotopes
Stream water

ABSTRACT

We present rare earth element (REE) patterns of small streams from a catchment basin in the Massif Central (France) in order to characterize the individual fractionation stages for the dissolved REE from the source to the catchment outlet. The upper part of the catchment is located on a basalt plateau, followed downstream by deep and narrow valleys within granitic and orthogneissic bedrock. Basalt-normalized 0.45 μm filtered stream water has REE patterns slightly depleted in the light REE (La–Sm, LREE) on the basalt plateau close to the source, followed by a continuous amplification of this LREE depletion downstream. At the same time also a negative Ce anomaly develops in the adsorbed fraction of >0.45 μm particles, which has been isolated by leaching with 1 M HCl. Strontium and Neodymium isotope ratios of stream water demonstrate that the dissolved REE are essentially of basaltic origin, even in the lower, granitic and gneissic part of the catchment. Mixing with gneiss or granite derived REE thus cannot explain the observed evolution of the REE patterns.

Our data suggest that the REE of the <0.45 μm fraction are associated to Fe colloids, which grow during transport downstream to Fe oxyhydroxide particles exceeding 0.45 μm in size. Precipitation of these oxyhydroxide particles leads to selective removal of LREE from 0.45 μm filtered stream water, and of Ce adsorbed on >0.45 μm particles. In contrast to earlier studies, we found no link between REE behavior and organic colloids or organic complexes. This scenario is confirmed by a detailed analysis of the REE patterns at 3 stream confluences. The results show that the REE do not behave conservatively during mixing at stream confluences, but that the LREE and Ce are preferentially removed similarly to what has been observed at catchment scale. Our study thus underlines the importance of Fe colloids for the transport and fractionation of the REE in stream water.

1. Introduction

The rare earth element concentrations in river water, river suspensions and in marine fine grained detrital sediments are extensively used to trace the erosional history of continents and to establish erosion budgets (Goldstein et al., 1984; Goldstein and Jacobsen, 1987, 1988a,b; Allègre et al., 1996; Gaillardet et al., 1997). Several studies have dealt with the evolution of dissolved rare earth elements (REE) in streams from large scale catchment basins and shown that there is no direct link between the REE distribution patterns of the dissolved load and bedrock (e.g. Dupré et al., 1996; Gaillardet et al., 1997; Sholkovitz et al., 1999). Other studies however indicate that REE distribution patterns and Eu anomalies of stream water in small catchment basins might be strongly lithology dependent (Tricca et al., 1999). Preferential dissolution of REE minerals during weathering, variable complex stabilities for the individual REE, and preferential removal of certain REE from solution by colloids and newly formed minerals are the most cited processes to explain the behavior of REE in aqueous solutions (e.g. Öhlander et al., 1996; Tricca et al., 1999; Dia et al., 2000; Ingri et al., 2000; Andersson et al., 2001; Aubert et al., 2001; Hannigan and Sholkovitz, 2001; Stille et al., 2003; Gruau et al., 2004). More recently, it has been shown that vegetation might be another important factor controlling REE fractionation and especially LREE depletion in river water (Stille et al., 2006).

The aim of the present study is to characterize in detail REE transport and fractionation processes within a small catchment situated on a mixed basaltic–granitic–orthogneissic bedrock. This catchment basin has been chosen because the contrasting lithologies allow to trace basalt derived REE from the source area downstream, and to quantify the exchange of stream water with the different bedrock lithologies using Sr and Nd isotopes.

2. Setting and methods

2.1. Regional setting

The catchment basin is located in the southern part of the French "Massif Central" (Fig. 1). The basin is underlain by Quaternary basalts

* Corresponding author. UMR 6249 Chrono-Environnement, Université de Franche, Comté, 16 route de Gray, 25030 Besançon, France. Tel.: +33 3 81 66 65 46; fax: +33 3 81 66 65 58.
E-mail address: marc.steinmann@univ-fcomte.fr (M. Steinmann).

0009-2541/$ – see front matter © 2008 Published by Elsevier B.V.
doi:10.1016/j.chemgeo.2008.04.004

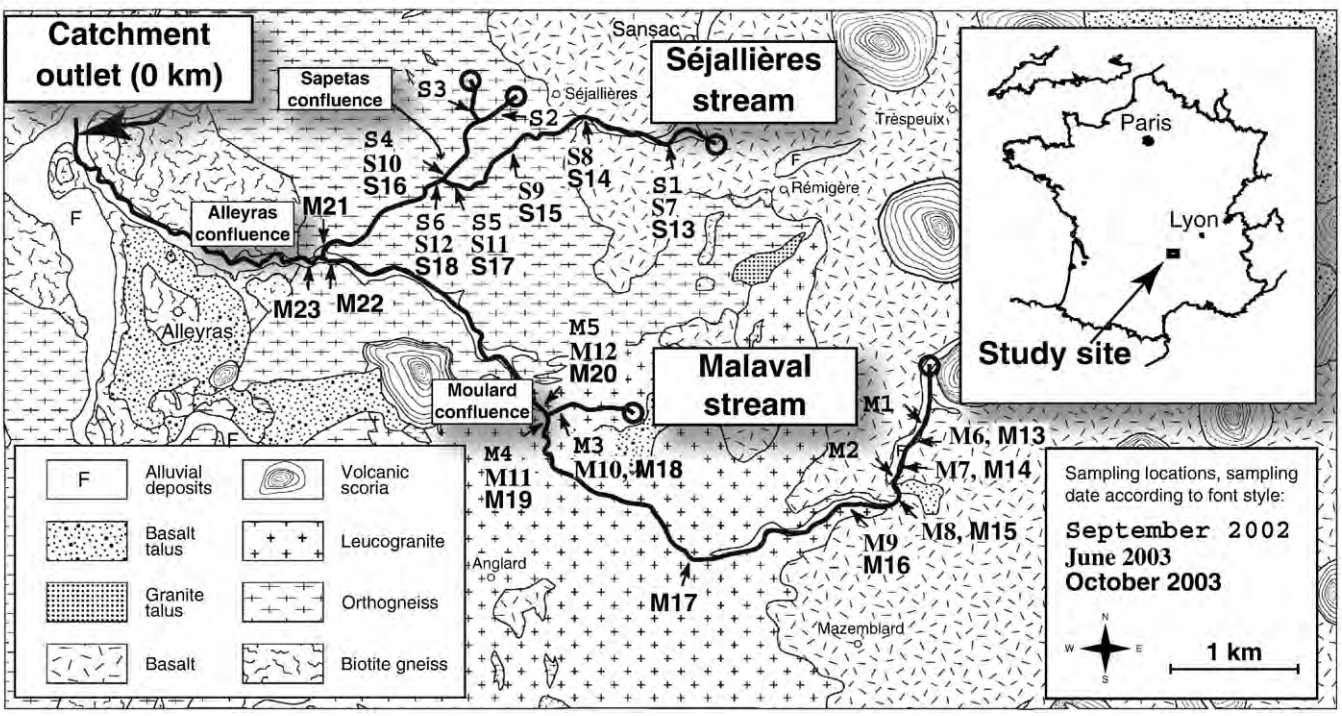

Fig. 1. Geographic location and simplified geological map of the study site according to Bouiller et al. (1978) with the sampling sites of the Séjallières and Malaval streams. The altitude of the basaltic plateau to the east is about 1200–1300 m, the outlet of the catchment basin of both streams into the main river named "Allier" to the west is located at 714 m.

in its upper part to the east and by Hercynian granites and orthogneisses in its lower part to the west. The catchment covers an area of about 68 km^2 at altitudes ranging from 1301 m on the basalt plateau to the east down to 714 m at its outlet to the Allier river to the west. The low inclination of the basalt plateau favors the formation of well developed soil profiles and swampy areas. In contrast, the slopes in the granitic and orthogneissic terrains to the west are steep, the soils are poorly developed and covered by forest. The climate is temperate oceanic mountainous with dominating west winds. The mean annual precipitation is about 800 mm and the annual mean temperature 10 °C. The basalt plateau is mainly covered by pastures and conifer forests (mainly spruce and pine), whereas mixed deciduous (beech, oak) — conifer forests and only little pasture areas occupy the steep slopes to the west.

2.2. Field sampling and analytical methods

Field sampling was realized in 3 campaigns in September 2002, June 2003, and October 2003 during dry periods with low stream discharge. The sampling order was from upstream to downstream, the stream Séjallières was sampled in 1 day and the stream Malaval in 2 days. The location of the sampling points is given in Table 1 as the upstream distance from the catchment outlet in kilometers, which is common for both streams (Fig. 1). This labeling has been chosen in order to plot the data of both streams together with a common kilometer scale. Table 1 gives furthermore the bedrock lithology for each stream water sampling point.

Sample aliquots for trace elements, REE and Nd–Sr isotope analysis were filtered on site using 0.45 μm Sartorius cellulose acetate filters of 47 mm diameter and a Nalgene filtering unit with a manual vacuum pump. Typically, 2 L of stream water were filtered and the filters were changed up to 16 times per sample depending on the particle load. The filtered samples were immediately acidified to pH 1–2 with sub-boiled distilled HCl and stored in acid-cleaned HDPE bottles for major cation and trace element analysis. Filtered, but non-acidified aliquots were kept to determine major anions. For DOC analyses an additional filtered aliquot of 100 mL was treated in the field with 5 drops of concentrated H_3PO_4 in order to stop microbial activity and stored at −18 °C after arrival in the laboratory. Conductivity, pH and Eh were measured on site using a portable WTB MultiLine P3 device and are given in Table 1. Bicarbonate was determined in the evening of each sampling day by titration with H_2SO_4.

The major cation and anion composition of the water samples was determined at the department of Geosciences, University of Franche-Comté, Besançon (France). Ca^{2+} was measured by potentiometric titration with a TitraLab 90 apparatus from Radiometer Analytical. The cations Na^+, K^+, Mg^{2+} were analyzed with a Perkin Elmer 1100 atomic absorption spectrophotometer, and the anions F^-, Cl^-, NO_3^-, and SO_4^{2-} with a Dionex DX100 high-pressure ion chromatograph. The DOC analyses were done at the common analytical center (SERAC) of the University of Franche-Comté, Besançon (France) using a Dohrmann carbon analyzer according to the method NF EN 1484.

All trace metals including the REE were determined by ICP-AES (Jobin Yvon) and ICP-MS (Fisons VG-Plasma Quad PQ2+) at the Centre de Géochimie de la Surface at CNRS Strasbourg (France). The REE concentrations of the waters range between 0.5 and 10 ng/L for Lu and 50 to 250 ng/L for Nd and are below the detection limit of traditional quadrupole ICP-MS. Therefore, a liquid–liquid extraction technique using HDEHP as organic solvent was used to enrich the REE by a factor of at least 100 (Shabani et al., 1990; Shabani and Masuda, 1991; Tricca et al., 1999). Typically, 1 L of filtered stream water was necessary to achieve concentrations above detection limit. This sample enrichment was realized in a clean lab at the department of Geosciences in Besançon. A detailed description of the procedure and reagents used is given by Steinmann and Stille (1998). This liquid–liquid extraction removes efficiently Ba and other matrix elements from the REE fraction leading to a significant reduction of mass interferences, in particular between BaO and Eu on mass 151 (Shabani and Masuda, 1991). The total procedure blank was determined by running the complete extraction procedure with 18 MΩ ultrapure water from a Millipore Simplicity system. Only La, Ce, and Gd were present in detectable amounts in the 14 blank samples and the blank contribution to stream

Table 1
Field parameters (pH, Eh, conductivity, temperature), chemical composition, saturation index (SI) for goethite, and total dissolved solid (TDS) values for 0.45 μm filtered water samples

	Upstream distance	Bedrock lithology	Sampling date	pH	Eh	Conductivity	Temperature	F^-	Cl^-	NO_3^-	SO_4^{2-}	HCO_3^-	PO_4^{3-}	Ca^{2+}	Na^+	K^+	Mg^{2+}	Charge balance	DOC	Fe	Rb	Sr	SI goethite	TDS
	[km]				[mV]	[μS/cm]	[°C]	[mg/L]	[mg/L]	[mg/L]	[mg/L]	[mg/L]	[mg/L]	[mg/L]	[mg/L]	[mg/L]	[mg/L]		[mg/L]	[μg/L]	[μg/L]	[μg/L]		[mg/L]
Water samples September 2002																								
M 1	9.1	BA	13/09/02	7.7	217	89	12.3	0.3	5.0	0.5	1.7	43	<0.1	6.0	3.1	0.9	5.4	−1.0%		33	3.8	69	7.3	80
M 2	8.5	BA	13/09/02	7.8	150	104	11.3	0.02	3.0	0.5	2.0	54	<0.1	8.1	3.3	0.8	6.4	−4.3%		80	3.6	91	7.2	95
M 3	4.9 (T)	GSC	14/09/02	7.8	42	126	11.1	0.06	10.8	14.2	8.9	29	<0.1	10.0	4.8	1.3	4.3	4.2%		<5	2.6	95	4.1	101
M 4	4.8	GSC	14/09/02	7.7	39	107	10.7	0.04	4.4	2.1	5.5	46	<0.1	8.1	4.3	1.0	5.2	−0.8%		<5	2.1	78	3.7	97
M 5	4.7	GSC	14/09/02	7.7	41	106	10.9	0.04	4.7	2.1	5.6	46	<0.1	8.3	4.4	1.0	5.6	3.0%		10	2.2	79	4.2	97
S 1	5.7	BA	11/09/02	7.9	189	202	15.9	0.06	6.1	0.4	6.7	100	<0.1	12.8	4.6	3.2	14.4	−3.8%		58	4.4	459	7.6	171
S 2	4.5 (T)	OG	12/09/02	7.7	176	211	11.7	0.00	6.4	1.9	7.0	107	<0.1	16.2	5.4	4.3	12.7	−2.1%		14	4.4	172	6.6	188
S 3	4.4 (T)	OG	12/09/02	7.1	120	106	10.4	0.00	6.0	0.0	4.1	49	<0.1	8.2	4.7	1.0	5.3	−0.8%		33	0.7	68	4.1	94
S 4	3.8 (T)	OG	12/09/02	7.8	228	192	11.2	0.05	6.7	0.2	6.9	91	<0.1	12.9	5.4	3.7	11.1	−1.7%		<5	2.6	145	6.7	162
S 5	3.7	OG	12/09/02	7.9	221	188	11.5	0.06	6.6	5.0	6.8	85	<0.1	13.5	4.7	2.8	11.8	−3.7%		56	2.7	139	7.8	159
S 6	3.6	OG	12/09/02	7.9	216	192	11.4	0.00	6.6	2.8	7.0	84	<0.1	13.8	5.0	3.1	11.5	−5.0%		<5	2.6	139	6.7	156
Water samples June 2003																								
M 6	8.9	BA	20/06/03	7.4	192	116	13.2	0.04	1.9	2.5	3.1	72	<0.1	7.4	3.7	0.4	6.8	9.3%		35	1.5	91	6.3	149
M 7	8.8	BA	20/06/03	7.6	171	119	13.5	0.04	2.8	2.8	3.5	56	<0.1	8.1	3.8	0.9	7.2	−3.3%		58	4.3	112	6.9	134
M 8	8.4	BA	20/06/03	7.8	188	125	16.4	0.05	3.3	3.1	3.8	59	<0.1	10.7	4.3	1.5	7.4	−7.5%		162	5.8	110	8.0	143
M 9	8.0	GSC	20/06/03	7.7	245	103	15.5	0.05	2.7	2.8	3.6	47	<0.1	6.1	4.3	1.1	5.6	−0.7%		21	2.9	84	7.2	128
M 10	4.9 (T)	GSC	21/06/03	7.7	180	168	14.5	0.20	2.8	0.7	6.8	95	<0.1	14.9	11.3	1.0	6.5	0.0%		8	4.7	130	6.4	164
M 11	4.8	GSC	21/06/03	7.5	265	95	12.8	0.09	3.3	2.5	5.9	36	<0.1	5.6	5.3	0.9	4.6	−4.1%		9	2.7	62	6.7	112
S 7	5.7	BA	18/06/03	7.4	172	175	21.7	0.06	6.7	5.5	4.6	87	<0.1	12.9	5.4	3.9	10.7	−1.7%		326	4.8	150	7.5	197
S 8	5.0	BA	19/06/03	7.8	178	176	11.9	0.07	6.6	6.1	5.1	90	<0.1	12.4	5.2	3.0	11.8	−1.0%		279	3.5	149	7.9	193
S 9	4.3	OG	19/06/03	8.0	204	180	16.8	0.07	7.2	9.8	5.7	74	<0.1	12.2	3.5	3.4	11.6	−3.3%		17	2.9	150	7.2	179
S 10	3.8 (T)	OG	19/06/03	8.2	250	188	14.5	0.05	7.5	3.1	5.5	89	<0.1	13.4	7.6	4.9	11.6	−6.7%		11	2.8	157	7.1	193
S 11	3.7	OG	19/06/03	8.1	258	174	15.5	0.07	6.9	8.1	5.9	73	<0.1	11.0	5.4	3.3	11.1	−4.0%		3	3.1	141	6.8	173
S 12	3.6	OG	19/06/03	8.1	253	178	15.9	0.09	7.1	6.7	5.9	76	<0.1	12.1	6.6	3.7	11.1	−6.4%		9	3.0	144	6.9	179
Water samples October 203																								
M 13	8.9	BA	16/10/03	7.8	264	178	7.3	0.02	3.3	2.1	3.6	121	<0.1	10.8	5.4	24.9	9.5	−0.3%	87.7	25	68.7	134	7.5	230
M 14	8.8	BA	16/10/03	6.6	222	134	8.4	0.01	2.7	0.8	5.0	72	<0.1	8.9	5.4	2.6	7.5	0.3%	4.3	59	3.6	121	4.6	154
M 15	8.4	BA	16/10/03	6.3	241	233	10.8	0.02	2.7	1.0	3.9	76	<0.1	7.7	5.7	1.8	7.7	3.6%	10.8	78	6.2	115	4.1	158
M 16	8.0	GSC	16/01/03	6.2	249	219	10.2	0.03	2.1	2.5	3.0	58	<0.1	5.8	5.3	1.3	5.6	4.7%	4.5	20	2.7	85	3.5	142
M 17	6.5	GSC	16/10/03	6.5	236	211	10.1	0.06	2.5	1.9	4.3	55	<0.1	5.0	6.5	1.2	5.0	5.6%	3.9	15	2.2	76	4.1	135
M 18	4.9 (T)	GSC	17/10/03	6.9	241	311	7.3	0.26	2.4	2.0	6.8	105	<0.1	15.1	11.5	1.3	6.0	5.1%	3.0	6	5.4	106	4.6	196
M 19	4.8	GSC	17/10/03	5.8	248	111	7.7	0.05	2.6	2.1	4.9	48	<0.1	5.0	6.3	1.0	4.3	4.7%	4.3	7	2.5	64	1.8	121
M 20	4.7	GSC	17/10/03	5.6	271	109	8.3	0.05	3.4	1.7	4.9	48	<0.1	5.3	6.4	1.0	4.5	4.1%	4.6	7	2.8	64	1.7	123
M 21	2.6 (T)	OG	17/10/03	8.4	247	259	9.6	0.07	6.9	3.6	6.4	86	<0.1	9.7	7.3	1.9	9.7	3.9%	2.8	7	2.0	134	7.0	176
M 22	2.5	OG	17/10/03	5.7	230	145	9.5	0.06	4.0	3.6	5.4	70	<0.1	7.9	6.5	1.3	6.9	5.1%	2.8	21	3.1	111	1.5	156
M 23	2.4	OG	17/10/03	5.7	223	150	9.5	0.06	4.9	3.5	5.6	73	<0.1	8.3	6.6	1.9	7.7	4.1%	3.1	11	2.9	116	1.3	161
S 13	5.7	BA	19/10/03	8.1	−13	170	6.8	0.03	6.3	6.6	6.1	74	<0.1	8.8	6.1	2.3	8.5	5.1%	3.4	121	3.3	130	4.9	174
S 14	5.0	BA	18/10/03	7.9	140	189	8.5	0.03	6.5	5.2	5.7	77	<0.1	8.9	6.3	2.4	8.9	3.9%	3.4	246	3.6	132	7.7	170
S 15	4.3	OG	18/10/03	8.1	183	190	11.3	0.05	6.9	8.6	5.3	82	<0.1	9.5	6.5	2.2	10.0	4.0%	3.7	28	2.3	141	7.5	179
S 16	3.8 (T)	OG	18/10/03	8.3	219	287	7.0	0.05	6.6	0.9	6.3	100	<0.1	10.0	8.1	2.9	10.4	5.0%	2.5	13	1.9	156	7.3	196
S 17	3.7	OG	18/10/03	8.2	218	180	7.1	0.05	6.1	6.4	5.6	83	<0.1	9.4	6.3	1.4	10.0	4.1%	2.6	7	2.1	136	7.0	173
S 18	3.6	OG	18/10/03	8.1	192	184	7.5	0.04	6.2	4.2	5.8	116	<0.1	10.6	8.1	3.1	10.5	10.4%	2.4	10	2.0	142	7.1	209

The SI values are <1 for all other commonly occurring secondary mineral phases. The column "upstream distance" gives the distance of the sampling point from the catchment outlet.

Table 2
REE and Y concentrations for 0.45 μm filtered water samples in ng/L, corresponding basalt-normalized Ce and Eu anomalies, and La/Yb, Nd/Yb and Y/Ho ratios

	Upstream distance	Bedrock lithology	La	Ce	Nd	Sm	Eu	Gd	Tb	Dy	Y	Ho	Er	Yb	Lu	Ce/Ce^*_{basalt}	Eu/Eu^*_{basalt}	La/Yb_{basalt}	Nd/Yb_{basalt}	Y/Ho_{basalt}
	[km]																			
Water samples September 2002																				
M 1	9.1	BA				88	27.3	81		52	322	10.4	32	32	5.6		0.9			1.1
M 2	8.5	BA			236	47	15.4	52	5.1	30	166	5.5	17	13	20		0.9		0.9	1.1
M 3	4.9 (T)	GSC				141	47.9	119		140	828	27.2	80	83	12.8		1.0			1.1
M 4	4.8	GSC			165	38	14.3	38	4.5	28	163	5.6	17	15	2.3		1.1		0.5	1.1
M 5	4.7	GSC			155	35	13.7	37	4.4	29	164	5.8	17	15	2.2		1.1		0.5	1.0
S 1	57	BA			170	37	11.6	49	4.6	27	162	5.5	16	13	2.1		0.8		0.6	1.1
S 2	4.5 (T)	OG			71	15	5.3	24	2.0	1.2	75	2.4	7	7	1.1		0.8		0.5	1.1
S 3	4.4 (T)	OG			196	59	21.0	58	9.6	74	454	15.5	44	32	4.4		1.0		0.3	1.1
S 4	3.8 (T)	OG			74	18	6.7	22	2.6	18	105	3.6	11	10	1.5		1.0		0.3	1.1
S 5	3.7	OG			83	19	6.6	26	2.7	17	99	3.5	10	10	1.5		0.8		0.4	1.0
S 6	3.6	OG			77	17	6.3	27	2.6	17	97	3.4	11	9	1.6		0.8		0.4	1.0
Extraction yield (n=3)																				
		Average			17%	17%	18%	24%	25%	19%	19%	19%	18%	16%	16%					
		SD			2%	2%	2%	2%	9%	2%	2%	2%	2%	2%	2%					
Water samples June 2003																				
M 6	8.9	BA	90	417	59	11	4.0	15	1.9	8	49	1.7	5	4	0.8	2.8	0.9	1.0	0.7	1.1
M 7	8.8	BA	109	459	84	17	5.8	20	2.5	11	64	2.3	6	5	0.8	2.4	0.9	1.0	0.8	1.0
M 8	8.4	BA	129	471	93	18	5.9	21	2.6	12	57	2.2	6	5	0.8	2.1	0.9	1.1	0.9	1.0
M 9	8.0	GSC	70	284	54	11	4.2	13	1.6	8	43	1.5	5	4	0.7	2.3	1.0	0.7	0.6	1.0
M 10	4.9 (T)	GSC	109	215	136	34	12.4	36	6.6	35	196	6.8	18	16	2.3	0.9	1.0	0.3	0.4	1.1
M 11	4.8	GSC	99	502	65	15	6.5	19	2.5	12	67	2.5	7	8	1.4	3.0	1.1	0.5	0.4	1.0
M 12	4.7	GSC	78	319	63	14	6.3	16	2.3	12	62	2.4	7	8	1.3	2.3	1.2	0.4	0.4	0.9
S 7	5.7	BA	309	945	292	58	19.8	68	9.4	44	209	8.7	23	18	2.7	1.6	0.9	0.	0.8	0.9
S 8	5.0	BA	228	835	181	37	11.5	43	5.7	27	118	5.2	14	11	1.8	2.1	0.8	0.9	0.8	0.8
S 9	4.3	OG	63	278	50	12	4.4	15	2.3	12	66	2.7	8	9	1.5	2.5	0.9	0.3	0.3	0.9
S 10	3.8 (T)	OG	72	268	70	18	7.1	23	3.8	21	107	4.4	14	15	2.4	2.0	1.0	0.2	0.2	0.9
S 11	3.7	OG	113	792	46	11	4.2	19	2.2	11	58	2.5	8	8	1.5	4.6	0.8	0.6	0.3	0.8
S 12	3.6	OG	82	492	45	11	4.2	17	2.3	12	67	2.6	8	9	1.5	3.7	0.9	0.4	0.2	0.9
Extraction yield (n=5)																				
		Average	27%	30%	23%	23%	23%	25%	23%	24%	24%	25%	24%	21%	19%					
		SD	4%	10%	3%	3%	3%	3%	4%	3%	3%	3%	3%	3%	3%					
Water samples October 2003																				
M 13	8.9	BA	188	1000	122	26	10.7	31	4.1	16	114	3.7	12	9	1.5	3.2	1.0	0.9	0.7	1.1
M 14	8.8	BA	98	434	81	17	5.5	19	2.6	10	63	2.1	6	6	0.7	2.6	0.9	0.8	0.7	1.1
M 15	8.4	BA	73	290	62	14	4.6	16	2.2	8	54	1.9	5	5	1.0	2.2	0.9	0.6	0.6	1.0
M 16	8.0	GSC	75	209	70	16	7.0	16	2.7	11	59	2.2	5	5	1.1	1.5	1.2	0.6	0.6	1.0
M 17	6.5	GSC	83	139	98	20	10.3	21	3.3	17	106	3.5	11	9	1.4	0.8	1.4	0.4	0.5	1.1
M 18	4.9 (T)	GSC	92	173	106	27	11.3	27	5.1	26	164	5.3	15	12	1.7	0.9	1.2	0.3	0.4	1.1
M 19	4.8	GSC	86	326	83	19	9.1	19	3.0	14	84	2.8	9	10	1.4	2.0	1.4	0.4	0.4	1.1
M 20	4.7	GSC	74	205	76	19	8.3	18	2.9	13	84	3.1	8	9	1.4	1.4	1.3	0.3	0.4	1.0
M 21	2.6 (T)	OG	55	165	63	17	5.6	18	3.2	17	104	3.4	11	11	1.7	1.5	0.9	0.2	0.3	1.1
M 22	2.5	OG	97	579	67	16	7.5	21	3.1	15	88	2.9	10	9	1.1	3.5	1.2	0.5	0.4	1.1
M 23	2.4	OG	57	128	65	17	7.1	19	3.5	16	98	3.7	10	10	1.8	1.1	1.1	0.2	0.3	1.3
S 13	5.7	BA	182	878	122	26	8.8	32	3.8	17	110	3.2	9	6	1.1	2.6	0.9	1.4	1.0	1.3
S 14	5.0	BA	164	596	129	25	8.2	30	3.1	16	91	2.8	8	7	0.7	2.1	0.8	1.1	0.9	1.2
S 15	4.3	OG	60	322	42	10	3.9	13	1.7	8	55	1.6	5	3		3.1	0.9	0.7	0.6	1.3
S 16	3.8 (T)	OG	50	173	50	13	6.3	16	2.7	14	91	2.6	8	9	1.1	1.8	1.2	0.2	0.3	1.3
S 17	3.7	OG	44	221	34	8	4.2	10	1.8	9	56	1.7	5	5	1.0	2.9	1.3	0.4	0.3	1.2
S 18	3.6	OG	37	80	48	13	5.1	13	2.3	11	77	2.3	8	8	1.4	1.0	1.1	0.2	0.3	1.2
Extraction yield (n=3)																				
		Average	18%	17%	16%	17%	17%	18%	17%	19%	18%	19%	18%	18%	15%					
		SD	2%	1%	1%	1%	1%	2%	1%	2%	2%	2%	1%	1%	0%					
Calculated mixing patterns																				
M 12 calc			99	498	66	15	6.6	19.2	2.5	12	69	2.6	8	8	1.4	3.0	1.1	0.5	0.4	1.0
M 20 calc			86	326	83	19	9.1	18.9	3.0	14	84	2.9	9	10	1.4	2.0	1.4	0.4	0.4	1.1
M 23 calc			88	486	66	16	7.1	20.0	3.1	1.5	92	3.0	10	9	1.2	3.2	1.1	0.4	0.3	1.1
S 12 calc			112	784	46	11	4.3	19.2	2.2	12	59	2.6	8	8	1.5	4.6	0.8	0.6	0.3	0.8
S 18 calc			44	221	34	8	4.2	10.1	1.8	9	56	1.7	5	5	1.0	2.9	1.3	0.4	0.3	1.2
Alteration profile in basalt																				
FB1 (90 cm)			57	99	51	10	3.4	8.5	1.3	6	30	1.2	3	2	0.3	0.9	1.0	1.2	1.2	0.9
FB2 (75 cm)			65	111	57	11	3.7	9.3	1.4	7	31	1.3	3	2	0.3	0.9	1.0	1.3	1.3	0.9
FB3 (55 cm)			52	93	46	9	2.9	7.6	1.1	6	27	1.1	2	2	0.3	1.0	1.0	1.3	1.3	0.9
FB4 (38 cm)			57	109	52	10	3.3	8.7	1.3	7	31	1.2	3	2	0.3	1.0	1.0	1.2	1.2	0.9
FB5 (20 cm)			55	112	51	10	3.2	8.7	1.3	7	32	1.2	3	2	0.3	1.1	0.9	1.1	1.1	1.0

The La and Ce concentrations of the sample series from September 2002 are omitted because of a blank problem during the enrichment procedure. The extraction yields have been determined for each sample series using standard solutions (n = number of standards) and been used to calculate the effective sample concentrations. The calculated mixing patterns are based on REE data from stream confluences and Sr isotopic compositions.
Concentrations for water samples in ng/L, in ppm for basalt alteration profile.

water samples never exceeded 10% for La and Ce, and 2% for Gd. Only exception was the September 2002 sample series, where the blank contributions were above 20% for La and Ce. Therefore, no La and Ce data are given for these samples. The extraction yield has been determined for each individual sample series using ultrapure water spiked with standard solutions and the resulting yield values are given in Table 2. The variations between the individual extraction series are due to changing reagent batches that were replaced for each series.

For isotope analysis, extraction of Sr and Nd from the water samples was conducted in the same clean lab as the REE extractions using Sr Spec, TRU Spec, and Ln Spec resins from Eichrom technologies (Pin et al., 1994). The same liquid–liquid preconcentration procedure as for the bulk REE was used to enrich Nd prior to separation on TRU Spec and Ln Spec columns. One liter of filtered stream water typically yielded 10–25 ng of Nd for isotope analysis. For Sr isotope analysis, 20 mL of water was evaporated prior to loading on Sr Spec columns. Nd and Sr isotope analysis were performed on a Nu-Plasma multi-collector ICP-MS at the laboratory for isotope geology at the University of Bern (Switzerland) using the ratios $^{86}Sr/^{88}Sr = 0.1194$ and $^{146}Nd/^{144}Nd = 0.7219$ for fractionation correction. The Nd in house standard was diluted to 40 ng Nd/L in order to have concentrations comparable to our water samples and yielded $^{143}Nd/^{144}Nd = 0.511058 \pm 23$ (±SD, $n = 7$) value of 0.511848 for the La Jolla standard. The NBS 987 Sr standard was measured at $^{87}Sr/^{88}Sr = 0.710250 \pm 22$ (±SD, $n = 10$). Some additional isotope measurements detailed in Table 3 were realized at the Centre de Géochimie de la Surface at CNRS Strasbourg (France) with a VG Sector thermal ionisation mass spectrometer (TIMS) with a 5-cup multi-collector. On the VG TIMS in Strasbourg the NBS 987 Sr standard yielded $^{87}Sr/^{88}Sr = 0.710259 \pm 8$ (±SD, $n = 12$) and the La Jolla Nd standard $^{143}Nd/^{144}Nd = 0.511871 \pm 8$ (±SD, $n = 14$).

For the study of the particulate matter, all 0.45 µm Sartorius cellulose acetate filters have been weighted prior to field sampling. After sampling, the filters were dried at 40 °C and weighted again in order to determine the suspension load for each filter. For the chemical analyses of the particulate load, for each sample one half of a filter was weighted and leached during 10 min with 15 mL of 1 M sub-boiled distilled HCl under continuous agitation in 50 mL polypropylene centrifuge tubes, and finally centrifuged at 3000 rpm during 5 min. After centrifugation, the supernatant later on called "leachate" was recovered by decantation and directly analyzed by ICP-MS and ICP-AES. The analytical precision is <±10% for the ICP-AES and <±5% for the ICP-MS on the first sigma level. The remaining filters were transferred into Savillex Teflon vials, ashed at 200 °C, completely dissolved in sub-boiled distilled 15 M HNO_3 and HF 40% of supra-pure quality (Merck), evaporated, and finally redissolved in 15 mL of 1 M HNO_3 for ICP analysis. The absolute elemental concentrations for the leachates and the residues were calculated by multiplying the analyzed concentrations with the 15 mL of solution volume and normalized to the particle weight contained in the filter half prior to leaching.

All bedrock samples were crushed, milled in an agate mill, fused with Li_2BO_4, and then dissolved in 20 mL of a HNO_3–glycerine solution for

Table 3
Sr and Nd isotope data of whole rock and water samples

	Upstream distance	Bedrock lithology	$^{87}Sr/^{86}Sr$	$^{87}Rb/^{86}Sr$	% basaltic Sr	Lab	$^{143}Nd/^{144}Nd$	$^{147}Sm/^{144}Nd$	ε_{Nd}	% basaltic Nd	Lab
Water samples June 2003											
	[km]										
M 10	4.9 (T)	GSC	0.709749(10)	0.105	63%	Sb					
M 11	4.8	GSC	0.706340(10)	0.118	83%	Sb					
M 12	4.7	GSC	0.706448(14)	0.125	82%	Sb					
S 10	3.8 (T)	OG	0.704790(10)	0.051	97%	Sb					
S 11	3.7	OG	0.704450(10)	0.063	97%	Sb					
S 12	3.6	OG	0.704599(10)	0.060	97%	Sb					
Water samples October 2003											
	[km]										
M 13	8.9	BA	0.703807(10)	1.482	98%	Be	0.512887(17)	0.130	4.9(0.3)	98%	Be
M 15	8.4	BA	0.703770(9)	0.155	98%	Be	0.512743(28)	0.124	2.1(0.5)	78%	Be
M 17	6.5	GSC	0.705733(13)	0.082	86%	Be	0.512780(59)	0.125	2.8(1.1)	83%	Be
M 18	4.9 (T)	GSC	0.710723(10)	0.147	57%	Be	0.512430(22)	0.154	−4.1(0.4)	34%	Be
M 19	4.8	GSC	0.706478(9)	0.115	82%	Be	0.512622(22)	0.138	−0.3(0.4)	61%	Be
M 20	4.7	GSC	0.706574(13)	0.125	81%	Be	0.512624(36)	0.147	−0.3(0.7)	61%	Be
M 21	2.6 (T)	OG	0.704968(12)	0.044	96%	Be	0.512693(34)	0.166	1.1(0.7)	66%	Be
M 22	2.5	OG	0.705211(9)	0.081		Be	0.512751(28)	0.144	2.2(0.5)		Be
M 23	2.4	OG	0.705125(11)	0.073		Be	0.512702(27)	0.157	1.3(0.5)		Be
S 13	5.7	BA	0.703927(10)	0.073	99%	Be	0.512798(15)	0.127	3.1(0.3)	83%	Be
S 14	5.0	BA	0.704002(10)	0.078	99%	Be	0.512788(17)	0.118	2.9(0.3)	81%	Be
S 16	3.8 (T)	OG	0.704762(11)	0.036	97%	Be	0.512779(27)	0.161	2.8(0.5)	80%	Be
S 17	3.7	OG	0.704501(9)	0.045	97%	Be	0.512744(53)	0.151	2.1(1.0)	74%	Be
S 18	3.6	OG	0.704664(9)	0.041	97%	Be	0.512775(32)	0.165	2.7(0.6)	79%	Be
Whole rock samples											
BA 1	Basalt		0.703348(11)	0.086		Sb	0.512940(4)	0.126	5.9(0.8)		Sb
BA 2	Basalt		0.703430(10)	0.112		Sb	0.512891(7)	0.128	4.9(0.1)		Be
SC 1	Volc. Scoria		0.703384(12)	0.060		Sb	0512874(4)	0.131	4.6(0.9)		Be
GSC 1	Granite		0.722319(13)	2.690		Sb	0.512197(6)	0.129	−8.6(0.1)		Be
GSC 2	Granite		0.718799(10)	2.046		Sb	0.512187(6)	0.118	−8.8(0.1)		Be
OG 1	Orthogneiss		0.751991(13)	4.525		Sb	0.512283(5)	0.147	−6.9(0.9)		Be
OG 2	Orthogneiss		0.739454(12)	4.203		Sb	0.512292(5)	0.147	−6.8(0.1)		Be

The errors given for the isotope ratios and ε_{Nd} values are ±2 sigma mean values and refer to the last digits. ε_{Nd} values are defined as $\varepsilon_{Nd} = 1E4 * ((^{143}Nd/^{144}Nd_{sample} - ^{143}Nd/^{144}Nd_{chondrite}) / ^{143}Nd/^{144}Nd_{chondrite})$ using 0.512638 for chondrite composition. The values "% basaltic Sr" and "% basaltic Nd" for water samples have been calculated by the formula: % basaltic Sr or Nd = $100 * \{(IR_{Sample} - IR_{Granite\ or\ Orthogneiss}) / (IR_{Basalt} - IR_{Granite\ or\ Orthogneiss})\}$, where "IR" stands for $^{87}Sr/^{86}Sr$ or $^{143}Nd/^{144}Nd$. A granitic end member was used for samples M13–M19, and an orthogneiss end member for samples S13 to S18 and M21. No percentages are given for samples M22 and M23 because these waters have in contrast to the other samples not been in contact with 2, but with 3 different lithologies (Fig. 1). The column "Lab" indicates the laboratory where the isotope measurements were made: Sb for Strasbourg and Be for Bern.

analysis by ICP-AES and ICP-MS at the Centre de Géochimie de la Surface at CNRS Strasbourg (France).

3. Results and discussion

3.1. The REE patterns of the bedrock

The REE data including yttrium and the major element composition of the whole rock samples are given in Table 4. The REE patterns of the basalts and the volcanic scoria are identical, whereas the granites are characterized by higher, and the orthogneisses by lower La/Yb ratios. Both, granite and orthogneiss, have negative Eu anomalies when normalized to basalt. We use a REE normalization with respect to average local basalt (BA1 to BA3 in Table 4) because most evolutions of the REE patterns of the stream water data discussed below are more obvious using this normalization rather than Chondrite or Upper Continental Crust (PAAS).

3.2. Major element composition, dissolved organic carbon, and physico-chemical parameters of stream water

The major element composition of the 0.45 μm filtered stream water samples are given in Table 1. The waters are generally of the Ca–Mg–HCO_3-type and in a Piper diagram no significant evolution of the major element chemistry can be observed from upstream to downstream. The pH values vary little and remain between 7 and 8 in most cases without systematic variations. Only the Malaval stream in October 2003 yielded downstream decreasing pH values with a minimum close to 6 near the catchment outlet (Table 1). The Eh values are almost always strongly positive becoming in general more oxidizing downstream where stream water is more agitated because of the steeper slopes. The conductivity values decrease like the total dissolved solid values (TDS) calculated with Aquachem 4 (www.waterloohydrogeologic.com) slightly downstream (Table 1).

3.3. Nd–Sr isotope data of the bedrock and 0.45 μm filtered stream water

The aim of the Nd–Sr isotope analysis was to identify and to quantify the impact of the different bedrock lithologies on the chemical composition of stream water. The study site is particularly suitable for such an approach because of the highly different Sr and Nd isotopic compositions between the upper basaltic, and lower granitic and gneissic portion of the catchment. This allows, in contrast to concentration data, to identify and to quantify even small exchanges of stream water with each bedrock type.

The Rb–Sr isotope data of the bedrock and the 0.45 μm filtered water samples are given in Table 3. The Sr isotopic ratios of the streams are close to basalt composition in the source area, followed by an increase as soon as the streams leave the basalt and reach the leucogranitic or orthogneissic bedrock. The shift is stronger for the Malaval than for the Séjallières stream. However, even for the Malaval stream the Sr isotopic compositions never exceed 0.707. Only sample M18 from a small tributary, whose catchment area is almost entirely located within leucogranite, has a $^{87}Sr/^{86}Sr$ ratio approaching 0.711. Simple end member calculations based on the Sr isotope data show that the Malaval stream never contains less than 80% of Sr of basaltic origin. Even the Malaval tributary samples M10 and M18 with most radiogenic $^{87}Sr/^{86}Sr$ ratios still contain 60% of basaltic Sr (Table 3). The Sr isotopic compositions of the Séjallières stream water samples remain always very close to basalt values demonstrating that all

Table 4
Major and trace element composition of whole rock samples of the different bedrock lithologies (BA = basalt, SC = volcanic scoria, GSC = leucogranite, OG = orthogneiss)

Basalt				Volcanic scoria			Leucogranite			Orthogneiss		
Sample	BA 1	BA 2	BA 3	SC 1	SC 2	SC 3	GSC 1	GSC 2	GSC 3	OG 1	OG 2	OG 3
LOI 1000 °C	0.75	0.20	−0.21	2.13	3.51	1.20	1.05	0.86	1.66	1.15	0.83	0.79
Major element (%)												
SiO_2	44.4	43.3	48.3	43.9	49.2	44.5	72.8	72.3	70.3	74.4	73.6	78.3
Al_2O_3	13.9	13.2	14.2	15.6	13.0	12.3	14.7	14.8	15.2	13.9	14.5	11.1
MgO	9.8	11.8	8.2	9.8	8.8	12.9	0.3	0.4	0.4	0.6	0.6	0.2
CaO	10.0	9.3	8.5	8.8	8.1	10.3	0.5	0.9	0.5	0.7	0.6	0.3
Fe_2O_3	13.0	12.9	12.5	12.9	10.9	12.8	1.2	1.2	1.8	2.2	1.7	1.7
MnO	0.189	0.182	0.173	0.183	0.159	0.184	0.037	0.016	0.020	0.026	0.026	0.016
TiO_2	2.55	2.33	2.85	2.48	2.18	2.39	0.17	0.18	0.26	0.28	0.21	0.11
Na_2O	2.07	2.75	3.35	1.89	1.76	2.34	3.42	3.67	3.68	2.67	2.32	2.33
K_2O	1.46	1.49	1.58	0.61	1.36	0.48	4.50	4.14	4.97	4.01	5.72	4.58
P_2O_5	0.52	0.55	0.66	0.41	0.49	0.67	0.10	0.11	0.10	0.22	0.22	0.30
Sum	98.7	98.1	100.1	98.7	99.4	100.1	98.8	98.5	98.9	100.7	100.3	99.7
Trace elements (ppm)												
Rb	27	30	33	17	57	56	174	170	204	129	168	240
Sr	923	779	695	836	508	705	187	240	437	83	116	27
La	39.9	35.0	36.8	40.3	45.3	39.6	23.6	27.2	42.8	24.0	20.9	7.1
Ce	70.1	65.9	71.3	77.0	85.8	75.3	45.7	50.1	76.3	49.9	41.9	15.3
Pr	8.8	7.7	8.7	9.4	10.1	9.0	5.1	5.7	8.1	5.9	5.0	1.8
Nd	34.8	30.8	35.3	37.2	38.7	34.7	17.3	19.7	27.3	22.1	17.8	6.3
Sm	7.3	6.5	7.5	8.0	7.7	7.1	3.7	3.8	4.5	5.4	4.3	1.9
Eu	2.24	2.05	2.41	2.58	2.28	2.21	0.64	0.84	1.04	0.70	0.77	0.16
Gd	5.71	5.13	5.61	5.93	6.56	5.75	2.43	2.64	3.40	4.46	3.49	1.66
Tb	0.92	0.83	0.91	0.94	1.01	0.94	0.35	0.33	0.46	0.88	0.66	0.45
Dy	4.82	4.26	4.97	5.04	5.13	4.57	1.70	1.60	2.32	5.23	4.01	3.25
Y	25.1	22.5	25.1	23.8	27.2	24.9	8.9	8.9	12.4	32.6	24.7	18.9
Ho	0.91	0.83	0.94	0.93	0.97	0.87	0.28	0.26	0.44	1.09	0.79	0.62
Er	2.03	1.78	2.01	2.01	2.27	2.15	0.59	0.56	1.08	2.53	1.85	1.23
Tm	0.29	0.27	0.32	0.29	0.34	0.31	0.10	0.07	0.18	0.40	0.28	0.20
Yb	1.71	1.54	1.62	1.68	1.87	1.61	0.62	0.50	0.97	2.39	1.60	0.91
Lu	0.25	0.25	0.24	0.26	0.27	0.25	0.09	0.06	0.14	0.35	0.24	0.11
Eu/Eu^*_{basalt}	0.97	0.99	1.04	1.05	0.90	0.97	0.60	0.74	0.75	0.40	0.56	0.26
La/Yb_{basalt}	1.01	0.99	0.99	1.04	1.05	1.07	1.66	2.37	1.92	0.44	0.57	0.34

The major elements as well as Sr and Y have been analyzed by ICP-AES, Rb and the REE by ICP-MS.

Table 5
Trace element concentrations for 1 M HCl leachates and residues of suspended particles (fraction > 0.45 μm)

Fraction method	Upstream distance	Bedrock lithology	Suspension weight	Si	Al	Fe	Mn	P	Cr	Co	Ni	As	Sr	Mo	Si	Al	Fe	Mn	Rb	Sr
				Leach 1	Leach 1	Leach 1	Leach 1	Leach 1	Leach 1	Leach 2	Leach 1	Leach 2	Leach 2	Leach 2	Residue 1	Residue 1	Residue 1	Residue 1	Residue 2	Residue 2
	[km]		[mg/L]	[ppm]	[ppm]	[ppm]	[ppm]	[ppm]	[ppb]	[ppb]	[ppb]	[ppb]	[ppb]	[ppb]	[ppm]	[ppm]	[ppm]	[ppm]	[ppb]	[ppb]
Samples June2003																				
M6	8.9	BA	17.4	0.7	0.8	6.1	0.1	0.4	b.d.l.	1.0	b.d.l.	2090	19	0.2						
M7	8.8	BA	16.0	1.1	1.0	9.7	0.2	0.6	52	2.2	19	1766	28	0.5						
M8	8.4	BA	52.2	2.0	2.0	15.4	0.3	0.8	237	3.9	140	1328	48	0.3						
M9	8.0	GSC	180.4	2.2	2.7	15.4	0.6	1.2	329	7.7	195	1196	135	0.4						
M10	4.9 (T)	GSC	1.3	0.7	2.2	11.0	1.1	1.3	1650	4.4	898	4299	90	3.5						
M11	4.8	GSC	5.5	1.1	2.1	10.2	0.5	0.9	630	5.2	375	1278	76	1.2						
M12	4.7	GSC	7.2	0.3	0.4	4.4	0.1	0.3	616	5.8	344	864	22	1.6						
S7	5.7	BA	47.8	0.6	0.6	10.7	0.2	0.3	1786	6.6	919	1381	15	6.4						
S8	5.0	BA	58.1	1.1	1.3	14.0	0.7	1.4	1792	11.4	977	1395	49	6.6						
S9	4.3	OG	17.5	0.9	1.5	10.1	0.4	0.6	1382	8.8	724	1057	43	4.9						
S10	3.8 (T)	OG	19.7	0.8	1.2	9.9	0.4	0.5	1358	8.5	732	930	41	4.5						
S11	3.7	OG	5.6	0.8	1.1	9.6	0.4	0.5	1294	9.1	681	903	37	4.5						
S12	3.6	OG	6.3	1.0	1.3	10.3	0.5	0.6	12330	8.7	662	838	46	3.9						
Samples October 2003																				
M13	8.9	BA	5.0	5.3	7.5	56.4	1.0	2.8	4447	16.5	2460	4977	64	14.2	0.58	35.7	23.5	0.26	17	104
M14	8.8	BA	6.2	3.4	9.8	33.0	1.7	2.7	2119	12.2	1298	2541	63	8.3	0.20	50.7	35.1	0.48	25	142
M15	8.4	BA	1.6	5.1	3.8	64.9	0.9	1.9	7688	39.3	4198	8615	79	34.1	0.26	17.4	11.0	0.18	9	57
M16	8.0	GSC	3.5	3.7	4.0	20.8	0.6	1.1	2980	17.2	1662	3116	66	12.1	b.d.l.	5.1	3.9	0.06	4	12
M17	6.5	GSC	0.7	0.9	2.8	39.2	0.9	1.4	9151	51.2	5125	10216	30	41.1	b.d.l.	8.4	5.1	0.05	11	16
M18	4.9 ('0	GSC	5.2	0.4	2.2	13.7	1.0	0.7	2877	11.5	1522	2614	60	10.3	b.d.l.	22.7	9.9	0.28	58	20
M19	4.8	GSC	0.7	1.1	3.4	39.0	1.1	1.8	8777	46.2	4992	8322	80	34.2	0.74	29.0	17.1	0.18	39	51
M20	4.7	GSC	1.9	1.0	2.0	22.6	0.6	1.1	5190	29.1	2803	4786	54	20.2	b.d.l.	24.6	12.7	0.12	40	47
M21	2.6 (T)	OG	0.7	0.7	2.3	39.4	1.1	1.7	9798	59.2	5344	8875	59	40.1	b.d.l.	16.0	8.1	0.13	19	31
M22	2.5	OG	0.8	3.3	3.0	37.6	1.4	1.8	6759	42.5	3749	5757	47	27.3	b.d.l.	10.9	6.9	0.10	16	28
M23	2.4	OG	0.6	11.1	15.0	172.7	6.9	9.0	28809	170.8	15586	23020	173	107.9	b.d.l.	54.2	26.7	0.41	64	113
S13	5.7	BA	7.8	1.6	1.8	39.4	0.8	1.4	7643	29.6	4107	5908	33	29.6	b.d.l.	19.6	13.6	0.14	9	37
S14	5.0	BA	1.3	1.0	1.7	29.9	0.8	0.7	7333	36.8	3832	4245	50	20.9	b.d.l.	28.2	18.4	0.23	19	60
S15	4.3	OG	3.1	2.0	1.8	28.2	1.0	1.1	4017	23.3	2177	2513	68	11.7	b.d.l.	33.3	21.8	0.68	48	64
S16	3.8 (T)	OG	1.8	1.2	2.0	30.3	0.9	1.1	7223	37.2	3773	4248	49	20.7	b.d.l.	23.3	10.9	1.05	25	25
S17	3.7	OG	1.2	2.9	2.3	45.2	0.9	1.4	7339	37.8	3845	4265	37	21.4	b.d.l.	8.3	4.2	0.11	9	19
S18	3.6	OG	2.5	1.3	2.0	26.5	1.0	0.9	5356	30.2	2801	3112	68	15.6	b.d.l.	25.4	17.8	0.28	37	48

1 = ICP-AES, 2 = ICP-MS, b.d.l. = below detection limit.
All concentrations are normalized to suspension weight before leaching.

samples contain at least 96% Sr of basaltic origin. The 6 Sr isotopic compositions of the sample series from June 2003 fit perfectly in this general picture.

The Sm–Nd isotope data of the bedrock and the 0.45 μm filtered water samples from October 2003 are given in Table 3. The Nd isotopic composition of stream water shows a similar evolution as Sr isotopes with basalt-like compositions on the basaltic plateau followed by a slight decrease towards more crustal values within the granite and the gneiss. Mixing calculations show, similar to Sr isotopes, that even the samples with lowest ε_{Nd} values still contain 60% of basaltic REE (Table 3). Only the tributary sample 18 at 4.9 km has a strongly crustal ε_{Nd} value of −4 indicating the presence of about only 30% of basaltic REE.

Thus both, the Sr and Nd the isotope data suggest that stream water acquires its isotopic composition mainly during water–rock interaction on the basalt plateau and that the contribution from the other granitic and gneissic terrains is very limited. This finding is in agreement with the field observation that a significant regolith cover allowing water–rock interaction is only present on the basalt plateau, whereas the granites and gneisses crop out on steep slopes with only poorly developed soils.

3.4. The REE of the suspended particle load

This section presents the chemical composition of particles recovered on 0.45 μm filters that were leached with 1 M HCl in order to separate the particle load into a leachable and a residual pool. The trace element and the REE data of the 1 M HCl leachates and the corresponding residues are given in Tables 5 to 7.

In Fig. 2 the leachate concentrations of trace elements and REE are compared to those of the untreated suspended load samples. According to this figure, leaching removed 90–100% of the total As, Cr, Ni, and Mo, followed by Si, Mn, Co, and Fe, where 70 to 90% were mobilized. The absolute element concentrations in the leachate are by far highest for Fe (Table 5). The high proportion of silica removed by leaching may be a hint that silica is in the present case mostly derived from diatoms, which are common organisms in stream water (e.g. Kelly, 2003), rather than from silicate mineral particles. This is supported by the fact that silica was present in detectable quantities in only 4 residues (Table 5). The correlation matrix given in Table 8 furthermore indicates, that all these readily leachable elements are highly intercorrelated and all correlation factors are above 0.9 when plotted against Fe ($n=30$). All these observations suggest that almost all As, Cr, Ni, Mo, Si, and Co removed from the particulate load during leaching has been associated to a Fe–Mn oxyhydroxide phase, and eventually to diatom tests. The link with Fe–Mn oxyhydroxides can be due to surface adsorption on oxyhydroxide particles and particle coatings, or alternatively, to mobilization of trace elements fixed within oxyhydroxides. A similar removal of trace elements associated to secondary Fe–Mn oxyhydroxides by the same leaching procedure with 1 M HCl has already been described by Steinmann and Stille (1997) for soils. In the present case, these Fe–Mn oxyhydroxide particles and coatings contain also considerable amounts of P and Al as suggested by similarly good correlations between these elements

Table 6
REE and Y concentrations (REY) and corresponding basalt-normalized Ce/Ce*, Eu/Eu*, La/Yb, Nd/Yb, and Y/Ho ratios for 1 M HCl leachates of suspended particles (fraction > 0.45 μm)

	Upstream distance [km]	Bedrock lithology	La	Ce	Pr	Nd	Sm	Eu	Gd	Tb	Dy	Y	Ho	Er	Tm	Yb	Lu	Ce/Ce*$_{basalt}$	Eu/Eu*$_{basalt}$	La/Yb$_{basalt}$	Nd/Yb$_{basalt}$	Y/Ho$_{basalt}$
Samples June2003																						
M6 L	8.9	BA	3.4	5.8	0.8	3.2	0.64	0.19	0.64	0.08	0.44	1.98	0.08	0.19	0.03	0.16	0.03	0.90	0.81	0.93	0.98	0.95
M7 L	8.8	BA	5.2	8.2	1.2	4.9	0.91	0.29	1.08	0.13	0.65	2.99	0.12	0.30	0.04	0.22	0.04	0.84	0.81	1.03	1.07	0.94
M8 L	8.4	BA	10.9	20.8	2.5	10.5	1.87	0.62	2.03	0.28	1.42	6.22	0.25	0.65	0.08	0.46	0.07	1.00	0.89	1.04	1.11	0.92
M9 L	8.0	GSC	17.0	28.7	4.0	16.4	3.08	1.03	3.17	0.44	2.17	10.50	0.39	1.05	0.14	0.77	0.12	0.89	0.92	0.96	1.03	0.98
M10 L	4.9 (T)	GSC	12.8	15.6	3.4	14.6	3.41	1.10	3.54	0.59	3.28	15.43	0.52	1.41	0.17	1.01	0.13	0.60	0.89	0.55	0.70	1.09
M11 L	4.8	GSC	12.6	17.6	3.0	12.7	2.68	0.92	2.68	0.35	1.88	9.48	0.35	0.85	0.11	0.67	0.09	0.72	0.97	0.82	0.92	0.99
M12 L	4.7	GSC	13.9	20.0	3.3	14.1	2.87	1.01	2.84	0.40	2.06	10.80	0.38	1.01	0.12	0.70	0.11	0.74	0.99	0.86	0.97	1.05
S7 L	5.7	BA	2.1	4.4	0.5	2.1	0.39	0.13	0.43	0.06	0.28	1.67	0.05	0.11	0.01	0.09	0.01	1.08	0.86	1.07	1.18	1.18
S8 L	5.0	BA	4.8	7.8	1.2	4.8	0.96	0.31	1.03	0.16	0.79	4.28	0.14	0.37	0.05	0.27	0.04	0.84	0.88	0.78	0.86	1.11
S9 L	4.3	OG	6.5	10.9	1.6	6.6	1.47	0.47	1.61	0.24	1.28	6.86	0.24	0.64	0.08	0.47	0.06	0.87	0.85	0.60	0.69	1.04
S10 L	3.8 (T)	OG	6.3	10.5	1.5	6.3	1.32	0.43	1.40	0.21	1.17	6.22	0.23	0.57	0.07	0.42	0.06	0.87	0.88	0.66	0.73	1.01
S11 L	3.7	OG	5.3	8.8	1.3	5.3	1.00	0.31	1.04	0.15	0.82	3.97	0.15	0.38	0.05	0.26	0.04	0.87	0.86	0.87	0.96	0.97
S12 L	3.6	OG	6.6	11.2	1.6	6.6	1.36	0.40	1.38	0.20	1.10	5.58	0.20	0.54	0.06	0.37	0.06	0.88	0.82	0.78	0.87	1.01
Samples October 2003																						
M13 L	8.9	BA	12.3	18.4	2.8	10.4	1.96	0.62	1.85	0.25	1.42	6.39	0.21	0.61	0.07	0.46	0.06	0.82	0.91	1.18	1.10	1.12
M14 L	8.8	BA	14.3	24.6	3.2	13.2	2.34	0.76	2.35	0.31	1.69	7.91	0.29	0.78	0.09	0.54	0.08	0.92	0.90	1.15	1.18	1.00
M15 L	8.4	BA	5.5	9.5	1.2	5.1	0.84	0.18	0.71	0.08	0.50	2.88	0.07	0.18	b.d.l.	b.d.l.	b.d.l.	0.92	0.67			1.43
M16 L	8.0	GSC	7.5	12.4	1.7	7.1	1.21	0.41	1.36	0.16	0.95	4.31	0.15	0.39	0.05	0.29	0.05	0.88	0.90	1.13	1.17	1.05
M17 L	6.5	GSC	2.5	3.3	0.5	2.3	b.d.l.	b.d.l.	0.51	b.d.l.	0.21	1.73	b.d.l.	b.d.l.	b.d.l.	b.d.l.	b.d.l.	0.71				
M18 L	4.9 (T)	GSC	8.0	10.5	2.1	8.8	1.93	0.69	2.28	0.40	2.23	10.91	0.36	0.94	0.11	0.62	0.08	0.66	0.91	0.56	0.68	1.13
M19 L	4.8	GSC	8.5	10.9	2.0	7.4	1.41	0.50	1.60	0.23	1.08	6.31	0.18	0.38	0.05	0.24	b.d.l.	0.70	0.94	1.55	1.51	1.27
M20 L	4.7	GSC	6.8	9.7	1.5	6.5	1.38	0.42	1.180	0.15	0.86	4.96	0.16	0.39	0.03	0.35	0.03	0.76	0.92	0.85	0.90	1.12
M2 1 L	2.6 (T)	OG	3.4	4.9	0.7	3.2	0.79	0.19	0.80	0.09	0.64	3.34	0.07	0.25	b.d.l.	b.d.l.	b.d.l.	0.77	0.67			1.83
M22 L	2.5	OG	3.3	4.8	0.8	3.3	0.51	0.14	0.69	0.09	0.48	2.97	0.09	0.18	b.d.l.	b.d.l.	b.d.l.	0.75	0.68			1.19
M23 L	2.4	OG	13.7	21.1	2.9	12.5	2.44	0.54	2.68	0.33	2.18	12.04	0.31	1.07	b.d.l.	0.46	b.d.l.	0.82	0.60	1.31	1.33	1.43
S13 L	5.7	BA	5.4	11.4	1.2	5.2	1.06	0.29	1.07	0.15	0.63	4.26	0.13	0.26	b.d.l.	0.23	b.d.l.	1.11	0.76	1.03	1.09	1.25
S14 L	5.0	BA	7.3	15.3	1.7	7.0	1.17	0.37	1.27	0.16	0.91	4.54	0.15	0.44	0.05	0.24	0.03	1.11	0.85	1.32	1.41	1.13
S15 L	4.3	OG	8.3	14.1	2.0	8.1	1.74	0.50	1.71	0.26	1.34	7.35	0.25	0.65	0.08	0.47	0.05	0.89	0.81	0.78	0.83	1.06
S16 L	3.8 (T)	OG	4.9	7.9	1.2	5.1	1.09	0.33	1.18	0.16	0.94	5.31	0.17	0.38	0.05	0.29	0.04	0.82	0.81	0.74	0.85	1.13
S17 L	3.7	OG	2.5	4.0	0.5	2.2	0.36	0.12	0.42	0.06	0.30	2.12	0.04	0.12	b.d.l.	b.d.l.	b.d.l.	0.87	0.87			1.87
S18 L	3.6	OG	7.8	12.9	1.8	7.7	1.46	0.48	1.67	0.24	1.28	7.32	0.25	0.67	0.07	0.49	0.05	0.86	0.86	0.69	0.75	1.06

The leachate concentrations are normalized to suspension weight before leaching. For the calculation of the Ce and Eu anomalies the following formulas have been used: $Ce/Ce^* = 3 * Ce_{basalt} / \{2 * La_{basalt} + Nd_{basalt}\}$; $Eu/Eu^* = Eu_{basalt} / \{Sm_{basalt} * Gd_{basalt}\}^{0.5}$.
All concentrations in ppb, b.d.l. = below detection limit.

Table 7
REE and Y concentrations (REY) and corresponding basalt-normalized Ce/Ce*, Eu/Eu*, La/Yb, Nd/Yb, and Y/Ho ratios for 1 M HCl residues of suspended particles (fraction>0.45 μm)

	Upstream distance	Bedrock lithology	La	Ce	Pr	Nd	Sm	Eu	Gd	Tb	Dy	Y	Ho	Er	Tm	Yb	Lu	Ce/Ce^*_{basalt}	Eu/Eu^*_{basalt}	La/Yb_{basalt}	Nd/Yb_{basalt}	Y/Ho_{basalt}
Samples October 2003																						
M13 R	8.9	BA	5.4	13.2	1.1	4.1	0.69	0.36	0.80	0.11	0.57	2.39	0.13	0.27	0.06	0.28	0.05	1.39	1.34	0.83	0.70	0.67
M14 R	8.8	BA	9.0	26.5	1.7	6.3	1.26	0.49	1.18	0.16	0.86	3.51	0.14	0.43	0.07	0.40	0.07	1.73	1.12	0.98	0.75	0.89
M15 R	8.4	BA	8.8	16.7	1.2	2.5	0.61	0.18	0.72	0.07	0.32	1.28	0.07	0.21	b.d.l.	0.23	b.d.l.	1.32	0.78	1.64	0.52	0.69
M16 R	8.0	GSC	1.7	7.4	0.2	0.9	0.26	0.08	0.17	0.03	0.11	0.50	0.02	0.06	b.d.l.	0.09	b.d.l.	2.73	1.01	0.86	0.51	0.73
M17 R	6.5	GSC	2.5	10.9	0.4	0.9	0.47	0.10	0.26	b.d.l.	0.23	0.95	0.06	b.d.l.	b.d.l.	0.19	b.d.l.	2.94	0.79	0.56	0.23	0.63
M18 R	4.9 (T)	GSC	4.2	9.7	0.9	3.3	0.57	0.14	0.60	0.10	0.46	2.19	0.08	0.19	0.04	0.22	0.03	1.30	0.66	0.82	0.72	1.04
M19 R	4.8	GSC	10.9	32.8	2.1	7.7	1.68	0.24	1.50	0.19	0.84	2.75	0.12	0.29	0.05	0.28	b.d.l.	1.76	0.42	1.69	1.32	0.83
M20 R	4.7	GSC	18.7	25.4	2.9	7.4	1.47	0.29	1.55	0.16	0.69	3.02	0.13	0.36	0.06	0.34	0.05	0.90	0.54	2.40	1.05	0.89
M21 R	2.60	OG	2.9	11.8	0.5	1.6	0.48	0.11	0.34	b.d.l.	0.30	0.98	0.07	0.11	b.d.l.	0.16	b.d.l.	2.51	0.79	0.77	0.45	0.52
M22 R	2.5	OG	3.3	9.0	0.5	1.6	0.38	0.12	0.43	0.05	0.27	0.96	0.06	0.14	b.d.l.	0.09	b.d.l.	1.73	0.80	1.54	0.82	0.62
M23 R	2.4	OG	12.2	67.0	1.7	6.5	1.10	0.50	1.31	0.22	1.03	3.99	0.23	0.50	b.d.l.	0.56	b.d.l.	3.43	1.17	0.95	0.56	0.63
S13 R	5.7	BA	6.3	8.4	1.0	2.6	0.46	0.19	0.59	0.06	0.33	1.13	0.06	0.13	0.04	0.20	b.d.l.	0.88	1.03	1.38	0.63	0.65
S14 R	5.0	BA	4.4	9.3	0.8	2.8	0.55	0.24	0.45	0.07	0.41	1.61	0.08	0.19	0.03	0.24	0.04	1.27	1.34	0.80	0.56	0.76
S15 R	4.3	OG	7.2	18.0	1.5	5.5	1.01	0.25	1.02	0.14	0.64	2.54	0.11	0.26	0.03	0.25	0.03	1.42	0.68	1.26	1.07	0.82
S16 R	3.80	OG	9.8	25.1	2.1	7.6	1.29	0.18	1.28	0.14	0.68	2.39	0.12	0.24	0.03	0.21	b.d.l.	1.45	0.38	2.08	1.78	0.75
S17 R	3.7	OG	1.8	3.0	0.3	1.0	0.23	0.07	0.22	0.03	0.16	0.52	0.03	0.07	b.d.l.	0.08	b.d.l.	1.03	0.84	0.97	0.57	0.58
S18 R	3.6	OG	5.0	11.3	1.0	3.8	0.81	0.21	0.77	0.08	0.50	2.26	0.10	0.27	0.04	0.26	0.04	1.28	0.76	0.82	0.69	0.79

The residue concentrations are normalized to suspension weight before leaching.
All concentrations in ppb, b.d.l. = below detection limit.

and Fe and Si (Table 8). Such high concentrations of P and Al in secondary Fe–Mn oxyhydroxides are well documented in the literature (Norrish and Taylor, 1961; Schwertmann and Taylor, 1989; Alvarez et al., 2007). However, most Al of the suspended load remained in the residual phase during leaching (Fig. 2).

The lack of correlations between Nd and Fe in the leachates demonstrates that the REE do not follow the behavior of the trace elements mentioned above (Table 8). The only weak correlation can be observed between Nd and Sr ($r=0.595$, $n=30$), and leaching with HCl has only removed about 60% of the total REE content of the particulate load, thus less than for the other traces elements (Fig. 2). Most basalt-normalized REE patterns of the leachates are characterized by negative Ce anomalies and by an enrichment of Gd, Tb, and the heavy REE (not shown). All these data indicate that the REE are, in contrast to other trace elements, not associated to Fe–Mn oxyhydroxides, but they do not furnish more detailed information on the speciation of the leachable REE. Knowing that leaching with HCl mobilizes adsorbed elements and elements fixed in HCl soluble solid phases (Steinmann and Stille, 1997), our data simply show that the REE are in the present case adsorbed or fixed elsewhere than in Fe–Mn oxyhydroxides. This absence of a link with oxyhydroxides is ascertained by the negative Ce anomaly of the leachate patterns, because REE fixed in oxyhydroxides are in general characterized by positive Ce anomalies (Bau, 1999).

The REE of the residues are in contrast to the leachable REE strongly correlated with Al, Fe, and Th. Only the 3 residue samples with the highest Nd concentrations (above 7 ppb, M19 R, M20 R, S16 R; Table 7) do not exactly match the general trend, but the 14 remaining samples yield r values of 0.962 and 0.935 for Nd vs Al, and Nd vs Fe, respectively (Table 9). The average molar ratio of Al over Fe in the residues is of about 3.5±0.6. (±SD, $n=17$), indicating that the Al and Fe carrier phase in the residues is an aluminosilicate rich in Fe rather than a Fe oxyhydroxide. The correlation of Nd with Al and Fe thus indicates that this Fe-rich aluminosilicate is also the principal REE carrier in the residues.

3.5. The REE of the <0.45 μm fraction

The trace element and REE data for the 0.45 μm filtered water samples are given in Tables 1 and 2, respectively. The total REE concentrations of these <0.45 μm fractions are in general highest on the basalt plateau and decrease downstream, with a strong drop at the break between basalt plateau and slope. The corresponding basalt-normalized REE patterns are shown in Fig. 3. Most of the samples are characterized by positive Ce and Gd anomalies, which however show no regular evolution with distance. In contrast, a regular trend can be observed for the fractionation between LREE and HREE. On the basalt plateau close to the source area, the samples are slightly depleted in the LREE with basalt-normalized Nd/Yb ratios ranging between 0.7 and 0.9 (Table 2, Fig. 4). With increasing distance, the LREE become more and more depleted as shown by downstream decreasing Nd/Yb ratios reaching minimum values as low as 0.3. Fractionation between LREE and HREE is expressed here by basalt-normalized Nd/Yb rather than La/Yb ratios because no La data are available for the samples from September 2002. However, the evolution is almost identical for those sample series where both ratios are available (Table 2).

The Nd isotope data presented in Section 3.3 have demonstrated that the REE of the <0.45 μm fraction of stream water from the basalt plateau are directly derived from the basalt. Consequently, the slight depletion of the LREE in the water samples from the basalt plateau as well as the positive Ce and Gd anomalies must have occurred during water–rock interaction. This is confirmed by the data from an alteration profile sampled in the source area of the Malaval stream close to sampling point M1 (Fig. 1) showing

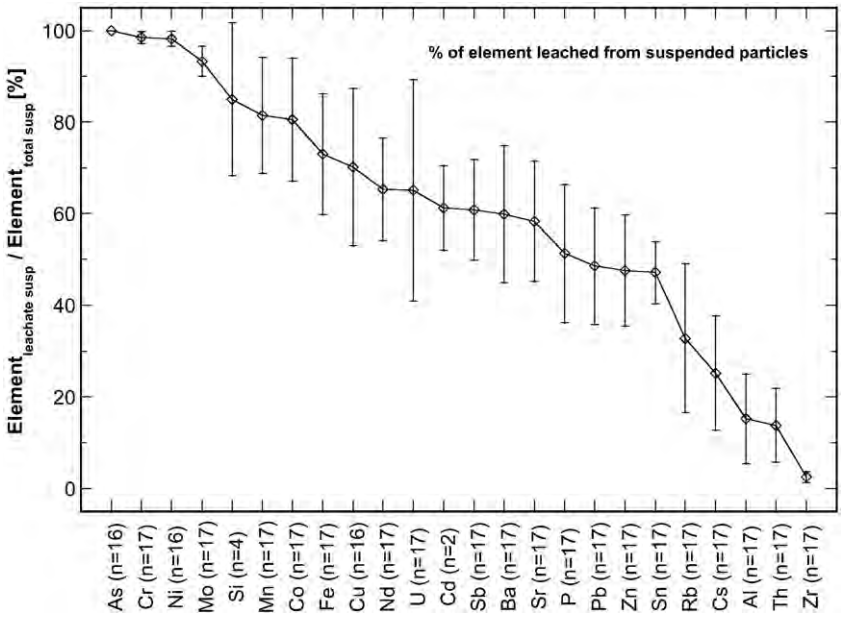

Fig. 2. Average percentage with standard deviation of trace elements removed from the particle fraction by leaching with HCl 1 M. The average values are based on percentages calculated for each individual sample by the formula % leached = 100 * {conc leachate / (conc leachate + conc residue)}.

that Nd/Yb and La/Yb ratios decrease towards the surface, whereas Ce/Ce* increases (Table 2, Bontemps, 2006). The evolution of the Ce/Ce* ratios can directly be related to the replacement of Fe-bearing primary minerals such as clinopyroxene and olivine by secondary Fe oxyhydroxides. In contrast, no direct mineralogical transformation could be observed to explain the LREE depletion towards the surface. A possible explanation may be preferential absorption of LREE by vegetation as shown by Stille et al. (2006) for the granitic Strengbach catchment in the Vosges mountains.

The downstream decreasing REE concentrations as well as the fractionation of the LREE are not correlated with conductivity or total dissolve solid values (TDS, Table 1), demonstrating that it is not a simple dilution effect. Furthermore, the Nd isotope data show that there is no important admixture of REE from other sources downstream that could explain the observed evolution of the Nd/Yb ratios (Section 3.3). We could also not find any relations between REE fractionation and major element chemistry or physico-chemical parameters such as pH or Eh.

Recent studies based on field observations, experimental data, and speciation modeling on dissolved REE suggest that solution complexation with organic matter may play an important role for REE solubility and fractionation (Tang and Johannesson, 2003; Johannesson et al., 2004; Sonke and Salters, 2006; Pourret et al., 2007a,b). In the present case, dissolved organic carbon concentrations have only been analyzed for the samples from October 2003, but the data show no correlation between DOC and Nd concentrations as described by Johannesson et al. (2004) for organic-rich blackwaters, and there is also no link between DOC and Ce/Ce* as reported by Dia et al. (2000) for organic-rich groundwaters or by Davranche et al. (2005, 2008) for experimental data. We found furthermore no relation between DOC and other REE parameters such as Nd/Yb, La/Yb, or Y/Ho. Therefore we suggest that solution complexation with organic ligands does not play a dominant role for REE speciation and fractionation at catchment scale.

In contrast, the REE concentrations of the <0.45 μm fraction are positively correlated with Fe (Fig. 5A). The points plotting off the general trend are samples with Nd concentrations above 100 ng/L, low Fe, but high organic carbon concentrations (up to 87.7 mg/L, Table 1). They all stem from pasture areas with cattle breeding on the basalt plateau or from tributaries. Therefore, we suggest that the offset of the

Table 8
Correlation factors *r* for the 1 M HCl leachates of the suspended load

	As	Cr	Ni	Mo	Si	Mn	Co	Fe	P	Al	Sr
As											
Cr	**0.964**										
Ni	**0.969**	**1.000**									
Mo	**0.982**	**0.990**	**0.993**								
Si	0.732	0.725	0.726	0.718							
Mn	**0.866**	**0.887**	**0.888**	**0.869**	**0.836**						
Co	**0.956**	**0.991**	**0.991**	**0.984**	0.734	**0.905**					
Fe	**0.931**	**0.942**	**0.943**	**0.934**	**0.901**	**0.925**	**0.936**				
P	**0.870**	**0.862**	**0.865**	**0.856**	**0.901**	**0.970**	**0.875**	**0.949**			
Al	0.720	0.693	0.700	0.690	**0.888**	**0.863**	0.702	**0.841**	**0.924**		
Sr	0.585	0.551	0.554	0.535	0.676	0.731	0.585	0.645	0.730	0.681	
Nd	−0.031	−0.090	−0.086	−0.116	0.222	0.232	−0.059	0.062	0.253	0.364	0.595

The matrix is based on 30 samples. *r* values > 0.8 are in bold.
n = 30.

Table 9
Correlation factors *r* for the 1 M HCl residues of the suspended load

	Al	Fe	Mn	Rb	Sr	Th
Al						
Fe	**0.954**					
Mn	0.468	0.408				
Rb	0.629	0.452	0.371			
Sr	**0.910**	**0.948**	0.268	0.313		
Th	0.771	0.697	0.488	0.707	0.578	
Nd	0.711	0.619	0.621	0.641	0.504	**0.953**

The matrix is based on 17 samples. *r* values>0.8 are in bold. The *r* values for Nd vs Al and Nd vs Fe improve to 0.962 and 0.935, respectively, when 3 offsetting points with Nd concentrations>7 ppb are omitted.
n=17.

plateau samples from the general trend in Fig. 5a is due to high organic carbon concentrations leading locally to soluble organic REE complexes.

Within the <0.45 μm fraction, not only the REE concentrations are linked with Fe, but also the Nd/Yb ratios (Fig. 5b). The basalt-normalized Nd/Yb ratios are about 1, thus unfractionated, when Fe concentrations are highest, and the ratios decrease with decreasing Fe concentrations. When looking at the evolution of the concentration data with distance, one can note a general decrease from upstream to downstream for Fe and the LREE such as Nd, whereas the concentrations for the HREE such as Yb vary only little (Tables 1 and 2). A similar decoupling between LREE and HREE has been reported by Shiller (2002), who showed in a time series for the Mississippi river that the LREE concentrations varied together with Mn, whereas the HREE concentrations remained almost constant.

3.6. The fractionation of the REE of the <0.45 μm fraction and the link with the colloidal and suspended particle load

A comparison between the Nd concentrations of the dissolved load and the Nd concentrations of the HCl leachates for the Malaval and Séjallières streams in June 2003 (Tables 2 and 6) shows that they are anticorrelated, i.e. dissolved Nd decreases downstream whereas leachable Nd increases. This leads within the basalt plateau to rapidly decreasing Nd dissolved/Nd leachate ratios, and the ratios become almost constant beyond the edge of the plateau (Fig. 6). The data thus document a transfer of Nd from the <0.45 μm pool to the >0.45 μm particle pool during transport. However, no comparable trend can be observed for the samples from October 2003, where also leachate data are available. A possible explication for this different behavior may be the particle load (Table 5), which was in most cases above 10 mg/L in June 2003 (average±SD of 33±48 mg/L), but lower than 5 mg/L in October 2003 (average±SD of 3±2 mg/L). We suggest that it was the high particle load in June 2003 that led to the observed regular transfer of Nd from the <0.45 μm to the >0.45 μm fraction, whereas the low particle load in October 2003 had no systematic impact on the dissolved Nd fraction. However, this REE transfer cannot explain the fractionation between light and heavy REE (expressed by the Nd/Yb ratios), because this fractionation is also present for the sample series from October 2003 (Fig. 4). Consequently, the fractionation of the Nd/Yb ratios must be related to another process.

It has been shown in Section 3.5 that the Nd concentrations and the Nd/Yb ratios of the <0.45 μm fraction decrease with Fe concentrations downstream (Fig. 5a and b). Fig. 5c furthermore shows that also the negative Ce anomaly of the HCl-leachable particle load is linked to Fe of the <0.45 μm fraction. The Fe concentration of the <0.45 μm fraction thus seems to control at the same time the REE concentration and fractionation in the <0.45 μm fraction and the Ce anomaly of the >0.45 μm HCl-leachable particle fraction.

These relationships are together with the high Fe concentrations in the <0.45 μm fraction (up to 330 μg/L) hints that the Fe of the <0.45 μm fraction is not present in dissolved but rather in colloidal form. This hypothesis is ascertained by the saturation indexes (SI), which show that all samples are strongly oversaturated with respect to Fe oxyhydroxides yielding SI values for goethite between 1.5 and 8 (Table 1). The saturation indexes for all other typically occurring secondary mineral phases are systematically <1.

In Fig. 7 the Nd/Yb ratios of the <0.45 μm fraction are plotted against the SI values for goethite for the Séjallières and Malaval streams in June and October 2003. The diagrams show that the basalt-normalized Nd/Yb ratios are close to 1 on the basalt plateau where also the SI values for goethite are highest. In Fig. 7a, c, and d the SI values increase within the plateau. But as soon as the streams reach the edge of the plateau, the SI values and the Nd/Yb ratios start to decrease simultaneously. This evolution of the Nd/Yb ratios and SI values for goethite is independent from pH.

Previous studies on REE in river water (Sholkovitz, 1992; Viers et al., 1997; Dupré et al., 1999; Ingri et al., 2000, Andersson et al., 2001; Pokrovsky and Schott, 2002; Andersson et al., 2006; Pokrovsky et al., 2006) and in estuaries (Elderfield et al., 1990; Sholkovitz, 1993, 1995; Nozaki et al., 2000; Sholkovitz and Szymczak, 2000, Lawrence and Kamber, 2006; Kulaksiz and Bau, 2007) have demonstrated that colloids are important REE carriers and that they scavenge preferentially the LREE. For the Kalix river in northern Sweden it has been shown that colloids are more abundant in summer and that the REE-bearing colloidal fraction is composed of Fe oxyhydroxides and organic matter (Ingri et al., 2000; Andersson et al., 2006; Dahlqvist et al., 2007). These authors furthermore show that in winter small (~3 nm) organic-rich colloids, and larger (~10–12 nm) Fe-oxyhydroxide colloids can be distinguished, whereas combined Fe-organic matter colloids of about 3 nm in size occur during spring and summer. This distinction into 2 different colloidal pools is also confirmed by Fe isotopes (Ingri et al., 2006). The detailed analysis of the winter colloids reveals that the LREE are preferentially associated with Fe colloids, whereas the HREE have stronger affinity for organic colloids (Andersson et al., 2006). A similar occurrence of REE-bearing organic and Fe colloids has been reported by Pokrovsky and Schott (2002) for rivers in Karelia and by Pokrovsky et al. (2006) for Siberian rivers.

We interpret the observed relations between REE concentrations, Nd/Yb ratios, Fe concentrations and goethite oversaturation by the presence of Fe-rich colloids that form on the basalt plateau and which continue to grow when the streams enter the steep slope, where stream water becomes agitated and well aerated as shown by the increasing Eh values (Table 1). This growth of the colloids finally leads to the formation of Fe-oxyhydroxide particles exceeding 0.45 μm in size. The link between Nd/Yb ratios and SI values indicates that the newly formed particles scavenge preferentially the light REE whereas the heavy REE remain in the <0.45 μm fraction. This scenario is in agreement with the study of Andersson et al. (2006), who showed that the LREE are preferentially associated with Fe colloids.

In contrast to the studies cited above, we found no correlation between Fe concentrations and organic carbon for the <0.45 μm fraction (Table 1), suggesting that Fe occurs in the present case exclusively as inorganic Fe colloids and not as combined Fe-organic colloids. Our data furthermore indicate no link between REE and organic colloids, which is another difference to earlier studies. A first reason for this may be that the organic carbon content of our stream water samples is in most cases lower than for the rivers of the studies cited above. A second reason may be that the previous studies have dealt with rivers with a flow regime much more regular than for our streams, where water is strongly agitated and thus well oxygenated.

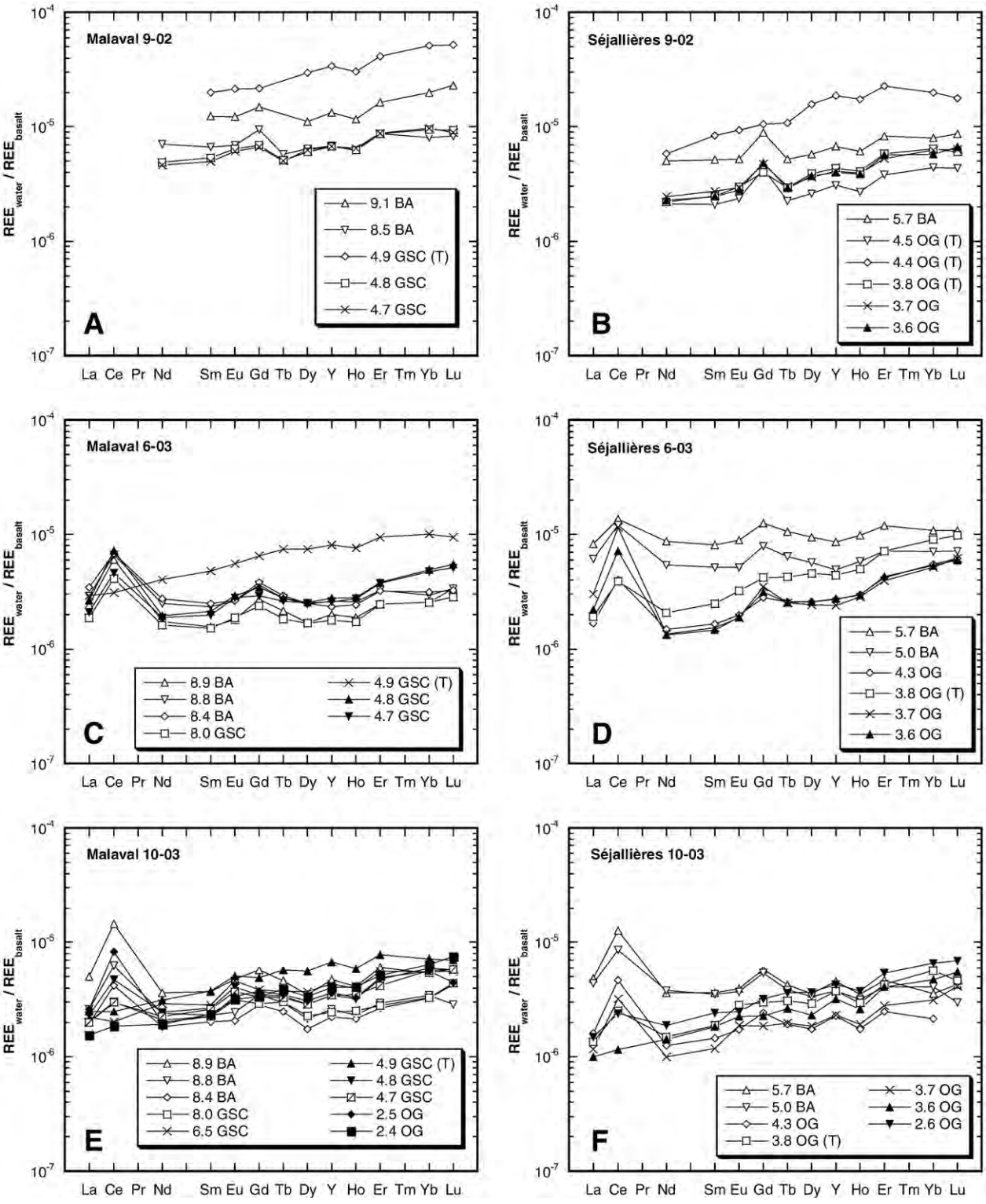

Fig. 3. REE distribution patterns for the <0.45 μm fractions of stream water samples from September 2002, June 2003, and October 2003 normalized to average basalt. The numbers in the legend give the distance upstream from the catchment outlet in kilometers, and the letters stand for the bedrock lithology of the sampling points: BA for basalt, OG for orthogneiss, and GSC for granite. The label "T" identifies tributaries.

This good oxygenation facilitates spontaneous precipitation of Fe oxyhydroxides and could explain why Fe colloids dominate over organic colloids.

As mentioned before, the Fe colloids of the <0.45 μm fraction control not only the Nd/Yb ratios of the <0.45 μm fraction, but also the negative Ce anomalies of the particle leachates (Fig. 5C). This is supported by the positive correlation between the Ce anomalies of the leachates and Nd/Yb of the <0.45 μm fraction (r=0.626). The basalt-normalized Ce anomalies of the particle leachates are closest to one, thus basalt-like, on the plateau and become more and more negative

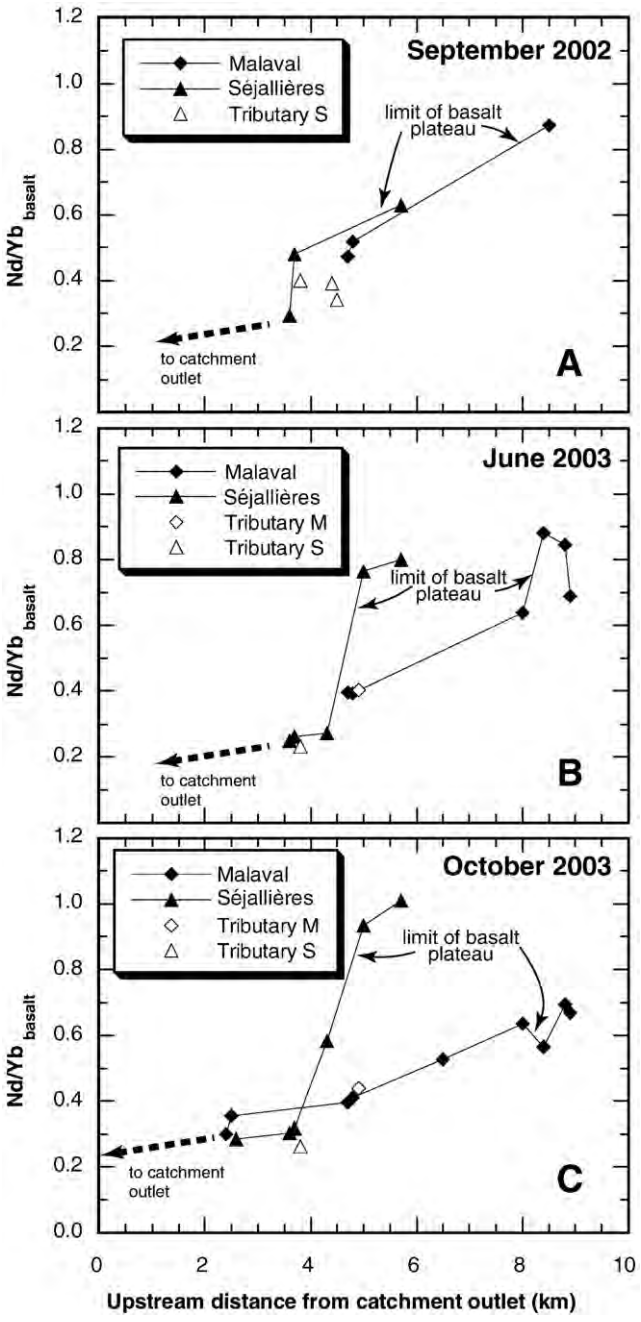

Fig. 4. Nd/Yb ratios of the <0.45 μm fractions of stream water samples shown in Fig. 3. The ratios decrease systematically from upstream to downstream.

downstream. Thus they manifest the same distance dependent variation as the Nd/Yb ratios of the <0.45 μm fraction in Fig. 4. This suggests that the growth of Fe colloids and the subsequent precipitation as Fe oxyhydroxide particles does not only remove LREE from the <0.45 μm fraction, but also Ce from the adsorbed particle load. These precipitating Fe-oxyhydroxide particles are most probably sedimented, because the HCl-leachable REE of the particle load are, as

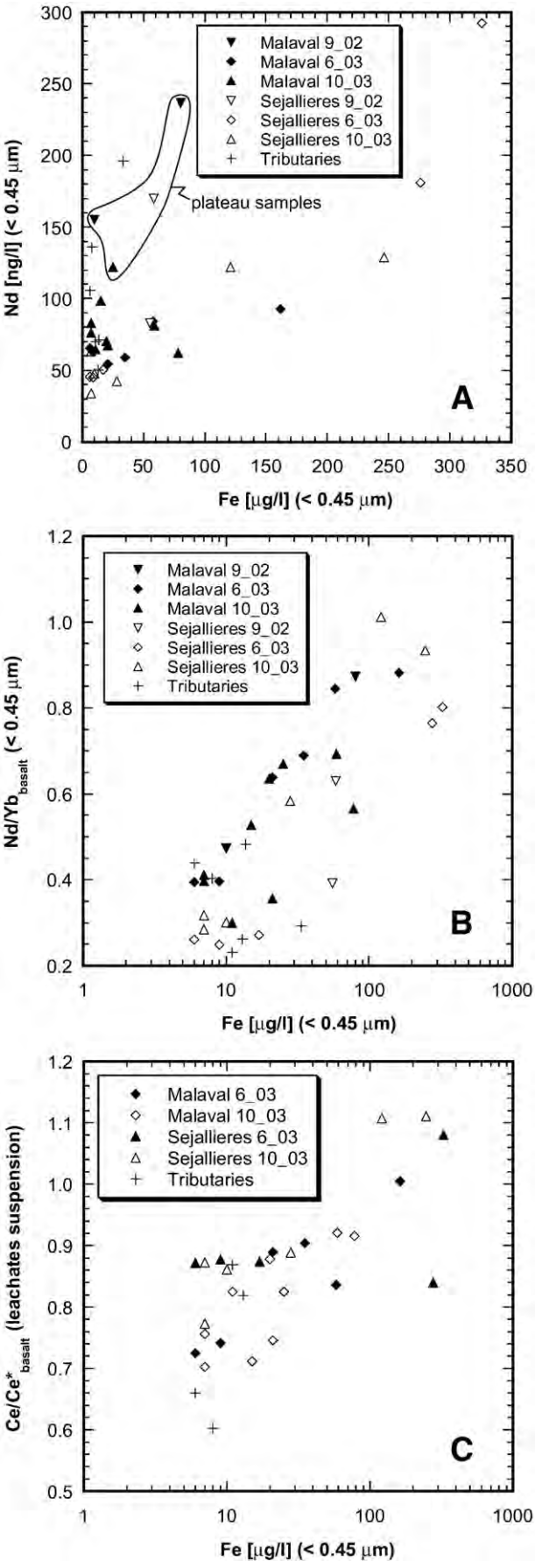

Fig. 5. Relation between Nd concentrations (A), Nd/Yb ratios (B) and Fe in the <0.45 μm stream water fractions, as well as between Ce/Ce* of the HCl leachates and Fe of the <0.45 μm stream water fraction (C). The samples from September 2002 are not shown in c because no leachate data are available. Note that the scale of the *X*-axis in diagram b and c is logarithmic.

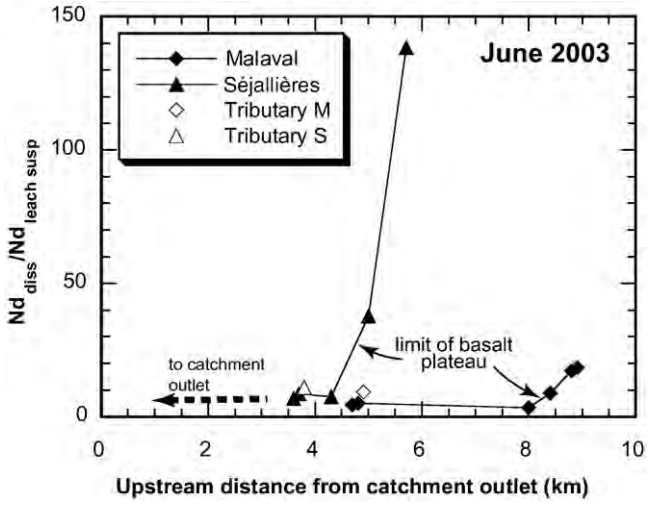

Fig. 6. Nd concentration ratios between the <0.45 μm fraction over leachate particulate fraction for the sample series from June 2003. The decreasing ratios from upstream to downstream suggest a REE transfer from the <0.45 μm fraction to the adsorbed particle fraction.

discussed in Section 3.4, not associated with Fe oxyhydroxides and their Ce anomaly is negative.

3.7. REE mixing at stream confluences

The central question that arises from the above discussion is whether the REE behave conservatively during water mixing at stream confluences or whether the processes identified at catchment scale would also occur at stream confluences and lead to fractionation of the REE. To answer this question, 3 stream confluences named "Sapetas", "Moulard", and "Alleyras" (Fig. 1) have been studied in detail. For each confluence, the REE patterns and the Sr isotopic composition of the <0.45 μm fraction have been analyzed for the main stream before and after the confluence, as well as for the tributary. For the main stream after the confluence the fractions "fA" and "fB" of water stemming from the main stream before the confluence and from the tributary, respectively, have been calculated from $^{87}Sr/^{86}Sr$ isotope ratios and Sr concentrations using the equations described by Faure (1986) for congruent mixing in binary systems:

$$fA[\%] = 100^{*}\left[\frac{\left(^{87}Sr/^{86}Sr^{*}Sr_M\right) - \left(^{87}Sr/^{86}Sr_B{}^{*}Sr_B\right)}{\left(^{87}Sr/^{86}Sr_A{}^{*}Sr_A\right) - \left(^{87}Sr/^{86}Sr_B{}^{*}Sr_B\right)}\right]$$

and

$$fB[\%] = 100 - fA$$

whereas "$^{87}Sr/^{86}Sr$" and "Sr" are Sr isotopic compositions and strontium concentrations, respectively, both given in Tables 1 and 3, respectively. The suffixes signify: A = main stream before confluence, B = tributary, M = main stream after confluence.

The resulting percentages "fA" and "fB" are compiled in Table 10. These values have been used together with the REE patterns analyzed for the main stream before the confluence and the tributary to calculate a synthetic REE pattern for the main stream after the confluence using the relation:

$$REE_{\text{main stream after}} = fA^{*}REE_{\text{main stream before}} + fB^{*}REE_{\text{tributary}}.$$

The resulting calculated patterns are listed in Table 2 and compared with the observed patterns in Fig. 8. The comparison shows that the Ce anomaly is systematically less positive for the observed than for the calculated patterns, suggesting that Ce is removed from solution during stream water mixing. Furthermore, the La/Yb and Nd/Yb ratios are systematically higher for the calculated REE patterns, i.e. that the slopes of the calculated patterns are less steep than for the observed ones. The ratios of the calculated over the observed values for the Ce anomalies and the La/Yb ratios are listed in Table 10 and compared in Fig. 9 with the fB value of the percentage of stream water derived from the tributary. The diagrams show that there is a slight trend between fB and Ce ratios, and that there is an almost linear relation between fB and La/Yb fractionation. This finding is similar as for the downstream evolution of the Ce anomalies and the La/Yb and Nd/Yb ratios presented in Section 3.6, i.e. that the LREE and in particular Ce are removed preferentially from the <0.45 μm fraction. This comparison between calculated and observed REE patterns at stream confluences thus demonstrates that the REE do not behave conservatively during stream water mixing. We suggest in continuity with the discussion inSection 3.6 that agitation and oxygenation of stream water at stream confluences triggers precipitation of Fe-hydroxide particles, which preferentially remove the LREE and Ce from the colloid controlled <0.45 μm fraction. To test this hypothesis, we also looked at the Fe concentrations at the stream confluences. Unfortunately, the concentrations are close to the detection limit of 5 μg/L for the confluences "Sapetas" and "Moulard" (Table 1) and there is no significant difference between calculated and observed Fe concentrations. In contrast, for the confluence "Alleyras", where Fe concentrations are highest, the observed concentration is almost 40% below the calculated value and thus in agreement with the hypothesis of precipitating Fe-hydroxide particles.

4. Summary and conclusions

The Sr and Nd isotope data show that the REE budget of stream water of the 68 km^2 Malaval catchment basin is dominated by REE issued from basalt alteration in the source area. This dominance of basaltic REE is due to local topography leading to well developed alteration profiles on basalt and only limited water–rock interaction on granite and gneiss. Close to the source area, the basalt-normalized stream waters are slightly depleted in the LREE and enriched in Ce. This first stage of fractionation can directly be related to water–rock interaction and probably also preferential absorption of the LREE by vegetation.

During transport downstream, the basalt-normalized REE patterns of the <0.45 μm fraction become progressively depleted in the LREE and the positive Ce anomaly of the REE adsorbed on >0.45 μm particles diminishes at the same time. The parameter controlling this coupled behavior of the REE is Fe of the <0.45 μm stream water fraction. The observation that this Fe controls simultaneously the REE patterns of the <0.45 and the >0.45 μm stream water fraction suggests, together with the link between Fe-oversaturation and REE fractionation, that Fe is not present in dissolved, but in colloidal form. The downstream evolution of the REE patterns and the saturation indexes for Fe oxyhydroxides indicate, that the Fe colloids grow during transport to Fe oxyhydroxide particles exceeding 0.45 μm in size, which selectively remove the LREE from the <0.45 μm and adsorbed Ce from the >0.45 μm stream water fractions leaving behind the REE patterns observed downstream. Fig. 10 gives a summary of these processes. Our data indicate in contrast to previous studies no significant impact of organic solution complexation and organic colloids on REE transport and fractionation. These earlier studies have dealt with rivers and we relate the above discrepancy to the lower organic carbon content of our streams and to their much more agitated flow regime leading to well oxygenated waters, which facilitates precipitation of Fe colloids.

The preferential removal of the LREE and Ce from stream water at catchment scale is confirmed by the results from 3 different

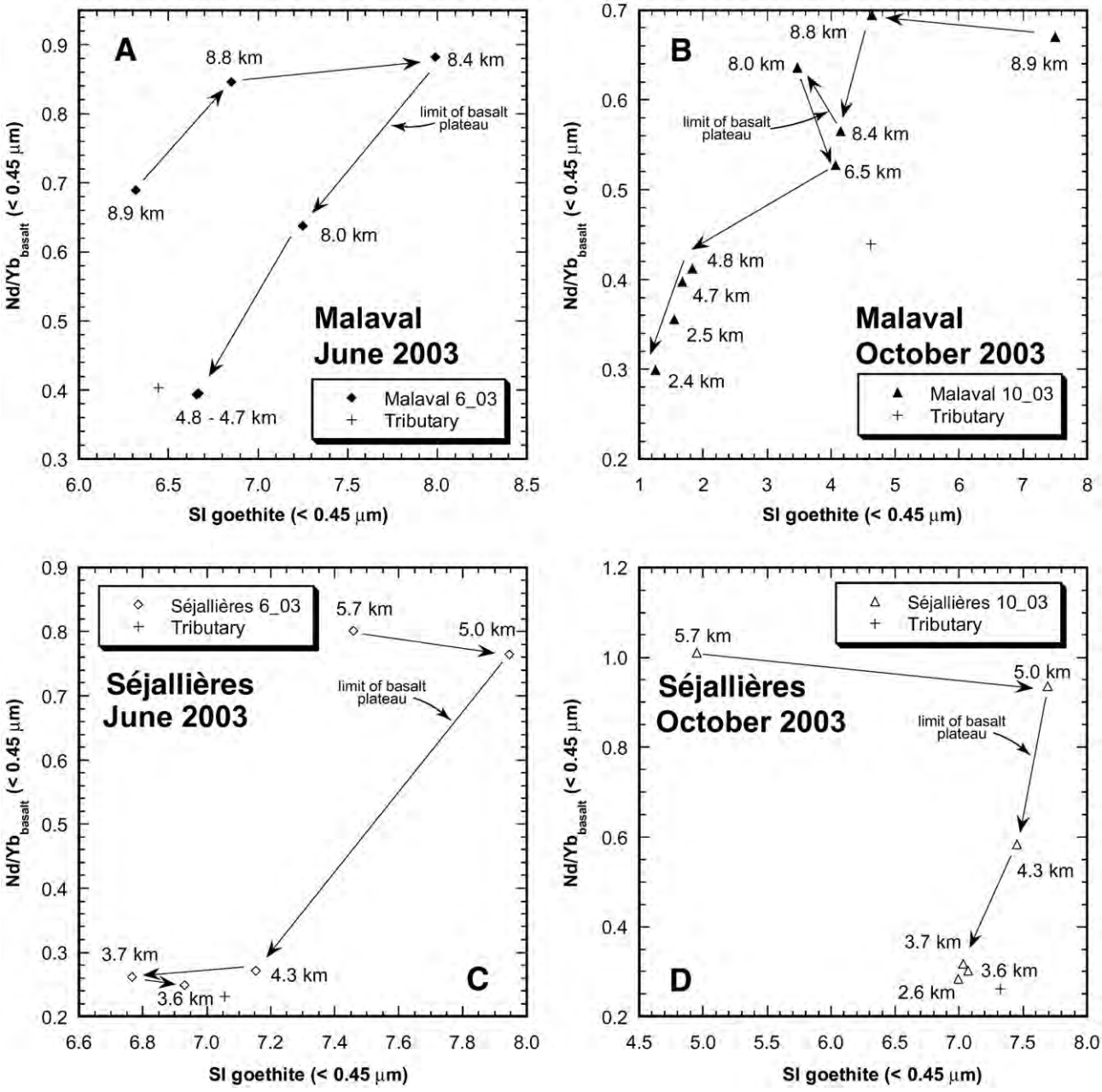

Fig. 7. Plots of Nd/Yb ratios vs saturation index (SI) of goethite for the <0.45 μm. Both values decrease systematically from upstream to downstream suggesting that goethite particles are removed from the <0.45 μm fraction scavenging preferentially the light REE such as Nd whereas Yb and the other heavy REE remain in solution.

stream confluences. The REE patterns measured in the main stream below a confluence have been compared with patterns calculated from the REE and Sr isotope data of the tributary and the main stream above the confluence. The results show that the observed patterns are with respect to the calculated patterns systematically depleted in the LREE and Ce demonstrating that the REE do not

Table 10
REE mixing at stream confluences

	Date	Samples	% main river (fA)	% tributary (fB)	$Ce/Ce^*_{calc/obs}$	$La/Yb_{calc/obs}$
Sapetas	June 2003	S10, S11, S12	81%	19%	1.2	1.4
	Oct. 2003	S16, S17, S18	70%	30%	2.8	1.8
Moulard	June 2003	M10, M11, M20	98.55%	1.45%	1.3	1.2
	Oct. 2003	M18, M19, M20	99.98%	0.02%	1.4	1.1
Alleyras	Oct. 2003	M21, M22, M23	78%	22%	2.8	1.7

The values "fA" and "fB" give the volume percentages of water derived from the main stream and the tributary, respectively. They have been calculated from $^{87}Sr/^{86}Sr$ values and Sr concentrations. The values "$Ce/Ce^*_{calc/obs}$" and "$La/Yb_{calc/obs}$" are the ratios of the basalt-normalized Ce anomalies and La/Yb ratios of the calculated over the observed REE pattern for the main stream after the confluence and have been calculated from the Ce/Ce^*_{basalt} and La/Yb_{basalt} values given in Table 2. All "$Ce/Ce^*_{calc/obs}$" and "$La/Yb_{calc/obs}$" are above 1 demonstrating that the calculated patterns have systematically more positive Ce anomalies and higher La/Yb ratios than the observed patterns.

behave conservatively during stream water mixture. This preferential removal of the LREE and Ce is similar to what has been observed at catchment scale and we therefore suggest that it is similarly due to precipitation of oxyhydroxide particles issued from the growth of Fe colloids.

All these REE fractionation processes from upstream to downstream could be identified thanks to the contrasting geochemical composition of the upper and lower part of the catchment area, which allowed the use of Sr and Nd isotopes to identify the origin of the REE in the individual samples. Another important point is local topography, that leads to strong water–rock interaction on the basalt plateau

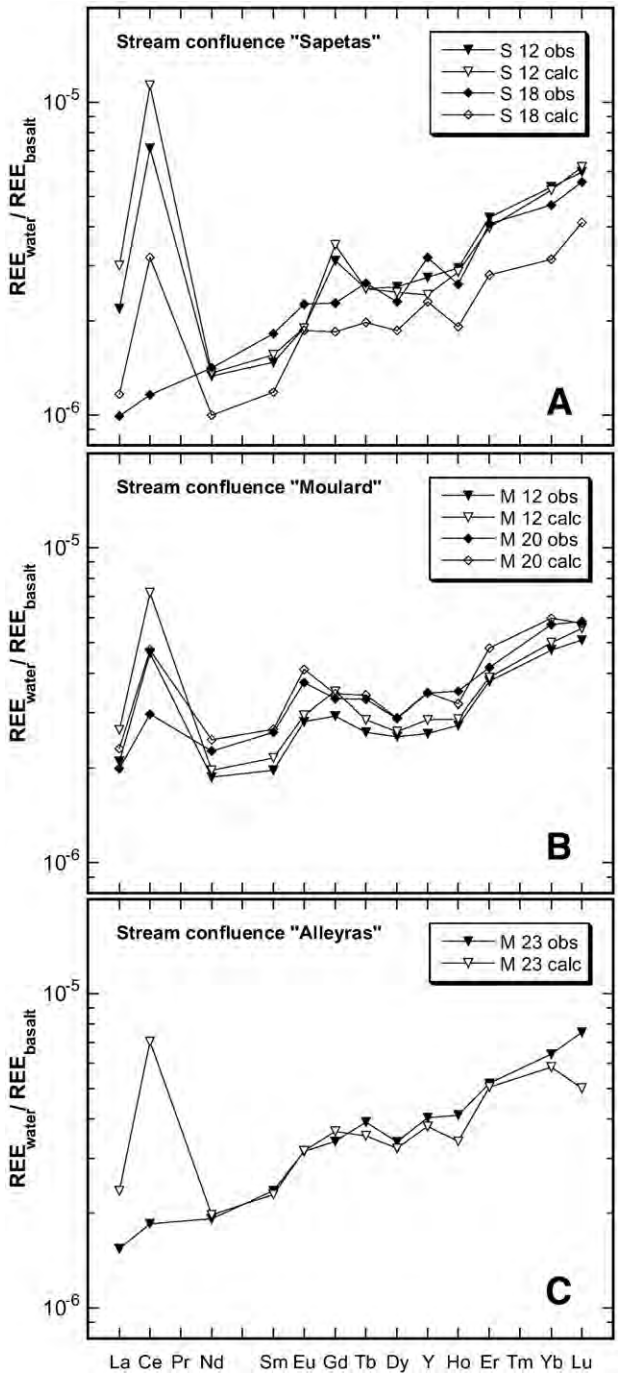

Fig. 8. Comparison between observed and calculated REE patterns from the stream confluences "Sapetas", "Moulard", and "Alleyras". Note that Ce anomalies are systematically more positive for the calculated patterns indicating that Ce is removed from solution during water mixing at stream confluences.

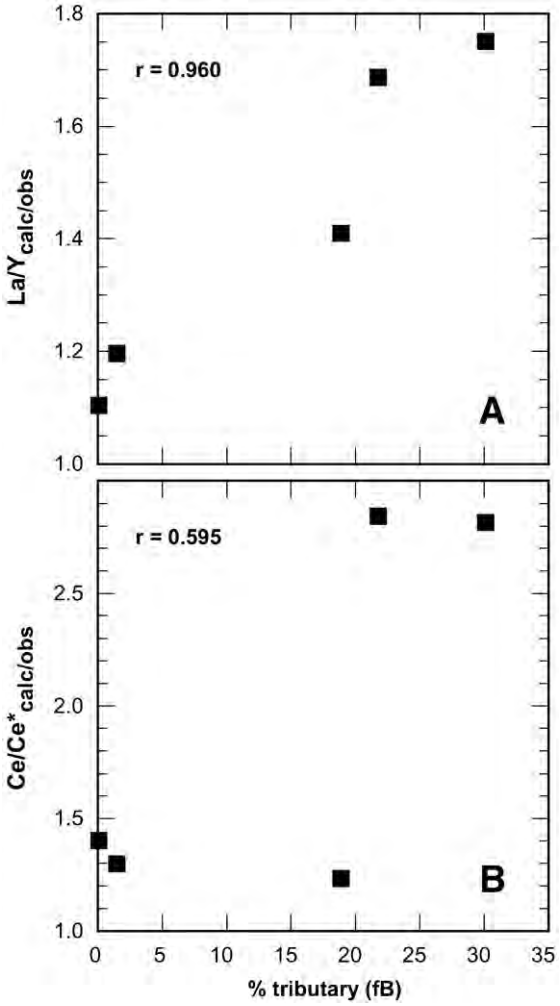

Fig. 9. Relation between % water from the tributary, Ce anomaly and La/Yb in the main stream after the confluence. The values "$La/Yb_{calc/obs}$" and "$Ce/Ce^*_{calc/obs}$" are the ratios of the basalt-normalized La/Yb ratios and Ce anomalies of the calculated over the observed REE pattern.

in the source area, whereas there is almost no chemical exchange with the granitic and gneissic bedrock further downstream. This furnishes a unique opportunity to study REE transport and fractionation with stream flow almost completely isolated from mixing with REE from adjacent lithologies.

Acknowledgments

We would like to thank S. Decitre and S. Bontemps for help in the clean lab in Besançon, and Th. Nägler, I. Villa, J. Kramers, M. Wille and D. Rufer for their support on the mass spectrometer in Bern. We also thank R. Boutin and Th. Perrone at CNRS Strasbourg for their technical assistance. M. Rossy (Besançon) is thanked for his advice for the selection of the field area. The constructive reviews of A. Shiller and an anonymous reviewer helped to improve an earlier version of the manuscript. This is EOST contribution 2008.204-UMR7517.

References

Allègre, C.J., Dupré, B., Négrel, P., Gaillardet, J., 1996. Sr–Nd–Pb isotope systematics in Amazon and Congo River systems: constraints about erosion processes. Chem. Geol. 131, 93–112.

Alvarez, M., Rueda, E.H., Sileo, E.E., 2007. Simultaneous incorporation of Mn and Al in the goethite structure. Geochim. Cosmochim. Acta 71 (4), 1009–1020.

Andersson, P.S., Dahlqvist, R., Ingri, J., Gustafsson, O., 2001. The isotopic composition of Nd in a boreal river: a reflection of selective weathering and colloidal transport. Geochim. Cosmochim. Acta 65 (4), 521–527.

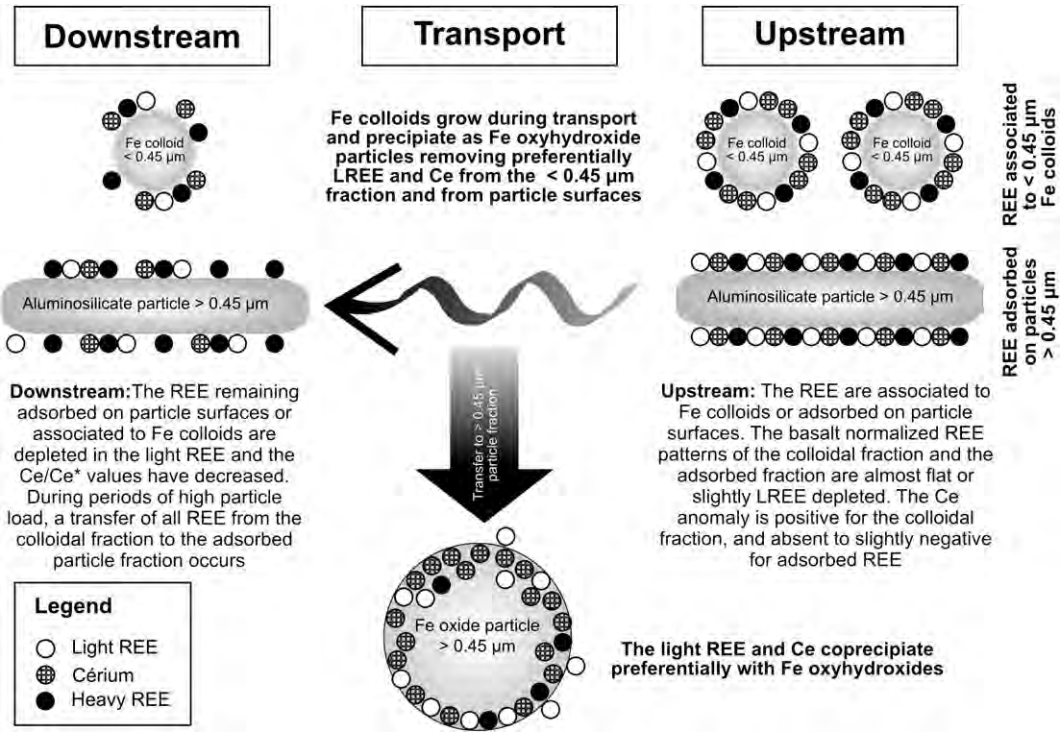

Fig. 10. Summary of parameters controlling transport and fractionation of the REE in stream waters of the study site.

Andersson, K., Dahlqvist, R., Turner, D., Stolpe, B., Larsson, T., Ingri, J., Andersson, P., 2006. Colloidal rare earth elements in a boreal river: changing sources and distributions during the spring flood. Geochim. Cosmochim. Acta 70 (13), 3261–3274.

Aubert, D., Stille, P., Probst, A., 2001. REE fractionation during granite weathering and removal by waters and suspended loads: Sr and Nd isotopic evidence. Geochim. Cosmochim. Acta 65 (3), 387–406.

Bau, M., 1999. Scavenging of dissolved yttrium and rare earths by precipitating iron oxyhydroxide: experimental evidence for Ce oxidation, Y–Ho fractionation, and lanthanide tetrad effect. Geochim. Cosmochim. Acta 63 (1), 67–77.

Bontemps, S., 2006. Mobilisation et transfert des éléments majeurs, en traces et terres rares au cours de l'altération dans le bassin versant de Malaval (Massif Central), Master thesis, Unversité de Franche-Comté, Besançon, 30 pp.

Bouiller, R., Couturier, J.P., Féraud, J., 1978. BRGM, carte géologique de la France à 1/50000, Feuille 815 Cayres, Orléans.

Dahlqvist, R., Andersson, K., Ingri, J., Larsson, T., Stolpe, B., Turner, D., 2007. Temporal variations of colloidal carrier phases and associated trace elements in a boreal river. Geochim. Cosmochim. Acta 71 (22), 5339–5354.

Davranche, M., Pourret, O., Gruau, G., Dia, A., Le Coz-Bouhnik, M., 2005. Adsorption of REE(III)–humate complexes onto MnO_2: experimental evidence for cerium anomaly and lanthanide tetrad effect suppression. Geochim. Cosmochim. Acta 69 (20), 4825–4835.

Davranche, M., Pourret, O., Gruau, G., Dia, A., Jin, D., Gaertner, D., 2008. Competitive binding of REE to humic acid and manganese oxide: impact of reaction kinetics on development of cerium anomaly and REE adsorption. Chem. Geol. 247 (1–2), 154–170.

Dia, A., Gruau, G., Olivie-Lauquet, G., Riou, C., Molenat, J., Curmi, P., 2000. The distribution of rare earth elements in groundwaters: assessing the role of source-rock composition, redox changes and colloidal particles. Geochim. Cosmochim. Acta 64 (24), 4131–4151.

Dupré, B., Gaillardet, J., Rousseau, D., Allègre, C.J., 1996. Major and trace elements of river-borne material: the Congo Basin. Geochim. Cosmochim. Acta 60 (8), 1301–1321.

Dupré, B., Viers, J., Dandurand, J.-L., Polve, M., Benezeth, P., Vervier, P., Braun, J.-J., 1999. Major and trace elements associated with colloids in organic-rich river waters: ultrafiltration of natural and spiked solutions. Chem. Geol. 160 (1–2), 63–80.

Elderfield, H., Upstill-Goddard, R., Sholkovitz, E.R., 1990. The rare earth elements in rivers, estuaries, and coastal seas and their significance to the composition of ocean waters. Geochim. Cosmochim. Acta 54 (4), 971–991.

Faure, G., 1986. Principles of Isotope Geology. John Wiley & sons, New York. 589 pp.

Gaillardet, J., Dupré, B., Allègre, C.J., Negrel, P., 1997. Chemical and physical denudation in the Amazon River Basin. Chem. Geol. 142 (3–4), 141–173.

Goldstein, S.J., Jacobsen, S.B., 1987. The Nd and Sr isotopic systematics of river-water dissolved material: implications for the sources of Nd and Sr in seawater. Chem. Geol. 66, 245–272.

Goldstein, S.J., Jacobsen, S.B., 1988a. Rare earth elements in river waters. Earth Planet. Sci. Lett. 89, 35–47.

Goldstein, S.L., Jacobsen, S.B., 1988b. Nd and Sr isotopic systematics of river water suspended material: implications for crustal evolution. Earth. Planet. Sci. Lett. 87, 249–265.

Goldstein, S.L., O'Nions, R.K., Hamilton, P.J., 1984. A Sm–Nd isotopic study of atmospheric dusts and particulates from major river systems. Earth Planet. Sci. Lett. 70, 221–236.

Gruau, G., Dia, A., Olivie-Lauquet, G., Davranche, M., Pinay, G., 2004. Controls on the distribution of rare earth elements in shallow groundwaters. Water Res. 38 (16), 3576–3586.

Hannigan, R.E., Sholkovitz, E.R., 2001. The development of middle rare earth element enrichments in freshwaters: weathering of phosphate minerals. Chem. Geol. 175 (3–4), 495–508.

Ingri, J., Widerlund, A., Land, M., Gustafsson, Ö., Andersson, P., Öhlander, B., 2000. Temporal variations in the fractionation of the rare earth elements in a boreal river; the role of colloidal particles. Chem. Geol. 166, 23–45.

Ingri, J., Malinovsky, D., Rodushkin, I., Baxter, D.C., Widerlund, A., Andersson, P., Gustafsson, O., Forsling, W., Ohlander, B., 2006. Iron isotope fractionation in river colloidal matter. Earth Planet. Sci. Lett. 245 (3–4), 792–798.

Johannesson, K.H., Tang, J., Daniels, J.M., Bounds, W.J., Burdige, D.J., 2004. Rare earth element concentrations and speciation in organic-rich blackwaters of the Great Dismal Swamp, Virginia, USA. Chem. Geol. 209 (3–4), 271–294.

Kelly, M.G., 2003. Short term dynamics of diatoms in an upland stream and implications for monitoring eutrophication. Environ. Pollut. 125 (2), 117–122.

Kulaksiz, S., Bau, M., 2007. Contrasting behaviour of anthropogenic gadolinium and natural rare earth elements in estuaries and the gadolinium input into the North Sea. Earth Planet. Sci. Lett. 260 (1–2), 361–371.

Lawrence, M.G., Kamber, B.S., 2006. The behaviour of the rare earth elements during estuarine mixing — revisited. Mar. Chem. 100 (1–2), 147–161.

Norrish, K., Taylor, R.M., 1961. The isomorphous replacement of iron by aluminium in soil goethites. J. Soil Sci. 14, 179–187.

Nozaki, Y., Lerche, D., Alibo, D.S., Snidvongs, A., 2000. The estuarine geochemistry of rare earth elements and indium in the Chao Phraya River, Thailand. Geochim. Cosmochim. Acta 64 (23), 3983–3994.

Öhlander, B., Land, M., Ingri, J., Widerlund, A., 1996. Mobility of rare earth elements during weathering of till in northern Sweden. Applied Geochem. 11, 93–99.

Pin, C., Briot, D., Bassin, C., Poitrasson, F., 1994. Concomitant separation of strontium and samarium–neodymium for isotopic analysis in silicate samples, based on specific extraction chromatography. Anal. Chim. Acta 298 (2), 209–217.

Pokrovsky, O.S., Schott, J., 2002. Iron colloids/organic matter associated transport of major and trace elements in small boreal rivers and their estuaries (NW Russia). Chem. Geol. 190 (1–4), 141–179.

Pokrovsky, O.S., Schott, J., Dupré, B., 2006. Trace element fractionation and transport in boreal rivers and soil porewaters of permafrost-dominated basaltic terrain in Central Siberia. Geochim. Cosmochim. Acta 70 (13), 3239–3260.

Pourret, O., Davranche, M., Gruau, G., Dia, A., 2007a. Organic complexation of rare earth elements in natural waters: evaluating model calculations from ultrafiltration data. Geochim. Cosmochim. Acta 71 (11), 2718–2735.

Pourret, O., Dia, A., Davranche, M., Gruau, G., Henin, O., Angee, M., 2007b. Organo-colloidal control on major- and trace-element partitioning in shallow groundwaters: confronting ultrafiltration and modelling. Appl. Geochem. 22 (8), 1568–1582.

Schwertmann, U., Taylor, R.M., 1989. Iron oxides. In: Dixon, J.B., Weed, S.B. (Eds.), Minerals in Soil Environments. Soil Science Society of America, Madison, Wisconsin, USA, pp. 379–438.

Shabani, M.B., Masuda, A., 1991. Sample introduction by on-line two-stage solvent extraction and back-extraction to eliminate matrix interference and to enhance sensitivity in the determination of rare earth elements with inductively coupled plasma mass spectrometry. Anal. Chem. 63, 2099–2105.

Shabani, M.B., Akagi, T., Shimizu, H., Masuda, A., 1990. Determination of trace lanthanides and yttrium in seawater by inductively coupled plasma mass spectrometry after preconcentration with solvent extraction and back-extraction. Anal. Chem. 62, 2709–2714.

Shiller, A.M., 2002. Seasonality of dissolved rare earth elements in the lower Mississippi River. Geochem. Geophys. Geosyst. 3 (11).

Sholkovitz, E.R., 1992. Chemical evolution of rare earth elements: fractionation between colloidal and solution phases of filtered river water. Earth Planet. Sci. Lett. 114, 77–84.

Sholkovitz, E.R., 1993. The geochemistry of the rare earth elements in the Amazon river estuary. Geochim. Cosmochim. Acta 57, 2181–2190.

Sholkovitz, E.R., 1995. The aquatic chemistry of rare earth elements in rivers and estuaries. Aquat. Geochem. 1, 1–34.

Sholkovitz, E., Szymczak, R., 2000. The estuarine chemistry of rare earth elements: comparison of the Amazon, Fly, Sepik and the Gulf of Papua systems. Earth Planet. Sci. Lett. 179 (2), 299–309.

Sholkovitz, E.R., Elderfield, H., Szymczak, R., Casey, K., 1999. Island weathering: river sources of rare earth elements to the Western Pacific Ocean. Mar. Chem. 68 (1–2), 39–57.

Sonke, J.E., Salters, V.J.M., 2006. Lanthanide-humic substances complexation. I. Experimental evidence for a lanthanide contraction effect. Geochim. Cosmochim. Acta 70 (6), 1495–1506.

Steinmann, M., Stille, P., 1997. Rare earth element behavior and Pb, Sr, Nd isotope systematics in a heavy metal contaminated soil. Appl. Geochem. 12 (5), 607–623.

Steinmann, M., Stille, P., 1998. Strongly fractionated REE patterns in salts and their implications for REE migration in chloride-rich brines at elevated temperatures and pressures. C.R. Acad. Sci. Paris, série II a 327, 173–180.

Stille, P., Gauthier-Lafaye, F., Jensen, K.A., Salah, S., Bracke, G., Ewing, R.C., Louvat, D., Million, D., 2003. REE mobility in groundwater proximate to the natural fission reactor at Bangombe (Gabon). Chem. Geol. 198 (3–4), 289–304.

Stille, P., Steinmann, M., Pierret, M.C., Gauthier-Lafaye, F., Chabaux, F., Viville, D., Pourcelot, L., Matera, V., Aouad, G., Aubert, D., 2006. The impact of vegetation on REE fractionation in stream waters of a small forested catchment (the Strengbach case). Geochim. Cosmochim. Acta 70 (13), 3217–3230.

Tang, J., Johannesson, K.H., 2003. Speciation of rare earth elements in natural terrestrial waters: assessing the role of dissolved organic matter from the modeling approach. Geochim. Cosmochim. Acta 67 (13), 2321–2339.

Tricca, A., Stille, P., Steinmann, M., Kiefel, B., Samuel, J., Eikenberg, J., 1999. Rare earth elements and Sr and Nd isotopic compositions of dissolved and suspended loads from small river systems in the Vosges mountains (France), the river Rhine and groundwater. Chem. Geol. 160 (1–2), 139–158.

Viers, J., Dupre, B., Polve, M., Schott, J., Dandurand, J.-L., Braun, J.-J., 1997. Chemical weathering in the drainage basin of a tropical watershed (Nsimi-Zoetele site, Cameroon): comparison between organic-poor and organic-rich waters. Chem. Geol. 140 (3–4), 181–206.

Thématique : "Les transferts des terres rares à l'interface géosphère – biosphère"

Stille, P., **Steinmann, M**., Pierret, M.C., Gauthier-Lafaye, F., Chabaux, F., Viville, D., Pourcelot, L., Matera, V., Aouad, G. and Aubert, D., 2006. The impact of vegetation on REE fractionation in stream waters of a small forested catchment (the Strengbach case). Geochim. Cosmochim. Acta, 70(13): 3217-3230.

Available online at www.sciencedirect.com
SCIENCE DIRECT®
Geochimica et Cosmochimica Acta 70 (2006) 3217–3230
Geochimica
www.elsevier.com/locate/gca

The impact of vegetation on REE fractionation in stream waters of a small forested catchment (the Strengbach case)

P. Stille [a,*], M. Steinmann [b], M.-C. Pierret [a], F. Gauthier-Lafaye [a], F. Chabaux [a], D. Viville [a], L. Pourcelot [c], V. Matera [d], G. Aouad [a], D. Aubert [a,e]

[a] CGS, CNRS, UMR 7517, EOST, F-67084 Strasbourg, France
[b] EA 2642 Géosciences, Université de Franche-Comté, F-25030 Besançon, France
[c] Institut de Radioprotection et de Sûreté Nucléaire IRSN, Cadarache, F-13108 St. Paul Lez Durance, France
[d] Inst. Géol., Université de Neuchâtel, CH-2007 Neuchâtel, Switzerland
[e] CEFREM, UMR 5110, Université de Perpignan, F-66860 Perpignan, France

Received 15 September 2005; accepted in revised form 26 April 2006

Abstract

Previous studies on waters of a streamlet in the Vosges Mountains (Eastern France) have shown that strontium and rare earth elements (REE) mainly originate from preferential dissolution of apatite during weathering. However, stream water REE patterns normalized to apatite are still depleted in the light REE (LREE, La–Sm) pointing to the presence of an additional LREE depleting process. Vegetation samples are strongly enriched in LREE compared to stream water and their Sr and Nd isotopic compositions are comparable with those of apatite and stream water. Thus, the preferential LREE uptake by vegetation might lead to an additional LREE depletion of surface runoff in the forested catchment. Mass balance calculations indicate, that the yearly LREE uptake by vegetation is comparable with the LREE export by the streamlet and, therefore, might be an important factor controlling LREE depletion in river water. This is underlined by the observation that rivers from arctic and boreal regions with sparse vegetation appear to be less depleted in LREE than rivers from tropical environments or boreal environments with a dense vegetation cover.

1. Introduction

Natural waters are the main pathway for the transport of elements and particles from the surface and subsurface of the continents to the oceans. Their chemical and isotopic composition is the result of interaction with the environment and especially controlled by erosional processes. Therefore, major river systems have been studied to estimate the fluxes of continent-derived material to the oceans and to shed light upon erosion processes on a global scale (Martin and Meybeck, 1979; Stallard and Edmond, 1983; Meybeck, 1987; Négrel et al., 1993; Blum et al., 1994; Gaillardet et al., 1995, 1997; Dupré et al., 1996). Alteration leads to the disaggregation of rocks and minerals, the formation of soils and also allows the removal of chemical elements as well as of larger and smaller particles from altered rocks and soils by surface runoff. Previous studies have shown that REE are powerful geochemical tracers that provide information about the origin of the suspended and the dissolved river load and about elemental fractionation between particulate and solution phases (Goldstein et al., 1984; Stordal and Wasserburg, 1986; Goldstein and Jacobsen, 1987, 1988a,b; Elderfield et al., 1990; Sholkovitz, 1992; Allègre et al., 1996; Tricca et al., 1999; Stille et al., 2003). The fractionation of the REE in river water between dissolved and particulate load as well as immobilization of the REE in the river sediment can be extensive and is strongly controlled by weathering reactions, surface adsorption and solution chemistry (Sholkovitz, 1995; Byrne and Sholkovitz, 1996; Byrne and Liu, 1998). With the exception of Ce (IV) the lanthanides have trivalent

* Corresponding author. Fax: +33 03 90 240 402.
E-mail address: pstille@illite.u-strasbg.fr (P. Stille).

0016-7037/$ - see front matter © 2006 Elsevier Inc. All rights reserved.
doi:10.1016/j.gca.2006.04.028

oxidation state in most natural waters. The elements of the lanthanide series are characterized by a gradual decrease in the ionic radii with increasing atomic number ("lanthanide contraction" from La^{3+} to Lu^{3+}; e.g., Brookins, 1989) leading to a slightly different behavior for heavy REE (HREE, Dy–Lu) and light REE (LREE, La–Sm) during chemical processes such as coprecipitation, adsorption or complexation. The configuration of the valence electrons does not change throughout the series because the additional electrons are systematically filled into the f-electron shell. From the literature it is known that competition between free and complexed REE ions, surface adsorption as well as REE scavenging by colloidal particles may strongly fractionate the relative lanthanide concentrations (Byrne and Kim, 1990; Byrne and Li, 1995; Byrne and Sholkovitz, 1996). As a consequence, REE concentrations in natural waters and fractionation of their distribution patterns strongly depend on pH, availability of potential complex ligands, and the presence of particles and colloids (Byrne and Sholkovitz, 1996).

Besides weathering, solution and surface chemistry, other factors such as vegetation have rarely been considered to be of importance for the REE distributions in river water although plants are actually known to accumulate REE under natural conditions (Sun et al., 1999; Yang et al., 1999; Zhimang et al., 2000; Ozaki and Enomoto, 2001; Akagi et al., 2002; Krachler et al., 2003). Therefore, vegetation might, especially in tropical and temperate zones, be an important REE sink potentially capable of fractionating the REEs in surface runoff. The aim of the present study is to determine in how far vegetation may fractionate the relative lanthanide concentrations in natural surface waters. To do this, the Strengbach streamlet and its uppermost catchment in the Vosges mountains (France) has been chosen, because the isotopic and REE characteristics of this site have already previously been extensively studied (Amiotte-Suchet et al., 1999; Riotte and Chabaux, 1999; Tricca et al., 1999; Aubert et al., 2001, 2002a,b, 2004).

2. Site setting

The Strengbach forested catchment covering an area of 80 ha is located in the eastern part of the Vosges mountains (Northeastern France) at altitudes ranging from 883 m at the outlet to 1146 m at the top (Fig. 1). This uppermost catchment site of the Strengbach has been thoroughly investigated since 1986 and has become a completely equipped environmental observatory with permanent sampling and measuring stations (http://ohge.u-strasbg.fr). A review of earlier geochemical, mineralogical and biological studies realized on the site is given by Probst et al. (1990) and Aubert et al. (2002a). The bedrock of the catchment is a homogeneous Hercynian leucogranite. Temperate oceanic mountainous climate with west wind dominates. The monthly averages of daily mean temperatures range from −2 °C to 14 °C (Probst et al., 1990). Rainfall occurs over the whole year with an annual average of 1400 mm (Probst et al., 1995). The forest is dominated by conifers (80%) and beech (20%). The average annual stream discharge is about 680,000 m^3/year. Weathering products and secondary mineral phases in soils and saprolite have previously been characterized (El Gh'Mari, 1995; Fichter et al., 1998). Hydrological processes have been studied extensively (Viville et al., 1993; Lu et al., 1995; Idir et al., 1999; Ladouche et al., 2001; Aubert et al., 2002a). After leaving the uppermost catchment and during its travel of about 15 km down to the Rhine valley, the Strengbach stream crosses different lithologies and mixes up with smaller influent streams from adjoining catchments. As a consequence, pH and major element composition of stream water evolve from upstream to downstream (Riotte and Chabaux, 1999; Tricca et al., 1999).

3. Analytical methods

The water samples were filtered on site through 0.45 μm pore size Millipore cellulose acetate filters. The solution which passed this filter is called the dissolved load and includes dissolved ions and <0.45 μm colloids. The filtered samples were acidified with bidistilled HCl to pH 1–2 and stored in acid-cleaned HDPE bottles. The solid sample fraction (>0.45 μm; suspended load) as well as bottom sediments and soils were considered to consist of two major phases: an unleachable residue and a leachable pool (Sholkovitz et al., 1994).

Leaching experiments with 1 N HCl at room temperature for 15 min have been performed on soil samples, stream water particles (>0.45 μm) and bottom sediments in order to recover the leachable pool which is considered to represent adsorbed REE and REE fixed in HCl-soluble mineral phases such as Fe–Mn oxy-hydroxides (Steinmann and Stille, 1997). Some of these HCl leachable cations can under natural conditions potentially go into solution and enter surface and subsurface runoff. Of course, the unleachable detritus and the leachable pool are operationally defined because there is always a continuum between leachable and residual phases (Stille and Clauer, 1994; Steinmann and Stille, 1997).

The REE concentrations of the filtered water samples (<0.45 μm) are below the detection limit of traditional quadrupole ICP MS (0.01μg/L) and therefore a specific enrichment method was required. A liquid–liquid extraction technique using HDEHP as organic solvent has been applied to enrich the REE by a factor of at least 100 (Shabani and Masuda, 1991; Tricca, 1997; Tricca et al., 1999). Some 0.5–2 L of samples was necessary to achieve concentrations above detection limit. The same extraction technique has been used to obtain sufficient Nd (at least 20 ng) for isotope determinations. The cations have been measured by AAS with a Perkin-Elmer 430 Spectrometer and the anions with a Dionex Ionic Chromatograph. The error is less than 1% for both analyses. A Shimadzu TOC 5000 apparatus has been used to determine DOC (dissolved organic carbon) concentrations.

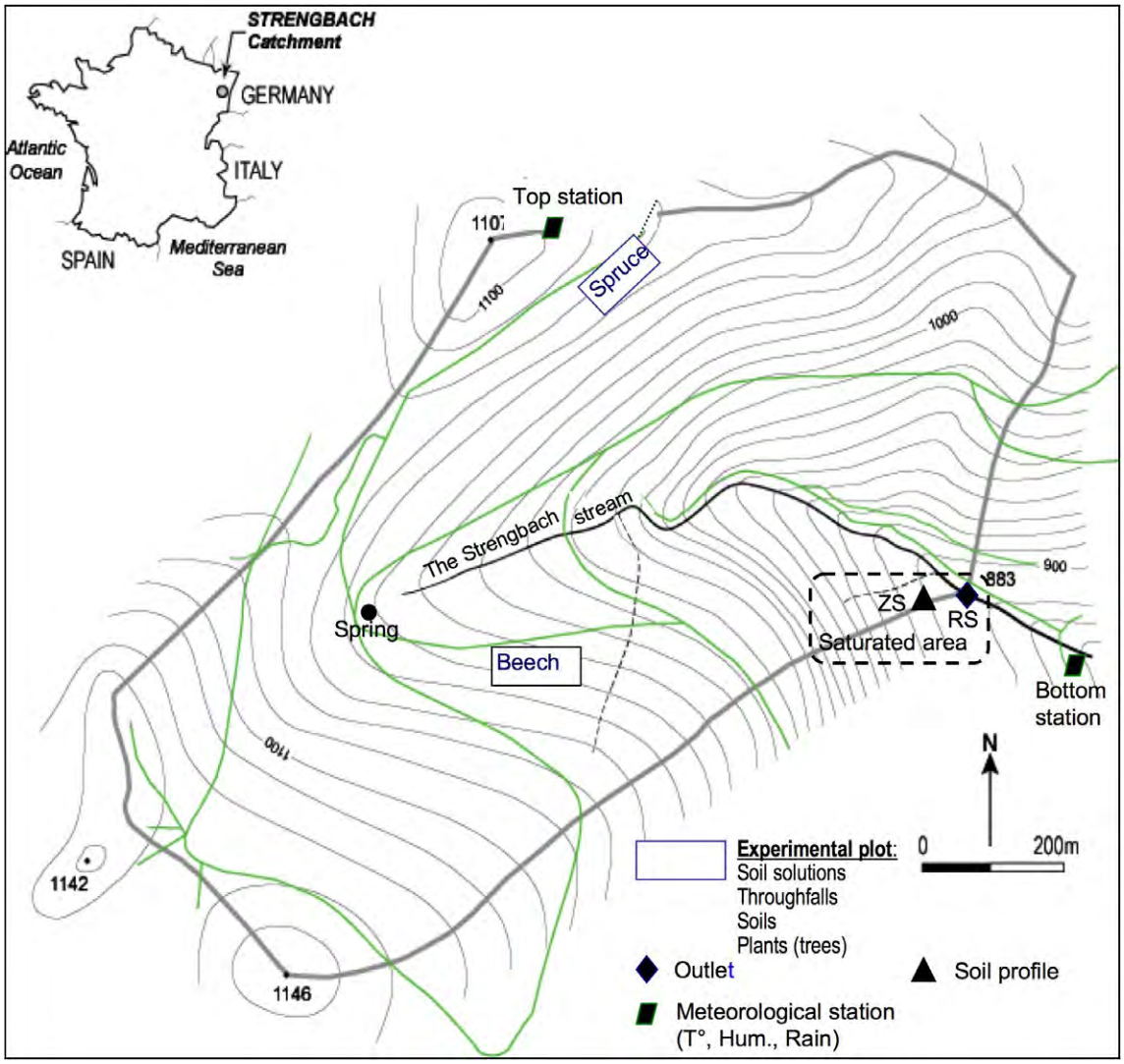

Fig. 1. Uppermost Strengbach catchment with sampling sites. ZS: soil profile in the water saturated zone close to the catchment outlet.

Throughfall has been collected under conifers using 2 m-long open gutters. The recovered solution has been conditioned and analyzed like stream water samples. All trees sampled for this study are older than 100 years. Before drying, leaves and roots were treated during 15 min in an ultrasonic bath with distilled water in order to remove atmospheric dust and soil particles. The bark material has not been washed in order to get information about the atmospheric isotopic composition. Clean powder samples from trunks and branches were obtained with an ultra-clean Ti-drill. All tree samples were dried at 80 °C during 24 h. Afterwards, 100–500 mg were completely digested in savillex vials using hot HNO_3 and H_2O_2. The REE concentrations of trees, soil leachates and waters were measured by inductively coupled plasma mass spectrometry (ICP-MS) in Strasbourg (Aubert et al., 2001) and Neuchâtel. The error of measurement is <5%. Standard techniques were applied for Sr and Nd isotopic analyses (Steinmann and Stille, 1997) and it was possible to run some of the beech samples. However, bad emissions on the mass spectrometer prevented precise Sr and Nd isotope determinations on conifers. The Sr isotopic compositions were determined using a fully automatic VG Sector thermal ionization mass spectrometer at CNRS Strasbourg with a 5-cup multicollector after enrichment and separation from the bulk sample using cation exchange resin. During the measuring period the NBS 987 Sr standard yielded $^{87}Sr/^{86}Sr = 0.710258 \pm 5$ ($\pm$SD, $n = 9$). The Nd isotopic composition were determined using a Nu instruments MC-ICP-MS at the branch of Isotope Geology at the University of Bern. The in house standard yielded $^{143}Nd/^{144}Nd = 0.51105 \pm 1$ ($\pm$SD, $n = 7$) corresponding to the La Jolla Standard value of 0.511843.

4. Results and discussion

4.1. REE and Sr–Nd isotope signatures of Strengbach waters in the uppermost catchment

In a previous study, it has been shown that the Strengbach waters close to the source have Sr and Nd isotopic compositions very similar to values of primary apatite from

the granitic bedrock and the overlaying soil (Aubert et al., 2001; Table 1; Fig. 2). However, stream water normalized to apatite is still depleted in LREE pointing to an additional LREE depletion after apatite dissolution in the soil as expressed by a apatite normalized La_N/Yb_N ratio of <1 (Table 2; Fig. 3).

The pH of Strengbach water rises from 6.2 upstream (in the uppermost catchment) to 8.1 downstream (in the Rhine valley; Table 2). At the same time the major element composition of stream water (Table 3) evolves from Ca–Na–SO_4 type water upstream to Na–Ca–Cl–SO_4–HCO_3 type water downstream. Nevertheless, the evolution of pH and major element chemistry appear to have no direct impact on the REE distribution patterns which remain almost unchanged from upstream to downstream.

The DOC concentrations (Table 3) and La_N/Yb_N ratios (apatite normalized) (Table 2) of the uppermost catchment site (3999, 4015, 4109) are low, vary weakly and range between 1.2 and 1.4 mg/L and 0.12 and 0.22, respectively.

Leaching experiments performed on suspended load samples and bottom sediments of the Strengbach and on soil samples from a soil profile (0–50 cm depth) located in the water saturated zone close to the catchment outlet (ZS; Fig. 1) show that surface adsorption might be one of the mechanisms responsible for the observed additional depletion of the LREE (Fig. 4).

The Sr and Nd isotopic compositions of a 1 M HCl leachate of a >0.45 μm suspended load sample from the catchment are comparable to those of the Strengbach stream water (Tricca et al., 1999). Similarly, 1 M HCl leachates from the lower part of a soil profile (20–50 cm) in the water saturated zone (ZS; Fig. 1; 510L2 and 512L2; Table 1) have stream water-like Sr and Nd isotopic compositions (triangle, #2 and 3 in Fig. 2). This indicates that leachable Sr and Nd adsorbed on the suspended load and soil minerals originate from surface water.

The REE patterns of the leached soil samples are the most LREE enriched with respect to stream water (Fig. 4) with stream water normalized La_N/Yb_N ratios of 2.2–2.7 (Table 4). The leachates of the suspended load samples have similar REE patterns with stream water normalized La_N/Yb_N ratios close to 2 (Fig. 4, Table 4), whereas the stream water normalized La_N/Yb_N ratios of bottom sediment leachates range between 1.8 and 1.9. Consequently, adsorption on suspended particles, bottom sediment and soil minerals might to some extend be responsible for the LREE depletion of stream water. However, the leachates of all sample categories remain LREE depleted

Table 1
Sr and Nd isotope data

Sample	Depth	$^{87}Sr/^{86}Sr$	$^{143}Nd/^{144}Nd$
Soil-508L2 (HCl leach.)	0–10 cm	0.72805(1)	0.51215(1)
Soil-510L2 (HCl leach.)	20–30 cm	0.72872(3)	0.51221(1)
Soil-512L2 (HCl leach.)	40–50 cm	0.73044(3)	0.51223(2)
508P (roots, <1 mm)	#2/0–10 cm #4/20–30 cm	0.72458(3)	0.51218(8)
510P (roots, <1 mm)		0.72974(1)	0.51211(1)
136 (bark wood; beech)		0.7251(5)	0.51212(4)
LP2 (leaves; beech)		0.72753(2)	0.51225(7)
LP19 (branch wood; beech)		0.72586(3)	0.51209(5)
PRH (roots wood; beech)		0.7336(2)	0.51217(3)
Lichen		0.71887(5)	0.51205(1)
Throughfall(a)		0.71857[a]	0.51212(5)
Rainwater(b)		0.711–0.7146	n.d.
Soil solution(a)		0.72289(5)	0.51218(5)
Spring water(c)		0.72606(2)	0.51224(4)
Stream water(c)		0.72481(3)	0.51224(1)
Stream water 2(d)		0.72447(1)	0.51226(1)
Suspended load leach(d)		0.72023(5)	0.51224(1)
Apatite(a)		0.71612(1)	0.51228(1)

The errors given for the Sr and Nd isotopic compositions are two sigma mean values and refer to the last digits (values in parentheses). n.d., not determined.
(a) Aubert et al. (2002a,b); (b) Chabaux et al. (2005); (c) Aubert et al. (2001); (d) Tricca et al. (1999).
[a] Three samples.

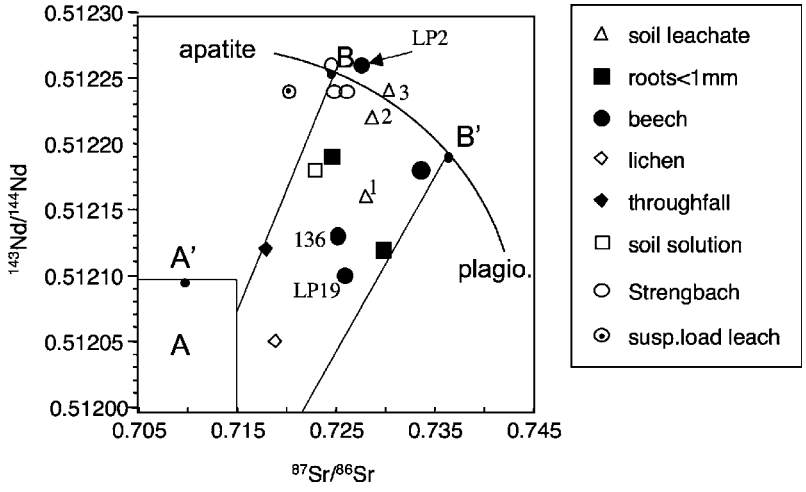

Fig. 2. Comparison of Sr and Nd isotope data of soil leachates and beech samples with Strengbach waters. Data of suspended load leachates, soil solution and stream waters from Aubert et al. (2001) and Tricca et al. (1999). A: atmospheric pool. B–B': range of Sr and Nd isotopic compositions of the alteration component taken up by the trees. All samples are from the uppermost Strengbach catchment. Most of the samples contain an atmospheric component A. Open triangle: soil leachates from ZS profile (depth: #1, 0–10 cm; #2, 20–30 cm; #3, 40–50 cm).

Table 2
REE concentration data of Strengbach waters, river Rhine and groundwater (nmol/L); distance in km from upper catchment[a]

Samples	Dist. from catchment	La	Ce	Pr	Nd	Sm	Eu	Gd	Tb	Dy	Ho	Er	Tm	Yb	Lu	LaN/YbN apatite
3999	up.catchm.	0.06	0.13	0.03	0.17	0.07	0.01	0.08	0.01	0.08	0.01	0.04	n.d.	0.05	0.01	0.12
4015[b]	up.catchm.	0.11	0.21	0.05	0.29	0.13	0.02	0.15	0.03	0.14	0.03	0.07	n.d.	0.04	0.01	0.22
4109	up.catchm.	0.12	0.28	0.06	0.39	0.15	0.03	0.18	0.03	0.17	0.03	0.07	n.d.	0.06	0.01	0.17
4108	1.5 km	0.15	0.24	0.05	0.28	0.11	0.02	0.13	0.02	0.14	0.03	0.07	n.d.	0.08	0.01	0.19
4016	2 km	0.09	0.11	0.03	0.15	0.05	0.02	0.06	0.01	0.07	0.02	0.04	n.d.	0.03	0.01	0.24
4112	3 km	0.08	0.14	0.03	0.18	0.07	0.01	0.08	0.01	0.09	0.02	0.05	n.d.	0.06	0.01	0.11
4017	5 km	0.14	0.15	0.04	0.20	0.07	0.01	0.08	0.01	0.08	0.02	0.05	n.d.	0.05	0.01	0.26
4019	5.5 km	0.09	0.10	0.03	0.15	0.05	0.01	0.06	0.01	0.05	0.01	0.02	n.d.	0.01	0.00	0.73
4020	7.5 km	0.11	0.15	0.03	0.18	0.06	0.01	0.08	0.01	0.07	0.02	0.05	n.d.	0.06	0.01	0.16
4022	14 km	0.09	0.11	0.02	0.10	0.03	0.01	0.05	0.01	0.05	0.01	0.04	n.d.	0.07	0.01	0.11

n.d.: not determined.
[a] Data from Tricca et al. (1999).
[b] Used for normalization.

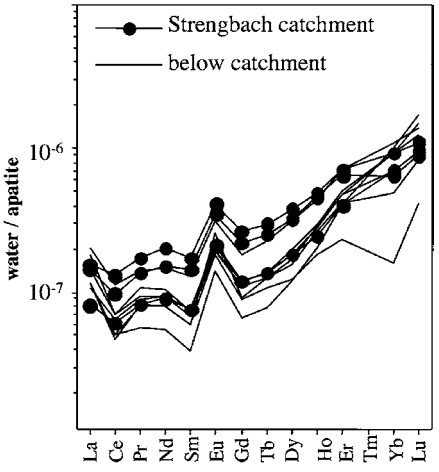

Fig. 3. Strengbach waters from the uppermost catchment (observatory) and from below the observatory normalized to apatite (Table 4).

when normalized to apatite demonstrating that LREE adsorption alone cannot explain the observed LREE depletion of stream water. All leachates show a positive stream water normalized Ce anomaly (Sholkovitz, 1993) ranging between +1.2 and 2.2 (Table 4) indicating that suspended load and soil particles are also sites for the oxidation of Ce (III) to Ce (IV).

4.2. The Sr–Nd isotope signatures of vegetation

Fig. 2 shows Nd and Sr isotopic compositions of the Strengbach waters from the uppermost catchment together

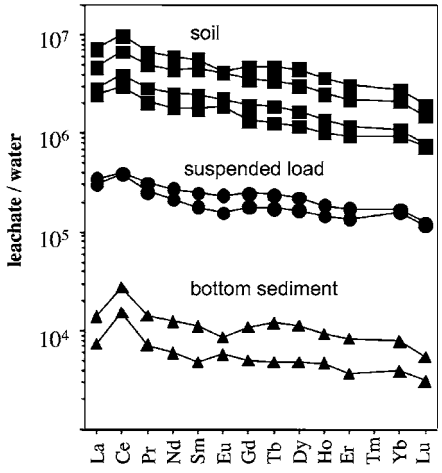

Fig. 4. REE of soil (from ZS profile), suspended load and bottom sediment leachates normalized to stream water (4015, Table 2). Suspended load and bottom sediment of the Strengbach are taken in the uppermost catchment. All samples are LREE enriched compared to Strengbach waters and have a positive Ce anomaly.

Table 3
Major cations and anions of Strengbach water; distance in km from upper catchment[a]

Sample	3999 up. catchm.	4015 up. catchm.	4109 up. catchm.	4108 1.5 km	4016 2 km	4112 3 km	4017 5 km	4019 5.5 km	4020 7.5 km	4022 14 km
Na^+ (mmol/L)	0.091	0.095	0.087	0.247	0.22	0.264	0.256	0.23	0.252	1.1
Mg^{2+} (mmol/L)	0.028	0.029	0.025	0.03	0.11	0.038	0.109	0.139	0.126	0.201
K^+ (mmol/L)	0.023	0.022	0.016	0.04	0.044	0.048	0.043	0.048	0.044	0.133
Ca^{2+} (mmol/L)	0.083	0.087	0.076	0.106	0.185	0.116	0.201	0.246	0.244	0.473
HCO_3^- (mmol/L)	0.034	0.005	0.027	0.133	0.331	0.17	0.332	0.469	0.437	1.12
NO_3^- (mmol/L)	0.049	0.051	0.029	0.036	0.057	0.048	0.06	0.069	0.068	0.082
SO_4^{2-} (mmol/L)	0.093	0.099	0.094	0.089	0.097	0.093	0.107	0.112	0.118	0.346
Cl^- (mmol/L)	0.061	0.079	0.06	0.175	0.235	0.195	0.259	0.226	0.245	0.629
Σ cations (meq/L)	0.336	0.349	0.305	0.559	0.854	0.620	0.919	1.05	1.04	2.58
Σ anions (meq/L)	0.330	0.333	0.304	0.522	0.817	0.599	0.865	0.99	0.99	2.52
DOC (mg/L)	1.27	1.23	1.44	2.05	1.43	2.77	1.60	1.79	1.88	3.31
pH	6.2	6.4	6.2	6.8	7.4	7.3	7.4	7.6	7.5	8.1

[a] Tricca (1997).

Table 4
REE concentrations of soil, bottom sediment and suspended load leachates (ppm)

Samples	La	Ce	Pr	Nd	Sm	Eu	Gd	Tb	Dy	Ho	Er	Tm	Yb	Lu	La/Yb norm.	Ce/Ce*
Soil 508L2	37.0	87.7	14.6	75.7	34.0	6.6	32.6	5.4	27.2	4.4	10.4	1.2	7.3	1.0	2.59	1.35
Soil 510L2	43.8	115.2	20.1	106.1	47.2	7.8	46.5	7.9	38.3	5.9	13.0	1.5	8.3	1.0	2.69	1.42
Soil 512L2	70.6	196.3	35.2	188.8	86.3	14.2	86.4	14.3	70.7	10.9	24.5	2.8	16.2	2.0	2.24	1.46
Soil 515L2	108.3	285.2	47.2	251.0	108.2	14.8	113.1	20.1	103.4	15.6	34.1	3.9	21.6	2.6	2.58	1.45
Susp. load 4109/32[b]	5.2	11.6	2.2	11.5	4.8	0.82	5.9	1	5.1	0.8	1.9	0.23	1.3	0.16	2.05	1.24
Susp. load 4108/33[b]	4.6	11.3	1.8	9	3.4	0.55	4.3	0.7	3.8	0.63	1.5	0.19	1.2	0.15	1.97	1.41
Bottom sedi. 4109/32[b]	0.21	0.79	0.1	0.52	0.21	0.03	0.26	0.05	0.26	0.04	0.09	0.01	0.06	0.007	1.8	2.02
Bottom sedi. 4108/33[b]	0.11	0.44	0.05	0.25	0.09	0.02	0.12	0.02	0.11	0.02	0.04	0.01	0.03	0.004	1.88	2.21
Apatite[a]	103.3	298.1	51.2	276.8	132.8	10.0	109.1	16.8	71.4	9.4	16.9	2.3	11.9	1.5		

La/Yb and Ce/Ce*: water normalized (see Table 2).
[a] Aubert et al. (2002a,b).
[b] Tricca et al. (1999).

with a calculated mixing curve defined by the end-members apatite and plagioclase extracted from local bedrock (mixing curve of alteration products; Aubert et al., 2001). All other bedrock and soil minerals plot far off this mixing curve towards more radiogenic Sr isotope ratios outside the range of Fig. 2 (Aubert, 2001; Aubert et al., 2001). Thus, there is no soil sample or mineral plotting to the left of this mixing curve. However, atmospheric precipitations which are additional Sr and Nd sources for the Strengbach catchment have low $^{143}Nd/^{144}Nd$ and $^{87}Sr/^{86}Sr$ ratios and plot to the left of the mixing curve. Their Nd–Sr isotopic compositions have been deduced from eolian particles and rain water plotting to the lower left of the diagram (A, Fig. 2) (Aubert et al., 2002b). Lichens, whose nutrients are known to derive largely from airborne particulate matter (e.g., Rossbach et al., 1999) have been sampled at the surface of tree barks and analyzed for Sr and Nd isotopes (Table 1). Their $^{87}Sr/^{86}Sr$ ratio is 0.71887 and similar to that of throughfall (0.71857, Table 1) and slightly higher than rainwater values that vary between 0.711 and 0.7146 (Chabaux et al., 2005). The $^{143}Nd/^{144}Nd$ ratio is only slightly different for lichens and throughfall (0.51205 and 0.51212, respectively). Therefore, soil samples, soil solutions or trees plotting to the lower left of the mixing curve for alteration products suffered atmospheric contamination.

Only one of the beech samples (LP2, young leaves) has Sr and Nd isotopic compositions (0.7275 and 0.51225, respectively) which are close to those of surface waters (average: 0.725 and 0.51225, respectively). Its isotopic composition is close to the alteration component taken up by the tree and defined in Fig. 2 as point B and composed by 15 wt% of apatite and 85 wt% of plagioclase (Aubert et al., 2001).

The two root samples (<1 mm) shown in Fig. 2 originate from the ZS soil profile discussed in Section 4.1 (Table 1; 508P, 510P). Their Sr and Nd isotopic composition values are shifted towards atmospheric composition and plot close to soil solution and to the topsoil leachate (triangle #1 in Fig. 2; ZS 508L2; 0–10 cm depth; Table 1). Similar $^{87}Sr/^{86}Sr$ isotopic composition values ranging between 0.725 and 0.734 have also been found in four beech samples (roots, bark, branches and leaves). Their $^{143}Nd/^{144}Nd$ isotopic composition values vary between 0.51209 and 0.51225. The bark (#136) and the wood of a beech (LP19; branch) contain important quantities of atmospheric Sr and Nd as indicated by their low $^{87}Sr/^{86}Sr$ and $^{143}Nd/^{144}Nd$ ratios.

The throughfall and lichen samples plot closest to A (Aubert et al., 2002b; A', 0.71 and 0.5121, respectively). Using these atmospheric end-member isotopic compositions and an alteration component B' on the mixing curve of alteration products (containing 5 wt% of apatite and 95 wt% of plagioclase; corresponding to $^{87}Sr/^{86}Sr$ and $^{143}Nd/^{144}Nd$ values of 0.735 and 0.51219, respectively; for more details see model of Aubert et al., 2001), one can deduce that throughfall contains up to 50% and soil solution more than 20% of atmospheric Sr and Nd (Aubert et al., 2002b). Similarly, high atmospheric contributions can be estimated for the beech samples with lowest Sr and Nd isotopic compositions closely situated to throughfall and lichen samples (#136, LP19; Table 1). The estimation of the atmospheric contribution remains very approximative because the isotopic composition of the atmospheric component is not yet precisely known. The new data from the beech (#136, LP19) and lichen samples point to a Nd isotopic composition for the atmospheric component that is even lower than that of point A' in Fig. 2. If some of the bark contained detrital REE of the soil, then the atmospheric contribution would even be higher than estimated because all soil minerals have much higher $^{87}Sr/^{86}Sr$ isotopic ratios than the atmospheric component and plot to the right of the mixing curve in Fig. 2.

4.3. The LREE uptake by vegetation

The trees REE concentrations (Table 5) were normalized to Strengbach water sampled close to its source (sample 4015, Table 2) (Fig. 5a) because tree samples without atmospheric contribution (e.g., LP2; Table 1) carry

Table 5
REE concentrations in plants (ppb)

Sample	La	Ce	Pr	Nd	Sm	Eu	Gd	Tb	Dy	Ho	Er	Tm	Yb	Lu	SREE	Eu/Eu[a]	La/Yb[a]	La/Yb[b]	La/Yb[c]	La/Yb[d]	Eu/Eu[d]
LP2/leaves, beech[e]	65	62	7	25	4	3	5	1	3	1	2	0.2	1	0.3	178	3.7	31	7	12.1	54	6
LP16/bark, beech[e]	26	38	5	18	4	17	4	n.d.	2	1	2	0.3	1	0.3	118	27.9	17	4	5.8	26	54
LP19/branch, beech[e]	51	62	7	27	5	12	7	1	3	1	2	0.3	1	0.2	179	12.2	20	4	7.0	31	23
P22/bark, beech[e]	75	163	19	70	14	5	14	2	8	2	4	0.5	3	0.4	380	2.2	14	3	4.3	19	3
LP25/roots, beech, 1 mm[e]	190	411	49	182	40	16	39	5	25	4	11	1.5	8	1.4	984	2.4	12	3	3.4	15	4
LP26/roots, beech, 5–8 mm[e]	26	54	6	23	5	8	6	1	3	1	1	0.2	1	0.2	136	9.4	12	3	3.5	16	18
PRH roots, beech[e]	986	2039	245	878	173	33	160	19	82	14	39	4.6	31	4.5	4707	1.2	17	4	5.6	25	1
RIH/roots, beech[e]	279	603	69	248	49	13	48	6	28	5	12	1.7	12	1.6	1375	1.6	12	3	3.8	17	2
508P/roots<1 mm[e]	63	129	19	82	28	5	24	4	18	3	7	1	6	0.9	389	1.2	6	1	0.9	4	1
510P/roots<1 mm[e]	1718	3805	539	2490	815	116	718	109	527	79	178	21	123	15	11,254	0.9	7	2	1.5	6	0.5
512P/roots<1 mm[e]	2270	5320	817	4037	1485	219	1350	213	1047	159	362	43	252	31	17,606	0.9	5	1	0.3	1	0.6
515P/roots<1 mm[e]	4781	11278	1668	7846	2728	352	2493	392	1884	284	640	76	448	55	34,925	0.8	5	1	0.7	3	0.3
A5: bark, beech[e]	243	127	66	249	51	16	43	9	32	8	16	4	12	4	880	2.1	10	2	2.9	13	3
F1/stem, beech[f]	71	158	22	75	13	19	14	3	13	3	7	2	7	1	408	8.6	5			3	16
F2/stem, beech[f]	28	74	8	24	4	4	3	n.d.	2	n.d.	n.d.	n.d.	1	n.d.	148	7.0	14			21	13
F206/leaves,beech[f]	265	490	55	195	37	16	39	8	26	7	12	4	9	4	1167	2.6	15			22	4
F4/stem, conifer[f]	34	80	11	35	9	8	10	2	6	1	3	1	3	1.0	204	5.1	6			4	9
H2/stem, conifer[f]	27	53	6	19	5	2	3	n.d.	4	1	2	n.d.	1	n.d.	123	3.2	14			20	5
15/bark, limetree[g]	728	1650	198	851	194	48	227	34	194	37	104	15	89	13	4382	1.4	4			1	2
16/stem, limetree[g]	33	58	10	37	8	3	5	1	6	2	3	1	2	2	171	2.9	8			9	5
P6/bark, limetree[g]	506	931	130	470	83	20	88	11	70	13	37	5	30	4	2398	1.4	9			9	2
P7/stem, limetree[g]	19	21	4	13	3	3	2	n.d.	2	n.d.	1	n.d.	n.d.	n.d.	68	7.5					14
P1/bark, beech[g]	404	779	102	376	73	18	69	11	55	10	27	5	22	4	1955	1.5	9			11	2
A8/lichen[e]	184	354	42	166	36	7	29	4	22	5	13	2	12	2	878	1.3	8	1.8			

n.d., not detected.
[a] Strengbach-norm. (in Table 2).
[b] Apatite norm.
[c] Apatite norm. and atmos. correct. (50%).
[d] Strengbach-norm. and atmos. correction (50% contr.): 2*((La_N/Yb_N) plant)–(La_N/Yb_N) lichen; 2*(Eu/Eu* (plant))–(Eu/Eu*) lichen.
[e] Strengbach catch.
[f] Black Forest.
[g] Strasbourg.

essentially the isotopic signature of stream water. The trees are strongly REE enriched with respect to stream water. Most enriched (up to 100,000 times) are small roots with 1–2 mm in diameter. Larger roots are up to 1000 times enriched. Wood and bark of branches and trunks have lower REE concentrations with a strong positive Eu anomaly (Fig. 5). Furthermore, a strong LREE enrichment can be observed in some of the tree samples (Fig. 6). Normalized to Strengbach water, these samples show La_N/Yb_N ratios ranging between 5 and 30. The smallest roots (508P, 510P, 512P, 515P; Table 5) are least LREE enriched with lowest La_N/Yb_N ratios between 5 and 7.

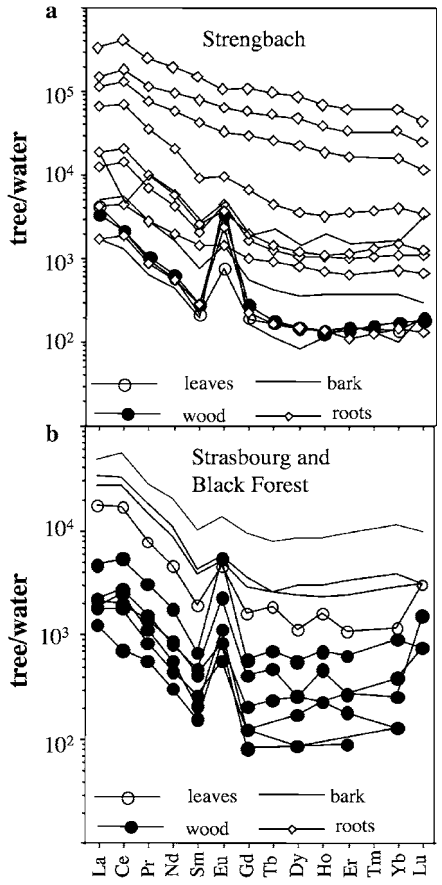

Fig. 5. Plant samples from the Strengbach catchment [Vosges Mountains (a)] and Strasbourg and Black Forest (b) normalized to the REE composition of the filtered stream water (sample 4015; Table 2). Wood stands for trunk and branch.

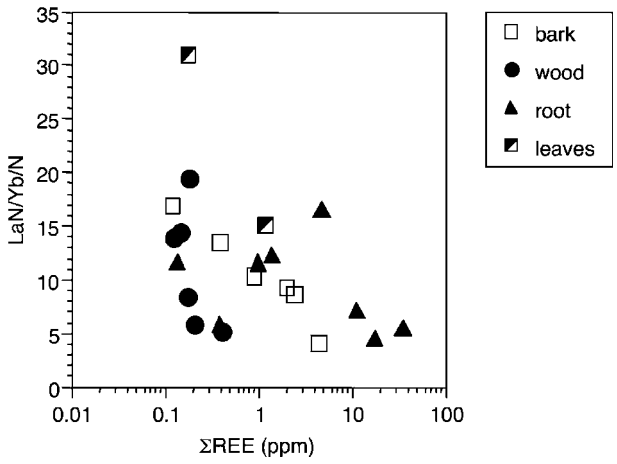

Fig. 6. La/Yb ratios in plants normalized to the REE composition of the filtered stream water (sample 4015; Table 2) and compared with the total REEs. Wood stands for trunk and branch.

The stream water normalized Eu anomalies and La_N/Yb_N ratios given in Table 5 have been corrected for atmospheric contamination using the REE distribution pattern of a lichen sample (see Table 5 for calculation details). The atmosphere corrected Eu anomalies and La/Yb ratios are generally higher than the uncorrected ones because the Eu anomaly (1.3 when normalized to stream water) and the LaN/YbN ratios of lichen (8 when normalized to stream water) are lower than for most vegetation samples (Table 5). Trees from outside the catchment from the city of Strasbourg in the Rhine valley further to the North and in the Black Forest on the other side of the Rhine Valley show very similar REE patterns (Fig. 5b) indicating that this kind of fractionation with LREE- and Eu-enrichment is not a local phenomenon.

The distribution patterns of plants normalized to apatite (Fig. 7), which is the most important REE source for plants and waters as shown by the Sr and Nd isotope data (Fig. 2), point to LREE enrichments with atmosphere corrected La_N/Yb_N ratios equal or lower than 12 (Table 5). The apatite normalized REE distribution patterns of the smallest roots are least fractionated and emphasize the idea, that most of the REE in the plants of the Strengbach catchment originate from apatite dissolution. Plant roots are known to attack specifically apatite, an important phosphate source for plant growth (Wallander et al., 1997). Upward in the tree, REE concentrations decrease in trunk, bark and leaves, simultaneously with the appearance of a strong positive Eu anomaly and a strong LREE enrichment (Figs. 6 and 8).

This general evolution suggests that REE fractionation is controlled by metabolic processes within the plant rather than by preferential uptake of LREE and Eu at the root–soil interface, e.g., due to bacterial activity, because major fractionation occurs within the plant and not at the soil–plant interface. This is in agreement with earlier observations indicating that the roots fractionate the REE during uptake from soil solution much less than other parts of the plant during transport and deposition within stem and leaves (Li et al., 1998; Bei Wen et al., 2001; Zhang et al., 2002). However, similar to our study (e.g., Fig. 6) it has also been observed that the root is the most REE-enriched part of the plant and that roots of rice and wheat have always lower La/Yb ratios than corresponding leaves (e.g., Bei Wen et al., 2001). Recent studies indicate that rare earth elements have a dual effect on the physiological and biochemical reactions in the plant development (Zeng et al., 2003 and citations therein). Important resemblances exist between Eu^{3+} and Ca^{2+} in their atomic radius and

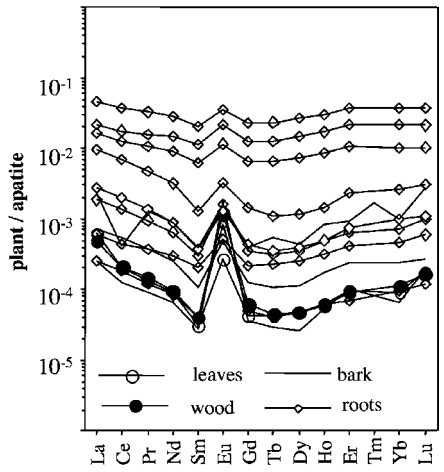

Fig. 7. REE of plant samples from the Strengbach catchment normalized to apatite (Table 4). Wood stands for trunk and branch.

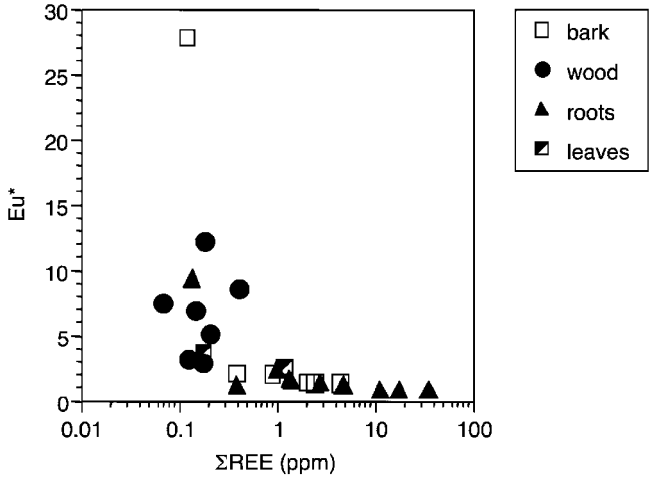

Fig. 8. Eu anomaly in plants as a function of total REEs. Wood stands for trunk and branch.

structures of the valence electron and Zeng et al. showed that Eu^{3+} might replace Ca^{2+} in plants (e.g., *Amarathus caudatus*) and promote calcium transportation across plasma membrane. Thus, possibly some of the trees Ca, which plays a vital role in the formation and the stabilization of the plants cellular walls, in the stabilization of membranes and in the regulation of the intracellular metabolism, might have been replaced by Eu^{3+}. The concentration of free and active Ca^{2+} in the cytoplasm of plant cell must remain low and is controlled by the precipitation of oxalate crystals which allows the storing of inactive Ca and probably also of Eu in the old plant organs.

More than 99% of the dry mass of a beech or a spruce corresponds to branches, stem, coarse roots (>2 mm) and leaves. The smallest roots (<2 mm) represent less than 0.5% of the whole tree mass (Scarascia-Mugnozza et al., 2000). Therefore, the REE pattern of the bulk tree reflects the REE distribution of bark, trunk and leaves, i.e., characterized by a strong LREE enrichment and a positive Eu anomaly (stream water normalized). The weaker LREE enrichment (stream water normalized) of the small roots completely disappears in this total budget in spite of their elevated REE concentrations. Consequently, our data clearly demonstrate that vegetation preferentially accumulates LREE and Eu. Vegetation thus represents an important sink for LREE in forested catchments. In the following section we will discuss how preferential accumulation of LREE by vegetation might modify the REE budget at catchment scale.

4.4. The impact of vegetation on the REE budget of the Strengbach catchment

The REE of soil and soil solutions of a small catchment might be exported by draining waters and/or vegetation. Both of them, the annual flow rate of the Strengbach at the outlet and the annual growth rate of vegetation are known. Based on long-term monitoring an average discharge rate of 20 L/s can be deduced (Probst and Viville, 1999). However, during dry years the mean flow rate can be as low as 9 L/s (Probst et al., 1995; Aubert et al., 2002a). The average discharge rate of 20 L/s leads to an annual dissolved LREE (La–Nd) and HREE (Er–Lu) export of 0.248 mol (35 g) to 0.532 mol (76 g) for LREE and 0.061 mol (10 g) to 0.091 mol (16 g) for HREE. The source data for this calculation are given in Table 6.

For the vegetation of the Strengbach catchment an average growth rate of 7 m^3/ha/year has been determined (Prevosto, 1988). Taking this value and 80 ha for the catchment surface and the additional parameters given in Table 6, one can calculate that vegetation extracts at least 0.319 mol (45 g) of LREE and 0.009 mol (1.5 g) of HREE per year. These values are deduced from tree samples whose average LREE and HREE concentrations are 0.952 nmol g^{-1} (0.135 ppm) and 0.027 nmol g^{-1} (0.005 ppm), respectively. These concentrations include correction for weight loss due to drying and for atmospheric contribution. Using tree samples including larger roots, a LREE and HREE export of 0.816 mol (114 g) and 0.018 mol (2.7 g), respectively, can be calculated. All samples (except the smallest roots representing less than 0.5% of the whole tree mass) can be used to calculate similar export values for LREE and HREE of 131 and 4 g, respectively. These results are only semi-quantitative because parameters such as wood density and water content used for this estimation are variable. Nevertheless they clearly indicate that the yearly LREE uptake by vegetation is comparable with the yearly LREE export by the streamlet. It appears that the LREE export by vegetation can even be higher than that of stream discharge. However, the HREE discharge by the Strengbach stream with 0.076 mol (13 g) in average and with extreme values of 0.061 mol (10 g) to 0.091 mol (16 g) is always more important than the uptake by plants (Table 6, Fig. 9).

Table 6
Flux parameters for REE

(a) Strengbach (catchment)							
Samples 3999, 4015, 4109; (Table 2):							
Concentrations:			Average		Low		High	
			ng/L	nmol/L	ng/L	nmol/L	ng/L	nmol/L
LREE (La–Nd)			89	0.618	56	0.393	120	0.843
HREE (Er–Lu)			20	0.121	17	0.097	25	0.145
Average annual discharge: 20 L/s								
			g	mol	g	mol	g	mol
Export LREE:			56	0.390	35	0.248	76	0.532
Export HREE:			13	0.076	10	0.061	16	0.091
(b) Vegetation (catchment)								
catchment surface:	80 ha							
Growth rate of vegetation:	7 m^3/ha/a							
	560 m^3/a							
Wood density:	0.6 kg/dm^3							
http://www.worldagroforestry.org/sea/Products/AFDbases/WD/Index.htm								
(A) samples (catchment) without roots LP2, LP16, LP19, P22, LP25, LP26, A5:								
(B) with roots (catchment; except the smallest samples 508P–515P)								
(C) all samples (including those from outside the catchment, except 508P–515P)								
			A		B		C	
			µg/g	nmol/g	µg/g	nmol/g	µg/g	nmol/g
LREE in dried sample:			0.34	2.379	0.855	6.073	0.88	6.258
HREE in dried sample:			0.011	0.066	0.02	0.135	0.03	0.202
25% wt loss during drying								
LREE in wet sample:			0.27	1.903	0.68	4.858	0.70	5.006
HREE in wet sample:			0.009	0.053	0.016	0.108	0.024	0.161
50% atmospheric origin								
LREE in vegetation:			0.135	0.952	0.34	2.429	0.35	2.503
HREE in vegetation:			0.0045	0.027	0.008	0.054	0.012	0.081
			g	mol	g	mol	g	mol
Export LREE:			45	0.319	114	0.816	118	0.841
Export HREE:			1.5	0.009	2.7	0.018	4	0.027

4.5. The fate of vegetation hosted REE after degradation

The results of the budget calculations presented in Section 4.4 demonstrate that LREE uptake by vegetation can explain the observed LREE depletion of stream water. Fig. 9 also implies that degradation of LREE-enriched plant tissue should lead to the formation of a LREE-enriched litter layer in the topsoil which, however, is not confirmed by our data. Consequently, there must be a process that exports these LREE from the catchment. Some of the LREE in the litter layer may also directly be recycled and re-absorbed by vegetation. However, the fact that the roots show compared to other parts of the plant only a relatively weak LREE enrichment suggests that this recycling does not significantly influence the REE budget at catchment scale. If LREE recycling would play an important role one might suggest that older plants are more LREE enriched than younger plants. This however is not the case. We found similar La/Yb ratios in adult trees and in only 30 days old corn plants.

In previous studies, it has been shown that two principal pools for REE in 0.22 or 0.45 µm-filtered river water exist: a REE-rich colloidal pool with shale-like distribution patterns and a dissolved pool with HREE enrichment (Elderfield et al., 1990). Thus, the presence of different quantities of colloidal phases in the <0.45 µm fraction may explain the variable degree of LREE depletion of the different samples. A more recent study on the boreal Kalix river confirms that colloidal particles dominate the transport of filter-passing REE and that the colloidal fraction shows a flat to slightly LREE-enriched pattern, whereas the "truly" dissolved <3 kDa fraction shows HREE-enriched patterns with respect to bedrock (Ingri et al., 2000). However, this study also indicates that the REE in the colloidal and particulate fraction are associated with an organic-rich and Fe-rich inorganic phase. The authors further show that La concentrations are positively correlated with dissolved organic carbon (DOC) and water discharge. Especially during flood events (e.g., in spring) when the river has a large exchange surface with vegetation, woodland and soil, DOC and La concentrations are high. Similarly, the study on river waters from a small catchment in the Cameroon shows that the Mengong river with DOC contents of up to 24 mg/L has much higher

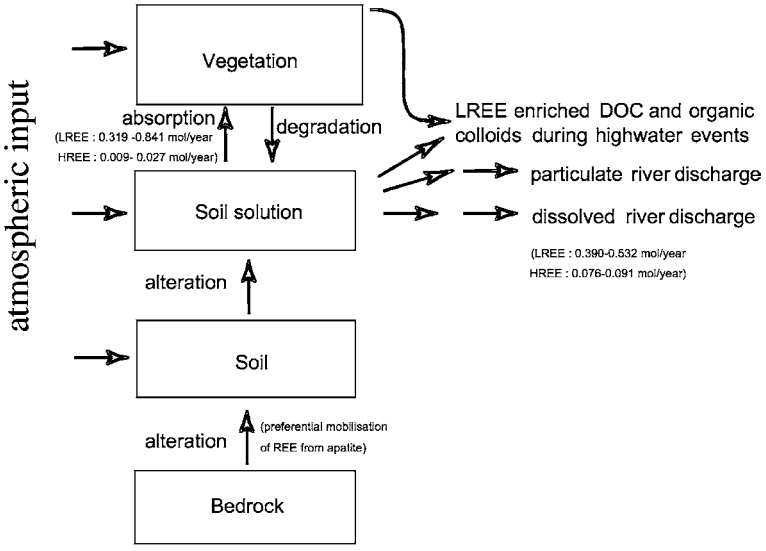

Fig. 9. Flux boxmodel for LREE and HREE at the atmosphere–water–soil–plant interface. The yearly LREE uptake by vegetation is comparable with the yearly LREE export by the streamlet. LREE export from catchment basins with DOC during high water events might be the process that counterbalances plant-derived LREE accumulation in the litter layer of the topsoil.

La_N/Yb_N ratios (0.8; PAAS norm) than the Nyong river with DOC contents of up to 14 mg/L (0.5; PAAS norm; Viers et al., 1997). These examples demonstrate that increasing DOC contents correlate with LREE enrichments in waters, which is in agreement with the concept that DOC in river water is mainly derived from decomposition of plant tissue. Consequently, LREE export from catchment basins with DOC during high water events might be the process that counterbalances plant-derived LREE accumulation in the litter layer of the topsoil. LREE and DOC export seems to occur mainly during high water events, whereas normal river discharge is characterized by LREE-depleted patterns inherited from soil water.

However, REE in organic-rich blackwaters (filtered at 0.45 μm) of the Great Dismal Swamp (Virginia) behave differently and are all enriched in the middle REEs when normalized to upper continental crust and not in the LREE as suggested in our case (Johannesson et al., 2004). Johannesson et al. show that organic complexes are the predominant form for dissolved REE despite significant competition with Fe and Al. One possible explanation for this different behavior might be the fact that these relatively quiet lake and swamp waters contain comparatively small quantities of organic-rich suspended particles. Therefore, the MREE-enriched organic complexes of the Great Dismal Swamp might be issued from solution complexation under hydrodynamically quiet conditions with little or no suspended particles, whereas rivers and streams drain, especially after flood events, suspended organic- and LREE-rich particulates and colloidal phases.

Unfortunately in the case of the Strengbach catchment no REE water data are available for flood events. However, previous uranium isotope studies in the catchment have shown that during flood events parts of U are supplied by superficial horizons of soils, probably complexed by organic colloids or adsorbed on organic particles (Riotte and Chabaux, 1999). DOC and U contents increase significantly at the beginning of a storm event in the catchment and, particularly, the DOC behavior reflects the leaching of the upper soil layers enriched in organic matter (Soulsby, 1992, 1995; Ladouche et al., 2001). Similar to the existing Sr and U isotope data (Riotte and Chabaux, 1999; Ladouche et al., 2001; Aubert et al., 2002a,b) new Ca isotope data also suggest that chemical fluxes from the topsoil become more important with increasing discharge (Schmitt, 2003; Schmitt et al., 2003; Schmitt and Stille, 2005). This is indicated by the positive correlation between $\delta^{44}Ca$ values and discharge at the outlet of the Strengbach catchment. The high $\delta^{44}Ca$ corresponding to a high discharge rate has been explained by an enhanced contribution of soil water. Interstitial soil water is depleted in the light ^{40}Ca isotope due to biological activity in the topsoil. Plants are recognized to absorb preferentially the light ^{40}Ca isotope (Schmitt et al., 2003; Schmitt and Stille, 2005 and citations therein) leading to a ^{40}Ca depletion of soil water. All these data thus show, that important quantities of organic matter are extracted from the topsoil of the Strengbach catchment during high water events similar to the Kalix catchment. We suggest in analogy to the Kalix study of Ingri et al. (2000) that LREE-enriched small organic matter particles/colloids are exported from the Strengbach catchment during high water events preventing formation of LREE-enriched topsoil.

4.6. REE absorption by vegetation at a global scale

Until now the impact of vegetation on the distribution of dissolved REE has only been discussed at the scale of the Strengbach catchment. In the following this impact shall be considered on a geographically larger scale. At

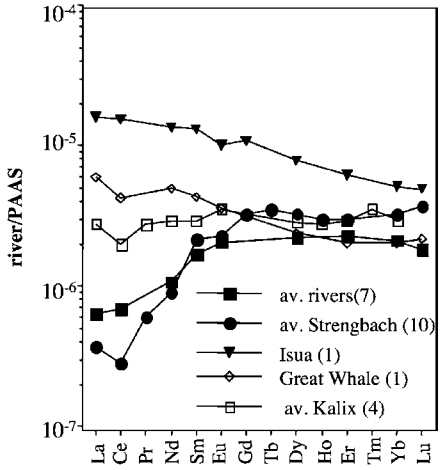

Fig. 10. PAAS normalized filtered 0.45–0.2μm river water from different climate zones. For temperate and tropical zones: average rivers [7 samples: Mississippi, Ohio, Rhine, Pampanga, Shinano, Amazon, Indus (Goldstein and Jacobsen, 1988a,b; Tricca et al., 1999)] and average Strengbach (10 samples; Tricca et al., 1999). Boreal zone: Kalix river (4 samples; filtered <0.2 μm; their PAAS normalized La_N/Yb_N ratios range between 0.5 and 2; Ingri et al., 2000). Arctic zone: Lake Isua, Great Whale (Goldstein and Jacobsen, 1988a,b).

regional scale, bedrock lithology plays only a minor role in defining the REE chemistry of river water (Elderfield et al., 1990). In Fig. 10 are shown the PAAS (post-Archean Australian shales) normalized dissolved load REE patterns of the Strengbach (average value of 10 samples) and large rivers draining temperate and tropical regions (average value of Amazon, Indus, Mississippi, Ohio, Pampanga, Shinano, Rhine) together with data from boreal and arctic zones (Kalix river in northern Sweden, Great Whale in NW Quebec and lake Isua in Eastern Greenland) (Goldstein and Jacobsen, 1988a; Tricca et al., 1999; Ingri et al., 2000). The comparison shows that the small Strengbach streamlet has REE distribution patterns very similar to those of large rivers and that rivers draining temperate or tropical regions are more depleted in LREE than rivers from boreal and arctic zones. The PAAS normalized average La_N/Yb_N ratio of the Strengbach is 0.12 whereas the ratios of the tropical and temperate rivers range between 0.12 and 0.39. The Kalix river (filtered <0.2 μm), draining a boreal region in Northern Sweden (Ingri et al., 2000), shows PAAS normalized La_N/Yb_N ratios ranging between 0.5 and 2. Even more LREE enriched are water samples from arctic regions (Goldstein and Jacobsen, 1988a), with a La_N/Yb_N of 2.9 for Great Whale and 3.1 for lake Isua.

The LREE depletion which apparently tends to disappear at higher latitudes is probably either the result of the successive disappearance of vegetation, the important sink for LREE, or of the superposition of both effects, the disappearance of vegetation and the increasing importance of colloidal phases. At this point it is impossible to distinguish between the superposing effects of organic/inorganic colloid induced LREE enrichment and the decreasing effect of LREE depletion due to the disappearance of vegetation. The only exceptions that do not follow this general trend are the Mengong river in Cameroon (Viers et al., 1997) with high DOC concentrations (25 mg/L) and the Kalix river (Ingri et al., 2000) during flood events. The Kalix river has high filtered La (<0.45 μm) and high dissolved organic carbon contents (0.7 μm) which can, as discussed in Section 4.5, be related to the presence of LREE-enriched organic colloids. $^{143}Nd/^{144}Nd$ ratios and $^{147}Sm/^{144}Nd$ ratios of the same Kalix river waters confirm the important influence of dissolved organic carbon on the REE composition of the 0.45 μm filtered water fraction (Öhlander et al., 2000; Andersson et al., 2001). These ratios are significantly lower than those of the average bedrock but show a closer resemblance with ratios found in humic and plant material.

Further studies shall help to answer these questions. Nevertheless, the Strengbach case study has shown that REE uptake by vegetation is besides apatite dissolution, complexation and lanthanide adsorption on colloids, suspended load and river ground sediments another important factor controlling the LREE fractionation in waters.

5. Summary and conclusions

Sr and Nd isotope data show that the dissolved REE of stream water mainly originate from dissolution of apatite during weathering. However, stream water REE patterns normalized to apatite are still depleted in light REE pointing to the presence of an additional LREE depleting process.

The leaching experiments performed on suspended load samples, bottom sediments of the Strengbach and on soil samples indicate that surface adsorption is one of the mechanisms responsible for the observed additional depletion of the LREE. It has also been shown that suspended load and soil particles are sites for the oxidation of Ce (III) to Ce (IV). Thus, due to adsorption processes some of the waters circulating in the soil are already additionally depleted in LREE and Ce before they enter the stream.

Vegetation might be another important factor controlling LREE depletion of river water. Vegetation samples are strongly enriched in LREE compared to surface and soil water and their Sr and Nd isotopic composition is after correction of the atmospheric contribution comparable with that of apatite and stream water. Mass balance calculations indicate that the yearly LREE uptake by vegetation is comparable with the LREE export by stream water.

The data further imply that degradation of LREE-enriched plant tissue should lead to the formation of a LREE-enriched litter layer in the topsoil. We suggest that this subsequent LREE enrichment is counterbalanced by LREE export from catchment basins together with DOC and small organic matter particles/colloids during high water events when the surface waters have a large exchange surface with vegetation and soil.

The LREE depletion is observable for nearly all large river systems. It apparently tends to disappear at higher

latitudes and is probably either the result of the successive disappearance of vegetation or due to the superposition of both effects, the disappearance of vegetation and the increasing importance of LREE-enriched colloidal phases.

Acknowledgments

We sincerely thank K. Johannessson, E. Sholkovitz and an anonymous reviewer for their constructive comments and R.H. Byrne for editorial handling. The hospitality at the branch of Isotope Geology of the University of Berne and the great help of Th. Nägler during the Nd isotope measurements on the MC-ICPMS is greatfully acknowledged. We also thank R. Boutin, J.-J. Frey, B. Kiefel and Th. Perrone of the Centre de Géochimie de la Surface at Strasbourg for their technical assistance and analytical work. This study has been financially supported by REALISE (REseau Alsace de Laboratoires en Ingénierie et Sciences pour l'Environnement) and the region of the Alsace. This is EOST contribution 2006.202-UMR7517.

Associate editor: Robert H. Byrne

References

Akagi, T., Fu, F.F., Yabuki, S., 2002. Absence of Ce anomaly in the REE patterns of peat moss and peat grass in the Ozegahara peatland. *Geochem. J.* **36**, 113–118.

Allègre, C.J., Dupré, B., Négrel, P., Gaillardet, J., 1996. Sr–Nd–Pb isotope systematics in Amazon and Congo river systems: constraints about erosion processes. *Chem. Geol.* **131**, 93–112.

Amiotte-Suchet, P., Aubert, D., Probst, J.L., Gauthier-Lafaye, F., Probst, A., Viville, D., Andreux, F., 1999. $\delta^{13}C$ pattern of dissolved inorganic carbon in a small catchment: the Strengbach case study (Vosges mountains, France). *Chem. Geol.* **159**, 129–145.

Andersson, P.S., Dahlqvist, R., Ingri, J., Gustafsson, Ö., 2001. The isotopic composition of Nd in a boreal river: a reflection of selective weathering and colloidal transport. *Geochim. Cosmochim. Acta* **65**, 521–527.

Aubert, D., 2001. Contribution de l'altération et des apports atmosphériques aux transferts de matières en milieu silicaté: traçage par le strontium et les terres rares. Cas du bassin versant du Strengbach (Vosges, France). PhD Thesis, University of Strasbourg.

Aubert, D., Stille, P., Probst, A., 2001. REE fractionation during granite weathering and removal by waters and suspended loads: Sr and Nd isotopic evidence. *Geochim. Cosmochim. Acta* **65**, 387–406.

Aubert, D., Probst, A., Stille, P., Viville, D., 2002a. Evidence of hydrological control of Sr behavior in stream water (Strengbach catchment, Vosges mountains, France. *Appl. Geochem.* **17**, 285–300.

Aubert, D., Stille, P., Probst, A., Gauthier-Lafaye, L., Pourcelot, L., DelNero, M., 2002b. Characterization and migration of atmospheric REE in soils and surface waters. *Geochim. Cosmochim. Acta* **66**, 3339–3350.

Aubert, D., Probst, A., Stille, P., 2004. Distribution and origin of major and trace elements (particularly REE, U and Th) into labile and residual phases in an acid soil profile (Vosges Mountains, France). *Appl. Geochem.* **19**, 899–916.

Wen, Bei, Yuan, Dong-an, Shan, Xiao-quan, Li, Fu-liiang, Zhang, Shuzhen, 2001. The influence of rare earth element fertilizer application on the distribution and bioaccumulation of rare earth elements in plants under field conditions. *Chem. Spec. Bioavail.* **13**, 39–48.

Blum, J.D., Erel, Y., Brown, K., 1994. $^{87}Sr/^{86}Sr$ ratios of Sierra Nevada stream waters: implications for relative mineral weathering rates. *Geochim. Cosmochim. Acta* **58**, 5019–5025.

Brookins, D.G., 1989. Aqueous geochemistry of rare earth elements. In: Lippin, B.R., McKay, G.A. (Eds.), *Reviews in Mineralogy: Geochemistry and Mineralogy of Rare Earth Elements*, vol. 21. Mineral Society of America, Washington, DC, pp. 201–223.

Byrne, R.H., Kim, K.H., 1990. Rare earth element scavenging in seawater. *Geochim. Cosmochim. Acta* **54**, 2645–2656.

Byrne, R.H., Li, B.Q., 1995. Comparative complexation behavior of rare earths. *Geochim. Cosmochim. Acta* **59**, 4575–4589.

Byrne, R.H., Sholkovitz, E.R., 1996. Marine chemistry and geochemistry of the lanthanides. In: Gschneidner, K.A., Jr.Jr., Eyring, L. (Eds.), *Handbook on the Physics and Chemistry of Rare Earth Elements*. Elsevier, Amsterdam, pp. 497–593.

Byrne, R.H., Liu, X., 1998. A coupled riverine-marine fractionation model for dissolved rare earths and yttrium. *Aquat. Geochem.* **4**, 103–121.

Chabaux, F., Riotte, J., Schmitt, A.-D., Carignan, J., Herckes, P., Pierret, M.-C., 2005. Variations of U and Sr isotope ratios in Alsace and Luxembourg rain waters: origin and hydrogeochemical implications. *CR Geosci.* **337** (16), 1447–1456.

Dupré, B., Gaillardet, J., Rousseau, D., Allègre, C.J., 1996. Major and trace elements of river-borne material: The Congo basin. *Geochim. Cosmochim. Acta* **60** (8), 1301–1321.

Elderfield, H., Upstill-Goddard, R., Sholkovitz, E.R., 1990. The rare earth elements in rivers, estuaries, and coastal seas and their significance to the composition of ocean waters. *Geochim. Cosmochim. Acta* **54**, 971–991.

El Gh'Mari, A., 1995. Etude minéralogique, pétrophysique et géochimique de la dynamique d'altération d'un granite soumis au dépôts atmosphériques acides (Bassin versant du Strengbach, Vosges, France) mécanismes, bilans et modélisations. PhD Thesis, ULP Strasbourg, 202 p.

Fichter, J., Turpault, M.P., Dambrine, E., Ranger, J., 1998. Mineral evolution of acid forest soils in the Strengbach catchment (Vosges mountains, N-E France). *Geoderma* **82**, 315–340.

Gaillardet, J., Dupré, B., Allègre, C.J., 1995. A global geochemical mass budget applied to the Congo basin rivers: erosion rates and continental crust composition. *Geochim. Cosmochim. Acta* **59**, 3469–3485.

Gaillardet, J., Dupré, B., Allègre, C.J., Négrel, P., 1997. Chemical and physical denudation in the Amazon river basin. *Chem. Geol.* **142**, 141–173.

Goldstein, S.L., O'Nions, R.K., Hamilton, P.J., 1984. A Sm–Nd isotopic study of atmospheric dusts and particulates from major river systems. *Earth Planet. Sci. Lett.* **70**, 221–236.

Goldstein, S.J., Jacobsen, S.B., 1987. The Nd and Sr isotopic systematics of river-water dissolved material: Implications for the sources of Nd and Sr in seawater. *Chem. Geol.* **66**, 245–272.

Goldstein, S.J., Jacobsen, S.B., 1988a. Rare earth elements in river waters. *Earth Planet. Sci. Lett.* **89**, 35–47.

Goldstein, S.J., Jacobsen, S.B., 1988b. Nd and Sr isotopic systematics of river water suspended material: implications for crsutal evolution. *Earth Planet. Sci. Lett.* **87**, 249–265.

Idir, S., Probst, A., Viville, D., Probst, J.L., 1999. Contribution des surfaces saturées et des versants aux flux d'eau et d'éléments exportés en période de crue: Traçage à l'aide du carbone organique dissous et de la silice. Cas du petit bassin versant du Strengbach (Vosges, France). *CR Acad. Sci.* **328**, 101–106.

Ingri, J., Widerlund, A., Land, M., Gustafsson, Ö., Andersson, P., Öhlander, B., 2000. Temporal variations in the fractionation of the rare earth elements in a boreal river; the role of colloidal particles. *Chem. Geol.* **166**, 23–45.

Johannesson, K.H., Tang, J., Daniels, J.M., Bounds, W.J., Burdige, D.J., 2004. Rare earth element concentrations and speciation in organic-rich blackwaters of the Great Dismal Swamp, Virginia, USA. *Chem. Geol.* **209**, 271–294.

Krachler, M., Mohl, C., Emons, H., Shotyk, W., 2003. Two thousand years of atmospheric rare earth element (REE) deposition as revealed by an ombrotrophic peat bog profile, Jura Mountains, Switzerland. *J. Environ. Monit.* **5**, 111–121.

Ladouche, B., Probst, A., Viville, D., Idir, S., Baqué, D., Loubet, M., Probst, J.-L., Bariac, T., 2001. Hydrograph separation using isotopic, chemical and hydrological approaches (Strengbach catchment, France). *J. Hydrol.* **242**, 255–274.

Li, Fuliang, Shan, Xiaoquan, Zhang, Tianhong, Zhang, Shuzhen, 1998. Evaluation of plant availability of rare earth elements in soils by chemical fractionation and multiple regression analysis. *Environ. Poll.* **102**, 269–277.

Lu, P., Biron, P., Breda, N., Granier, A., 1995. Water relations of adult Norway spruce (*Picea abies* (L) Karst) under soil drought in the Vosges mountains: water potential, stomatal conductance and transpiration. *Ann. Sci. For.* **52**, 117–129.

Martin, J.M., Meybeck, M., 1979. Element mass-balance of material carried by major world rivers. *Mar. Chem.* **7**, 173–206.

Meybeck, M., 1987. Global chemical weathering from surficial rocks estimated from river dissolved loads. *Am. J. Sci.* **287**, 401–428.

Négrel, P., Allègre, C.J., Dupré, B., Lewin, E., 1993. Erosion sources determined by inversion of major and trace element ratios in river water: The Congo basin case. *Earth Planet. Sci. Lett.* **120**, 59–76.

Öhlander, B., Ingri, J., Land, M., Schöberg, H., 2000. Change of Sm–Nd isotope composition during weathering of till. *Geochim. Cosmochim. Acta* **64**, 813–820.

Ozaki, T., Enomoto, S., 2001. Uptake of rare earth elements by *Dryopteris erythrosora* (autumn fern). *Focused New Trends Bio-Trace Elem. Res.* **35**, 84–87.

Prevosto, B., 1988. Flux des éléments minéraux dans un ecosystème forestier déperissant. Impact de la pollution atmosphérique acide; Mémoire de 3ème année. INRA, Champenoux-54280 Seichamps.

Probst, A., Dambrine, E., Viville, D., Fritz, B., 1990. Influence of acid atmospheric inputs on surface water chemistry and mineral fluxes in a declining spruce stand within a small granitic catchment (Vosges massif, France). *J. Hydrol.* **116**, 101–124.

Probst, A., Fritz, B., Viville, D., 1995. Mid-term trends in acid precipitation, streamwater chemistry and element budgets in the Strengbach catchment (Vosges mountains, France). *Water Air Soil Pollut.* **79**, 39–59.

Probst, A., Viville, D., 1999. Bilan hydrogéochimique du petit bassin versant forestier du Strengbach à Aubure (Haut Rhin). In: *Rapport scientifique activités de recherche, 7e réunion du conseil de direction scientifique*, Ifare/DFIU, 66–72.

Riotte, J., Chabaux, F., 1999. ($^{243}U/^{238}U$) activity ratios in freshwaters as tracers of hydrological processes: the Strengbach watershed, Vosges, France. *Geochim. Cosmochim. Acta* **63**, 1263–1275.

Rossbach, M., Jayasekera, R., Kniewald, G., Nguyen, Huu Thang, 1999. Large scale air monitoring: lichen vs. air particulate matter analysis. *Sci. Tot. Env.* **232**, 59–66.

Scarascia-Mugnozza, G., Bauer, G.A., Persson, H., Mattaeucci, G., Masci, A., 2000. Tree biomass, growth and nutrient pools. In: Schulze, E.-D. (Ed.), *Carbon and Nitrogen Cycling in European Forest Ecosystems*. Springer, New York, pp. 49–62.

Schmitt, A.-D., 2003. Les isotopes du calcium: développements analytiques-applications au bilan océanique présent et passé. Ph. D. Thesis, University of Strasbourg.

Schmitt, A.-D., Chabaux, F., Stille, P., 2003. The calcium riverine and hydrothermal isotopic fluxes and the oceanic calcium mass balance. *Earth Planet. Sci. Lett.* **213**, 503–518.

Schmitt, A.-D., Stille, P., 2005. The source of calcium in wet atmospheric deposits: Ca–Sr isotope evidence. *Geochim. Cosmochim. Acta* **69**, 3463–3468.

Shabani, M.B., Masuda, A., 1991. Sample introduction by on-line two-stage solvent extraction and back-extraction to eliminate matrix interference and to enhance sensitivity in the determination of rare earth elements with inductively coupled plasma spectrometry. *Anal. Chem.* **63**, 2099–2105.

Sholkovitz, E.R., 1992. Chemical evolution of rare earth elements: fractionation between colloidal and solution phases of filtered river water. *Earth Planet. Sci. Lett.* **114**, 77–84.

Sholkovitz, E.R., 1993. The geochemistry of rare earth elements in the Amazon river estuary. *Geochim. Cosmochim. Acta* **57**, 2181–2190.

Sholkovitz, E.R., Landing, W.M., Lewis, B.L., 1994. Ocean particle chemistry: the fractionation of rare earth elements between suspended particles and seawater. *Geochim. Cosmochim. Acta* **58**, 1567–1579.

Sholkovitz, E.R., 1995. The aquatic chemistry of rare earth elements in rivers and estuaries. *Aquat. Geochem.* **1**, 1–34.

Soulsby, C., 1992. Hydrological controls on acid runoff generation in an forested headwater catchment at Llyn Brianne, Mid-Wales. *J. Hydrol.* **138**, 431–448.

Soulsby, C., 1995. Contrasts in storm event hydrochemistry in an acidic afforested catchment in Upland Wales. *J. Hydrol.* **170**, 159–179.

Stallard, R.F., Edmond, J.M., 1983. Geochemistry of the Amazon 2. The influence of geology and weathering environment on the dissolved load. *J. Geophys. Res.* **88**, 9671–9688.

Steinmann, M., Stille, P., 1997. Rare earth element behavior and Pb, Sr, Nd isotope systematics in a heavy metal contaminated soil. *Appl. Geochem.* **12**, 607–624.

Stille, P., Clauer, N., 1994. The process of glauconitization: chemical and isotopic evidence. *Contrib. Mineral. Petrol.* **117**, 253–262.

Stille, P., Gauthier-Lafaye, F., Jensen, K.A., Salah, S., Bracke, G., Ewing, R.C., Louvat, D., Million, D., 2003. REE mobility in groundwater proximate to the natural fission reactor at Bangombé (Gabon). *Chem. Geol.* **198**, 289–304.

Stordal, M.C., Wasserburg, G.J., 1986. Neodymium isotopic study of Baffin Bay water: sources of REE from very old terranes. *Earth Planet. Sci. Lett.* **77**, 259–272.

Sun, H., Wang, X., Wang, Q., Wang, H., Chen, Y., Dai, L.C., 1999. The effects of chemical species on bioaccumulation of rare earth elements in rice grown in nutrient solution. *Toxicol. Environ. Chem.* **69**, 75–85.

Tricca, A., 1997. Transport mechanism of trace elements in surface and groundwater: Sr, Nd, U isotope and REE evidence. PhD Thesis, University of Strasbourg.

Tricca, A., Stille, P., Steinmann, M., Kiefel, B., Samuel, J., Eikenberg, J., 1999. Rare earth elements and Sr and Nd isotopic compositions of dissolved and suspended loads from small river systems in the Vosges mountains (France), the river Rhine and the groundwater. *Chem. Geol.* **160**, 139–158.

Viers, J., Dupré, B., Polvé, M., Schott, J., Dandurand, J.-L., Braun, J.-J., 1997. Chemical weathering in the drainage basin of a tropical watershed (Nsimi-Zoétélé site, Cameroon): comparison between organic-poor and organic-rich waters. *Chem. Geol.* **140**, 181–206.

Viville, D., Biron, P., Granier, A., Dambrine, E., Probst, A., 1993. Interception in a mountainous declining spruce stand in the Strengbach catchment (Vosges, France). *J. Hydrol.* **144**, 273–282.

Wallander, H.k., Wickman, T., Jacks, G., 1997. Apatite as a P source in mycorrhizal and non-mycorrhizal *Pinus sylvestris* seedlings. *Plant Soil* **196** (1), 123–131.

Yang, L., Wang, X., Sun, H., Zhang, H., 1999. The effect of EDTA on rare earth elements bioavailability in soil ecosystem. *Chemosphere* **38**, 2825–2833.

Zeng, F., Tian, H.E., Wang, Z., An, Y., Gao, F., Zhang, L., Li, F., Shan, L., 2003. Effect of rare earth element europium on amaranthin synthesis in *Amarathus caudatus* seedlings. *Biol. Trace Elem. Res.* **93**, 271–282.

Zhang, Z.Y., Wang, Y.Q., Li, F.L., Xiao, H.Q., Chai, Z.F., 2002. Distribution characteristics of rare earth elements in plants from a rare earth ore area. *J. Radioanal. Nucl. Chem.* **252**, 461–465.

Zhimang, G., Xiaorong, W., Jing, C., Liansheng, W., Lemei, D., 2000. Effects of sulfate on speciation and bioavailability of rare earth elements in nutrient solution. *Chem. Spec. Bioavailab.* **12**, 53–58.